

AFRL-SR-BL-TR-98-

sources, gathering  
of this collection of  
ivis Highway. Suite

077

**Reproduced From  
Best Available Copy**

UNITED STATES AIR FORCE  
SUMMER RESEARCH PROGRAM -- 1993  
SUMMER RESEARCH EXTENSION PROGRAM FINAL REPORTS

VOLUME 2

PHILLIPS LABORATORY

RESEARCH & DEVELOPMENT LABORATORIES

5800 Uplander Way  
Culver City, CA 90230-6608

Program Director, RDL  
Gary Moore

Program Manager, AFOSR  
Major David Hart

Program Manager, RDL  
Scott Licoscas

Program Administrator, RDL  
Gwendolyn Smith

Program Administrator  
Johnetta Thompson

Submitted to:

AIR FORCE OFFICE OF SCIENTIFIC RESEARCH

Bolling Air Force Base

Washington, D.C.

November 1994

DTIC QUALITY INSPECTED 3

19981211 022

## **PREFACE**

This volume is part of a five-volume set that summarizes the research of participants in the 1993 AFOSR Summer Research Extension Program (SREP). The current volume, Volume 2 of 5, presents the final reports of SREP participants at Phillips Laboratory.

Reports presented in this volume are arranged alphabetically by author and are numbered consecutively -- e.g., 1-1, 1-2, 1-3; 2-1, 2-2, 2-3, with each series of reports preceded by a 35 page management summary. Reports in the five-volume set are organized as follows:

<b>VOLUME</b>	<b>TITLE</b>
1A	Armstrong Laboratory (part one)
1B	Armstrong Laboratory (part two)
2	Phillips Laboratory
3	Rome Laboratory
4A	Wright Laboratory (part one)
4B	Wright Laboratory (part two)
5	Arnold Engineering Development Center Frank J. Seiler Research Laboratory Wilford Hall Medical Center

# 1993 SREP FINAL REPORTS

## Armstrong Laboratory

### VOLUME 1A

<b>Report #</b>	<b>Report Title Author's University</b>	<b>Report Author</b>
1	Three-Dimensional Calculation of Blood Flow in a Thick -Walled Vessel Using the University of Missouri, Rolla, MO	Dr. Xavier Avula Mechanical & Aerospace AL/AO Engineering
2	A Study of the Contrast Detection Modeling for Human Eye and its Application to Wright State University, Dayton, OH	Dr. Jer-sen Chen Computer Science & AL/CF Engineering
3	An Approach to On-Line Assessment and Diagnosis of Student Troubleshooting Knowl New Mexico State University, Las Cruces, NM	Dr. Nancy Cooke Psychology AL/HR
4	An Experimental Investigation of Hand Torque Strength for Tightening Small Fast Tennessee Technological University, Cookeville, TN	Dr. Subramaniam Deivanayagam Industrial Engineering AL/HR
5	Determination of Total Peripheral Resistance, Arterial Compliance and Venous Com North Dakota State University, Fargo, ND	Dr. Dan Ewert Electrical Engineering AL/AO
6	A Computational Thermal Model and Theoretical Thermodynamic Model of Laser Induc Florida International University, Miami, FL	Dr. Bernard Gerstman Physics AL/OE
7	A Comparison of Various Estimators of Half-Life in the Air Force Health Study University of Maine, Orono, ME	Dr. Pushpa Gupta Mathematics AL/AO
8	The Effects of Exogenous Melatonin on Fatigue, Performance and Daytime Sleep Bowling Green State University, Bowling Green, OH	Mr. Rod Hughes Psychology AL/CF
9	A New Protocol for Studying Carotid Baroreceptor Function  Georgia Institute of Technology, Atlanta, GA	Dr. Arthur Koblasz Civil Engineering AL/AO
10	Adaptive Control Architecture for Teleoperated Freflex System  Purdue University, West Lafayette, IN	Dr. A. Koivo Electrical Engineering AL/CF
11	A New Construct for Interpreting the Fundamental Dilemma of Insufficient Tissue University of Tennessee, Memphis, TN	Dr. Robert Kundich Biomedical Engineering AL/CF
12	An Empirical Test of a Method for Comparison of Alternative Multiship Aircraft Arizona State University, Tempe, AZ	Dr. William Moor Industrial & Management AL/HR Engineering
13	Remote Monitoring and Reduction of Emotionality in Air Force Laboratory Primates University of Georgia Research, Athens, GA	Dr. B. Mulligan Psychology AL/OE



# 1993 SREP FINAL REPORTS

## Armstrong Laboratory

### VOLUME 1B

Report #	Report Title Author's University	Report Author
14	Simulation of the Motion of Single and Linked Ellipsoids Representing Human Body Wright State University, Dayton, OH	Dr. David Reynolds Biomedical & Human AL/CF Factors
15	Bioeffects of Microwave Radiation on Mammalian Cells and Cell Cultures Xavier University of Louisiana, New Orleans, LA	Dr. Donald Robinson Chemistry AL/OE
16	Analysis of Isocyanate Monomers and Oligomers in Spray Paint Formulations Southwest Texas State University, San Marcos, TX	Dr. Walter Rudzinski Chemistry AL/OE
17	Development of the "Next Generation" of the Activities Interest Inventory for Se Wayne State University, Detroit, MI	Dr. Lois Tetrick Industrial Relations Prog AL/HR
18	Investigations on the Seasonal Bionomics of the Asian Tiger Mosquito, Aedes Albo Macon College, Macon, GA	Dr. Michael Womack Natural Science and AL/OE Mathematics
19	Difficulty Facets Underlying Cognitive Ability Test Items  Ohio State University, Columbus, OH	Dr. Mary Roznowski Psychology AL/HR
20	A Simplified Model for Predicting Jet Impingement Heat Transfer North Carolina A & T State University, Greensboro, NC	Mr. Mark Kitchart Mechanical Engineering AL/EQ
21	Geostatistical Techniques for Understanding Hydraulic Conductivity Variability Washington State University, Pullman, WA	Dr. Valipuram Manoranjan Pure and Applied AL/EQ Mathematics
22	An Immobilized Cell Fluidized Bed Bioreactor for 2,4-Dinitrotoluene Degradation Colorado State University, Fort Collins, CO	Dr. Kenneth Reardon Agricultural and Chemical AL/EQ Engineering
23	Applications of Superconductive Devices in Air Force  Alfred University, Alfred, NY	Dr. Xingwu Wang Electrical Engineering AL/EQ

# 1993 SREP FINAL REPORTS

## Phillips Laboratory

### VOLUME 2

Report #	Report Title Author's University	Report Author
1	Optimal Passive Damping of a Complex Strut-Built Structure Iowa State University, Ames, IA	Dr. Joseph Baumgarten Mechanical Engineering PL/VT
2	Theoretical and Experimental Studies on the Effects of Low-Energy X-Rays on Elec University of Arizona, Tucson, AZ	Dr. Raymond Bellem Electrical & Computer Engineering PL/VT
3	Ultrawideband Antennas with Low Dispersion for Impulse Radars University of Alabama, Huntsville, AL	Dr. Albert Biggs Electrical Engineering PL/WS
4	Experimental Neutron Scattering Investigations of Liquid-Crystal Polymers Arkansas Technology University, Russellville, AR	Dr. David Elliott Engineering PL/RK
5	High Temperature Spectroscopy of Alkali Metal Vapors for Solar to Thermal Energy University of Iowa, Iowa City, IA	Mr. Paul Erdman Physics and Astronomy PL/RK
6	A Detailed Investigation of Low-and High-Power Arcjet Plume Velocity Profiles Us University of Southern California, Los Angeles, CA	Dr. Daniel Erwin Aerospace Engineering PL/RK
7	Measurements of Ion-Molecule Reactions at High Temperatures University of Puerto Rico, Mayaguez, PR	Dr. Jeffrey Friedman Physics PL/GP
8	Final Design and Construction of Lidar Receiver for the Starfire Optical Range Georgia Institute of Technology, Atlanta, GA	Dr. Gary Gimmestad Research Institute PL/LI
9	Dynamics of Gas-Phase Ion-Molecule Reactions Carnegie Mellon University, Pittsburgh, PA	Dr. Susan Graul Chemistry PL/WS
10	A Numerical Approach to Evaluating Phase Change Material Performance in Infrared University of Texas, San Antonio, TX	Mr. Steven Griffin Engineering PL/VT
11	An Analysis of ISAR Imaging and Image Simulation Technologies and Related Post University of Nevada, Reno, NV	Dr. James Henson Electrical Engineering PL/WS
12	Optical and Clear Air Turbulence Worcester Polytechnic Institut, Worcester, MA	Dr. Mayer Humi Mathematics PL/LI
13	Rotational Dynamics of Lageos Satellite North Carolina State University, Raleigh, NC	Dr. Arkady Kheyfets Mathematics PL/LI
14	Study of Instabilities Excited by Powerful HF Waves for Efficient Generation of Polytechnic University, Farmingdale, NY	Dr. Spencer Kuo Electrical Engineering PL/GP

# 1993 SREP FINAL REPORTS

## Phillips Laboratory

### VOLUME 2

cont'd

Report #	Report Title Author's University	Report Author
15	Particle Stimulation of Plasmas University of Missouri, Kansas City, MO	Dr. Richard Murphy Physics PL/WS
16	A Universal Equation of State for Shock in Homogeneous Materials California State University, Northridge, CA	Dr. Jon Shively Engineering & Computer Science PL/VT
17	Speed-Up of the Phase Diversity Method Via Reduced Region & Optimization Dimen. University of Houston, Victoria, TX	Dr. Johanna Stenzel Arts & Sciences PL/LI
18	Analysis of Solwind P-78 Fragmentation Using Empirical And Analytical Codes Alabama A & M University, Normal, AL	Dr. Arjun Tan Physics PL/WS
19	Experimental Investigations of Homogeneous and Heterogeneous Nucleation/Condensa University of Missouri, Rolla, MO	Dr. Philip Whitefield Physics PL/LI

# 1993 SREP FINAL REPORTS

## Rome Laboratory

### VOLUME 3

Report #	Report Title Author's University	Report Author
1	Analysis and Code for Treating Infinite Arrays of Tapered Antennas Printed on Bo California State University, Sacramento, CA	Dr. Jean-Pierre Bayard Electrical & Electronic RL/ER Engineering
2	Comparing Pattern Recognition Systems Syracuse University, Syracuse, NY	Dr. Pinyuen Chen Mathematics RL/IR
3	Wideband ATM Networks for the Dynamic Theater Environment University of Southwestern Louisiana, Lafayette, LA	Dr. Robert Henry Electrical & Computer RL/C3 Engineering
4	Congestion Control For ATM Network in a Tectical Theater Environment Polytechnic University, Brooklyn, NY	Mr. Benjamin Hoe Electrical Engineering RL/C3
5	Automated Natural Language Evaluators (ANLF) Southwest Texas State College, San Marcos, TX	Dr. Khosrow Kaikhah Computer Science RL/IR
6	System Analysis and Applications for a Photonic Delay Line Le Moyne College, Syracuse, NY	Dr. Evelyn Monsay Physics RL/OC
7	An Exploratory Investigaton of Multimedia Data Reinforcement for Large-Scale Inf Syracuse University, Syracuse, NY	Dr. Michael Nilan Information Studies RL/C3
8	Supporting Systematic Testing for Reusable Software Components University of Alabama, Tuscaloosa, AL	Dr. Allen Parrish Computer Science RL/C3
9	Use of Turnable Fiber Ring Lasers in Optical Communications SUNY/Institute of Technology, Utica, NY	Dr Salahuddin Qazi Optical Communications RL/OC
10	Further Monte Carlo Studies of a Theoretical Model for Non-Gaussian Radar Clutte SUNY College at Cortland, Cortland, NY	Dr. Jorge Romeu Assistant Prof. of RL/OC Mathematics
11	Hierarchical Modeling and Simulation Syracuse University, Syracuse, NY	Dr. Robert Sargent Engineering and Computer RL/XP Science
12	Metamodel Applications Using TAC Brawler Virginia Polytechnic Institute, Blacksburg, VA	Dr. Jeffery Tew Industrial & Systems RL/IR Engineering
13	Automatic Detection of Prominence in Spontaneous Speech New Mexico Institute of Mining, Socorro, NM	Dr. Colin Wightman Electrical Engineering RL/IR

# 1993 SREP FINAL REPORTS

## Wright Laboratory

### VOLUME 4A

Report #	Report Title Author's University	Report Author
1	Integrated Estimator/Guidance/Autopilot for Homing Missiles University of Missouri, Rolla, MO	Dr. S. Balakrishnan Mechanical & Aerospace WL/MN Engineering
2	Studies of NTO Decomposition Memphis State University, Memphis, TN	Dr. Theodore Burkey Chemistry WL/MN
3	Investigation of Ray-Beam Basis Functions for Use with the Generalized Ray Expan Ohio State University, Columbus, OH	Dr. Robert Burkholder Electrical Engineering WL/AA
4	Wave Mechanics Modeling of Terminal Ballistics Phenomenology Louisiana Tech University, Ruston, LA	Dr. Eugene Callens, Jr. Mechanical and Industrial WL/MN Engineer
5	Modeling for Aeroelastic Parameter Estimation of Flexing Slender Bodies in a Bal University of California, Berkeley, CA	Dr. Gary Chapman Mechanical Engineering WL/MN
6	Using VHDL in VSL Bist Design Synthesis and its Application to 3-D Pixel Graphic Wright State University, Dayton, OH	Dr. Chien-In Chen Electrical Engineering WL/EL
7	Study of Part Quality and Shrinkage for Injection Molded Aircraft Transparencies Florida International University, Miami, FL	Dr. Joe Chow Industrial and Systems WL/FI Engineering
8	Implementation of Noise-Reducing Multiple-Source Schlieren Systems Purdue University, West Lafayette, IN	Dr. Steven Collicott Aeronautics and WL/FI Astronautical Engineering
9	Performing Target Classification Using Fussy Morphology Neural Networks Iowa State University, Ames, IA	Dr. Jennifer Davidson Electrical Engineering WL/MN
10	Turbulent Heat Transfer In Counter-Rotating Disk System University of Dayton, Dayton, OH	Dr. Jamie Ervin Mechanical and Aerospace WL/ML Engineering
11	Modelling of Biomaterials for Non-Linear Optical Applications University of Virginia, Charlottesville, VA	Dr. Barry Farmer Materials Science and WL/ML Engineering
12	Passive Ranging, Roll-angle Approximation, and Target Recognition for Fuze Appli Florida State University, Tallahassee, FL	Dr. Simon Foo Electrical Engineering WL/MN
13	A Role of Oxygen and Sulfur Compounds in Jet Fuel Deposit Formation Eastern Kentucky University, Richmond, KY	Ms. Ann Gillman Chemistry WL/PO
14	Effect of Aeroelasticity on Experimental Nonlinear Indicial Responses Measured Ohio University, Athens, OH	Dr. Gary Graham Mechanical Engineering WL/FI

## Wright Laboratory

VOLUME 4A  
cont'd

<b>Report #</b>	<b>Report Title Author's University</b>	<b>Report Author</b>
15	<b>Virtual Reality Information Presentation Technology for Avionics New Mexico Highlands University, Las Vegas, NM</b>	<b>Dr. Elmer Grubbs Electrical Engineering WL/AA</b>
16	<b>An Investigation of the Thermal Stability of an AlC/Ti-22Al-23Nb Metal Matrix Co University of Delaware, Newark, DE</b>	<b>Dr. Ian Hall Materials Science WL/ML</b>
17	<b>Investigation of the Combustion Characteristics of Confined Coannular Jets with Brigham Young University, Provo, UT</b>	<b>Dr. Paul Hedman Chemical Engineering WL/PO</b>
18	<b>Morphology of High-Velocity Perforation of Laminated Plates University of New Orleans, New Orleans, LA</b>	<b>Dr. David Hui Mechanical Engineering WL/FI</b>

# 1993 SREP FINAL REPORTS

## Wright Laboratory

### VOLUME 4B

Report #	Report Title Author's University	Report Author
19	Evaluation of Variable Structure Control for Missile Autopilots Using Reaction Auburn University, Auburn, AL	Dr. Mario Innocenti Aerospace Engineering WL/MN
20	Laser Imaging and Ranging (LIMAR) Processing  Wright State University, Dayton, OH	Dr. Jack Jean Computer Science & WL/AA Engineering
21	Applications of Wavelet Subband Decomposition in Adaptive Arrays Lafayette College, Easton, PA	Dr. Ismail Jouny Electrical Engineering WL/AA
22	Micromechanics of Matrix Cracks In Brittle Matrix Composites With Frictional Int University of South Florida, Tampa, FL	Dr. Autar Kaw Mechanical Engineering WL/ML
23	A Physics-Based Heterojunction Bipolar Transistor Model Including High-Current, Universtiy of Central Florida, Orlando, FL	Dr. Juin Liou Electrical and Computer WL/EL Engineering
24	Electrical and Thermal Modeling of Switched Reluctance Machines San Francisco State Univesity, San Francisco, CA	Dr. Shy-Shenq Liou Engineering WL/PO
25	Process Migration Facility for the quest Distributed VHDL Simulator University of Cincinnati M.L., Cincinnati, OH	Mr. Dallas Marks Electrical and Computer WL/AA Engineering
26	Investigation of Third Order Non-Linear Optical Properties of Strained Layer Sem Columbia University, New York, NY	Dr. Mary Potasek Applied Physics WL/ML
27	Development of Control Design Methodologies for Flexible Systems with Multiple Arizona State University, Tempe, AZ	Dr. Armando Rodriguez Electrical Engineering WL/MN
28	Enhanced Liquid Fuel Atomization Through Effervescent Injection Virginia Polytechnic Inst & State Coll., Blacksburg, VA	Dr Larry Roe Mechanical Engineering WL/PO
29	Sensor Fusion for IR/MMW Dual-Mode Sensors Using Artificial Neural Networks Auburn University, Auburn, AL	Dr. Thaddeus Roppel Electrical Engineering WL/MN
30	Characterizing the Solid Fragment Population in a Debris Cloud Created by a Hype University of Alabama, Huntsville, AL	Dr. William Schonberg Civil and Environmental WL/MN Engineering
31	Digital Signal Processing Algorithms for Digital EW Receivers  Wright State University, Dayton, OH	Dr. Arnab Shaw Electrical Engineering WL/AA
32	An Analytical Model of Laminated Composite Plates for Determination of Stresses University of Cincinnati, Cincinnati, OH	Mr. Robert Slater Mechanical & Industrial WL/FI Engineering

# 1993 SREP FINAL REPORTS

## Wright Laboratory

### VOLUME 4B

cont'd

<b>Report #</b>	<b>Report Title Author's University</b>	<b>Report Author</b>
33	Detection of Internal Defects in Multilayered Plates By Lamb Wave Acoustic Micro Universtiy of Arizona, Tucson, AZ	Dr. Kundu Tribikram Civil Engineering and WL/ML Engineering
34	Wavelet Analysis of Ultrasonic Signals for Non-Destructive Evaluation of Composi University of Dayton, Dayton, OH	Dr. Theresa Tuthill Electrical Engineering WL/ML
35	Stochastic Modeling of MBE Growth of Compoud Semiconductors University of Nevada, Las Vegas, NV	Dr. Ramasubrama Venkatasubraman Electrical and Computer WL/ML Engineering
36	Performance Evaluation And Improvement of a Resonant DC Link Inverter With A Lim North Dakota State University, Fargo, ND	Dr. Subbaraya Yuvarajan Electrical Engineering WL/PO
37	Three Component LDV Measurements in a Swirl Combustor  North Carolina State University, Raleigh, NC	Dr. Richard Gould Mechanical and Aerospace WL/PO Engineering



# 1993 SREP FINAL REPORTS

## VOLUME 5

Report #	Report Title Author's University	Report Author
<b>Arnold Engineering Development Center</b>		
1	<b>Performance Enhancement for a TI TMS320C40 version of Multigraph</b> Vanderbilt University, Nashville, TN	<b>Mr. Ben Abbott</b> Electrical Engineering AEDC/
2	<b>System Integration Software for Parallel Hardware Architectures</b> Vanderbilt University, Nashville, TN	<b>Dr. Csaba Biegl</b> Electrical Engineering AEDC/
3	<b>Heat Load Structural Failure Prediction for the AEDC Heat-Hi Test Unit Nozzle</b> Georgia Institute of Technology, Atlanta, GA	<b>Dr. Kurt Gramoll</b> Aerospace Engineering AEDC/
4	<b>Coupling of an Inductive Generator with Plasma Erosion Opening Switch (PEOS) to</b> Morehouse College, Atlanta, GA	<b>Dr. Carlyle Moore</b> Physics AEDC/
<b>Frank J Seiler Research Laboratory</b>		
5	<b>Active and Passive Control Designs for the FJSRL Flexible Structure Testbeds</b> Old Dominion University, Norfolk, VA	<b>Dr. Thomas Alberts</b> Mechanical Engineering FJSRL/
6	<b>Three Dimensional Characterization of Non-Linear Optical Thin Films</b> University of Colorado, Colorado Springs, CO	<b>Dr. Thomas Christensen</b> Physics FJSRL/
7	<b>Electrochemistry of Lithium in Room Temperature Molten Salt Electrolytes</b> Houghton College, Houghton, NY	<b>Dr. Bernard Piersma</b> Chemistry FJSRL/
<b>Wilford Hall Medical Center</b>		
8	<b>Enhanced Physiologic Monitoring of Patients with Closed Head-Injury</b> Memphis State, Memphis, TN	<b>Dr. Michael Daley</b> Electrical Engineering WHMC/
9	<b>Rheological, Biochemical and Biophysical Studies of Blood at Elevated Temperatures</b> University of Miami, Coral Gables, FL	<b>Dr. Walter Drost-Hansen</b> Chemistry WHMC

# **1993 SUMMER RESEARCH EXTENSION PROGRAM (SREP) MANAGEMENT REPORT**

## **1.0 BACKGROUND**

Under the provisions of Air Force Office of Scientific Research (AFOSR) contract F49620-90-C-0076, September 1990, Research & Development Laboratories (RDL), an 8(a) contractor in Culver City, CA, manages AFOSR's Summer Research Program. This report is issued in partial fulfillment of that contract (CLIN 0003AC).

The Summer Research Extension Program (SREP) is one of four programs AFOSR manages under the Summer Research Program. The Summer Faculty Research Program (SFRP) and the Graduate Student Research Program (GSRP) place college-level research associates in Air Force research laboratories around the United States for 8 to 12 weeks of research with Air Force scientists. The High School Apprenticeship Program (HSAP) is the fourth element of the Summer Research Program, allowing promising mathematics and science students to spend two months of their summer vacations working at Air Force laboratories within commuting distance from their homes.

SFRP associates and exceptional GSRP associates are encouraged, at the end of their summer tours, to write proposals to extend their summer research during the following calendar year at their home institutions. AFOSR provides funds adequate to pay for 75 SREP subcontracts. In addition, AFOSR has traditionally provided further funding, when available, to pay for additional SREP proposals, including those submitted by associates from Historically Black Colleges and Universities (HBCUs) and Minority Institutions (MIs). Finally, laboratories may transfer internal funds to AFOSR to fund additional SREPs. Ultimately the laboratories inform RDL of their SREP choices, RDL gets AFOSR approval, and RDL forwards a subcontract to the institution where the SREP associate is employed. The subcontract (see Appendix 1 for a sample) cites the SREP associate as the principal investigator and requires submission of a report at the end of the subcontract period.

Institutions are encouraged to share costs of the SREP research, and many do so. The most common cost-sharing arrangement is reduction in the overhead, fringes, or administrative charges institutions would normally add on to the principal investigator's or research associate's labor. Some institutions also provide other support (e.g., computer run time, administrative assistance, facilities and equipment or research assistants) at reduced or no cost.

When RDL receives the signed subcontract, we fund the effort initially by providing 90% of the subcontract amount to the institution (normally \$18,000 for a \$20,000 SREP). When we receive the end-of-research report, we evaluate it administratively and send a copy to the laboratory for a technical evaluation. When the laboratory notifies us the SREP report is acceptable, we release the remaining funds to the institution.

## 2.0 THE 1993 SREP PROGRAM

**SELECTION DATA:** A total of 719 faculty members (SFRP Associates) and 286 graduate students (GSRP associates) applied to participate in the 1992 Summer Research Program. From these applicants 185 SFRPs and 121 GSRPs were selected. The education level of those selected was as follows:

1992 SRP Associates, by Degree			
SFRP		GSRP	
PHD	MS	MS	BS
179	6	52	69

Of the participants in the 1992 Summer Research Program 90 percent of SFRPs and 25 percent of GSRPs submitted proposals for the SREP. Ninety proposals from SFRPs and ten from GSRPs were selected for funding, which equates to a selection rate of 54 % of the SFRP proposals and of 34 % for GSRP proposals.

1993 SREP: Proposals Submitted vs. Proposals Selected			
	Summer 1992 Participants	Submitted SREP Proposals	SREPs Funded
SFRP	185	167	90
GSRP	121	29	10
TOTAL	306	196	100

The funding was provided as follows:

Contractual slots funded by AFOSR	75
Laboratory funded	14
Additional funding from AFOSR	<u>11</u>
Total	100

Six HBCU/MI associates from the 1992 summer program submitted SREP proposals; six were selected (none were lab-funded; all were funded by additional AFOSR funds).

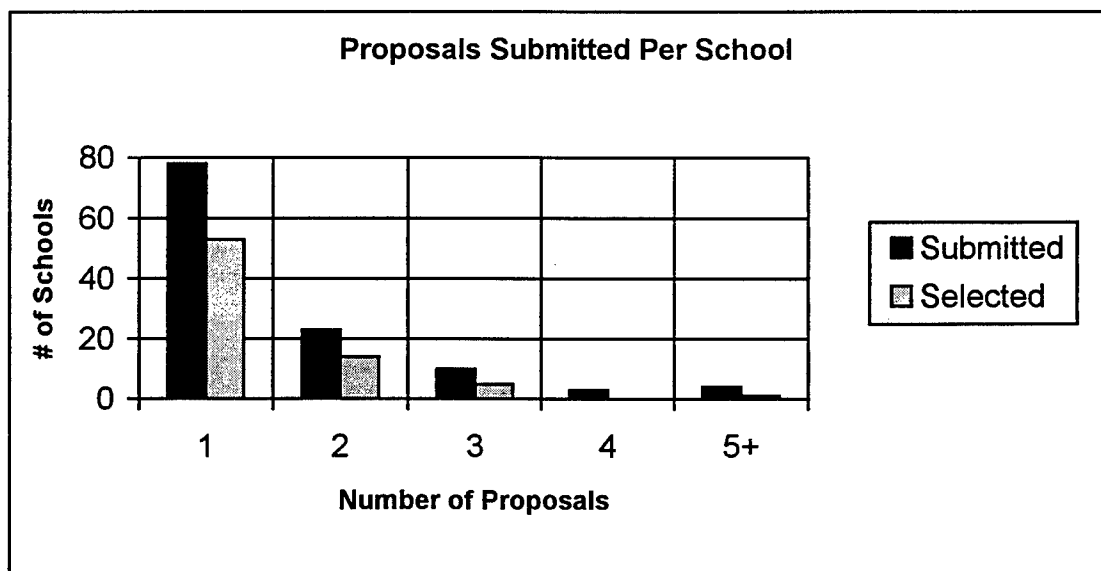
<b>Proposals Submitted and Selected, by Laboratory</b>		
	<b>Applied</b>	<b>Selected</b>
Air Force Civil Engineering Laboratory	9	4
Armstrong Laboratory	41	19
Arnold Engineering Development Center	12	4
Frank J. Seiler Research Laboratory	6	3
Phillips Laboratory	33	19
Rome Laboratory	31	13
Wilford Hall Medical Center	2	1
Wright Laboratory	62	37
<b>TOTAL</b>	<b>196</b>	<b>100</b>

Note: Phillips Laboratory funded 3 SREPs; Wright Laboratory funded 11; and AFOSR funded 11 beyond its contractual 75.

The 306 1992 Summer Research Program participants represented 135 institutions.

<b>Institutions Represented on the 1992 SRP and 1993 SREP</b>		
<b>Number of schools represented in the Summer 92 Program</b>	<b>Number of schools represented in submitted proposals</b>	<b>Number of schools represented in Funded Proposals</b>
135	118	73

Forty schools had more than one participant submitting proposals.



The selection rate for the 78 schools submitting 1 proposal (68%) was better than those submitting 2 proposals (61%), 3 proposals (50%), 4 proposals (0%) or 5+ proposals (25%). The 4 schools that submitted 5+ proposals accounted for 30 (15%) of the 196 proposals submitted.

Of the 196 proposals submitted, 159 offered institution cost sharing. Of the funded proposals which offered cost sharing, the minimum cost share was \$1000.00, the maximum was \$68,000.00 with an average cost share of \$12,016.00.

<b>Proposals and Institution Cost Sharing</b>		
	<b>Proposals Submitted</b>	<b>Proposals Funded</b>
With cost sharing	159	82
Without cost sharing	37	18
Total	196	100

The SREP participants were residents of 41 different states. Number of states represented at each laboratory were:

<b>States Represented, by Proposals Submitted/Selected per Laboratory</b>		
	<b>Proposals Submitted</b>	<b>Proposals Funded</b>
Air Force Civil Engineering Laboratory	8	4
Armstrong Laboratory	21	13
Arnold Engineering Development Center	5	2
Frank J. Seiler Research Laboratory	5	3
Phillips Laboratory	16	14
Rome Laboratory	14	7
Wilford Hall Medical Center	2	1
Wright Laboratory	24	20

Eleven of the 1993 SREP Principal Investigators also participated in the 1992 SREP.

**ADMINISTRATIVE EVALUATION:** The administrative quality of the SREP associates' final reports was satisfactory. Most complied with the formatting and other instructions provided to them by RDL. Ninety seven final reports and two interim reports have been received and are included in this report. The subcontracts were funded by \$1,991,623.00 of Air Force money. Institution cost sharing totaled \$985,353.00.

**TECHNICAL EVALUATION:** The form used for the technical evaluation is provided as Appendix 2. ninety-two evaluation reports were received. Participants by laboratory versus evaluations submitted is shown below:

	Participants	Evaluations	Percent
Air Force Civil Engineering Laboratory	*	*	*
Armstrong Laboratory	23 <sup>1</sup>	20	95.2
Arnold Engineering Development Center	4	4	100
Frank J. Seiler Research Laboratory	3	3	100
Phillips Laboratory	19 <sup>2</sup>	18	100
Rome Laboratory	13	13	100
Wilford Hall Medical Center	1	1	100
Wright Laboratory	37	34	91.9
Total	100 <sup>3</sup>	93	95.9

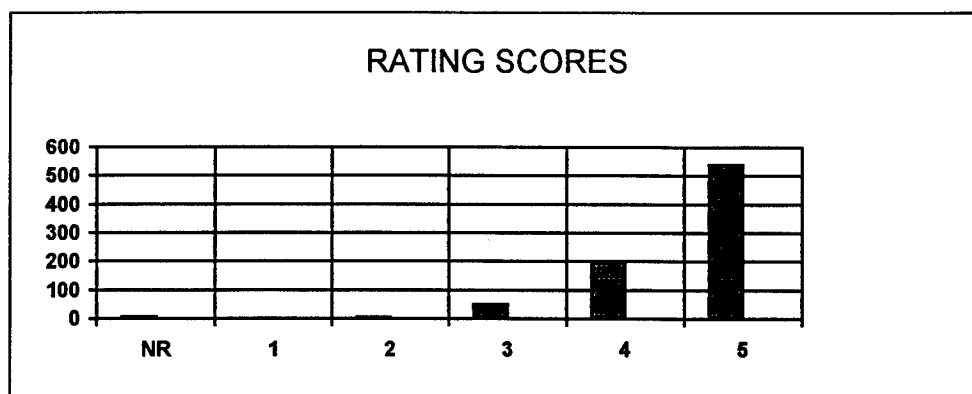
\*AFCEL was combined with Wright Laboratory's Flight Dynamics Directorate and Armstrong Laboratories Environics Directorate in 1993. All four of AFCEL's SREP awards went to Armstrong Laboratories Environics Directorate, and their reports are included with Armstrong Lab.

Notes:

- 1: Research on two of the final reports was incomplete as of press time so there aren't any technical evaluations on them to process, yet. Percent complete is based upon 20/21=95.2%
- 2: One technical evaluation was not completed because one of the final reports was incomplete as of press time. Percent complete is based upon 18/18=100%
- 3: See notes 1 and 2 above. Percent complete is based upon 93/97=95.9%

The number of evaluations submitted for the 1993 SREP (95.9%) shows a marked improvement over the 1992 SREP submittals (65%).

**PROGRAM EVALUATION:** Each laboratory focal point evaluated ten areas (see Appendix 2) with a rating from one (lowest) to five (highest). The distribution of ratings was as follows:

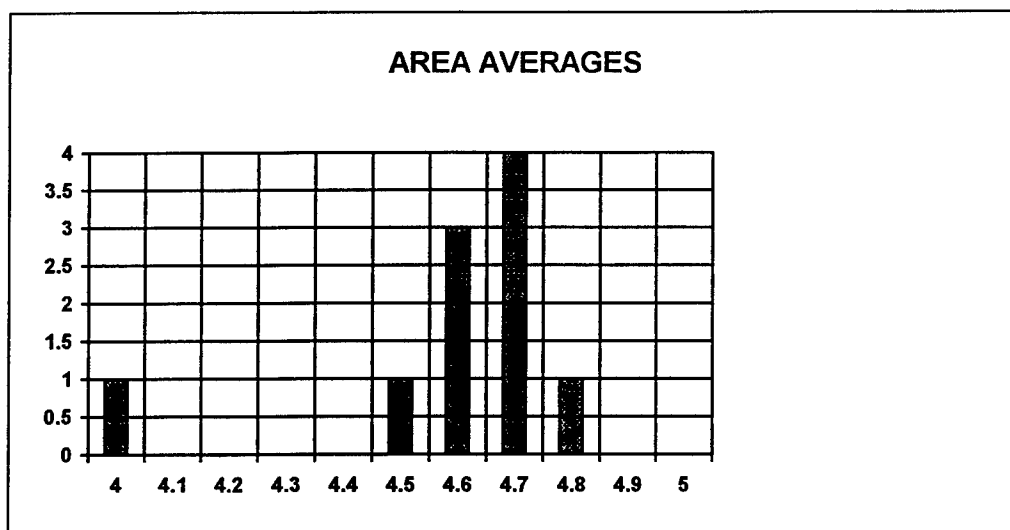


Rating	Not Rated	1	2	3	4	5
# Responses	7	1	7	62 (6%)	226 (25%)	617 (67%)

The 8 low ratings (one 1 and seven 2's ) were for question 5 (one 2) "The USAF should continue to pursue the research in this SREP report" and question 10 (one 1 and six 2's) "The one-year period for complete SREP research is about right", in addition over 30% of the threes (20 of 62) were for question ten. The average rating by question was:

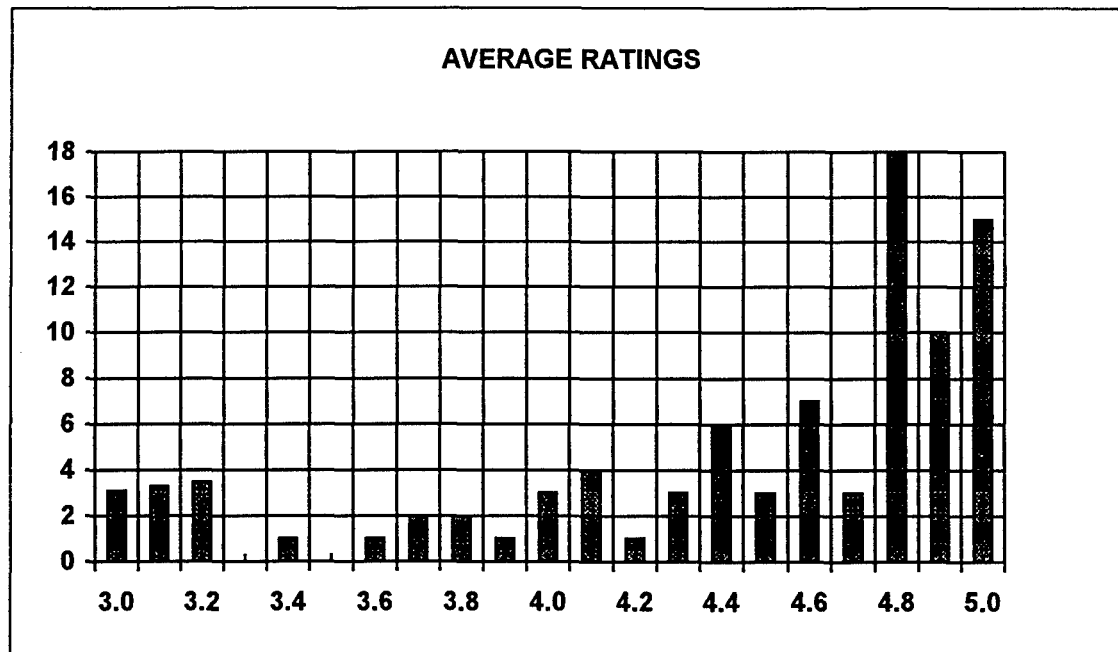
Question	1	2	3	4	5	6	7	8	9	10
Average	4.6	4.6	4.7	4.7	4.6	4.7	4.8	4.5	4.6	4.0

The distribution of the averages was:



Area 10 "the one-year period for complete SREP research is about right" had the lowest average rating (4.1). The overall average across all factors was 4.6 with a small sample standard deviation of 0.2. The average rating for area 10 (4.1) is approximately three sigma lower than the overall average (4.6) indicating that a significant number of the evaluators feel that a period of other than one year should be available for complete SREP research.

The average ratings ranged from 3.4 to 5.0. The overall average for those reports that were evaluated was 4.6. Since the distribution of the ratings is not a normal distribution the average of 4.6 is misleading. In fact over half of the reports received an average rating of 4.8 or higher. The distribution of the average report ratings is as shown:



It is clear from the high ratings that the laboratories place a high value on AFOSR's Summer Research Extension Programs.



### 3.0 SUBCONTRACTS SUMMARY

Table 1 provides a summary of the SREP subcontracts. The individual reports are published in volumes as shown:

<u>Laboratory</u>	<u>Volume</u>
Air Force Civil Engineering Laboratory	*
Armstrong Laboratory	1
Arnold Engineering Development Center	5
Frank J. Seiler Research Laboratory	5
Phillips Laboratory	2
Rome Laboratory	3
Wilford Hall Medical Center	5
Wright Laboratory	4A, 4B

\*AFCEL was combined with Wright Laboratory's Flight Dynamics Directorate and Armstrong Laboratories Environics Directorate in 1993. All four of AFCEL's SREP awards went to Armstrong Laboratories Environics Directorate, and their reports are included with Armstrong Lab.

# 1993 SREP SUB-CONTRACT DATA

TABLE 1: SUBCONTRACTS SUMMARY

Report Author Author's University	Author's Degree	Sponsoring Lab	Performance Period		Contract Amount Univ. Cost Share
Abbott , Ben Electrical Engineering Vanderbilt University, Nashville, TN	M.S.	AEDC/	01/01/93	12/31/93	\$19619.00 \$0.00
Alberts , Thomas Mechanical Engineering Old Dominion University, Norfolk, VA	PhD	FJSRL/	01/01/93	04/15/94	\$20000.00 \$8000.00
Avula , Xavier Mechanical & Aerospace Engineering University of Missouri, Rolla, MO	PhD	AL/AO	01/01/93	04/15/94	\$20000.00 \$1836.00
Balakrishan , S. Mechanical & Aerospace Engineering University of Missouri, Rolla, MO	PhD	WL/MN	12/01/92	12/14/93	\$20000.00 \$3996.00
Baumgarten , Joseph Mechanical Engineering Iowa State University, Ames, IA	PhD	PL/VT	01/01/93	04/01/94	\$19916.00 \$9083.00
Bayard , Jean-Pierre Electrical & Electronic Engineering California State University, Sacramento, CA	PhD	RL/ER	01/01/93	12/31/93	\$20000.00 \$7423.00
Bellem , Raymond Electrical & Computer Engineering University of Arizona, Tucson, AZ	PhD	PL/VT	01/01/93	02/28/94	\$19956.00 \$0.00
Biegl , Csaba Electrical Engineering Vanderbilt University, Nashville, TN	PhD	AEDC/	01/01/93	12/31/93	\$19999.00 \$0.00
Biggs , Albert Electrical Engineering University of Alabama, Huntsville, AL	PhD	PL/WS	01/01/93	12/31/93	\$19975.00 \$0.00
Burkey , Theodore Chemistry Memphis State University, Memphis, TN	PhD	WL/MN	01/01/93	12/31/93	\$20000.00 \$18648.00
Burkholder , Robert Electrical Engineering Ohio State University, Columbus, OH	PhD	WL/AA	01/01/93	12/31/93	\$20000.00 \$6727.00
Callens, Jr. , Eugene Mechanical and Industrial Engineer Louisiana Tech University, Ruston, LA	PhD	WL/MN	01/01/93	12/31/93	\$20000.00 \$5700.00
Chapman , Gary Mechanical Engineering University of California, Berkeley, CA	PhD	WL/MN	01/01/93	12/31/94	\$20000.00 \$0.00
Chen , Chien-In Electrical Engineering Wright State University, Dayton, OH	PhD	WL/EL	01/01/93	12/31/93	\$20000.00 \$32065.00
Chen , Jer-sen Computer Science & Engineering Wright State University, Dayton, OH	PhD	AL/CF	01/01/93	12/31/93	\$20000.00 \$31763.00

# 1993 SREP SUB-CONTRACT DATA

Report Author Author's University	Author's Degree	Sponsoring Lab	Performance Period		Contract Amount Univ. Cost Share
Chen , Pinyuen Mathematics Syracuse University, Syracuse, NY	PhD	RL/IR	01/01/93	12/31/93	\$20000.00 \$0.00
Chow , Joe Industrial and Systems Engineering Florida International University, Miami, FL	PhD	WL/FI	01/01/93	01/14/94	\$20000.00 \$2500.00
Christensen , Thomas Physics University of Colorado, Colorado Springs, CO	PhD	FJSRL/	01/01/93	12/31/93	\$20000.00 \$5390.00
Collicott , Steven Aeronautics and Astronautical Engineering Purdue University, West Lafayette, IN	PhD	WL/FI	01/01/93	12/31/93	\$20000.00 \$13307.00
Cooke , Nancy Psychology New Mexico State University, Las Cruces, NM	PhD	AL/HR	01/01/93	12/31/93	\$20000.00 \$6178.00
Daley , Michael Electrical Engineering Memphis State, Memphis, TN	PhD	WHMC/	01/01/93	12/31/93	\$20000.00 \$18260.00
Davidson , Jennifer Electrical Engineering Iowa State University, Ames, IA	PhD	WL/MN	01/01/93	02/28/94	\$19999.00 \$0.00
Deivanayagam , Subramaniam Industrial Engineering Tennessee Technological University, Cookeville, TN	PhD	AL/HR	02/01/93	12/31/93	\$20000.00 \$12491.00
Elliott , David Engineering Arkansas Technology University, Russellville, AR	PhD	PL/RK	10/01/92	08/15/93	\$20000.00 \$50271.00
Erdman , Paul Physics and Astronomy University of Iowa, Iowa City, IA	M.S.	PL/RK	01/01/93	12/31/93	\$20000.00 \$26408.00
Ervin , Jamie Mechanical and Aerospace Engineering University of Dayton, Dayton, OH	PhD	WL/ML	01/01/93	12/31/93	\$18632.00 \$3000.00
Erwin , Daniel Aerospace Engineering University of Southern California, Los Angeles, CA	PhD	PL/RK	01/01/93	12/31/93	\$19962.00 \$12696.00
Ewert , Dan Electrical Engineering North Dakota State University, Fargo, ND	PhD	AL/AO	01/01/93	12/31/93	\$20000.00 \$2100.00
Farmer , Barry Materials Science and Engineering University of Virginia, Charlottesville, VA	PhD	WL/ML	01/01/93	02/28/94	\$20000.00 \$2000.00
Foo , Simon Electrical Engineering Florida State University, Tallahassee, FL	PhD	WL/MN	01/01/93	12/31/93	\$19977.00 \$0.00

# 1993 SREP SUB-CONTRACT DATA

Report Author Author's University	Author's Degree	Sponsoring Lab	Performance Period	Contract Amount Univ. Cost Share
Friedman , Jeffrey Physics University of Puerto Rico, Mayaguez, PR	PhD	PL/GP	01/01/93 12/31/93	\$20000.00 \$10233.00
Gerstman , Bernard Physics Florida International University, Miami, FL	PhD	AL/OE	01/01/93 04/30/94	\$19947.00 \$2443.00
Gillman , Ann Chemistry Eastern Kentucky University, Richmond, KY	M.S.	WL/PO	01/01/93 12/31/93	\$20000.00 \$15618.00
Gimmestad , Gary Research Institute Georgia Institute of Technology, Atlanta, GA	PhD	PL/LI	01/01/93 12/31/93	\$20000.00 \$0.00
Gould , Richard Mechanical and Aerospace Engineering North Carolina State University, Raleigh, NC	PhD	WL/PO	01/01/93 12/31/93	\$20000.00 \$8004.00
Graham , Gary Mechanical Engineering Ohio University, Athens, OH	PhD	WL/FI	01/01/93 12/31/93	\$20000.00 \$5497.00
Gramoll , Kurt Aerospace Engineering Georgia Institute of Technology, Atlanta, GA	PhD	AEDC/	01/01/93 12/31/93	\$19707.00 \$14552.00
Graul , Susan Chemistry Carnegie Mellon University, Pittsburgh, PA	PhD	PL/WS	01/01/93 03/31/94	\$20000.00 \$0.00
Griffin , Steven Engineering University of Texas, San Antonio, TX	M.S.	PL/VT	01/01/93 12/31/93	\$20000.00 \$0.00
Grubbs , Elmer Electrical Engineering New Mexico Highlands University, Las Vegas, NM	PhD	WL/AA	01/01/93 12/31/93	\$20000.00 \$6747.00
Gupta , Pushpa Mathematics University of Maine, Orono, ME	PhD	AL/AO	01/01/93 12/31/93	\$20000.00 \$1472.00
Hall , Ian Materials Science University of Delaware, Newark, DE	PhD	WL/ML	01/01/93 12/31/93	\$20000.00 \$9580.00
Hedman , Paul Chemical Engineering Brigham Young University, Provo, UT	PhD	WL/PO	01/01/93 12/31/93	\$19999.00 \$7755.00
Henry , Robert Electrical & Computer Engineering University of Southwestern Louisiana, Lafayette, LA	PhD	RL/C3	12/01/92 05/31/93	\$19883.00 \$11404.00
Henson , James Electrical Engineering University of Nevada, Reno, NV	PhD	PL/WS	01/01/93 12/31/93	\$19913.00 \$9338.00

# 1993 SREP SUB-CONTRACT DATA

Report Author Author's University	Author's Degree	Sponsoring Lab	Performance Period	Contract Amount Univ. Cost Share
Hoe , Benjamin Electrical Engineering Polytechnic University, Brooklyn, NY	M.S.	RL/C3	09/01/92 05/31/93	\$19988.00 \$7150.00
Hughes , Rod Psychology Bowling Green State University, Bowling Green, OH	M.S.	AL/CF	01/01/93 04/15/94	\$20000.00 \$20846.00
Hui , David Mechanical Engineering University of New Orleans, New Orleans, LA	PhD	WL/FI	01/01/93 12/31/93	\$20000.00 \$0.00
Humi , Mayer Mathematics Worcester Polytechnic Institut, Worcester, MA	PhD	PL/LI	01/01/93 12/31/93	\$20000.00 \$5000.00
Innocenti , Mario Aerospace Engineering Auburn University, Auburn, AL	PhD	WL/MN	01/01/93 02/28/94	\$20000.00 \$12536.00
Jean , Jack Computer Science & Engineering Wright State University, Dayton, OH	PhD	WL/AA	01/01/93 12/31/93	\$20000.00 \$34036.00
Jouny , Ismail Electrical Engineering Lafayette College, Easton, PA	PhD	WL/AA	01/01/93 12/31/93	\$19381.00 \$4500.00
Kaikhah , Khosrow Computer Science Southwest Texas State College, San Marcos, TX	PhD	RL/IR	01/01/93 12/31/93	\$20000.00 \$0.00
Kaw , Autar Mechanical Engineering University of South Florida, Tampa, FL	PhD	WL/ML	01/01/93 12/31/93	\$20000.00 \$22556.00
Kheyfets , Arkady Mathematics North Carolina State University, Raleigh, NC	PhD	PL/LI	01/01/93 12/31/93	\$20000.00 \$2500.00
Kitchart , Mark Mechanical Engineering North Carolina A & T State University, Greensboro, NC	M.S.	AL/EQ	01/01/93 12/31/93	\$20000.00 \$0.00
Koblasz , Arthur Civil Engineering Georgia Institute of Technology, Atlanta, GA	PhD	AL/AO	01/01/93 12/31/93	\$19826.00 \$0.00
Koivo , A. Electrical Engineering Purdue University, West Lafayette, IN	PhD	AL/CF	01/01/93 06/30/94	\$20000.00 \$0.00
Kundich , Robert Biomedical Engineering University of Tennessee, Memphis, TN	PhD	AL/CF	01/01/93 12/31/94	\$20000.00 \$23045.00
Kuo , Spencer Electrical Engineering Polytechnic University, Farmingdale, NY	PhD	PL/GP	01/01/93 04/30/94	\$20000.00 \$9731.00

# 1993 SREP SUB-CONTRACT DATA

Report Author Author's University	Author's Degree	Sponsoring Lab	Performance Period		Contract Amount Univ. Cost Share
Liou , Juin Electrical and Computer Engineering Universtiy of Central Florida, Orlando, FL	PhD	WL/EL	01/01/93	12/31/93	\$20000.00 \$9073.00
Liou , Shy-Shenq Engineering San Francisco State Univesity, San Francisco, CA	PhD	WL/PO	01/01/93	12/31/93	\$20000.00 \$13387.00
Manoranjana , Valipuram Pure and Applied Mathematics Washington State University, Pullman, WA	PhD	AL/EQ	01/01/93	12/31/93	\$19956.00 \$10041.00
Marks , Dallas Electrical and Computer Engineering University of Cincinnati M.L., Cincinnati, OH	M.S.	WL/AA	10/01/92	06/30/93	\$20000.00 \$4731.00
Monsay , Evelyn Physics Le Moyne College, Syracuse, NY	PhD	RL/OC	01/01/93	12/31/93	\$19634.00 \$1510.00
Moor , William Industrial & Management Engineering Arizona State University, Tempe, AZ	PhD	AL/HR	01/01/93	12/31/93	\$20000.00 \$4833.00
Moore , Carlyle Physics Morehouse College, Atlanta, GA	PhD	AEDC/	01/01/93	12/31/93	\$20000.00 \$4880.00
Mulligan , B. Psychology University of Georgia Research, Athens, GA	PhD	AL/OE	01/01/93	04/15/94	\$19998.00 \$13936.00
Murphy , Richard Physics University of Missouri, Kansas City, MO	PhD	PL/WS	01/01/93	12/31/93	\$20000.00 \$13022.00
Nilan , Michael Information Studies Syracuse University, Syracuse, NY	PhD	RL/C3	01/01/93	12/31/93	\$19998.00 \$13016.00
Parrish , Allen Computer Science University of Alabama, Tuscaloosa, AL	PhD	RL/C3	01/01/93	12/31/93	\$19919.00 \$20599.00
Piersma , Bernard Chemistry Houghton College, Houghton, NY	PhD	FJSRL/	01/01/93	12/31/93	\$20000.00 \$4000.00
Potasek , Mary Applied Physics Columbia University, New York, NY	PhD	WL/ML	12/01/93	11/30/93	\$20000.00 \$7806.00
Qazi , Salahuddin Optical Communications SUNY/Institute of Technology, Utica, NY	PhD	RL/OC	01/01/93	12/31/93	\$20000.00 \$68000.00
Reardon , Kenneth Agricultural and Chemical Engineering Colorado State University, Fort Collins, CO	PhD	AL/EQ	01/01/93	01/31/94	\$19996.00 \$12561.00

# 1993 SREP SUB-CONTRACT DATA

Report Author Author's University	Author's Degree	Sponsoring Lab	Performance Period	Contract Amount Univ. Cost Share
Reynolds , David Biomedical & Human Factors Wright State University, Dayton, OH	PhD	AL/CF	01/01/93 06/30/94	\$20000.00 \$14063.00
Robinson , Donald Chemistry Xavier University of Louisiana, New Orleans, LA	PhD	AL/OE	01/01/93 06/30/94	\$20000.00 \$12935.00
Rodriguez , Armando Electrical Engineering Arizona State University, Tempe, AZ	PhD	WL/MN	01/01/93 12/31/93	\$20000.00 \$0.00
Roe , Larry Mechanical Engineering Virginia Polytechnic Inst & State Coll., Blacksburg, VA	PhD	WL/PO	01/01/93 12/31/93	\$20000.00 \$11421.00
Romeu , Jorge Assistant Prof. of Mathematics SUNY College at Cortland, Cortland, NY	PhD	RL/OC	01/01/93 12/31/93	\$19997.00 \$7129.00
Roppel , Thaddeus Electrical Engineering Auburn University, Auburn, AL	PhD	WL/MN	01/01/93 12/31/93	\$20000.00 \$21133.00
Roznowski , Mary Psychology Ohio State University, Columbus, OH	PhD	AL/HR	01/01/93 03/31/94	\$19953.00 \$6086.00
Rudzinski , Walter Chemistry Southwest Texas State University, San Marcos, TX	PhD	AL/OE	01/01/93 12/31/93	\$20000.00 \$10120.00
Sargent , Robert Engineering and Computer Science Syracuse University, Syracuse, NY	PhD	RL/XP	01/01/93 12/31/93	\$20000.00 \$11931.00
Schonberg , William Civil and Environmental Engineering University of Alabama, Huntsville, AL	PhD	WL/MN	01/01/93 12/31/93	\$19991.00 \$5083.00
Shaw , Arnab Electrical Engineering Wright State University, Dayton, OH	PhD	WL/AA	01/01/93 12/31/93	\$20000.00 \$4766.00
Shively , Jon Engineering & Computer Science California State University, Northridge, CA	PhD	PL/VT	01/01/93 12/31/93	\$20000.00 \$9782.00
Slater , Robert Mechanical & Industrial Engineering University of Cincinnati, Cincinnati, OH	M.S.	WL/FI	01/01/93 12/31/93	\$20000.00 \$8257.00
Stenzel , Johanna Arts & Sciences University of Houston, Victoria, TX	PhD	PL/LI	01/01/93 12/31/93	\$20000.00 \$9056.00
Tan , Arjun Physics Alabama A & M University, Normal, AL	PhD	PL/WS	01/01/93 12/31/93	\$20000.00 \$1000.00

# 1993 SREP SUB-CONTRACT DATA

Report Author Author's University	Author's Degree	Sponsoring Lab	Performance Period		Contract Amount Univ. Cost Share
Tetrick , Lois Industrial Relations Prog Wayne State University, Detroit, MI	PhD	AL/HR	01/01/93	12/31/93	\$20000.00 \$17872.00
Tew , Jeffery Industrial & Systems Engineering Virginia Polytechnic Institute, Blacksburg, VA	PhD	RL/IR	05/31/93	12/31/93	\$16489.00 \$4546.00
Tribikram , Kundu Civil Engineering and Engineering Universtiy of Arizona, Tucson, AZ	PhD	WL/ML	01/01/93	12/31/93	\$20000.00 \$9685.00
Tuthill , Theresa Electrical Engineering University of Dayton, Dayton, OH	PhD	WL/ML	01/01/93	12/31/93	\$20000.00 \$24002.00
Venkatasubraman , Ramasubrama Electrical and Computer Engineering University of Nevada, Las Vegas, NV	PhD	WL/ML	01/01/93	12/31/93	\$20000.00 \$18776.00
Wang , Xingwu Electrical Engineering Alfred University, Alfred, NY	PhD	AL/EQ	01/01/93	12/31/93	\$20000.00 \$10000.00
Whitefield , Philip Physics University of Missouri, Rolla, MO	PhD	PL/LI	01/01/93	03/01/94	\$20000.00 \$11040.00
Wightman , Colin Electrical Engineering New Mexico Institute of Mining, Socorro, NM	PhD	RL/IR	01/01/93	12/31/93	\$20000.00 \$1850.00
Womack , Michael Natural Science and Mathematics Macon College, Macon, GA	PhD	AL/OE	01/01/93	06/30/94	\$19028.00 \$6066.00
Yuvarajan , Subbaraya Electrical Engineering North Dakota State University, Fargo, ND	PhD	WL/PO	01/01/93	12/31/93	\$19985.00 \$22974.00



**APPENDIX 1:**  
**SAMPLE SREP SUBCONTRACT**

AIR FORCE OFFICE OF SCIENTIFIC RESEARCH  
1993 SUMMER RESEARCH EXTENSION PROGRAM SUBCONTRACT 93-133

BETWEEN

Research & Development Laboratories  
5800 Uplander Way  
Culver City, CA 90230-6608

AND

San Francisco State University  
University Comptroller  
San Francisco, CA 94132

REFERENCE: Summer Research Extension Program Proposal 93-133  
Start Date: 01/01/93 End Date: 12/31/93  
Proposal Amount: \$20,000.00

- (1) PRINCIPAL INVESTIGATOR: Dr. Shy Shenq P. Liou  
Engineering  
San Francisco State University  
San Francisco, CA 94132
- (2) UNITED STATES AFOSR CONTRACT NUMBER: F49620-90-C-09076
- (3) CATALOG OF FEDERAL DOMESTIC ASSISTANCE NUMBER (CFDA): 12.800  
PROJECT TITLE: AIR FORCE DEFENSE RESEARCH SOURCES PROGRAM
- (4) ATTACHMENTS 1 AND 2: SREP REPORT INSTRUCTIONS

\*\*\* SIGN SREP SUBCONTRACT AND RETURN TO RDL \*\*\*


1. **BACKGROUND:** Research & Development Laboratories (RDL) is under contract (F49620-90-C-0076) to the United States Air Force to administer the Summer Research Programs (SRP), sponsored by the Air Force Office of Scientific Research (AFOSR), Bolling Air Force Base, D.C. Under the SRP, a selected number of college faculty members and graduate students spend part of the summer conducting research in Air Force laboratories. After completion of the summer tour participants may submit, through their home institutions, proposals for follow-on research. The follow-on research is known as the Summer Research Extension Program (SREP). Approximately 75 SREP proposals annually will be selected by the Air Force for funding of up to \$20,000; shared funding by the academic institution is encouraged. SREP efforts selected for funding are administered by RDL through subcontracts with the institutions. This subcontract represents such an agreement between RDL and the institution designated in Section 5 below.
  
2. **RDL PAYMENTS:** RDL will provide the following payments to SREP institutions:
  - 90 percent of the negotiated SREP dollar amount at the start of the SREP Research period.
  - the remainder of the funds within 30 days after receipt at RDL of the acceptable written final report for the SREP research.
  
3. **INSTITUTION'S RESPONSIBILITIES:** As a subcontractor to RDL, the institution designated on the title page will:
  - a. Assure that the research performed and the resources utilized adhere to those defined in the SREP proposal.
  - b. Provide the level and amounts of institutional support specified in the RIP proposal.
  - c. Notify RDL as soon as possible, but not later than 30 days, of any changes in 3a or 3b above, or any change to the assignment or amount of participation of the Principal Investigator designated on the title page.

- d. Assure that the research is completed and the final report is delivered to RDL not later than twelve months from the effective date of this subcontract, but no later than December 31, 1993. The effective date of the subcontract is one week after the date that the institution's contracting representative signs this subcontract, but no later than January 15, 1993.
- e. Assure that the final report is submitted in accordance with Attachment 1.
- f. Agree that any release of information relating to this subcontract (news releases, articles, manuscripts, brochures, advertisements, still and motion pictures, speeches, trade association meetings, symposia, etc.) will include a statement that the project or effort depicted was or is sponsored by: Air Force Office of Scientific Research, Bolling AFB, D.C.
- g. Notify RDL of inventions or patents claimed as the result of this research as specified in Attachment 1.
- h. RDL is required by the prime contract to flow down patent rights and technical data requirements in this subcontract. Attachment 2 to this subcontract contains a list of contract clauses incorporated by reference in the prime contract.

4. All notices to RDL shall be addressed to:

RDL Summer Research Program Office  
5800 Uplander Way  
Culver City, CA 90230-6608

5. By their signatures below, the parties agree to the provisions of this subcontract.



Abe S. Sopher  
RDL Contracts Manager

\_\_\_\_\_  
Signature of Institution Contracting Official

\_\_\_\_\_  
Typed/Printed Name

\_\_\_\_\_  
Date

\_\_\_\_\_  
Title

\_\_\_\_\_  
Institution

\_\_\_\_\_  
(Date/Phone)

**ATTACHMENT 2**  
**CONTRACT CLAUSES**

This contract incorporates by reference the following clauses of the Federal Acquisition Regulations (FAR), with the same force and effect as if they were given in full text. Upon request, the Contracting Officer or RDL will make their full text available (FAR 52.252-2).

<b><u>FAR CLAUSES</u></b>	<b><u>TITLE AND DATE</u></b>
52.202-1	DEFINITIONS (SEP 1991)
52.203-1	OFFICIALS NOT TO BENEFIT (APR 1984)
52.203-3	GRATUITIES (APR 1984)
52.203-5	COVENANT AGAINST CONTINGENT FEES (APR 1984)
52.304-6	RESTRICTIONS ON SUBCONTRACTOR SALES TO THE GOVERNMENT (JUL 1985)
52.203-7	ANTI-KICKBACK PROCEDURES (OCT 1988)
52.203-12	LIMITATION ON PAYMENTS TO INFLUENCE CERTAIN FEDERAL TRANSACTIONS (JAN 1990)
52.204-2	SECURITY REQUIREMENTS (APR 1984)
52.209-6	PROTECTING THE GOVERNMENT'S INTEREST WHEN SUBCONTRACTING WITH CONTRACTORS DEBARRED, SUSPENDED, OR PROPOSED FOR DEBARMENT (NOV 1992)
52.212-8	DEFENSE PRIORITY AND ALLOCATION REQUIREMENTS (SEP 1990)
52.215-1	EXAMINATION OF RECORDS BY COMPTROLLER GENERAL (APR 1984)
52.215-2	AUDIT - NEGOTIATION (DEC 1989)
52.222-26	EQUAL OPPORTUNITY (APR 1984)
52.222-28	EQUAL OPPORTUNITY PREAWARD CLEARANCE OF SUBCONTRACTS (APR 1984)

- 52.222-35 AFFIRMATIVE ACTION FOR SPECIAL DISABLED AND VIETNAM ERA VETERANS (APR 1984)
- 52.222-36 AFFIRMATIVE ACTION FOR HANDICAPPED WORKERS (APR 1984)
- 52.222-37 EMPLOYMENT REPORTS ON SPECIAL DISABLED VETERAN AND VETERANS OF THE VIETNAM ERA (JAN 1988)
- 52.223-2 CLEAN AIR AND WATER (APR 1984)
- 52.232-6 DRUG-FREE WORKPLACE (JUL 1990)
- 52.224-1 PRIVACY ACT NOTIFICATION (APR 1984)
- 52.224-2 PRIVACY ACT (APR 1984)
- 52.225-13 RESTRICTIONS ON CONTRACTING WITH SANCTIONED PERSONS (MAY 1989)
- 52.227-1 AUTHORIZATION AND CONSENT (APR 1984)
- 52.227-2 NOTICE AND ASSISTANCE REGARDING PATENT AND COPYRIGHT INFRINGEMENT (APR 1984)
- 52.227-10 FILING OF PATENT APPLICATIONS - CLASSIFIED SUBJECT MATTER (APR 1984)
- 52.227-11 PATENT RIGHTS - RETENTION BY THE CONTRACTOR (SHORT FORM) (JUN 1989)
- 52.228-6 INSURANCE - IMMUNITY FROM TORT LIABILITY (APR 1984)
- 52.228-7 INSURANCE - LIABILITY TO THIRD PERSONS (APR 1984)
- 52.230-5 DISCLOSURE AND CONSISTENCY OF COST ACCOUNTING PRACTICES (AUG 1992)
- 52.232-23 ASSIGNMENT OF CLAIMS (JAN 1986)
- 52.237-3 CONTINUITY OF SERVICES (JAN 1991)

52.246-25	LIMITATION OF LIABILITY - SERVICES (APR 1984)
52.249-6	TERMINATION (COST-REIMBURSEMENT) (MAY 1986)
52.249-14	EXCUSABLE DELAYS (APR 1984)
52.251-1	GOVERNMENT SUPPLY SOURCES (APR 1984)

**APPENDIX 2:**

**SAMPLE TECHNICAL EVALUATION FORM**



## 1993 SUMMER RESEARCH EXTENSION PROGRAM

RIP NO.: 93-0092

RIP ASSOCIATE: Dr. Gary T. Chapman

Provided are several evaluation statements followed by ratings of (1) through (5). A rating of (1) is the lowest and (5) is the highest. Circle the rating level number you best feel rates the statement. Document additional comments on the back of this evaluation form.

Mail or fax the completed form to :

RDL

Attn: 1993 SREP TECH EVALS

5800 Uplander Way

Culver City, CA 90230-6608

(FAX: 310 216-5940)

- |     |   |   |   |   |   |   |
|-----|---|---|---|---|---|---|
| 1.  | This SREP report has a high level of technical merit.                           | 1 | 2 | 3 | 4 | 5 |
| 2.  | The SREP program is important to accomplishing the labs's mission               | 1 | 2 | 3 | 4 | 5 |
| 3.  | This SREP report accomplished what the associate's proposal promised.           | 1 | 2 | 3 | 4 | 5 |
| 4.  | This SREP report addresses area(s) important to the USAF                        | 1 | 2 | 3 | 4 | 5 |
| 5.  | The USAF should continue to pursue the research in this SREP report             | 1 | 2 | 3 | 4 | 5 |
| 6.  | The USAF should maintain research relationships with this SREP associate        | 1 | 2 | 3 | 4 | 5 |
| 7.  | The money spent on this SREP effort was well worth it                           | 1 | 2 | 3 | 4 | 5 |
| 8.  | This SREP report is well organized and well written                             | 1 | 2 | 3 | 4 | 5 |
| 9.  | I'll be eager to be a focal point for summer and SREP associates in the future. | 1 | 2 | 3 | 4 | 5 |
| 10. | The one-year period for complete SREP research is about right                   | 1 | 2 | 3 | 4 | 5 |

\*\*\*\*USE THE BACK OF THIS FORM FOR ADDITIONAL COMMENTS\*\*\*\*

LAB FOCAL POINT'S NAME (PRINT): \_\_\_\_\_

OFFICE SYMBOL: \_\_\_\_\_ PHONE: \_\_\_\_\_

**PASSIVE DAMPING PREDICTION AND OPTIMIZATION  
FOR THE SPICE STRUCTURE  
USING A MAXWELL STRUCTURAL MODEL**

Thomas J. Thompson  
Graduate Assistant

Joseph R. Baumgarten  
Professor Emeritus

Donald R. Flugrad  
Associate Professor

Department of Mechanical Engineering  
Iowa State University  
2025 H. M. Black Engineering Building  
Ames, Iowa 50011

Final Report for:  
Summer Research Extension Program  
Phillips Laboratory

Sponsored by:  
Air Force Office of Scientific Research  
Bolling Air Force Base, Washington, D.C.

and

Iowa State University

March 1994

**PASSIVE DAMPING PREDICTION AND OPTIMIZATION  
FOR THE SPICE STRUCTURE  
USING A MAXWELL STRUCTURAL MODEL**

Thomas J. Thompson  
Graduate Assistant  
Mechanical Engineering  
Iowa State University

Abstract

Proposed future space missions involve large structures which must maintain precise dimensional tolerances even during dynamic maneuvers. In order to reduce disturbances in the many vibrational modes of such a structure, active and passive vibration control are proposed. The passive control is to be achieved by placing viscous or viscoelastic members or materials within a structure in order to absorb vibrational energy. Ascertaining the best combination of locations for such treatments is difficult due to the large number of cases, and since computationally expensive complex eigenvalue analyses of a finite element model is necessary to compute modal damping values for each case.

The purpose of this work is to develop and use a simpler model of structural damping which could accurately estimate modal damping ratio for any damping case based on a relatively small number of real eigenvalue (normal modes) analyses. The motion of the spring-mass system assumed by this Maxwell model is modified by placing the damper to be added in series with another stiffness inherent to the structure for each mode and damper location. The resulting expression for damping is easily evaluated and optimized.

Based on the Maxwell model, candidate damping locations for the SPICE structure were evaluated and ranked in order of effectiveness; locations which spanned the octahedral cells of the tetrahedron truss of its bulkhead ranked highest. Damping struts were placed in these locations and optimized using the Maxwell model.

# PASSIVE DAMPING PREDICTION AND OPTIMIZATION FOR THE SPICE STRUCTURE USING A MAXWELL STRUCTURAL MODEL

Thomas J. Thompson

## 1. NOMENCLATURE

$c$	Damping rate
$C$	Damping matrix
$F(s)$	Laplace expression for force
$j$	$\sqrt{-1}$
$k_{Aj}$	Modal stiffness, $j$ th mode
$k_{Bij}$	Series stiffness for $i$ th strut location, $j$ th mode
$k_s$	Equivalent stiffness of strut
$K$	Stiffness matrix
$M$	Mass matrix
$n$	Total number of struts
$q_i, \tilde{q}_i$	Generalized coordinates
$Q(s)$	Laplace expression for displacement of generalized coordinates
$r$	Damper ratio
$r^*$	Damper ratio at which maximum loss factor occurs
$s$	Laplace operator
$x$	Displacement in a system
$X(s)$	Laplace expression for displacement in a system
$\alpha_{ij}$	Influence coefficient (not in traditional sense), $i$ th strut, $j$ th mode
$\zeta, \tilde{\zeta}$	Damping ratio
$\eta$	Loss factor (or structural damping factor)
$\eta^*$	Maximum loss factor
$\kappa$	Stiffness ratio
$\kappa_s$	Stiffness ratio with respect to $k_s$
$\lambda_i, \tilde{\lambda}_i$	$i$ th eigenvalue
$\phi_i, \tilde{\phi}_i$	Eigenvector for $i$ th mode
$\Phi$	Modal matrix
$\omega$	Forcing natural frequency or mode frequency
$\omega_B$	Damper constant
$\omega_o$	Undamped natural frequency
$\omega_i$	Natural frequency of $i$ th mode
$\omega_s$	Natural frequency with strut stiffness in structure

## 2. INTRODUCTION

Large space structures proposed for use as space stations, telescopes, or laser platforms require active control systems to suppress vibrational disturbances and maintain precise dimensions. The SPICE (Space Integrated Control Experiment) [1] is a scale model of such a structure. Active control strategies such as HAC-LAC (high-authority control, low-authority control) used on such structures work best when passive damping is present in the structure to prevent instabilities in spill-over modes.

Such passive damping is incorporated in strut-built structures such as SPICE by means of inserting struts which introduce viscous (D-Strut) [2] or viscoelastic (V-Strut) damping; these struts normally have high static stiffness, which limits damping effectiveness. It has been proposed that inserting viscous dampers without static stiffness could produce more effective damping. This will be referred to as diagonal damping, since it would span diagonally across node pairs which are not spanned by structural elements.

The purpose of the research of this report was to evaluate the effectiveness of such diagonal damping in achieving optimal modal damping in several target modes using as few struts as possible. This was done by developing and implementing a procedure to estimate the damping coefficient produced by combinations of struts placed in various locations.

In order to estimate modal damping for the structure without repeated, expensive finite element complex eigenvalue analyses, each structural mode was characterized by Maxwell models. A limited number of real eigenvalue analyses led to a simple expression for predicting the modal damping achieved by dampers in any given set of locations. Based on this expression, strut locations were ranked, and effectiveness of diagonal damping was evaluated.

## 3. REQUIREMENTS

The requirements applied in seeking the best locations to implement damping are given below.

The Model used is an MSC-NASTRAN finite element model of the SPICE Structure. The actual structure, Figure 1, developed by the Air Force, is around 8 meters tall and possesses 62 modes below 75 Hz. The finite element model, developed by Lockheed Missiles and Space Company, has been correlated to experimental data with a high degree of accuracy.

The damping is to be provided by a viscous damping device such as a D-strut. The mathematical model of this device will be developed later.

The bulkhead truss of the SPICE structure (SPICE lab version) is pictured in Figure 2. (This model is used in example computations later.) A given damping strut may replace any one of the existing struts shown, producing "in-line" damping, or may span across any one of the 27 octahedral cells in one of up to three directions, producing diagonal damping. The node locations for the bulkhead portion of the Lockheed version of the NASTRAN model of the complete SPICE structure is shown in Figure 3. One-third of the 72 diagonal and 234 in-line candidate damper locations for this model are listed in Appendix A. Note that not all of the node locations of Figure 2 match those of Figure 3.

The goal for passive damping is to provide a minimum required damping in each of several target modes in order to provide better gain margins for the active control system.

The ultimate goal in this study is to find the best locations to provide the required damping in these modes

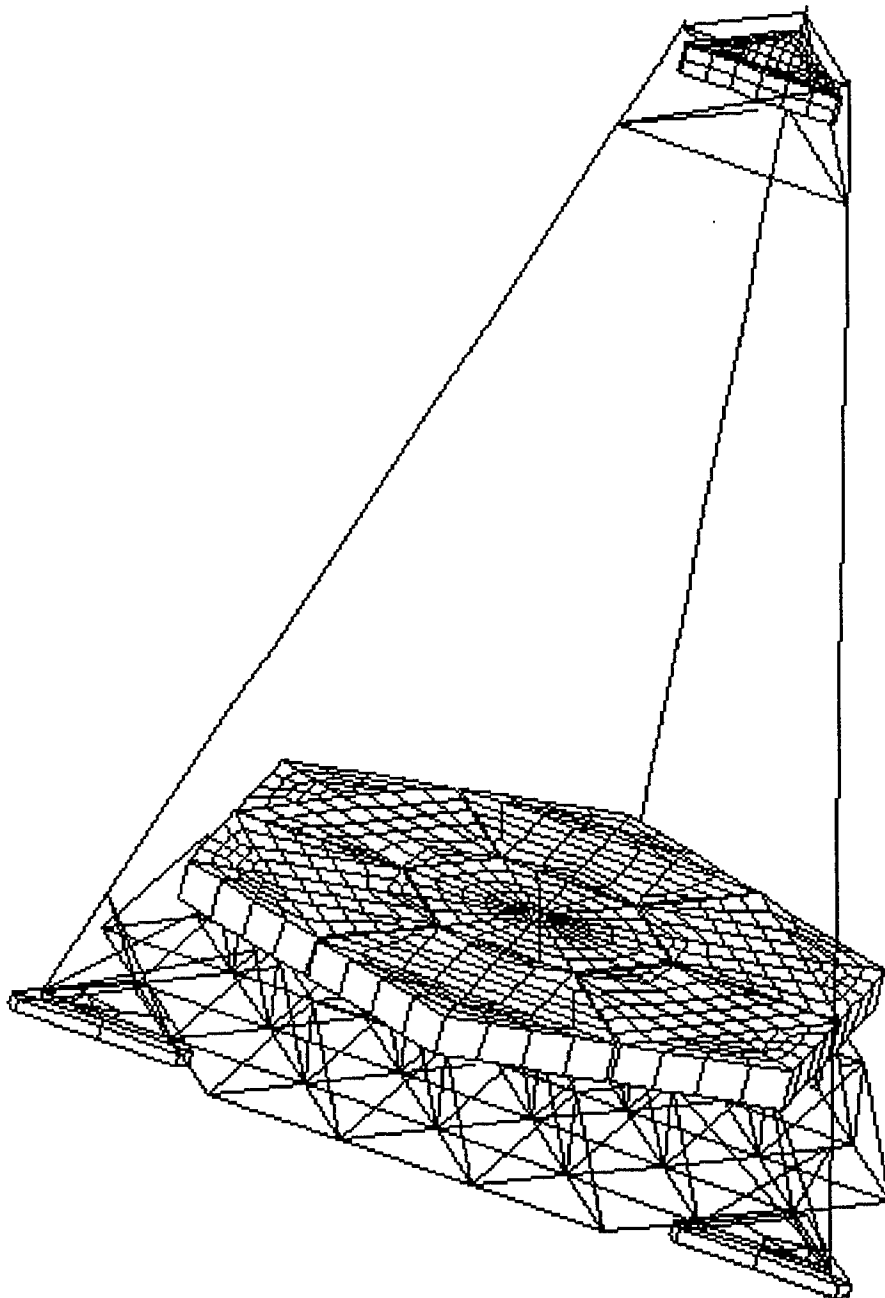


Figure 1: SPICE

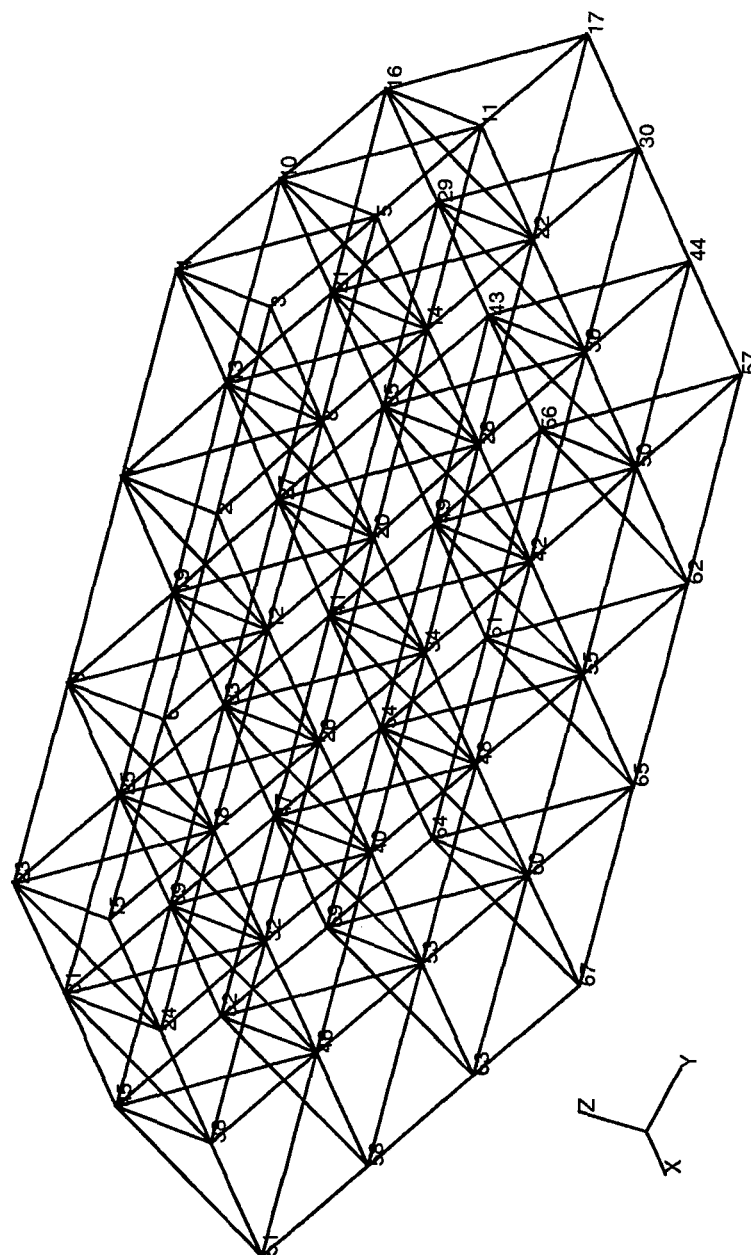


Figure 2: The SPICE Bulkhead Structure

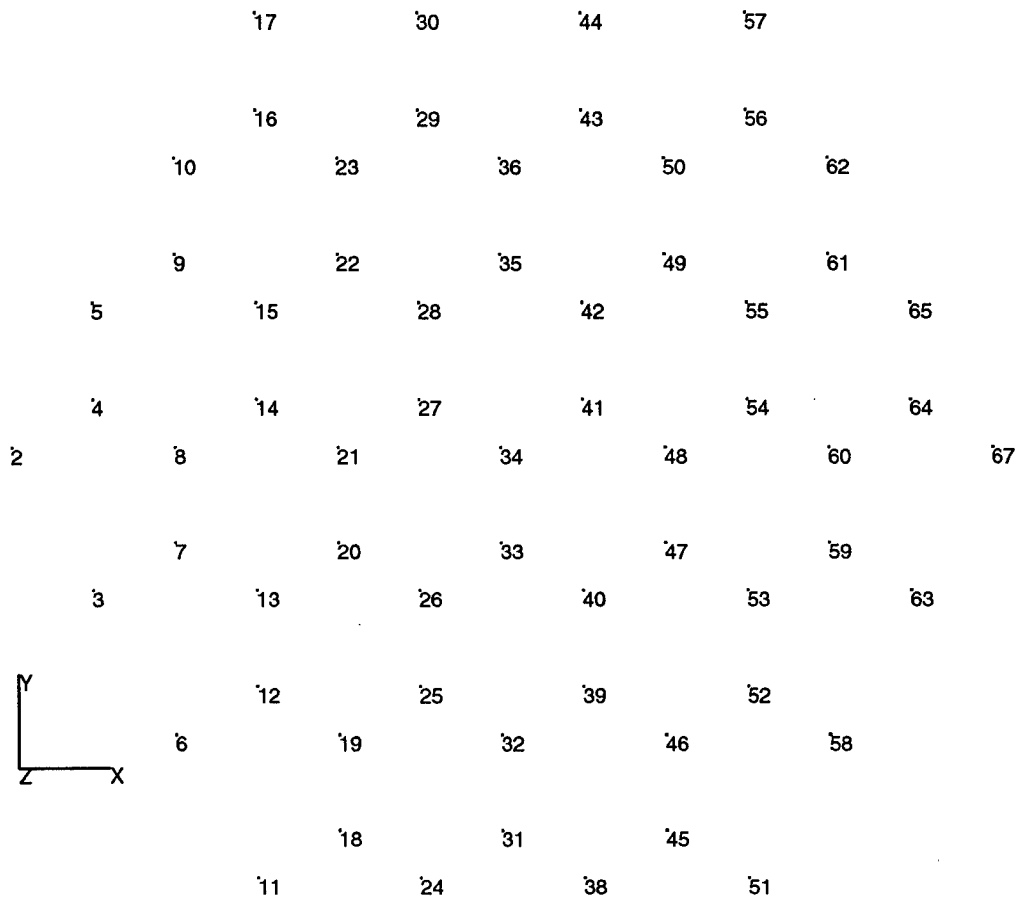


Figure 3: The SPICE Bulkhead Nodes (Lockheed)



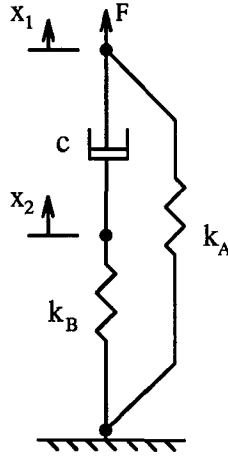


Figure 4: Model of a D-Strut

using the smallest possible number of D-struts. An intermediate step in achieving this goal is the characterize the effect of damping struts placed in each of the strut locations and rank their effectiveness. Once strut locations are ranked, the most promising combinations were tried, each with modal damping performance index being optimized with respect to viscous damping coefficient according to the simple expression of the Maxwell structural model. In the work all damping struts possess identical values of viscous damping coefficient  $c$ , but individual values of  $c$  could also be handled fairly easily with this model.

#### 4. MAXWELL MODEL OF A DAMPING STRUT

The first step in modeling the structural damping was to model the physical damping element which is to be inserted between given nodes of the SPICE bulkhead. These elements are called (Honeywell) D-struts [2][3], and can be modeled as two springs—one in “series” and one in “parallel”—with a dashpot. See Figure 4. This arrangement implies that the damping value of the dashpot can be “tuned” to optimize the damping, as was shown in references [3] and [4]. The same mathematical model is developed briefly below.

The transfer function relating force to displacement at the free end of the model in Figure 4 is

$$\frac{F}{X}(s) = k_A + \frac{k_B c s}{k_B + c s}. \quad (1)$$

Here  $s$  denotes the Laplace transform.

In order to simplify analysis, define the stiffness ratio

$$\kappa = \frac{k_B}{k_A},$$

the damper constant

$$\omega_B = \frac{k_B}{c},$$

the damper ratio

$$r = \frac{\omega}{\omega_B} = \frac{\omega c}{k_B},$$

and

$$j = \sqrt{-1}$$

where  $\omega$  is the forcing frequency. It is apparent that  $r$  increases proportionally with either  $\omega$  or  $c$ .

Substituting  $s = j\omega$  into the transfer function results in

$$\frac{F}{X}(\omega) = k_A \left( 1 + \kappa \frac{j\omega}{\omega_B + j\omega} \right) \quad (2)$$

$$\frac{F}{X}(r) = k_A \left( 1 + \kappa \frac{r^2}{1+r^2} + \kappa \frac{jr}{1+r^2} \right). \quad (3)$$

The loss factor, or structural damping factor,  $\eta$ , which is related to the fraction of the total strain energy in the element which is dissipated each cycle, can be written as the ratio of the imaginary part to the real part of the transfer function [5]. The loss factor is then

$$\eta(r) = \frac{\kappa \frac{r}{1+r^2}}{1 + \kappa \frac{r^2}{1+r^2}}. \quad (4)$$

Note that at  $r$  (or  $c$  or  $\omega$ ) = 0, the loss factor  $\eta = 0$ . As  $r$  is increased,  $\eta$  takes on some positive value which diminishes to zero as  $r \rightarrow \infty$ .

Setting the derivative of  $\eta$  with respect to  $r$  equal to zero results in the maximum loss factor

$$\eta^* = \frac{\kappa}{2\sqrt{1+\kappa}} \quad (5)$$

which occurs at

$$r^* = \frac{1}{\sqrt{1+\kappa}}. \quad (6)$$

Note that this depends only upon the spring ratio,  $\kappa$ .

In [4] and [5], it was further shown that for a system including mass and moderate damping, the conventional damping ratio in the equation of motion

$$\ddot{x} + 2\zeta\omega_o\dot{x} + \omega_o^2x = 0 \quad (7)$$

can be approximated by

$$\zeta \approx \frac{\eta}{2} \quad (8)$$

at frequency near  $\omega_o$ . This establishes a relationship between loss factor and damping coefficient.

## 5. MAXWELL MODEL OF STRUCTURAL MODES

### 5.1. Modes of a Structure

A structure can be modeled mathematically as

$$M\ddot{x} + C\dot{x} + Kx = [0] \quad (9)$$

where  $M$  is the mass matrix,  $C$  is the damping matrix,  $K$  is the stiffness matrix, and  $x(t)$  is the vector of displacements. Dot notation represents differentiation with respect to time.

When  $C = [0]$ , a real eigenvalue analysis results in a modal matrix  $\Phi$  of eigenvectors  $\phi_i$  and a set of eigenvalues  $\lambda_i$  which decouple the modes of the system into equations of the form [6]

$$\phi_i^T M \phi_i \ddot{q}_i + \phi_i^T K \phi_i q_i = 0 \quad (10)$$

where  $q_i$  is the  $i$ th member of the vector  $q$  containing generalized coordinates, and

$$x = \Phi q . \quad (11)$$

If  $\phi_i$  are mass-normalized,

$$\ddot{q}_i + \omega_i^2 q_i = 0 \quad (12)$$

and

$$\lambda_i = \omega_i^2 .$$

If  $C \neq [0]$ , then Equation 9 leads to the eigenvalue problem [6]

$$(\tilde{\lambda}_i^2 M + \tilde{\lambda}_i C + K) \tilde{\phi}_i = 0 \quad (13)$$

where  $\tilde{\lambda}_i$ ,  $\tilde{\phi}_i$ , and  $\tilde{q}_i$  are, in general, complex. The modal damping can then be computed as

$$\tilde{\zeta}_i = -\frac{Real[\tilde{\lambda}_i]}{\omega_i} . \quad (14)$$

The modal damping coefficients,  $\tilde{\zeta}_i$ , must be computed in order to optimize the passive damping of the SPICE bulkhead structure, as mentioned earlier. Complex eigenvalue analysis is computationally expensive, so a method to accurately estimate the modal damping coefficients can save much effort. The modal strain energy method [8] is able to estimate modal damping produced by (in-line) damping struts which replace existing struts. However, it is not able to predict modal damping produced by damping struts placed in (diagonal) locations where no strut exists in the original structure. However, the modes of the structure can be considered Maxwell models, and each damping coefficient estimated in relation to the loss factor of that mode's Maxwell model. This procedure is the basis of the damping estimation of this report, and is described below.

## 5.2. Description of Maxwell Model of a Structure

If one was to insert a damper into an arbitrary location in a large structure (Figure 5) and look at the resulting damping ratio as the damping  $c_i$  of the strut increased from zero to infinity, one might expect the damping ratio of a given mode to start at zero, increase to some point, and then "level off." One might also expect the damping ratio to decrease and again approach zero as the value of  $c_i$  approached infinity. This provides the intuitive basis for modeling each mode of a structure as a Maxwell model.

Figure 6 shows the Maxwell model of a mode  $j$  of a structure. In this figure,  $k_{Aj}$  represents the modal stiffness of the undamped mode; with a mass-normalized system,  $m = 1$ , and  $k_{Aj} = \omega_j^2$ . Any parallel stiffness  $k_p$  in the damper must be included in  $k_{Aj}$ . The symbol  $k_{Bij}$  represents compliances within the structure which influence the way the series components of the  $i$ th d-strut,  $c_i$  and  $k_i$ , affect the modal damping ratio. The  $\alpha_{ij}$  is an influence coefficient which "scales" the values of  $c_i$  and  $k_i$  for each mode  $j$  and each strut  $i$ .

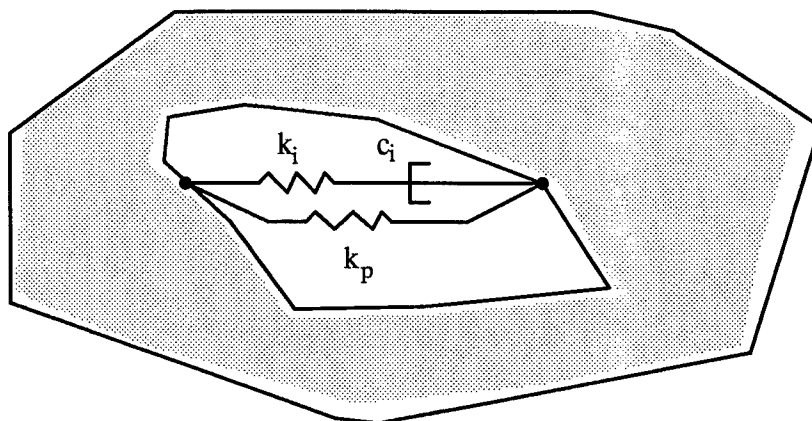


Figure 5: Model of a Damper Inserted into a Structure

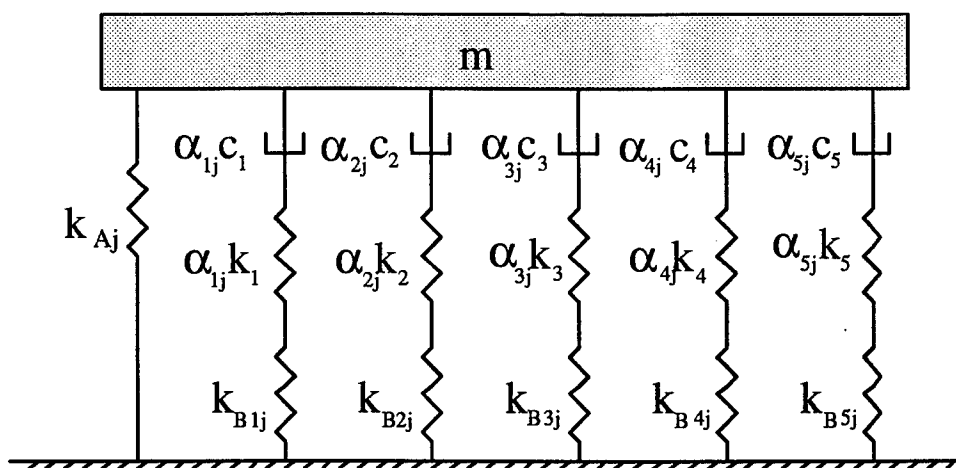


Figure 6: Maxwell Model of a Structural Mode

In this model,  $k_{Aj}$ ,  $k_{Bij}$ , and  $\alpha_{ij}$  must be determined for each mode and strut location. Then  $k_i$  and  $c_i$  can be set to optimize a performance index using damping ratios estimated through the modal loss factor of the model.

### 5.3. Modal Loss Factor of Maxwell Model of Structure

The treatment in this section parallels that of the Maxwell model of the strut presented earlier. Now looking only at the stiffness and damping components, the transfer function relating force to displacement  $q_{ij}$  of a given mode  $j$  is

$$\frac{F_j}{Q_j}(s) = k_{Aj} + \sum_{i=1}^n \frac{k_{sij}\alpha_{ij}c_i s}{k_{sij} + \alpha_{ij}c_i s} \quad (15)$$

where  $n$  is the number of struts. Making the substitutions

$$\kappa_{sij} = \frac{k_{sij}}{k_{Aj}} \quad (16)$$

$$\omega_{Bij} = \frac{k_{sij}}{\alpha_{ij}c_i} \quad (17)$$

$$r_{ij} = \frac{\omega}{\omega_{Bij}} \quad (18)$$

$$s = j\omega \quad (19)$$

results in

$$\frac{F_j}{Q_j}(\omega) = k_{Aj} \left( 1 + \sum_{i=1}^n \kappa_{sij} \frac{j\omega}{\omega_{Bij} + j\omega} \right) \quad (20)$$

or

$$\frac{F_j}{Q_j}(r_{ij}) = k_{Aj} \left\{ 1 + \sum_{i=1}^n \left( \kappa_{sij} \frac{r_{ij}^2}{1 + r_{ij}^2} + \kappa_{sij} \frac{j r_{ij}}{1 + r_{ij}^2} \right) \right\} \quad (21)$$

Taking modal loss factor to be the ratio of the real to imaginary parts of this transfer function,

$$\eta_{ij}(r_{ij}) = \frac{\sum_{i=1}^n \kappa_{sij} \frac{r_{ij}}{1 + r_{ij}^2}}{1 + \sum_{i=1}^n \kappa_{sij} \frac{r_{ij}^2}{1 + r_{ij}^2}} \quad (22)$$

It is stated without proof that the maximum loss factor estimate for a given mode  $j$  occurs when  $c_i$  is set such that

$$r_{ij} = r_{i+1,j}$$

$$i = 1, 2, 3, \dots, n-1.$$

It occurs at

$$r_j^* = \frac{1}{\sqrt{1 + \sum_{i=1}^n \kappa_{sij}}} \quad (23)$$

at a value of

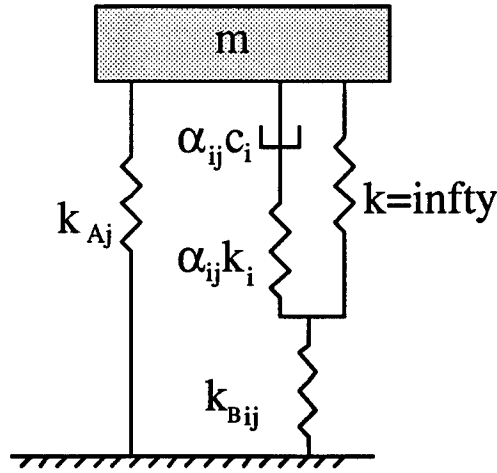


Figure 7: Model for Finding  $k_{Bij}$

$$\eta_j^*(r_{ij}) = \frac{\sum_{i=1}^n \kappa_{sij}}{2\sqrt{1 + \sum_{i=1}^n \kappa_{sij}}} \quad (24)$$

Finding the optimal damping is not so simple if the performance index includes several modes.

#### 5.4. Methods of Finding Properties of the Maxwell Structural Model

##### 5.4.1. Method of Infinite Stiffnesses

In order to find the values of  $k_{Aj}$ ,  $k_{Bij}$ , and  $\alpha_{ij}$ , for a given mode  $j$  and strut location  $i$ , the following procedure can be used. First, a real eigenvalue analysis is performed on the structure alone without any added spring elements in parallel to damper locations included. Mass normalization is used, so that for mode  $j$ ,

$$k_{Aj} = \omega_{Aj}^2 \quad (25)$$

The value of  $k_{Bij}$  is found by placing a spring of infinite stiffness into the damper location, as Figure 7 shows. Assuming that the modal mass does not change, the value of  $k_{Bij}$  is determined by assuming that  $k_{Aj}$  and  $k_{Bij}$  act in parallel. With  $\omega_{Bij}^2$  from the resulting real eigenvalue analysis,

$$k_{Bij} = \omega_{Bij}^2 - k_{Aj} \quad (26)$$

Next, the value of the influence coefficient  $\alpha_{ij}$  must be found. A spring of stiffness identical to that of  $k_i$  is placed across the damper location. This is equivalent to placing an infinitely-stiff spring in parallel with damper  $c_i$ . A third real eigenvalue analysis is done. Using the series-parallel properties of the springs in the model, a new spring equivalent to the combination of  $k_i$  and  $k_{Bij}$  is found.

$$\omega_{sij}^2 - k_{Aj} = k_{sij} = \frac{\alpha_{ij} k_i k_{Bij}}{\alpha_{ij} k_i + k_{Bij}} \quad (27)$$

With  $k_i$  having been selected and  $k_{Bij}$  and  $k_{sij}$  known,

$$\alpha_{ij} = \frac{1}{k_i} \frac{k_{sij} k_{Bij}}{(k_{Bij} - k_{sij})} \quad (28)$$

Performing two more real eigenvalue analyses per strut and repeating the same computations completely determine the Maxwell model of the structure for any mode being analyzed. Knowing the values of  $k_{Aj}$ ,  $k_{Bij}$ , and  $\alpha_{ij}$  of the structure along with specifying  $k_i$  provide enough information to compute  $\kappa_{sij}$ .

#### 5.4.2. Method of Finite Stiffnesses

A second method of finding the values  $\kappa_{sij}$  and  $\alpha_{ij}$  for the Maxwell structural model is to analyze the shifts in frequencies caused by individually inserting two massless springs of known stiffness.

The parallel stiffness of the mode,  $k_{Aj}$ , is given by Equation 25. Insertion of the value of the known strut stiffness  $k_i$  and computation of the frequencies determine  $k_{sij}$  (and so  $\kappa_{sij}$ ) by Equation 27. The value of  $\alpha_{ij}$  is found by repeating the frequency analysis with a massless spring of another known stiffness,  $k_{di} = dk_i, d > 0$ . If  $\omega_{sdi}^2$  is the resulting eigenvalue, then

$$\omega_{sdi}^2 - k_{Aj} = k_{sdi} . \quad (29)$$

Then

$$\alpha_{ij} = \frac{d-1}{dk_i} \left( \frac{k_{dsi}k_{si}}{k_{si} - k_{dsi}} \right) . \quad (30)$$

It is recommended that  $d$  is set to  $1/2$ . Then

$$\alpha_{ij} = \frac{1}{k_i} \left( \frac{k_{dsi}k_{si}}{k_{si} - k_{dsi}} \right) . \quad (31)$$

The value  $k_{Bij}$  does not need to be found unless one desires to vary  $k_i$  in applying the model, in which case  $k_{Bij}$  is evaluated by rearranging Equation 27.

Like the method of infinite stiffnesses, this method requires  $2n + 1$  real eigenvalue analyses, where  $n$  is the number of strut locations being analyzed.

#### 5.4.3. Method of Frequency Slopes

This method reduces the number of eigenvalue analyses necessary to characterize the Maxwell structural model by extracting information about  $\alpha_{ij}$  from the eigenvalue analysis of the original structure (very slightly modified). It consists of placing springs of very small stiffness ( $k_2 = 2$  units, which is relatively close to zero) in all of the candidate locations for the eigenvalue analysis on the original structure and setting each  $\alpha_{ij}$  equal to the mass-normalized strain energy in mode  $j$  for the element  $i$  of stiffness  $k_2$ . The value  $k_{Aj}$  and  $k_{sij}$  are determined as in the method of finite stiffnesses and the method of infinite stiffnesses, except the springs of stiffness  $k_2$  are included in all computations.

The method of extracting  $\alpha_{ij}$  is substantiated as follows. Insert a spring  $k_i$  into location  $i$  of the structure. The Maxwell model predicts the frequency  $j$  of the structure to change to

$$\omega_{ij}^2 = k_{Aj} + \frac{\alpha_{ij}k_i k_{Bij}}{\alpha_{ij}k_i - k_{Bij}} . \quad (32)$$

The derivative of this eigenvalue with respect to  $k_i$  at  $k_i = 0$  is

$$(\omega_{ij}^2)'|_{k_i=0} = \alpha_{ij} . \quad (33)$$

Next, take the derivative of the eigenvalue problem (mass-normalized) with respect to massless  $k_i$ .

$$(\omega_{ij}^2)'|_{k_i=0} = \phi_j^T K' \phi_j, \quad (34)$$

where  $K'$  is the derivative of the stiffness matrix with respect to  $k_i$ . (For a one-dimensional problem, one can visualize that the non-zero elements of  $K'$  would be  $K'(i, i) = K'(j, j) = -K'(i, j) = -K'(j, i) = 1$ .) The right side of Equation 34 can also be seen as the square of the axial modal displacement across element  $k_i$ . The strain energy in  $k_i$  is then

$$SE_{ij} = \frac{1}{2} k_i \phi_j^T K' \phi_j = \frac{1}{2} k_i \alpha_{ij}. \quad (35)$$

Any other method of computing the value of the square of the axial modal displacements between nodes would be acceptable means of finding  $\alpha_{ij}$ . The method of frequency slopes requires only  $n+1$  real eigenvalue analyses to characterize the Maxwell model of the structure.

### 5.5. Ranking of Struts for Optimization

The ultimate objective of the passive damping treatment is to achieve a minimum value of modal damping in each of several target modes with the fewest number of damping struts. In order to do this, one must compute and optimize the damping values for many combinations of struts. The Maxwell model makes this much easier to do. In order to search intelligently for the best combinations, struts should be ranked according to their ability to contribute to overall modal damping. The basis for this ranking is now developed.

One possible performance index for optimizing the damping of a combination of damping struts is to do a weighted summation of the damping achieved in each of the target modes. This optimization problem can be stated as follows.

Maximize with respect to  $c$

$$J = \sum_{j=1}^m w_j \eta_j \quad (36)$$

subject to

$$\eta_{ij}(r_{ij}) = \frac{\sum_{i=1}^n \kappa_{sij} \frac{r_{ij}}{1+r_{ij}^2}}{1 + \sum_{i=1}^n \kappa_{sij} \frac{r_{ij}^2}{1+r_{ij}^2}}, \quad (37)$$

$$r_{ij} = \frac{\alpha_{ij} \omega_j c}{k_{sij}}, \quad (38)$$

and

$$\kappa_{sij} = \frac{k_{sij}}{k_{A_j}}, \quad (39)$$

where  $w_j$  is a set of modal weighting factors chosen by the designer. Due to the complexity of the expression for  $\eta_{ij}$  (Equation 37), it is difficult to completely separate out the contribution of each strut  $i$ . However, the denominator is relatively insensitive to the contribution of any one strut, so the numerator is used as a ranking criterion. The resulting estimation of the relative contribution of each strut is given by

$$\tilde{J}_i = \max_c \left( \sum_{j=1}^m w_j \kappa_{sij} \frac{r_{ij}}{1+r_{ij}^2} \right). \quad (40)$$



## 6. COMPUTATIONS

### 6.1. Bulkhead with One Damping Strut

In order to check the accuracy of the Maxwell model in predicting modal damping, the effect of placing one damping strut into the NASTRAN model of the SPICE lab version of the bulkhead (translated from the Patran file blkcorr.pat) was studied. This model is shown in Figure 2.

The damper was inserted between nodes 51 and 52 of the bulkhead. Since this position spans across two corners of an octahedral cell near the edge of the bulkhead, this is a diagonal damper.

The values of  $\kappa_{sij}$  and  $\alpha_{ij}$  were obtained by means of the method of zero slopes. For frequencies at which there was more than one mode, the values of  $\alpha_{ij}$  obtained were allocated totally to the mode with the higher value of  $\kappa_{sij}$ . Using the Maxwell model, the estimated values of modal loss factor for 13 modes ranging in frequency from 50 to 150 Hz were computed as a function of damping coefficient  $c$  of the strut and plotted in Figure 8.

For comparison purposes, modal damping coefficients ( $2\zeta$ ) were also computed using NASTRAN. They are plotted as symbols. Note that the values computed by the Maxwell model correlate to the "correct" values computed by complex eigenvalue analysis with a high degree of accuracy.

### 6.2. Bulkhead with Five Damping Struts

To see how well the Maxwell model predicts the modal damping achieved by multiple damping struts, a similar test was run, this time including five damping struts in the structure.

In-line damping struts were included between the node pairs 56-61, 6-18, 27-28, 28-34, and 29-30 of the SPICE lab finite element model of the bulkhead (see Figure 2).

Again, the values of  $\kappa_{sij}$  and  $\alpha_{ij}$  were found by the method of frequency slopes. This time, for modes of duplicated eigenvalues, the values of  $\kappa_{sij}$  at a given frequency were re-allocated so that they were proportional to those of the corresponding  $\alpha_{ij}$ . The Maxwell model was used to compute loss factor for each mode as a function of  $c$ , and the values were plotted in Figure 9.

Then the values of modal damping coefficient as computed by complex eigenvalue analysis were plotted. This time, the modes 3, 4, and 5, which were not repeated eigenvalues, correlated well, but the modes at repeated eigenvalues were not predicted as accurately. Apparently, the damping was not distributed properly among each set of duplicated modes.

However, the value of the performance index, the summation of the modal loss factors for all 13 modes evaluated, was plotted in Figure 10. Although damping prediction was not allocated correctly between modes of repeated eigenvalues, the summation of the damping values correlates well with the "correct" summation obtained through complex eigenvalue analysis. The prediction due to the Maxwell model compares favorably to that of the modal strain energy method [8] (the static stiffness of damping strut in the computation was not decreased to compensate for the increased dynamic stiffness due to the presence of the viscous damper in the modal strain energy method computation).

LOSS FACTOR ESTIMATED BY MAXWELL MODEL  
Alpha Estimated by Strain Energy of Springs of k=2  
Case 5152; All-or-Nothing Kappas and Alphas

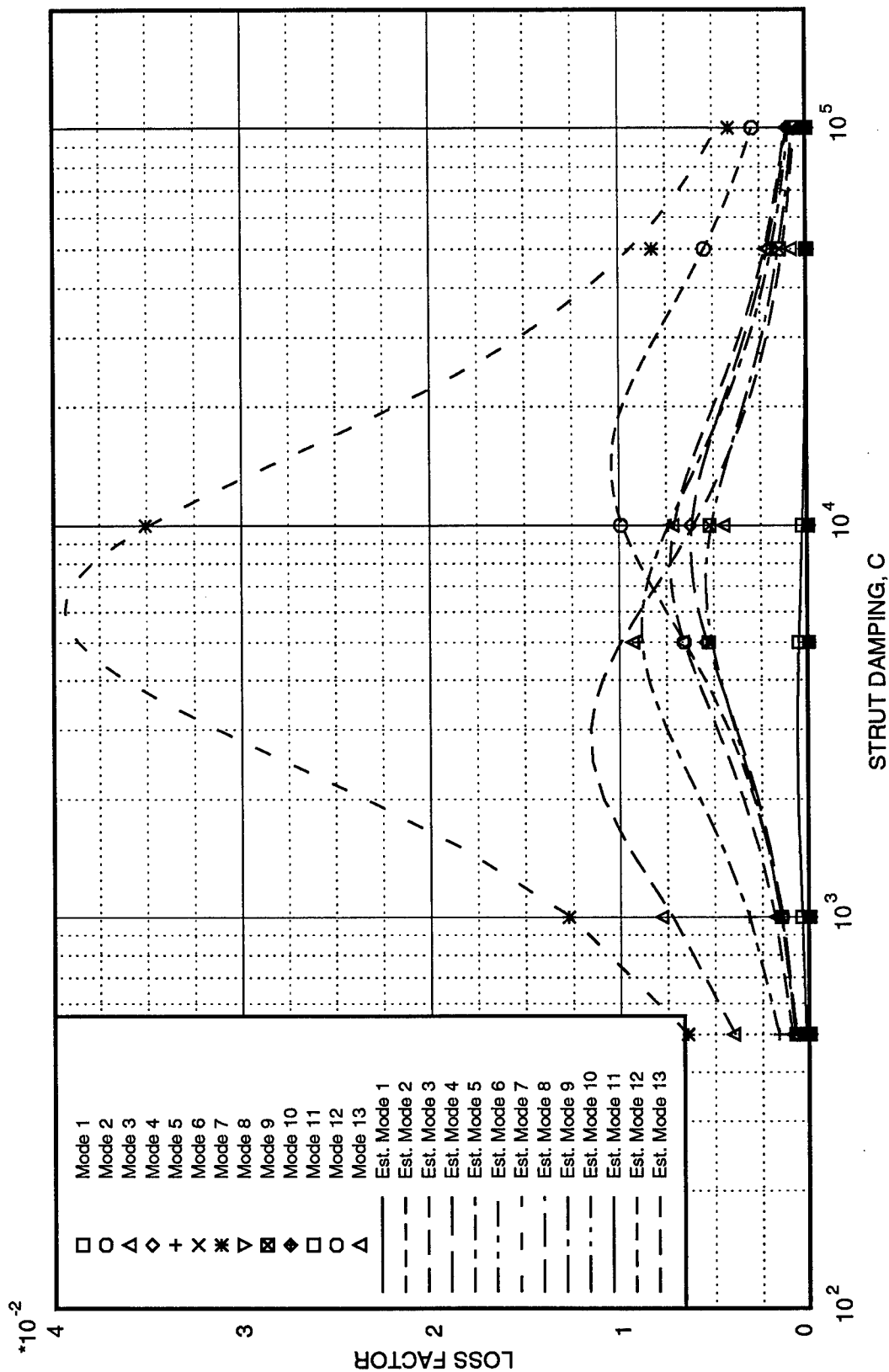


Figure 8: Modal Loss Factor Due to Damper in Location 5152

# LOSS FACTOR ESTIMATED BY MAXWELL MODEL

Alpha Estimated by Strain Energy of Springs of  $k=2$   
Case 1: 5661, 618, 2728, 2834, 2930

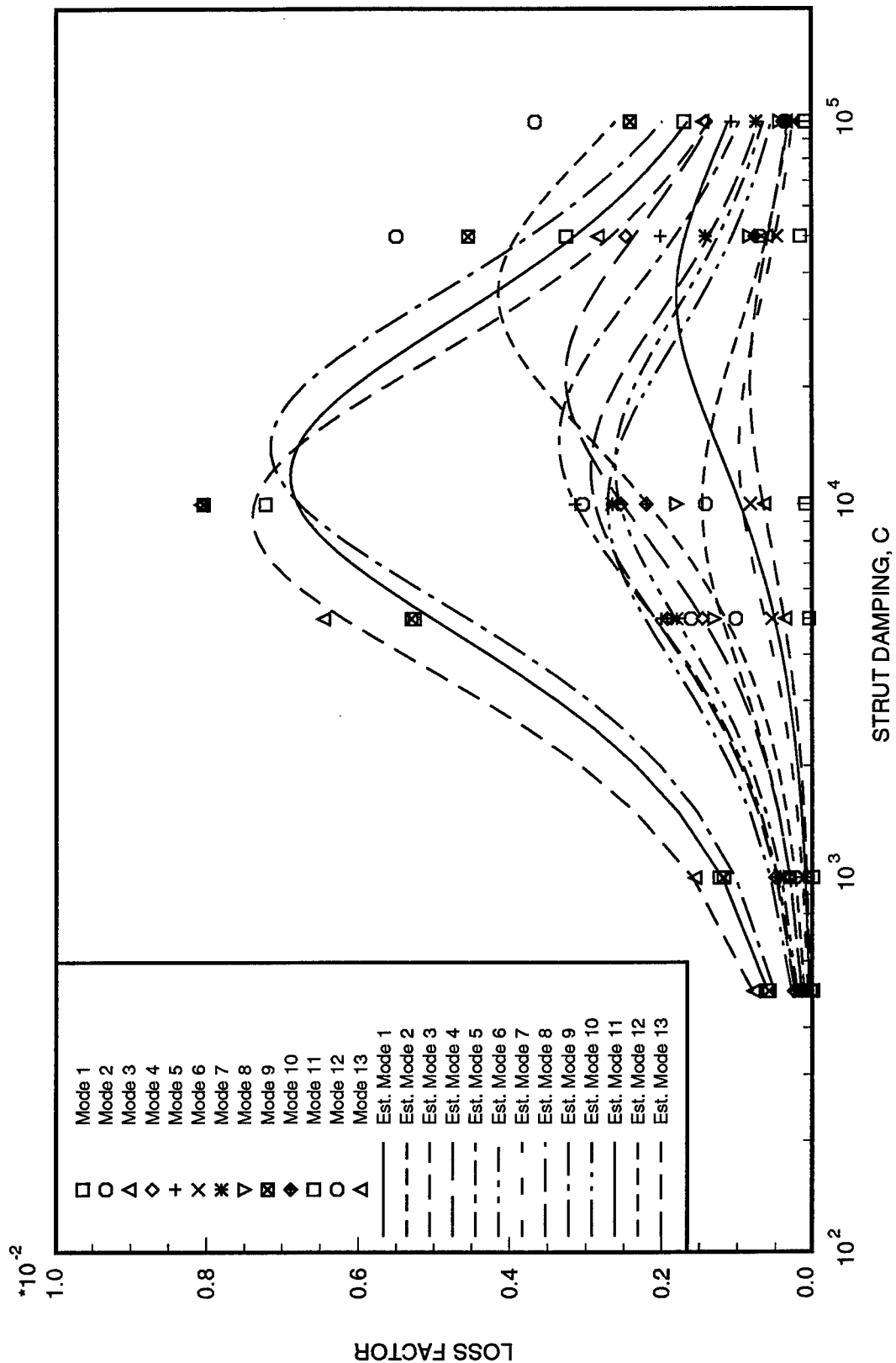


Figure 9: Loss Factor for Five Struts  
1-18

# SUM OF DAMPING FOR ALL MODES Case 1: 5661, 618, 2728, 2834, 2930

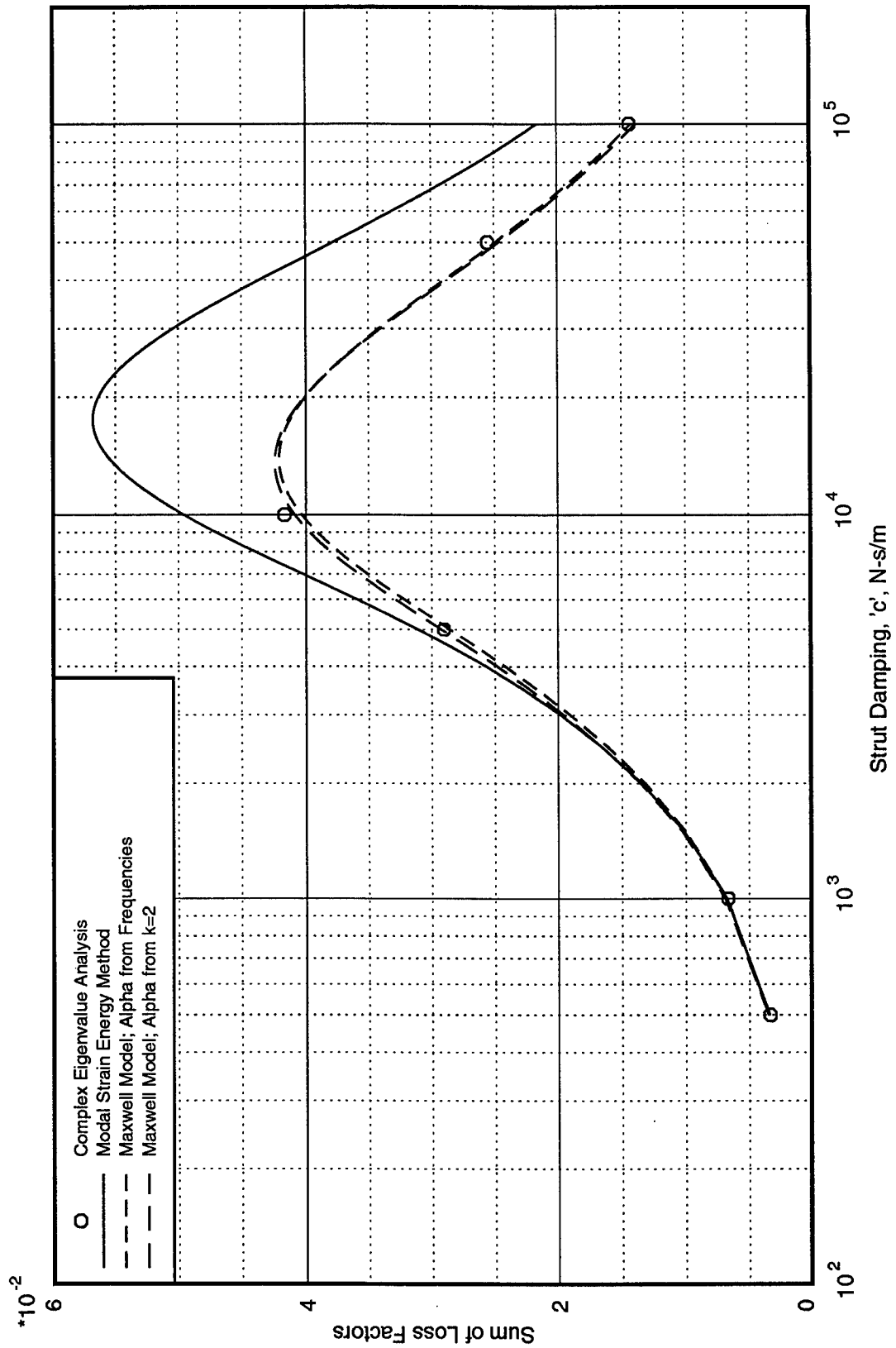


Figure 10: Summation of Modal Loss Factors

### 6.3. Optimization on the SPICE Structure

In order to begin to solve the problem of optimizing damping of the whole SPICE structure, the Maxwell model was characterized, the strut locations were ranked according to effectiveness, and the structural damping was optimized for a set of the dampers in the "best" locations.

#### 6.3.1. Characterization of the Maxwell Model

The values of  $\kappa_{sij}$  and  $\alpha_{ij}$  for the Maxwell model of the Lockheed version of the whole SPICE structure (NASTRAN model spc5a.dat, see Figure 3 for the bulkhead node numbers) were found by the method of frequency slopes.

The whole SPICE structure contains many more low-frequency modes than the bulkhead model alone, and it has many more nodes, making eigensolutions more expensive. Target modes for high passive damping have been identified for the SPICE structure; however, it has also been observed that passive damping of about 2% for all modes in a HAC-LAC control system would be highly desirable. Therefore, the 50 modes between 41 and 103 Hz were chosen for study.

Because of time limitations and symmetry, only  $\frac{1}{3}$  of the strut locations were studied. The strut locations which made a  $0^\circ$  or  $30^\circ$  angle with the  $x$  axis when viewed from the vertical ( $z$  axis) line of sight were chosen.

The same values of  $k_i$  (series stiffness of the damping strut) were used in this study of the whole SPICE structure as were used in the present examples. That value for in-line strut locations was  $17.16 \times 10^6 \frac{N}{m}$ , based on total series stiffness achieved on proposed D-struts [9]. This includes compliance of bellows. Since the diagonal strut locations are longer by a factor of  $\sqrt{2}$ , and it was assumed that the same cross-section would be used, and  $k_i$  for these locations was set to  $12.13 \times 10^6 \frac{N}{m}$ .

Once the values of  $\kappa_{sij}$  and  $\alpha_{ij}$  for each strut  $i$  and mode  $j$  had been obtained, the effectiveness of each strut was evaluated according to the criteria outlined in Section 5.5. The modified index  $\tilde{J}_i$  was optimized over  $c$  for each strut, and the struts were ranked according to the maximum values of  $\tilde{J}_i$ .

Table 1 shows the highest-ranking node pairs along with the maximums of  $\tilde{J}_i$  and the corresponding value of  $c$ . Those locations with positive cell numbers are diagonal locations which span one of the 27 octahedral cells of the bulkhead. Note that the nine most highly ranked locations are diagonal.

### 6.4. Optimization Example on the SPICE Structure

This section describes the optimization of damping on the SPICE structure for an example combination of strut locations.

#### 6.4.1. Method

Since the Maxwell model of the SPICE structure has been fully characterized of the modes and strut locations in question, it is easy to use the damping expression Equation 37 to optimize damping for various combinations of struts or performance criteria. In this section, the performance criteria comprising the summation of modal damping in all the measured modes is used. The contribution of each mode is weighted equally.

In order to find the value of  $c$  (same for all struts) at which the performance criterion  $J$  was at a maximum,

Table 1: Strut Ranking

Strut Rank	Strut Number	Node 1	Node 2	Cell Number	$\tilde{J}_i^*$	$c^* (\frac{N_s}{m})$
1	97	45	58	22	7.761e-02	1.591e+04
2	84	16	30	9	6.983e-02	1.629e+04
3	96	43	57	21	6.612e-02	1.534e+04
4	102	59	67	27	6.177e-02	1.356e+04
5	86	20	34	11	5.154e-02	2.287e+04
6	87	22	36	12	4.731e-02	1.836e+04
7	94	39	53	19	4.609e-02	1.814e+04
8	95	41	55	20	4.275e-02	2.655e+04
9	100	52	63	25	3.786e-02	2.185e+04
10	6	6	19	0	3.641e-02	3.559e+04
11	9	46	58	0	3.565e-02	3.514e+04
12	23	3	21	0	3.447e-02	3.136e+04
13	68	21	27	0	3.304e-02	3.418e+04
14	92	33	48	17	3.267e-02	2.457e+04
15	83	14	28	8	3.170e-02	1.987e+04
16	77	23	29	0	3.163e-02	2.703e+04
17	54	46	52	0	3.159e-02	2.704e+04
18	89	27	42	14	3.136e-02	2.473e+04
19	88	25	40	13	3.134e-02	1.972e+04
20	59	40	47	0	2.749e-02	2.559e+04
21	71	28	35	0	2.745e-02	2.553e+04
22	69	42	49	0	2.744e-02	2.624e+04
23	62	26	33	0	2.711e-02	3.327e+04
24	63	48	54	0	2.674e-02	2.657e+04
25	80	7	21	5	2.459e-02	1.939e+04
26	82	12	26	7	2.445e-02	1.934e+04
27	98	47	60	23	2.419e-02	1.903e+04
28	93	35	50	18	2.325e-02	1.854e+04
29	65	34	41	0	2.296e-02	3.978e+04
30	12	39	52	0	2.247e-02	3.381e+04
31	81	9	23	6	2.232e-02	1.982e+04
32	74	15	22	0	2.223e-02	2.834e+04
33	91	31	46	16	2.202e-02	1.965e+04
34	56	32	39	0	2.194e-02	2.809e+04
35	57	53	59	0	2.002e-02	3.119e+04

a program was written which used the values of  $\kappa_{sij}$  and  $\alpha_{ij}$  for all the strut locations in question, evaluated  $J$  at various values of  $c$ , and found the maximum value  $J^*$  along with  $c^*$  by means of the method of golden section. Since  $J$  is quick to evaluate, repeated searches can be done very quickly, but for the purposes of this report, only a few combinations were considered.

Once the optimal value of  $c$  was found, the computed values of  $\eta_j$  for several modes were compared to data point acquired using complex eigenvalue analysis, in a range near the maximum value of  $J$ .

#### 6.4.2. Results

The results of the set of damping optimizations performed using the Maxwell model are given in Table 1. First, the strut locations are given. The next column shows the maximum values of damping and the values of viscous damping  $c$  at which the maximum was achieved. Strut locations may be correlated with nodal locations by referencing Appendix A, where the first column is the strut location and the second and third columns represent nodal locations. Note that the combination which achieved the highest damping comprised the five highest-ranking strut locations.

Table 2: Optimizations of Various Combinations

Trial Number	First Strut	Second Strut	Third Strut	Fourth Strut	Fifth Strut	$J^*$	$c^* (\frac{Ns}{m})$
1	97	84	96	102	86	3.1890e-01	1.6095e+04
2	87	94	95	100	92	2.0283e-01	2.1213e+04
3	6	9	23	68	77	1.6903e-01	3.2086e+04
4	97	84	96	6	9	2.7010e-01	1.9454e+04

Due to time constraints, the optimizations for these combinations of struts using the Maxwell structural model were not confirmed by finite element complex eigenvalue analysis.

Table 3 shows the amount of time it took to analyze the entire SPICE structure for the following cases.

1. Real eigenvalue analysis for 50 modes.
2. Optimization of four (4) sets of five (5) struts over 50 modes using the Maxwell Model.
3. Complex eigenvalue analysis for five (5) struts and one (1) mode.

Since the computations performed different functions and ran on different machines, their run times cannot be compared head-to-head; these data are included for the purpose of qualitative comparison only.

Table 3: Run Times (minutes:seconds)

Solution	Machine	Real	User	System
Real Eigenvalue	SGI r4000 Indigo	41:10.	17:00.	3:06.
Optimization	DEC 5000/25	5.8	3.0	0.9
Complex Eigenvalue	DEC 5000/133	285:19.	73:07.	42:07

## 7. Conclusions and Recommendations

### 7.1. Usefulness of the Maxwell Model

In order to speed the search for optimal combinations of either in-line or diagonal strut viscous damping in a large space structure like SPICE, an accurate method of predicting the approximate values of modal damping without complex eigenvalue analysis was developed. The modal strain energy method is very useful, but does not allow one to predict the effect of damping struts placed in diagonal locations. The Maxwell structural model can handle in-line and diagonal damper locations equally well and results in an expression for modal loss factor estimation which is quickly evaluated and optimized.

### 7.2. Effectiveness of Diagonal Damping Struts

One of the key motivations for this research is to evaluate how well dampers placed in diagonal locations contribute to modal damping. When damping locations were ranked according to each strut's estimated contribution to modal damping based on the Maxwell model, diagonal strut locations ranked higher than locations collinear with an existing structural member.

### 7.3. Recommended Future Work

The optimization criterion used in this report was a simple summation of the modal loss factors for various modes. Once values of  $\kappa_{sij}$  and  $\alpha_{ij}$  for all locations of the structure have been found, this criterion could be restated to best facilitate control of the structure. That is, specific modes could be targeted for high damping, or all modes could be required to attain low-level damping, with little increase in the performance index due to higher damping in a given mode. With any such restatement of the optimization problem, the optimization search could proceed based on the Maxwell model without more eigenvalue analysis.

If passive damping is incorporated into the SPICE structure for future control experiments, it is recommended that damping struts be placed in diagonal damping locations with the highest damping performance index.

Modes at duplicated frequencies presented problems in the Maxwell model. The proper way of distributing  $\kappa_{sij}$  and  $\alpha_{ij}$  between sets of such modes for a given combination of struts should be developed.

The Maxwell structural model itself provides an interesting perspective on the effects which local changes have on structural vibrational characteristics. It should be augmented to include changes in point mass. The simplicity with which the model predicts or is determined by frequency shifts could make it useful in structural control or failure detection systems.

## 8. ACKNOWLEDGMENT

The help of Mr. R. Ninneman, Phillips Lab VT/SA, Air Force, in suggesting this problem is acknowledged.

## References

- [1] Blankenship, R.M., Breakwell, J.A., Dettmer, J.W., Hamilton, B.D., Richardson, J.M., 1992, "The SPICE Program," *Proceedings, Rocky Mountain Guidance and Control Conference*, Keystone, Colorado, Feb.



- [2] Yiu, Y.C., Davis, L.P., Napolitano, K., and Ninneman, R., 1992, "Design, Analysis, and Testing of High Frequency Passively Damped Struts," *Fifth NASA-DoD Controls-Structures-Interaction Technology Conference*, Lake Tahoe, Nevada, March.
- [3] Davis, L.P., and Ginter, S.D., 1991, "An Advanced D-Strut," *Proceedings, Damping '91*, USAF Wright Lab., Flight Dynamics Dir., WL-TR-91-3078, San Diego, California, Feb. (reprint courtesy Honeywell).
- [4] Thompson, T.J. and Baumgarten, J.R., 1993, "A Brief Study of Passive Viscous Damping for the SPICE Bulkhead Structure," *Proceedings, The 14th Biennial Conference on Mechanical Vibration and Noise (ASME)*, Albuquerque, New Mexico, Sept.
- [5] Thomson, William T., 1981, *Theory of Vibration with Applications*, 2nd ed., p.75
- [6] Yiu, Y.C., and Weston, E.L., 1992, "Computation of Complex Modes in Reduced Vector Subspaces," *33rd AIAA/ASME/ASCE/AHS/ASC Structures, Structural Dynamics, and Materials Conference*, Paper 92-2515, Dallas, Texas, Feb.
- [7] Young, M.I., 1989, "On Passive Spot Damping Anomalies," *Proceedings of Damping '89*, USAF Wright Aeronautical Lab., WRDC-TR-89-3116, West Palm Beach, Florida, Feb., pp.DCB1-DCB14
- [8] Johnson, C.D., and Kienholz, D.A., 1982, "Finite Element Prediction of Damping in Structures with Constrained Viscoelastic Layers," *AIAA Journal*, Vol. 20, No. 9, pp. 1284-1290, Sept.
- [9] Yiu, Y.C., Davis, L.P., and Kienholz, D.A., 1992, "Development of High Frequency Passively Damped Struts," Final Report for Subtask 02-08, Task 4, Space Integrated Controls Experiment Program, Contract No: F29601-89-C0015, pp. 23-26, April.

## A. LIST OF STRUT LOCATIONS

The file shown below lists the node pairs for the strut locations of the SPICE model which was investigated. The second and third columns contain the node numbers, and the fourth column gives the cell number (non-zero for diagonal struts).

1	11	24	0
2	24	38	0
3	38	51	0
4	18	31	0
5	31	45	0
6	6	19	0
7	19	32	0
8	32	46	0
9	46	58	0
10	12	25	0
11	25	39	0
12	39	52	0
13	3	13	0
14	13	26	0
15	26	40	0
16	40	53	0
17	53	63	0
18	7	20	0
19	20	33	0
20	33	47	0
21	47	59	0
22	2	8	0
23	3	21	0
24	21	34	0
25	34	48	0
26	48	60	0
27	60	67	0
28	4	14	0
29	14	27	0
30	27	41	0
31	41	54	0
32	54	64	0
33	5	15	0
34	15	28	0
35	28	42	0
36	42	55	0
37	55	65	0
38	9	22	0
39	22	35	0
40	35	49	0
41	49	61	0
42	10	23	0
43	23	36	0
44	36	50	0
45	50	62	0

46	16	29	0
47	29	43	0
48	43	56	0
49	17	30	0
50	30	44	0
51	44	57	0
52	38	45	0
53	24	31	0
54	46	52	0
55	11	18	0
56	32	39	0
57	53	59	0
58	19	25	0
59	40	47	0
60	60	64	0
61	6	12	0
62	26	33	0
63	48	54	0
64	13	20	0
65	34	41	0
66	55	61	0
67	3	7	0
68	21	27	0
69	42	49	0
70	8	14	0
71	28	35	0
72	50	56	0
73	2	4	0
74	15	22	0
75	36	43	0
76	5	9	0
77	23	29	0
78	10	16	0
79	4	15	3
80	7	21	5
81	9	23	6
82	12	26	7
83	14	28	8
84	16	30	9
85	18	32	10
86	20	34	11
87	22	36	12
88	25	40	13
89	27	42	14
90	29	44	15
91	31	46	16
92	33	48	17
93	35	50	18
94	39	53	19
95	41	55	20
96	43	57	21

97	45	58	22
98	47	60	23
99	49	62	24
100	52	63	25
101	54	65	26
102	59	67	27

ANALYTICAL AND EXPERIMENTAL DOSIMETRY TECHNIQUES FOR  
CALIBRATING LOW ENERGY X-RAY RADIATION SOURCE

Raymond D. Bellem  
Associate Professor  
Department of Electrical Engineering

Embry-Riddle Aeronautical University  
3200 Willow Creek Rd.  
Prescott, AZ 86301

Final Report for;  
Summer Research Extension Program  
Phillips Laboratory

Sponsored by:  
Air Force Office of Scientific Research  
Bolling Air Force Base, Washington, D.C.

and

Embry-Riddle Aeronautical University

April 1994

# ANALYTICAL AND EXPERIMENTAL DOSIMETRY TECHNIQUES FOR CALIBRATING A LOW ENERGY X-RAY RADIATION SOURCE

Raymond D. Bellem  
Associate Professor  
Department of Electrical Engineering  
Embry-Riddle Aeronautical University

## Abstract

This paper describes the methodology used to calibrate a large-volume continuous X-ray irradiation test chamber. Analytical tools and experimental dosimetry techniques were developed to map the radiation field intensity and resulting material dose deposition profiles for a tungsten target bremsstrahlung X-ray spectrum with end point energies up to 160 keV. Three detector types, an X-ray vacuum diode, silicon PIN diodes, and PMOS FETs, were used to measure radiation intensity and dose deposition in silicon devices. CEPXS and PHOTCOEF electron-photon transport codes were used to calculate the X-ray tube spectrum and the radiation transport and energy deposition in the detectors. Calculated and experimental diode detector responses correlated within 30% over the full energy range. PMOS FETs were used to establish dose-deposition correlation with Cobalt-60 ionizing radiation exposure. The results of this effort provide dosimetry and analysis tools needed to perform ionizing radiation testing of large area ( $0.25\text{m}^2$ ) electronic subsystems.

# ANALYTICAL AND EXPERIMENTAL DOSIMETRY TECHNIQUES FOR CALIBRATING A LOW ENERGY X-RAY RADIATION SOURCE

R.D. Bellem

## I. INTRODUCTION

Testing the radiation tolerance of microelectronic parts and subsystems in the high total dose ionizing radiation environments required for some military space and missile systems dictates the use of large, expensive simulators. High dose-rate Cobalt-60 gamma sources or pulsed linear electron accelerators are commonly used for qualification testing of electronic parts. Due to their convenience, safety and lower cost, low energy X-ray sources are being used, where possible, for hardness assurance screening on individual parts. Many device manufacturers are screening their microelectronic parts for radiation tolerance using low energy X-ray test systems such as the Aracor Model 4100 Automatic Semiconductor Irradiation System [1]. The Aracor Model 4100 uses a bremsstrahlung X-ray spectrum with a 10 keV mean photon energy and a 50 keV maximum energy. This system is designed to perform high total dose irradiations for production screening of semiconductor devices at the wafer fabrication stage. The Aracor system is limited, however, to irradiating a maximum area of a few square centimeters. A larger X-ray test facility would be needed however to test larger structures such as circuit boards and small subsystems. Such an X-ray system would reduce the cost of evaluation when compared to the larger simulators now in use such as Cobalt-60 and flash X-ray.

A large shielded X-ray test cell which can illuminate entire electronic assemblies has been designed and built by the USAF Phillips Laboratory, PL/VTET in Kirtland AFB, NM. This facility is referred to as LEXR (Low Energy X-Ray). The radiation source for LEXR

is a Phillips Model MCN 165 X-ray Unit which uses a tungsten target anode with input power levels up to 3.6k. The facility provides ionizing-radiation dose rates in the range from 0.1-1000 krad(Si)/min with spectral end-point energies between 20 and 160 keV. LEXR was developed to perform ionizing radiation research and evaluation of microelectronic and photonic devices, circuits and subsystems in accordance with the methods outlined in ASTM F-1467 [2].

The facility is depicted in Figure 1. and consists of a lead-lined room with the X-ray source exposing a test area of approximately 0.25 m<sup>3</sup>.

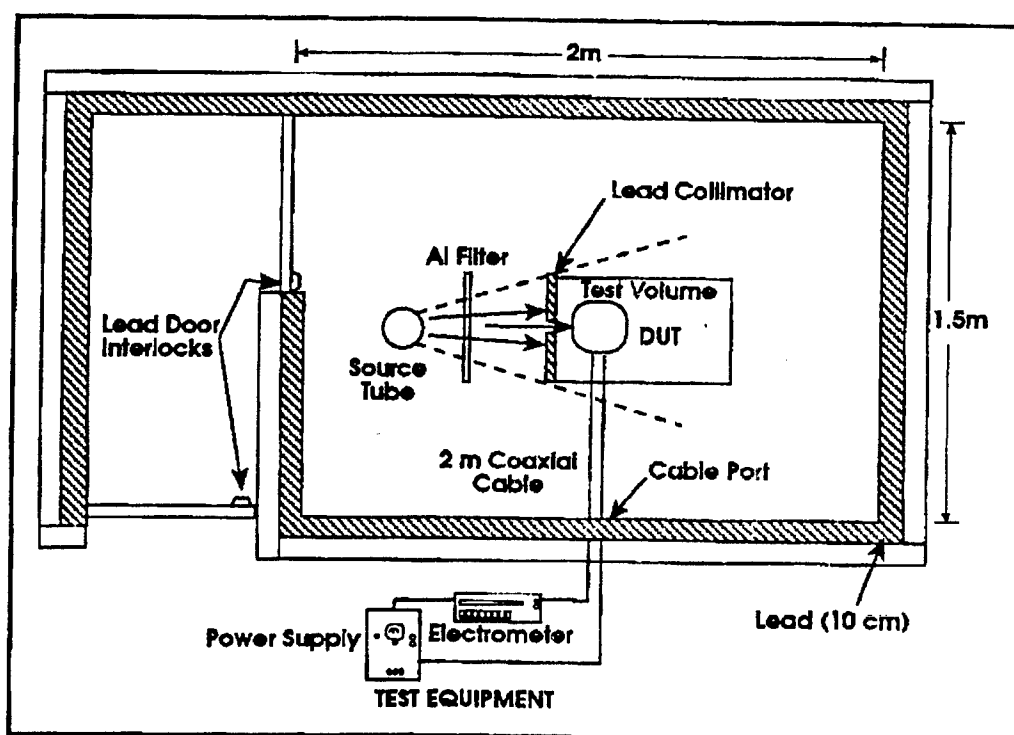


Figure 1: LEXR and Test Equipment Layout



The technical challenge inherent implementing use of the test set-up in Fig. 1 is to develop the analytical and experimental dosimetry techniques needed to calibrate the radiation field over the entire test volume. Figure 2 depicts this problem broken down into three distinct physical processes: a) the bremsstrahlung spectrum generation in the tube and the accurate spectral characterization of the X-ray beam exiting the Beryllium window; b). the air attenuation associated with the X-ray radiation transport, collimation and accurate characterization of the resultant spectrum incident on the detector; c) the interaction of the incident spectrum with the detector (example of Ge detector in shown Figure 2) or an electronic device under test and the resultant energy deposition in the detector.

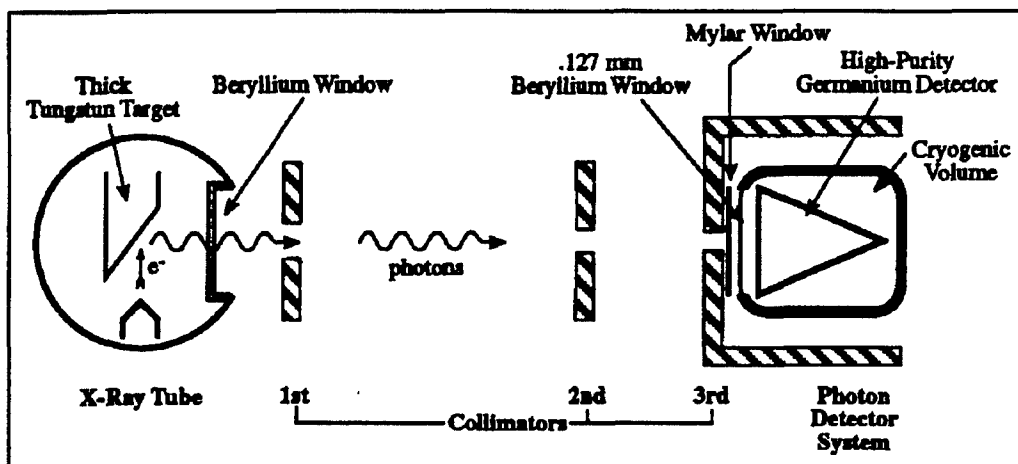


Figure 2: LEXR Problem (Generation, Propagation and Deposition)

The overall objective of the work described in this paper was to establish calibration procedures and techniques for the X-ray facility over the full energy range of the x-ray source (end-point energies up to 160 keV). Analytical tools were selected, developed and demonstrated which provide an accurate means to calculate the generation, propagation and

deposition of the X-ray energy. Measurement techniques were developed to measure dose and dose-rate under test conditions of interest. X-ray detectors were selected which are sensitive to the tube spectrum and their response can be correlated directly to the material systems to be studied (Si and SiO<sub>2</sub>). These X-ray detectors are calibrated and their measurements are used to establish valid dosimetry and to provide confidence in the analysis tools being used. All techniques developed will allow the use of the radiation test methods as set forth in ASTM F-1467, Standard Guide for X-ray Testers [2]. All dosimetry was traceable to NIST measurement standards wherever possible.

## II. APPROACH

Some of the experimental and theoretical analyses used in this effort were reported in the authors previous report under the AFOSR Summer Program and at the 1993 and 1994 HEART Conferences [3,4,5,]. Some of this published work will be included in the following discussion for completeness. Figure 3 shows the steps and the interrelationships of the calculations and the experimental work followed in this effort. Each step in the process described in Fig. 3 will be discussed in detail in the next several sections.

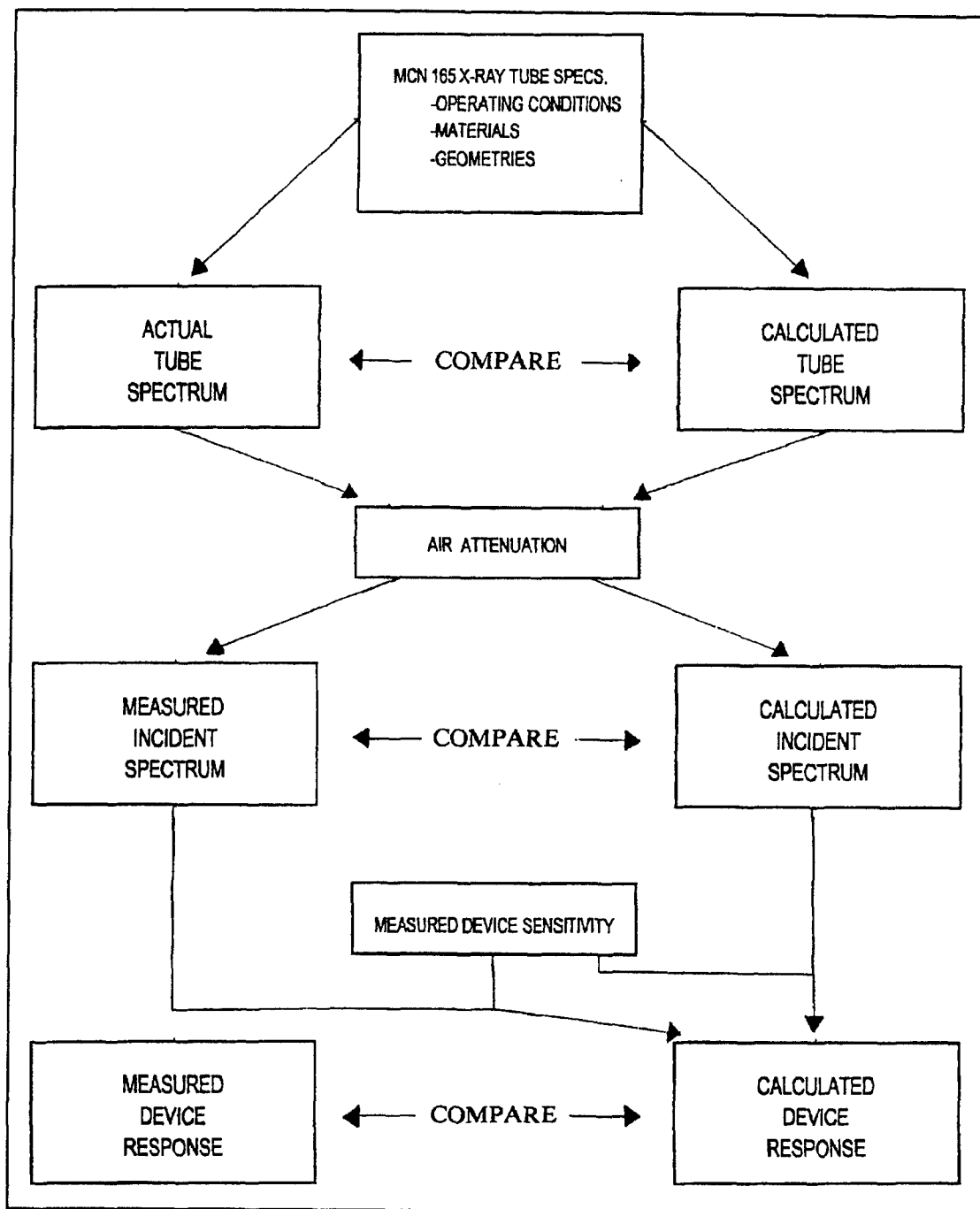


**Figure 3: Calculation/Measurement Flowchart Required for Complete Characterization of LEXR Facility.**

The theoretical calculations followed a four step process:

- (1) Calculate the MCN 165 x-ray tube output differential energy spectrum using proven electron-photon transport codes.
- (2) Calculate the spectral attenuation during radiation transport from the tube output window to the detector using proven electron-photon transport codes.
- (3) Calculate the detector response using calibrated detector sensitivity and the calculated incident spectrum from (2).
- (4) Compute  $^{60}\text{Co}$ -equivalent dose-rates in X-ray chamber.

The experimental portion of this effort consists of the following steps:

- (5) Calibrate the detector response using a calibrated standard.
- (6) Measure the detector responses in the x-ray chamber for different spectra and location (vary tube voltage, current, and distance).
- (7) Correlate theoretical and calculated detector responses.

### III. DETECTORS

There were three radiation detectors selected for this effort: a) an x-ray vacuum diode (XRD), b) a silicon PIN diode, and c) PMOS Field-Effect Transistors (FETs).

The X-ray vacuum diode selected, referred to as the SEMIRAD (Secondary Electrons Mixed Radiation Dosimeter), is an evacuated chamber constructed to collect secondary electron emissions from a gold film cathode within the chamber [6]. The SEMIRAD is applicable for high-intensity radiation environments; its use at low dose rates is not recommended because of its low sensitivity. The SEMIRAD is ideally suited to measure a constant high intensity X-ray beam with radiation intensities at energies up to 160 keV. A

cross-sectioned illustration of the construction of the SEMIRAD is shown in Figure 4.

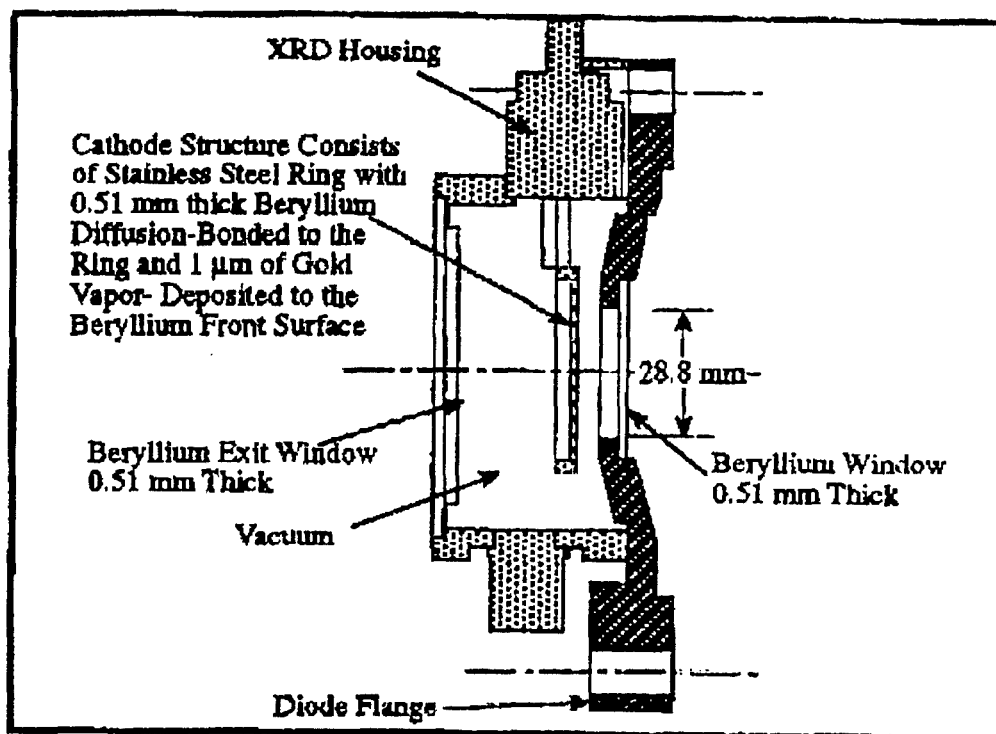


Figure 4: SEMIRAD X-Ray Diode (SRD-SN018) Illustration

The PIN diodes (Quantrand 010PIN025) used in this effort were purchased from Aracor. This type diode has been used successfully for dose-rate measurements in the Aracor 4100 machine for several years. Calibration data was provided with the diodes which have a nominal area of 10 mm<sup>2</sup> and an effective collection depth of about 25  $\mu$ m. The diodes provide a direct readout of the current corresponding to dose-rate and can accurately measure dose rates up to 200 krad(Si)/min.

The PMOS FETs used in this evaluation were manufactured by the AT&T Allentown Microelectronics Facility. The devices, which were packaged by the Sandia National Laboratories, are typical of hardened MOS technology using polysilicon gate: SiO<sub>2</sub>:Si

structures with a hardened gate oxide thickness less than 20 nm. The devices were fabricated in a test strip with a variety of gate lengths and widths. Four transistors were selected with a gate width of 30  $\mu\text{m}$  and gate lengths of 1.50, 1.75, 2.00, and 5.00  $\mu\text{m}$ .

#### IV. THEORETICAL CALCULATIONS

Calculated and measured spectra of commonly used X-ray tubes, similar to the Phillips MCN 165 have been reported in the literature [7,8]. Dozier at the Naval Research Laboratory (NRL) calculated the MCN 165 tube spectrum using the tube specifications as input parameters to the NRL TUBE electron-photon transport program [9]. The accuracy of the code, when compared with experimental data for tungsten targets, is within 30% point-by-point and within 10% for the integral intensity [7].

Differential energy spectra were calculated for anode voltages of 20, 30, 50, 60, 80, 100, 120, 140 and 160 KV. (Note: CEPXS can also be used to calculate the X-ray tube output spectrum. Appendix I will present the results of the CEPXS calculations however the TUBE spectral calculations have greater fidelity and will be used to obtain results and comparisons.)

Figure 5 shows plots of the calculated spectral data using TUBE for three of the spectra used in the analysis reported in this paper. These differential energy spectra data are then entered as input data into the PHOTCOEF and CEPXS electron-photon transport codes for further calculations.

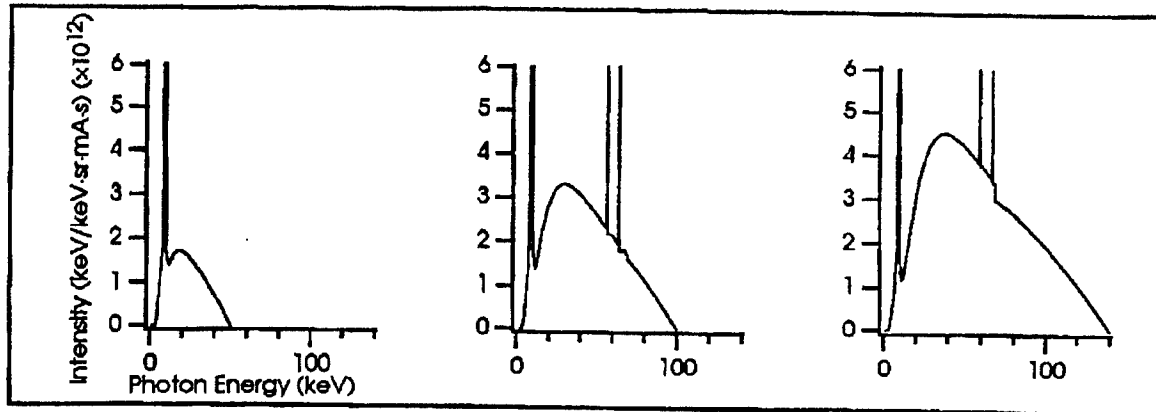


**Figure 5:** Calculated X-Ray Tube Differential Spectra using TUBE for Anode Voltages of 50, 100 and 140 kV (L-Lines Truncated).

The intensity units in Figure 5 were selected so that the data is independent of detector distance and X-ray tube current. More familiar units can be obtained by scaling the intensity data as shown in Equation(1):

$$\Phi \left( \frac{\text{keV}}{\text{keV} \cdot \text{cm}^2 \cdot \text{s}} \right) = \Phi \left( \frac{\text{keV}}{\text{keV} \cdot \text{sr} \cdot \text{mA} \cdot \text{s}} \right) I_t d^{-2} \quad (1)$$

where

$I_t$  = X-ray tube current(mA)

$d$  = source-detector distance(cm)

The spectrum at the x-ray tube face, as calculated by Dozier and shown in Figure 5, was the starting point for all transport computations.

CEPXS and PHOTCOEF were chosen to calculate attenuation and dose deposition in the detector structures [10,11]. PHOTCOEF is a 1D semi-empirical code which runs under DOS. PHOTCOEF is used to calculate shielding and dose deposition profiles. CEPXS is a

1D deterministic code used to calculate shielding and dose deposition. In both cases, the X-ray tube spectrum and a description of the intervening materials were input to the programs. The codes then computed the spectrum that was incident on the detector. Since the intensity of the incident spectrum is a function of the X-ray tube current, anode voltage and the distance from the source, several calculations were required to simulate the variety of experimental conditions.

The device response is then calculated by integrating the incident spectrum with the experimentally measured detector sensitivity. A computer program was written (Shown in Appendix II) to integrate the product of these two quantities, that is:

$$I_d = A_a \int_0^{50 \text{ keV}} \Phi'(E) S(E) dE \quad (2)$$

where

$\Phi'(E)$  = Calculated incident spectrum (keV/keV•cm<sup>2</sup>•s)

$A_a$  = Aperture area (cm<sup>2</sup>)

$S(E)$  = Diode sensitivity data (C/keV)

$I_d$  = Diode current (A)

By combining the results of all three steps above, the response of the XRD PIN was calculated for each spectrum at predetermined locations within the test cell.

## V. DETECTOR CALIBRATION

The first experimental step was to calibrate the detectors using a source which could



be traced to NIST standards. The XRD and the PIN diode sensitivity curves were determined by irradiating the devices at the SAIC/DNA facility in Albuquerque. Bremsstrahlung-induced K-fluorescent monochromatic x-rays from a selection of target materials were used in the SAIC/DNA facility to obtain the sensitivity curves.

The SEMIRAD diode was calibrated from 4.96 keV (the K-line for Ti) up to 115 keV (the K-line for U) by measuring the current response[11]. A plot of the sensitivity data obtained for the SEMIRAD diode calibration is shown in Figure 6.

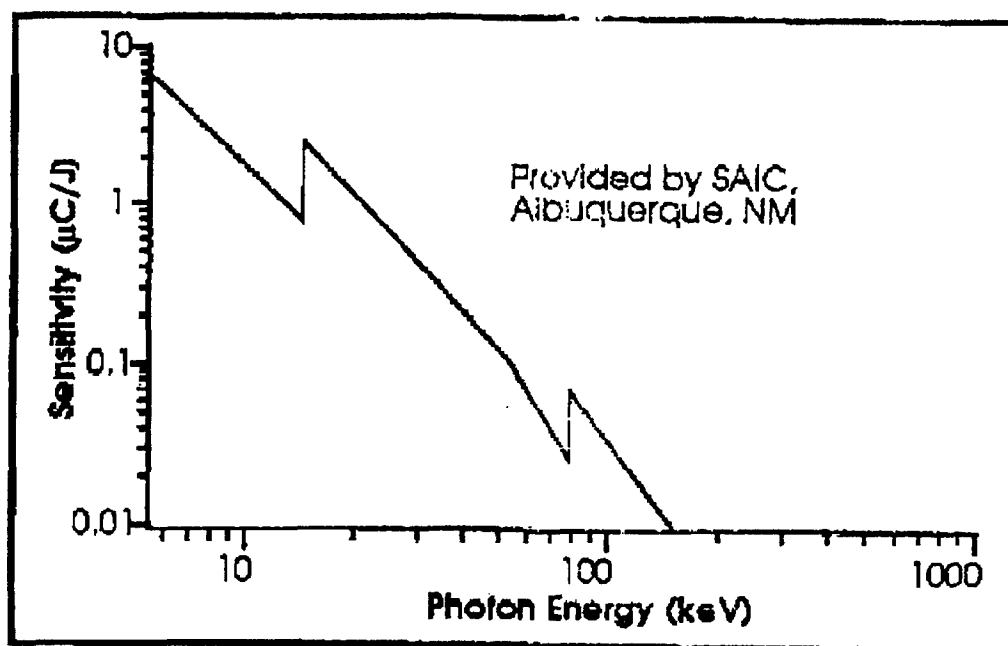


Figure 6: SEMIRAD X-Ray Diode (XRD-SN018)  
Sensitivity versus Photon Energy

The calibrated errors are estimated at less than 5% over the energy range from 5 keV to 40 keV with the error increasing to about 10% as the energy approaches 160 keV [12]. Below 5 keV, errors are introduced in the sensitivity due to the M-lines of Au, however this

error will have no effect in our calculations since most of the energy in the spectrum below 5 keV is removed by filtering.

The PIN diode was calibrated at the SAIC/DNA facility from 4.96 keV to 50 keV.

The PIN diode response is shown in Figure 7.

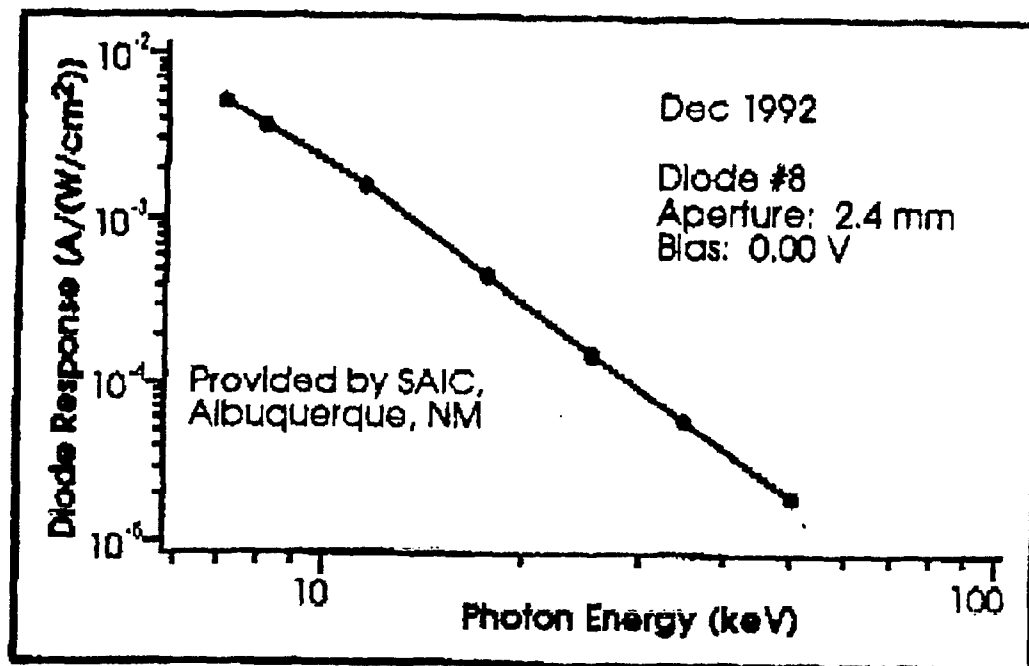


Figure 7: ARACOR PIN Diode (CS1003) Sensitivity versus Photon Energy

The PMOS transistors were calibrated at the Phillips Laboratory (PL) free-field  $^{60}\text{Co}$  gamma facility using the MIL-STD 883C Test Method 1019.4 procedures [13]. It was not necessary to use a Pb/Al container since the level of the low-energy scattered radiation was not sufficient to cause dosimetry errors. The PL  $^{60}\text{Co}$  facility is calibrated annually in accordance with ASTM Standard Practice E668 [14]. Facility calibration is traceable to NIST through a calibrated ionization chamber. The PMOS devices were delidded to minimize enhancement effects due to gold flashing on the lids. Electrical parameter

measurements were made on the devices before and after each irradiation. Devices were biased with -5 V on the gate during irradiations. The elapsed time between exposure and post-exposure measurements was less than 5 minutes. Gate threshold voltage shifts ( $\Delta V_{th}$ ) versus total dose were recorded for dose-rates of 6, 12 and 20 krad(Si)/min. A representative plot of these data are presented in Figure 8.

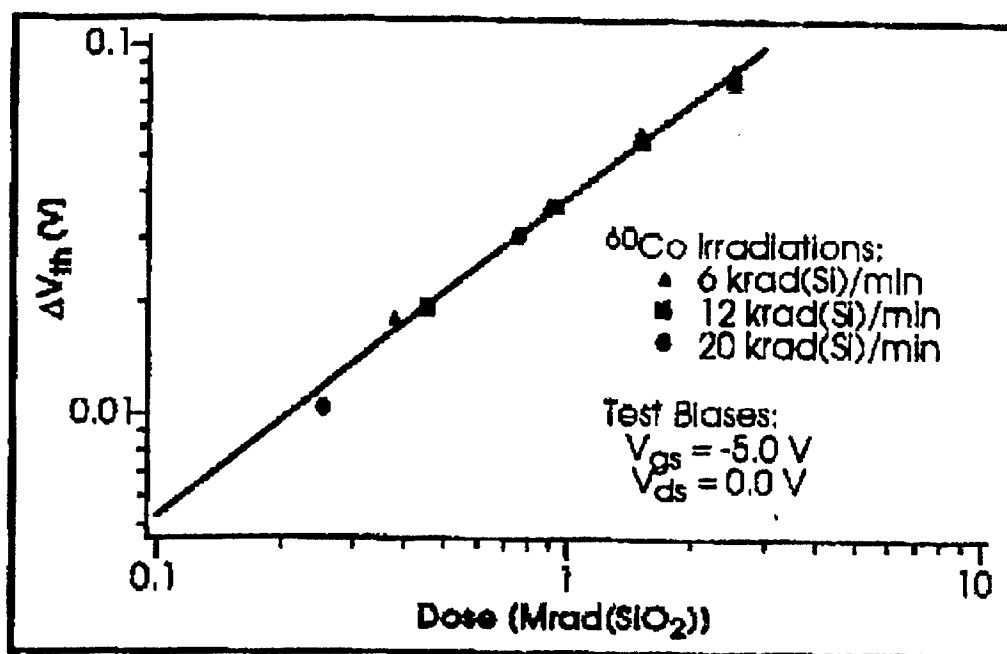


Figure 8:  $\Delta V_{th}$  versus <sup>60</sup>Co Dose for P-Channel FETs

The equation for calculating  $\Delta V_{th}$  as a function of applied <sup>60</sup>Co dose was determined using a curve fit routine as:

$$\Delta V_{th} = 0.038 D^{0.87}$$

where

$V_{th}$  = Threshold voltage (volts)

D = Dose in rad (Si)

## VI. DEVICE RESPONSE MEASUREMENTS

The final experimental measurement is to directly measure the response of the devices to the x-ray spectrum by measuring the current in the SEMIRAD and PIN and the voltage shift in the FET under constant radiation exposure. The experimental setup for these measurements was shown in Figure 1. One inch thick lead collimators were used in front of the devices so that only the active device areas were exposed. The remainder of the detectors were shielded with 0.6 cm of lead to reduce the effects of x-ray scatter within the cell. For the SEMIRAD measurements, a 25  $\mu\text{m}$  piece of mylar was placed in front of the SEMIRAD beryllium window to eliminate low-energy ( $< 5$  keV) electrons that scattered off the lead collimator. Data was taken with and without the aluminum filter shown in the figure. ASTM F-1467 prescribes a .0025 cm aluminum filter to attenuate photons with energies below 5 keV. It was found, however, that air provided sufficient attenuation of those photons for distances greater than 25 cm. In-flux responses were recorded with a Keithley electrometer using cables shielded against radiation-generated noise. Data was taken for anode voltages of 50, 100 and 140 kV at detector distances of 25, 50 and 75 cm. A similar test set-up was used for collecting the PMOS data with additional equipment to provide the proper bias in-flux.

## VII. RESULTS

SEMIRAD DIODE - A plot of the SEMIRAD diode current for different x-ray tube anode voltages at distances of 25, 50 and 75 cm is shown in Figure 9. Note that, as expected, the diode current is a linear function of the X-ray tube current.

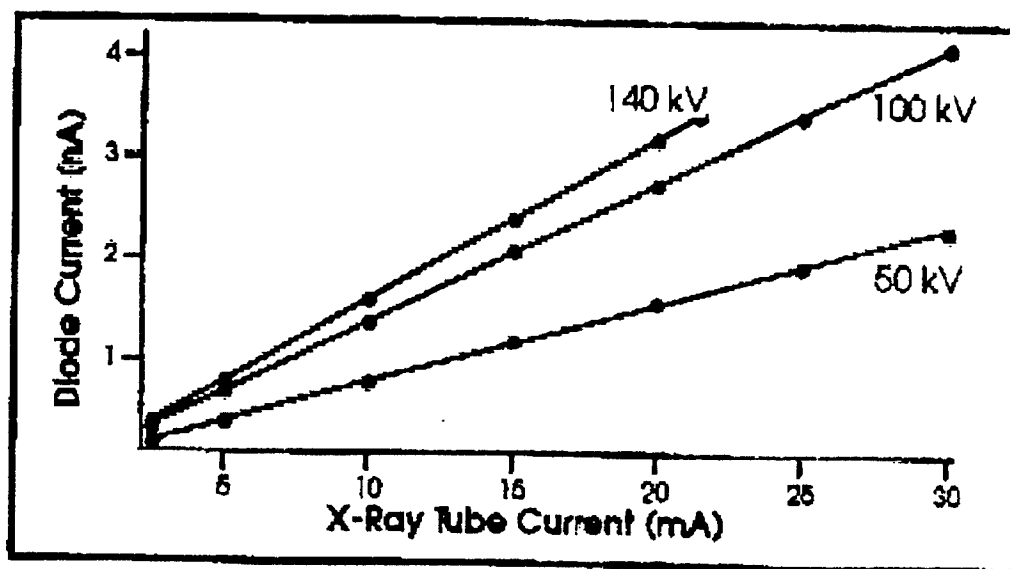


Figure 9: SEMIRAD Diode Current for X-Ray Tube Voltages

Using the theoretically calculated X-ray diode currents from Eqn. 2, a comparison between calculated and measured diode currents at 25 mA for 25, 50 and 75 cm is shown in Table I. The diode currents also demonstrated the expected  $1/d^2$  intensity attenuation where  $d$  is the tube/detector distance.

Table I. Calculated and Measured XRD Response

Anode voltage (keV)	Tube Current (mA)	Detector Distance (cm)	Calc'd Diode Current (pA)	Measured Diode Current (pA)	Relative Difference (%)
50	25	25	1546	1957	21.0
50	25	50	330.8	420	21.2
50	25	75	129.5	167	22.5
100	25	25	2500	3440	27.3
100	25	50	555.6	704	27.3
100	25	75	223.9	306	26.8
140	25	25	2264	3210	29.6
140	25	50	511.5	721	29.0
140	25	75	208.6	293	28.8

A combination of errors can be introduced in the calculations based on estimated errors discussed earlier. An error analysis was done using the following error estimates: 20% for the differential spectral intensity across the calculated spectrum, 10% for the diode sensitivity curves and 2% for the numerical integration procedure. Using standard error analysis techniques, the maximum overall error in the calculations was estimated to be 23%. Measurement errors were estimated to be less than 10%. The relative error between calculated and measured values as shown in Table I is relatively constant at approximately 30%, which is within the estimation described above.

PIN DIODE - In the previous paper[4], the PIN diode was found to be an accurate dosimeter for measuring dose rate in silicon. Due to the noise limitations in calibrating the PIN above

50 keV and the potential for PIN degradation due to oxide charge buildup from the collimator shield leakage, the PIN is limited to spectral energies less than 50 keV. In theory, however, the PIN diode responds to all incident radiation. Therefore, to determine dose rates for end-point energies above 50 keV, a method which combines measured and calculated results was used. PHOTCOEF was used to calculate the theoretical dose/dose rate in the PIN structure for end-point energies of 50 keV, 100 keV and 140 keV. A typical plot of a PHOTCOEF depth-dose calculation is shown in Figure 10. (Note: CEPXS was used to make the same calculations and compared with PHOTCOEF. Appendix III presents these results for all energies).

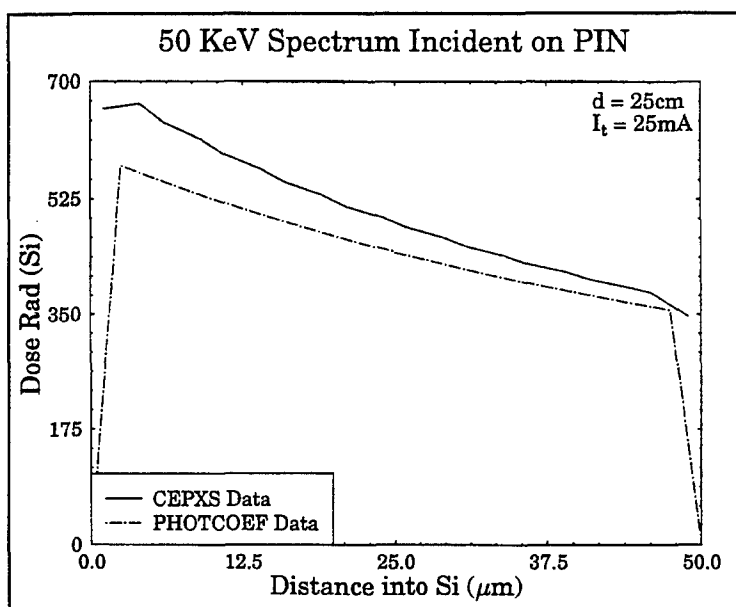


Figure 10: 50 keV Depth-Dose Plot for PIN Structure

Using the ratios of calculated dose rates, scaling factors were calculated to be:

$$D(100 \text{ keV}) = 1.43 * D(50 \text{ keV})$$

and

$$D(140 \text{ keV}) = 1.487 * D(50 \text{ keV})$$

For a given tube current and distance, the dose rate at the higher anode voltage (e.g., 100 kV) was estimated by scaling the PIN dose rate measured for a 50 kV anode voltage. The absolute errors in our calculations were shown to be effectively constant from 50 to 140 keV.

PMOS FETs - This approach used above was verified using PMOS FETs. Response data of PMOS FETs irradiated in  $^{60}\text{Co}$ , compared with data from PMOS FETs irradiated in the X-ray chamber confirmed that the scaling factor described above is accurate. The dose rate in the X-ray chamber was set using the scaling factor. The PMOS FET data shown in Figure 8 is now correlated back to the calibrated  $^{60}\text{Co}$  source as discussed in ASTM F-1467. Figure 11 shows a plot of  $V_{th}$  versus dose for 50 keV, 100 keV and 140 keV end point energies.



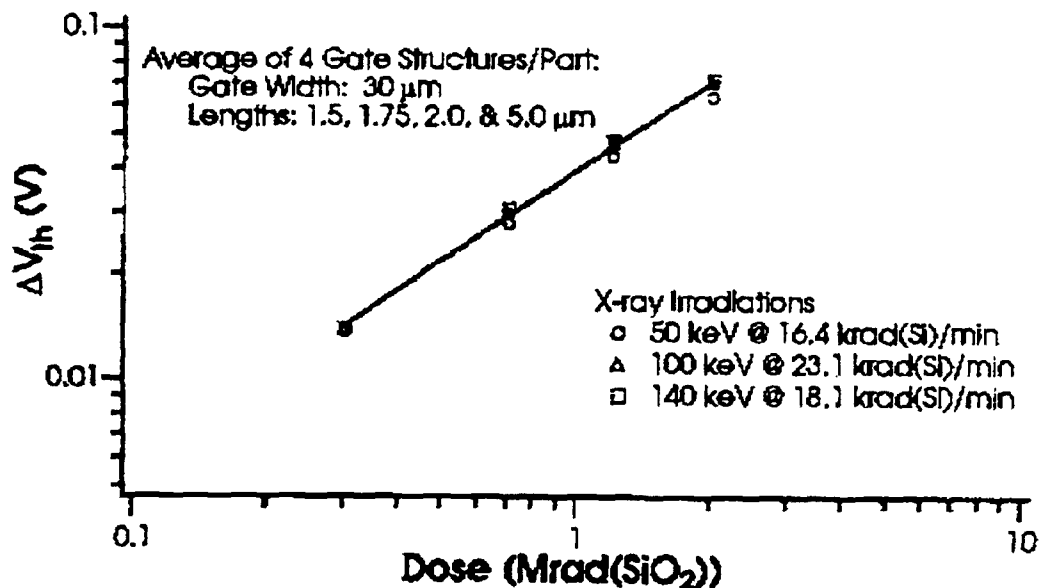


Figure 11: Threshold Voltage Shift of PMOS FETs Irradiated with 50, 100 and 140 keV X-Rays

An overlay comparison of X-ray data in Figure 11 with  $^{60}\text{Co}$  data from Figure 8 is shown in Figure 12.

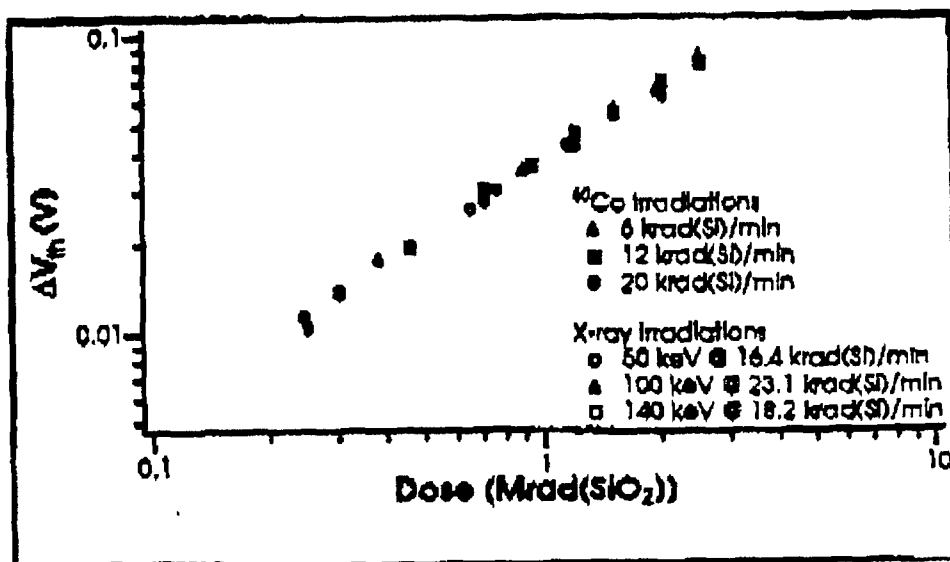


Figure 12: Threshold Voltage Shift of PMOS FETs with X-Ray and  $^{60}\text{Co}$  Data Overlaid

The maximum variation between data points in Figure 12 is less than 10%. This correlation is excellent for these type measurements over the broad range of photon energies being considered.

## VII. CONCLUSIONS

TUBE, CEPXS and PHOTCOEF provided excellent electron-photon transport calculations with which to calculate the x-ray tube output spectrum, spectral attenuation during radiation transport and depth-dose profiles in Si/SiO<sub>2</sub> detector materials over X-ray energies up to 160 keV. Detector response estimates based on these calculations were accurate to within 30% of values measured experimentally. This accuracy is consider excellent based on similar work by other investigators. Comparisons of PHOTCOEF and CEPXS were excellent for lower energy spectra but then began to diverge at energies greater than 80 keV as shown in Appendix III. More investigation is required in this area. PHOTCOEF and CEPXS are valuable electron-photon transport codes which provide calculational support for test analysis with the accuracy needed to support testing.

The SEMIRAD X-ray diode provides an accurate detector to measure X-ray test chamber integral intensities at all energies of interest. Due to it's simplicity, stability, and ease of calibration, the SEMIRAD is also an excellent device with which to validate analysis codes

The PIN diode provides an excellent dosimeter for directly measuring dose-rate in Si and SiO<sub>2</sub> . The calibration of dose rate in Si at 50 kV scaled to higher spectral end-point energies based on analyses using PHOTCOEF provides a means to accurately establish the

dose rate for all x-ray tube anode voltages. This provides accurate dosimetry for the entire spectrum of X-ray energies available in LEXR.

The PMOS FET response to X-rays correlates well with  $^{60}\text{Co}$  for all X-ray energies, using the PIN diode to set dose-rate in the X-ray chamber. This demonstrates that the dosimetry established can be directly traced to NIST standards through the  $^{60}\text{Co}$  calibrated dosimetry.

The techniques developed by this effort provide the tools to do complete and accurate analyses of radiation transport and it also establishes the dosimetry for the LEXR X-ray facility needed to test electronic devices, circuits and subsystems in accordance with ASTM F1467.

## REFERENCES

- [1] L. Palkuti and J. LePage, "X-ray Wafer Probe for Total Dose Testing," IEEE Trans. on Nuclear Sci., NS-29, Dec. 1982.
- [2] ASTM Standard F1467 "Std. Guide for the Use of an X-Ray Tester (10keV) in Ionizing Radiation Effects Testing of Microelectronic Devices."
- [3] R. Bellem *et al.* "Application of Analytical and Experimental Dosimetry Techniques to a Low-Energy X-Ray Radiation Source," to be published in 1993 Journal of Radiation Effects Research & Engineering.
- [4] R. Bellem "Calibration Techniques for a Low Energy X-Ray Irradiation Chamber," AFOSR Final Report, Summer Research Program 1992.
- [5] R. Bellem *et al.* "Calibration Techniques for Bremsstrahlung X-Ray Sources With End-

Point Energies Up To 160 keV," to be published in the 1994 Journal of Radiation Effects Research & Engineering.

[6] Kronenberg, "A Monograph on High-Intensity Radiation Dosimetry with SEMIRAD," The United States Army Research and Development Series, No.3, Fort Monmouth, NJ, Sept. 1966.

[7] D. B. Brown and D. J. Nagel, "Calculation of Spectra from Electron-Impact X-Ray Sources," 1981 AIP Conference Proceedings No. 75, David T. Attwood and Burton L. Henke, Eds. (American Institute of Physics, New York, 1981), pg. 253.

[8] D.B. Brown, J.V. Gilfrich and M.C. Packerar, "Measurement and Calculation of Absolute Intensities of X-Ray Spectr," Journal of Applied Physics, Vol. 46, No. 10, Oct 1975

[9] Private Communication, C. Dozier, Naval Research Laboratory, Washington, D.C.

[10] L.J. Lorence, J.E. Morel, G.D. Valdez, "User's Guide to CEPXS/ONEDANT: A One-Dimensional Coupled Electron-Photon Discrete Ordinates Code Package, Sandia Report SAND89-1661.

[11] PHOTCOEF A Nuclear Physics Utilities Program Written for IBM PC's and Compatible Microcomputers, AIC Software, P.O. Box 544, Grafton, Mass. 01519

[12] Private Communication, R. Miller & D. Arion, SAIC Albuquerque.

[13] Available from Standardization Documents Order Desk, Bldg. 4 Section D, 700 Robbins Ave., Philadelphia, PA 19111

[14] E 668, "Standard Practice for the Application of Thermoluminescence-Dosimetry (TLD) Systems for Determining Absorbed Dose in Radiation-Hardness Testing of Electronic

Devices." American Society for Testing and Materials, 1916 Race St., Philadelphia, PA  
19103.

## APPENDIX I. CEPXS CALCULATIONS OF X-RAY TUBE SPECTRUM

CEPXS was used to calculate the bremsstrahlung emission spectra using a monoenergetic beam of electrons incident on a slab of tungsten. An example of the CEPXS input file, CEPINP, for 50 keV electrons is shown below:

```
title
50 KeV electrons normal on 0.254 cm Tungsten
energy 0.05
cutoff 0.001
legendre 15
photons
  linear 50
electrons
  linear 50
electron-source
  full-coupling
material W
print
  rows
geometry 1
  1 50 0.254
direction
  normal
```

The resulting CEPXS output file, CURRE, is shown plotted below as reverse photon number flux differential in energy. This spectrum is also shown converted to a reverse energy flux.

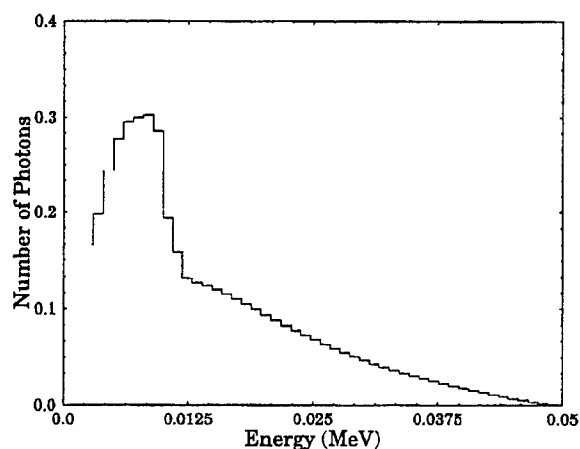


Figure 13: 50 keV on .025 cm

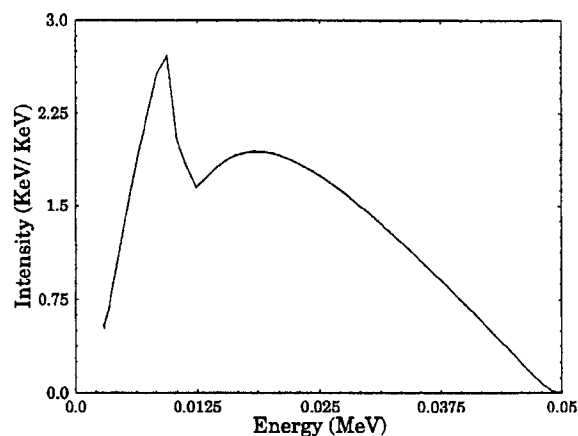


Figure 14: 50 keV on .025 cm

The CEPXS calculated tube output spectrum shown above for 50 keV, was used as an input energy spectrum to both CEPXS and PHOTCOEF and used to calculate air transmission/attenuation and depth-dose calculations in materials systems such as the PIN structure.

## APPENDIX II

This appendix shows the computer program used to calculate the diode current as shown in Eqn. 2.

```

**This program is called INTEGRATE.BAS**
' It can be used to integrate a function  $y=f(x)$ 
' that is defined by a table of data points in
' file.

DECLARE SUB transpose (n!, x!(), y!())
DIM x(200), y(200)
INPUT "Function File Name ?", fileone$
OPEN fileone$ FOR INPUT AS #1
INPUT "OUTPUT FILE NAME ?", FILETWO$
OPEN FILETWO$ FOR OUTPUT AS #2

n = 1
DO WHILE NOT EOF(1)
INPUT #1, x(n), y(n)
n = n + 1
LOOP
n = n - 1
sum = 0
xleft = x(1)
xright = x(2)
yleft = y(1)
yright = y(2)
i = 3
again:
area = ABS(xright - xleft) * (yleft + yright) / 2
sum = sum + area
K = xright
SUM1 = sum
PRINT #2, K, SUM1

i = i + 1
IF i <= n THEN
    xleft = xright
    yleft = yright
    xright = x(i)
    yright = y(i)
    GOTO again

```



END IF

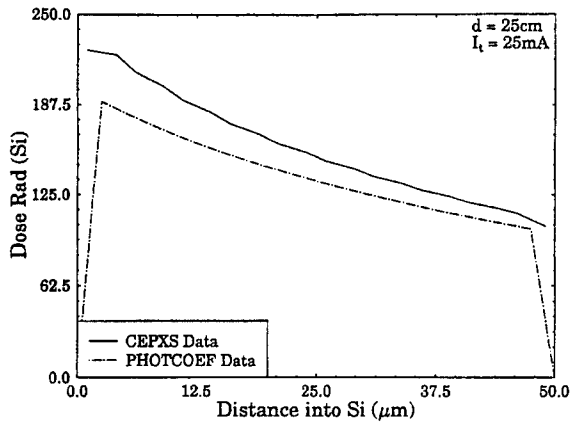
PRINT "N=", n  
PRINT "SUM = ", sum  
CLOSE #1  
CLOSE #2  
END

SUB transpose (n, x(), y())  
DIM XX(200), YY(200)  
FOR j = 1 TO n  
XX(j) = x(n + 1 - j)  
YY(j) = y(n + 1 - j)  
NEXT j  
FOR j = 1 TO n  
x(j) = XX(j)  
y(j) = YY(j)  
NEXT j  
END SUB

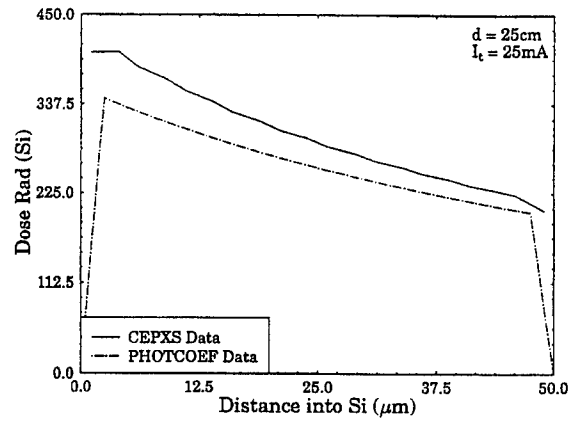
### APPENDIX III.

This appendix shows plots of CEPXS and PHOTCOEF calculations of depth-dose profiles in the PIN structure overlayed for comparison purposes. The plots show that for lower energies the calculations are within 10-15%. At higher energies (above 80 keV) the calculations begin to diverge. It appears that the CEPXS results need to be further studied to understand this difference. Further work in this area will be done in the next phase of this effort.

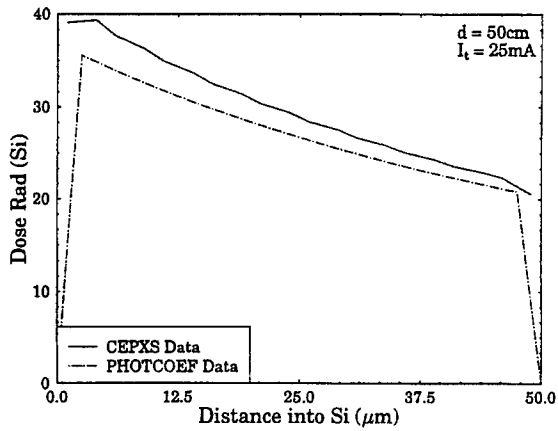
20 KeV Spectrum Incident on PIN



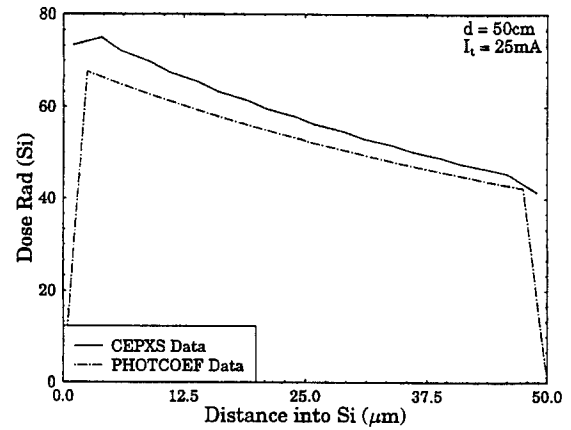
30 KeV Spectrum Incident on PIN



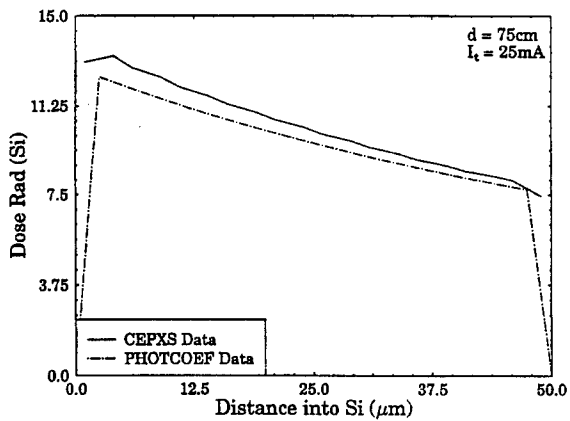
20 KeV Spectrum Incident on PIN



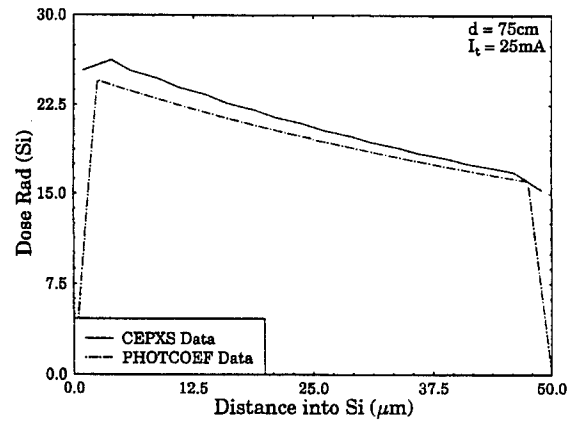
30 KeV Spectrum Incident on PIN



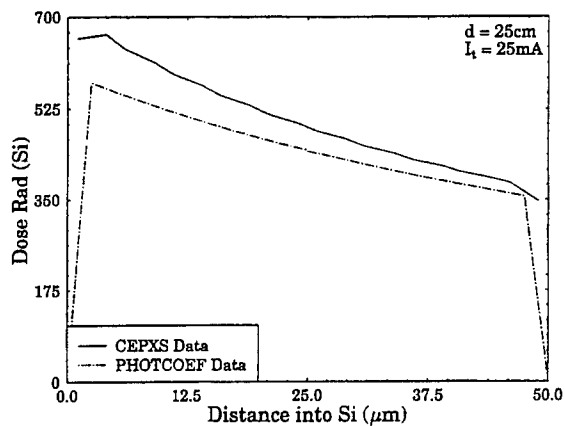
20 KeV Spectrum Incident on PIN



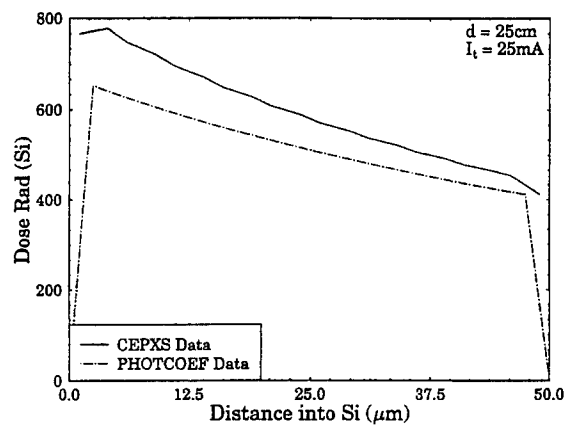
30 KeV Spectrum Incident on PIN



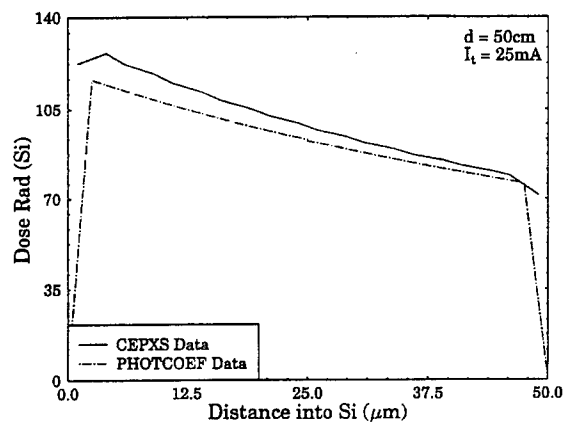
50 KeV Spectrum Incident on PIN



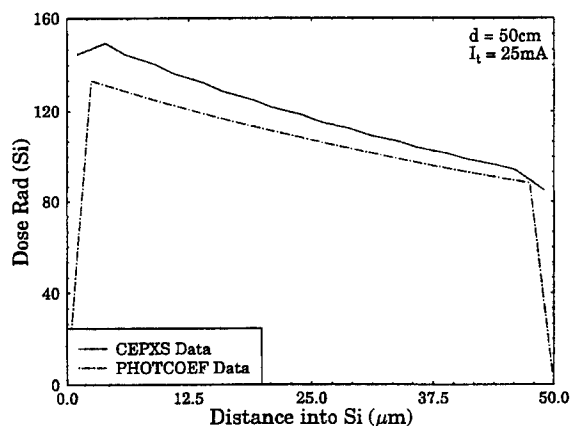
60 KeV Spectrum Incident on PIN



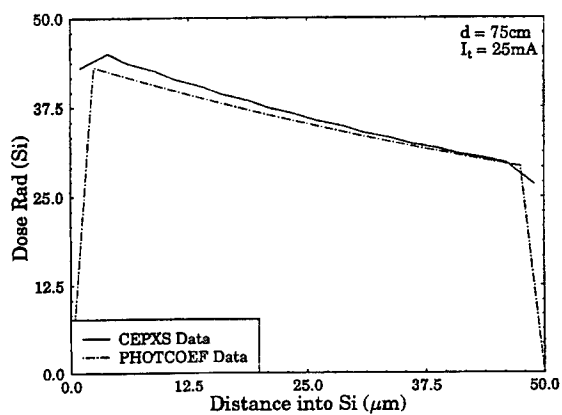
50 KeV Spectrum Incident on PIN



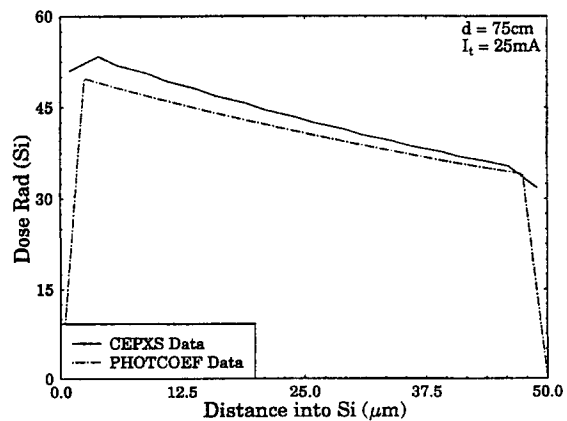
60 KeV Spectrum Incident on PIN



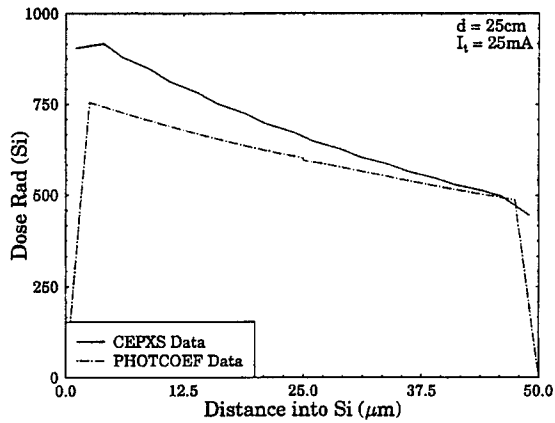
50 KeV Spectrum Incident on PIN



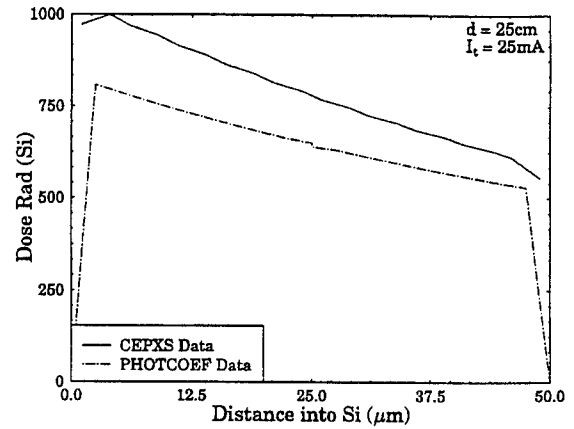
60 KeV Spectrum Incident on PIN



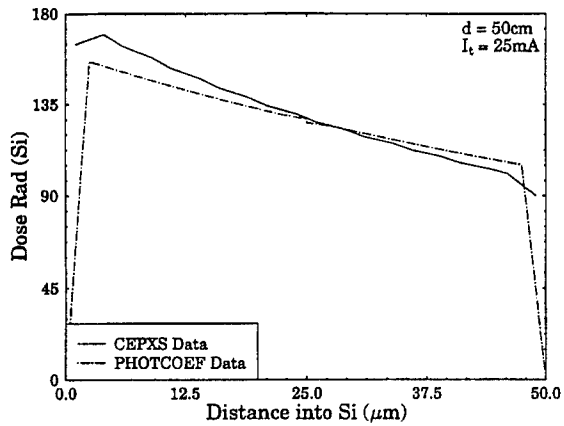
80 KeV Spectrum Incident on PIN



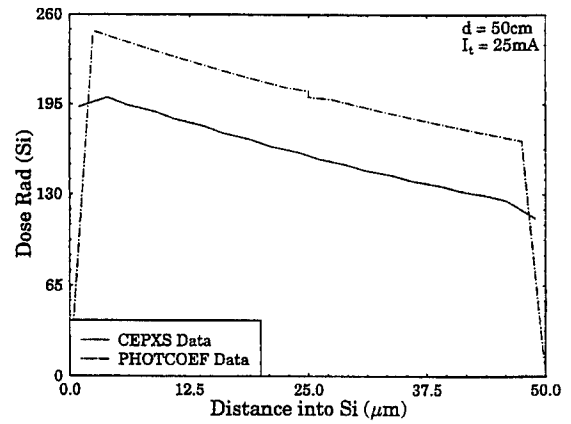
100 KeV Spectrum Incident on PIN



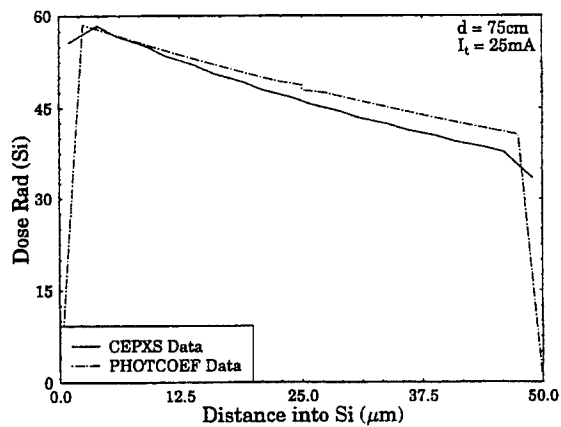
80 KeV Spectrum Incident on PIN



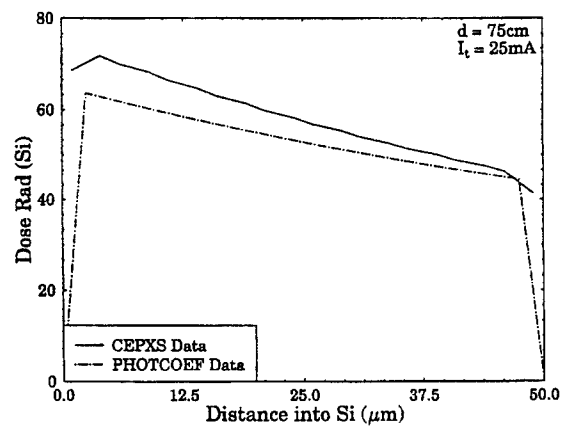
100 KeV Spectrum Incident on PIN



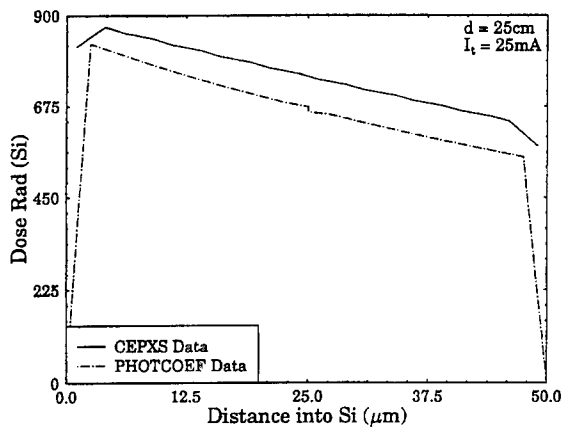
80 KeV Spectrum Incident on PIN



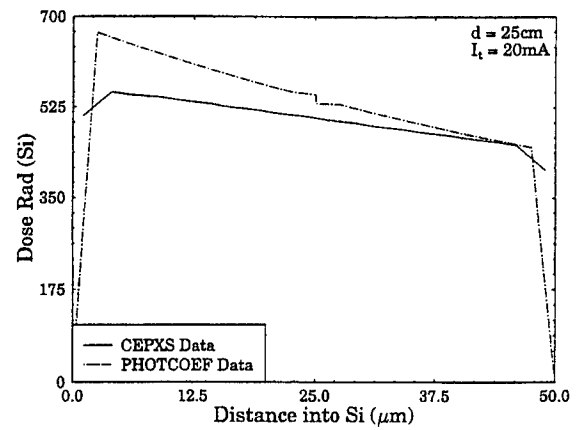
100 KeV Spectrum Incident on PIN



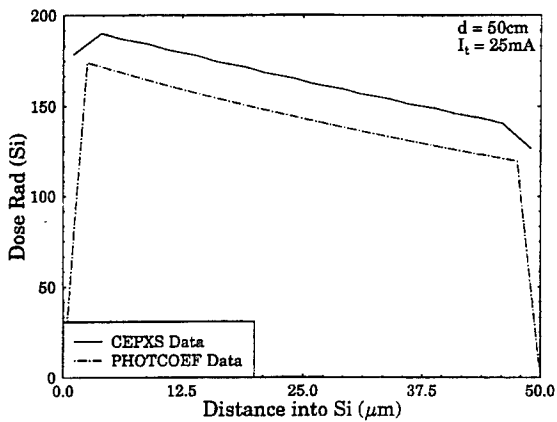
120 KeV Spectrum Incident on PIN



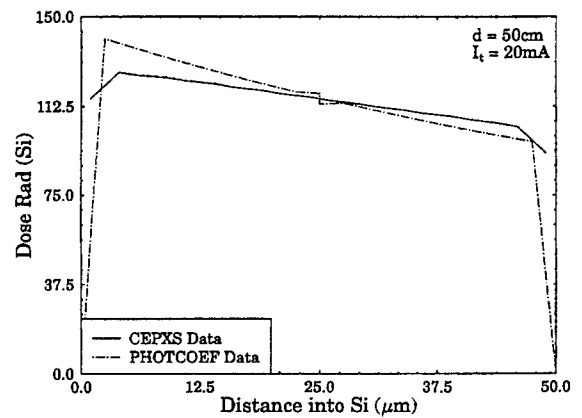
140 KeV Spectrum Incident on PIN



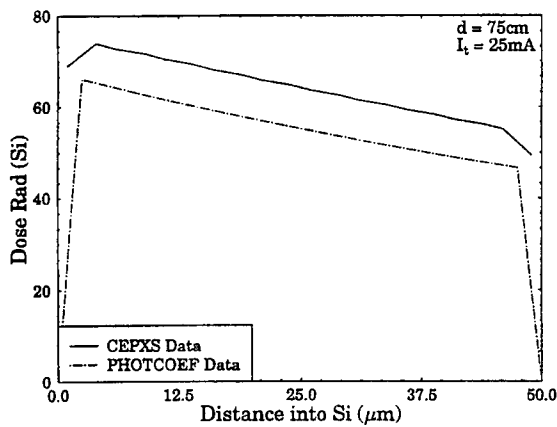
120 KeV Spectrum Incident on PIN



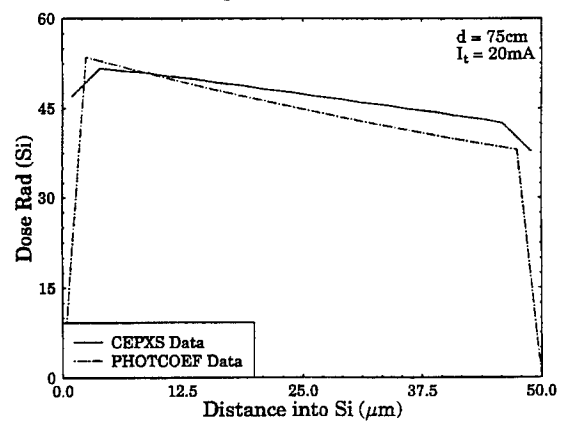
140 KeV Spectrum Incident on PIN



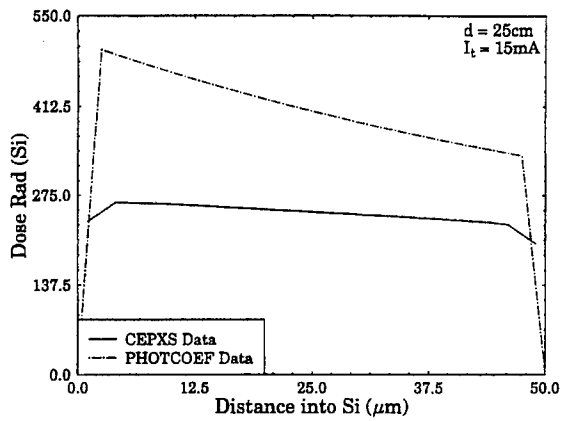
120 KeV Spectrum Incident on PIN



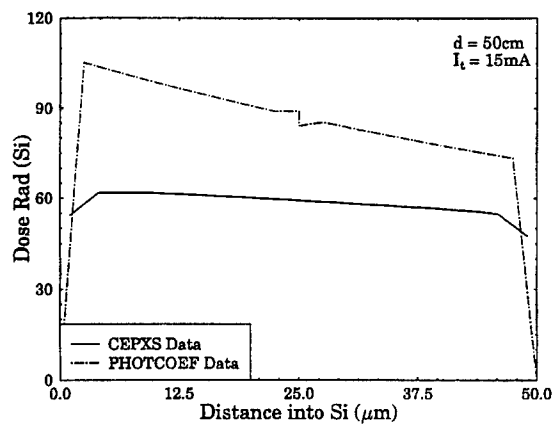
140 KeV Spectrum Incident on PIN



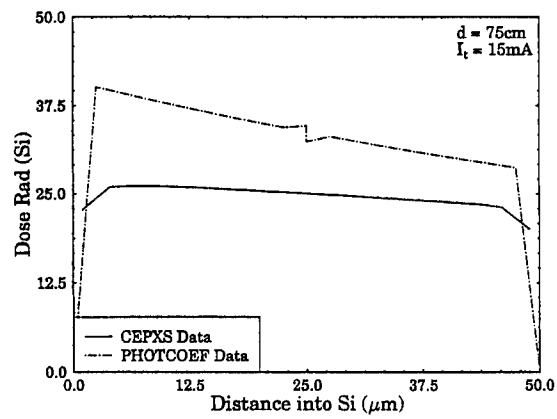
160 KeV Spectrum Incident on PIN



160 KeV Spectrum Incident on PIN



160 KeV Spectrum Incident on PIN



# **FREQUENCY DISPERSIVE PHENOMENA IN ULTRA WIDEBAND RADARS**

**Albert W. Biggs**

**Professor**

**Department of Electrical and Computer Engineering  
The University of Alabama in Huntsville  
Huntsville, AL 35899**

**Final Report for:**

**Summer Research Extension Program**

**Sponsored by:**

**Air Force Office of Scientific Research  
Bolling Air Force Base, Washington, DC**

**December 1993**



# **FREQUENCY DISPERSIVE PHENOMENA IN ULTRA WIDEBAND RADARS**

**Albert W. Biggs**

Professor

Department of Electrical and Computer Engineering

The University of Alabama in Huntsville

Huntsville, AL 35899

## **ABSTRACT**

Results of frequency dispersive phenomena on pulse distortion are applied to design of ultra wideband radars (UWBR). Distortions, made by higher attenuation of high frequency components in the pulses, were observed when transmission lines, waveguides, and propagation media were lossy. Propagation media are included with frequency dispersion because UWBR will be used as Ground Penetrating Radars (GPR) for detecting buried unexploded ordnance (UXO) like bombs, mines, or artillery rounds.

Frequency dispersions in waveguides and antennas are created by phase velocities changing with frequency. Pulse distortion decreased with higher frequency components in the pulses.

Transient responses of pyramidal horn antennas were analyzed and experimentally verified to observe pulse distortion and dispersion and to develop models for UWBR. The narrow bandwidth of the antenna creates a high frequency dispersion in the form of a long transient damped sinusoidal response.

Another example of frequency dispersion is the log periodic dipole array (LPDA). LPDAs have high gains and bandwidths almost unlimited, but cannot be used for transmission and reception of ultra wideband signals. The strong frequency dispersions for LPDAs and similar antennas creates substantial distortion of pulse shapes. A simple change in geometry of LPDAs is described to reduce dispersion effects to negligible levels.

# **FREQUENCY DISPERSIVE PHENOMENA IN ULTRA WIDEBAND RADARS**

**Albert W. Biggs**

## **INTRODUCTION**

Millions of acres of government lands are contaminated with buried unexploded ordnance (UXO). UXOs include bombs, mines, artillery projectiles, grenades, missiles, rockets, and submunitions, and they originated from operations at military training areas, functional test ranges, impact ranges, and open burn/open detonation areas. Several installations with known or assumed UXOs have been selected for base alteration and closing. Some are previous defense facilities and several are active military installations that plan alternate uses for the UXO sites. It is necessary to accurately and reliably locate and identify the distribution of buried UXOs (bombs, mines, etc.).

Detection and identification of UXO's must be completed before range sites can be transferred or sold to other government agencies or private entities. Range site terrains are pockmarked with shell craters and not accessible by roads or sidewalks for surface vehicles. Unexploded mines, on and near the terrain surface, and other UXOs make manual probing or digging hazardous to one's health. These limitations, combined with extremely extensive areas, imply that airborne sensors are necessary in terms of cost and time.

Sensor output must resemble the UXO shape and indicate its depth, and also resemble several buried UXOs being imaged. Microwave imaging radars, often called ground penetrating radars (GPR) when the propagation medium is the ground, detect and identify subsurface targets with radar images. These radar images are similar to those made with weather radar, side looking airborne radar (SLAR), and microwave remote sensing radar [1]. When the depths of the burial of UXOs, and UXOs in a group or cluster, decrease, resolution and contrast or discrimination of buried targets (bombs or mines) improve. The image is like a photograph, with bombs at other depths appearing out-of-focus.

Subsequent sections describe frequency dispersive phenomena encountered when ultra wideband (or short) pulses are radiated from a narrowband pyramidal (or rectangular) horn antenna, fed by highly dispersive rectangular waveguide, and reduction of frequency dispersion encountered in conventional log periodic dipole arrays (LPDA) by simple modifications of the LPDA geometry. Frequency dispersion is demonstrated by measurements made with both narrowband horns and wideband TEM horns. These measurements provided frequency dispersive phenomena in both transmitting and receiving antennas. The original and modified LPDAs were compared with computer simulation to demonstrate frequency dispersion reduction.

### **ULTRA WIDEBAND RADARS**

UWBRs include impulse radars, "chirp" or linear FM radars, stepped FM radars, and radars with pseudorandom coding or other techniques. Ground penetrating radars (GPRs) have better detection and penetration capabilities with UWBRs than with narrowband radars (NBRs) and since NBRs have no dispersion, only UWBRs are studied here. In the set of UWBRs, only impulse radars and chirp radars are evaluated, "Chirp" was first used by B. Oliver in an internal Bell Lab memo, "Not with a Bang, but with a Chirp," in 1951. It describes how radar detection ranges are increased without loss of resolution or increase of peak power. Transmitted radar pulses with long periods  $T$  and low peak power (Chirp), have Frequency Modulated (FM) carriers that sweep frequencies across bandwidth  $B$  during each period. The pulses are backscattered from clouds, meteors, or buried UXOs to radar receivers and compressed with matched filters into  $(\sin x) / x$  shapes as narrow pulses with high peak powers (Bang).

Pulse compression ratios are ratios of original pulse period  $T$  to collapsed pulse width  $(1/B)$ , or  $BT$ . Typical  $BT$  ratios vary from 10 to 100,000. The product  $BT$  is the increase in peak power due to pulse compression. With  $BT$  equal to 20, 100 watts increases to 2 kilowatts after compression. Chirped pulse compression is achieved in transmit modes with ultra wideband (UWB) antennas such as LPDAs, where the matched filters are the antennas.

When the LPDAs are transmitting and/or receiving antennas for Chirp radars, they can be modeled as matched filters, possessing both amplitude-frequency and phase-frequency responses. Their phase conjugate functions can be shown to produce chirp pulse compression.

Frequency dispersion is introduced into LPDAs to create chirped pulses. When FM pulses are fed into the high frequency (HF) at the beginning of the LPDA, HF components at the front of the pulses are radiated from the HF dipoles in the LPDA. As the pulses travel to the low frequency (LF) end of the LPDA, LF components at the back of the pulses are radiated from the LF dipoles in the LPDA. The frequency dispersed components are spatially separated, and recombined in a matched filter. The early arriving HF components have slower phase velocities and later LF components have faster phase velocities.

When pulsed waveforms are introduced into LPDAs, all frequency components arrive at the same time but are radiated at different locations. This frequency dispersion increases with the increase of the difference in wavelength of HF and LF dipoles in the array.

### **FREQUENCY DISPERSION IN PYRAMIDAL HORNS AND LPDAs**

The observed distortion of a short pulse (wide bandwidth) from LPDAs was described by Pulfer [2]. Raz Mittra [3] gave an analytical discussion of this distortion, and resulting pulse length increase, in which he suggested that it was a result of frequency dispersion. An analytical model [4] combines suggestions by Mittra, Pulfer, and others. Figure 1(a) from Pulfer [2] and Knop [4], has a pulsed voltage  $v(t)$  applied at the apex (actually at the first dipole of length A) terminals. For an input pulse of short duration  $T$ , the envelope of the radiated pulse is seen in Figure 1(b) along the same time scale as that of the input pulse. The envelope reaches a maximum at a time  $t' = a / \omega_p$ , where  $a$  is the antenna parameter  $a = \frac{\pi}{2 \tan \alpha}$  and  $\alpha$  is the LPDA apex angle. The frequency  $\omega_p$  is approximately  $\sqrt{\omega_L \omega_U}$  with  $\omega_L$  and  $\omega_U$  being the lower and upper frequencies of the array (with wavelengths  $A/2$  and  $B/2$ , where A and B are dipole lengths). The resemblance to band pass filters is seen in the mean value  $\omega_p$  in the

passband,  $\omega_U - \omega_L$ , but its exact location depends on the input pulse spectrum and on the LPDA passband characteristics.

Another example of frequency dispersion is seen in Figure 2 from Mittra [3], who has an input pulse to a spiral antenna (pulse length about 1.0 microsecond) and a radiated pulse length exceeding 45 microseconds.

The third example of frequency dispersion is observed in the transmitting and receiving responses of a pyramidal horn antenna. A Gaussian pulse with a pulse width of about one nanosecond is inversely proportional to the center frequency of a pyramidal horn antenna. The pulse is fed into the pyramidal horn antenna from a coaxial line to rectangular waveguide transition seen in Figure 3. Two feeds are seen, one with the center conductor of the coaxial line shorted to the opposite wall of the guide and the other with the center conductor ending as an open circuit.

Side view and end view of the horn antenna appear in Figure 4. The short-circuited probe configuration is used here. Radiation from the antenna was measured with a J-dot probe (1.8 GHz 3 dB point) in the antenna far field.

All shots or pulse transmissions were an average of 128 pulses (for each shot). The Fast Fourier Transform (FFT) used a rectangular window. The feed probe from the coaxial line, RG 223, was the short circuit configuration in Figures 3 and 4. All coaxial cables in radiated pulse measurements were RG 223.

The anticipated dispersive properties of the pyramidal horn agree with analytical results [5]. These are a series of Bessel functions of the first kind with order zero. The arguments of the Bessel functions are proportional to the odd TE modes of the rectangular guide, and are seen in the measured responses. Inside dimensions of the waveguide are 9.750 inches by 4.875 inches (designation WR-975), nominal cutoff frequency is 605 MHz, and specified operating frequency is 0.75 to 1.12 GHz. The first peak in the radiated pulse is about 760 MHz, and the second peak is at 1347 MHz or square root (3) times greater. This does not match TE 30 modes.

Figure 5 describes the measurement configuration for pulse distortion. It shown the power supply, the Tektronix 109 Pulse Generator connected to the horn antenna with 20 feet of RG 223 coaxial cable, the J-dot probe, and the Hewlett Packard 602A Digital Signal Analyzer connected to the probe with 30 feet of RG 223 coaxial cable. A 40 dB attenuator is not shown. Some pulse spreading was observed from the 20 feet cable feeding the horn. Figures 6 and 7 are measurement locations for Shots #8 through #11, and #12 through #14, respectively.

Figure 8 is the reference input pulse at the LPDA input terminals. It originates with the Tektronix 109 pulse generator, and is averaged over 128 pulses. Some pulse spreading was observed along the 20 feet of RG 223 coaxial cable. The pulse in Figure 8 has a 3-dB width of about one nanosecond. The arrow indicates the beginning of the pulse. The frequency spectrum of the pulse has a gradual decreasing amplitude from 14.648 MHz to 1.2353 GHz (linear frequency scale of 122.07 MHz per division). The frequency spectral response of the pulse is calculated with the FFT.

Figure 9 is the radiated pulse waveform for Shot #8 after dispersion created by the antenna. The frequency spectral response of the radiated pulse is also calculated with the FFT. The J-dot probe is centered 3 meters in front of the antenna.

Figure 10 is the radiated pulse waveform for Shot #9 after dispersion created by the antenna. The frequency spectral response of the radiated pulse is also calculated with the FFT. The J-dot probe is located in the mouth of the antenna, and on the bottom wall.

Figure 11 is the radiated pulse waveform for Shot #10 after dispersion created by the antenna. The frequency spectral response of the radiated pulse is also calculated with the FFT. The J-dot probe is located 3 meters in front of the antenna, and 2 meters to the left of the antenna axis.

Figure 12 is the radiated pulse waveform for Shot #11 after dispersion created by the antenna. The frequency spectral response of the radiated pulse is also calculated with the FFT. The J-dot probe is located in front of the antenna, and in line with the bottom edge of the antenna.

Figure 13 is the radiated pulse waveform for Shot #12 after dispersion created by the antenna. The frequency spectral response of the radiated pulse is also calculated with the FFT. The J-dot probe is located 6 meters in front of the antenna.

Figure 14 is the radiated pulse waveform for Shot #13 after dispersion created by the antenna. The frequency spectral response of the radiated pulse is also calculated with the FFT. The J-dot probe is located in the mouth of the antenna, and on the left hand wall.

Figure 15 is the radiated pulse waveform for Shot #14 after dispersion created by the antenna. The frequency spectral response of the radiated pulse is also calculated with the FFT. The J-dot probe is located 3 meters in front of the antenna, and 2 meters to the right of the antenna axis.

### **REDUCTION OF DISTORTION IN TRANSIENT AND CHIRPED PULSES IN LPDAs**

Phase-frequency distortion in transient and chirped pulses was described in previous sections for LPDAs, log spiral antennas, and pyramidal horns. This section introduces two techniques for eliminating the dispersive distortion found in transmitting and receiving LPDA antennas. The first technique is a modification of the dipole geometrical spacing from logarithmic periodicity to arithmetic periodicity. This modification is made by altering the equations relating the lengths and distances between the dipole elements [6]. There is some deterioration of the bandwidth in the "arithmetic periodic dipole array" (APDA) in comparison with that of the LPDA [6].

The second technique is a modulation change which allows compression of super wideband signals on conventional LPDAs.

The radiation field of an LPDA is described by

$$E(\theta, \phi, \omega) = E_o(\omega) \frac{e^{-jkr}}{4\pi r} \sqrt{G(\omega)} F(\theta, \phi, \omega) e^{j\psi(\theta, \phi, \omega)}, \quad (1)$$

where  $E_o(\omega)$  is the Fourier transform of the pulse at the antenna input,  $G(\omega)$  is the antenna gain,  $\psi(\theta, \phi, \omega)$  is the phase of the array pattern, and  $F(\theta, \phi, \omega)$  is the normalized antenna pattern. The phase  $\psi(\theta, \phi, \omega)$  and amplitude  $F(\theta, \phi, \omega)$  are functions of  $\theta(\omega)$  and  $\phi(\omega)$ , where  $(\omega)$  is included because  $\theta$  and  $\phi$  change with frequency. Since these terms vary with frequency, we define the antenna frequency response as

$$H(\theta, \phi, \omega) = \sqrt{G(\omega)} F(\theta, \phi, \omega) e^{j\psi(\theta, \phi, \omega)}, \quad (2)$$

relating the antenna input  $E_o(\omega)$  to the observation point  $(r, \theta, \phi)$ . The far field  $e(\theta, \phi, t)$  is found by the convolution of  $h(\theta, \phi, t)$  and  $e_o(t)$ ,

$$e(\theta, \phi, t) = h(\theta, \phi, t) e_o(t) = \int_{-\infty}^{\infty} h(t-x) e_o(x) dx, \quad (3)$$

where  $E_o(\omega)$  is related to  $E_o(t)$  by

$$E_o(\omega) = \int_{-\infty}^{\infty} e_o(t) e^{-j\omega t} dt \quad (4)$$

with the same result when two sided Laplace transforms are used (and  $s = j\omega$ ).

In chirp radar, where pulses are linear FM, and in impulse radar, where pulses are usually Gaussian-like functions of time or damped sine waves, undistorted waveforms are obtained when the phase is a linear function of frequency and when the antenna gain is constant over the bandwidth of the pulse. In conventional LPDAs, where the amplitude is relatively constant in the pulse bandwidth, the phase response is a logarithmic function of frequency,

$$\psi(\theta, \phi, \omega) = \frac{\pi}{\ln \tau} \ln\left(\frac{\omega}{\omega_1}\right), \quad (5)$$



where  $\omega_1$  is the resonant frequency of the length  $\ell_1$  of the largest dipole, and the constant scale factor  $\tau$ ,

$$\tau = \frac{\omega_{n-1}}{\omega_n} = \frac{\ell_n}{\ell_{n-1}} = \frac{R_n}{R_{n-1}}, \quad (6)$$

$$\tau^{n-1} = \frac{\omega_1}{\omega_n} = \frac{\ell_n}{\ell_1} = \frac{R_n}{R_1}, \quad 0 < \tau < 1 \quad (7)$$

where  $n$  is the index for the  $n^{th}$  dipole,  $n = 1, 2, 3, \dots, N$ , seen in Figure 16, lengths  $\ell_n$  of  $n^{th}$  dipoles, with distances  $R_n$  from dipoles to the apex. When  $n = N$ , it identifies the shortest dipole with the highest frequency in the array. Each dipole element is a half wavelength  $\lambda_n / 2$ .

For undistorted pulse radiation, the phase versus frequency characteristic must be linear and the antenna gain versus frequency characteristic must be constant. As the phase versus frequency characteristic becomes more linear, distortion decreases. By modifying the geometry of LPDAs, linearity is achieved with the arithmetic periodicity,

$$\omega_n = \omega_1 + (n-1) \delta\omega, \quad n = 1, 2, \dots, N, \quad (8)$$

where  $\omega_1$  is the resonant frequency of the lowest frequency dipole and  $\delta\omega$  is the incremental change to the next frequency  $\omega_2$ . Dipole lengths must satisfy a nonlinear relationship,

$$\ell_n = \frac{\ell_1}{[1 + (n-1) \delta\omega / \omega_1]}. \quad (9)$$

When the frequency is increased by  $\delta\omega$ , the current on the  $(n+1)$  dipole will have the value it had on the  $(n)$  dipole at the initial frequency with a phase shift of  $\pi$  due to the crossover in the LPDA. (Crossover is the herringbone pattern.) This results in a phase versus frequency slope of  $-\pi / \delta\omega$ . The constant slope has the linear form

$$\psi(\omega) = -\pi \omega / \delta \omega . \quad (10)$$

Combining Equations (8) and (10) lead to

$$\psi(\omega_n) = \psi(\omega_1) - (n-1) \pi \quad (11)$$

where the phase response is changed by  $\pi$  as  $n$  changes by one. When a pulse is compressed, similar linearity is achieved with Equation (11). A chirped pulse, linearly modulated FM with rectangular envelope, has the form

$$e_o(t) = E_o \cos(\omega_o t + \frac{\Delta \omega}{2T} t^2) = 0, \quad -\frac{T}{2} \leq t \leq \frac{T}{2}, \quad t > \left| \frac{T}{2} \right|, \quad (12)$$

where  $\frac{\Delta \omega}{T}$  is the linear FM rate,  $T$  is the pulse period or length, and  $\Delta \omega$  is frequency swept in period  $T$ .

The Fourier transform of Equation (12) is the spectrum of  $e_o(t)$ ,

$$\begin{aligned} E(\omega) = & E_o \sqrt{\frac{\pi T}{4 \Delta \omega}} e^{j \frac{(\omega - \omega_o)^2}{2 \Delta \omega} T} \cdot \{[C(x_1) + C(x_2)] + j[S(x_1) + S(x_2)]\} \\ & + E_o \sqrt{\frac{\pi T}{4 \Delta \omega}} e^{j \frac{(\omega + \omega_o)^2}{2 \Delta \omega} T} \cdot \{[C(x_3) + C(x_4)] + j[S(x_3) + S(x_4)]\}, \end{aligned} \quad (13)$$

where Fresnel integrals  $C(x)$  and  $S(x)$  are

$$C(x) = \int_0^{\infty} \cos \frac{\pi}{2} y^2 dy, \quad S(x) = \int_0^{\infty} \sin \frac{\pi}{2} y^2 dy \quad (14)$$

and

$$\begin{aligned}
 x_1 &= [\frac{\Delta\omega}{2} + (\omega_o - \omega)] / \sqrt{\frac{\pi\Delta\omega}{T}} \\
 x_2 &= [\frac{\Delta\omega}{2} - (\omega_o - \omega)] / \sqrt{\frac{\pi\Delta\omega}{T}} \\
 x_3 &= [\frac{\Delta\omega}{2} + (\omega_o + \omega)] / \sqrt{\frac{\pi\Delta\omega}{T}} \\
 x_4 &= [\frac{\Delta\omega}{2} - (\omega_o + \omega)] / \sqrt{\frac{\pi\Delta\omega}{T}} .
 \end{aligned} \tag{15}$$

For chirped pulses, linearity is met with

$$\omega_n = \omega_1 + \Delta\omega \left[ \left\{ 0.5 + \frac{t}{T} \right\} - \sqrt{\left\{ 0.5 + \frac{t}{T} \right\}^2 - \frac{2\pi(n-1)}{T\Delta\omega}} \right] \tag{16}$$

where  $t = T_o = \frac{T}{2}$  to the center of the pulse, and

$$\omega_n = \omega_1 + \Delta\omega \left[ 1 - \sqrt{1 - \frac{2\pi(n-1)}{T\Delta\omega}} \right] \cong \omega_1 + \Delta\omega \left[ 1 - \left( 1 - \frac{\pi(n-1)}{T\Delta\omega} \right) \right] = \omega_1 + (n-1) \frac{\pi}{T} , \tag{17}$$

where  $\frac{\pi}{T}$  is the increment in frequency and

$$\ell_n = \frac{\ell_1 \omega_1}{\omega n} = \frac{\ell_1}{1 + \frac{\pi}{\omega_1 T} (n-1)} . \tag{18}$$

Figure 17 is a linear FM pulse with low to high frequencies progressing to the right. When used in Chirp radar, frequency dispersion is part of the matched filter for pulse compression, but unwanted frequency dispersion is introduced with conventional LPDAs with FM pulses in Figure 17. This is altered by the exponential FM pulse envelope in Figure 18. The amplitude and phase response to the esponentially modulated pulse in Figure 18 appears in

Figure 19 as a function of time. The amplitude and phase spectra for Figure 19 appear in Figure 20, and the resulting output waveform is chirped without distortion in Figure 21.

## **REFERENCES**

- [1] Albert W. Biggs, "Radar and Infrared Remote Sensing of Terrain, Water, Arctic Sea Ice, and Agriculture," *32nd Symposium of EWPP/AGARD, NATO, Oberammergau, Germany*, May 24-28, 1983.
- [2] J. K. Pulfer, "Frequency dispersive properties of broad-band antennas," *Proc. IRE*, Vol. 49, pp. 644-536, March 1961.
- [3] Raz Mittra, "Log periodic antennas," in *Antenna Theory, Part II*, F. J. Zucker and R. E. Collin, McGraw Hill, NY, pp. 376-380, 1969.
- [4] Charles M. Knop, "Transient radiation from a log periodic dipole array," *IEEE Trans. Antennas Propagat.*, Vol. AP-18, pp. 807-810, November 1970.
- [5] Robert E. Collin, *Field Theory of Guided Waves*, McGraw Hill Book Co., New York, pp. 258-307, 1960.
- [6] Victor A. Yatskevich and Leon I. Fedosenko, "Antennas for radiating ultra wideband signals," *Izvestiya VUZ. Radioelektronika*, Vol. 29, No. 2, pp. 69-74, February 1986.
- [7] Victor A. Yatskevich, "Reduction of the distortion of ultra wideband signals radiated by a log periodic antenna," *Izvestiya VUZ. Radioelektronika*, Vol. 34, No. 5, pp. 39-44, May 1991.

## FIGURE CAPTIONS

**Figure 1.** (a) Geometrical arrangement of elements in a log periodic dipole antenna array (LPDA). (b) Input and radiated pulse waveforms for the LPDA.

**Figure 2.** Input and output radiated pulse waveforms for log spiral antennas.

**Figure 3.** Transitions from coaxial lines to rectangular guides, which feed into horn antennas. Feeds have open- and short-circuit coaxial probes.

**Figure 4.** Horn antenna configuration with relevant dimensions in inches.

**Figure 5.** Measurement setup with power supply, pulse generator, antenna, recorder, and J-dot probe.

**Figure 6.** Measured waveform locations of the J-dot probes with respect to the horn antenna for Shots #8 through #11.

**Figure 7.** Measured waveform locations of the J-dot probes with respect to the horn antenna for Shots #12 through #14.

**Figure 8.** Measured waveform of Shot #7 of the input pulse amplitude and frequency spectrum.

**Figure 9.** Radiated pulse waveform for Shot #8 and its frequency response probe. Probe is centered 3 meters in front of the horn antenna.

**Figure 10.** Radiated pulse waveform for Shot #9 and its frequency response probe. Probe is in antenna mouth, on bottom wall.

**Figure 11.** Radiated pulse waveform for Shot #10 and its frequency response probe. Probe is 3 meters in front of antenna and then 2 meters to left.

**Figure 12.** Radiated pulse waveform for Shot #11 and its frequency response probe. Probe is 3 meters in front and in line with bottom of antenna.

**Figure 13.** Radiated pulse waveform for Shot #12 and its frequency response probe. Probe is 6 meters in front of antenna.

**Figure 14.** Radiated pulse waveform for Shot #13 and its frequency response probe. Probe is in antenna mouth, on left hand wall.

**Figure 15.** Radiated pulse waveform for Shot #14 and its frequency response probe. Probe is 3 meters in front of antenna and then 2 meters to right.

**Figure 16.** Geometrical arrangement of LPDA.

**Figure 17.** Square wave modulation envelope of a linear Frequency Modulated (FM) pulse with low to high frequencies.

**Figure 18.** Exponentially modulated FM pulse to reduce unwanted frequency distortion.

**Figure 19.** Amplitude and phase responses as functions of time for exponential pulse in Figure 18.

**Figure 20.** Amplitude and phase frequency spectra of Figure 19.

**Figure 21.** Chirped pulse with distortion reduced.

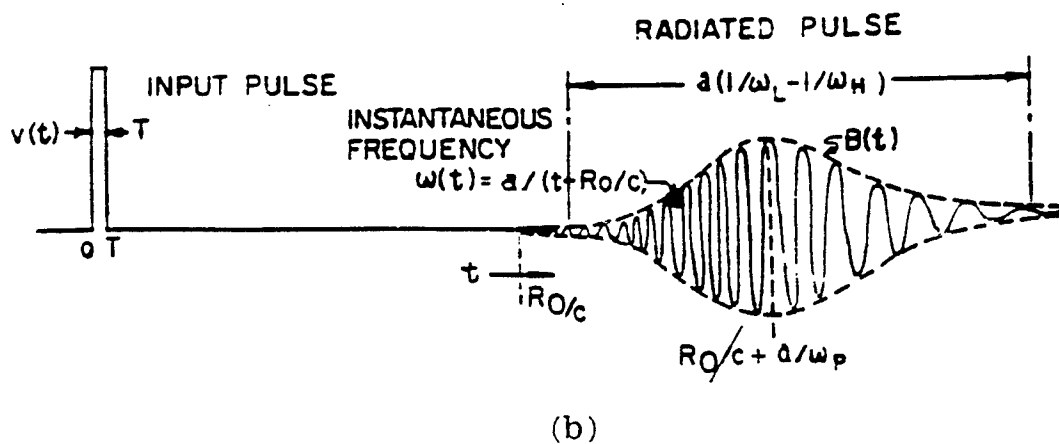
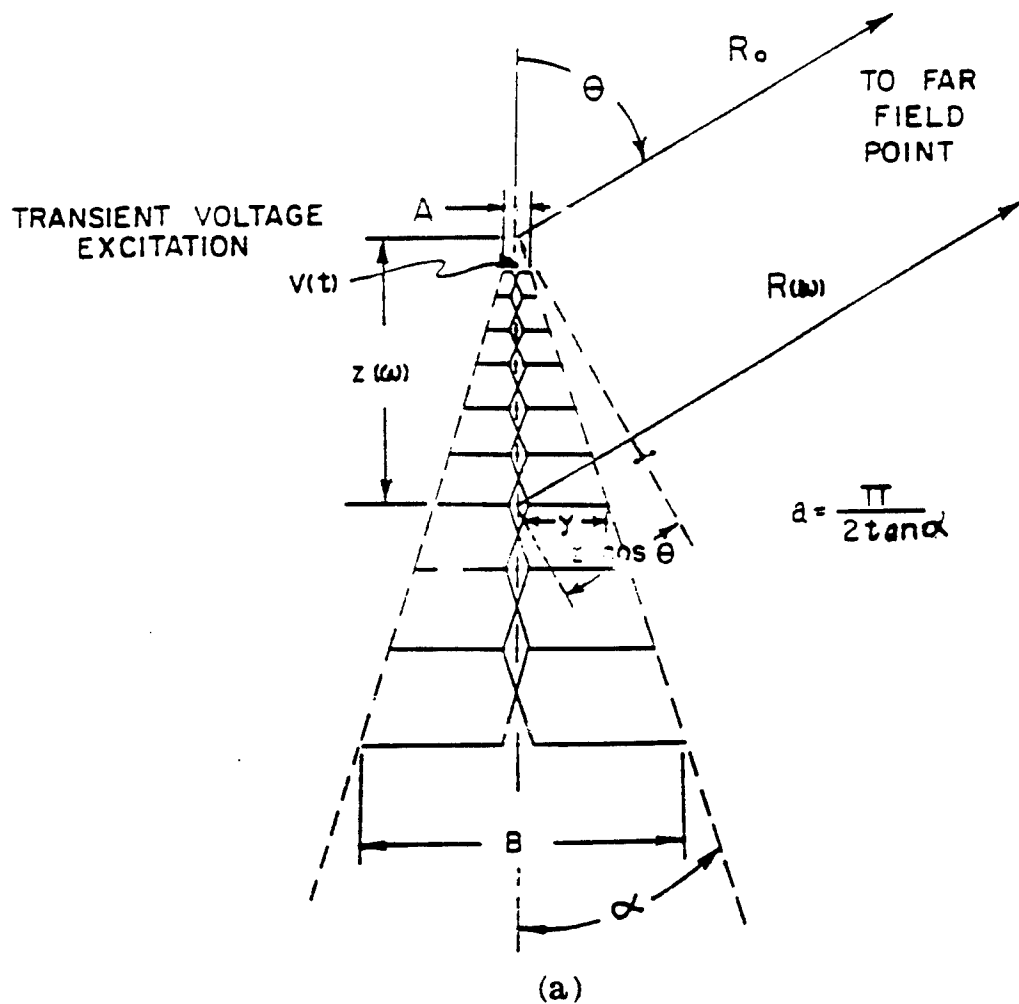


**Figure 1.** (a) Geometrical arrangement of elements in a log periodic dipole antenna array (LPDA). (b) Input and radiated pulse waveforms for the LPDA.



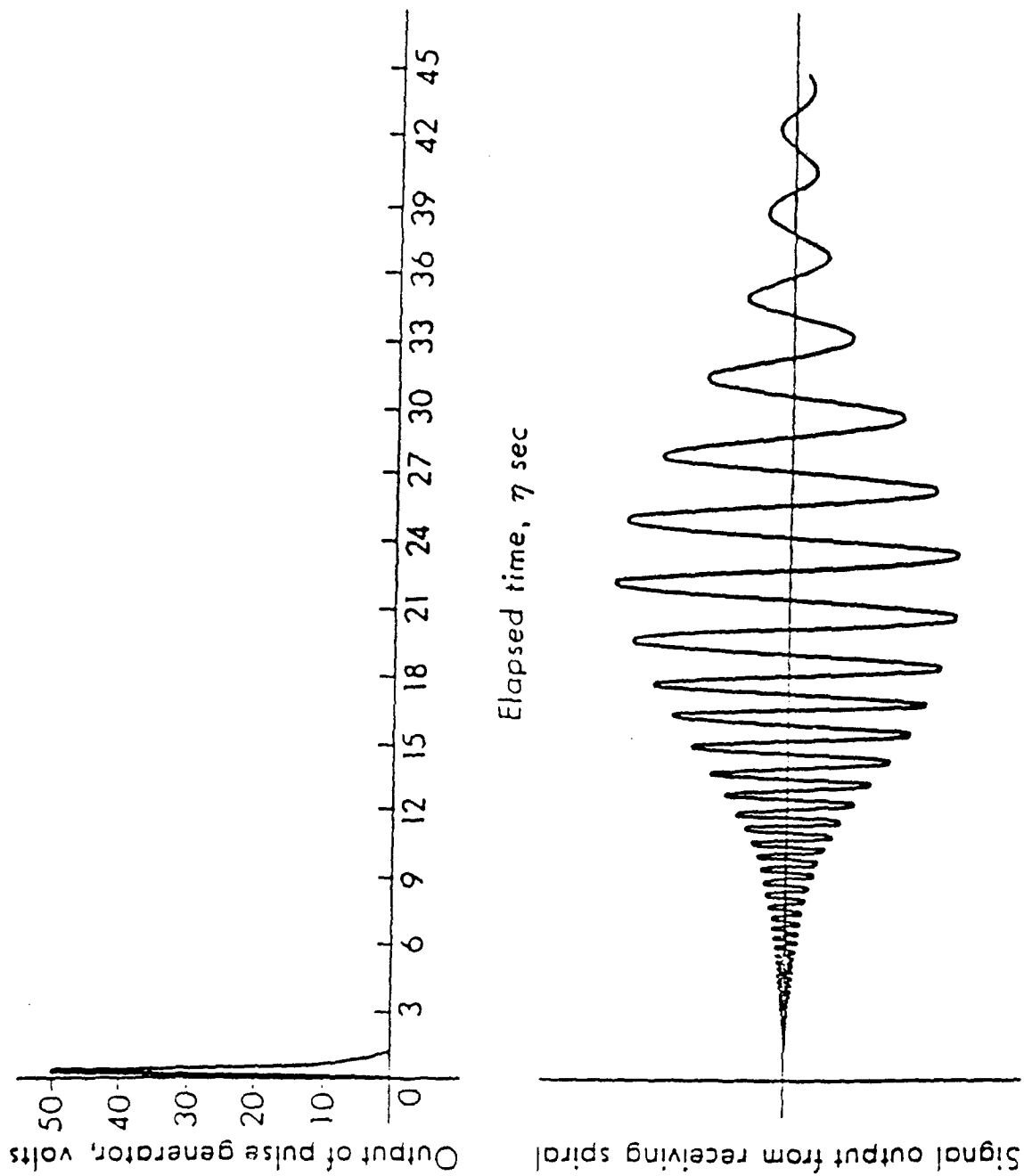


Figure 2. Input and output radiated pulse waveforms for log spiral antennas.

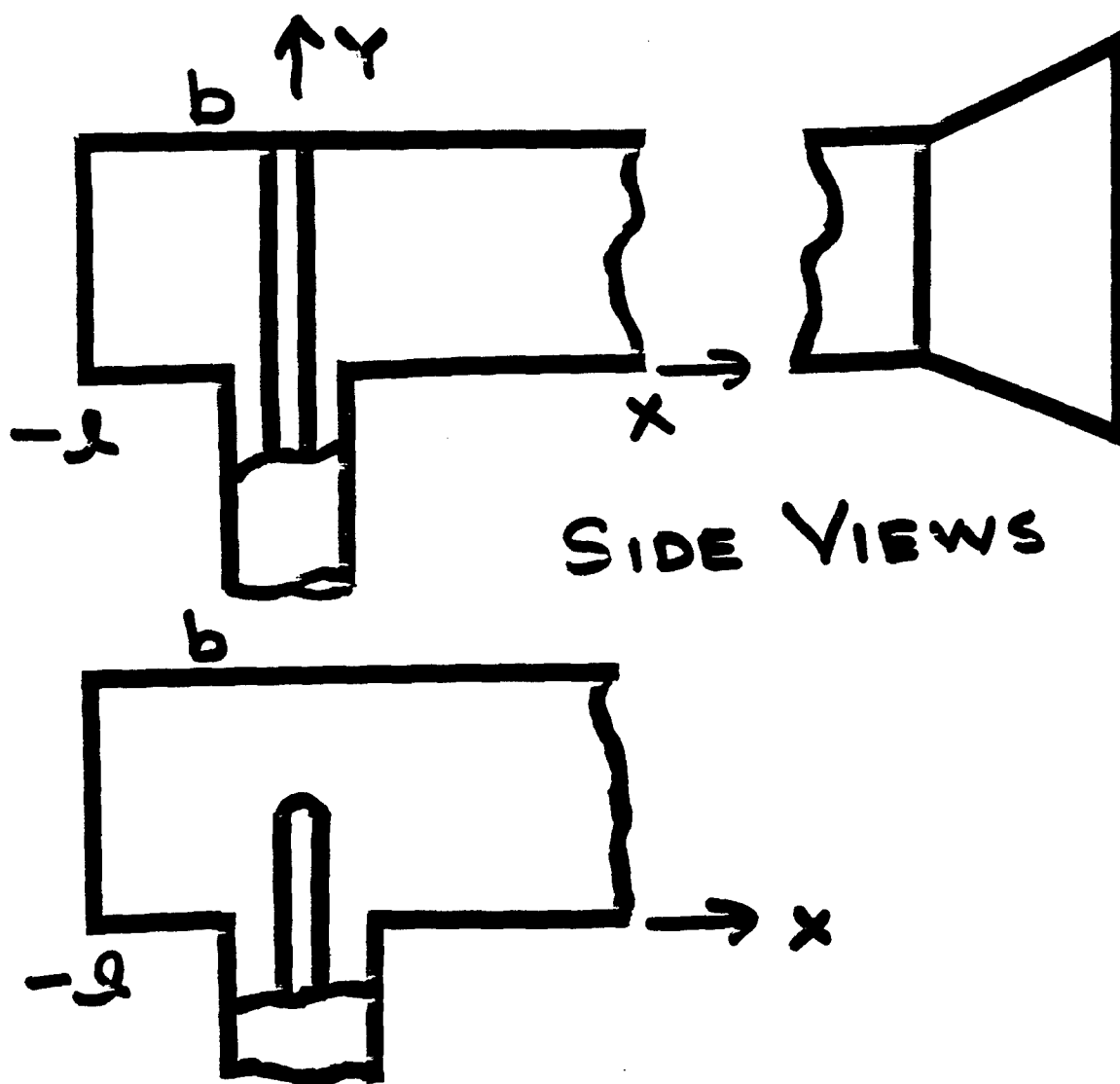


Figure 3. Transitions from coaxial lines to rectangular guides, which feed into horn antennas. Feeds have open- and short-circuit coaxial probes.

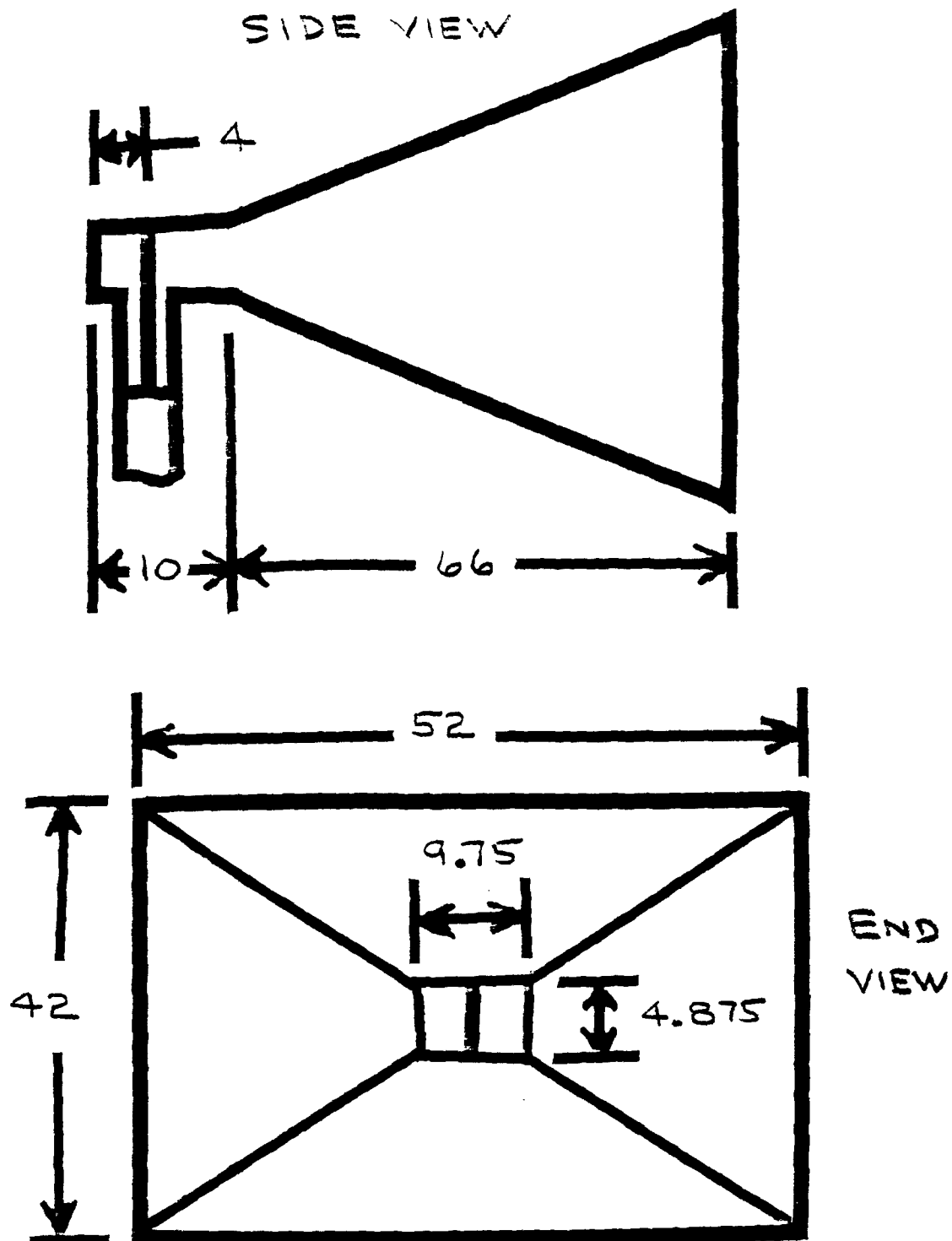
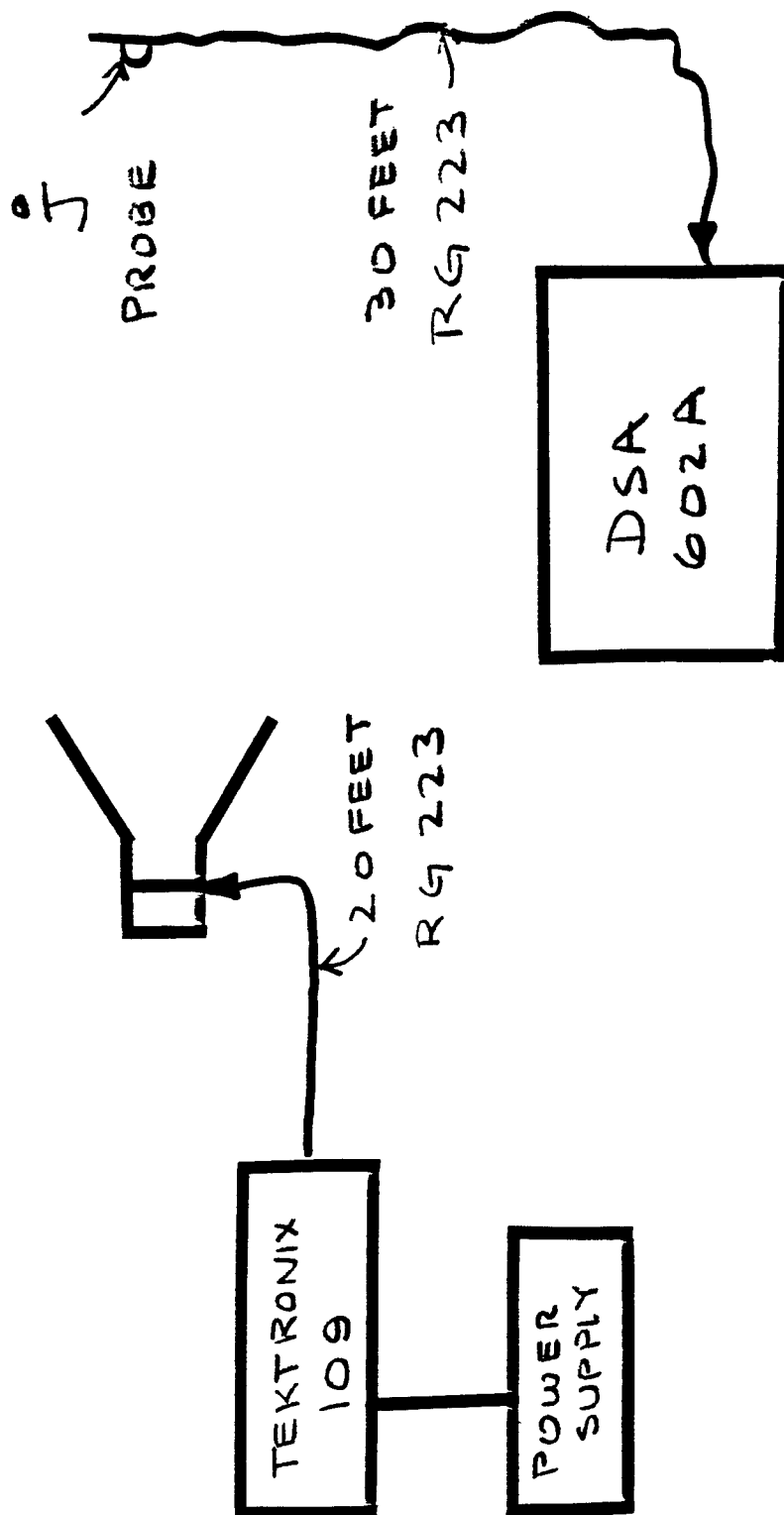


Figure 4. Horn antenna configuration with relevant dimensions in inches.

Figure 5. Measurement setup with power supply, pulse generator, antenna, recorder, and J-dot probe.



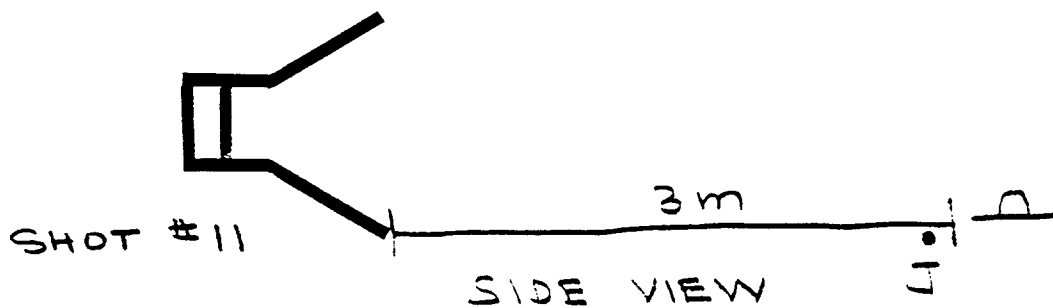
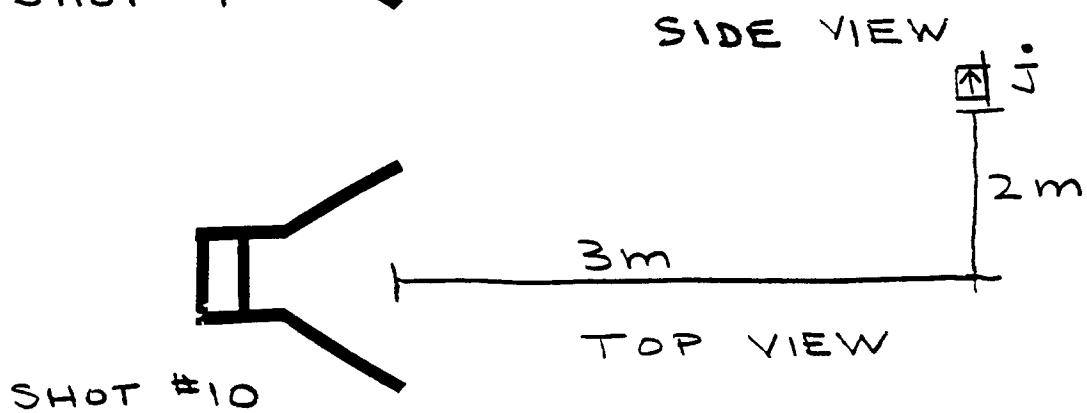
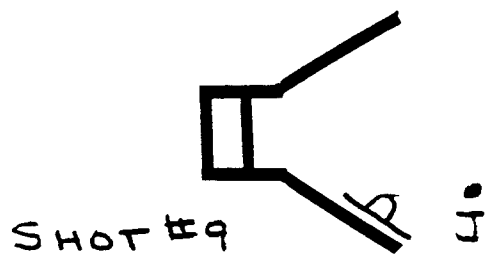
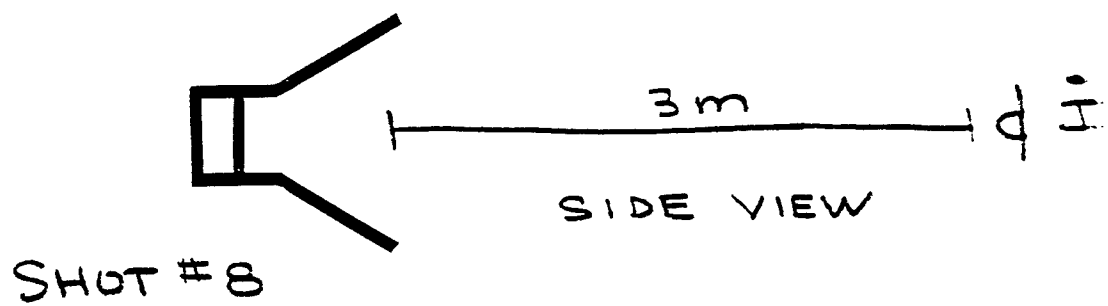
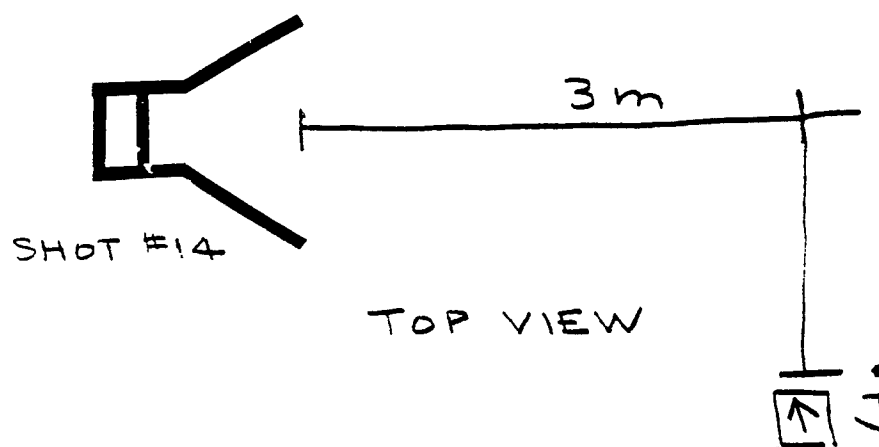
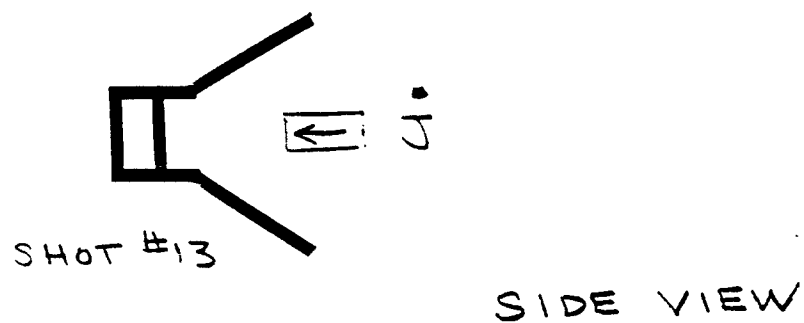
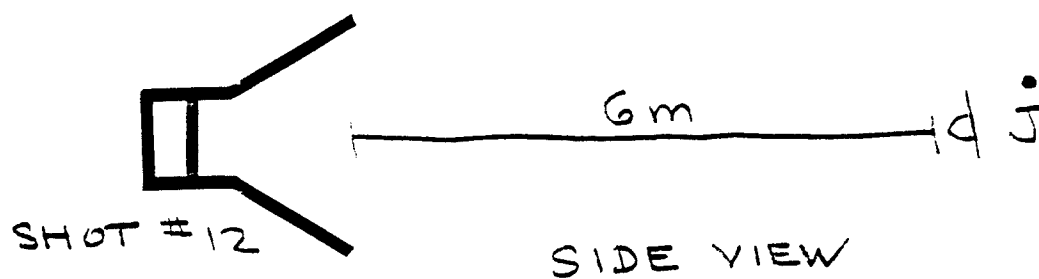


Figure 6. Measured waveform locations of the J-dot probes with respect to the horn antenna for Shots #8 through #11.



**Figure 7.** Measured waveform locations of the J-dot probes with respect to the horn antenna for Sots #12 through #14.

DSA 602A DIGITIZING SIGNAL ANALYZER

date: 12-JUN time: 18:37:10

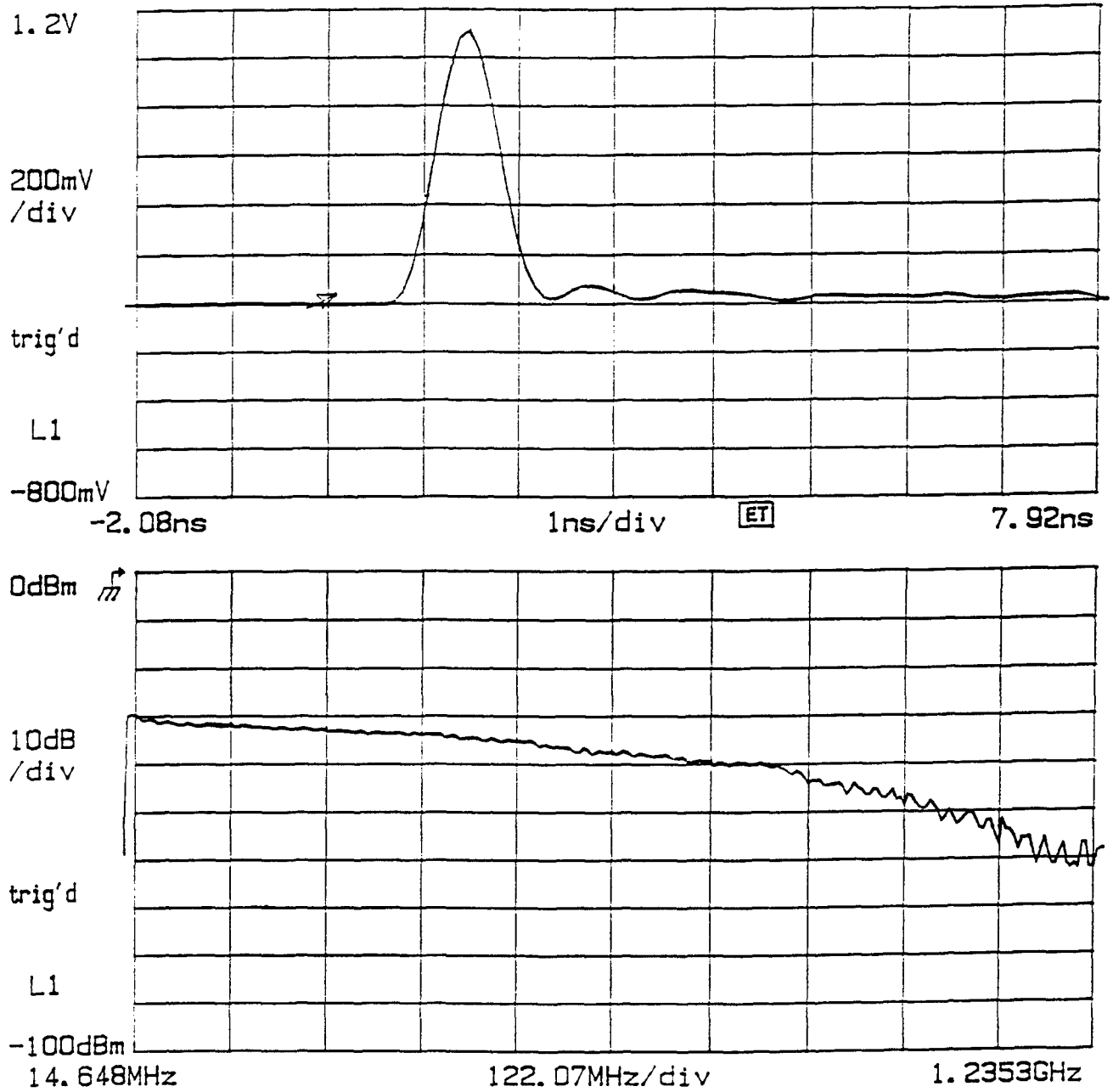
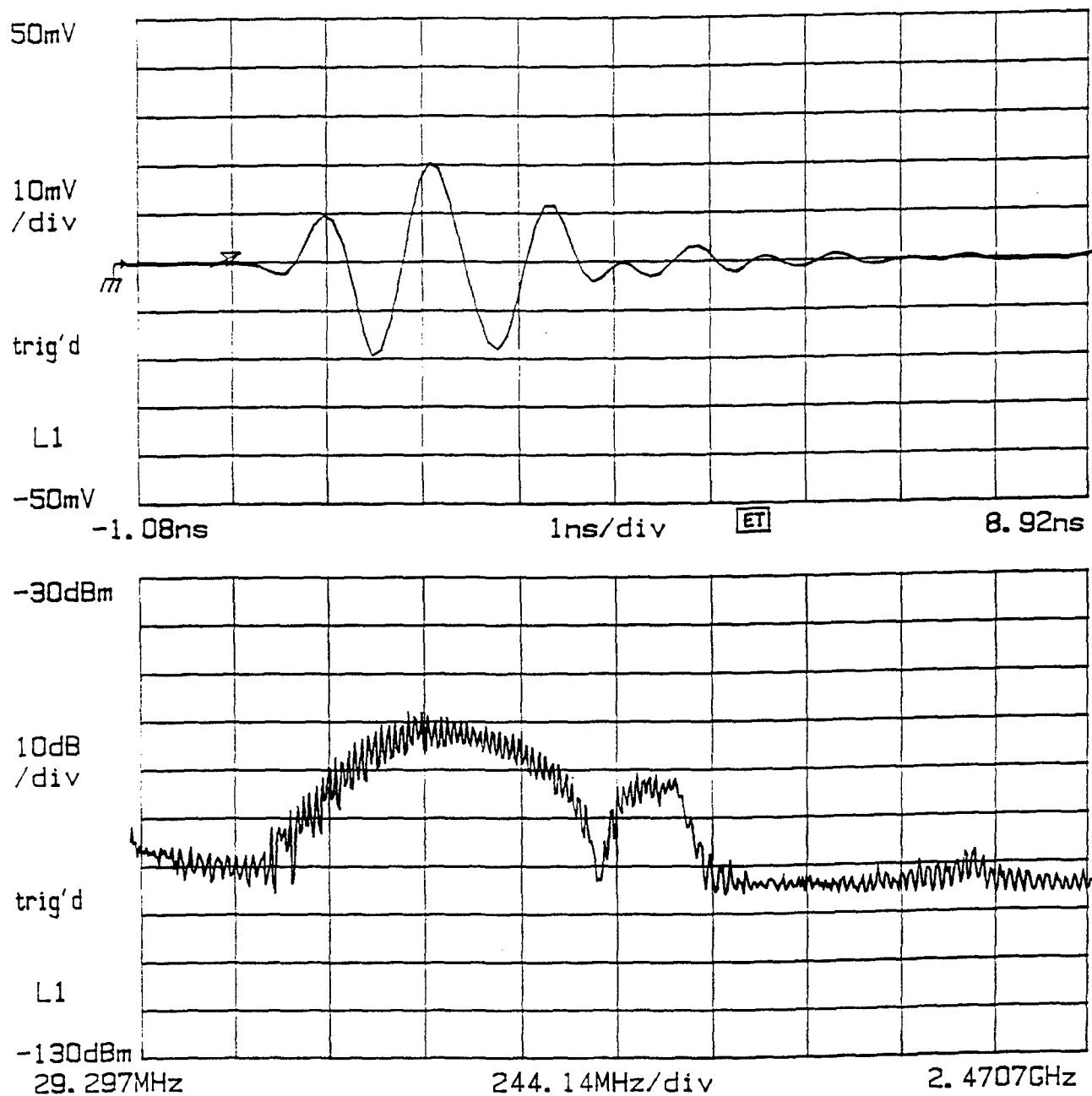


Figure 8. Measured waveform of Shot #7 of the input pulse amplitude and frequency spectrum.

DSA 602A DIGITIZING SIGNAL ANALYZER

date: 12-JUN time: 18:45:09



**Figure 9.** Radiated pulse waveform for Shot #8 and its frequency response probe. Probe is centered 3 meters in front of the horn antenna.



DSA 602A DIGITIZING SIGNAL ANALYZER

date: 12-JUN time: 18:49:35

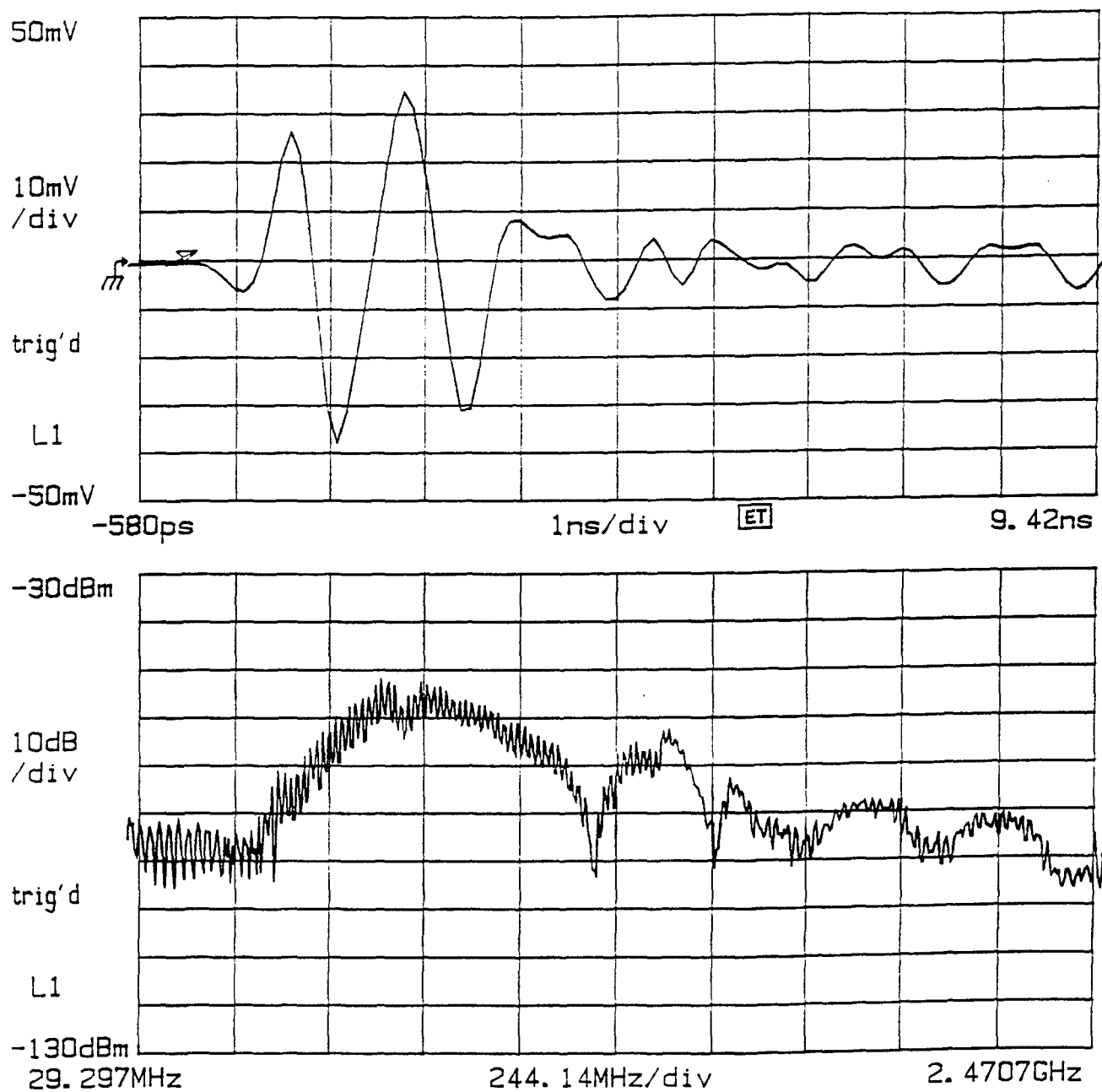


**Figure 10.** Radiated pulse waveform for Shot #9 and its frequency response probe. Probe is in antenna mouth, on bottom wall.

DSA 602A DIGITIZING SIGNAL ANALYZER

date: 12-JUN time: 19:01:09

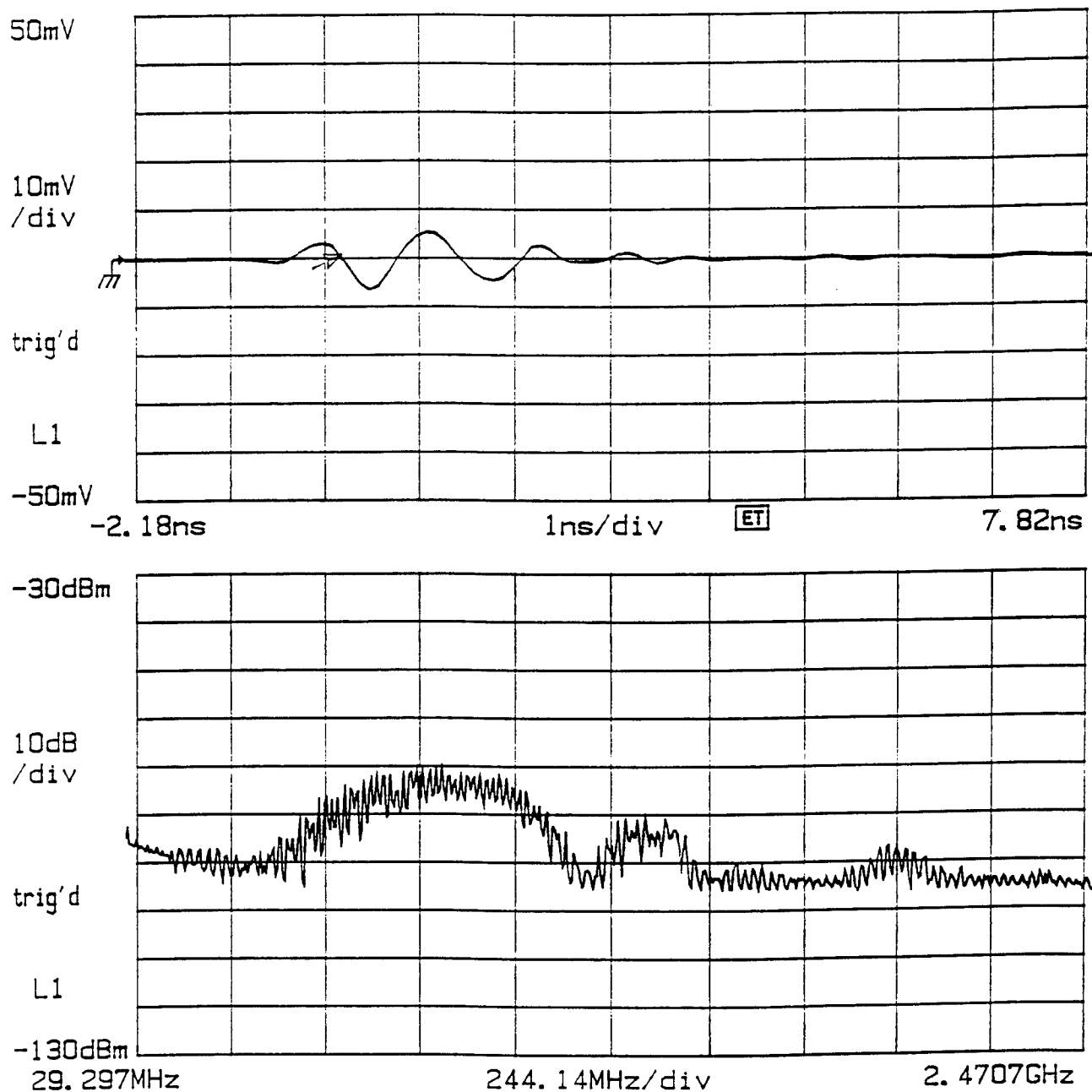


**Figure 11.** Radiated pulse waveform for Shot #10 and its frequency response probe. Probe is 3 meters in front of antenna and then 2 meters to left.

DSA 602A DIGITIZING SIGNAL ANALYZER

date: 12-JUN time: 19:07:12

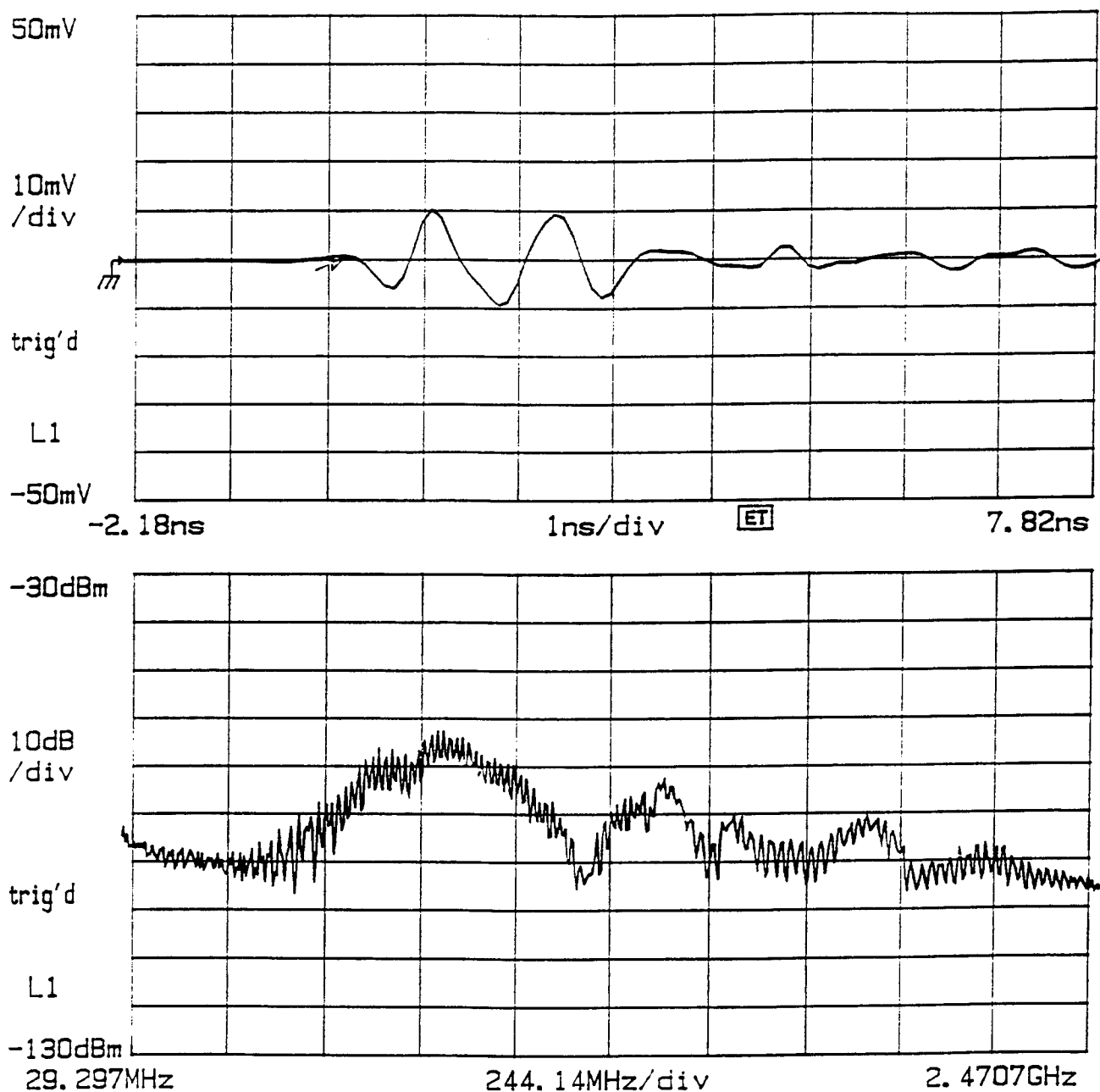


**Figure 12.** Radiated pulse waveform for Shot #11 and its frequency response probe. Probe is 3 meters in front and in line with bottom of antenna.

DSA 602A DIGITIZING SIGNAL ANALYZER

date: 12-JUN time: 19:12:46

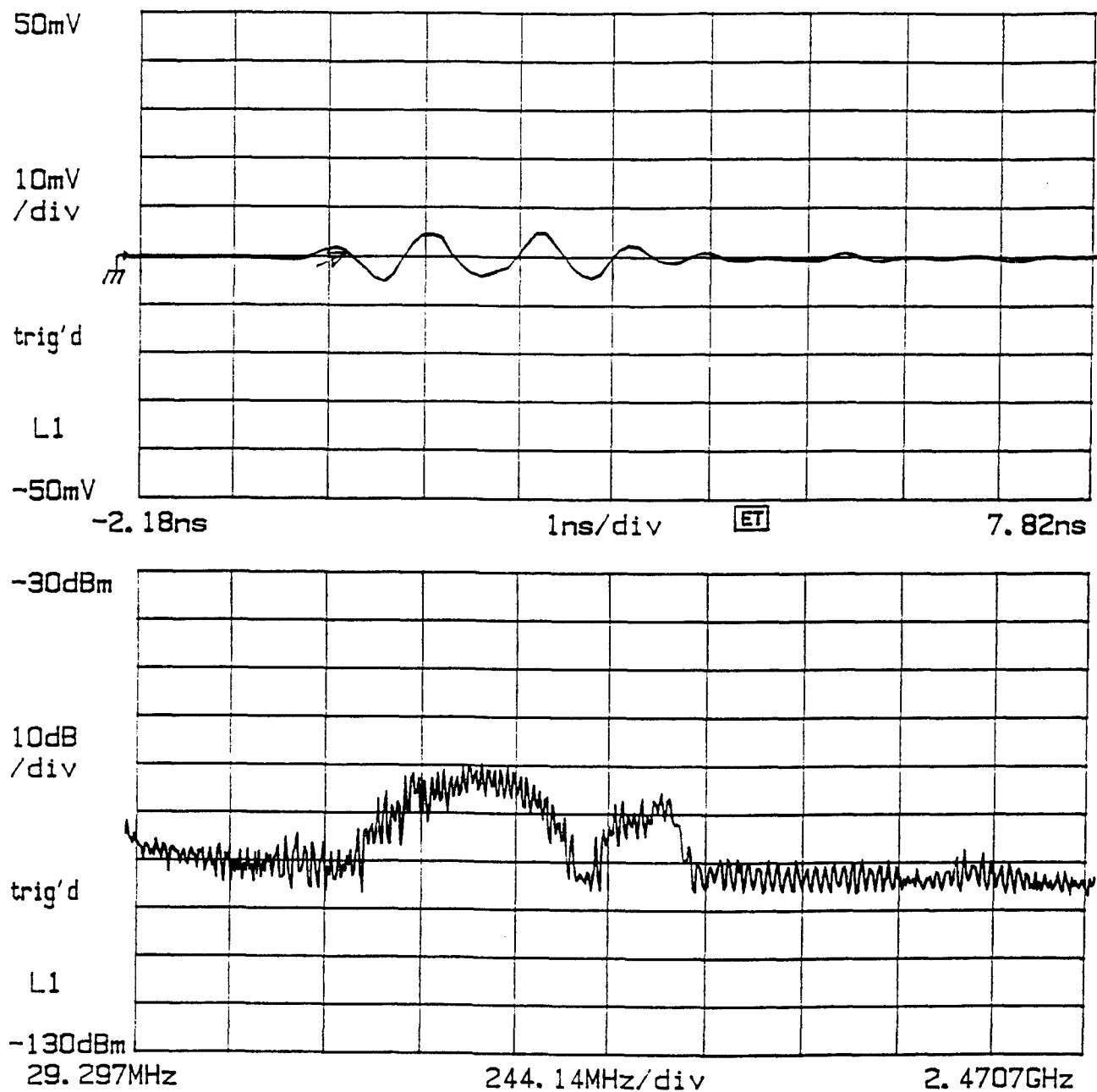


**Figure 13.** Radiated pulse waveform for Shot #12 and its frequency response probe. Probe is 6 meters in front of antenna.

DSA 602A DIGITIZING SIGNAL ANALYZER

date: 12-JUN time: 19:18:56

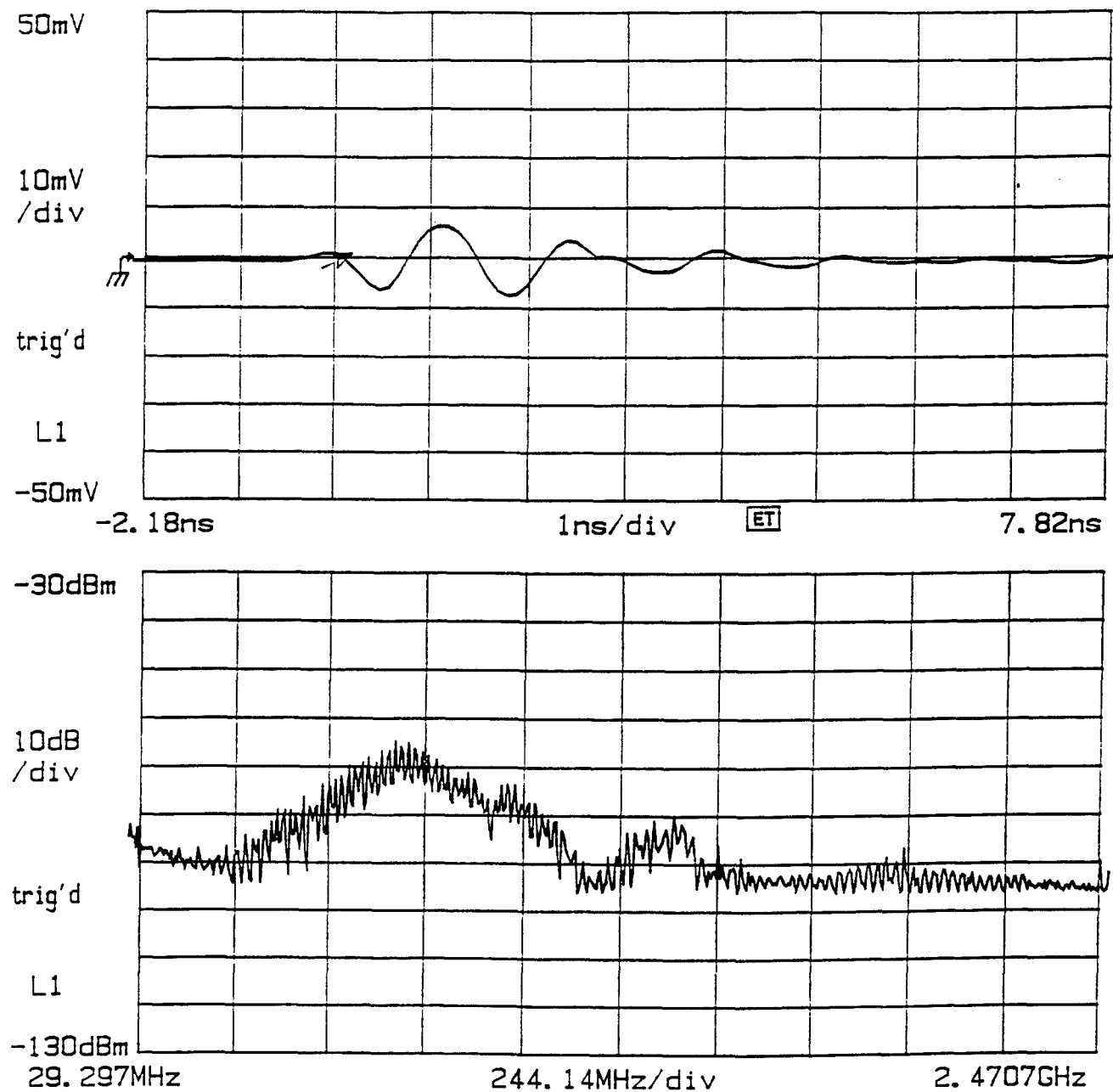


**Figure 14.** Radiated pulse waveform for Shot #13 and its frequency response probe. Probe is in antenna mouth, on left hand wall.

DSA 602A DIGITIZING SIGNAL ANALYZER

date: 12-JUN time: 19:28:09

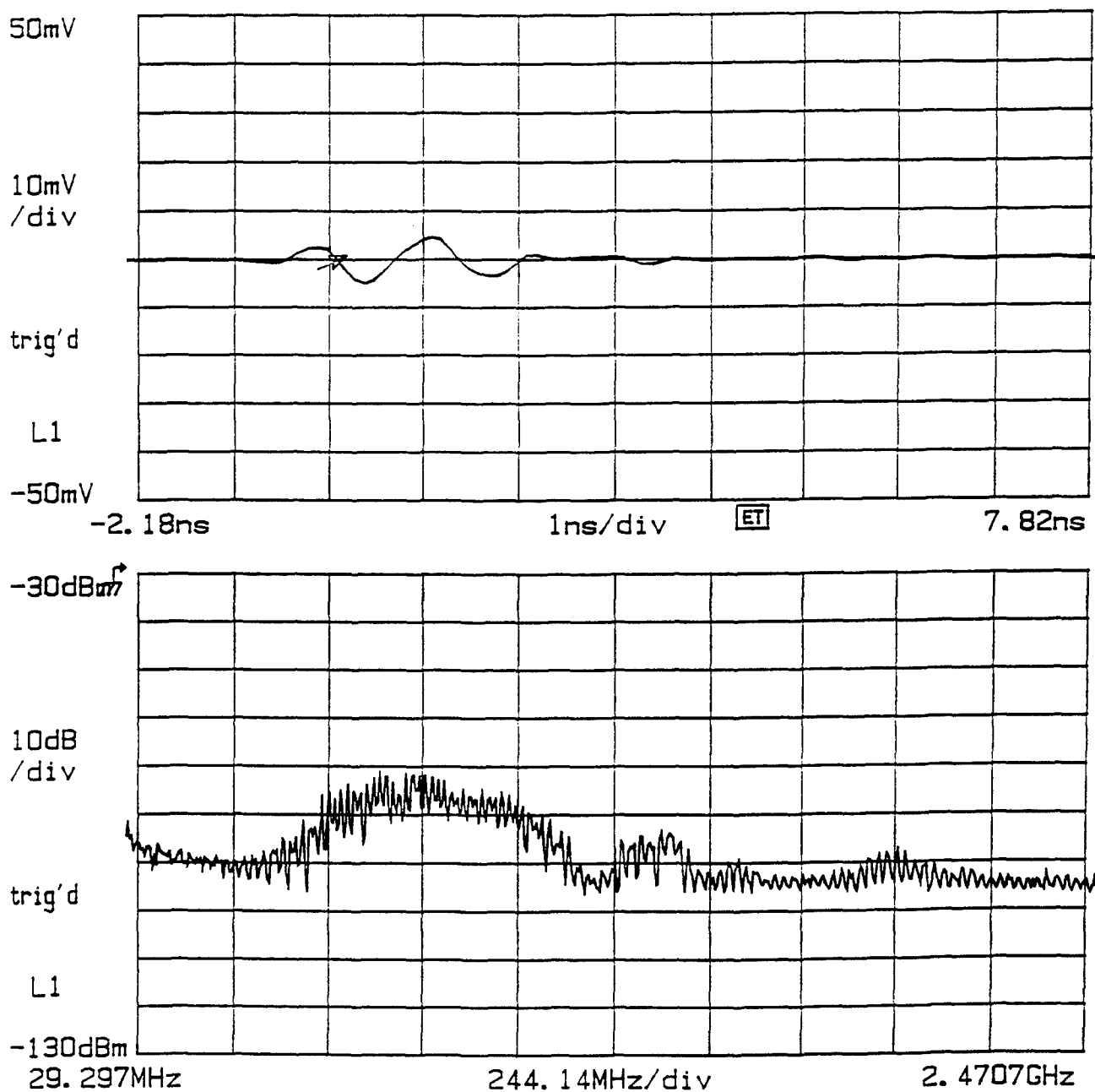


**Figure 15.** Radiated pulse waveform for Shot #14 and its frequency response probe. Probe is 3 meters in front of antenna and then 2 meters to right.

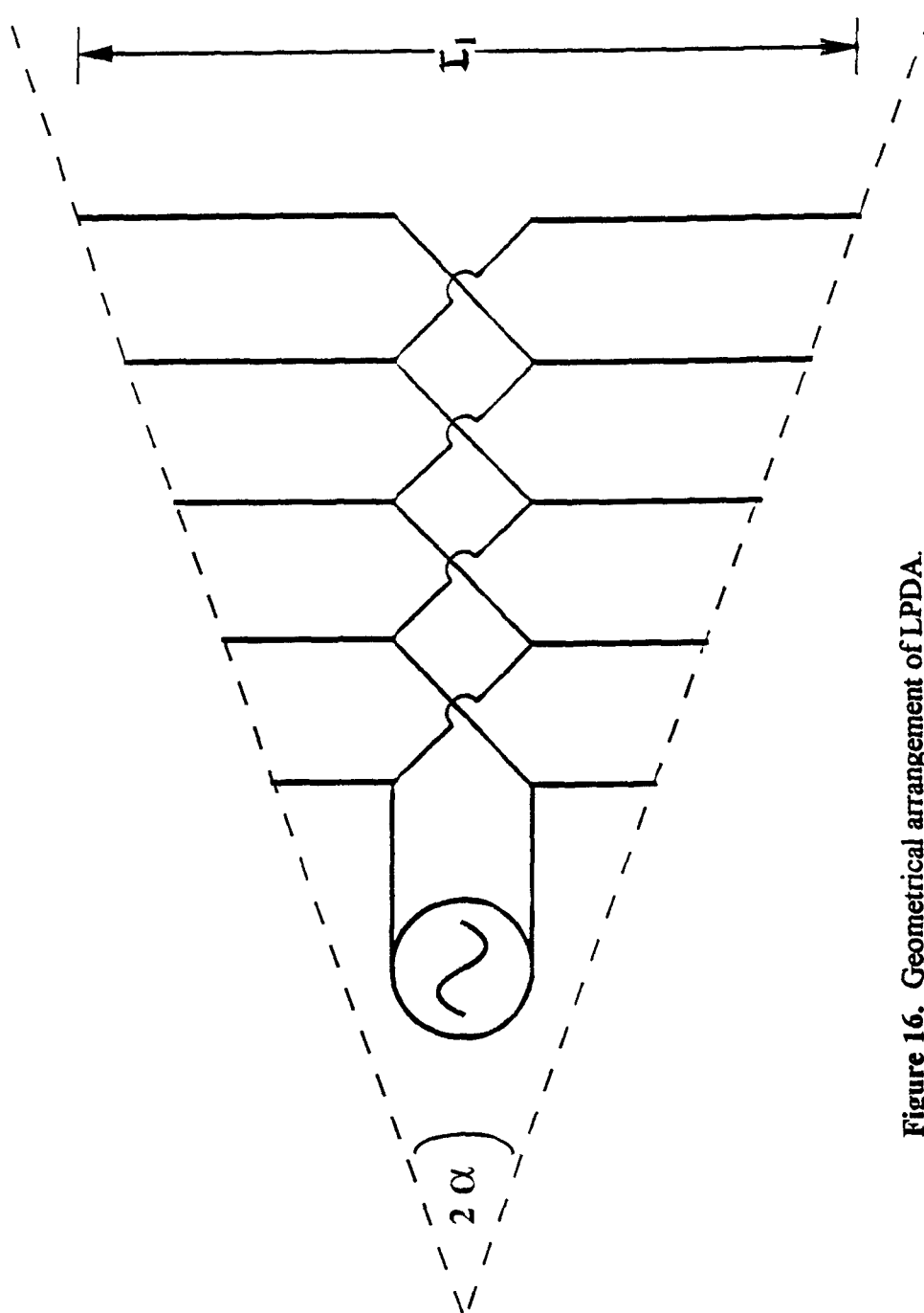
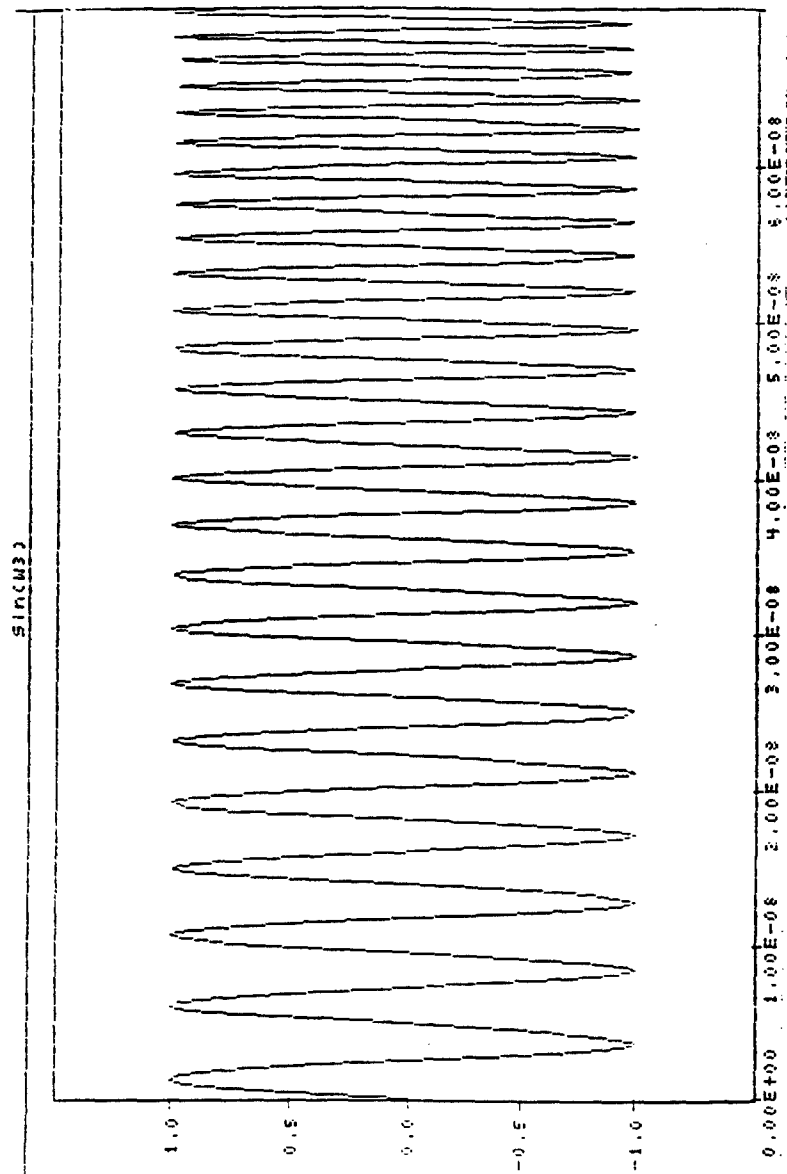
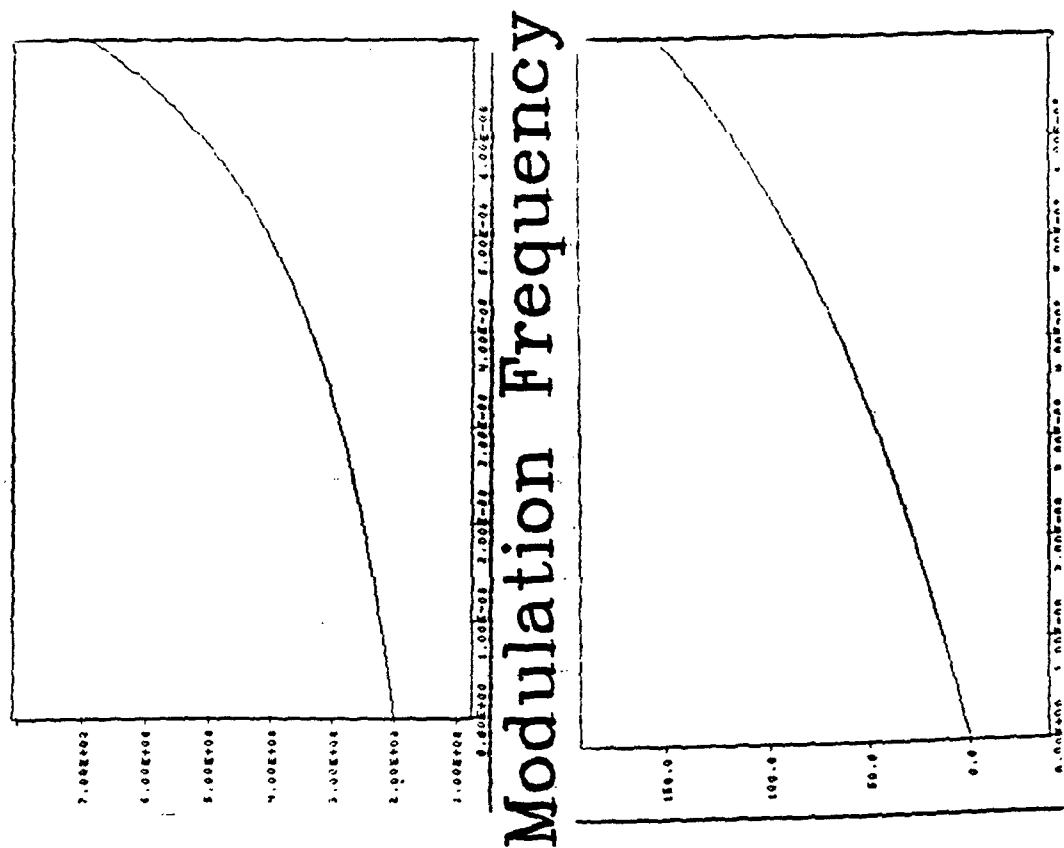


Figure 16. Geometrical arrangement of LPDA.



**Figure 17. Square wave modulation envelope of a linear Frequency Modulated (FM) pulse with low to high frequencies.**

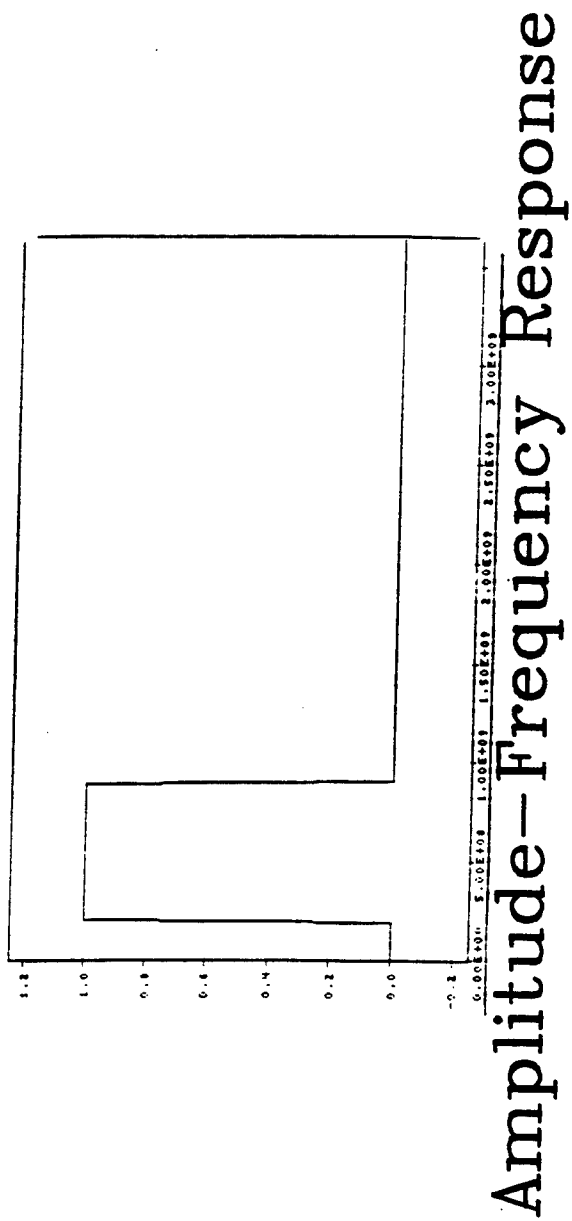




## Modulation Frequency

Phase (Integral of the frequency function)

Figure 18. Exponentially modulated FM pulse to reduce unwanted frequency distortion.



3-35

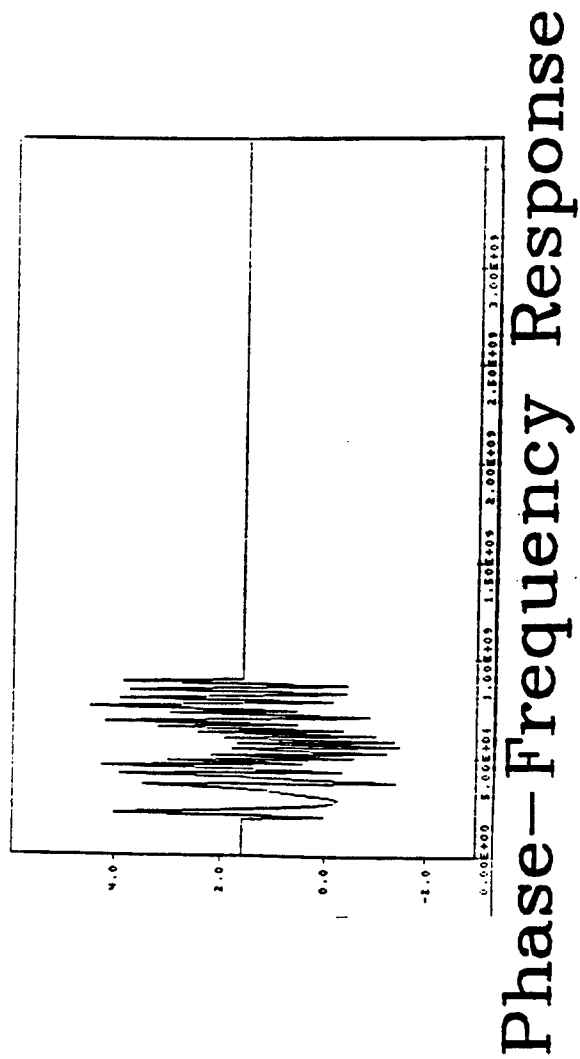


**Figure 19.** Amplitude and phase responses as functions of time for exponential pulse in Figure 18.

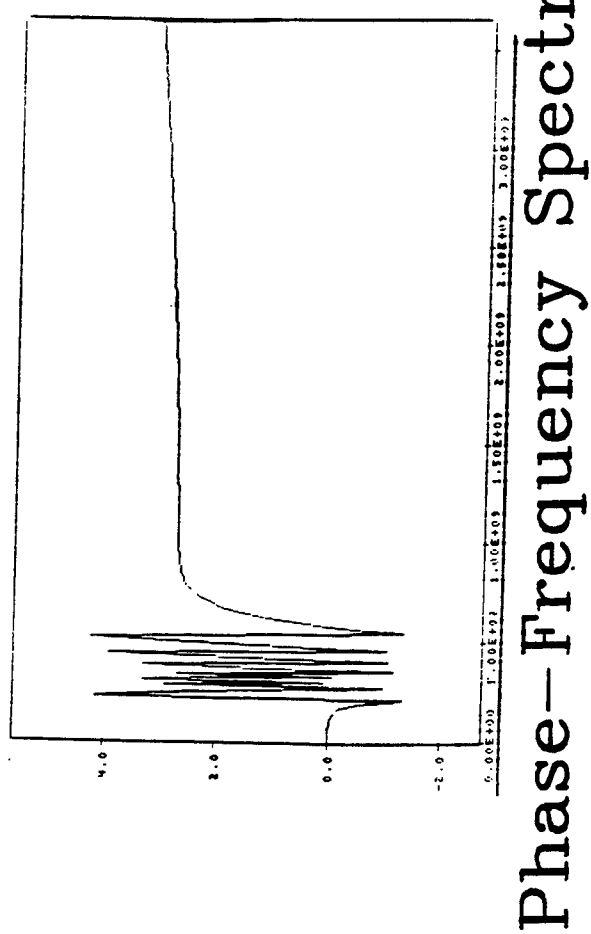
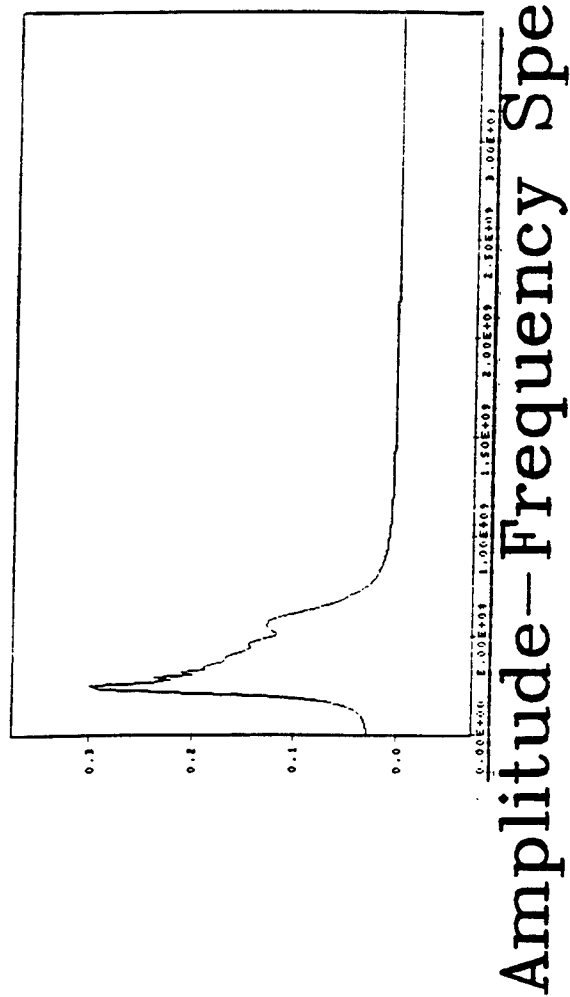
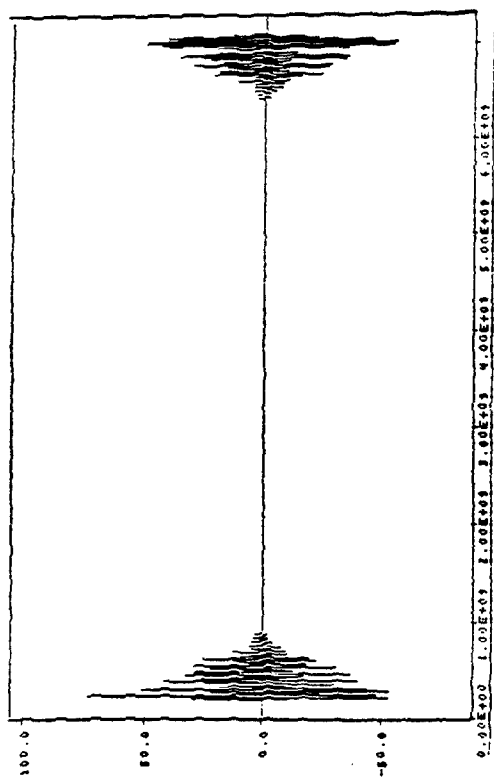
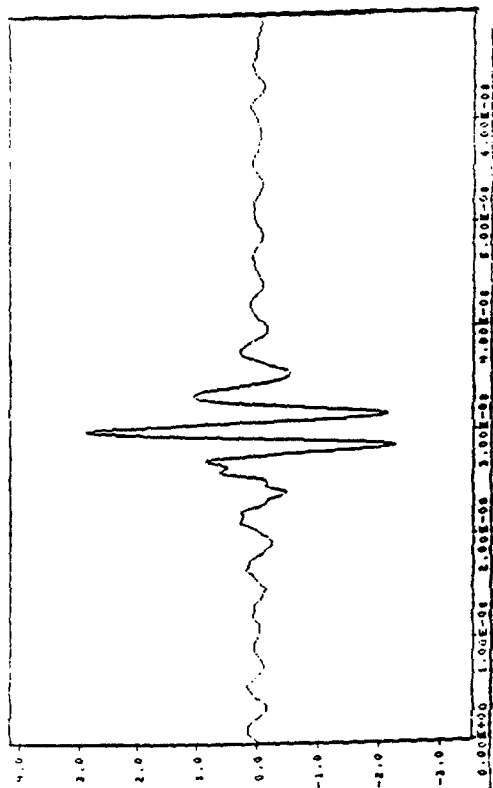


Figure 20. Amplitude and phase frequency spectra of Figure 19.

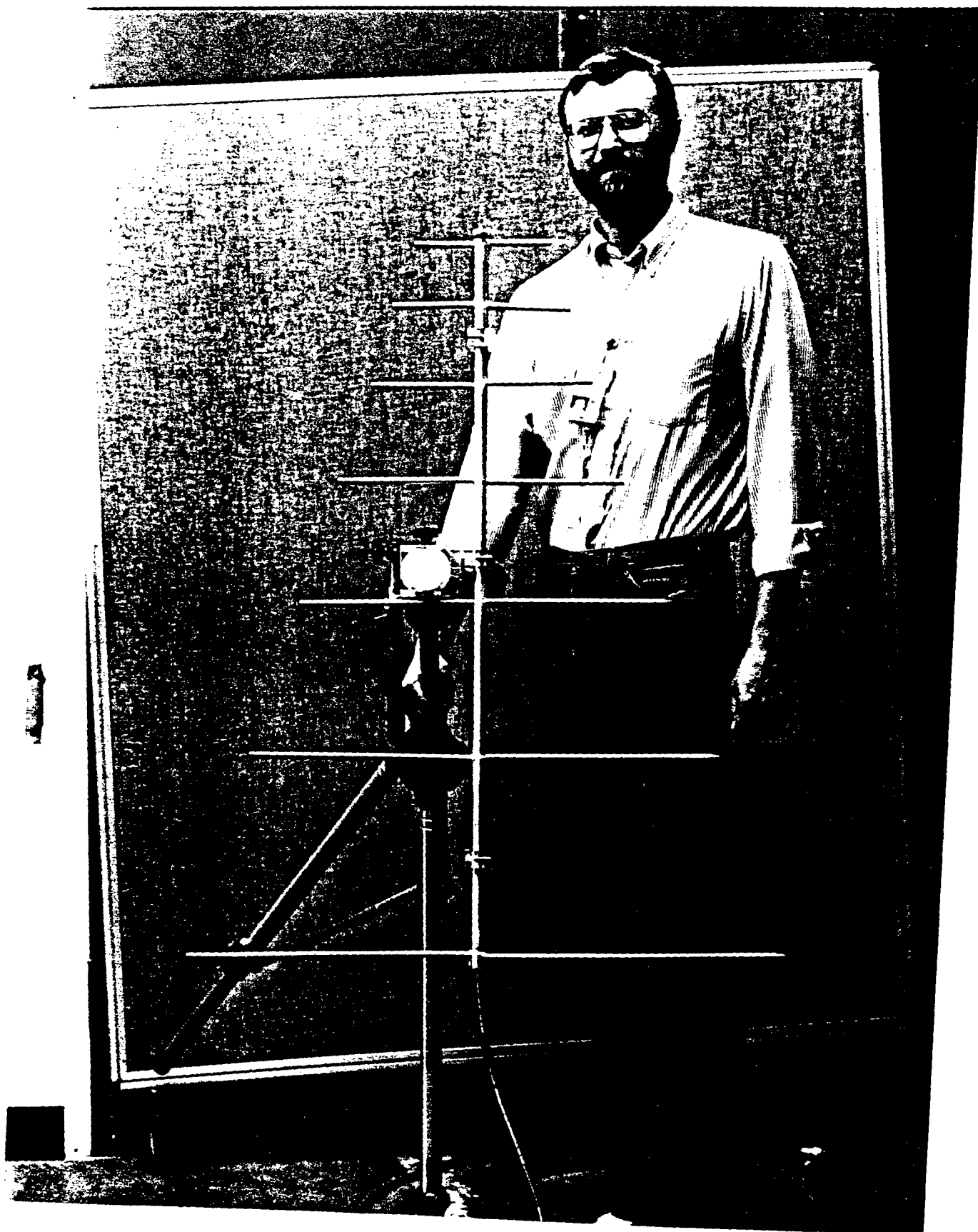


FFT of the Output Waveform



Time Form of the Output Waveform

Figure 21. Chirped pulse with distortion reduced.



A STUDY OF THERMOTROPIC LIQUID CRYSTAL POLYMERS

David M. Elliott  
Associate Professor  
Department of Engineering

Arkansas Tech University  
Russellville, AR 72801

Final Report for:  
Research Initiation Program  
Phillips Laboratory

Sponsored by:  
Air Force Office of Scientific Research  
Bolling Air Force Base, Washington, D.C.

and

Arkansas Tech University

November 1993

# A STUDY OF THERMOTROPIC LIQUID CRYSTAL POLYMERS

David M. Elliott  
Associate Professor  
Arkansas Tech University

## Abstract

Researchers at the Phillips Laboratory at Edwards Air Force Base have been instrumental in both the development and the characterization of thermotropic liquid crystal polymers (LCPs). The mechanical and chemical properties of parts made by injection molding some of these materials are known to dramatically improve upon thermal annealing. In order to realize the full potential of annealed LCPs, a firm understanding of the molecular and crystalline structure, morphology, texture, and the dynamics and mechanism of formation of the annealed state must be obtained.

Very little is known about the crystalline structure of injection molded LCPs and how that structure varies or changes with direction of flow into the mold and other mold processing variables or with thermal annealing of molded parts. The principal objective of this work was to assess the feasibility of using neutron diffraction as a tool to investigate the crystalline properties of these parts. Concurrent with work towards this objective, a number of other techniques of investigation were utilized to provide further information about the crystalline and mechanical properties. These other techniques included x-ray diffraction, tensile testing, hardness testing, and scanning electron microscopy of fracture surfaces.

It was found that the neutron diffraction technique is capable of establishing that these materials do have a crystalline structure and of measuring some of the crystalline properties but it is not capable of determining the crystalline structure itself. X-ray diffraction was found to be better, faster and less expensive for these measurements.

Injection molded parts made from five commercial LCPs were studied. It was found that both crystalline and mechanical properties were dramatically influenced by annealing in argon at 260 deg. C.

# A STUDY OF THERMOTROPIC LIQUID CRYSTAL POLYMERS

David M. Elliott

## INTRODUCTION

The development of advanced new materials possessing very high specific strength and specific modulus is critically important to the Air Force mission in both the exploration of interplanetary space and the development of higher performance and lower cost missile systems. Composite materials with superior mechanical properties have been made from high-strength fibers and graphite. Parts and structures made from these composite materials are, however, relatively costly because of the complexity of the manufacturing process. The high-strength fibers used in these composite materials are often prepared from stiff-chain aromatic polymers. These polymers are called stiff-chain polymers because the molecules tend to be quite elongated in solution or in the melt. These elongated molecules have a propensity to form a definite crystalline organization in the liquid state (either solution or melt) and consequently they are referred to as liquid-crystal polymers (LCPs). In addition to their use in high-strength fibers, LCPs can be injection or blow molded inexpensively into complex shapes. The liquid crystalline order persists and is often enhanced as the LCPs are carried into the solid state during the molding process. Solid materials molded from LCPs are, however, inhomogeneous and highly anisotropic. They can be thought of as molecular composites.

The mechanical properties of solid LCPs depend importantly on the processing as well as on the material itself. Flow, either in the spinning of fibers or in the molding of parts, can result in an increase in the crystalline order and this in turn can result in significant enhancements of both strength and modulus. Temperature is also an important processing variable. The relationships between molecular conformation and crystalline order and mechanical and chemical properties are not well known yet understanding these relationships is vital to developing these molecular composites to their full potential.

Recognizing this, researchers at the Phillips Laboratory are pursuing a program of both theoretical and experimental studies to characterize the molecular structure, dynamics, and mechanism of formation of the annealed state in selected linear LCPs. In addition, a number of Air Force installations are cooperating in a related program to fabricate injection molded parts from commercial LCPs, to measure the mechanical properties of these injection molded LCPs, and to use the parts in demonstration applications including solid rocket motors.



A process known as physico-chemical annealing is of particular interest in the design of parts made from LCPs. In this process, the material is heated to a temperature below the melting point and held there for a period of time. When the material is cooled it sometimes happens that the mechanical properties, particularly the modulus and the ultimate strength, are significantly improved, the resistance to solvents is improved and the material no longer melts; it decomposes instead. This annealing process is commonly utilized in making high-strength LCP fibers and the details of the process and its effects on physical and chemical properties are relatively well known in this field. The annealing process appears to work best when the long chain molecules of the material are highly oriented prior to annealing as they are in spun or drawn fibers.

Fundamental to all of these programs is the ability to determine and reliably measure the important crystalline properties and those mechanical properties essential for design purposes. Because of the highly anisotropic nature of injection molded LCP parts, it is necessary to determine these properties as functions of both orientation and position within the part. Because there is strong evidence that thermal annealing affects a number of these properties, it is desirable to measure the effect of annealing on each important property individually. The measurement of these properties requires a wide variety of the modern techniques of material science. It is unusual for all of the necessary equipment and investigative skills to exist in a single laboratory. As a consequence, cooperative efforts between a number of different organizations are usually required. The current program involves a number of Air Force installations and laboratories, other government facilities, both U.S. and foreign, universities, and industrial organizations. The work reported here is a joint effort involving the United States Air Force Phillips Laboratory, Arkansas Tech University, and the Australian Nuclear Science & Technology Organisation, ANSTO. The experimental work was carried out at the ANSTO facilities at Lucas Heights in Australia.

The principal objective of this work was to assess the feasibility of using neutron diffraction as a tool to investigate the crystalline properties of injection molded parts made from commercially available liquid crystal polymers. Because of the work was carried out at ANSTO where on site there is available a wide variety of world class experimental facilities and competent and genuinely helpful people, a number of other techniques were used to obtain additional data which added significantly to the knowledge base and suggested fruitful areas for further work. These other techniques included x-ray diffraction, tensile testing, hardness testing, and scanning electron microscopy of fracture surfaces.

HRPD is conventional in design but is carefully optimized for high resolution diffraction experiments. Both diffractometer operation and data collection are computerized. Figure 1. shows the basic geometry of a neutron diffraction experiment. Figure 2. is a diagram of the VANESSA powder diffractometer in Britain which is similar in design to HRPD.

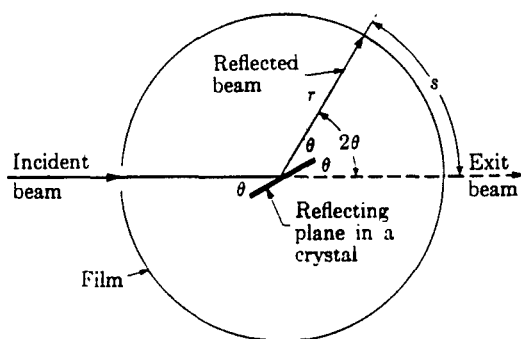


Figure 1. Basic geometry of a neutron diffraction experiment<sup>(1)</sup>

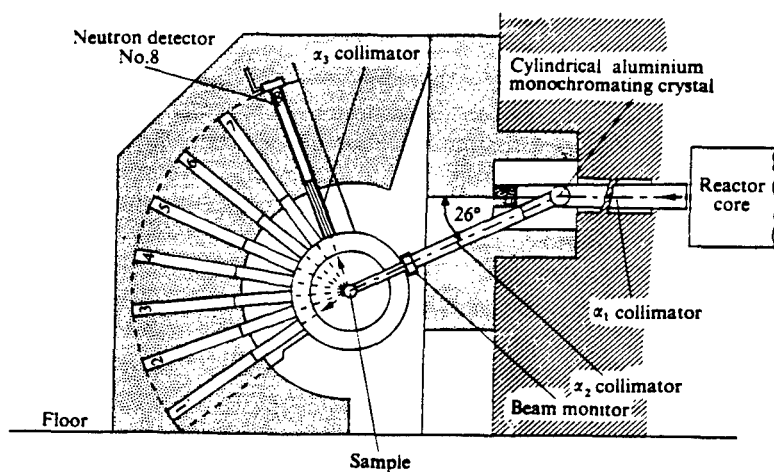


Figure 2. Diagram of the VANESSA powder diffractometer<sup>(2)</sup>

Like VANESSA, HRPD uses eight detectors spaced six degrees apart. These detectors rotate as a unit about the vertical axis through the sample. The sample itself can rotate during the experiment if the investigator so chooses. A monitor counter is placed in the beam at the point where it emerges from the concrete shield. This counter is used to assure uniform exposures. The important parameters of HRPD are given in Table 2.

Beam Hole	4H2
Monochromator	Ge (hhl)
Take Off Angle	120 degrees
Beam Size	20mm X 50mm
Flux at Sample	$5 \times 10^4$ n/cm <sup>2</sup> /sec
Available Wavelengths	1.377, 1.493, 1.893 Angstroms
Temperature Range	14K to 2000K

Table 2. HRPD parameters

All of the measurements reported in this work utilized a wavelength of 1.893 Angstroms and a two-theta step size of 0.05 or 0.1 degrees.

The results of a neutron diffraction experiment are usually presented in the form of a plot of intensity or counts vs the diffraction angle ( $2\theta$ ). For most samples of crystalline material, the plot looks like Figure 3. Note the presence of numerous well defined and relatively sharp peaks. In the case of liquid crystal polymers, however, the plot typically looks like Figure 4. In these plots there is typically only one peak that is well enough resolved to permit quantitative measurement. Sometimes there was evidence of one or two smaller peaks but these were not resolvable. The reason for this behavior is that the LCPs contain a high percentage of hydrogen. Hydrogen bound in crystals has a large incoherent scattering cross section. The effect of a high concentration of nuclei with a high incoherent scattering cross section is to smear the neutrons scattered from such nuclei rather uniformly over the total range of diffraction angles. The result is a very high background against which it is difficult to detect diffraction peaks. It should be mentioned that this problem could be significantly reduced by replacing the

normal hydrogen with deuterium. This is however, chemically difficult and extremely expensive.

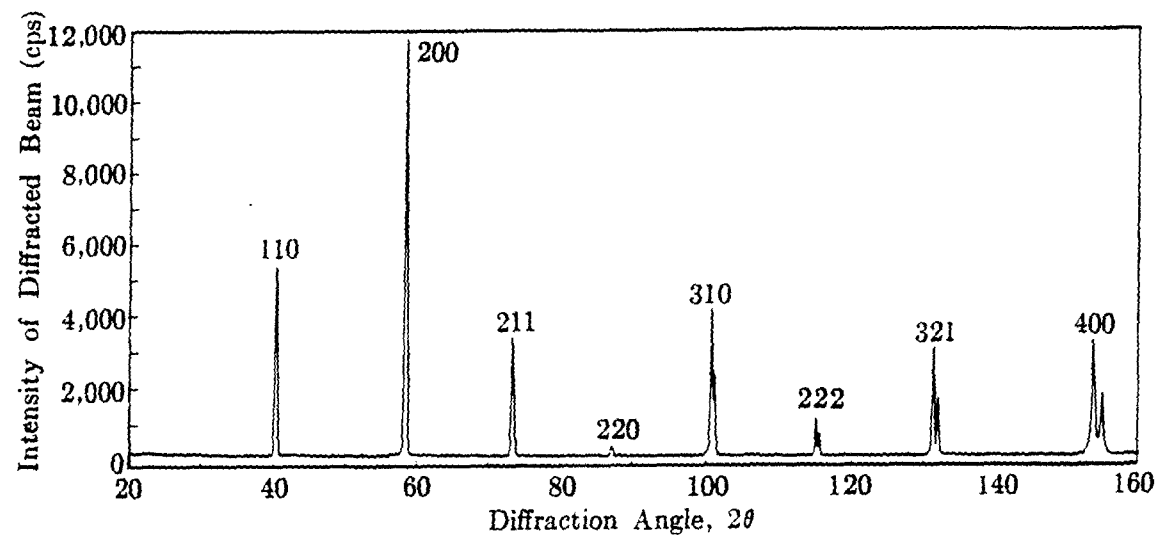


Figure 3. Typical neutron diffraction pattern for an inorganic crystalline material

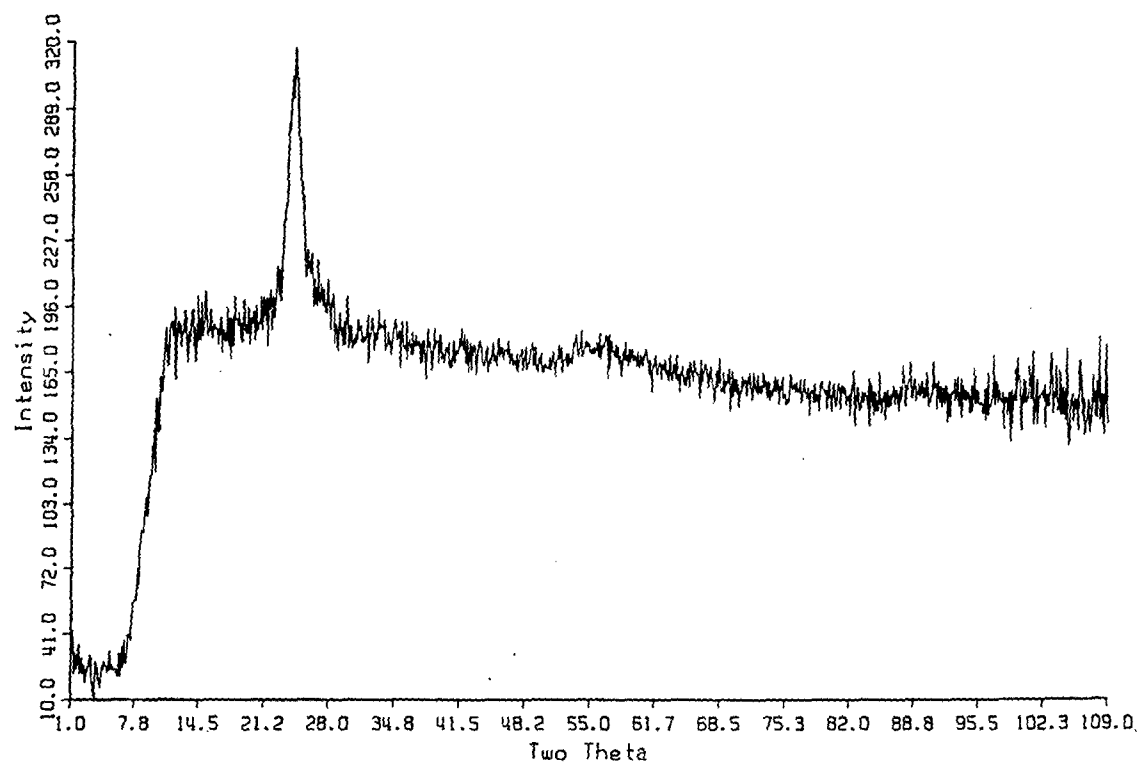


Figure 4. Typical neutron diffraction spectrum for a liquid crystal polymer

Given that there is only one peak to work with in these LCP diffraction patterns, one naturally asks: What useful information can be extracted from these data? The answer is a lot. First of all, the very presence of a peak indicates that the material is at least partially crystalline as opposed to wholly amorphous. Theory suggests that neutron diffraction peaks should be gaussian. A least squares fit to a gaussian riding on a linearly decreasing background was performed for each peak. The results of the fitting process yielded numerical values for the peak height, the peak width at half-maximum, and the location of the peak in  $2\theta$ . A relative area was calculated as the product of the peak height and the width at half-maximum. The location of the peak is related to the spacing of the reflecting planes in the crystal, the  $d$  spacing, through Bragg's law.

$$n\lambda = 2d\sin\theta$$

Changes in  $d$  spacing strongly suggest a change in the crystalline structure. The area of the peak is proportional to the intensity of neutrons scattered through  $2\theta$  which is in turn proportional to the square of the concentration of crystals with the proper orientation to satisfy Bragg's law. (Intensity is also proportional to the square of the structure factor which is a function of the positions of the atoms within the crystal.) The width of the peak is a measure of the degree of alignment of the set of individual crystals; the narrower the peak, the better the alignment. So even though there is only one peak (which precludes the determination of the exact crystal structure), the quantification of its parameters provides a great deal of interesting and useful information.

### **X-ray Diffraction**

The basic idea of x-ray diffraction is very similar to neutron diffraction. In both experiments, a beam of radiation is made to impinge on a sample and the intensity of the scattered radiation is measured as a function of the scattering angle. Figure 5 shows a schematic diagram of an x-ray diffractometer. A fundamental difference between the two experiments is that the x-rays interact with the orbital electrons in the sample while the neutrons interact with the sample nuclei. Bragg's law, however, applies in both cases. One result of this difference is that x-rays are strongly absorbed by the sample while neutrons are not. X-rays can, therefore, see only the sample surface and those atoms close to it. This can be an advantage or a disadvantage depending on what is wanted from the experiment. For polymers and other hydrogenous materials, x-ray diffraction does not suffer

from the problem of incoherent scattering from the bound hydrogen. The spectra are, therefore, much better resolved.

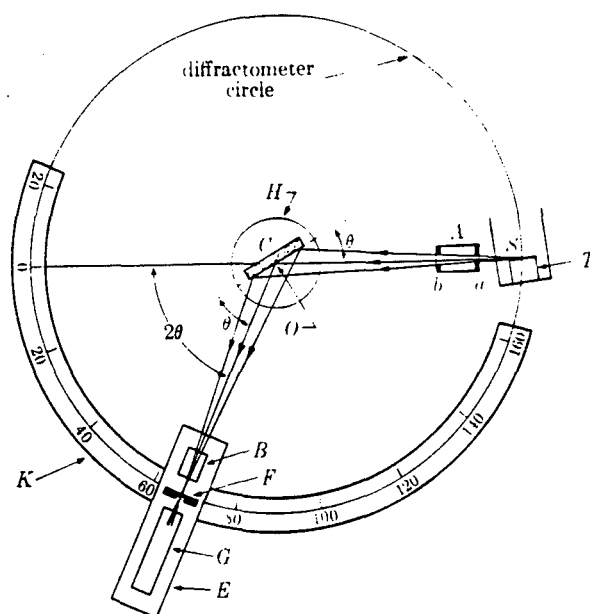


Figure 5. X-ray Diffractometer (schematic)

While the basic idea of x-ray and neutron diffraction is similar, in practice the two methods are very different. Neutron diffraction requires an intense source of neutrons, usually a nuclear reactor or a particle accelerator. Both types of neutron source are very large and very expensive to build and operate. The neutron diffractometers are usually custom built at the site where they will be used. X-ray diffractometers, on the other hand, are commercially available from a number of sources and cost only a few hundred thousand dollars. The source of the x-rays is part of the diffractometer package. Figure 6 shows a typical x-ray diffraction pattern obtained from a liquid crystal polymer.

The x-ray diffractometer used in this work was a Siemens model D-500. The wavelength was 1.789 Angstroms and the diffraction angle step size was 0.05 degrees.

#### Tensile Testing

Several of the mechanical properties of interest from a design standpoint can be measured utilizing standard tensile testing methods. For the current work, injection molded dogbone samples were subjected to tensile testing. The samples were 15 to 20cm in overall length and 3.1mm thick. The width of the gage

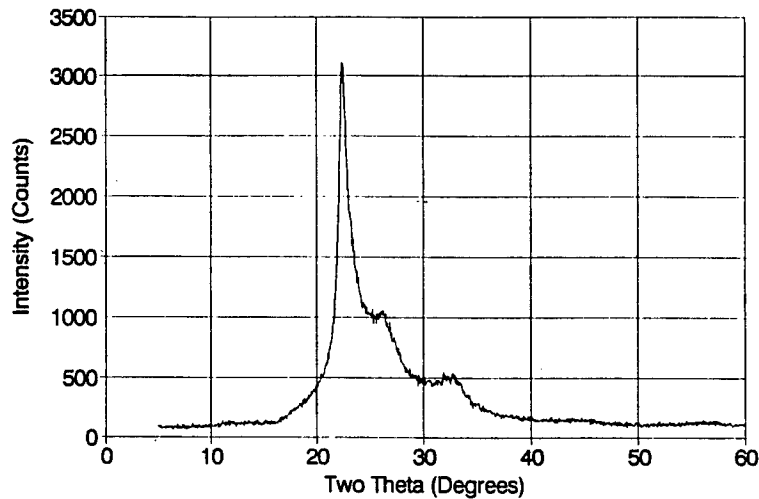


Figure 6. Typical x-ray diffraction pattern for a liquid crystal polymer

area was about 13.8mm. The testing machine was an Instron Model 8561 with a 100KN load. The extensometer was an Instron Model 045 with a 50mm gage length. The test environment was air at room temperature of 22 degrees C. All of the samples were tested in displacement control at a cross head rate of 0.01mm/sec. The following mechanical properties were measured: Elastic modulus, ultimate tensile strength, elongation at break, and reduction of area. It must be recognized that injection molded liquid crystal polymers are inhomogeneous and highly anisotropic. The tensile testing done in this work was restricted to uniaxial along the direction of flow into the mold.

#### Hardness Testing

Given the inhomogeneous and anisotropic nature of injection molded LCP parts, the interpretation of the results of standard hardness testing methods is difficult at best. All of these methods measure the extent to which a pointed probe penetrates the sample surface when pushed with a standard force. The Vickers method was chosen for this work because it uses an indenter in the form of a square pyramid with an apical angle of 136 degrees and because it uses much lighter loads. The other methods use spherical or conical indentors. The impression is measured by means of a medium-power compound microscope. In the

normal test, both dimensions of the diamond shaped indentation are measured and an average value is used. The Vickers hardness number is found from the relation

$$V = P/0.539d^2$$

where P is the imposed load in Kg and d is the diagonal of the indentation in mm. The anisotropy of the samples is evident from the different values of d parallel to and perpendicular to the direction of flow into the mold. Vickers hardness numbers are reported parallel to the flow direction, perpendicular to it, and as an average of these two values.

### **Scanning Electron Microscopy of Fracture Surfaces**

Scanning electron microscopy is preferred over optical microscopy for the examination of fracture surfaces because it has much better resolution and depth of field. These characteristics are very beneficial in revealing the topographical features of fracture surfaces. In scanning electron microscopy, the image is formed by reflected electron beams. It is necessary for the surface being examined to be electrically conductive. To provide this surface conductivity, the LCP fracture surfaces were coated with a thin layer of carbon by a sputtering process. The instrument used was a JEOL Model JXA-840 Scanning Microanalyzer. Photomicrographs were taken of the dogbone fracture surfaces of VECTRA A950 and HX 4000 both untreated and annealed for 16 hours at 260 deg. C.

## **RESULTS**

### **Neutron Diffraction Studies of Orientation**

The size of the peak obtained by neutron diffraction of injection molded LCP samples was found to be very dependent upon the orientation of the sample in the diffractometer. The peak was found to be larger in all cases when the sample was oriented in the diffractometer such that the direction the material flowed into the mold was aligned with the vertical axis of the diffractometer. In the results which follow, this direction is referred to as "vertical". The horizontal direction is, of course, rotated 90 degrees. Figures 7 and 8 show the spectra at both orientations and the difference between them for VECTRA B950T and HX 4000 respectively. The samples were 50mm X 50mm squares cut from injection molded sheets. The direction of flow into the mold was determined visually from the appearance of the surface of the sheets.



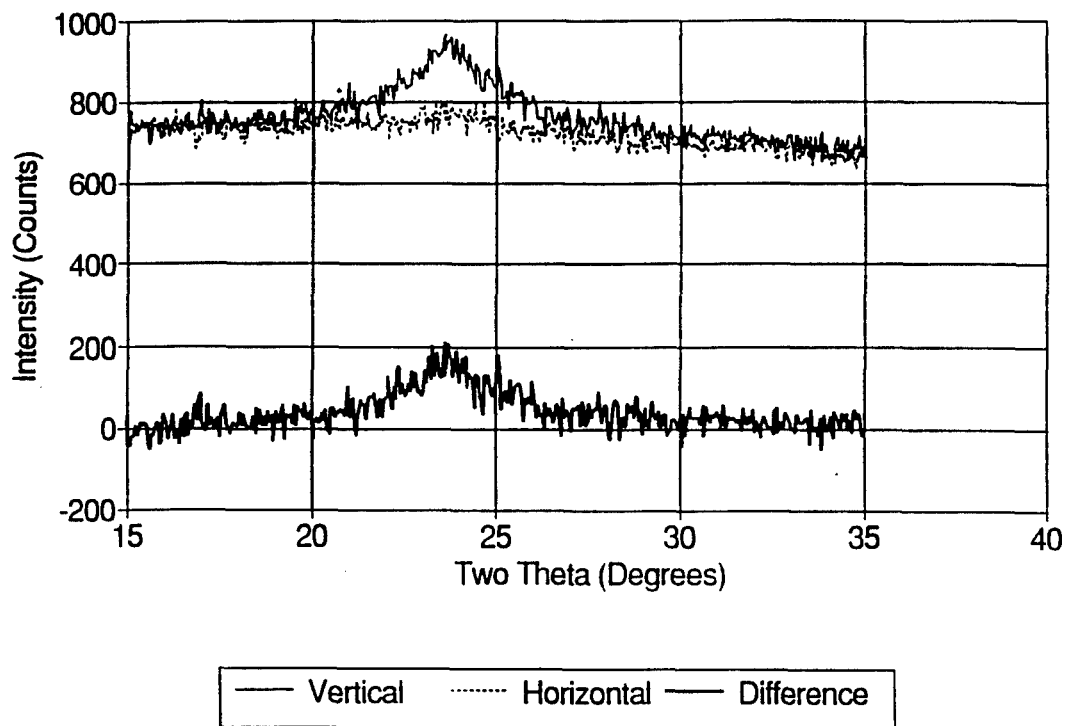


Figure 7. Neutron Diffraction Spectra as a Function of Orientation for VECTRA B950T

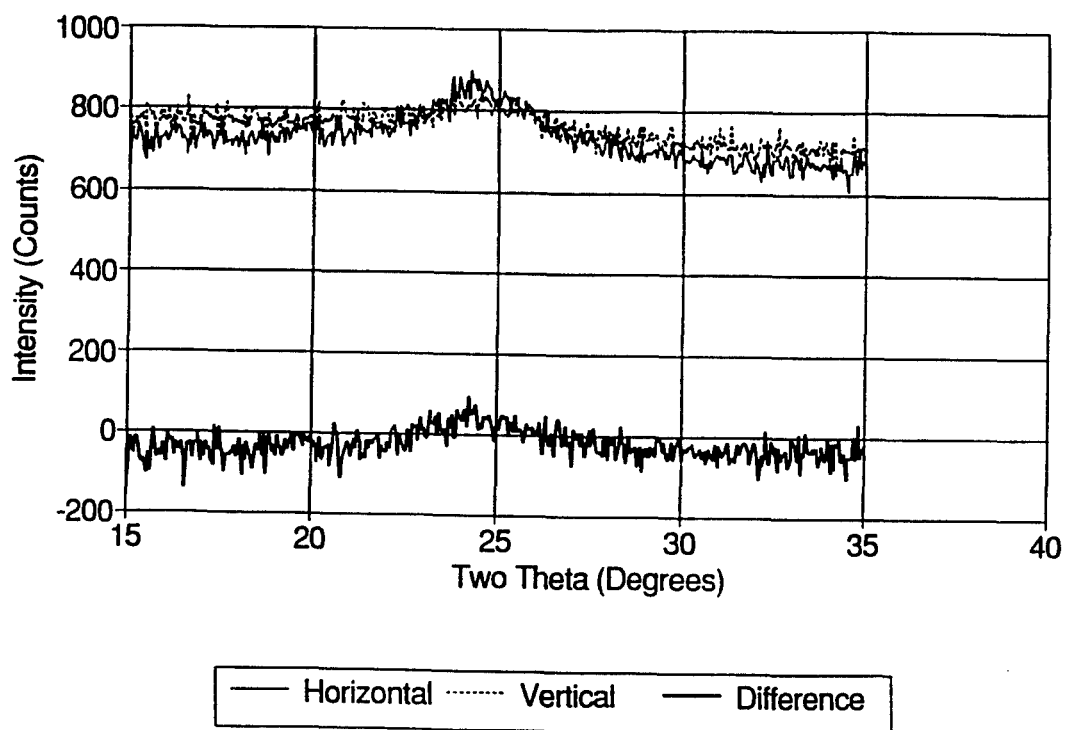


Figure 8. Neutron Diffraction Spectra as a Function of Orientation for HX 4000

Even though the peak is larger in the vertical direction for all materials tested, the extent to which it is larger varies considerably from one material to the next.

#### **Neutron Diffraction Studies of Annealing Versus Orientation**

Figures 9 through 11 show the measured neutron diffraction peak parameters individually for the two different orientations both for untreated LCPs and for LCPs which have been annealed for 16 hours in argon at 260 de. C. The legend "UV" means an untreated sample oriented in the vertical direction while "AH" means an annealed one oriented in the horizontal direction. The ordinates give the actual values calculated from the peak fits. The units of height are counts, width is in  $2\theta$  with units of degrees, area is the product of peak height and width, and d is in Angstroms calculated from Bragg's law. With the results presented in this way, it is easy to see the effects of orientation and annealing individually or combined.

Figures 12 through 14 show the same information as the previous figures but in a different format. Here the percent increase in the individual parameters after annealing is shown for both the vertical and horizontal directions.

#### **Neutron Diffraction Studies of Annealing of Powders**

When the molten LCP flows into the mold, the shear field tends to align the molecules in the direction of flow. In an attempt to remove this preferred alignment and obtain a diffraction pattern for randomly oriented crystals, a powder was made from two of the sheet samples by belt sanding the edges and collecting the dust. This was done for POLYMER A and for SRT 500. Half of the resultant powder for each material was annealed at 260 deg. C for 16 hours under argon and the other half was left untreated. The powder samples were put into vanadium sample cans. These sample cans were rotated about their vertical axis while being exposed to the neutron beam. The resultant spectra are shown in Figures 15 and 16. The background areas far removed from the peaks do not lie on top of each other either because the sample weights were (POLYMER A) different or the irradiation time was different (SRT 500). What is of most interest in both cases is that the peak does grow significantly with annealing.

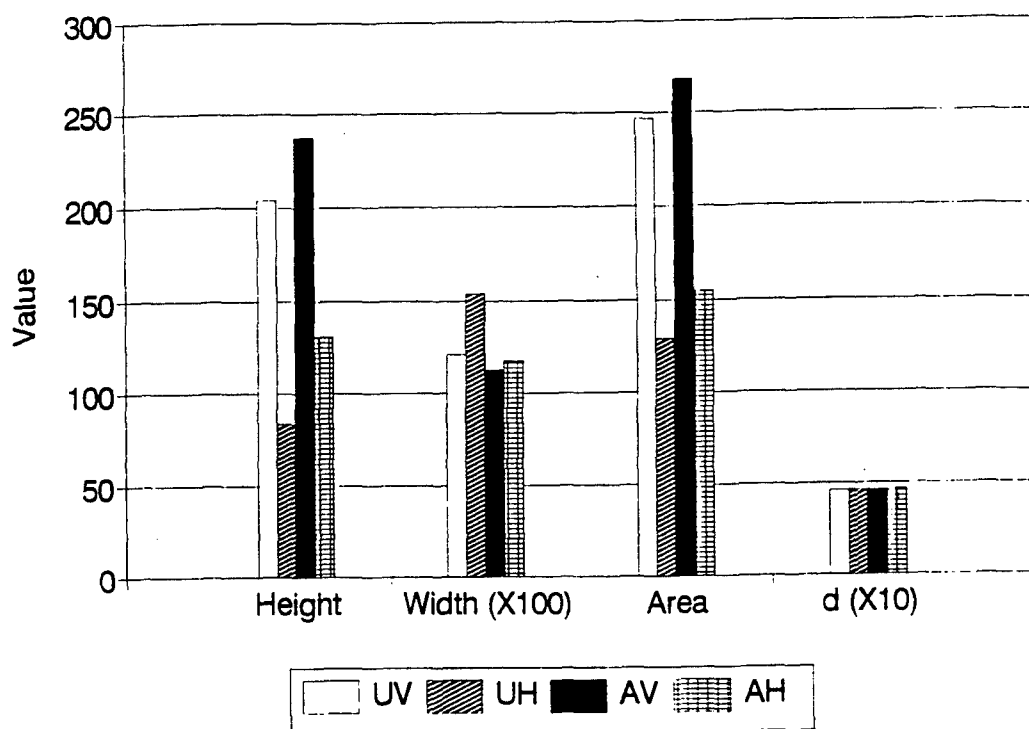


Figure 9. Peak parameters for POLYMER A

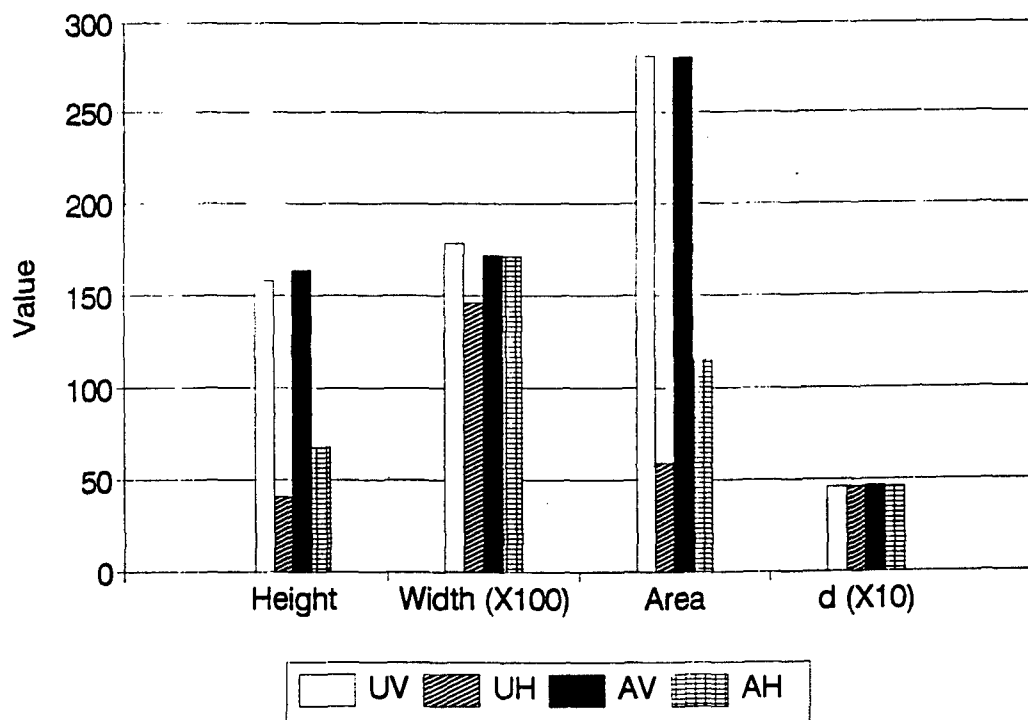


Figure 10. Peak parameters for VECTRA B950T

## **Neutron Diffraction Investigation of the Effect of Gamma Rays**

It was suggested by some that gamma rays might have an effect similar to thermal annealing. A sample of SRT 500 powder was exposed to 500 KGray of Co-60 gamma rays. Spectra of the exposed and unexposed powders are shown in Figure 17. There was no difference in the spectra (the difference curve is flat), suggesting that the gamma rays had no effect on the crystalline structure of SRT 500.

## **X-Ray Diffraction**

X-ray diffraction spectra were taken of both skin and core for POLYMER A and for HX 4000. This was done both for untreated and annealed samples. Because the x-rays do not penetrate deeply, the spectra of the skin region were taken of small pieces of sheet directly. To obtain surfaces of core material, the skin was milled off to a depth of about 0.3mm to expose the core. These spectra are shown in Figures 18 through 21.

These spectra are clearly more detailed than those produced by neutron diffraction. Changes with annealing in both the skin and core regions are evident. These spectra have not yet been quantified by peak fitting techniques. Fitting a spectrum with several peaks is significantly more difficult than fitting a single peak. Figure 19 shows that annealing causes the main peak to shrink in the core region of POLYMER A. This result is inconsistent with all of the other x-ray and neutron diffraction data and is therefore suspect. It is possible that the data sets were reversed inadvertently.

## **Tensile Testing**

Table 3 presents the results of the tensile testing on the injection molded commercial LCPs. The HX 4000N polymers were supplied in July, 1993 by Hill Air Force Base. They were from a different batch than the other HX 4000 samples. The suffix "(A16)" means annealed for sixteen hours while "(A32)" means annealed for 32 hours.

## **Hardness Testing**

Table 4. gives the results of Vickers hardness testing of two injection molded commercial liquid crystal polymers. The difference between the Vickers Hardness Numbers (VHN) in the vertical and horizontal directions is a clear indication of the anisotropy of the samples.

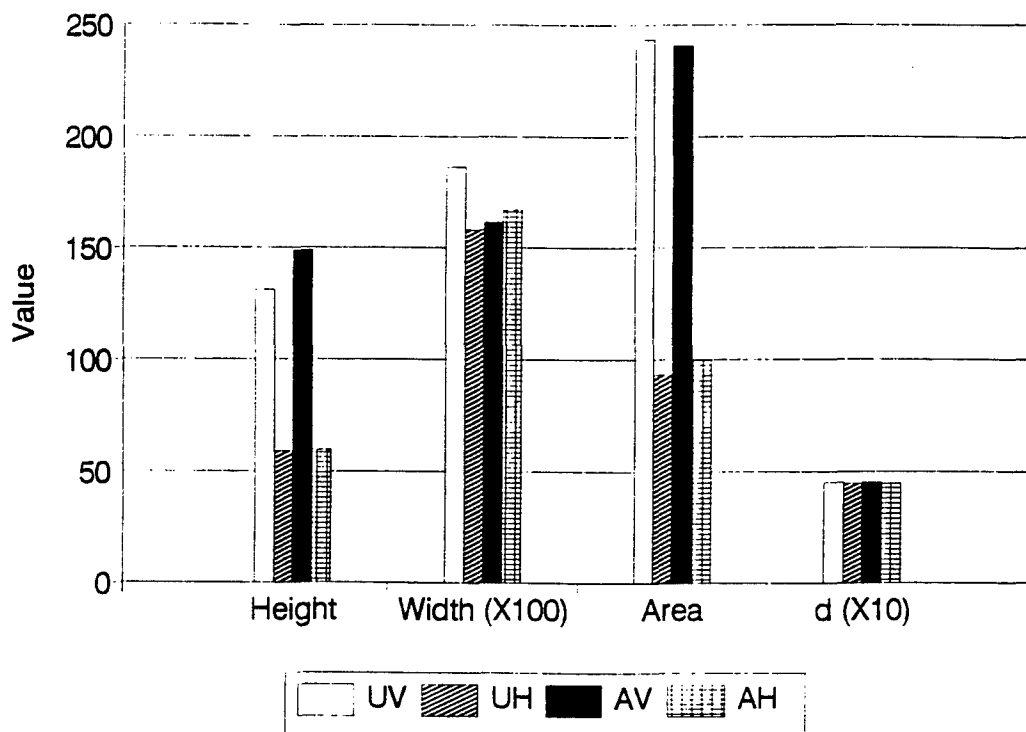


Figure 11. Peak parameters for HX 4000

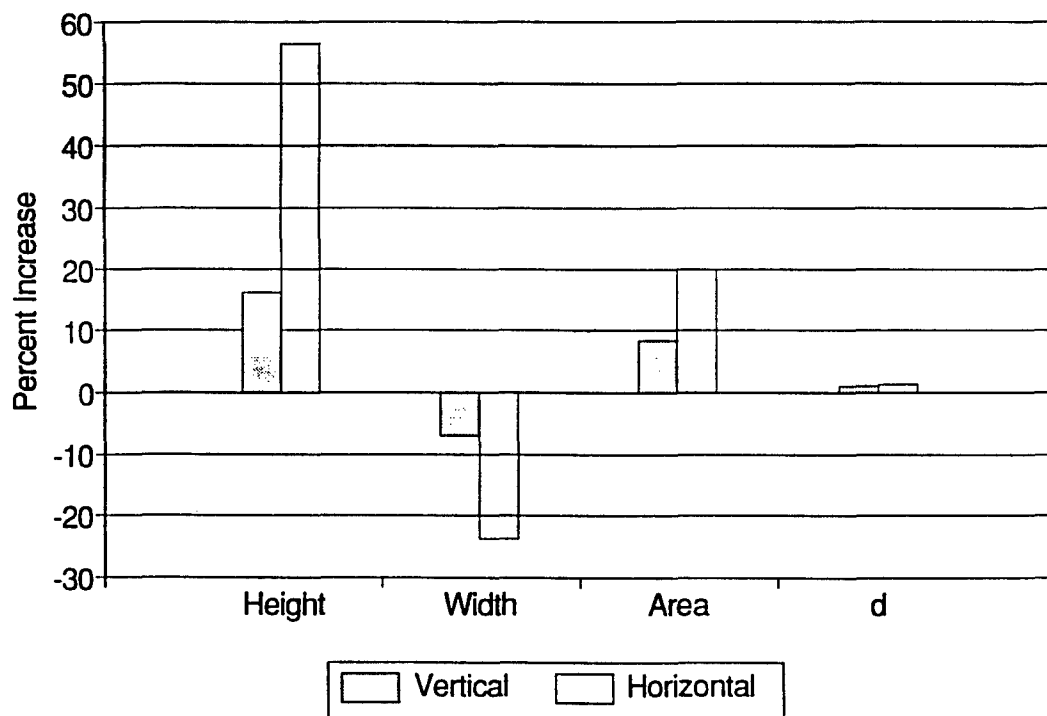


Figure 12 Percent change in peak parameters for POLYMER A

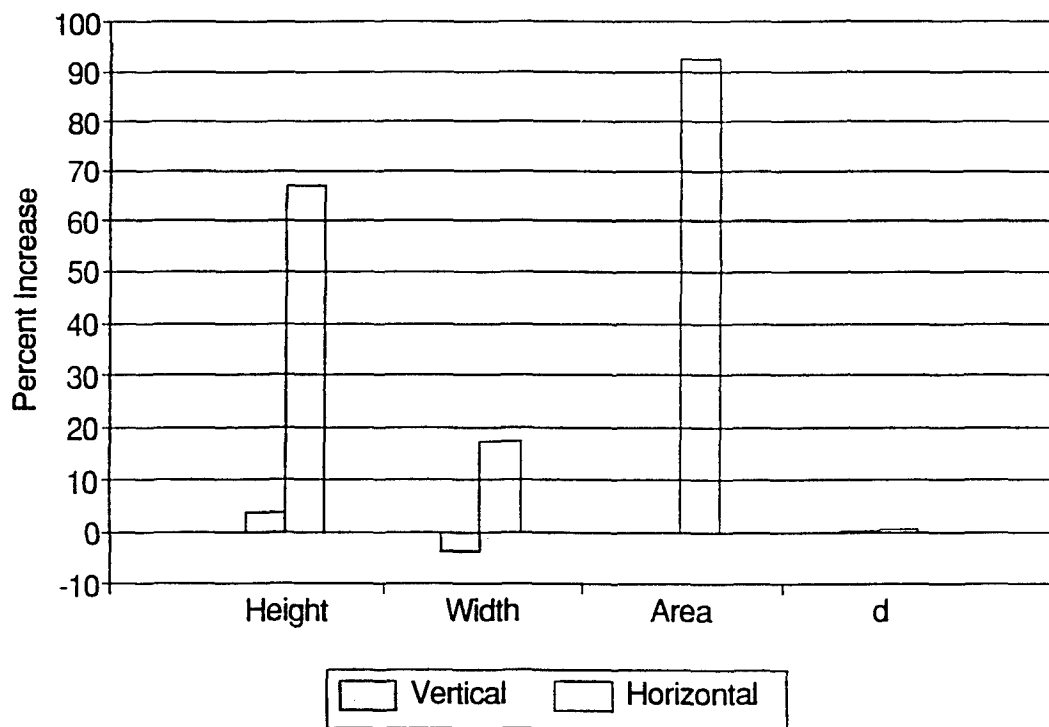


Figure 13. Percent change in peak parameters for VECTRA B950T

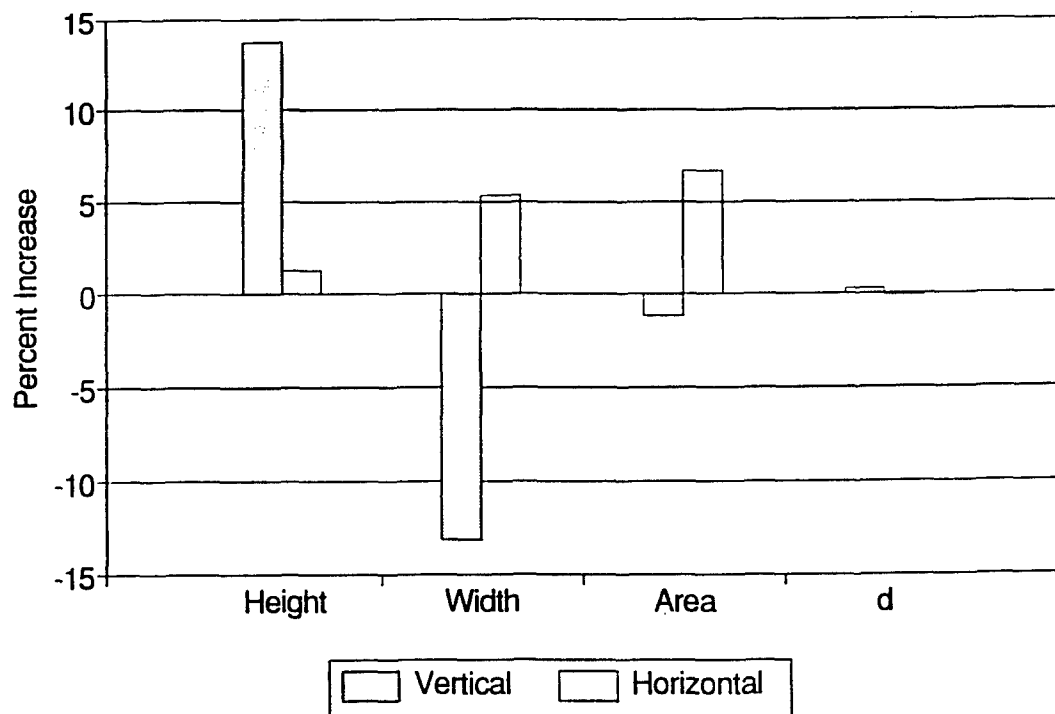


Figure 14. Percent change in peak parameters for HX 4000

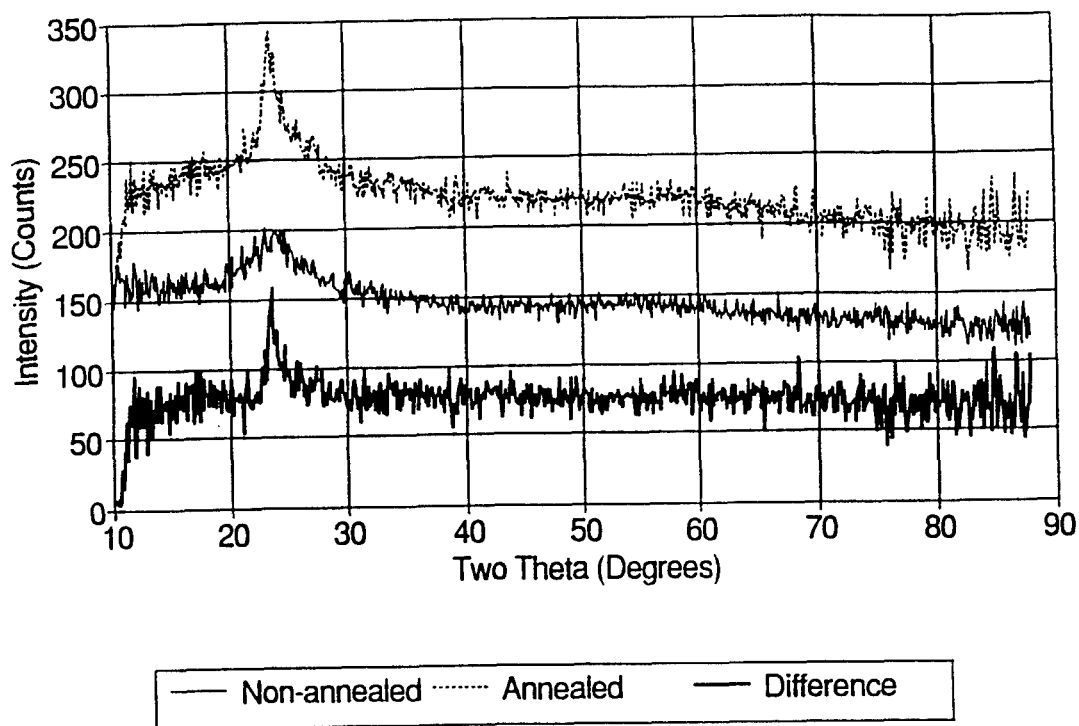


Figure 15 Powder spectra for POLYMER A

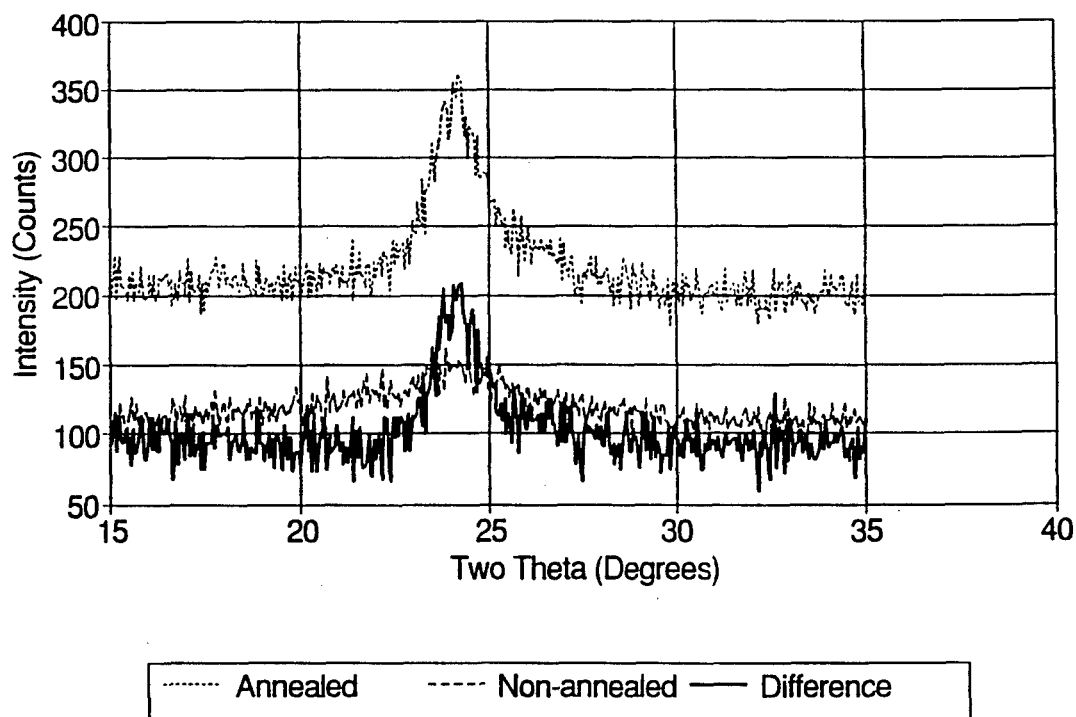


Figure 16. Powder Spectra for SRT 500

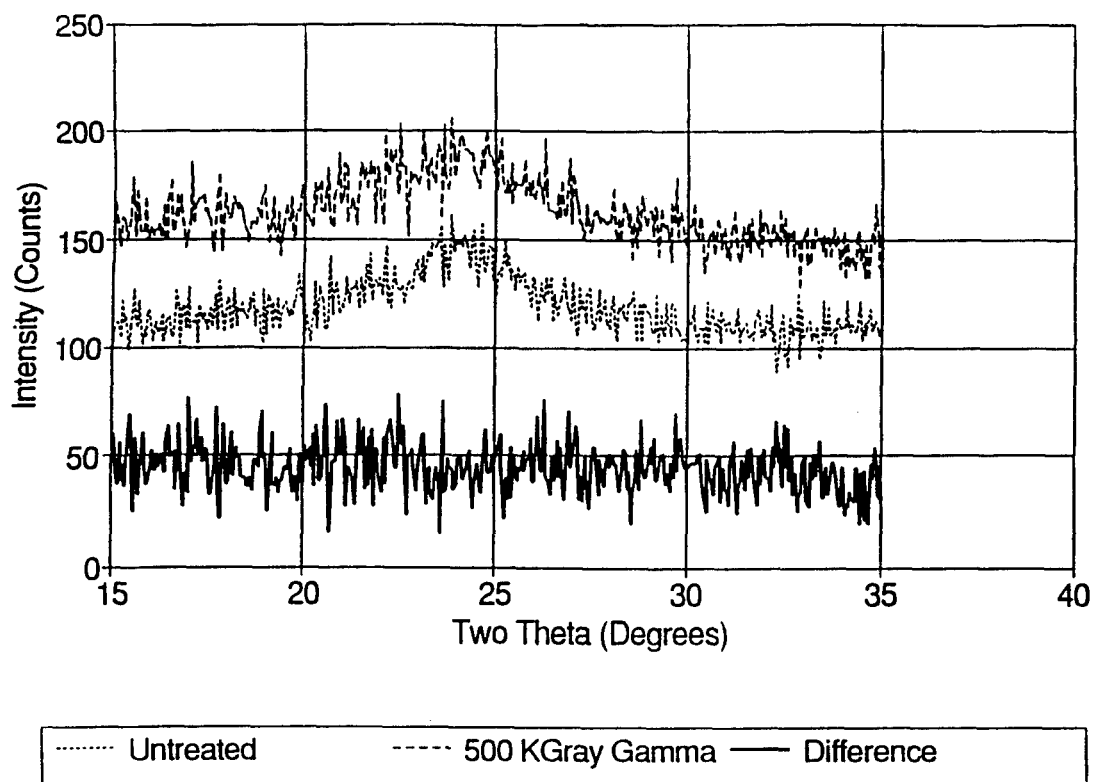


Figure 17. Spectra for SRT 500 powder untreated and exposed to 500 KGray of Co-60 gamma rays

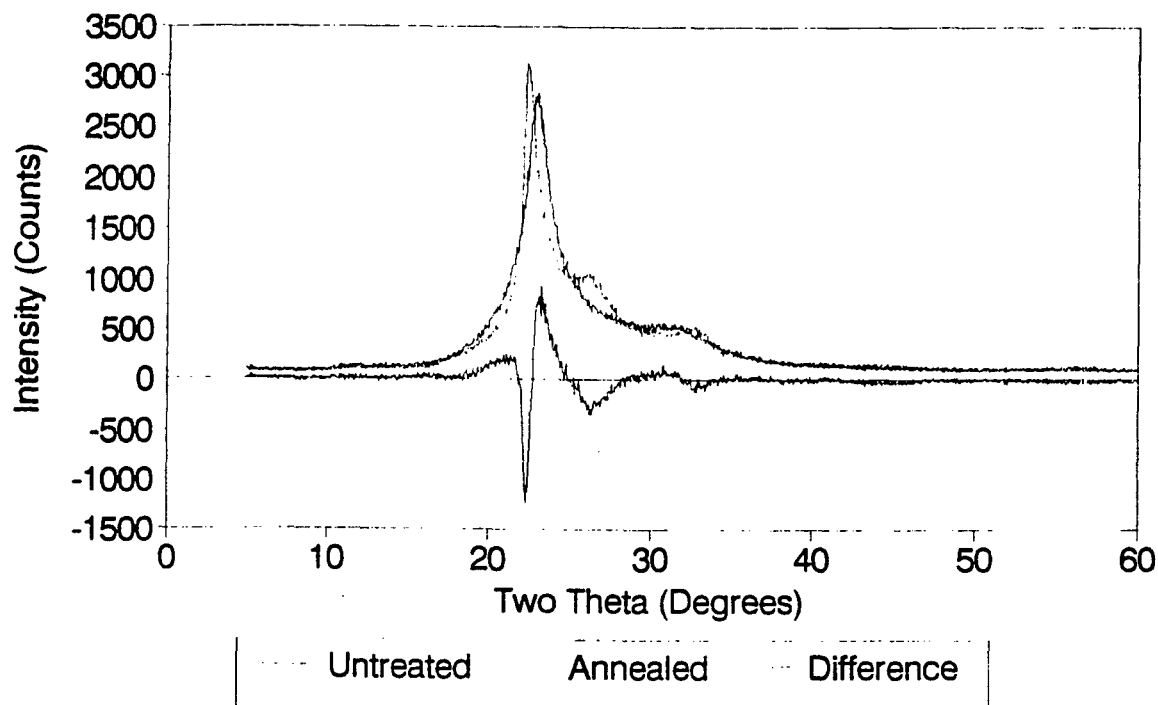


Figure 18. X-ray diffraction spectra for POLYMER A skin



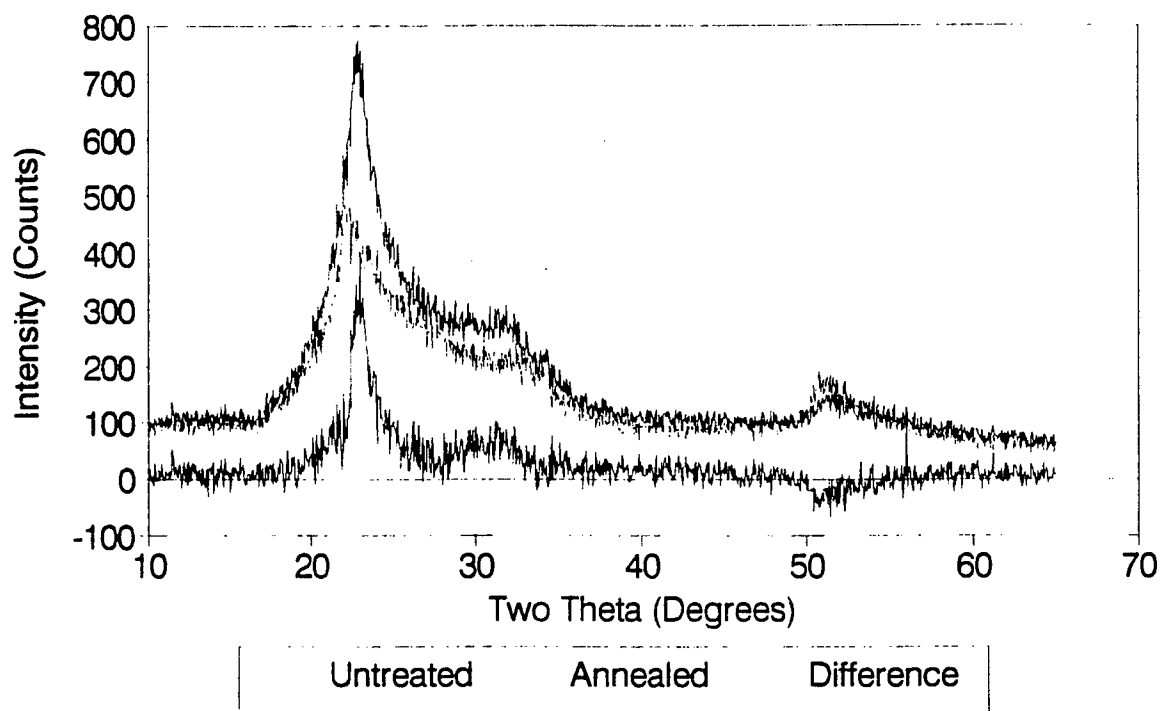


Figure 19. X-ray diffraction spectra for POLYMER A core

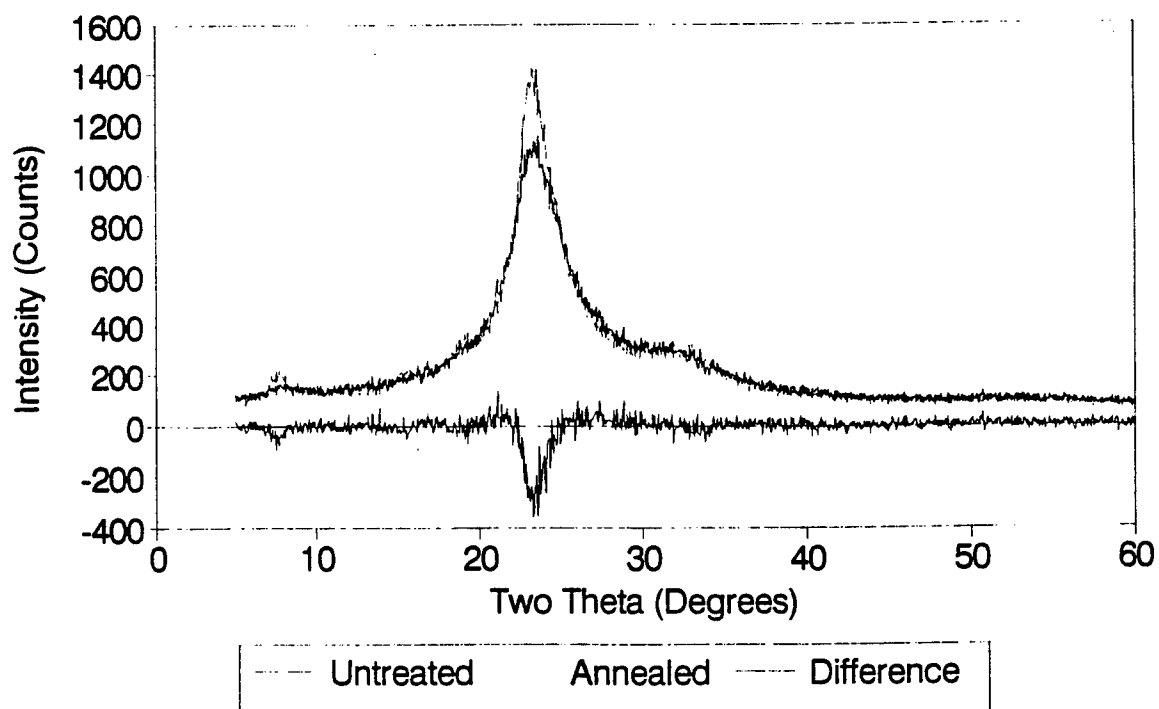


Figure 20. X-ray diffraction spectra for HX 4000 skin

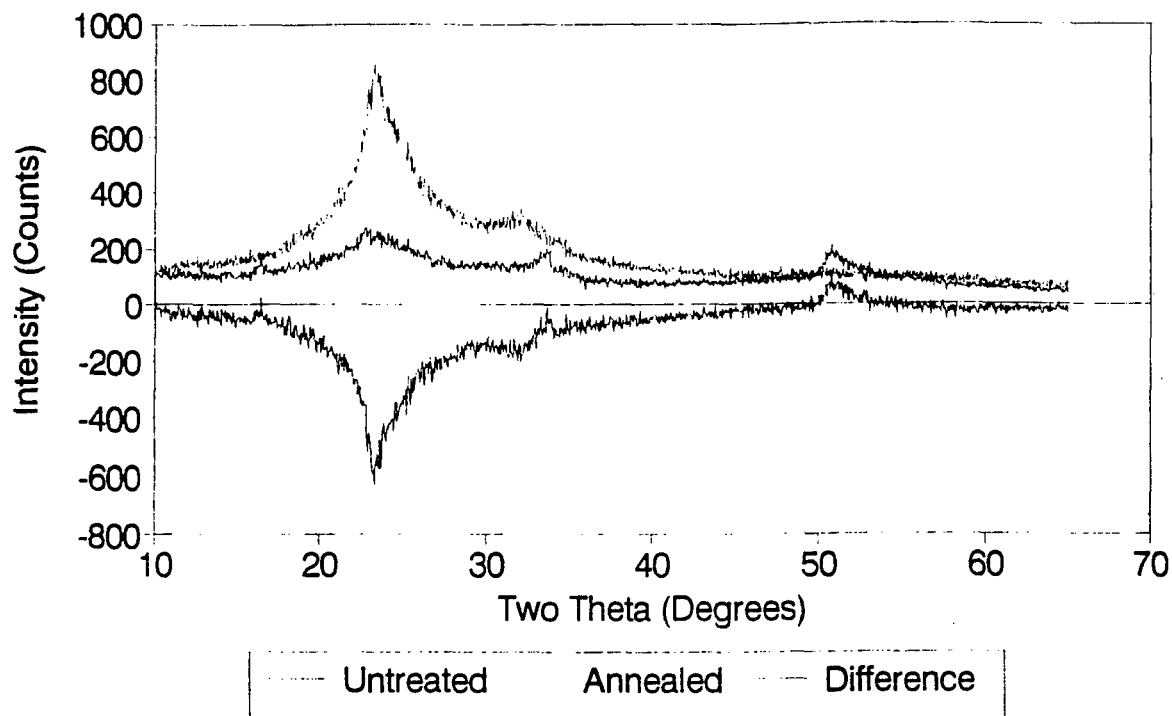


Figure 21. X-ray diffraction spectra for HX 4000 core

Material	E (GPa)	UTS (MPa)	Elong. (%)	ROA (%)
VECTRA A950	5.71	97.0	2.64	0.29
VECTRA A950 (A16)	6.25	97.8	1.78	-1.24
HX 4000	11.95	94.4	1.69	-2.16
HX 4000 (A16)	14.01	75.4	2.07	-3.04
HX 4000N	11.56	95.5	0.30	
HX 4000 (A16)	16.56	95.5	0.30	
HX 4000N (A32)	12.15	86.7	0.35	

Table 3. Effect of annealing on the mechanical properties of injection molded LCPs.

HX 4000		
Sample	d	VHN
4 Vertical	258	27.87
4 Horizontal	318	18.35
4A Vertical	269	25.64
4A Horizontal	302	20.34
Percent increase after annealing:		
Vertical -8.0%		
Horizontal 10.8%		
VECTRA A950		
Sample	d	VHN
2 Vertical	344	15.68
2 Horizontal	410	11.04
2A Vertical	274	24.71
2A Horizontal	328	17.25
Percent increase after annealing:		
Vertical 57.6%		
Horizontal 56.2%		

Table 4. Hardness testing results ("A" means annealed for 16 hours at 260 deg. C in argon.)

#### Scanning Electron Microscopy of Fracture Surfaces

Visual examination of the surfaces of injection molded LCP parts suggests that the mechanical properties might be anisotropic because the direction of flow of the material into the mold is obvious in most cases. Observation of cut surfaces reveals the highly inhomogeneous character of these parts. There are obviously distinct skin and core regions. The anisotropic and inhomogeneous character of these materials is dramatically confirmed when the fracture surfaces of parts failed in tension are observed under high magnification in a scanning electron microscope. In addition, there is clearly a major effect of annealing on the macroscopic structure.

The annealing was done before the samples were failed. Figure 22 shows the fracture surface of untreated VECTRA A950 and Figure 23 shows the fracture surface of annealed VECTRA A950. The magnification for both Figures 22 and 23 was 4000. Figure 24 shows the fracture surface of untreated HX 4000 and Figure 25 shows the fracture surface of annealed HX 4000. As with the VECTRA A950, the magnification in both cases for HX 4000 was 4000.

The most startling observation for the untreated fracture surfaces of both materials is their highly fibrous nature. The fibers do not look like random fibers embedded in an amorphous matrix. Instead they appear very distinct and individualized. There is little or no evidence amorphous material or matrix in either case. The appearance of the fracture surfaces for these materials after thermal annealing is noticeably different than the appearance of the untreated surfaces. In the case of VECTRA A950, the fibers in the annealed sample appear to have been softened and some of them appear to be bonded together. There are regions where the fibers appear to have melted together to form a sheet like texture. In the case of HX 4000, this transformation from a fibrous to a sheet like texture appears to be essentially complete.

#### CONCLUSIONS

The principal objective of this work was to assess the feasibility of using neutron diffraction as a tool to investigate the crystalline properties of injection molded parts made from commercially available liquid crystal polymers. Neutron diffraction spectra were obtained from parts made from five different LCPs. Spectra were obtained both from solid parts and from powders obtained from solid parts. In all cases, only one peak was resolvable. Because there was only one peak, no characterization of the crystal structure itself was possible. The peak parameters of location in  $2\theta$ , height, width at half maximum, and area were easily quantifiable and these were found to vary with orientation of the solid sample and with thermal annealing in argon at 260 de. C for 16 hours. Because very little is known about the crystalline properties of these materials, particularly in the injection molded form, the temptation to try to draw conclusions about such properties from these results was very great. The results, unfortunately do not warrant drawing any such conclusions. They are based on very few (usually only one) data points. Therefore, these results must be considered interesting and certainly suggestive but not definitive.

It must also be recognized that neutron diffraction is a time consuming

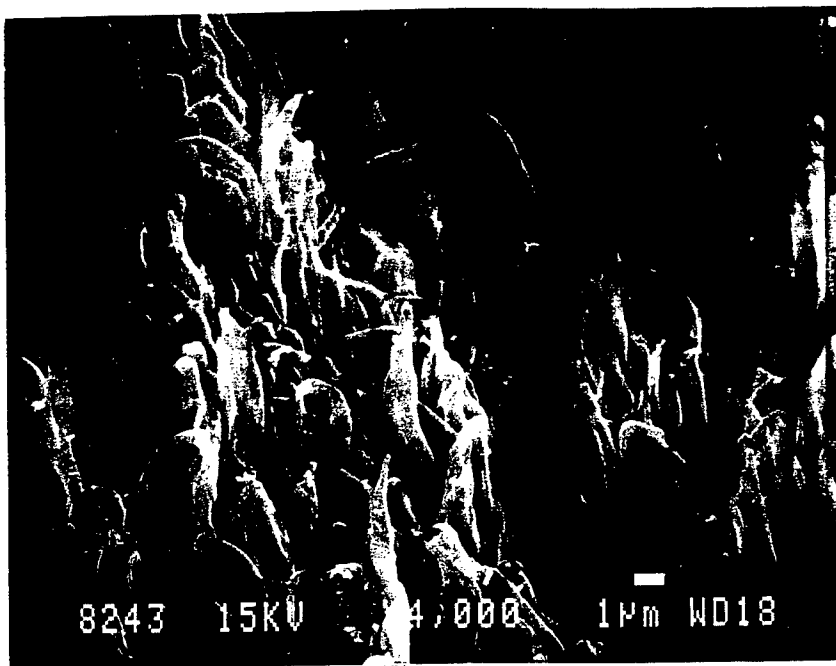


Figure 22 Fracture surface of untreated VECTRA A950

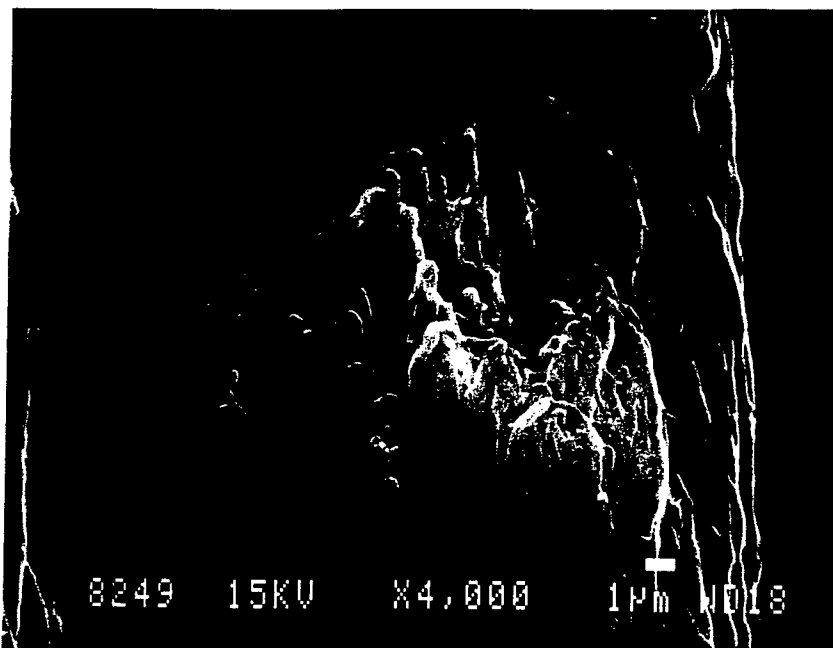


Figure 23 Fracture surface of annealed VECTRA A950

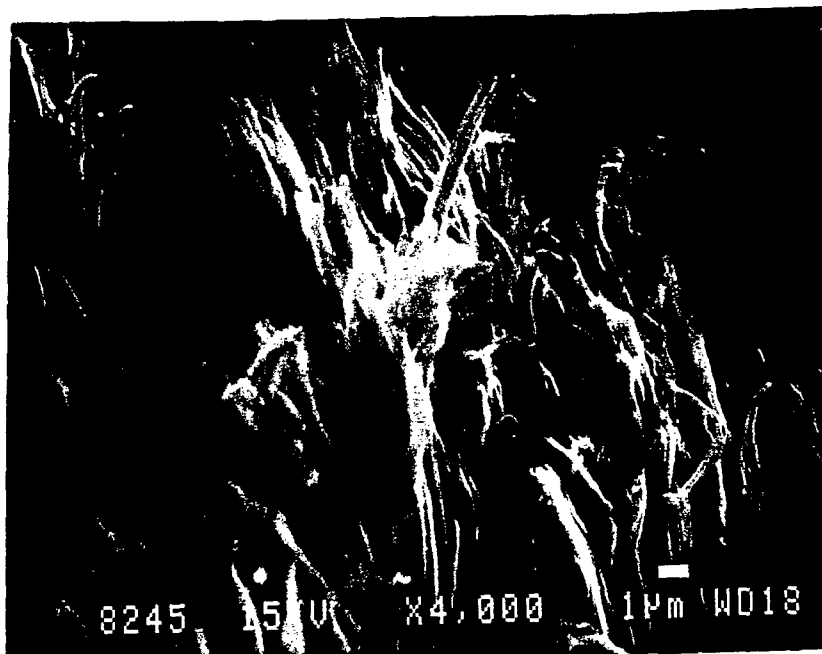


Figure 24 Fracture surface of untreated HX 4000

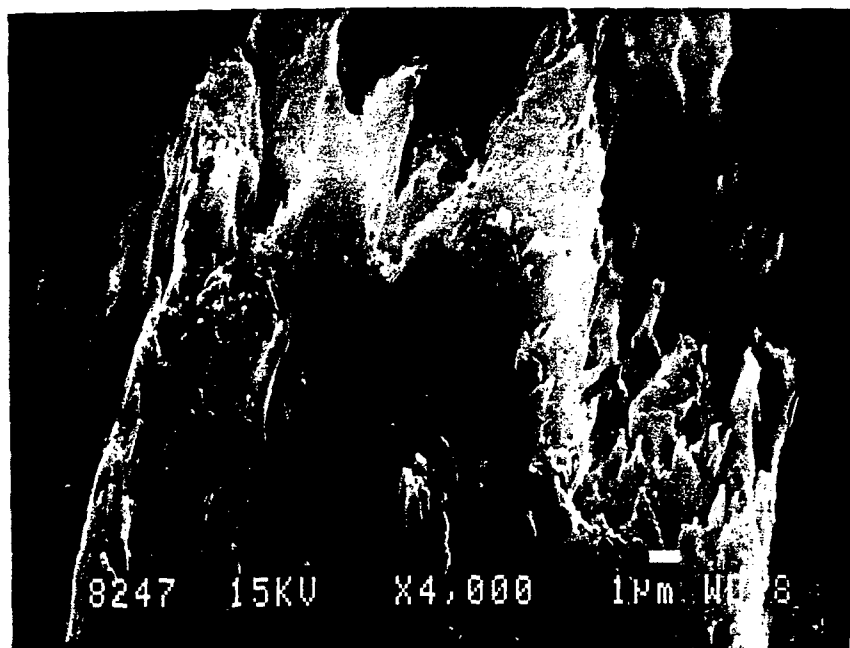


Figure 25 Fracture surface of annealed HX 4000

and expensive experimental technique. It takes from five to ten hours of dedicated beam time to obtain a single full range spectrum. Beam time, if it had to be paid for, would be very expensive. It can be concluded, therefore, that neutron diffraction is capable of measuring some but not all of the crystalline properties of injection molded LCPs. At the same time it must be observed that X-ray diffraction appears to be capable of measuring these same parameters while providing significantly more detailed information about the crystalline structure.

In summary, the several specific conclusions about the crystalline and mechanical properties of injection molded parts made from commercial liquid crystal polymers can be drawn from this work. The more important of these are listed below.

- o Neutron diffraction of injection molded LCPS using the HRPD at ANSTO is capable of resolving only a single peak.
- o All five of the commercial LCPs tested showed a strong peak corresponding to a d spacing of 4.4 to 4.6 Angstroms. All of these materials are, therefore, at least partially crystalline.
- o Changes in the peak parameters of position, height, width at half maximum, and area can be measured reliably and consistently.
- o The peak parameters are clearly affected by sample orientation and by annealing at 260 deg. C for 16 hours.
- o The measured d spacing corresponding to the single neutron diffraction peak increases by 1% to 1.5% on annealing for POLYMER A and VECTRA A950. The change is not measurable for the other samples.
- o For POLYMER A, VECTRA B950T, and HX 4000, The area of the neutron diffraction peak is greater in the vertical orientation.
- o For POLYMER A, VECTRA B950T, and HX 4000, the area of the neutron diffraction peak either stays essentially the same or grows with annealing. The peak growth is greater in the horizontal orientation.
- o For HX 4000, annealing for 16 hours causes substantial growth in the area of the vertically oriented neutron diffraction peak. Annealing for 32 hours results in the peak area returning nearly to its unannealed value.
- o For HX 4000, annealing for 16 hours causes a substantial increase in the elastic modulus (about 43%). Annealing for 32 hours results in the elastic modulus returning nearly to its unannealed value. This effect correlates well with the change in the area of

- the vertically oriented neutron diffraction peak.
- o Irradiation with Co-60 gamma rays to 500 KGray causes no measurable effect on the neutron diffraction peak.
  - o X-ray diffraction, being capable of resolving three or four peaks in injection molded commercial LCPs and being much cheaper and less time consuming than neutron diffraction is the preferred technique for investigating the crystalline properties of these materials.
  - o The elastic modulus increases with annealing in argon at 260 deg. C for 16 hours for VECTRA A950 and HX 4000. The increase for HX 4000 (17% to 43% depending on the sample batch) is greater than for VECTRA A950 (9%).
  - o Hardness measurements for these materials are difficult to perform and interpret. The Vickers method is uniquely capable of detecting difference in hardness as a function of orientation.
  - o The effect of annealing on hardness is very different for VECTRA A950 (56% increase) and HX 4000 (little effect).
  - o Both the crystalline and the mechanical properties of parts made from injection molded LCPs are profoundly affected by processing variables during the molding process.
  - o The fracture surfaces of HX 4000 and VECTRA A950 show an almost totally fibrous structure with little visible evidence of amorphous regions.
  - o Annealing at 260 deg. C in argon for 16 hours profoundly affects the macroscopic structure of the fracture surfaces of HX 4000 and VECTRA A950. The texture changes from fibrous to sheet like, the effect being much more pronounced in HX 4000.

#### RECOMMENDATIONS

Further experimental investigations of the crystalline and mechanical properties of injection molded liquid crystal polymers and how these properties are affected by processing variables, both during and after molding should be carried out. X-ray diffraction should be the primary technique for future investigations of the crystalline properties.

Molecular modelling of these materials is critical to understanding their behavior in the solid state. Theoretical studies should be pursued vigorously.



Design and preparation of samples optimized for each particular experiment is crucial in future efforts. Careful control of process variables is essential. Thin shear sheet samples could be used for both x-ray and neutron diffraction experiments as well as future small angle neutron scattering and inelastic neutron scattering experiments. These later experiments should provide answers to fundamental questions on interchain interactions.

A serious effort should be undertaken to model the crystalline properties of these materials as they exist in injection molded parts. Modelling of the crystalline structure might begin with consideration of the structure of KEVLAR fibers as reported in the literature <sup>(4)</sup> and how that structure changes with thermal annealing. Thin shear sheet samples should be useful in this effort as well as in support of the molecular modelling. X-ray diffraction appears to be a particularly promising technique here. Studies of the effects of thermal annealing in thin shear sheets can be done in situ with x-ray diffraction and such studies are highly recommended.

#### ACKNOWLEDGEMENTS

I would like to gratefully acknowledge the help with the experiments and the personal encouragement of Dr. Robert Knott, Dr. Sue Town, and Mr. Paul Stathers of the Australian Nuclear Science & Technology Organisation and members of their staffs. Dr. Kevin Chaffee and Dr. John Rusek of the Phillips Laboratory suggested this project and supported it throughout. Their efforts were crucial and are very much appreciated. The financial support provided by the Air Force Office of Scientific Research and Arkansas Tech University is also gratefully acknowledged.

#### REFERENCES

1. Elements of Physical Metallurgy, Third Edition, A.G. Guy and J.J. Hren, Addison-Wesley, Reading, MA, 1974
2. Neutron Diffraction, G.E. Bacon, Clarendon Press, Oxford, 1975
3. Elements of X-ray Diffraction, B.D. Cullity, Addison-Wesley, Reading, MA, 1956
4. Properties and Applications of Liquid-Crystalline Main-Chain Polymers, M.G. Dobb and J.E. McIntyre, Advances in Polymer Science 60/61, Springer-Verlag, Berlin, 1984

# HIGH TEMPERATURE SPECTROSCOPY OF ALKALI METAL VAPORS FOR SOLAR TO THERMAL ENERGY CONVERSION

Paul S. Erdman  
Graduate Research Assistant  
Department of Physics and Astronomy

University of Iowa  
Iowa City, IA 52242

and

William C. Stwalley  
Department Head  
Department of Physics

University of Connecticut  
2152 Hillside Road  
Storrs, CT 06269-3046

Final Report for:  
Summer Research Extension Program  
Phillips Laboratory

Sponsored by:  
Air Force Office of Scientific Research  
Bolling Air Force Base, Washington D.C.  
and  
University of Iowa

December 1993

# HIGH TEMPERATURE SPECTROSCOPY OF ALKALI METAL VAPORS FOR SOLAR TO THERMAL ENERGY CONVERSION

Paul S. Erdman  
Graduate Research Assistant  
Department of Physics and Astronomy  
University of Iowa

and

William C. Stwalley  
Department Head  
Department of Physics  
University of Connecticut

## Abstract

Solar plasma propulsion methods proposed by the Air Force have led to the study of high temperature optical absorption of metal vapors. The Plasma Spectroscopy Cell in the Phillips Laboratory at Edwards Air Force Base has been used to obtain an abundance of absorption spectra at temperatures approaching 2000 K and pressures of one atmosphere for lithium and sodium metal vapors. Tentative assignments of molecular transitions are improved upon by use of modern computational techniques for generating intensities of molecular transitions which possibly have been observed. Identification of contributing molecular transitions to overall absorption of radiant energy assists the efforts to develop propulsion methods which rely on the direct absorption of solar energy.

# HIGH TEMPERATURE SPECTROSCOPY OF ALKALI METAL VAPORS FOR SOLAR TO THERMAL ENERGY CONVERSION

Paul S. Erdman  
William C. Stwalley

## INTRODUCTION

It has been proposed by C.W. Larson of the Edwards AFB Phillips Laboratory that the direct use of solar energy to propel spacecraft from low earth orbit to geosynchronous orbit is best performed by absorbing radiant solar energy directly into the rocket propellant [1]. The absorbed radiant energy would be converted through collisions into thermal energy, heating the propellant to provide a high exhaust velocity. The solar plasma absorber has the advantage that it would be able to reach higher propellant temperatures than the alternately proposed blackbody absorber. Another advantage is the tendency of the plasma to trap reradiated energy, thus reducing loss and increasing efficiency.

The preferred gas for spacecraft propulsion is hydrogen, since as the lightest element it would provide the highest specific impulse. However, hydrogen is a poor absorber of solar energy, because it is transparent in the visible and near infrared region of the spectrum where the solar flux is greatest. To better absorb solar energy, the hydrogen propellant would have to be seeded with lightweight absorbing elements. The alkali metals would be excellent candidates for seedants, since it is already known that they absorb well in the visible and near infrared regions of the spectrum [2]. Alkali hydrides would also form and contribute to absorption [3]. In fact, it is likely that previously unobserved species  $M_xH_y$  (where M is an alkali metal) may also form and contribute to absorption [3].

## EXPERIMENT

In order to study candidate absorbing elements and their hydrides in the high tem-

perature, high pressure conditions that would exist in the solar plasma thruster, the Plasma Spectroscopy Cell (PSC) has been constructed in the Phillips Laboratory at Edwards AFB, California (see Figure 1). The PSC uses concentric gas flows and resistive heating elements to create high temperature (potentially 3000 K), high pressure (potentially 100 atmospheres) metal vapors which can be optically studied for their absorption properties.

The metals are loaded in a crucible surrounded by a rhenium resistive heating ring in a section of the PSC known as the atomizer or evaporator region. A neutral entrainment gas, such as helium or argon, carries the metal vapor through the central tube A into the region known as the hot zone. The hot zone is heated by a molybdenum susceptor which surrounds the concentric tubes A, B, and shroud tube. Tube B carries a gas which can be chosen as neutral or a reactive gas such as hydrogen. The metal vapor jet formed in the central region of the hot zone at the exits of tubes A and B contains the molecules of interest. Optical access to this area is available through four opposing windows on two perpendicular axes.

Absorption experiments carried out with the PSC over the last three years have generally followed the schematic shown in Figure 2. Both xenon and tungsten lamps have been used as sources to pass light through the PSC and into a spectrometer. In several experiments, the extra beam created by the beam splitter has been used with an additional spectrometer to obtain spectra of wider spectroscopic range or higher resolution in a region of particular interest.

## DATA

Much of the data obtained in the PSC experiments described above has been in the form of images 384 by 578 pixels. The long dimension corresponds to wavelength, the range of which was 330 to 665 nm. The shorter dimension corresponds to spatial position

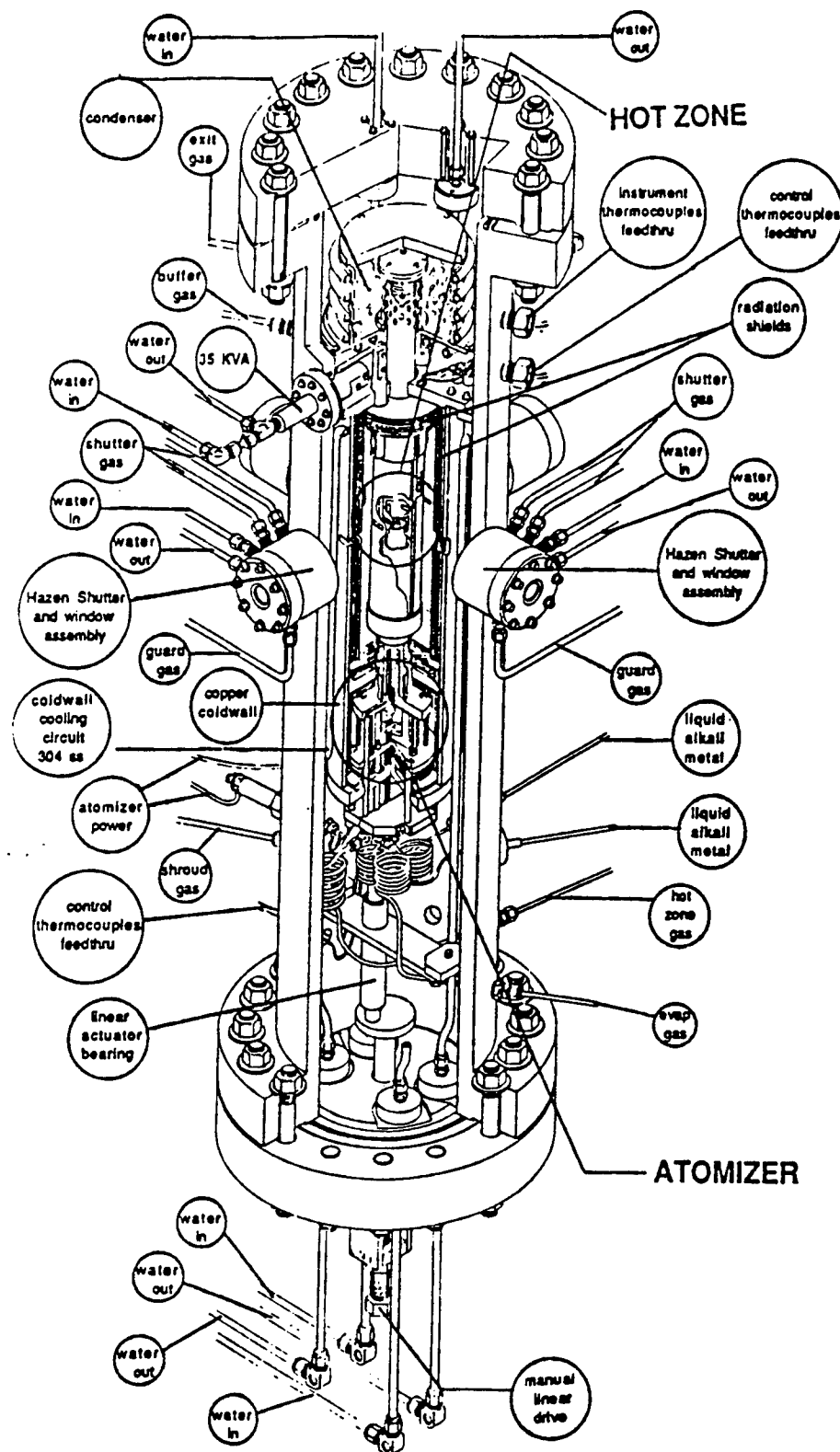


Figure 1. The Plasma Spectroscopy Cell [3].

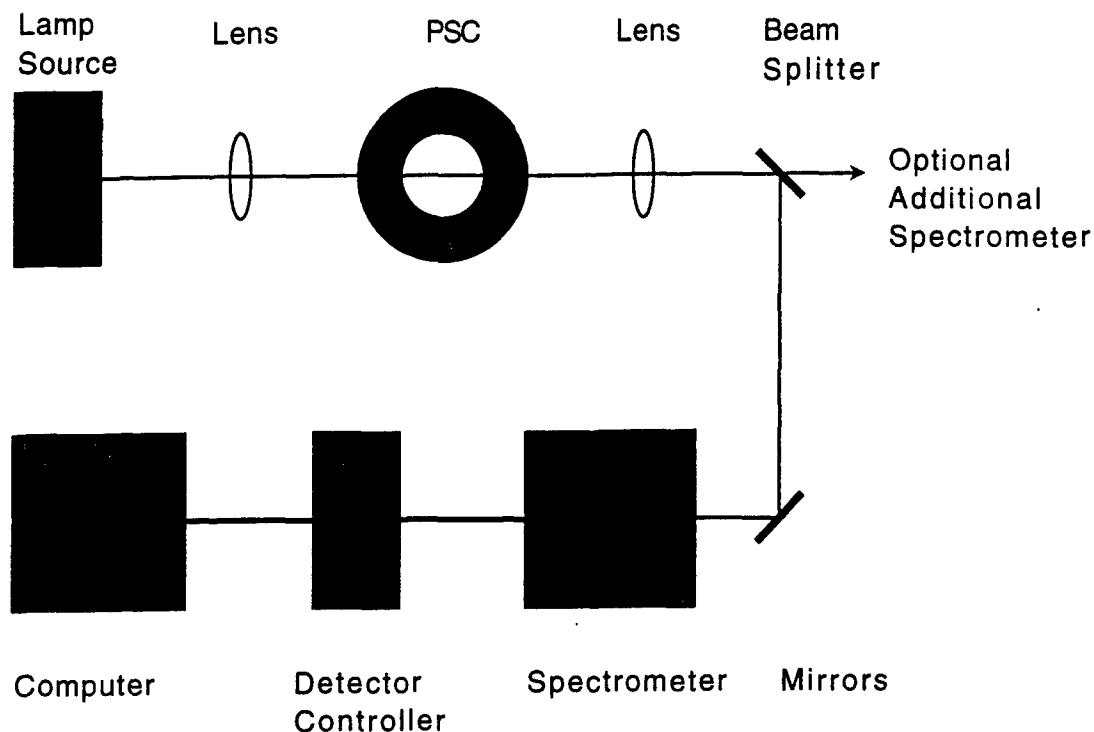


Figure 2. Schematic of PSC experiment.

across the width of the metal vapor jet. Thus, each image file contains 578 cross sections of intensity vs position, and 384 cross sections of intensity vs wavelength. The image files for the original intensity  $I_0$  of the source lamp and the transmitted intensity  $I$  through the metal vapor jet were used to calculate images of absorbance according to

$$\text{Absorbance} = \ln \left( \frac{I_0 - B_0}{I - B} \right)$$

where  $B_0$  and  $B$  are the appropriate background intensity images.

It is easier to reproduce and visualize a single absorbance intensity vs wavelength cross section of an image file rather than the whole image file. An example of such a cross section is shown in Figure 3, which shows absorbance by sodium at 1720 K and a pressure of one atmosphere. Prominent atomic lines are at 330 nm for the 3s-4p transition and the broad, saturated sodium D line at 589 nm for the 3s-3p transition. Centered on 500 nm is absorbance by the  $B^1\Pi_u - X^1\Sigma_g^+$  transition of  $\text{Na}_2$ . Another diatomic sodium

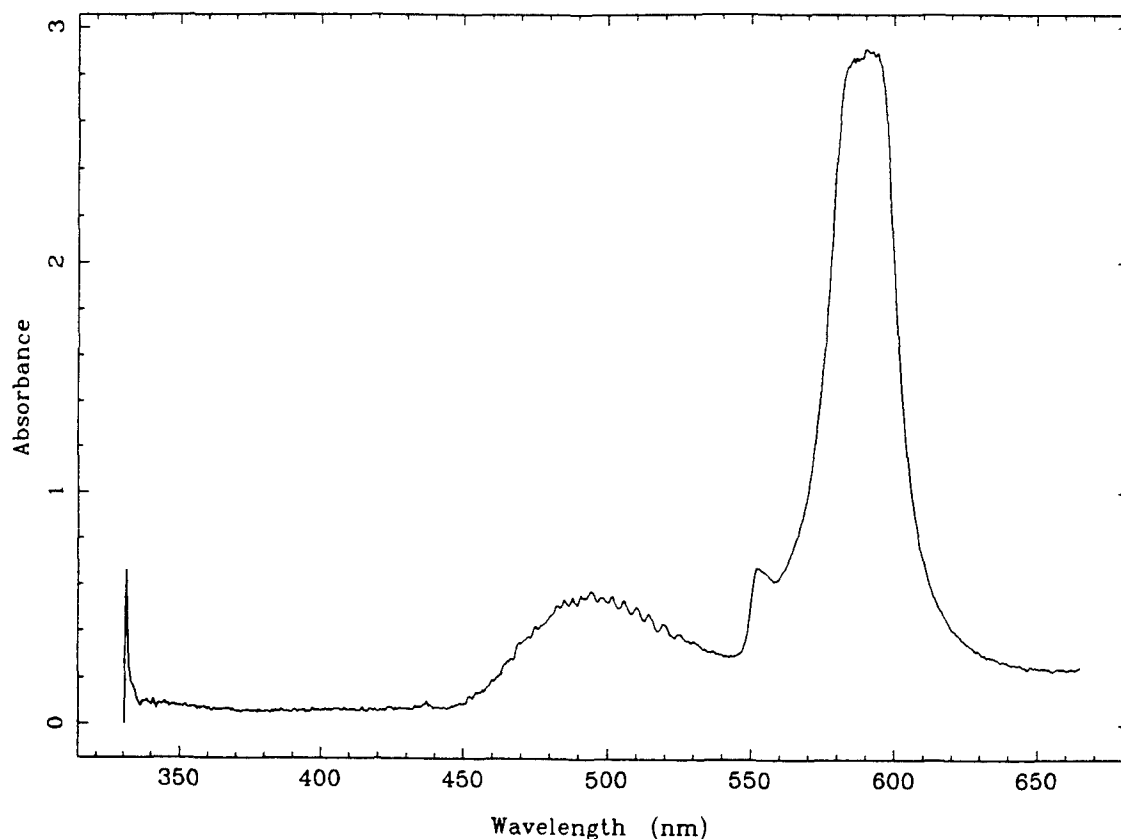


Figure 3. Absorbance of Na at 1720 K and 1 atmosphere

absorbance is the ridge between 550 and 560 nm, believed to be attributed to the  $1^3\Pi_g - 1^3\Sigma_u^+$  transition.

Experiments performed with a mix of lithium and sodium produced results such as the absorbance plot shown in Figure 4, taken at a temperature of 1600 K and pressure of one atmosphere. Again, the sodium atomic peaks for the 3s-4p and 3s-3p transitions appear, whereas the atomic 2s-2p transition of lithium at 670 nm is off the right edge of the range and only appears as a high ridge of line broadening mixed in with the  $A^1\Sigma_u^+ - X^1\Sigma_g^+$  transition of  $Li_2$ . The ridge centered on 500 nm with more sharply defined bandheads is the  $B^1\Pi_u - X^1\Sigma_g^+$  transition of  $Li_2$ . Transitions from NaLi and other Na



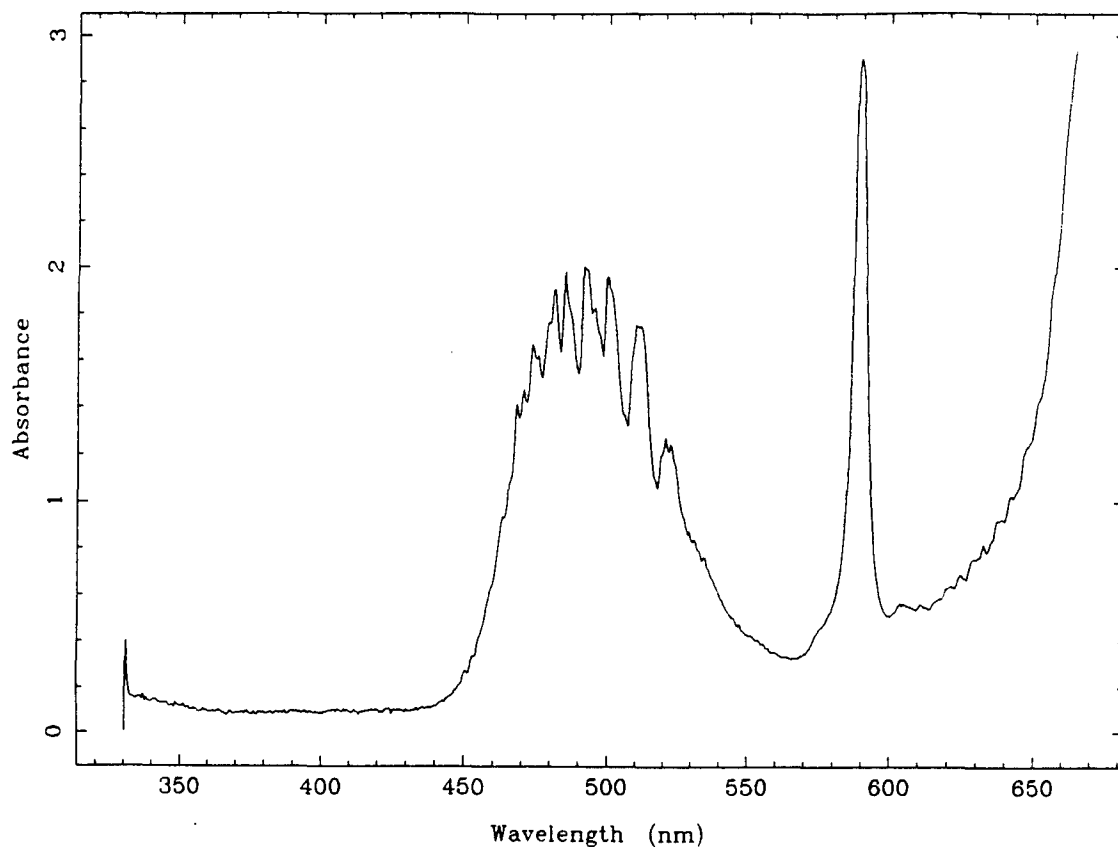


Figure 4. Absorbance of Na, Li mixture at 1600 K and 1 atmosphere.

and Li triplets may be mixed in with the Li and Na features identified so far.

Adding hydrogen as a reactive gas allows the possible formation of hydrides, e.g. LiH and NaH. Figure 5 shows a predominantly lithium absorption spectrum taken at 1900 K and one atmosphere. Residual sodium can still be seen to contribute atomic absorptions at 330 and 589 nm. The molecular transitions of B-X and A-X from Li<sub>2</sub> are seen around 500 nm and above 610 nm, respectively. The lithium atomic line for the 2p-3d transition can be seen at 610 nm to the right of a ridge believed to belong to the  $1^3\Pi_g - 1^3\Sigma_u^+$  transition of Li<sub>2</sub>. The remaining absorption bands from 330 to 430 nm are in the right range for both  $C^1\Pi_u - X^1\Sigma_g^+$  absorption of Li<sub>2</sub> and  $A^1\Sigma^+ - X^1\Sigma^+$  absorption of LiH.

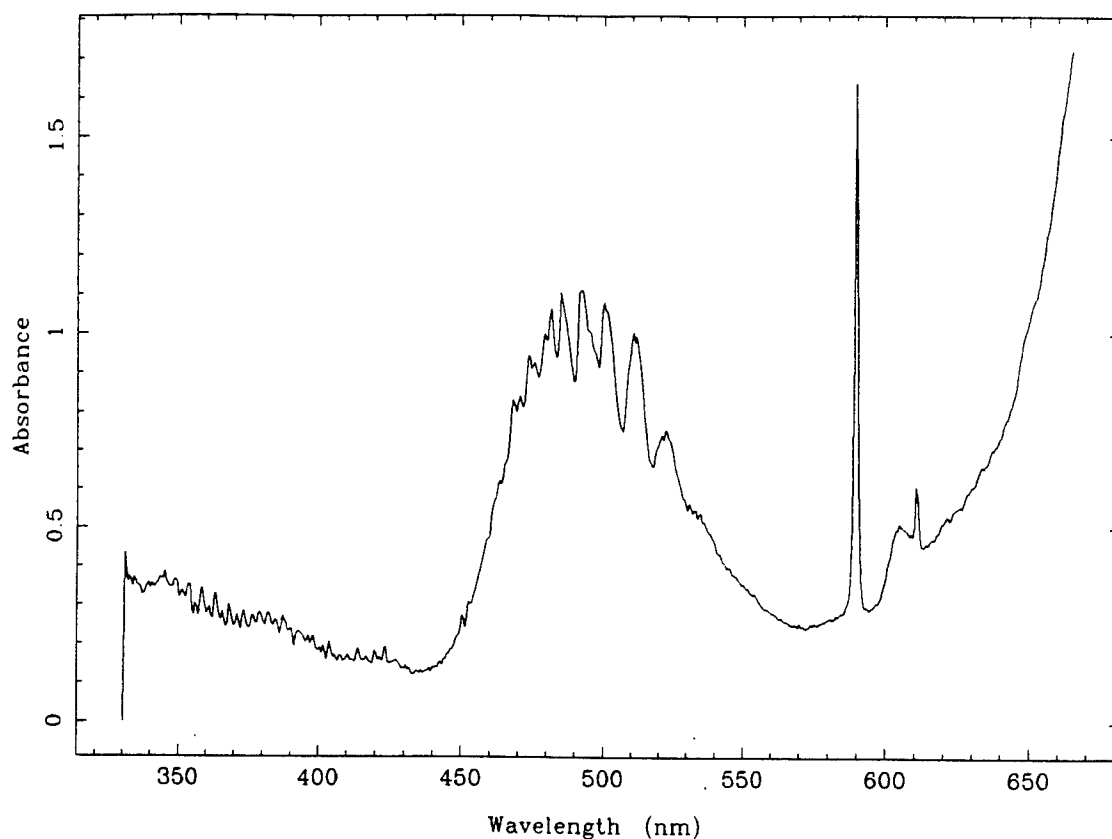


Figure 5. Absorbance of Na, Li, H mixture at 1900 K and 1 atmosphere.

### ANALYSIS

General references such as Huber and Herzberg's book on Molecular Spectra [4] can be used to give an indication where molecular transitions should occur in the electromagnetic spectrum. However, the absorption spectra obtained in the PSC experiments may have overlapping features contributed by various transitions from the same and different molecules in the chamber. In this mix of transitional spectra, it is more difficult to identify which species are contributing significantly to overall absorption of radiant energy. A more detailed analysis is necessary to identify the contributions potentially useful for the absorption of solar energy in the solar plasma thruster.

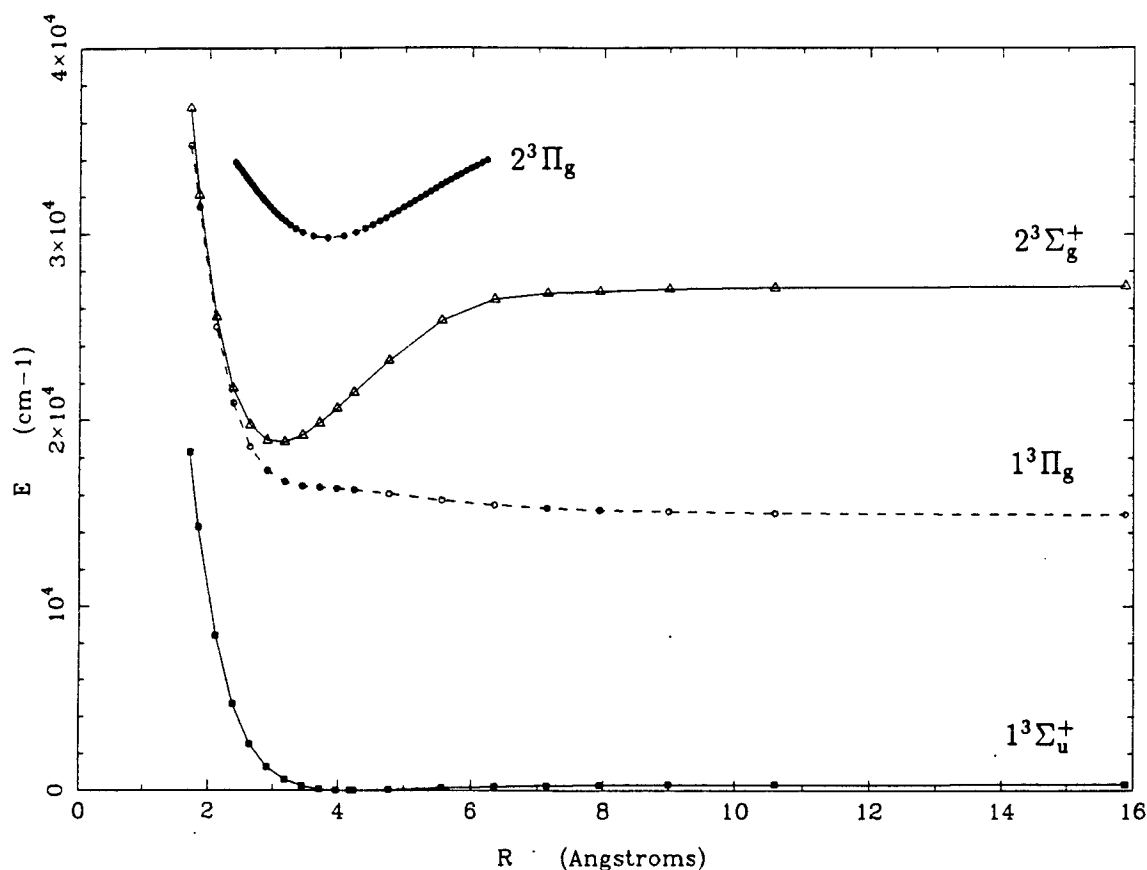


Figure 6. Potential curves of selected Li triplets [5,6,7].

To more carefully identify absorption spectra from specific transitions of a diatomic molecule, certain standard techniques of computation, based on molecular theory, have been developed. The method begins with the potential energy curves of the transitions in question. The potential curves are used to generate accurate eigenvalues of the radial Schrödinger equation. Both the potential curves and the eigenvalues can then be used to calculate the intensities for all rotational-vibrational energy levels of the two electronic states.

To illustrate the analysis, consider the triplet transitions of  $\text{Li}_2$  which should appear in the spectral range of the PSC absorption data (330 - 665 nm). Figure 6 shows the

potential curves for the  $1^3\Sigma_u^+$ ,  $1^3\Pi_g$ ,  $2^3\Sigma_g^+$ , and  $2^3\Pi_g$  states of  $\text{Li}_2$ . The lowest state,  $1^3\Sigma_u^+$ , is an RKR potential curve generated by Zemke and Stwalley [5], which has only eleven bound states. The  $1^3\Pi_g$  and  $2^3\Sigma_g^+$  states are from ab initio calculations of Schmidt-Mink, Müller and Meyer [6]. The  $1^3\Pi_g$  state is purely repulsive and has no bound states. The  $2^3\Sigma_g^+$  state was found to have 54 bound states. The portion of the  $2^3\Pi_g$  state shown in Figure 6 is an RKR potential curve generated from molecular constants provided by Xie and Field [7]. It will be necessary to merge the RKR curve with theoretical long range values before eigenvalues can be calculated.

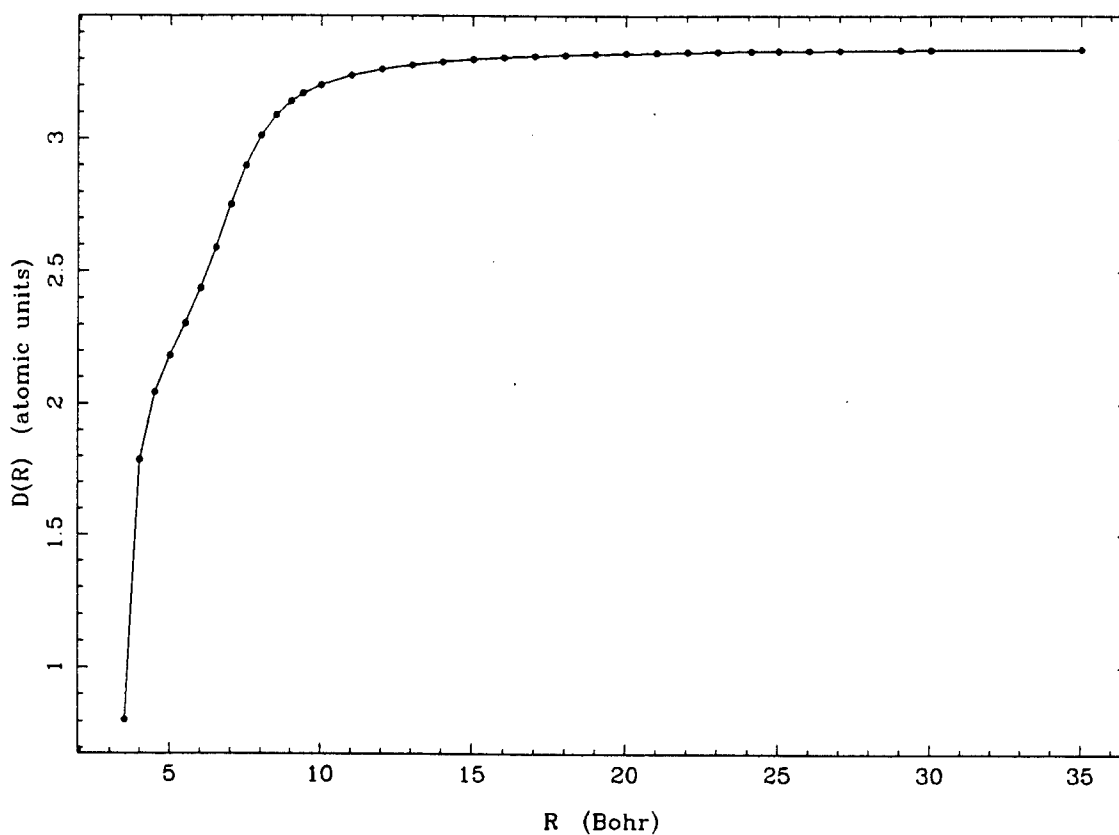


Figure 7. Electronic transition dipole moment for  $1^3\Sigma_u^+ - 1^3\Pi_g$  of  $\text{Li}_2$  [8].

Often when the intensity of molecular transitions are computed, the Franck-Condon Factors (FCFs) are calculated with the assumption that the electronic transition dipole

moment can be treated as a constant over the intermolecular distance. For this analysis, the full functions of the electronic transition dipole moments were used to calculate the Franck-Condon Factors, as they depart significantly from a constant at short range. Figures 7 and 8 show the functions used for the  $1^3\Sigma_u^+ - 1^3\Pi_g$  and  $1^3\Sigma_u^+ - 2^3\Sigma_g^+$  transitions of  $\text{Li}_2$ , respectively, as calculated by Ratcliff, Fish, and Konowalow [8].

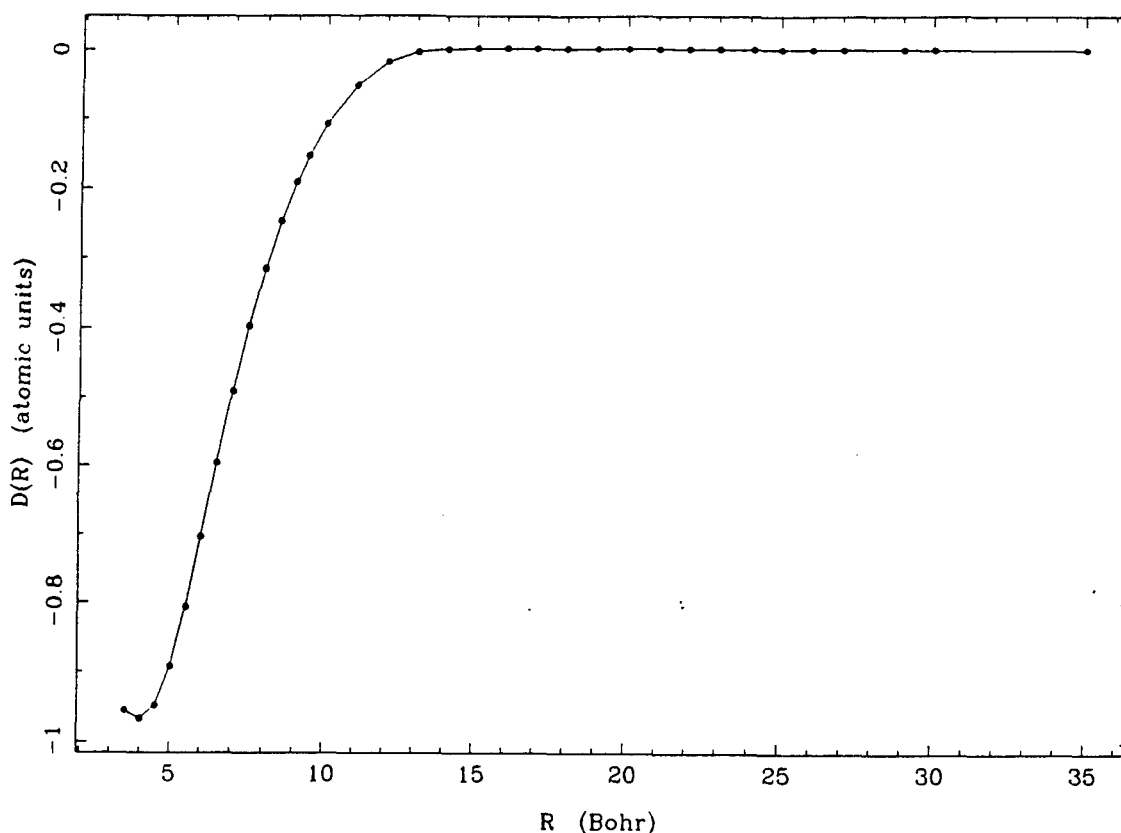


Figure 8. Electronic transition dipole moment for  $1^3\Sigma_u^+ - 2^3\Sigma_g^+$  of  $\text{Li}_2$  [8].

The intensities of the  $1^3\Sigma_u^+ - 2^3\Sigma_g^+$  transition of  $\text{Li}_2$  are represented by the Franck-Condon factors plotted in Figure 9. Intensities were only calculated for the rotationless transitions from the 11 vibrational states of  $1^3\Sigma_u^+$  to the 54 vibrational states of  $2^3\Sigma_g^+$ . Further calculations will be performed to include rotational energies in the transitions. The intensities can then be binned into small wavelength ranges corresponding to the 578

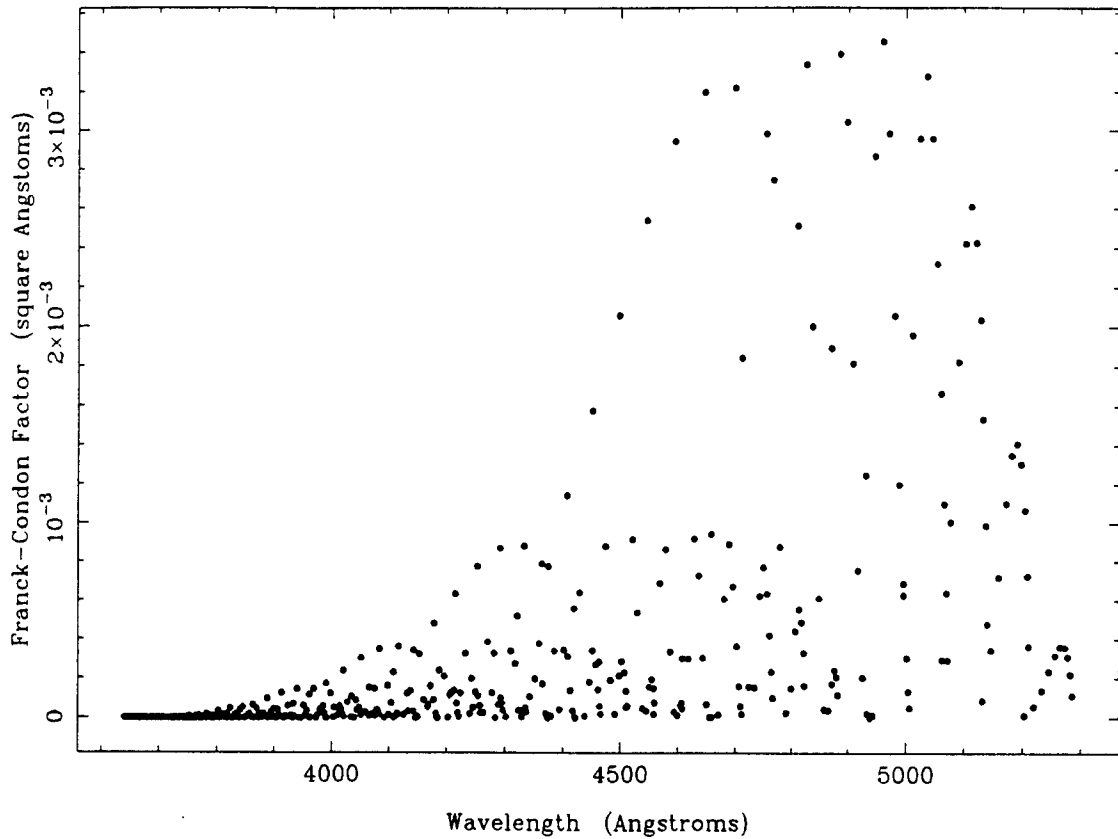


Figure 9. Rotationless Intensities of the  $1^3\Sigma_u^+ - 2^3\Sigma_g^+$  transition of  $\text{Li}_2$ .

pixels in the wavelength direction of the PSC image data for comparison to the data.

For bound-free absorption, the intensities are calculated directly in atomic units. Figure 10 shows the computed intensities for the  $1^3\Sigma_u^+ - 1^3\Pi_g$  transition at a temperature of 2000 K.

The jet profiles of absorbance vs position contained in the PSC image data are not true indications of the amount of absorbance per unit length occurring in the metal vapor jet. To obtain the radial profile, it is necessary to perform an Abel inversion on the lateral profile. For a measured lateral intensity profile  $N(x)$  of a specific wavelength, the

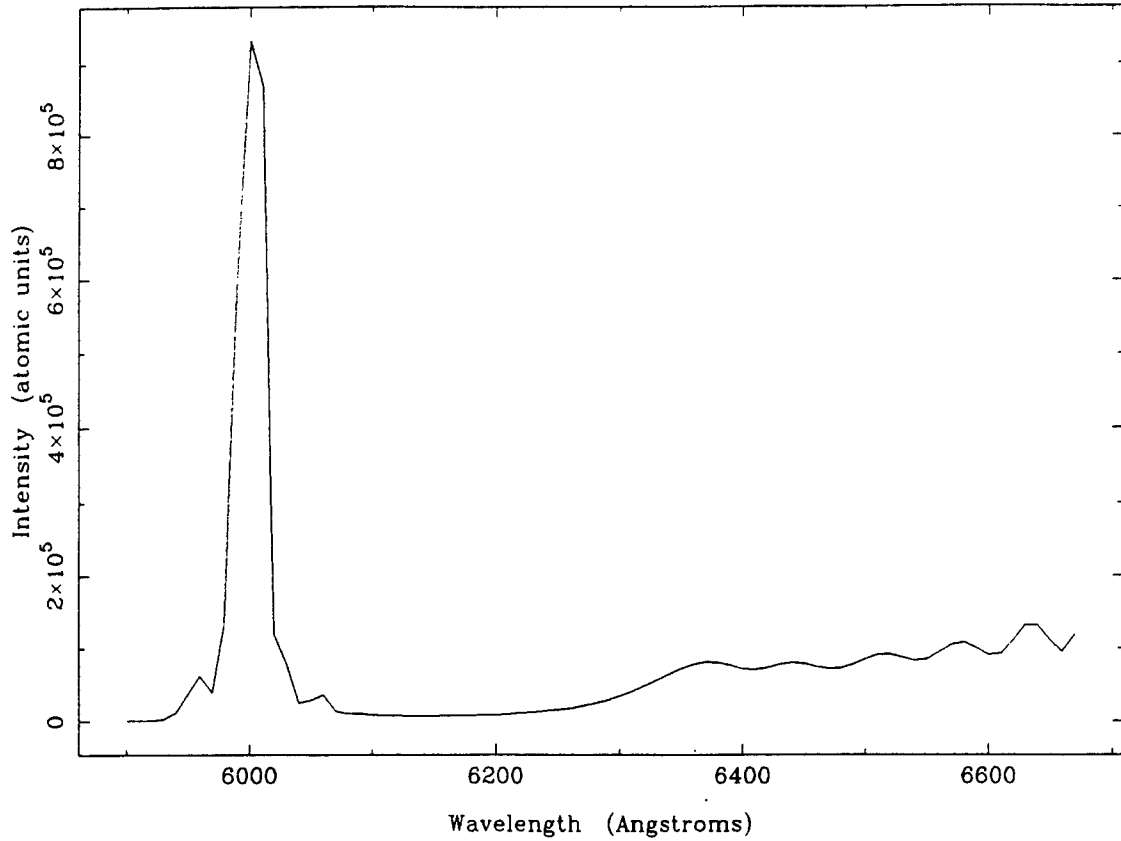


Figure 10. Intensities of the  $\text{Li}_2$   $1^3\Sigma_u^+ - 1^3\Pi_g$  transition at a temperature of 2000 K.

inverted profile  $f(r)$  is given by

$$f(r) = -\frac{1}{\pi} \int_r^R \frac{N'(x)dx}{(x^2 - r^2)^{\frac{1}{2}}}$$

where  $R$  is the edge of the lateral profile [9]. However, first performing a derivative on the data tends to amplify the effects of noise. A method recommended by Freeman and Katz [10] first rewrites the integral with the derivative on the outside as

$$f(r) = -\frac{1}{\pi r} \frac{d}{dr} \int_r^R \frac{N(x)xdx}{(x^2 - r^2)^{\frac{1}{2}}}.$$

Next, the data is fit to a curve of the form

$$N(x) = \sum_{i=0}^m C_i (R^2 - x^2)^i$$

which can be integrated by parts to give the Abel inversion

$$f(r) = \sum_i \lambda_i C_i (R^2 - r^2)^{i-\frac{1}{2}},$$

where

$$\lambda_i = \frac{2^{2i}(i!)^2}{\pi(2i)!}.$$

Using the above method, the data in Figure 11 was fit to a curve of eighth order. The resulting Abel inversion has been scaled by a factor of one hundred to show the narrower shape of the radial profile as compared to the original data.

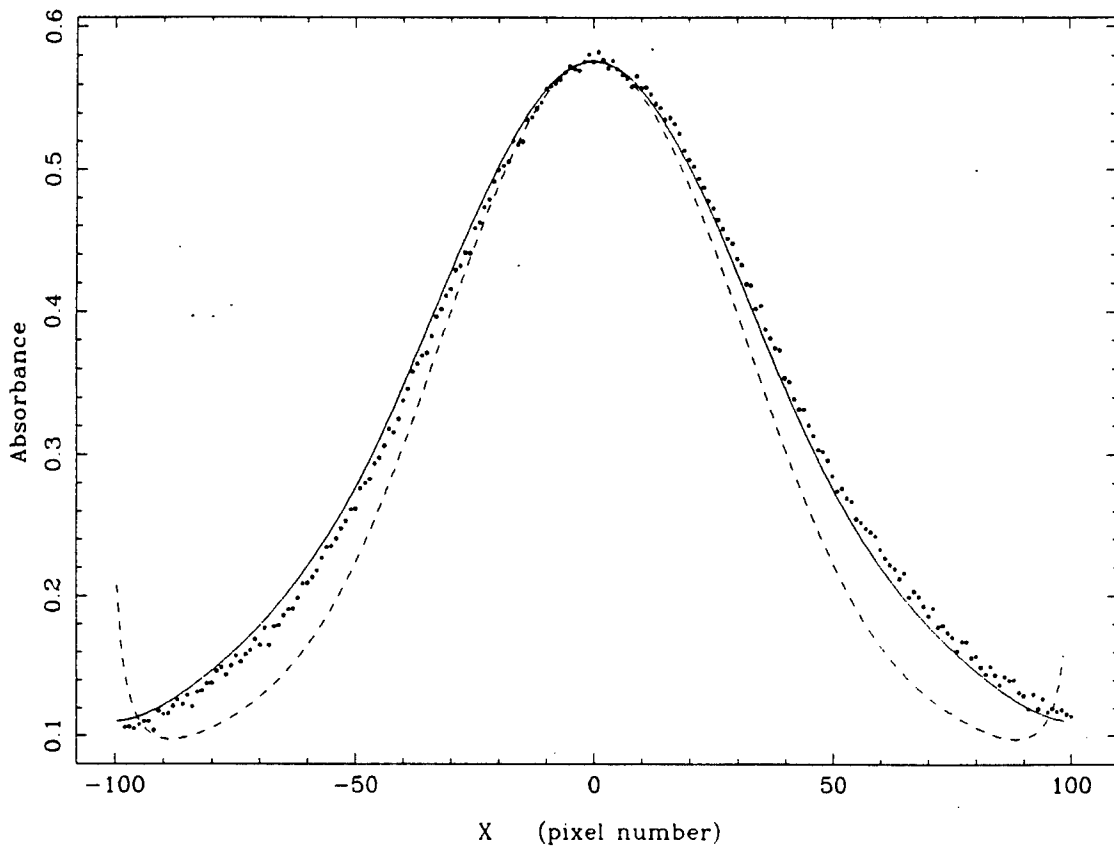


Figure 11. Abel Inversion. Original lateral data profile represented by small circles. Fit to lateral data profile shown as solid line. Dashed line is the Abel inversion multiplied by 100.



## CONCLUSIONS

High temperature lithium and sodium experiments in the Plasma Spectroscopy Cell have generated a large volume of data which can be analyzed with modern computational techniques. Calculations to date have shown that these techniques can be used to generate intensity profiles that will help to identify the specific molecular transitions observed in the PSC experimental data and thus help to characterize the mix of metal vapors to be used for solar plasma propulsion. Further development of these computational methods will enable the direct comparison of the calculated absorption profiles to the PSC data.

## REFERENCES

1. Larson, C.W. (1987), "Solar Plasma Propulsion," Report AFRPL TR-85-096 of the Air Force Propulsion Laboratory, Edwards Air Force Base, California.
2. Stwalley, W.C. and Koch, M.E. (1980), "Alkali Metal Vapors: Laser Spectroscopy and Applications," *Optical Engineering*, Vol. 19, No. 1, Jan./Feb., pp. 71-84.
3. Larson, C.W. (1988), "The Spectroscopy of Hydrogen/Metal-Vapor Mixtures at High Temperatures and Pressures," Report AL-TR-88-080 of the Air Force Astronautics Laboratory, Edwards Air Force Base, California.
4. Huber, K.P. and Herzberg, G. (1979) *Molecular Spectra and Molecular Structure IV*, Van Nostrand Reinhold Co., New York.
5. Zemke, W.T. and Stwalley, W.C. (1993), "Analysis of Long Range Dispersion and Exchange Interactions of Two Li Atoms," *Journal of Physical Chemistry*, Vol. 97, pp. 2053-2058.
6. Schmidt-Mink, I., Müller, W., and Meyer, W. (1985), "Ground- and Excited-state Properties of  $\text{Li}_2$  and  $\text{Li}_2^+$  from Ab Initio Calculations with Effective Core Polarization Potentials," *Chemical Physics*, Vol. 92, pp. 263-285.
7. Xie, X. and Field, R.W. (1986), "Perturbation Facilitated Optical-Optical Double

Resonance spectroscopy of the  ${}^6\text{Li}_2$   $3^3\Sigma_g^+$ ,  $2^3\Pi_g$ ,  $1^3\Delta_g$ ,  $b^3\Pi_u$ , and  $a^3\Sigma_u^+$  States," *Journal of Molecular Spectroscopy*, Vol. 117, pp. 228-244.

8. Ratcliff, L.B., Fish, J.L., and Konowalow, D.D. (1987), "Electronic Transition Dipole Moment Functions for Transitions among the Twenty-Six Lowest-Lying States of  $\text{Li}_2$ ," *Journal of Molecular Spectroscopy*, Vol. 122, pp. 293-312.

9. Tourin, Richard H. (1966), *Spectroscopic Gas Temperature Measurement*, Elsevier Publishing Co., New York.

10. Freeman, M.P. and Katz, S. (1963), "Determination of a Radiance-Coefficient Profile from the Observed Asymmetric Radiance Distribution of an Optically Thin Radiating Medium," *Journal of the Optical Society of America*, Vol. 53, pp. 1172-1179.

A DETAILED INVESTIGATION OF TIME RESOLVED  
LOW-POWER ARCJET PLUME PARAMETERS

Jeffrey A. Pobst  
Research Assistant  
Department of Aerospace Engineering

and

Daniel A. Erwin  
Associate Professor  
Department of Aerospace Engineering

University of Southern California  
University Park  
Los Angeles, California 90089-1191

Final Report for:  
Summer Research Extension Program (SREP)  
Phillips Laboratory

Sponsored by:  
Air Force Office of scientific Research  
Bolling Air Force Base, Washington, D.C.

December 1993

A DETAILED INVESTIGATION OF TIME RESOLVED  
LOW-POWER ARCJET PLUME PARAMETERS

Jeffrey A. Pobst  
Research Assistant  
Department of Aerospace Engineering

and

Daniel A. Erwin  
Associate Professor  
Department of Aerospace Engineering

University of Southern California  
University Park  
Los Angeles, California 90089-1191

Abstract

The behavior of the arcjet space thruster plume was studied using the Current Modulation Velocimetry(CMV) method whereby the gas plume axial velocity is observed to fluctuate as it expands from the arcjet nozzle. The diagnostic method provides time-accurate velocity measurements of high resolution and is based upon the Emission Ripple Velocimetry diagnostic that has been discussed in previous reports. Due to the initial results of the CMV diagnostic, further investigation into time-dependent parameters of arcjet operation is deemed necessary so time-resolved electron temperature and density are investigated using the Triple Langmuir Probe diagnostic. The nature of Laser-Induced Fluorescence(LIF) as a time-integrated measurement prevented it from enhancing this investigation into time-dependent behavior.

The use of the Phillips Laboratory Electric Propulsion Facilities also allowed examination of chamber background effects on arcjet plume properties. This demonstrated that previous arcjet plume measurements may be called into question due to the high background pressure environment in which they were performed.

A DETAILED INVESTIGATION OF TIME RESOLVED  
LOW-POWER ARCJET PLUME PARAMETERS

Jeffrey A. Pobst and Daniel A. Erwin

Department of Aerospace Engineering  
University of Southern California  
Los Angeles, California 90089-1191

Introduction

Arcjets are expected to play a strong role in future satellite space propulsion needs, particularly in the areas of on-orbit stationkeeping and orbit maneuvering. While the technology is considered viable enough to be deployed on a Telstar IV communications satellite,<sup>1</sup> arcjets are far from a mature technology. In order to compete successfully with chemical propulsion systems for orbit transfer missions, further improvements in arcjet propulsion systems are still required.<sup>2</sup> However, if these needed improvements in the performance level and efficiency of arcjets are to be achieved, an increased understanding of the fundamental physical processes that govern the operation of an arcjet is essential.

In order to increase the overall efficiency of an arcjet it is important to understand the major energy losses, of which the category of frozen flow losses is believed to be the dominant factor. Frozen flow losses of atomic species include: electronic excited states, unrecovered dissociation, and ionization, while molecular species also have rotational and vibrational energy states that are not fully converted to kinetic energy. Information pertaining to the frozen flow energy distribution of an arcjet would be beneficial for both designing next-generation thrusters and for comparison purposes with numerical models.

Although much research, both experimental and numerical, has been conducted on arcjet plume characterization over the last 30 years, almost all previous

studies assume that the arcjet operates in a steady-state mode. However, when current is provided by a high frequency switching power supply, it is found that the current delivered to the arcjet modulates at the PPU switching frequency. How this current modulation affects overall arcjet thruster performance is presently unclear. It is thought to potentially play a role in electrode erosion effects, while reference 3 clearly demonstrated that excited state frozen flow losses are affected by current modulation. It must still be resolved how fluctuations affect the more dominant frozen flow issues of dissociation, ionization and in the case of molecules, vibrational and rotational energy levels.

One of the goals of this work is to provide more insight into the time-dependent arcjet behavior. To address this, we present time-resolved measurements of the plume electron temperature, electron density and velocity. This type of information can indicate sources of error that arcjet researchers should be aware of. For example, measurement of the plume velocity fluctuations provides a velocity correction for the interpretation of steady-state Doppler broadened temperature measurements. These results also provide critical data for comparisons with numerical work.

In order to obtain velocity fluctuation data in an arcjet plume it was necessary to develop a new velocity diagnostic. This diagnostic, called current modulation velocimetry (CMV), is time-resolved and is based upon manipulation of the current to the arcjet. CMV is the only technique presently being employed that provides instantaneous velocity measurements of the arcjet plasma. The principal velocity diagnostic presently being used for arcjets is continuous wave (CW) laser induced fluorescence (LIF)<sup>4,5</sup> which provides accurate mean velocity measurements but with very limited temporal resolution. Although the CMV technique employs spatial averaging over a distance of several mm, temporal resolution is a few microseconds, enabling plume velocity fluctuations (if present) to be measured.

Data are taken over a range of typical facility conditions for arcjet research. How background pressure affects the arcjet plume is likewise discussed. In an effort to understand what background pressure is needed to simulate the conditions of space for arcjet research, a range of pressures (from 1.5 Torr down to 40 mTorr) is investigated.

#### Experimental Description

All experiments were conducted in the Optical Diagnostics Chamber (see Figure 1) of the Air Force Phillips Laboratory Electric Propulsion Lab. The arcjet used here is a 1-kW-class radiatively-cooled engine, constructed and furnished by NASA Lewis Research Center. Standard operating conditions were 110 V and 8.0 A, with 10 SLM of hydrogen propellant. Power was provided by a NASA Lewis 1-kW power processing unit (PPU). This PPU is a switching unit, operating at 16 kHz switching frequency. At the normal operating conditions, current ripple is about 20% peak-to-peak which depends somewhat on the line voltage.

The vacuum system consists of an aluminum chamber, 3 m in length and 2 m in diameter, with a large number of windowed ports for optical access. Two 9500-cfm Roots blowers evacuate the chamber; each is backed by a 1600-cfm blower and a mechanical pump.

For the optical emission measurements, two Hamamatsu R943-02 photomultiplier tubes (PMT) were used. A 10 nm Melles Griot interference filter ( $\lambda_0=656.3$  nm) and appropriate neutral density filters were placed in front of each PMT to insure that only the H $\alpha$  emission was observed. The optics train of each detection system is identical to that described in our previous work.<sup>3</sup> (Note that in the previous work only one detector system was used). All optical and triple probe signals were recorded on a DSA 601 digital signal analyzer.

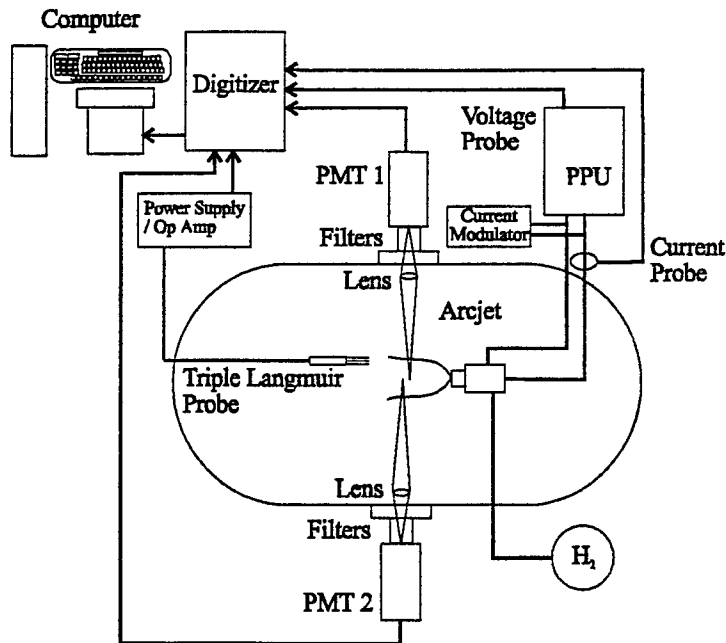


Figure 1: Experimental setup for emission diagnostics.

### Velocity Measurements

In our previous work<sup>3</sup> a velocity diagnostic called emission ripple velocimetry (ERV) was presented. In ERV, local optical emission oscillations are observed in the plume which are a result of current modulations from a high frequency switching power supply. Measurement of the delay of the emission signal with respect to the current waveform, as a function of axial position, allowed the axial flow velocity (averaged over the distance between two successive observation stations) to be calculated.

ERV, as implemented in reference 3, had two disadvantages which limited its usefulness:

1. An ERV measurement can only be obtained in the presence of significant high-frequency current ripple. It is thus inappropriate for use with, e.g., traditional ballasted welding power supplies.
2. The emission signals at different axial stations were obtained at different times (only one detector was used). Velocities so obtained must be time-averaged in order to be meaningful.



We present here a modification to the ERV technique, which we call current modulation velocimetry or CMV, which avoids these difficulties. In CMV, ambient current ripple is not used. Instead, a current spike is superimposed on the arcjet current. The consequent spike in emission is observed simultaneously at two axial locations (using two detectors) separated by several millimeters. The current spike and the emission spikes are all of duration a few microseconds. The time delay between the emission spikes at the two locations can be resolved to about one nanosecond, leading to a velocity measurement whose accuracy is in the range 30-60 m/s for plume velocities of order 5-10 km/s; this accuracy is comparable to those of recent CW-LIF results.<sup>4,5</sup>

Note that the velocity measurements obtained with CMV, while still position-averaged over the detector separation (here,  $3.29 \pm 0.05$  mm), are instantaneous. We know of no other plume velocimetry technique which has this property. LIF measurements, for example, determine the absorption lineshape by scanning in laser wavelength, which takes a minimum of several seconds to determine a velocity. In principle, a Doppler-shifted emission lineshape could be recorded instantaneously by a spectrograph and a gated imaging detector, but we know of no plume measurements in which Doppler shifts have been so measured. (In the recent Stuttgart work of Zube and Auweter-Kurtz,<sup>6</sup> instantaneous lineshapes were recorded in order to measure arc properties [gas excitation temperature and electron density].)

The current spike needed for CMV is generated by the simple RC shunt circuit of Figure 2, which is installed in parallel with the arcjet. Upon switch closure, the arcjet voltage appears across the shunt, charging the capacitor over several 1-microsec time constants. The shunt current is thus a several-ampere pulse lasting a few microseconds. The shunt current is subtracted from the arcjet current, which therefore shows a spiked current

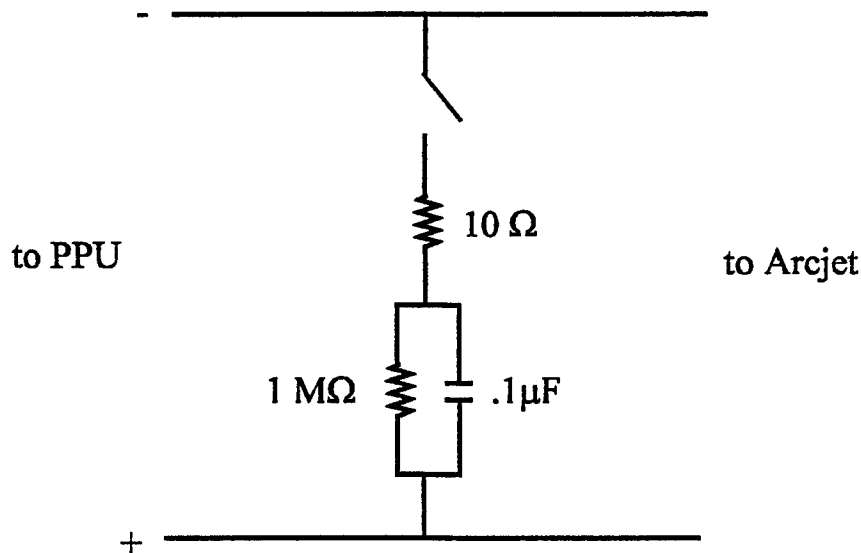


Figure 2: Current Modulation

dropout (the total current from the PPU is constant during this time, as it is held up by an output inductor of several mH).

The positive ring of the current pulse generates a sharp emission spike. See Figure 3, which shows the current pulse and the consequent emission spike. The emission spike is delayed with respect to the current spike; this delay is equal to the integral of  $1/v$  over the distance from the arc-heating region to the detection station, where  $v$  is the plume velocity as a function of axial position. A portion of the flow inside the arcjet is thus "tagged" by the current pulse.

Figure 4(a) shows two typical traces of emission spikes, taken simultaneously at the two detection stations. The second one (taken further out in the plume) is both smaller and time-delayed from the first. Figure 4(b) shows the two traces again, but the second trace has been translated and scaled to optimize the fit between the traces. (The optimization minimizes the integral of the square of the difference between the two curves.) The magnitude of the

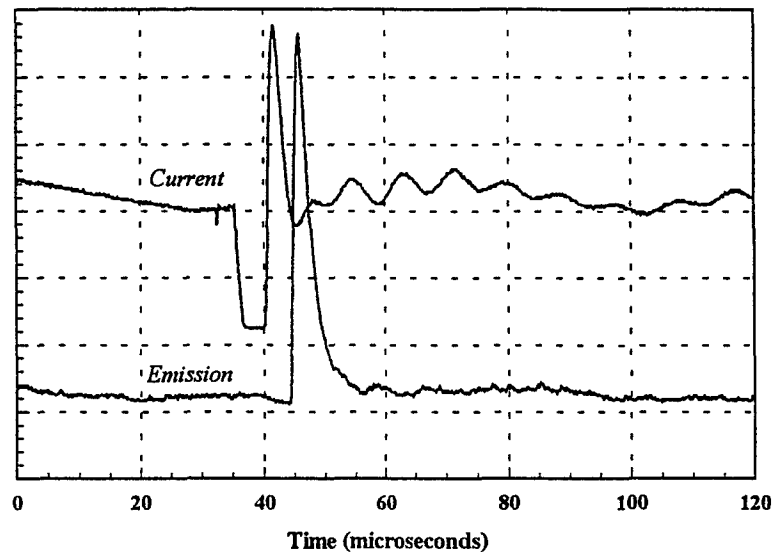


Figure 3: Current Pulse and Resulting Emission Spike

horizontal translation is the measured time delay between the original two traces, which allows the velocity to be calculated.

The best-fit transformation is determined using the standard Levenberg-Marquardt method.<sup>7</sup> The covariance matrix so obtained gives a measure of the confidence interval of the best-fit parameters, assuming the measurement of the optical signal to be subject to uniform, normally-distributed scatter. In this paper, the error bars given to indicate the precision of a measured velocity are computed using a one-standard-deviation confidence interval on the magnitude of the horizontal translation (time delay between the two emission spikes).

The optical emission from the arcjet plume is believed to come from electron recombination which repopulates the uppermost levels with the electrons subsequently cascading downward to populate the H excited states whose radiation is observed here. Electron recombination is a strong function of the electron temperature. In order to verify these ideas of how current

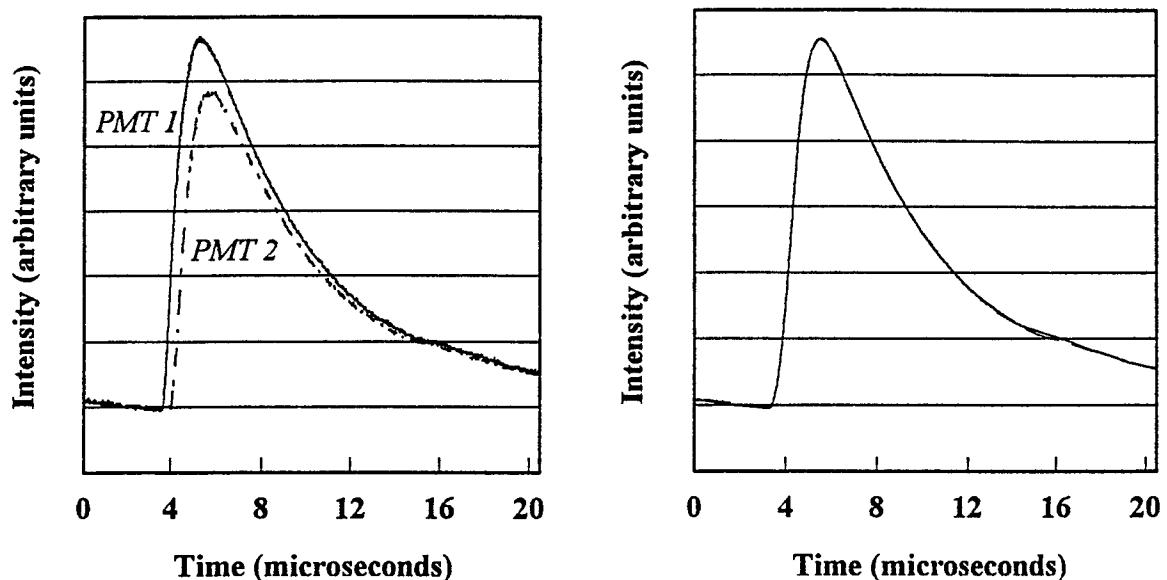


Figure 4 (a): Two simultaneous emission traces.

(b): Two traces, one shifted to determine time

modulation affects the arcjet plume signal, the electron temperature was measured.

#### Langmuir probe measurements of electron density and temperature

A triple Langmuir probe<sup>8,9</sup> was used to measure the electron temperature and electron density during the PPU switching cycle. The technique used to interpret the triple probe results and the explanation of triple probe theory is principally taken from Tilley et al.<sup>8</sup> The triple probe technique was chosen due to its simplicity of data reduction and its ability to instantaneously follow fluctuations of the plasma properties in the arcjet plume. A triple probe consists of three Langmuir probes that are electrically set up so that no voltage potential sweeps of the probes are required. Since curve fitting is not needed, data analysis is also much easier than for single or double probe techniques. The probes are placed as close together as possible without causing probe-to-probe sheath interaction. The larger control

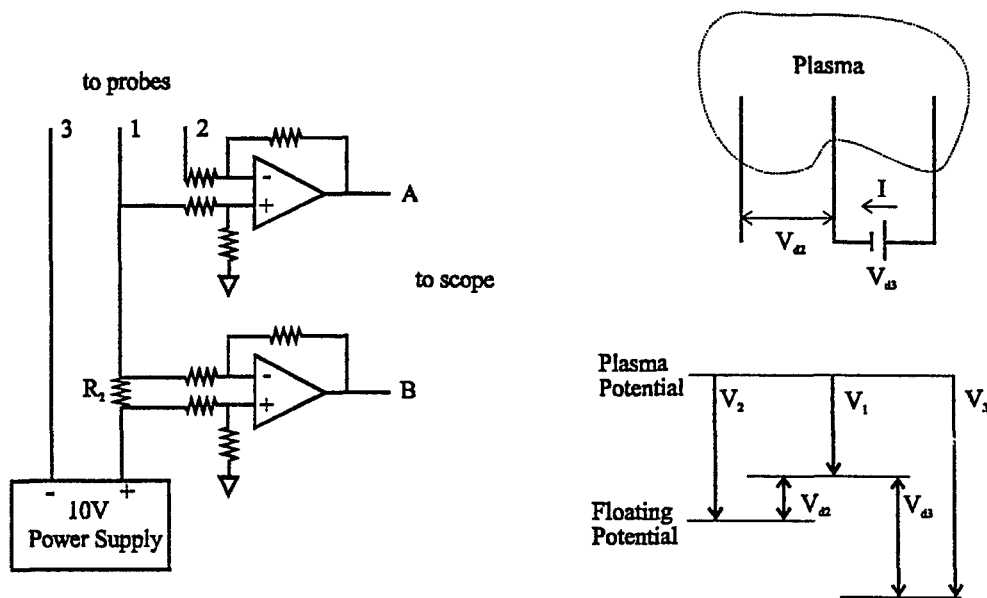


Figure 5: Triple Langmuir Probe Schematics

volume of the triple probe technique ( $\sim 2\text{mm} \times 2\text{mm} \times 3.5\text{mm}$ ) was not a concern for these measurements since an overall regional effect is being investigated. This is believed to be the first use of a triple probe on an arcjet; in reference 8, MPD thruster plumes were investigated.

The triple probe schematic, which can be seen in Figure 5, consists of electronics and three wire electrodes that provide  $T_e$  and  $n_e$  by measuring the voltage potential of probe 2 ( $V_{a2=2-1}$ ) and the current between probes 1 and 3. The circuit is floating and all electrodes become negatively biased with respect to the plasma potential due to the higher electron mobility. All potentials are actually measured with respect to the local plasma potential of the arcjet plume; however, the plasma potential value is not needed since it drops out in the equations. The thin sheath limit technique of Chen and Sekiguchi<sup>9</sup> is employed in this paper; based on error estimates, it was not considered necessary to employ the more accurate exact calculation of Laframboise. The primary equations, which assume singly ionized species, are:

$$\text{Electrode 1:} \quad I / A_1 = J_{\infty} \exp(-\chi_1) - J_i(\chi_1) \quad (1)$$

$$\text{Electrode 2:} \quad 0 = J_{\infty} \exp(-\chi_2) - J_i(\chi_2) \quad (2)$$

$$\text{Electrode 3:} \quad I / A_3 = J_{\infty} \exp(-\chi_3) - J_i(\chi_3) \quad (3)$$

In these expressions,  $J_{\infty} = n_e e (kT_e / 2\pi m_e)^{1/2}$  is the electron current at the sheath edge due to random thermal motion,  $\chi = e |V - V_p| / kT_e$  is the non-dimensional potential of the electrode with respect to the plasma potential,  $J_i(\chi)$  is the ion flux to the surface of the electrode, and  $A$  is the area of the electrode exposed to the plasma. An assumption of the thin sheath limit is that  $J_i$  is independent of  $\chi$  which enables  $T_e$  to be written implicitly as a function of  $V_{a2}$  and  $V_{a3}$ . The resulting implicit expression for  $T_e$  is:

$$\frac{1}{2} = \frac{1 - \exp(-\chi_{a2})}{1 - \exp(-\chi_{a3})} \quad (4)$$

where  $\chi_{a2} = \chi_2 - \chi_1$  and  $\chi_{a3} = \chi_3 - \chi_1$ . To obtain the electron number density, the Bohm sheath criteria is employed by Chen and Sekiguchi<sup>9</sup> to model the ion current as:  $J_i = \exp(-0.5) n_e (kT_e / M_i)^{1/2}$ . Number density is then obtained from equations (1) and (2) above as:

$$n_e = \frac{\exp(0.5) \frac{I}{A_1}}{e \left( \frac{kT_e}{M_i} \right)^{1/2} (\exp(\chi_{a2}) - 1)} \quad (5)$$

The major sources of triple probe error that were pointed out in Tilley<sup>8</sup> for the conditions of MPD thrusters were reevaluated for arcjet plasma conditions. The principal assumption employed in the thin-sheath theory is that the ion saturation current is independent of  $\chi$ . There are several concerns that need

to be addressed. One concern is the ion drift velocity perpendicular to the probe axis. However, since probe measurements were only taken on the centerline of the flow axis for these experiments, the component of flow perpendicular to the probe is considered negligible. The ratio of several length scales are considered pertinent: the ratio of probe radius to electron Debye length is calculated as 22.5, the ratio of ion-ion mean free path to probe radius equals approximately 60 and the ratio of probe spacing to electron Debye length is 270. All these ratios are considered acceptable. The probe end effect parameter was calculated to be on the order of 50 which is also negligible. A further source of probe error is contamination of the electrodes. A glow discharge is typically used for cleaning purposes. For these experiments, the electrodes were placed very close to the arcjet nozzle exit for several seconds. This caused the 0.010" tungsten electrodes to glow white hot due to particle-probe collisions and thus clean the wire surfaces. The exposed electrode lengths were 0.934 cm and the spacing between probes was 1.5 mm.

As a critical check of the background noise levels for the triple probe experiment, the arcjet was run with a glass enclosure placed around the triple probe. This test revealed a peak-to-peak noise level of  $\pm 4$  mV as compared to a triple probe voltage measurement ( $T_e$ ) on the order of 300 mV and a current shunt measurement ( $n_e$ ) on the order of 3.8 V.

## Results

### Electron Density and Temperature

Shown in Figure 6 is a comparison of how four arcjet operating parameters behave as a function of time: electron temperature, electron density, arcjet current modulation and the observed plume emission ripple of the  $H\alpha$  line. The modulation in the current delivered to the arcjet causes time-dependent

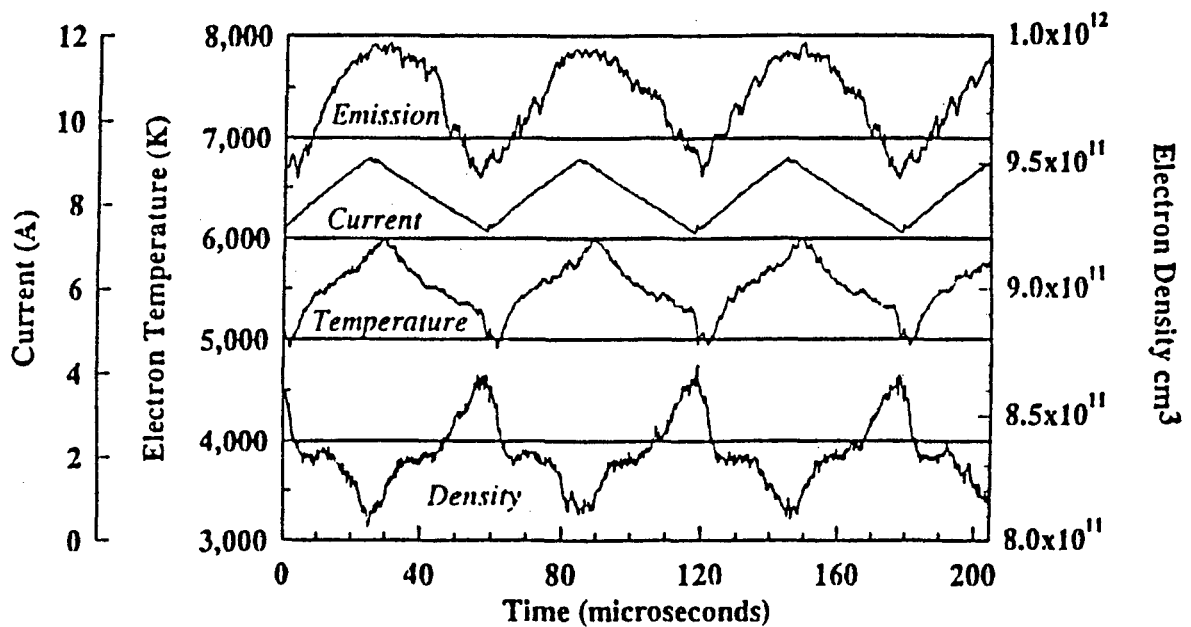


Figure 6: Time Resolved Measurements of Plume Parameters

variations in other operating parameters. The PPU current amplitude varies about 20% (p-p) around the mean value of 8.2 amps and modulates with the PPU switching frequency of 16.6 kHz. The electron temperature is observed to vary over a 20% range about the mean while electron densities fluctuate about 7% throughout the typical modulation cycle. Note that the current modulation, electron temperature and plume optical signals are all at the same frequency and almost in phase. A time delay between current ripple and both the observed electron temperature and plume emission fluctuations, which were observed at an axial location 2.5 cm downstream of the nozzle exit, is to be expected. There is approximately a 5.2  $\mu$ sec delay as the gas is convected downstream from the principal arcjet heating zone just in front of the cathode tip. The electron number density, although also strongly correlated with current, is 180° out of phase with the electron temperature. However, the observed plume emission is in phase with the electron temperature fluctuations. These observations imply that the electron temperature drives the excited state populations.



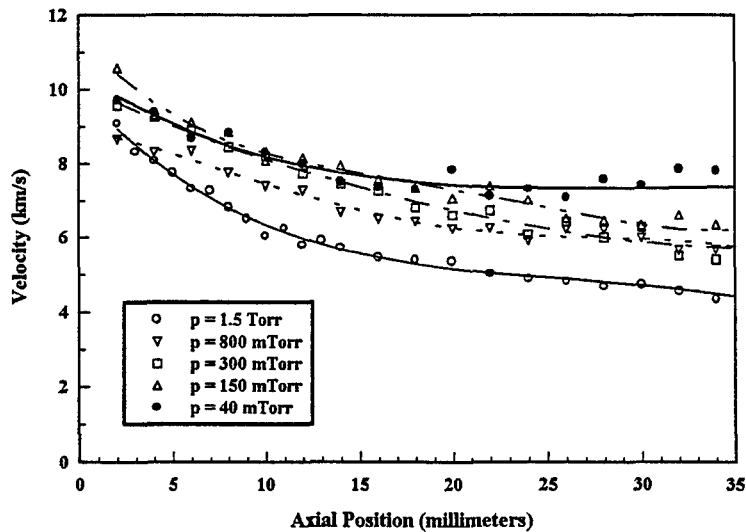


Figure 7: Axial Velocity vs. Chamber Pressure

#### Axial Velocity

Using the current modulation velocimetry technique, arcjet plume velocity measurements were taken along the centerline as a function of background pressure. (As will be discussed below, each data point is an average of ten measurements.) Velocity measurements for the lowest three pressure levels are very similar between the nozzle exit and two cm downstream. At this location, velocities for the 40 mTorr level remain constant or even are observed to rise slightly while velocities for 150 and 300 mTorr can be seen to decrease out to 3.5 cm downstream. Velocity measurements for 1.5 Torr chamber pressure are substantially lower than for the other background pressures tested. As expected, the 800 mTorr velocity curve falls between the high pressure level and the three lower pressure levels.

The trend for all the curves in Figure 7, for axial velocity to decrease with distance from the nozzle, is consistent with the measurements of Liebeskind et al.<sup>4</sup>

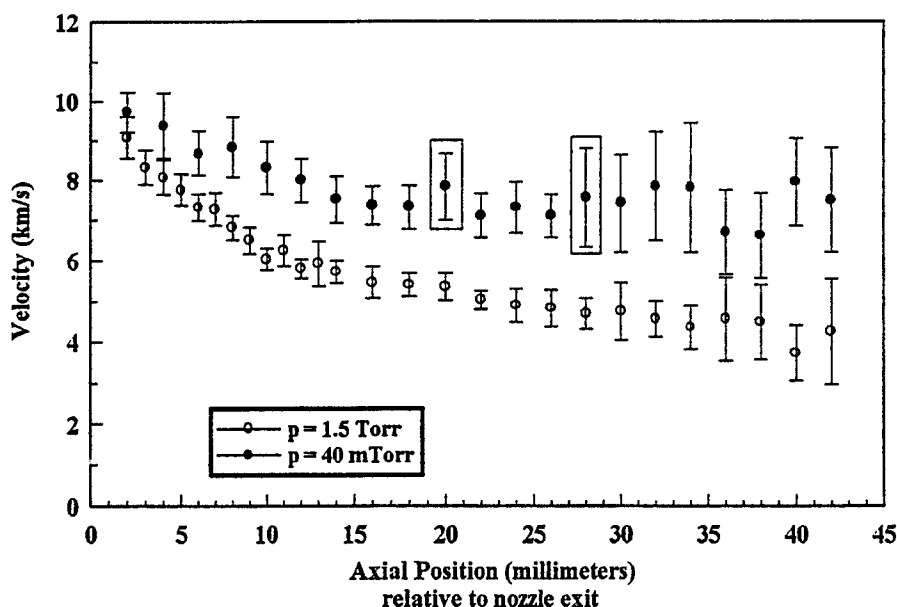


Figure 8: Axial Velocity Fluctuations. Each error bar represents the standard deviation of ten separate velocity measurements

Figure 8 presents the same data as Figure 7, for the lowest and highest pressure. Error bars are shown which represent one standard deviation of ten velocity measurements taken at separate times. We see that the plume velocity is not constant, but fluctuates by several percent or more.

In Figure 8, two points are shown with boxes around them. These boxed points are shown again in Figure 9, where the ten individual velocity measurements whose mean and deviation were seen in Figure 8, are shown separately. The error bars in Figure 9 are based on the accuracy of measurement of the time delay between a pair of emission traces. Note that this fit error is much smaller than the velocity spread.

In regard to velocity fluctuations, it is worth pointing out that a time-averaged Doppler lineshape will include the effects of fluctuations as well as translational temperature. Therefore, translational temperature

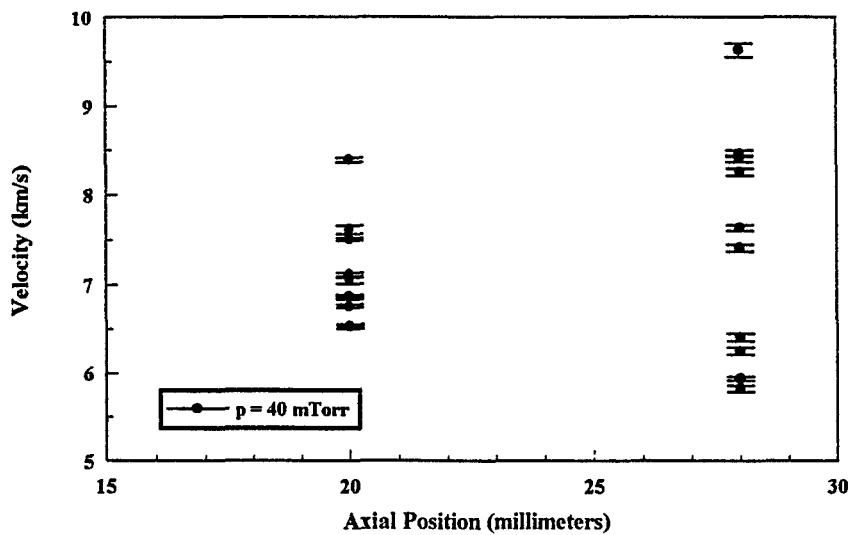


Figure 9: Examples of Raw Velocity Data and Confidence of Fit

obtained assuming a stationary flow is overestimated. However, this correction is small for the present results, only around one degree.

Figure 10 shows the variation of the CMV results for observations at several values of the radial coordinate (distance from the plume axis). It is important to note that these data have not been Abel inverted. Therefore, they do not exactly represent radially resolved axial velocities.

In order to obtain true radial variation of the instantaneous axial velocity, it would be necessary to simultaneously record two traces at each of many radial locations and Abel invert all radial data. Since we could only digitize two traces at once, it was impossible for us to record in this manner. Therefore, we deemed it inappropriate to Abel invert the data obtained here.

### Conclusions

A new velocity diagnostic is presented called Current Modulation Velocimetry (CMV) which allows instantaneous velocity measurements to be taken in the

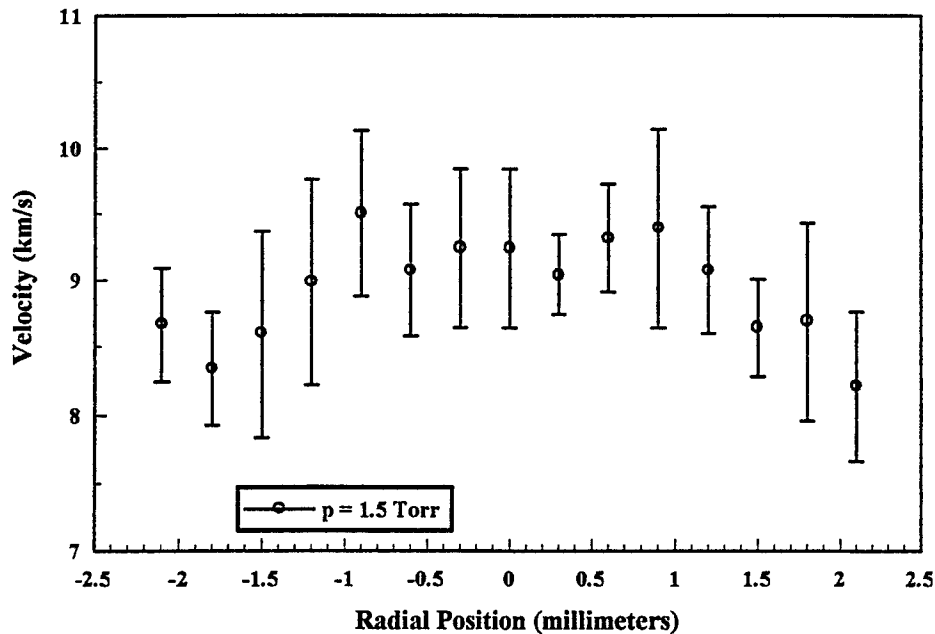


Figure 10: Radially Resolved Axial Velocity Fluctuations  
(Approximate; not Abel inverted)

arcjet plume to an accuracy of  $\pm 50$  m/s. Axial velocity measurements using CMV indicate that the plume is not steady, but fluctuates by 5% to 20% of the local mean value.

Axial velocity measurements show a significant variation in profile as a function of background pressure. Considerable differences in velocity are observed for pressures above 800 mTorr as opposed to below this pressure level. For the first two centimeters downstream of the nozzle exit, velocities for a background pressure of 1.5 Torr are 25% or more lower than velocity measurements taken below the 800 mTorr level.

Velocity fluctuations are found to increase with axial distance downstream. Axial velocity was found to decrease with distance from the nozzle exit in agreement with earlier CW-LIF results.

The electron temperature was found to oscillate at the same frequency and almost in phase with the current ripple from the PPU. The electron temperature ranges from a low of 4950K to a peak value of 6000K. The electron density was found to fluctuate 180° out of phase with the electron temperature, with a peak-to-peak amplitude of 7%.

The fact that the electron temperature fluctuates in phase with the arcjet current ripple and the plume optical emission, strongly supports a hypothesis from previous work<sup>3</sup> that plume radiation is predominantly due to electron recombination rather than to resonant scattering of arc emission.

#### References

1. W.W. Smith et al., "Low Power Hydrazine Arcjet Qualification," IEPC Paper 91-148, Viareggio, Italy, October 1991.
2. C. E. Vaughan and R. J. Cassady, "An Updated Assessment of Electric Propulsion Technology for Near-Earth Space Missions," AIAA 92-3202, July 1992.
3. R. A. Spores, J. A. Pobst, J. H. Schilling, and D. A. Erwin, "Performance Effects of Interaction Between a Low-Power Arcjet and its Power Processing Unit", AIAA 92-3238, 28th Joint Propulsion Conference, Nashville TN, July 6-8 1992.
4. J. G. Liebeskind, R. K. Hanson, and M. A. Cappelli, "Plume Characteristics of an Arcjet Thruster", AIAA 93-2530, 29th Joint Propulsion Conference, Monterey CA, June 28-30, 1993.
5. W. M. Ruyten and D. Keefer, "Laser Fluorescence Velocimetry of an Arcjet Exhaust Plume," IEPC-91-093, 22nd International Electric Propulsion Conference, Viareggio, Italy, October 1991.

6. D. M. Zube and M. Auweter-Kurtz, "Spectroscopic Arcjet Diagnostics under Thermal Equilibrium and Nonequilibrium Conditions," AIAA-93-1792, 1993.

7. W. H. Press, B. P. Flannery, S. A. Teukolsky, and W. T. Vetterling, *Numerical Recipes: The Art of Scientific Computing*, 1st ed. (Cambridge Univ. Press, Cambridge, 1986).

8. D. L. Tilley, A. J. Kelly, and R. G. Jahn, "The Application of the Triple Probe Method to MPD Thruster Plumes," AIAA-90-2667, 21st International Electric Propulsion Conference, Orlando, Florida, July 18-20, 1990.

9. S.L. Chen and T. Sekiguchi, "Instantaneous Direct-Display System of Probe Parameters by Means of Triple Probe," J. Appl. Phys., Vol. 36, No. 8, 1965, pp. 2363-2375.

This work published at the 23rd International Electric Propulsion Conference  
as paper 93-128 Time Resolved measurements of 1 kW Arcjet plumes using Current  
Modulation Velocimetry and Triple Langmuir Probes

# **MEASUREMENTS OF ION-MOLECULE REACTIONS AT HIGH TEMPERATURES**

**Jeffrey F. Friedman**  
**Assistant Professor**  
**Department of Physics**  
**University of Puerto Rico at Mayaguez**

**Thomas M. Miller**  
**Professor**  
**Department of Physics and Astronomy**  
**University of Oklahoma**

**Final Report for:**  
**Summer Research Extension Program**  
**Phillips Laboratory**

**Sponsored by:**  
**Air Force Office of Scientific Research**  
**Bollings Air Force Base, Washington, D.C.**

**and**  
**Recinto Universitaria Mayaguez**

**December 1993**

# MEASUREMENTS OF ION-MOLECULE REACTIONS AT HIGH TEMPERATURES

Jeffrey F. Friedman  
Assistant Professor  
Department of Physics  
University of Puerto Rico at Mayaguez

Thomas M. Miller  
Professor  
Department of Physics and Astronomy  
University of Oklahoma

## Abstract

We have begun measurements of ion-molecule reactions at temperatures up to 1300 K, greatly exceeding temperatures covered in all previous work. A new high-temperature flowing afterglow apparatus has been used. The research effort has been divided into (a) solving materials and design problems, (b) solving reaction chemistry problems, and (c) carrying out the actual measurements. In this report we describe plans for, and the: publishing of existing data, conducting additional research on the Phillips High Temperature Flowing Afterglow (HTFA) apparatus, the implementation of new design modifications, the formation and training of a new ion-molecule group at the University of Puerto Rico, Mayaguez, and the design and early construction phase of a new innovative High Temperature Flowing Afterglow at UPR-RUM.



# MEASUREMENTS OF ION-MOLECULE REACTIONS AT HIGH TEMPERATURES

Jeffrey F. Friedman, and Thomas M. Miller,

## INTRODUCTION

It has long been recognized that information on ion-molecule reactions at high temperatures is desirable for both scientific and practical reasons.<sup>1-4</sup> New reaction channels can open up at high temperatures as rotational and vibrational states are excited in both the ion and target molecule.<sup>5</sup> In addition, entropy differences between reactants and products may be significant enough at high temperatures to allow a reaction to proceed even if the reaction enthalpy is positive.<sup>3,4</sup>

Very little information is available on the dependence of ion-molecule reaction rates as a function of vibrational excitation of the neutral molecule.<sup>6</sup> A small fraction of the total ion-molecule literature includes measurements of reaction rate coefficients as a function of temperature.<sup>7</sup> These measurements typically extend into the 500-600 K range, limited by the type of materials and heaters used in the apparatus. A single experiment has gone beyond this conventional temperature limit, prior to the present work. In 1974, a group at NOAA modified the heaters on a flowing afterglow apparatus and measured reaction rate coefficients for several positive ion reactions involving atmospheric species, up to 900 K.<sup>2</sup>

We now have measurements as high as 1300 K<sup>5,8-14</sup> for roughly a dozen ion-molecule systems, and propose to finalize these measurements and to carry out further work, possibly at still higher temperatures made possible by the purchase of new clamshell heaters rated to 1500 K. Despite the numerous problems that we have encountered we believe that with a small number of additional modifications, briefly described below and to be detailed in a paper in progress<sup>15</sup> (this paper has been delayed because of several new modifications to the apparatus in process of implementation), routine measurements in the 1300 to 1500 K range will be easily attainable. We have operated the Air Force HT FLACH (High Temperature FLOWing Afterglow CHEmistry) apparatus for two 12 week sessions, regularly exceeding 1200 K, taken data, calibrated and tested all systems, and designed and implemented

modifications; all with relatively little down time for major repairs. Maintenance time is not unreasonable and routine data taking is easily within the scope of a single investigator. We note that Lindinger et al.<sup>2</sup> commented on their pioneering work at high temperatures, "...900 K, which seems to be about the practical limit for a flowing afterglow system."<sup>2</sup> Ferguson<sup>6</sup> added, "The materials problems at 900 K are horrendous, and the measured rate constants at 900 K had much larger uncertainties than the room temperature measurements." So, we feel that success even in the first stage of development of the apparatus warrants publication of the high temperature features and problems.

The U.S. Air Force sponsors a great deal of research on low-energy interactions of electrons, ions, atoms, and molecules because of the need to understand and influence plasmas which occur naturally (e.g., auroras and the ionosphere) or man-made (e.g., around transonic aircraft, re-entry vehicles, or engine exhausts). Generally speaking, the ultimate goal is to be able to eliminate free electrons locally from the plasma to enhance radio wave communications and/or reduce radar signatures. In order to gain control of a particular plasma, one must have developed a model of the plasma which utilizes perhaps thousands of reaction rate coefficients for the interacting species.

Many of the plasmas of interest to the Air Force exist at high temperature (say, 1000-2000 K). Plasma modelers are forced to make educated guesses as to the high temperature behavior of reaction rates and products, by extrapolating lower temperature data. A guide for extrapolation may be found in data on the kinetic energy dependence of reaction rates from experiments carried out in the presence of a weak electric field (drift experiments). The kinetic energies in such experiments correspond to temperatures of many thousands of degrees in translational energy. However, the translational energy data are not directly applicable to high temperature plasmas because the target molecules in those experiments were not at equivalently high temperatures, and the projectile ions may or may not be excited by successive collisions with a buffer gas.<sup>5, 7</sup>

As we shall see, comparisons of our high temperature data with kinetic energy data are useful to determine the relative importance of translational versus internal energy on the reaction rate coefficients and product distributions. This information may shed light on the reaction mechanisms.<sup>5</sup>

## EXPERIMENTAL METHOD

The data discussed were obtained with a newly constructed flowing-afterglow apparatus at Hanscom AFB that was specially designed for high temperatures. The flowing afterglow technique was developed in the 1960s for the study of ion-molecule reactions by a group at NOAA Laboratories (then part of the National Bureau of Standards).<sup>6</sup> The flowing afterglow method is now a well-established technique used in 20-30 laboratories around the world.

The experimental technique involves interacting a swarm of ions with a known number density ( $n$ ) of reactant molecules for a specific time ( $t$ ). Exponential attenuation of the primary ion signal ( $I$ ) will occur if reactions take place which generate other species:

$$I = I_0 \exp (-k n t),$$

where the signal at  $t=0$  is  $I_0$ , and the reaction rate coefficient is  $k$ . This experiment was carried out in a flowing buffer gas (0.3 - 0.9 torr helium) to effectively transform the time measurement into one of distance.

Mass spectra were used to identify the ionic products of the reaction under study. Electron detachment reactions were revealed by the lack of ionic product. Neutral products could not be observed, but could usually be inferred from known energetics. The recent addition of a residual gas analyzer helps in this regard, but has not, as yet, been placed in routine operation.

## APPARATUS

In the flowing afterglow apparatus, a plasma (e.g., consisting of  $O^+$  ions and various positive ions) was created by interaction between a source gas (e.g.,  $N_2O$  in helium) and an electron beam at the upstream end of the flow tube. These primary ions drifted approximately 40 cm toward an inlet for neutral reactants. The primary ions were allowed to mix with the neutrals, reacting for 63 cm before a sample of the final ion swarm was taken through an aperture into a mass spectrometer and detection chamber. We shall now focus on the special high-temperature aspects of the apparatus.

The apparatus is intended to reach temperatures as high as 2000 K in 3 stages of development. In the first (present) stage, the stainless steel flow tube is wrapped with the best commercial heating tapes available and zirconia insulation. A large vacuum box that surrounds the flow tube for additional thermal

insulation has only recently been employed to counteract leaks in the vacuum system that have resulted from temperature cycling fatigue in the stainless steel joint at the downstream end of the flow tube. The use of the vacuum box, contrary to expectations, did not yield any noticeable gain in attainable temperature. In addition thermal equilibrium, while very stable, took much longer to attain, and the box became very hot when working at high temperatures. When the ceramic flow tube is installed in phase 3 the large vacuum box will be necessarily employed as the downstream joint between the flow tube and mass analyzing region because of inadequate sealing materials, will leak considerably, but it is suggested

that for work with heating tapes (and possibly clamshell heaters) that this is not necessary and is probably detrimental because of the heat and inaccessibility of the flow tube.. The heating tapes are only rated for 1030 K, but this limitation is set by crystallization of the woven glass insulation; if the tape is not disturbed, temperatures "several hundred degrees higher may be reached." We have taken the flow tube temperature to over 1300 K and have yet to experience heater failure because of insulation breakdown, rather the limit is set by the current carrying capacity of the heating wires, which is about 5 amperes.

The ends of the flow tube are vacuum sealed with Viton o-rings at water-cooled flanges. At the downstream end of the reaction zone, the hot flow tube is supported by a thin (1/16-inch) stainless steel plate, which is inefficient at conducting heat away from the flow tube. The outer edge of the thin plate couples to the water-cooled flange. This joint, as mentioned above, has proven susceptible to leaks and is currently being redesigned. At high temperatures it bows over 1/4 inch from planar. The bowing was even greater before the installation of bellows type gas inlet feed lines. We consider this to be the last major original design weakness to be corrected. We are designing a bellows type expansion joint for this area.

In the final stage of development (ca. 2000 K) of this apparatus we will use a specially built furnace which utilizes a ceramic flow tube. Vacuum seal to the ceramic tube will not be perfect, but some leakage of helium will be allowable, into the large evacuated box surrounding the flow tube. This concept has already been proven with the successful operation of the apparatus with a very large leak in the flow tube's downstream weld. Although not critical, the pumping constraints on this box are considerable and a fairly large forepump is necessary. As stated above, the box is probably not needed

with a good stainless steel flow tube and zirconium, or other high grade, insulation to at least 1300K.

An intermediate stage of development (ca. 1500 K) using ceramic clam shell heaters around the stainless steel flow tube is currently being implemented. The heaters have been purchased and will be installed when the apparatus is reassembled after moving the laboratory. This stage represents a relatively minor modification to the apparatus, but experience has shown that each step of several hundred degrees upward in temperature reveals new materials problems, and it will be easier to solve these problems before the massive furnace is installed. For example, our first excursion to 1300 K resulted in total loss of ion signal. We found the electron multiplier (ion detector) completely plated with a thin white film and with its original metallic coating heavily etched, even though the detector chamber is supposed to be at room temperature. The plating seemed restricted to the electron multiplier. At this point we do not have an explanation for the failure of the electron multiplier (an \$800-900 item), and we do not know if it was a freak accident or a result of bombardment with ions or neutrals emitted by the 1300 K flow tube. Subsequent trials at 1300 K have been relatively free of problems, although we have had further multiplier failure due to other causes; one associated with evacuation of the large box which necessitated the redesign of the pumping system and the addition of another mechanical forepump. The lifetime of the multipliers is a legitimate concern at this time and it may prove necessary to provide additional cooling in the detector region. Heat buildup is through conduction as the vacuum in this region is fairly good and radiation is insufficient to account for the heating. This aspect of the work will require monitoring in future sessions to determine if any problem exists.

It is assumed that the regular use of the large vacuum box will be necessary near 1500 K to insure structural integrity of the stainless steel flow tube as it approaches its melting point. Additional internal cooling may also prove necessary as the detection and lensing chambers, as mentioned above, are heated by conduction from the flow tube. At 1300 K they are already too hot to touch with the unprotected hand.

Two other problems inherent to the high temperature experiment deserve mention. The first is that many common reactant gases will thermally dissociate (probably mostly on the hot flow tube walls)

even at the modest 1300 K temperatures reached thus far. Up to this point we have simply concentrated on reactants that are not expected to dissociate easily (e.g., H<sub>2</sub>, D<sub>2</sub>, CO, CH<sub>4</sub>). But eventually some routine form of residual gas analysis will be necessary, and an analyzer has recently been installed to do this. To reduce the chances of dissociation a new flow tube has been designed with a side reactant port with minimal length in the high temperature region. This is an acceptable solution for heating by tape or

clamsells, but it is not possible with the large oven, at least in its present configuration. The second problem is that all common materials evaporate impurities when heated. Our present molybdenum nose cone sampling plate (recently replaced with stainless steel) evaporates K<sup>+</sup> ions in noticeable amounts even at 700 K, and as 1300 K is approached, alkali metal ions are observed, in copious amounts, regardless of whether the electron-impact ion source is on or off. Therefore, at the present time, *positive* ion reactions cannot be studied without additional difficulty above about 1000 K at low buffer pressures (i.e. 0.3 - 0.5 torr). We have not found any similar problem with *negative* ions, at least as high as 1300 K. It remains to be seen what will happen with a ceramic flow tube. The stainless steel nose cone plate ameliorates this problem somewhat but causes other problems because of charge buildup on its surface. Operation at higher buffer pressure (i.e. 1.0 torr), as suggested by Smith<sup>17</sup> also seems to help.

Our measurements on the evaporation of alkali metal ions from the hot surface are consistent with the results of Datz and Taylor<sup>18</sup> (who studied other metal surfaces). We observe the evaporation of K<sup>+</sup> ions to follow the Saha-Langmuir equation,

$$[K^+]/[K] = 0.5 \exp (-0.33 \text{ eV}/kT),$$

where 0.5 is a statistical weight factor and, in this equation, *k* is Boltzmann's constant. At 1200 K, about 2.5% of the evaporated potassium is ionized. We do not now measure the absolute ion density, so neither of the concentrations [K<sup>+</sup>] nor [K] is known separately. We propose below to use a Langmuir probe to measure the plasma density [K<sup>+</sup>] as a function of temperature, from which [K] can be calculated. Residual gas analysis will show if these impurities play a role in the dissociation of neutral reactants, e.g., can CH<sub>3</sub>Br be converted to KBr on the hot flow tube surface? We have recently employed the two internal thermocouples as Langmuir probes for test purposes and the results were favorable so we intend to continue the practice.

## PRELIMINARY RESULTS

We first examined the classic nucleophilic displacement reaction<sup>8,9,11,12</sup>



The results agreed with other work, with a reaction rate coefficient that slowly declined with temperature up to nearly 600 K. We observed a shallow minimum in the reaction rate at about 550 K, followed by a rapid increase of almost two orders of magnitude by 1200 K. A similar effect was found in a kinetic energy study<sup>13a</sup> for  $^{37}\text{Cl}^- + \text{CH}_3^{35}\text{Cl}$ . While the rapid increase could be due to vibrational excitation, it is also likely that the  $\text{CH}_3\text{Br}$  reactant is thermally dissociating, yielding a more reactive product. Again, this problem can only be resolved by residual gas analysis. Similar data have been obtained for  $\text{CH}_3\text{I}$ . An abstract on this work was presented at the 1992 Gaseous Electronics Conference.<sup>12</sup> Additional work, as proposed, has not yet been done on these reactions, but is to be attempted after the construction of the new flow tube with a short reactant gas inlet.

To avoid the dissociation problem, we next used more stable reactants, studying reactions between  $\text{O}^-$ ,  $\text{O}^+$ , and  $\text{O}_2^+$  with  $\text{H}_2$ ,  $\text{D}_2$ ,  $\text{NO}$ ,  $\text{CO}$ ,  $\text{CH}_4$ , and  $\text{N}_2$ .<sup>10,11,14</sup> In the case of  $\text{O}^-$  the first four reactants lead to electron detachment, with a minor hydroxide channel for  $\text{H}_2$  and  $\text{D}_2$ . Reaction with  $\text{CH}_4$  gives solely hydroxide ionic product, and no reaction is observed for  $\text{O}^- + \text{N}_2$ . In each case, the reaction rate coefficients measured as a function of temperature agree well with drift field results<sup>20-24</sup> implying that translational energy effects dominate over internal energy effects for these systems, at least up to 1000 K. Data for  $\text{O}^- + \text{NH}_3$  and  $\text{N}_2\text{O}$  indicate that the  $\text{NH}_3$  and  $\text{N}_2\text{O}$  undergo dissociation into non reactive products above about 800 K.

We also have preliminary data on  $\text{Ar}^+$  reactions with various stable gases up to 1000 K, and results for  $\text{O}_2^+ + \text{CH}_4$  and  $\text{O}^-$  on  $\text{O}_2$ ,  $\text{D}_2$ , and  $\text{CH}_4$  up to 1300 K. The latter data correlate quite well with lower temperature data<sup>19</sup> obtained in this laboratory on a different apparatus, and indicate a strong  $\text{CH}_4$  vibrational energy effect on the reaction rate coefficient.<sup>5</sup> The  $\text{CH}_4$  data were very difficult to obtain. There are indications that the chemistry is temperature dependent in this reaction from the production of ions in down stream reactions. We propose to explore these possibilities in detail.

Based on our experience at Hanscom AFB, we have begun to assemble equipment to construct a smaller, inexpensive version of a high-temperature flowing-afterglow apparatus at the University of Puerto Rico. Most of the cost of the Hanscom AFB apparatus is in (a) the large mechanical pumps needed for the fast buffer gas flow, (b) the electric quadrupole mass spectrometer, and in (c) the machine shop time required for construction. A scaled-down apparatus would greatly simplify the heating problem and involve a smaller vacuum pump, and an in-house magnetic mass spectrometer with a Faraday cup detector would save on costs and will be constructed in the UPR physics department shop. It is premature to claim unequivocally that a scaled-down HTFA is feasible, but a furnace and several mechanical vacuum pumps are now available at UPR, machine shop time has been committed. We also have a UPR commitment for the use of a large variable field magnet for the mass spectrometer. A

student has already written, and is testing, a computer program to model the flow characteristics of the new flow tube. A second, independent, program has now been written and the output of the two programs will be compared to establish if their computations are reliable. Preliminary designs are being made for the construction of the new flow tube in conjunction with the UPR physics department's machinist.

Within the physics department the two faculty members who have expressed interest in forming a new research group and have begun the early phases of training. Dr. A. Leyderman is an experienced experimentalist and Dr. C. Condat is a theorist with experience in diffusion limited processes. In addition to his writing and design work Dr. Miller is preparing a workshop on Flowing Afterglows to be presented while he is in P.R. Dr. Friedman has prepared and is schedule a preliminary seminar to the physics and chemistry departments to attract other interested parties. Ms. Menendez-Barreto also presented a seminar for the physics department's graduate students.

Three AFOSR Summer Research Participants ( only Friedman and Menendez-Barreto participated in the program this past summer) carried out the research discussed above: University of Puerto Rico (UPR) Prof. Jeffrey F. Friedman, University of Oklahoma (OU) Prof. Thomas M. Miller, and now OU (formerly UPR) graduate student Ms. Melani Menendez-Barreto. This work was the subject of Ms. Menendez-Barreto's M.S. thesis<sup>25</sup>.



About half of the work outlined here - writing manuscripts, planning experiments, designing apparatus, and analyzing data - was done at the University of Puerto Rico, utilizing in large measure the requested computer system. The other half of the work - with the high temperature apparatus - was performed at Hanscom AFB.

The and Galileo ion detectors requested (only one was requested, but we have not ordered the amplifier requested because of suitable equipment already available in lieu of two more detectors, considered much more critical to the project) from AFOSR to solve nagging problems we have had with the present piece of equipment have been ordered. It is our intention that this item will eventually be used at UPR.

Some of the materials and supplies requested from AFOSR will be used for constructing a new flow tube at UPR. One new heaters was required and purchased. The MKS flow controllers were purchased by UPR and are ready for installation.

## REFERENCES

- <sup>1</sup>See, for example, *Gas Phase Ion Chemistry*, Vol. 2, Ed. M. T. Bowers (Academic Press, New York, 1979).
- <sup>2</sup>W. Lindinger, F. C. Fehsenfeld, A. L. Schmeltekopf, and E. E. Ferguson, *J. Geophys. Res.* **79**, 4753 (1974).
- <sup>3</sup>M. Meot-Ner (Mautner), *J. Phys. Chem.* **95**, 6580 (1991).
- <sup>4</sup>M. Meot-Ner (Mautner) and S. C. Smith, *J. Am. Chem. Soc.* **113**, 862 (1991).
- <sup>5</sup>A.A. Viggiano, R.A. Morris, T.M. Miller, J.F. Friedman, M. Menendez-Barreto, J.F. Paulson, H.H. Michels, and J.A. Montgomery, (submitted) *J. Chem. Phys.* (1993)
- <sup>6</sup>E. E. Ferguson, *J. Am. Soc. Mass Spectrum.* **3**, 479 (1992).
- <sup>7</sup>Y. Ikezoe, S. Matsuoka, M. Takebe, and A. Viggiano, *Gas Phase Ion-Molecule Reaction Rate Constants Through 1986* (Maruzen Company, Ltd., Tokyo, 1987).
- <sup>8</sup>M. Menendez-Barreto, J.F. Friedman, T.M. Miller, *SFRP Final Report*, (1992).
- <sup>9</sup>J.F. Friedman, M. Menendez-Barreto, A.A. Viggiano, T.M. Miller, J.M. Van Doren, R.A. Morris, A.E.S. Miller, J.F. Paulson, *Bull. Amer. Phys. Soc.*, **38**, 1103, (1993).
- <sup>10</sup>T.M. Miller, J.F. Friedman, M. Menendez-Barreto, A.A. Viggiano, R.A. Morris, A.E.S. Miller, and J.F. Paulson, *Proc. 6<sup>th</sup> Intl. Sem. on Electron and Ion Swarms*, (1993)
- <sup>11</sup>J.F. Friedman, M. Menendez-Barreto, *SFRP Final Report*, (1993).
- <sup>12</sup>M. Menendez-Barreto, J. F. Friedman, T. M. Miller, A. A. Viggiano, R. A. Morris, A. E. S. Miller, J. M. Van Doren, and J. F. Paulson, abstract 45th Gaseous Electronics Conference, Boston, October 1992, *Bull. Am. Phys. Soc.* Dec. (1992)
- <sup>13</sup>T.M. Miller, J.F. Friedman, M. Menendez-Barreto, A.A. Viggiano, R.A. Morris, A.E.S. Miller, and J.F. Paulson, (accepted for publication by) *Physica Scripta*.
- <sup>14</sup>J.F. Friedman, T.M. Miller, M. Menendez-Barreto, A.A. Viggiano, R.A. Morris, A.E.S. Miller, and J.F. Paulson, Boulder, June 1993, *10<sup>th</sup> Annual CEDAR conference*.
- <sup>15</sup>M. Menendez-Barreto, J. F. Friedman, T. M. Miller, A. A. Viggiano, R. A. Morris, and J. F. Paulson, abstract 46th Gaseous Electronics Conference, Montreal, October 1993, *Bull. Am. Phys. Soc.* Dec. (1993)
- <sup>16</sup>J.F. Friedman, T.M. Miller, M. Menendez-Barreto, J. Williamson, F. Dale, J.F. Paulson, A.A. Viggiano, R.A. Morris, (in preparation for) *Review of Scientific Instruments*.
- <sup>17</sup>D. Smith, Hanscom, April 1993 (personnel comm.).

- <sup>18</sup>S. Datz and E. H. Taylor, *J. Chem. Phys.* **25**, 389 (1956).
- <sup>19</sup>S. E. Barlow, J. M. Van Doren, and V. M. Bierbaum, *J. Am. Chem. Soc.* **110**, 7240 (1988).
- <sup>20</sup>W. Lindinger, D. L. Albritton, F. C. Fehsenfeld, and E. E. Ferguson, *J. Chem. Phys.* **63**, 3238 (1975).
- <sup>21</sup>M. McFarland, D. L. Albritton, F. C. Fehsenfeld, and E. E. Ferguson, *J. Chem. Phys.* **59**, 6629 (1973).
- <sup>22</sup>A. A. Viggiano, R. A. Morris, C. A. Deakyne, F. Dale, and J. F. Paulson, *J. Phys. Chem.* **94**, 8193 (1991).
- <sup>23</sup>A. A. Viggiano, R. A. Morris, C. A. Deakyne, F. Dale, and J. F. Paulson, *J. Phys. Chem.* **95**, 3644 (1991).
- <sup>24</sup>A. A. Viggiano, R. A. Morris, J. M. Van Doren, and J. F. Paulson, *J. Chem. Phys.* **96**, 275 (1992).
- <sup>25</sup>M. Menendez-Barreto, Mayaguez, May 1993, *Master of Science Thesis*.

**FINAL DESIGN AND CONSTRUCTION OF LIDAR RECEIVER  
FOR THE STARFIRE OPTICAL RANGE**

Gary G. Gimmestad  
Principal Research Scientist  
Georgia Tech Research Institute

Georgia Institute of Technology  
Atlanta, Georgia 30332

Final Report For:  
Research Initiation Program  
Phillips Laboratory

Sponsored by:  
Air Force Office of Scientific Research  
Bolling Air Force Base, Washington, DC

December, 1993

# **FINAL DESIGN AND CONSTRUCTION OF LIDAR RECEIVER FOR THE STARFIRE OPTICAL RANGE**

Gary G. Gimmestad  
Principal Research Scientist  
Georgia Tech Research Institute  
Georgia Institute of Technology

## **Abstract**

During the summer of 1992, a prototype lidar system was developed and evaluated at the Starfire Optical Range (SOR) at Kirtland AFB, New Mexico, with funding from the AFOSR Summer Research Program. The prototype lidar used SOR's copper vapor laser (CVL) and 1.5 meter telescope as a transmitter, and the receiver was based on a Celestron C-14 telescope which was mounted on the side of the 1.5 meter telescope. The prototype lidar system was operated on several occasions in 1992 and its sensitivity was demonstrated by observing thin, subvisual cirrus clouds which drifted over the site. However, when the receiver was mounted on the side of the 1.5 meter telescope, several alignment problems arose. The most serious problem was traced to flexing of components in the Celestron telescope as the elevation angle was changed, due to the changing direction of gravitational forces. Attempts were made to stiffen the Celestron telescope, but the flexing problem was never solved. In addition, several other problems related to convenience of operation were discovered. For these reasons, the work proposed under the Research Initiation Program was to eliminate all of these problems by redesigning and rebuilding the lidar receiver. Our methodology was to list the faults with the prototype receiver and develop a design which would eliminate them while maintaining the system's good features and excellent detection sensitivity. This project was successful. SOR now has an operational lidar system which is easy to use and very adaptable. The receiver has two channels with different entrance apertures, and the two channels can be independently configured with different field stops and optical filters to provide a wide range of sensitivities and operating wavelengths. All of the problems which occurred in the prototype have been eliminated.

# FINAL DESIGN AND CONSTRUCTION OF LIDAR RECEIVER FOR THE STARFIRE OPTICAL RANGE

Gary G. Gimmestad

## INTRODUCTION

During the summer of 1992, a prototype lidar system was developed and evaluated at the Starfire Optical Range (SOR) with funding from the AFOSR Summer Research Program. SOR, located at Kirtland Air Force Base in Albuquerque, New Mexico, uses high-power lasers to create artificial guide stars in the atmosphere. The guide stars are used in conjunction with adaptive optics techniques to provide high-resolution images of celestial objects and man-made satellites. The prototype lidar used SOR's copper vapor laser (CVL) and its projection optics as a transmitter, and the receiver was based on a Celestron C-14 telescope which was mounted on the side of the 1.5 meter telescope. This configuration has the advantages that the lidar is always pointing in the same direction as the main telescope yet it does not require any additional optics in the Coude path and it does not "steal" photons from other experiments.

The prototype lidar had two receiver channels, referred to as short range and long range. Each channel had its own narrow-band optical filter, so the receiver could also be operated as a two-color lidar if required. The short range channel was based on a 2-inch diameter objective lens and the long range channel used the full 14-inch aperture of the C-14 telescope. In practice, smaller apertures had to be used in both cases to avoid saturation in the photomultiplier tubes. The short range channel normally had an aperture about 1/2 inch in diameter, and the long range channel had about 1/3 of the full area of the C-14 aperture.

The prototype lidar system was operated on 13 occasions in 1992 and its sensitivity was demonstrated by observing thin, subvisual cirrus clouds which drifted over the site on August 18, 1992. However, these observations were made with the lidar receiver on a tripod. When the receiver was mounted on the side of the 1.5 meter telescope, several alignment problems arose. The most serious problem was traced to flexing of components in the Celestron telescope as the

elevation angle was changed, due to the changing direction of gravitational forces. Attempts were made to stiffen the Celestron telescope, but the flexing problem was never solved. In addition, several other problems were encountered which were related to convenience of operation. For these reasons, the work proposed under the Research Initiation Program was to eliminate all of these problems by redesigning and rebuilding the lidar receiver.

### DISCUSSION OF PROBLEM

The main problem with the prototype lidar receiver was lack of alignment stability. The alignment was not stable from day to day, and more importantly, it changed with telescope elevation angle. The movement of the receiver optic axis as the elevation angle changed was estimated to be about 1 milliradian. The receiver field of view was also about 1 milliradian (a small field of view is necessary in order to avoid saturation of the PMT) so the misalignment was drastic. This problem was aggravated by the fact that the Celestron telescope was mounted on the top and front of the 1.5 meter telescope tube, which meant that the telescope had to be inverted during alignment so that personnel could have access to the lidar receiver, and then returned to its normal orientation for operation. Efforts to stiffen the Celestron telescope were not successful. The alignment procedure was also very awkward. It required mounting the heavy lidar receiver with a boresite precision of a few milliradians, performing initial adjustments during daytime, and performing final adjustments at night while standing on scaffolding. The alignment fixtures were crude, and a special tool was required to remove the receiver cover.

Other problems included stray light which got into the long range receiver, especially with the short range receiver port open; the necessity to use several tools to operate and align the lidar; and the necessity to keep track of loose parts whenever the receiver ports were opened. In addition, the lidar receiver had a rough appearance due to its painted sheet metal cover and access ports.

### METHODOLOGY

Our approach to solving the problems listed above was to completely redesign and rebuild the lidar receiver. Our methodology was to list the faults with the prototype receiver and develop

a design which would eliminate them while maintaining the system's good features and excellent detection sensitivity, which had been demonstrated in 1992.

A schematic diagram of the new design is shown in Fig. 1. The two-channel feature has been preserved, with a two-inch aperture short range telescope (based on the prototype) and a six-inch long range telescope. The area of the six-inch aperture is approximately equal to that which was used during initial measurements with the prototype long-range receiver.

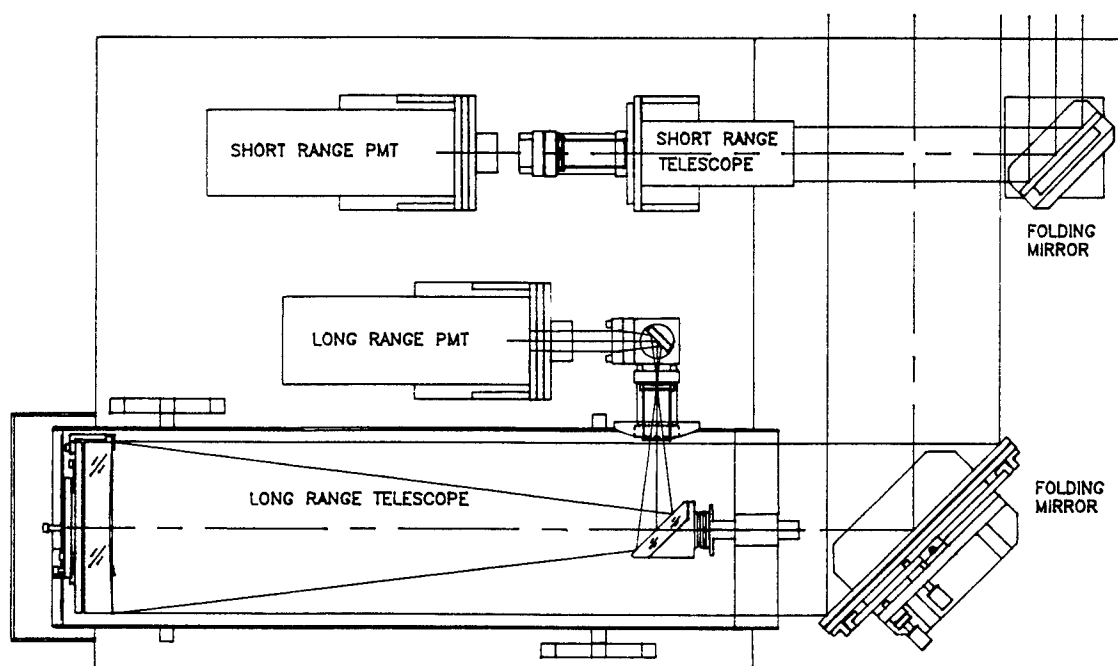


Fig. 1. Schematic diagram of the two-channel lidar receiver.

Ease of alignment has been facilitated by using adjustable folding mirrors in front of both telescopes. This means that the orientation of the receiver during installation is not critical at all, and that initial daytime alignment is not required. All alignment adjustments are performed with knobs on the mirror mounts (no tools or loose parts are required) while watching the lidar signal with an oscilloscope.

The amount of light reaching the telescopes is also adjustable. The short range receiver is equipped with an iris diaphragm which is accessible and easily adjusted by hand. The long



range telescope can be partially shadowed by a sliding shutter on the front of the receiver. This shutter is part of the dust cover for the folding mirrors, so it is normally closed when the receiver is not in operation.

Stray light is controlled by several levels of baffling. The left side of the receiver as shown in Fig. 1 is in a light-tight box. Light-tight gaskets are provided for both telescopes where they protrude through the box wall. Aluminum tubes, threaded inside and black-anodized, are provided between the telescopes and the field stops. In addition, tubes made of black cloth with drawstrings are used between the telescopes and the photomultiplier tubes (PMTs) to avoid cross-talk between receiver channels. The inside of the light-tight box is painted black.

Access ports for the mirror adjustments are equipped with Dzus fasteners so that they can be removed without tools and with no loose parts. The covers for the light-tight box are held on with screws, because the only reason to remove them is to change optical filters or field stops, and this would normally be done with the dome lights on, when tools and parts are not a problem. Even this procedure has been simplified, however, by providing flanges on the optical filter holders so that they can be easily gripped. No other alignment or adjustment is required inside the light-tight box and no special alignment fixtures are required.

Overall appearance of the receiver was improved by constructing the light-tight box and the dust cover from panels of varnished, brushed aluminum with flat black handles. The panels are fastened to a framework made of welded aluminum angle, which is painted flat black. Photographs of the lidar receiver with and without its covers are shown in Figs. 2 and 3.

One of the greatest improvements in convenience resulted from a new mounting position. The lidar receiver is now mounted closer to the back of the telescope. Alignment can be done while standing on a step stool with the 1.5 meter telescope inverted and elevated 45 degrees, or by standing on a stepladder with the 1.5 meter telescope pointed at the zenith.

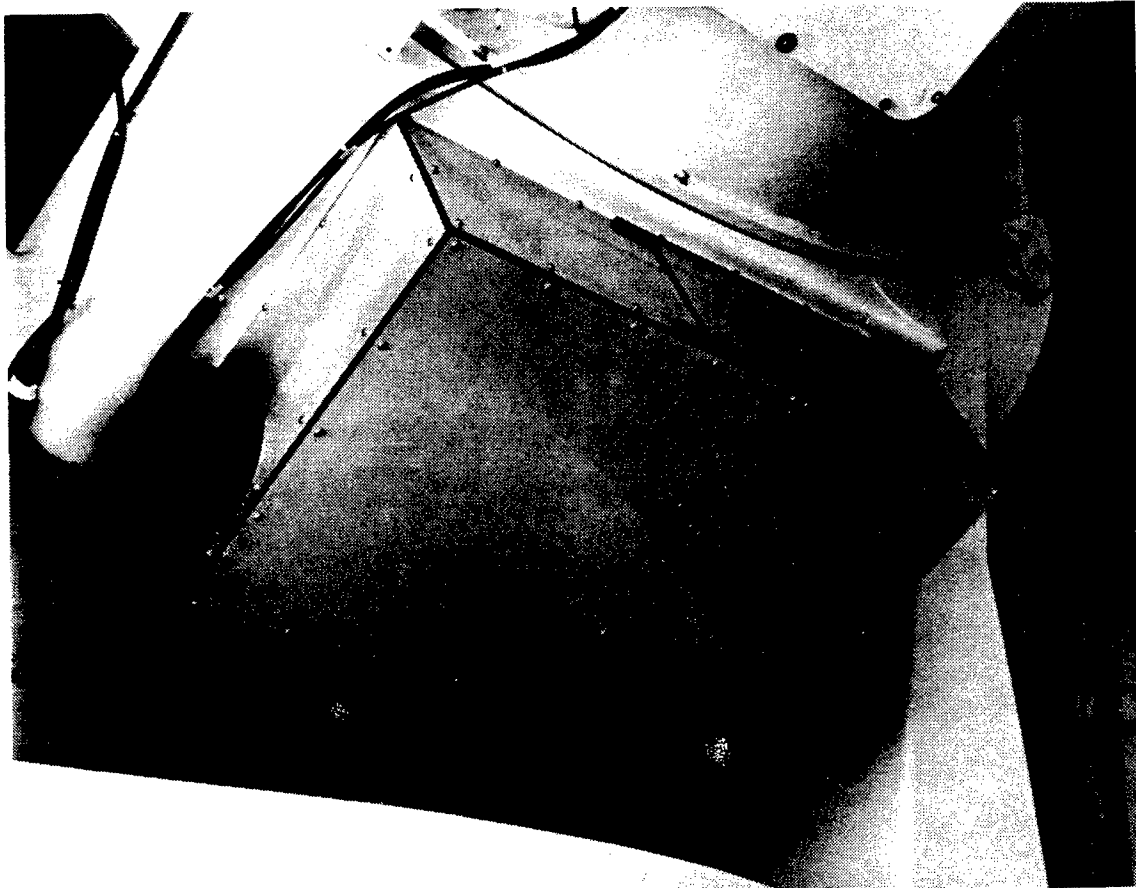


Fig. 2. The lidar receiver installed on the 1.5 meter telescope (covers on).

A great deal of design effort was expended in making the long range receiver rigid. Its field of view is normally one milliradian, and the design goal was to maintain alignment to one-tenth of the field of view. Because a given angular deflection in a mirror results in twice as large an angular deflection in light rays reflected from the mirror, the design goal was to keep mechanical deflection to 50 microradians or less as the telescope moved through its complete range of angles (from 45 to 90 degrees above the horizon when the laser is in operation). An additional constraint was that the overall weight of the receiver could not exceed 80 pounds, so the common approach of making optical mounts massive could not be used here. Using a 6-inch newtonian telescope instead of the 14" Celestron telescope saved over 30 pounds, and since the smaller telescope could be made stiffer, alignment stability was dramatically improved. Specific methods which were used to minimize flexure are explained in the numbered paragraphs below.

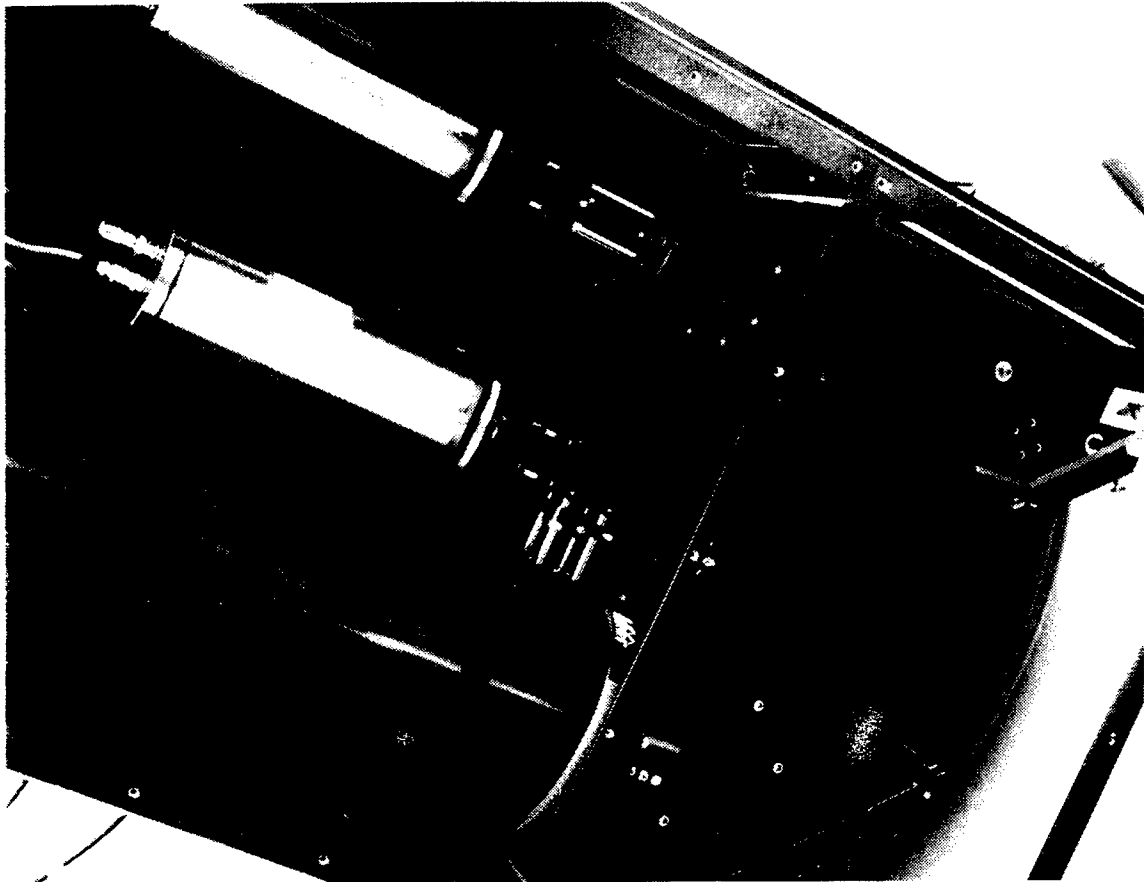


Fig. 3. The lidar receiver installed on the 1.5 meter telescope (covers off).

1. No ball bearings or sleeve bearings were used for angular adjustments because these types of bearings may have backlash. Metal flexures were used instead, because these rely on the bending of metal to provide rotation. Leaf flexures were used on the primary mirror mount and the secondary mirror mount. Lucas Free-Flex Pivots were used on the long-range receiver's steering mirror. Heavy shafts and bearing mounts were avoided by using flexures.
2. All angular adjustments inside the light-tight enclosure are locked down with screws to increase the stiffness of the flexures.
3. The long-range receiver's secondary mirror was bonded to its mount with a uniform layer of two-component RTV silicone rubber, preventing the mirror from

moving in its mount. The layer's thickness was controlled to .0001 inch by shims behind the mirror to minimize thermally induced tilts.

4. The spider holding the secondary in the long-range receiver has four sets of double-legs made from stainless steel, producing an extremely stiff structure and minimizing secondary mirror motion as the elevation angle of the telescope is changed.
5. The long-range receiver telescope is held to the lidar's baseplate by two low profile "tripod" mounts that wrap around the aluminum telescope tube. The bottom surface of each mount has three raised pads forming a triangle with mounting bolt holes through the pads. This approach ensures that the mounts will not rock on their mounting bolts, and that the stiffness gained by bolting the baseplate to the 1.5 meter telescope is passed on to the long-range receiver. Making the mounts as short as possible minimizes flexure while minimizing weight.
6. The short range receiver mount has raised pads on its bottom surface to keep the telescope from rocking on the baseplate. The mount also has stiffening brackets to minimize flexure. The stiffeners allowed the mount material to be reduced from 1/2-inch to 1/4-inch aluminum, reducing its weight.
7. The PMT mounts were designed similar to the short-range receiver mount to help keep the receiver weight within limits.
8. Additional optics used in the long and short-range receivers are mounted directly to the telescopes using Spindler & Hoyer Microbench components. This approach eliminated the need to use individual mounts for each optical component, reducing the weight of each assembly to about 1/3 of the weight of individual mounts.

When all of the receiver components had been fabricated and procured, the receiver was assembled in Atlanta to verify that all parts fit together properly. Power supplies were connected to the photomultipliers and dark current pulses were monitored with an oscilloscope in order to verify that the wiring was all done correctly. The alignment stability of the six-inch receiver telescope was investigated by using an autocollimator to measure angular deflection while applying forces at various places on the optics mounts. Pulling on the primary mirror mount with a force approximately equal to the mirror's weight produced an optical deflection of about 100 microradians. This deflection appeared to be within the design goals, because the force required was larger than the change in gravitational forces that the assembly would experience due to changes in telescope orientation during actual use. The receiver was partially disassembled, packed, and shipped to SOR.

On 13 July 93, the lidar receiver was mounted on the side of the 1.5 meter telescope and re-assembled. There were no technical problems. However, a complete checkout of the lidar was not possible during the installation trip due to the heavy clouds and rain which occurred on four successive nights. Checkout was therefore postponed until a drier time of year. The installed receiver is shown in Figs. 2 and 3, with and without its covers.

During the period 11-15 September 93, the new lidar receiver was finally operated and checked out. Initial adjustments were performed with a three-step procedure: first, the folding mirror orientation for each channel was adjusted so that the lidar signal as seen with an oscilloscope began to rise roughly where expected from geometrical crossover calculations; second, the shutter or iris diaphragm was adjusted so that the peak signal was in the range 3.0 - 3.5 volts; and third, the lidar signal was digitized, averaged, and analyzed. This procedure was iterated until the averaged signal had the correct crossover position and the peak signal was in the correct voltage range.

As mentioned earlier, the 1.5 meter telescope can only be operated at elevations in the 45 to 90 degree range when the laser is being propagated for safety reasons, and it is possible to align the lidar receiver with the telescope aimed at the zenith, so the lidar is only required to

operate properly over a 45 degree range of elevation angle after alignment. Nevertheless a more stringent test was performed on 15 September 93 in order to assess the amount of flexure in the new lidar receivers. In this test, a lidar data set was recorded with the 1.5 meter telescope at 45 degrees elevation with the lidar receiver on top (the normal position), then the telescope was flipped over and rotated in azimuth so that the lidar was underneath but pointed in the same direction in the sky, and another data set was recorded immediately. Any difference in the two data sets must be due to flexure in the receiver caused by changing the direction of gravitational forces by 90 degrees.

## RESULTS

The data from the flexure test were reduced by noting the range at which the lidar signal began to rise above its background level. This marks the range at which the laser beam just begins to enter the receiver field of view. For the long range receiver, the ranges were 396 meters for the lidar on top and 905 meters for the lidar on the bottom. The difference is caused by a tilt in the receiver optic axis relative to the laser beam under the changed gravitational forces. The amount of this tilt was estimated by a straightforward geometrical analysis which took into account the laser beam geometry and the separation between the transmitter and the receiver. This analysis has a limitation in that it is based on an assumption that the receiver and transmitter optic axes are initially coplanar and that they stay coplanar as the deflection occurs. This is not necessarily true, but the analysis can at least provide an approximate interpretation of the measured change in the lidar data. The total deflection of the receiver optic axis determined in this way was 340 microradians, which is presumably twice the deflection which would be experienced when operating in the normal range of zenith angles, so the deflection caused by mechanical flexure was taken to be 170 microradians. This is larger than the design goal of 100 microradians, but it is not large enough to cause major difficulties.

For the short range receiver, the ranges to the beginning of crossover were 34 and 56 meters. The total deflection in this case was calculated to be 3.4 milliradians. This value is too large to be caused by flexing of metal parts (we had not expected any measurable deflection) so

it must have another cause. The most likely cause is a shifting of the objective lens in its barrel. The lens is a loose fit in the barrel, and it is secured by a metal ring which was placed in the barrel after the lens and then cemented in place. This arrangement apparently does not prevent the lens from shifting in the barrel as the lidar orientation is changed. In any event, this deflection has little impact on operation of the lidar, because the short range receiver has such a large field of view.

## CONCLUSIONS

The project described here was successful. SOR now has an operational lidar system which is easy to use and very adaptable. The receiver has two channels with different entrance apertures, and the two channels can be independently configured with different field stops and optical filters to provide a wide range of sensitivities, crossover distances, and operating wavelengths. All of the problems in the prototype have been eliminated.

The system is in routine use for detecting subvisual cirrus clouds during imaging measurements using the CVL guide star, and it has also been configured for both ruby laser and doubled-Nd:YAG laser wavelengths.

## ACKNOWLEDGEMENTS

The author would like to acknowledge David W. Roberts of GTRI, who was the chief optical designer for both the prototype lidar and the final version. Dave also prepared all of the drawings for parts which were fabricated in the Georgia Tech shop, and he assembled and tested the new receiver and assisted with installation at SOR.

The author would also like to thank Dr. Robert Q. Fugate, Major Phil Leatherman, and the entire SOR staff for helping to make the project successful and enjoyable.

## REFERENCE

G. G. Gimmestad, "Development of a Prototype Lidar System at the Starfire Optical Range," Summer Research Initiation Program Final Report (1992), pp. 15-1 - 15-17.

**INTERIM REPORT ON PROGRESS:**  
**DYNAMICS OF GAS-PHASE ION-MOLECULE REACTIONS**

Susan T. Graul  
Assistant Professor of Chemistry  
Carnegie Mellon University

The proposal that was originally submitted to the Summer Research Extension Program in November 1992 is briefly outlined below for reference. We have encountered unexpected delays in obtaining adequate laboratory space, and this has hampered the initiation of the proposed research, although we have made progress on the theoretical studies. In this interim report, I will describe briefly the nature of the delays, and the progress that we were able to make on our research program. I am requesting a three-month extension to the grant period, and will describe below what I intend to accomplish during that three-month period.

The original proposal submitted in November, 1992 described the use of a guided-ion beam apparatus for the study of bimolecular gas-phase ion-molecule reactions. As stated in that proposal, our research program, once established, will involve the measurement of reaction kinetics and analysis of angular distributions and kinetic energy distributions of ionic products of reactions. This information will be used to learn about mechanisms and potential energy surfaces for reactions. The systems we are targeting for initial studies include the bimolecular reactions of the atomic oxygen negative and positive ions with various organic and inorganic species. We plan to compare the experimental results to predictions of theoretical models for ion-molecule reactions.

The laboratory space that my research group will eventually occupy is currently being renovated. This space amounts to a total of nearly 1400 square feet, but on my arrival at Carnegie Mellon University, was under-equipped with power, air handling, and cooling water, and was moreover sub-divided into four smaller areas. The renovations involved removing several walls, clearing out old cabinetry, and completely rewiring and replumbing the utilities. Partly as a consequence of competing renovation projects elsewhere on campus, the renovation of my lab



space was delayed by almost a year from the originally anticipated completion date of spring 1993, and is now slated to be finished in January 1994.

One focus of my SREP proposal was the construction of a guided-ion beam apparatus and the establishment of a new program for the study of ion chemistry and dynamics in the gas phase in the Department of Chemistry at Carnegie Mellon University. During the grant period (1/93-12/93), this apparatus was being designed and is still under construction. We have acquired several necessary components for the apparatus, including the quadrupole mass filter and controller, the Wien filter, an IBM 486-based personal computer, and miscellaneous tools and laboratory equipment. The quadrupole filter and Wien filter are in storage and will be moved into our new lab in January. In addition, during the past year, I modified my apparatus designs from the original 10-inch double octopole system to a meter-long double octopole ion guide, which I believe will enhance our capabilities for time-of-flight analysis and photodissociation studies. The machining for the guided-ion beam apparatus is done in-house, at the Mellon College of Science machine shop.

In the requested three-month extension, it is unlikely that we will be able to put together a working apparatus, although I expect to make significant progress toward that goal. Machining of the newly redesigned double octopole ion guide should be complete some time in the spring. In the meantime, we will be interfacing the ion source and quadrupole system with the IBM personal computer, and will be writing and modifying data acquisition software. I am further exploring the option of purchasing an electrospray ionization source, which should greatly enhance our capabilities for generating novel cluster ions.

During the grant period, we continued our collaborative work with Dr. Rainer Dressler of the Phillips Laboratory at Hanscom AFB. This work began in June 1992 under the Summer Faculty Research Program, and involved the study of the dynamics of the reactions of  $\text{Ar}^+$ ,  $\text{N}_2^+$ , and  $\text{Kr}^+$  with NO in the guided-ion beam apparatus at Phillips Laboratory. We collected experimental data on the reaction cross sections, product distributions, and product time-of-flight (TOF) distributions. Since returning to Carnegie Mellon, we have continued the analysis of the

experimental data, and have determined the velocity distributions and coarse angular distribution information for the  $\text{NO}^+$  product of the charge-transfer reactions. The time-of-flight distributions are characteristic of near-resonant charge-transfer processes. At all collision energies studied, the charge-transfer reactions are dominated by a direct mechanism, but below 1 eV, the formation of a long-lived intermediate complex is also significant.

In order to examine the extent of energy randomization within this intermediate complex, I have carried out theoretical calculations of the internal energy distributions that would be predicted for a process characterized by completely statistical energy partitioning. The calculated distribution for the reaction of  $\text{Ar}^+$  with NO at 0.79 eV is shown in Fig. 1, and the calculated distribution for the reaction of  $\text{N}_2^+$  with NO at 1.09 eV is shown in Fig. 2, along with the respective experimental results.

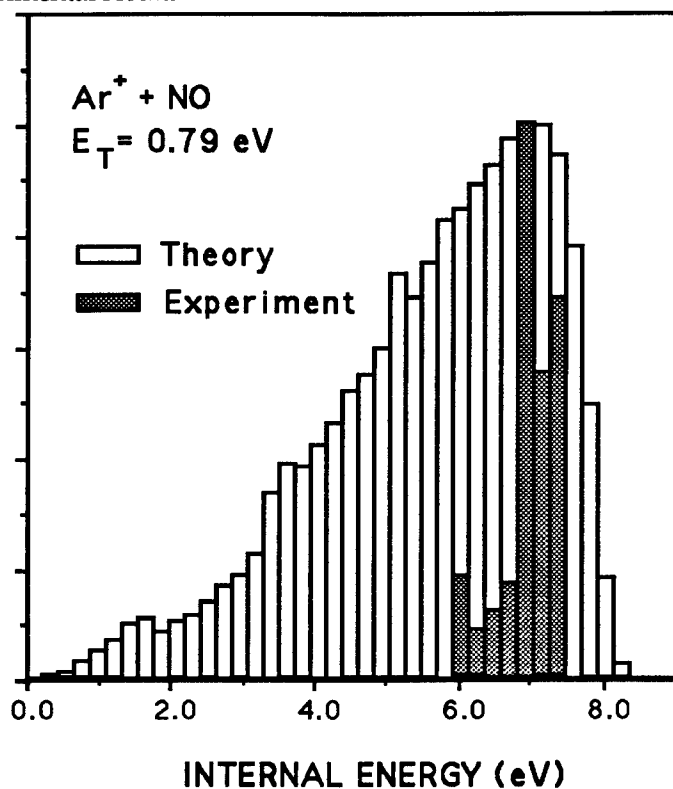


Fig. 1. Calculated (unshaded) and experimental (shaded)  $\text{Ar}^+ + \text{NO}$  charge-transfer product internal energy distributions. The internal energy scale assumes ground-state reactants.

The experimental distributions are characterized by a high probability for the internal energy that corresponds to a resonant charge transfer (6.50 eV for the  $\text{Ar}^+$  reactant and 6.32 eV for the  $\text{N}_2^+$

reactant). There is also a somewhat lower probability for redistribution of energy, which typically leads to products with internal energies in excess of the resonant charge-transfer case. This redistribution of energy most likely occurs within a long-lived collision complex. In the  $\text{N}_2^+ + \text{NO}$  reaction, the complex process results in a fairly smooth distribution peaking at an energy about equal to the collision energy plus the IP difference of 6.32 eV. Although the calculated statistical distributions peak near the same internal energies, they are considerably broader, and tail to much lower energies than the experimental result. In the  $\text{Ar}^+ + \text{NO}$  reaction, the experimental distribution shows some structure, which may indicate that Franck-Condon factors are important even within the complex. The calculated statistical distributions again are considerably broader.

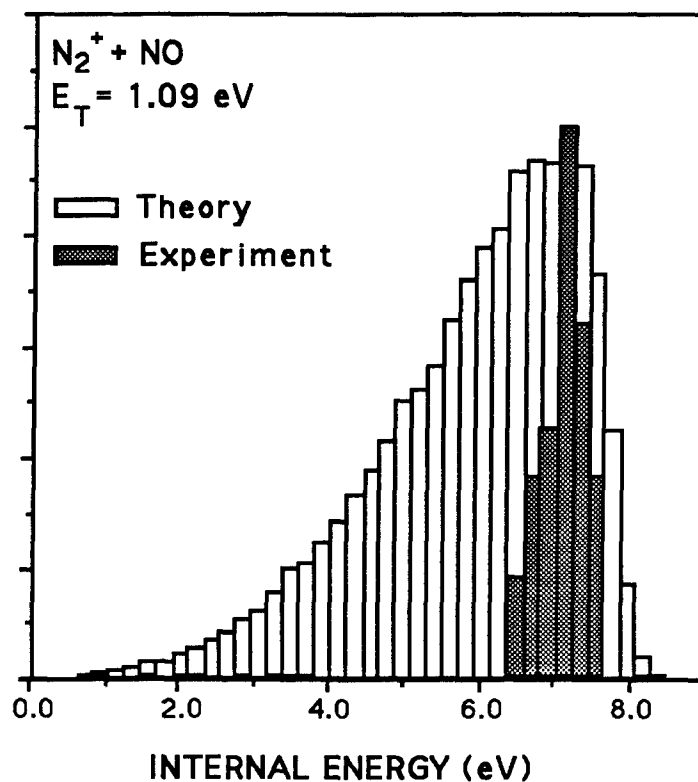


Fig. 2. Calculated (unshaded) and experimental (shaded)  $\text{N}_2^+ + \text{NO}$  charge-transfer product internal energy distributions. The internal energy scale assumes ground-state reactants.

These calculated distributions reflect the density of states available to the system at a given total energy. When carried out with relatively high energy precision of 25 or 50  $\text{cm}^{-1}$ , the calculated distributions do show some structure within the same broad envelop shown in Figs. 1

and 2. For lower energy resolution of about  $500\text{ cm}^{-1}$ , the structure is no longer visible. The experimental energy resolution is limited to perhaps  $500\text{-}1000\text{ cm}^{-1}$ , depending on the collision energy, and therefore the "low-resolution" calculations more accurately represent the experimental reality.

In addition to continuing the  $\text{Ar}^+$ ,  $\text{N}_2^+$ , and  $\text{Kr}^+ + \text{NO}$  charge transfer project, my student Richard Edgington and I returned to Dr. Dressler's laboratory at Hanscom AFB during July and August 1993, to study the reactions of  $\text{O}^+$  with  $\text{C}_2\text{H}_4$  and  $\text{C}_2\text{D}_4$ . This work was partially funded by a government contract to PhotoMetrics, Inc., under which I was sub-contracted. Edgington's participation was funded in part by Carnegie Mellon University, who covered his travel expenses, and in part by this SREP grant. He is currently analyzing the experimental data, and we will be carrying out modeling studies in the next few months as well.

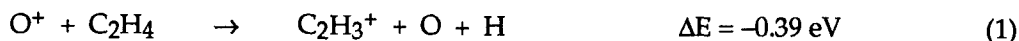
These reactions were examined in the collision energy range from near-thermal to slightly over ten eV. We observed primary product ions  $\text{C}_2\text{H}_n^+$  at mass-to-charge ratios ( $m/z$ ) of 26-28, and some higher mass ions, which probably correspond to products of secondary reactions of the initially formed  $\text{C}_2\text{H}_n^+$  ions with  $\text{C}_2\text{H}_4$ . These secondary reactions most likely involve primary product ions that are formed with very small translational energies, such that they remain in the reaction region long enough to encounter a second neutral reaction molecule. Generally, secondary product ions constituted less than 10-15% of the total product ion intensity.

Product ion velocity distributions were analyzed by means of time-of-flight measurements, and were converted to axial velocity distributions. Distributions were measured for conditions of high rf trapping voltage on the octopoles, in which case all product ions are collected, and for low rf voltages, in which case product ions with large transverse components of velocity are lost. The difference between these distributions gives an indication of the anisotropy of the angular distribution of the product ions.

The reaction of  $\text{O}^+$  with  $\text{C}_2\text{H}_4$  forms three primary ionic products throughout the collision energy range studied. These products are  $\text{C}_2\text{H}_2^+$ ,  $\text{C}_2\text{H}_3^+$ , and  $\text{C}_2\text{H}_4^+$ , in order of abundance. Formation of  $\text{C}_2\text{H}_4^+$  clearly occurs by charge transfer, and is 3.11 eV exothermic.

The other two ions may be formed by either dissociative charge transfer or by hydride transfers.

The relevant thermochemistry is given in eqs. 1-5.



Each of these reactions except eq 3 is exothermic for ground-state  $\text{O}^+$  ions. Because the energetics for the different mechanisms that form  $\text{C}_2\text{H}_3^+$  or  $\text{C}_2\text{H}_2^+$  differ strongly, we hope to be able to determine which mechanisms are active in the collision energy range studied.

Shown in Figure 3 are the cross sections for reaction of  $\text{O}^+$  with  $\text{C}_2\text{H}_4$  as a function of collision energy. The total cross section is about  $120 \text{ \AA}^2$  at  $0.2 \text{ eV}$  collision energy, and decreases with approximately an  $E^{-1/4}$  energy dependence until about  $1 \text{ eV}$ , where it levels off at  $80 \text{ \AA}^2$ . The cross sections for the three primary product ions ( $\text{C}_2\text{H}_2^+$ ,  $\text{C}_2\text{H}_3^+$ , and  $\text{C}_2\text{H}_4^+$ ) and one of the secondary product ions ( $\text{C}_2\text{H}_5^+$ ) are also shown in Fig. 3.

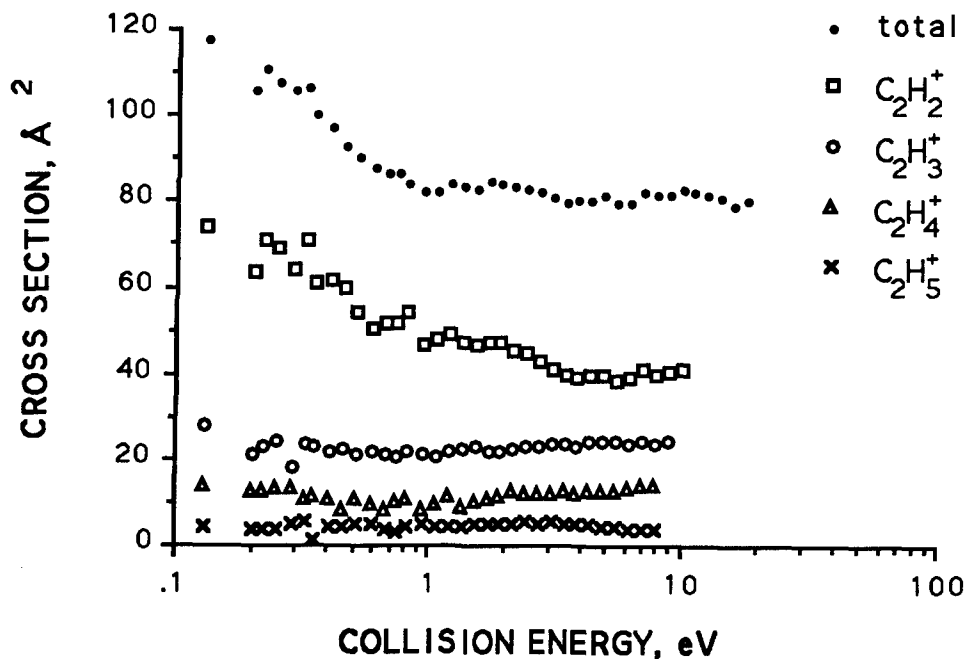


Figure 3. Collision energy dependence of the cross sections for reaction of  $\text{O}^+$  with  $\text{C}_2\text{H}_4$ .

Of the product ion cross sections, only that for  $C_2H_2^+$  shows a significant energy dependence. As shown in eqs. 3-5, this ion may be formed by three different mechanisms with very different energetics. No increase in cross section for formation of  $C_2H_2^+$  is observed above 4 eV, the energetic threshold for the endothermic dissociative charge transfer (eq 3). This implies that this mechanism is not an important one, and that neutral  $H_2O$  is not formed in this reaction. The high cross section at low collision energies and negative energy dependence for the cross section for formation of  $C_2H_2^+$  implies that the major reaction pathway is an exothermic one, i.e., eq 4 or 5. The cross section data alone is not sufficient to distinguish between these two mechanisms.

The total cross section for the reaction of  $O^+$  with  $C_2D_4$  is slightly higher, but displays similar energy dependence. The data for this reaction are shown in Figure 4.

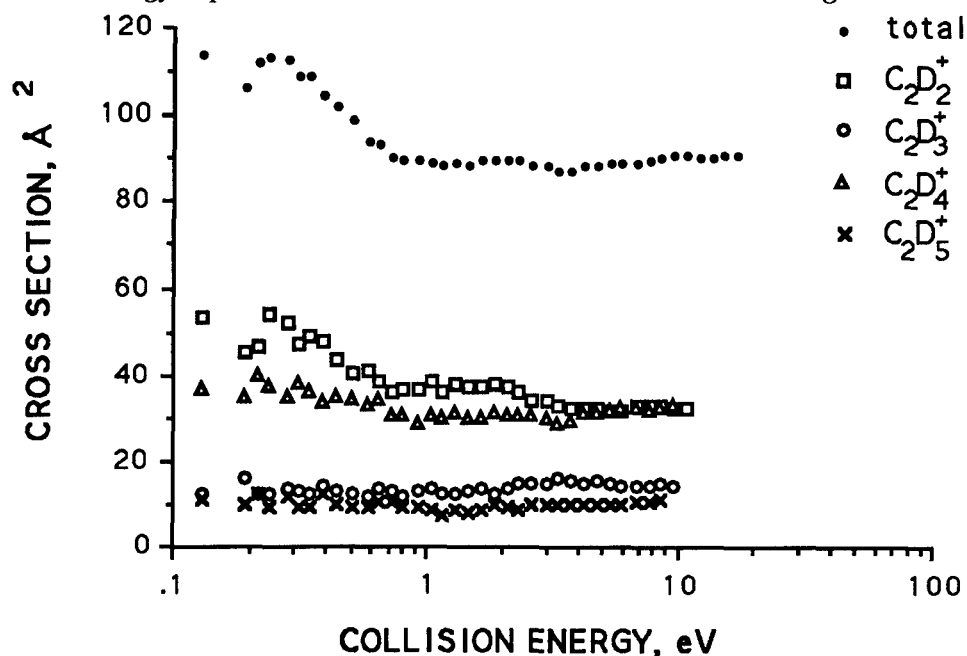


Figure 4. Collision energy dependence of the cross sections for reaction of  $O^+$  with  $C_2D_4$ .

Although the total cross section shows a similar energy dependence as was seen for the reaction of  $O^+$  with  $C_2H_4$ , the branching ratios are noticeably different. The  $C_2D_4^+$  product is more abundant than  $C_2D_3^+$  at all energies, and is almost as prominent as  $C_2D_2^+$ . This is in marked contrast to the results for  $C_2H_4$ , and almost certainly results from the primary kinetic isotope effect that favors cleavage of C-H bonds over C-D bonds. The less exothermic reactions shown

in eqs 1 and 4 would be expected to show stronger kinetic isotope effects than the strongly exothermic reactions shown in eqs 2 and 5. Whether the observed isotope effects are consistent with the weakly or strongly exothermic reactions requires a detailed kinetic analysis, and this question will be explored further in our ongoing analysis of these data.

It is interesting to note that in both the deuterated and undeuterated reactions, the  $C_2L_2^+$  ( $L=H, D$ ) ion is the only product to show a significant collision energy dependence. This energy dependence may indicate the intermediacy of an ion-molecule complex, formation of which is disfavored at higher collision energies. This observation is consistent with the fact that both of the exothermic pathways leading to formation of  $C_2H_2^+$  involve hydride or hydrogen transfer reactions. Such reactions may be expected to involve complex formation. In contrast,  $C_2H_3^+$ , which does not show a strong collision energy dependence, can be formed by dissociative charge transfer, which need not involve complex formation, and may occur at long range. The cross sections for this product and for  $C_2H_4^+$  are essentially constant, and do not appear to depend on collision energy.

Time-of-flight distributions were collected for each of the three primary products for several different collision energies and under conditions of high and low rf trapping voltage on the octopole. These distributions were converted to axial velocity distributions. An example of such a distribution is shown in Figure 5 for the formation of  $C_2H_4^+$  at 2.2 eV collision energy. The velocity distributions peak near zero and drop off rapidly, which indicates that the products are formed with relatively little translational energy, as in a long-range charge transfer. The similarity between the two distributions further indicates that the products are not formed with large transverse velocities. Moreover, the shape of the distribution suggests that the  $C_2H_4^+$  products are not formed in long-lived collision complexes, which should result in forward-scattered products with large axial velocities. This does not, however, rule out the intermediacy of long-lived collision complexes in the  $O^+ + C_2H_4$  reaction; such complexes may be implicated in the formation of  $C_2H_3^+$  and  $C_2H_2^+$ . Analysis of the velocity distributions for the  $C_2H_3^+$  and

$\text{C}_2\text{H}_2^+$  products is ongoing, and should help to answer the question of how these products are formed.

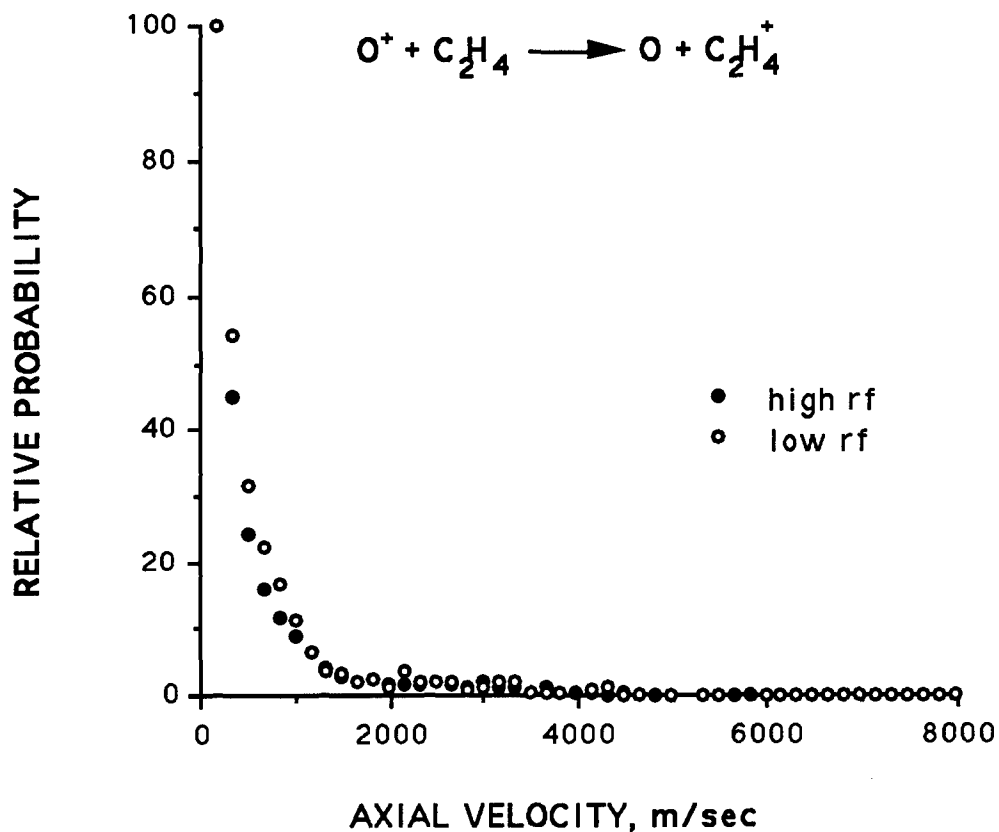


Figure 5. Axial velocity distributions for the  $\text{C}_2\text{H}_4^+$  product from the reaction of  $\text{O}^+$  with  $\text{C}_2\text{H}_4$  at 2.2 eV collision energy. The open circles correspond to the measurement at low rf trapping voltage, where products with large components of transverse velocity will not be collected. The closed circles are the measurements with high rf voltage, and complete product ion collection.



# **A Numerical Approach to Evaluating Phase Change Material Performance in Infrared Sensor Satellite Thermal Control**

**Steven E. Griffin  
Graduate Student  
Division of Engineering**

**University of Texas at San Antonio  
6900 N Loop 1604 W  
San Antonio, TX 78249-0665**

**Final Report for:  
1992 Summer Research Extension Program  
Air Force Phillips Laboratory**

**Sponsored by:  
Air Force Office of Scientific Research  
Bolling Air Force Base, Washington, D.C.**

**and**

**University of Texas at San Antonio**

**December 1993**

# A Numerical Approach to Evaluating Phase Change Material Performance in Infrared Sensor Satellite Thermal Control

Steven E. Griffin  
Division of Engineering  
University of Texas at San Antonio

## ABSTRACT

Latent thermal energy storage canisters containing phase change materials typically represent an exceptional technology for satellite thermal management because the phase change canisters are typically lightweight, provide long term energy storage, and exhibit relatively small temperature excursions near mounting surfaces. Thermal storage canisters are especially suited to space power thermal management systems where design is based not on the maximum heat/power load but on the average load. As a result, a set of satellite sensors can be thermally controlled via the phase change material's fusion temperature.

This paper looks into the thermal energy storage requirements of several canisters designed to enhance phase change energy storage rates and effectiveness for the removal of waste heat from satellite surveillance equipment and solar heating. The enhanced phase change canisters improve thermal transfer by increasing the unit's thermal conductivity while maintaining high energy storage densities. Specifically, by mounting rectangular fins to the base plate and parallel to the direction of heat transfer, the system experiences higher heat transfer rates and more effective heat penetration into the phase change material without sacrificing the canister's latent thermal storage.

The phase change model employs a modified enthalpy approach which can evaluate multiple phase fronts within the canister domain. Although intrinsically non-linear, phase front propagation can be modelled by coupling the heat conduction equation and a suitable piece-wise linear enthalpy equation to develop a set of algebraic equations resolved iteratively using the Gauss-Siedel method. Results from both a one-dimensional similarity solution and experimentally accepted data were compared with the numerical procedure to evaluate the accuracy of the numerical model.

## NOMENCLATURE

A	normalized control surface in the x, y, or z plane
B	discrete conductance coefficients
$c_p$	specific heat
D	maximum canister length: L, H, or W
f	functional time varying boundary condition
Fo	Fourier modulus $\equiv \alpha t / D^2$
h	enthalpy
H	domain height
i	discrete control volume centered around the $i^{\text{th}}$ element
j	discrete control volume centered around the $j^{\text{th}}$ element
k	thermal conductivity or discrete control volume centered around the $k^{\text{th}}$ element
L	domain length
n	normal component to the phase change interface
q	heat flux
Q	heat transfer
Ste	Stefan number $\equiv c_p \Delta T_{\text{ref}} / \lambda$
t	time
T	temperature
u	internal energy
v	interface propagation velocity
W	domain width
x	cartesian coordinate
y	cartesian coordinate
z	cartesian coordinate

## GREEK

$\alpha$	thermal diffusivity
$\gamma$	normalized maximum height factor
$\Delta$	system volume dimension difference
$\delta$	control volume dimension difference
$\varepsilon$	interface temperature range, $(T_f - \varepsilon) \leq T_f \leq (T_f + \varepsilon)$
$\eta$	canister thermal effectiveness
$\lambda$	latent heat of fusion
$\rho$	density
$\tau$	implicit time step factor
$\xi$	normalized maximum length factor
$\zeta$	normalized maximum width factor

## Subscripts

b	back finite difference coefficient
c	sub-subscript of enthalpy states {solid, phase transition, liquid, canister}
e	east finite difference coefficient
f	fusion temperature or front finite difference coefficient
i	interface or discrete x-location
j	discrete y-location
k	discrete j-location
liq	liquid
m	melt
n	north finite difference coefficient
ref	reference

s	solid or south finite difference coefficient
w	west finite difference coefficient
x	surface area reference, $\{\Delta y^* \Delta z^*\}$
y	surface area reference, $\{\Delta x^* \Delta z^*\}$
z	surface area reference, $\{\Delta x^* \Delta y^*\}$

### Superscripts

*	normalized
n	current time-level
n+1	next time-level

## TABLE OF CONTENTS

<u>SECTION</u>	<u>PAGE</u>
ABSTRACT	2
NOMENCLATURE	3
LIST OF TABLES	7
LIST OF FIGURES	7
CHAPTER 1 INTRODUCTION	8
1.1 Background Information	8
1.2 Purpose	11
CHAPTER 2 MATHEMATICAL STATEMENT	12
2.1 Heat Conduction Development	12
2.2 Finite Difference Formulation	15
2.3 Boundary Conditions	23
CHAPTER 3 NUMERICAL RESULTS	27
CHAPTER 4 DISCUSSION	30
CHAPTER 5 CONCLUSIONS	35
APPENDIX	37
PCM Analysis Computer Program [3½" Diskette] Located In Back Cover Insert:	
PCM_Anal.EXE	{Executable}
*.TPU	{Units}
BIBLIOGRAPHY	38

## LIST OF TABLES

<u>TABLE</u>	<u>PAGE</u>
3.1 Material properties of a water and brass canister combination	29
4.1 Thermal Storage Unit - Trade Study of Two-Dimensional Canister	31

## LIST OF FIGURES

<u>FIGURE</u>	<u>PAGE</u>
1.1 Typical Thermal Control System	8
2.1 Thermal Control Volume: Energy Balance	12
2.2 Collection of discrete control volumes	15
2.3 Piece-wise linear enthalpy model	19
2.4 Evaluation of exterior boundary nodes for corners, edges, and surfaces given both Neumann and/or Dirichlet prescribed boundary conditions	24
3.1 Similarity Solution vs. Numerical Model	28
4.1 Comparison of a) Percent Melt and b) Canister Effectiveness	32
4.2 Canister Effectiveness, $\eta(Fo = 0.1)$ , vs Number of Fins	33

# Chapter 1. Introduction

## 1.1 Background Information

Thermal management of spacecraft systems requires extensive design to predict satellite thermal-response characteristics to typical heating profiles during Air Force, Ballistic Missile Defense Organization, and other classified missions. Spacecraft equipment having power levels up to several kilo-watts (kW) can be controlled by thermal conduction to structural elements, radiating surfaces, or waste heat removal systems. Although many effective methods exist for removing waste heat, this paper focuses on the application of phase change thermal energy storage to provide satellite thermal control during critical orbit heat loads and corresponding temperatures which might effect sensitive electronic equipment such as infrared sensors.

In Figure 1, satellite radiators are mounted on opposite sides and are normal to the orbital plane and flight direction. Consequently, the radiators alternate in shadow and sun throughout the orbit. The colder, shadowed radiator radiates dissipated electrical sensor energy and parasitic heat leakage from the thermal control system. During the alternating crossover period, neither the shadow nor the sun radiator is cold enough to reject heat. For this period, sensor heat along with parasitic heat leakage is absorbed by a phase change material (PCM) housed within a thermal energy storage (TES) canister where the heat melts the subcooled material. When the shadowed radiator cools to its operating temperature, it radiates again and the PCM refreezes [1].

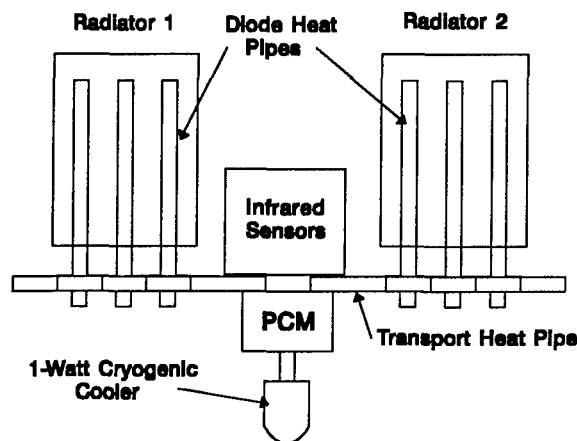


**Figure 1. Typical Thermal Control System**



Diode heat pipes transport heat from sensors and the PCM to the emitting radiator and block any reversing heat flows which occur when the sun or insulated radiator is at a higher temperature than the sensors and PCM. Consequently, a set of sensors are thermally controlled via the phase change material's fusion temperature which makes consistent melt/freeze cycles, behavior, and predictability paramount in this type of TES application.

The benefits from phase change thermal energy storage include reduction of satellite weight for pulsed heating with short pulse durations and solar heating with short orbit periods. Thermal energy storage canisters require little or no energy and are typically bolt-on or weld-in-place devices. The applications considered here assume that heat is transferred by conduction through the baseplate and cold-tip finger of the cryogenic or other refrigeration cooler and by radiation through the side walls using flux-prescribed heat parasitics. As a result, the TES unit depends on satellite equipment heat load profiles, heat rejection temperature, and environmental heating [2,3].

Unfortunately, thermal energy storage systems including phase change are extremely difficult to analyze because of the highly non-linear characteristics of the phase front, thermal properties of the materials, and canister shape. Even though several analytical methods have been applied to the resolution of moving boundaries (i.e. Stefan problems), the solution complexity becomes intrinsically more difficult as the number of dimensions and phase fronts increase within the system. This becomes apparent in the simultaneous solution of the three-dimensional, transient conduction equation, eqn. (1.1), and the interface compatibility constraint, eqn. (1.2), in the direction normal to the interface propagation.

$$\frac{\partial^2 T}{\partial x^2} + \frac{\partial^2 T}{\partial y^2} + \frac{\partial^2 T}{\partial z^2} = \frac{1}{\alpha} \frac{\partial T}{\partial t} \quad (1.1)$$

$$\frac{\partial T}{\partial n} \Big|_s = \frac{\partial T}{\partial n} \Big|_l + \rho \lambda v_n \quad (1.2)$$

The conduction equation assumes uniform properties within the control volume and is valid for both the solid, liquid, and canister regions. The interface compatibility constraint is highly non-linear in both the energy fluxes and the propagation velocity. Both equations coupled

together cannot be resolved with an exact solution for applications involving several phase fronts, multiple dimensions, and conduction enhancement fins. As a result, an enthalpy approach utilizing both sensible and latent heat terms will simulate the interface constraint.

The solution will take the form of a numerical Enthalpy Method developed by Shamsundar and Sparrow [4,5] in 1975 to predict the temperature time history of the phase change TES canister. Using a modified enthalpy approach first proposed by Schneider and Raw [6,7] in 1983, a single fully-implicit equation will be derived with assumptions made to account for the solid, phase transition, liquid, and canister regions of the entire system.

The idea behind the modified enthalpy method is to develop the heat diffusion equation and the interface compatibility constraint into a single equation that can generate a system of algebraic equations to be evaluated iteratively. The basic equation originates in finite difference form from the heat conduction equation, eqn. (1.1), and a piece-wise linear approximation relating enthalpy to temperature. Using the Stefan number to characterize the heat transfer during phase transition, this solution can track the interface location to within one mesh spacing.

Major assumptions of the numerical model include:

1. uniform specific properties for both solid and liquid phases and average conductive fluxes across the control volume,
2. the neglect of buoyancy induced natural convection for near zero-gravity satellite applications,
3. the neglect of conservation of mass velocity components that develop in the liquid portion of the PCM as a result of thermal expansion or contraction as well as changes from phase transition.

Assumption (1) holds throughout this paper. Assumption (2) holds for experiments performed in a gravity environment because the addition of a small metal wire-matrix or fins provides support for the solid during melting and freezing. Furthermore, density gradients (3) are neglected because the application of rectangular fins reduces the tendency of the canister to transport heat via natural convection induced flow.

Minor assumptions consider that the heat penetration, as in regular conduction, relies heavily on the size or depth in which heat must be transferred into or out of a region. As a result, the expectations of the program PCM\_Anal.EXE to analyze large TES units in any

direction is unrealistic because natural convection resulting from density gradients can no longer be neglected. The exact point where the two modes of heat transfer become indistinguishable is not known. Also, the idea of zero-subcooling and no thermal degradation is included.

Using the program, two general canister configurations are considered: the open cavity container and a conduction enhancement unit containing rectangular fins. The results of several numerical variations of fin to PCM volume are considered for comparative and demonstrative purposes. The fins are mounted vertically in the y-direction to a height not greater than the maximum Height of the canister and extend into the z-direction to a depth not greater than the maximum Depth.

## 1.2 Purpose

The following application of the enthalpy method provides a tool for the evaluation of thermal energy storage (TES) canisters using phase change materials (PCM). The employed enthalpy method is fully implicit and provides a general approach to discretizing the solution domain. Currently, the enthalpy method appears to provide the most applicable approach to evaluating multi-dimensional systems containing several phase change interfaces.

The phase change evaluations require a program that is capable of evaluating thermal energy storage rates ( $U = U(Fo)$ ) as a function of canister type (with or without fins), thermal energy stored, and percent melt for typical heating profiles. Various profiles affect the boundary conditions and include constant temperatures and/or thermal heat fluxes (also adiabatic), pulse power duty cycles (surveillance spacecraft dissipation - decaying function  $T_b = A \cdot Fo^B$ ), solar heating (absolute sinusoidal profiles  $T_b = \text{abs}(A \cdot \sin(B \cdot Fo))$ ), and other surface temperature excitations where the boundary temperature's functional dependence is on the Fourier modulus ( $T_b = f\{Fo\}$ ) and the constants A and B are user defined.

The software is a design tool for evaluating typical TES canisters in satellite applications. Analysis on multi-dimensional phase change TES units, which include rectangular fins for thermal conductivity enhancement, will demonstrate the flexibility of the enthalpy method to the design and analysis of future systems.

## Chapter 2. Mathematical Statement

### 2.1 Heat Conduction Development

A thermal control volume is provided in Figure 2.1 to demonstrate a fundamental basis for the three dimensional energy equation and its application to finite difference methods. The small control volume (CV) is assumed to have constant dimensions (i.e. volume), uniform heat fluxes across the faces, and appropriately averaged material properties at the center. For the three dimensional case, the conservation of energy states that the energy stored in a CV must equal the energy difference of the amount entering and leaving the system.

For a closed system with a rectangular control volume enclosing  $(x,y,z)$  and occurring over time, an energy balance governed by eqn. (2.1) results.

$$\sum \dot{Q}_{in} - \sum \dot{Q}_{out} = \frac{\partial E}{\partial t} = \frac{\partial U}{\partial t} \quad (2.1)$$

Heat transfers into the control volume through the left, bottom, and front control surfaces and out through the right, top, and back control surfaces. Approximating the heat transfer by a Taylor series expansion, that ignores second and higher order terms as shown in Figure 2.1, results in

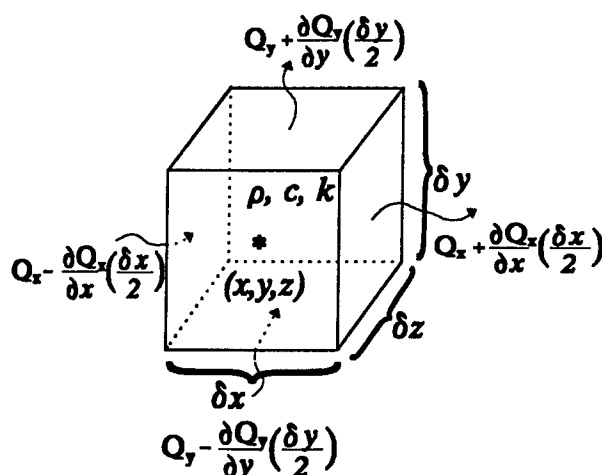


**Figure 2.1.** Thermal Control Volume: Energy Balance

the heat diffusion equation in terms of  $Q_x$ ,  $Q_y$ ,  $Q_z$ , and  $\rho u$ . Furthermore, by applying Fourier's conduction law, a solution for temperature over the entire spatial and temporal domain of any uniform property system (i.e. solid, liquid, canister) develops.

$$\frac{\partial}{\partial x} \left( k \frac{\partial T}{\partial x} \right) + \frac{\partial}{\partial y} \left( k \frac{\partial T}{\partial y} \right) + \frac{\partial}{\partial z} \left( k \frac{\partial T}{\partial z} \right) = \frac{\partial (\rho u)}{\partial t} \quad (2.2)$$

When density is not neglected, continuity requires velocity components to develop in the liquid portion of the PCM as a result of thermal contraction and expansion as well as changes due to phase transition [8]. The heat diffusion equation takes the form of eqn. (2.3) where  $(D/Dt)$  represents the substantial or total derivative.

$$\frac{\partial}{\partial x} \left( k \frac{\partial T}{\partial x} \right) + \frac{\partial}{\partial y} \left( k \frac{\partial T}{\partial y} \right) + \frac{\partial}{\partial z} \left( k \frac{\partial T}{\partial z} \right) = \frac{D(\rho u)}{Dt} \quad (2.3)$$

In the case of moving boundary or Stefan related phase-change problems, an interface compatibility constraint must be applied to account for the heat diffusion between the solid and liquid phase along with the latent heat energy transfer of the solid/liquid interface. The compatibility constraint takes on the independent variable  $n$  to represent the normal component of the interface within the system.

$$k_s \frac{\partial T}{\partial n} \Big|_s = k_l \frac{\partial T}{\partial n} \Big|_l + \rho \lambda v_n \quad (2.4)$$

Since both the energy and interface equation must be solved simultaneously, only simplifications involving one dimension and one phase front can be solved using either similarity transforms or other methods. An exact solution is virtually impossible with cases involving multiple dimensions and phase fronts. As a result, the following paper works to develop a single finite difference equation to solve moving boundary problems undergoing a change of phase. The numerical procedure takes the form of a finite difference method modelled after Shamsundar and Sparrow's [3,4] "enthalpy method" and expanded from Schneider and Raw's [5,6] modified solution to the enthalpy method. The solution will be in the form of a fully implicit equation which will generate a system of linear equations which can be resolved iteratively using Gauss-Siedel or another appropriate method.

To begin, the governing equation, eqn. (2.2), applies to both the solid and liquid phases and will be normalized before it undergoes a finite difference transformation using the variables shown in eqn. (2.5):

$$\left\{ \begin{array}{l} x^* = \frac{x}{L}; \quad y^* = \frac{y}{H}; \quad z^* = \frac{z}{W}; \quad FO = \frac{\alpha_{liq} t}{D^2} \\ k^* = \frac{k}{k_{liq}}; \quad \rho^* = \frac{\rho}{\rho_{liq}}; \quad c_p^* = \frac{c_p}{c_{p_{liq}}}; \quad \alpha_{liq} = \frac{k_{liq}}{c_{p_{liq}} \rho_{liq}} \\ T^* = \frac{T - T_f}{\Delta T_{ref}}; \quad u^* = \frac{u - u_f}{c_{p_{liq}} \Delta T_{ref}} \end{array} \right. \quad (2.5)$$

Note that in the Fourier modulus, the denominator D takes on the maximum dimension's value whether it is L, H, or W. The reference temperature  $\Delta T_{ref}$  represents the largest boundary prescribed temperature difference of either the Dirichlet ( $T_b - T_f$ ) or Nuemann ( $q_b D/k$ ) conditions. Normalizing the partial derivative of each independent variable and substituting them into the heat conduction equation, eqn. (2.2), results in eqn. (2.6).

$$\left[ \frac{1}{L^2} \frac{\partial}{\partial x^*} \left( k^* \frac{\partial T^*}{\partial x^*} \right) + \frac{1}{H^2} \frac{\partial}{\partial y^*} \left( k^* \frac{\partial T^*}{\partial y^*} \right) + \frac{1}{W^2} \frac{\partial}{\partial z^*} \left( k^* \frac{\partial T^*}{\partial z^*} \right) \right] = \frac{\rho_{liq} \alpha_{liq}}{k_{liq} \Delta T_{ref} D^2} \frac{\partial (\rho^* u)}{\partial FO} \quad (2.6)$$

After defining three other non-dimensional parameters based on the canister dimensions, a general form of the normalized heat conduction equation based on the above assumption that D takes on the largest value of the three canister lengths develops. For the special case of a cubic canister, the coefficients of eqn (2.7) take on the value of one.

$$\left\{ \begin{array}{l} \xi = \frac{D}{L} \\ \gamma = \frac{D}{H} \\ \zeta = \frac{D}{W} \end{array} \right. \quad (2.7)$$

The final form of the normalized heat diffusion equation develops in eqn. (2.8).

$$\xi^2 \frac{\partial}{\partial x^*} \left( k^* \frac{\partial T^*}{\partial x^*} \right) + \gamma^2 \frac{\partial}{\partial y^*} \left( k^* \frac{\partial T^*}{\partial y^*} \right) + \zeta^2 \frac{\partial}{\partial z^*} \left( k^* \frac{\partial T^*}{\partial z^*} \right) = \frac{\partial (\rho^* u^*)}{\partial Fo} \quad (2.8)$$

The heat diffusion equation is valid for any transient solution involving conduction between single phases - solid, liquid, and canister. Later, the heat diffusion equation will be coupled with a piece-wise linear equation of state that accurately represents the phase change material's current state (solid, transition, and liquid) and canister.

## 2.2 Finite Difference Formulation

Since the normalized energy equation was derived from an energy balance of the control volume centered about (x,y,z), we can integrate over the element using finite difference limits of a typical volume to develop eqn. (2.9) from eqn. (2.8). Each diffusion integral is evaluated at either the present time interval (i.e. an explicit solution) or the next time interval (i.e. implicit). A general finite difference solution using either form will be given the superscript (n +  $\tau$ ) to represent the time interval at which the average heat transfer rate across each control surface

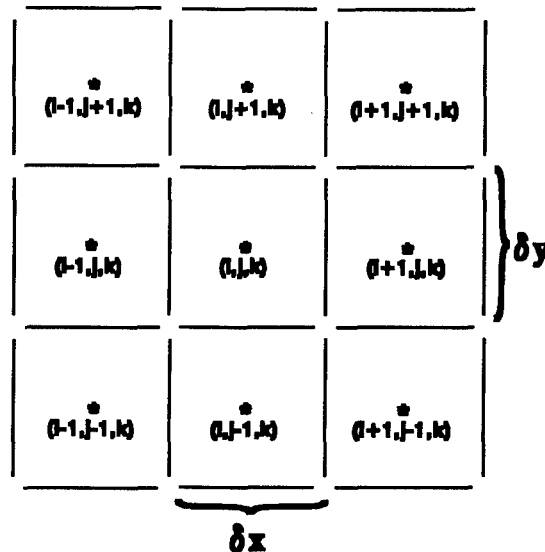


**Figure 2.2** Collection of discrete control volumes

should be evaluated. Using Figure 2.2, the limits of integration take on the value at the interface of each control surface and its location. Although the z-dimension is not shown in the figure, the same form of integration occurs over the control volume centered about a reference element (i, j, k).

The result from integration over the temporal domain uses the superscripts  $n$  and  $n+1$  to refer to the time intervals  $Fo$  and  $(Fo + \Delta Fo)$  in eqn. (2.9). The superscript  $(n + \tau)$  represents the time level required to provide an average conductive flux evaluation. By definition of a fully explicit solution ( $\tau = 0$ ) and a fully implicit procedure ( $\tau = 1$ ), the evaluation of the diffusion term may occur at  $(n \leq n+\tau \leq n+1)$ .

$$\begin{aligned}
 & \xi^2 \left[ \left( k^* \frac{\partial T^*}{\partial x^*} \right)_{i+\frac{1}{2}}^{n+\tau} - \left( k^* \frac{\partial T^*}{\partial x^*} \right)_{i-\frac{1}{2}}^{n+\tau} \right] \Delta y^* \Delta z^* \Delta Fo + \\
 & \gamma^2 \left[ \left( k^* \frac{\partial T^*}{\partial y^*} \right)_{j+\frac{1}{2}}^{n+\tau} - \left( k^* \frac{\partial T^*}{\partial y^*} \right)_{j-\frac{1}{2}}^{n+\tau} \right] \Delta x^* \Delta z^* \Delta Fo + \\
 & \zeta^2 \left[ \left( k^* \frac{\partial T^*}{\partial z^*} \right)_{k+\frac{1}{2}}^{n+\tau} - \left( k^* \frac{\partial T^*}{\partial z^*} \right)_{k-\frac{1}{2}}^{n+\tau} \right] \Delta x^* \Delta y^* \Delta Fo = \\
 & \Delta x^* \Delta y^* \Delta z^* \left[ (\rho^* u_{ijk}^*)^{n+1} - (\rho^* u_{ijk}^*)^n \right]
 \end{aligned} \tag{2.9}$$

The normalized control surfaces  $A_x^*$ ,  $A_y^*$ ,  $A_z^*$  are defined by the y-z, x-z, and x-y interfaces, respectively, along with a normalized control volume based on the element's normalized change in dimensions;  $\Delta V^* = \Delta x^* \Delta y^* \Delta z^*$ . The diffusion terms of eqn. (2.9) represent the time interval of an average heat flux crossing the corresponding control surfaces. To evaluate the diffusion terms, Fourier's conduction law is expressed in normalized finite difference form at the appropriate time interval and interface as in eqn. (2.10).

$$Q_{i+\frac{1}{2},jk}^{*n+\tau} = -k^* \Delta y^* \Delta z^* \left[ \frac{\partial T^*}{\partial x^*} \right]_{i+\frac{1}{2},jk}^{n+\tau} \tag{2.10}$$

Furthermore,  $Q^*$  represents a locally one-dimensional heat transfer rate evaluated and expressed in the normalized finite difference form for the east and other corresponding control surfaces:



$$Q_{i+\frac{1}{2}jk}^{*n+1} = - \left[ \frac{2k_i^* k_{i+1}^*}{\Delta x_i^* k_{i+1}^* + \Delta x_{i+1}^* k_i^*} \right] \Delta y^* \Delta z^* [T_{i+1jk}^{*n+1} - T_{ijk}^{*n+1}] \quad (2.11)$$

Since each element is evaluated based on the average heat transfer rate occurring at the CV interface, the conduction term represents an average conduction value between neighboring CVs in the corresponding direction. That is, the conduction term of  $k_i^*$  may represent the solid phase while  $k_{i+1}^*$  is allowed to take on a solid, phase transition, liquid, or canister phase conduction value. As a result, the location of the phase change (solid/liquid) interface can only be determined with an accuracy of one mesh spacing in any direction.

Substituting the locally one-dimensional heat transfer eqn. (2.10) into eqn. (2.9) results in an energy balance with heat leaving through the north, east, and back control surfaces, heat entering through the south, west, and front faces, and energy storage in the CV as in eqn. (2.12).

$$\begin{aligned} & \xi^2 \left[ -Q_{i+\frac{1}{2}jk}^{*n+1} + Q_{i-\frac{1}{2}jk}^{*n+1} \right] \Delta F_o + \\ & \gamma^2 \left[ -Q_{j+\frac{1}{2}jk}^{*n+1} + Q_{j-\frac{1}{2}jk}^{*n+1} \right] \Delta F_o + \\ & \zeta^2 \left[ -Q_{k+\frac{1}{2}jk}^{*n+1} + Q_{k-\frac{1}{2}jk}^{*n+1} \right] \Delta F_o = \Delta V^* [(\rho^* u_{ijk}^*)^{n+1} - (\rho^* u_{ijk}^*)^n] \end{aligned} \quad (2.12)$$

If we let  $B_e^*$ ,  $B_w^*$ ,  $B_n^*$ ,  $B_s^*$ ,  $B_f^*$ , and  $B_b^*$  represent the conduction terms on the east, west, north, south, front, and back control surfaces respectively, as in eqn. (2.13), then we can substitute both eqn. (2.10), along with the appropriate control surface counterparts, and eqn. (2.13) into the finite difference heat equation, eqn. (2.12), to yield eqn. (2.14).

$$\begin{cases} B_e^* = \left[ \frac{2k_i^* k_{i+1}^*}{\Delta x_i^* k_{i+1}^* + \Delta x_{i+1}^* k_i^*} \right] \Delta A_x^* & B_w^* = \left[ \frac{2k_i^* k_{i-1}^*}{\Delta x_i^* k_{i-1}^* + \Delta x_{i-1}^* k_i^*} \right] \Delta A_x^* \\ B_n^* = \left[ \frac{2k_j^* k_{j+1}^*}{\Delta y_j^* k_{j+1}^* + \Delta y_{j+1}^* k_j^*} \right] \Delta A_y^* & B_s^* = \left[ \frac{2k_j^* k_{j-1}^*}{\Delta y_j^* k_{j-1}^* + \Delta y_{j-1}^* k_j^*} \right] \Delta A_y^* \\ B_f^* = \left[ \frac{2k_k^* k_{k+1}^*}{\Delta z_k^* k_{k+1}^* + \Delta z_{k+1}^* k_k^*} \right] \Delta A_z^* & B_b^* = \left[ \frac{2k_k^* k_{k-1}^*}{\Delta z_k^* k_{k-1}^* + \Delta z_{k-1}^* k_k^*} \right] \Delta A_z^* \end{cases} \quad (2.13)$$

$$\begin{aligned}
& \xi^2 \left[ B_e^* (T_{i+1}^{*n+\tau} - T_i^{*n+\tau}) - B_w^* (T_i^{*n+\tau} - T_{i-1}^{*n+\tau}) \right] \Delta Fo + \\
& \gamma^2 \left[ B_n^* (T_{j+1}^{*n+\tau} - T_j^{*n+\tau}) - B_s^* (T_j^{*n+\tau} - T_{j-1}^{*n+\tau}) \right] \Delta Fo + \\
& \zeta^2 \left[ B_f^* (T_{k+1}^{*n+\tau} - T_k^{*n+\tau}) - B_b^* (T_k^{*n+\tau} - T_{k-1}^{*n+\tau}) \right] \Delta Fo = \Delta V_{ijk}^* \left[ (\rho^* u^*)^{n+1} - (\rho^* u^*)^n \right]
\end{aligned} \tag{2.14}$$

The finite difference heat diffusion equation can be simplified by collecting temperatures of similar time steps and letting a total conduction term, eqn. (2.15), represent the sum of all conduction components of each control surface. The diffusion terms of eqn. (2.14) have been simplified into nodal temperatures evaluated at either the present or the next time step, depending on either an explicit or implicit solution, respectively. The energy storage densities of the right-hand side, although considered uniform within the control volume, are not necessarily constant over the temporal domain. Furthermore, the consideration of the solid/liquid interface does not yet appear in eqn. (2.16).

$$B_{tot}^* = \xi^2 (B_e^* + B_w^*) + \gamma^2 (B_n^* + B_s^*) + \zeta^2 (B_f^* + B_b^*) \tag{2.15}$$

$$\begin{aligned}
& \xi^2 \left[ B_e^* T_{i+1,j,k}^{*n+\tau} + B_w^* T_{i-1,j,k}^{*n+\tau} \right] \Delta Fo + \\
& \gamma^2 \left[ B_n^* T_{i,j+1,k}^{*n+\tau} + B_s^* T_{i,j-1,k}^{*n+\tau} \right] \Delta Fo + \\
& \zeta^2 \left[ B_f^* T_{i,j,k+1}^{*n+\tau} + B_b^* T_{i,j,k-1}^{*n+\tau} \right] \Delta Fo - \\
& \left[ B_{tot}^* \right] T_{i,j,k}^{*n+\tau} \Delta Fo = \Delta V^* \left[ (\rho^* u_{i,j,k}^*)^{n+1} - (\rho^* u_{i,j,k}^*)^n \right]
\end{aligned} \tag{2.16}$$

What remains is one assumption: the specific internal energy equals the specific enthalpy. Based on Shamsundar and Sparrow's enthalpy method [4], a system undergoing a phase change experiences a change of pressure which is independent of time. As a result, the complex equation describing energy transfer from a control volume undergoing phase change can be simplified by assuming that  $\{\Delta(\rho^* u^*)^{n+1} \approx \Delta(\rho^* h^*)^{n+1}\}$ .

$$\{(\rho^* u^*)^{n+1} - (\rho^* u^*)^n\} \approx \{(\rho^* h^*)^{n+1} - (\rho^* h^*)^n\} \quad (2.17)$$

In eqn. (2.17),  $h^*$  is normalized with respect to  $c_p \Delta T_{ref}$  just like the normalized specific internal energy. Furthermore, the equation of state relating enthalpy to temperature can be modelled in a piece-wise linear fashion to include the solid, phase transition, liquid, and canister regions in a single equation. By designating the solid, melt, liquid, and canister phases with subscripts 1, 2, 3, and 4 respectively, a general equation of state develops from eqn. (2.18).

$$\frac{\partial h^*}{\partial T^*} = c_p^* \quad (2.18)$$

$$h^* = h_{ref_c}^* + c_{p_c}^*(T^* - T_{ref_c}^*), \quad c = 1, 2, 3, 4 \quad (2.19)$$

In the case above, the subscript (ref) denotes the reference value associated with each phase where typical values can be derived from Figure 2.3. Originally, Schneider and Raw [6,7] proposed a set of reference constants which only represent the latent heat component governing the region,  $h_3 - h_2 = \lambda$ . Since enthalpy is defined as the sum of sensible, latent, and chemical heat terms, a new collection of constants are proposed as reference values for each state.

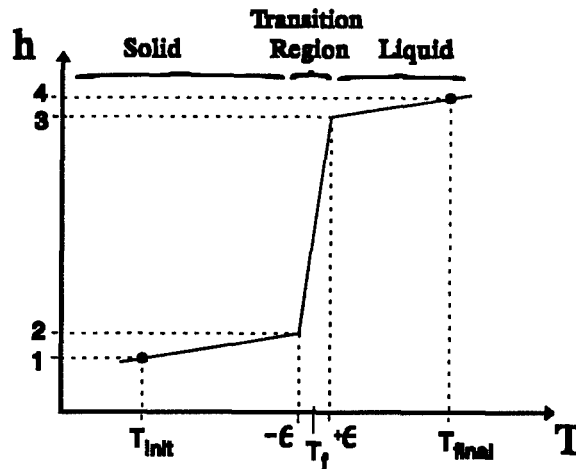


Figure 2.3 Piece-wise linear enthalpy model

Schneider's reference constants are appropriate for a latent heat approximation with two exceptions. In the first case, the temperature reference  $\epsilon$  represents a small temperature excursion across the phase front which needs to be associated with the fusion temperature and normalized with respect to  $\Delta T_{ref}$ . Secondly, the specific heat relationship of the phase transition region should not include  $\Delta T_{ref}$  which becomes more evident if eqn. (2.19) is rewritten to accommodate all the normalized terms as shown in eqn. (2.20).

$$\frac{h - h_f}{c_{p_l} \Delta T_{ref}} = \frac{h_{ref} - h_f}{c_{p_l} \Delta T_{ref}} + \frac{c_{p_c}}{c_{p_l}} \left[ \frac{T - T_f}{\Delta T_{ref}} - \frac{T_{ref} - T_f}{\Delta T_{ref}} \right] \quad (2.20)$$

The latent heat represents a fraction of its energy storage capability within the region, but reaches its total latent heat of fusion when the local temperature charges through the phase change transition temperature range of  $2\epsilon$ . Typical reference constants of eqn. (2.19) are proposed in ref. [6,7]. However, a new set of enthalpy coefficients below are specifically considered and highly recommended for thermal energy storage applications. In a single equation of state, the coefficients include the sensible heat from the initial temperature contained within the solid and canister regions, the latent heat from the phase transition region, and the sensible heat from the liquid region. As a result from the coefficients of eqn. (2.21), a melting process having an initial temperature within the solid region will gain heat while a liquid freezing will lose heat. A similar set of enthalpy reference coefficients can be derived for the freezing process having an initial temperature within the liquid region.

$$\left\{ \begin{array}{lll} h_{ref_1}^* = 0, & T_{ref_1}^* = \frac{T_{init} - T_f}{\Delta T_{ref}}, & c_{p_1}^* = \frac{c_{p_s}}{c_{p_l}} \\ h_{ref_2}^* = \frac{c_{p_s}[(T_p) - T_{init}]}{c_{p_l} \Delta T_{ref}}, & T_{ref_2}^* = \frac{(T_f - \epsilon) - T_f}{\Delta T_{ref}}, & c_{p_2}^* = \frac{c_{p_m}}{c_{p_l}} = \frac{\lambda}{(c_{p_l} 2\epsilon)} \\ h_{ref_3}^* = \frac{c_{p_s}[(T_p) - T_{init}]}{c_{p_l} \Delta T_{ref}} + \frac{1}{Ste}, & T_{ref_3}^* = \frac{(T_f + \epsilon) - T_f}{\Delta T_{ref}}, & c_{p_3}^* = \frac{c_{p_l}}{c_{p_l}} = 1 \\ h_{ref_4}^* = 0, & T_{ref_4}^* = \frac{T_{init} - T_f}{\Delta T_{ref}}, & c_{p_4}^* = \frac{c_{p_c}}{c_{p_l}} \end{array} \right. \quad (2.21)$$

Note that  $\epsilon$  (of the phase change constants) takes on a typically small value less than  $10^{-3}$  whose influence is equivalent to the representation of the phase transition region by a very large specific heat over a negligibly small temperature range. Furthermore, instead of the Stefan

number's introduction into the solution through the compatibility constraint, it appears in the above constants to permit an approximation of a single equation that accurately represents an energy balance between dissimilar control volumes for moving boundary problems [6,7].

To evaluate the diffusion terms, a general temperature relationship representing either an explicit or an implicit solution as in eqn. (2.22) can be used in conjunction with the enthalpy formulation of eqn. (2.19) to expand the diffusion and specific internal energy terms of eqn. (2.16). The result is an extremely flexible energy equation describing the energy transport of phase change problems.

$$T^{*n+\tau} = \tau T^{*n+1} - (\tau-1)T^{*n} \quad (2.22)$$

$$\begin{aligned} & \xi^2 \left[ B_e^* [\tau T_{i+1}^{*n+1} - (\tau-1)T_{i+1}^{*n}] + B_w^* [\tau T_{i-1}^{*n+1} - (\tau-1)T_{i-1}^{*n}] \right] \Delta Fo + \\ & \gamma^2 \left[ B_n^* [\tau T_{j+1}^{*n+1} - (\tau-1)T_{j+1}^{*n}] + B_s^* [\tau T_{j-1}^{*n+1} - (\tau-1)T_{j-1}^{*n}] \right] \Delta Fo + \\ & \zeta^2 \left[ B_f^* [\tau T_{k+1}^{*n+1} - (\tau-1)T_{k+1}^{*n}] + B_b^* [\tau T_{k-1}^{*n+1} - (\tau-1)T_{k-1}^{*n}] \right] \Delta Fo - \\ & \left[ B_{tot}^* \right] [\tau T_{i,j,k}^{*n+1} - (\tau-1)T_{i,j,k}^{*n}] \Delta Fo = \\ & \Delta V^* \left[ \{ \rho^* (h_{f_c}^* + c_{p_c}^* (T_{i,j,k}^* - T_{f_c}^*)) \}^{n+1} - \{ \rho^* (h_{f_c}^* + c_{p_c}^* (T_{i,j,k}^* - T_{f_c}^*)) \}^n \right] \end{aligned} \quad (2.23)$$

Note that the subscript *ref* has been replaced by *f* in the enthalpy substitution of eqn. (2.23).

Simplification of eqn. (2.23) results from collecting time constant terms, ( $\tau$ ) and ( $\tau-1$ ) for each set of temperature evaluations, and equating temperature terms evaluated at ( $n+1$ ) on the left and ( $n$ ) on the right, eqn. (2.24). Consequently, a solution representing either an explicit or implicit evaluation can be considered.

Since the solution employed throughout this paper is implicit (i.e.  $\tau = 1$ ), eqn. (2.24) can be reduced considerably to produce the final form of eqn. (2.25) for the moving boundary phase change problem. The result for  $T_{i,j,k}^{*n+1}$  represents a fully implicit solution to the Stefan problem in an equation solving sense rather than in the typical Crank-Nicholson case. Furthermore, the solution can be resolved into a set of linear algebraic equation representing the interior nodes of the TES unit and evaluated iteratively for some prescribed convergence accuracy.

$$\begin{aligned}
& \tau \left[ \xi^2 (B_e^* T_{i+1}^{*n+1} + B_w^* T_{i-1}^{*n+1}) + \gamma^2 (B_n^* T_{j+1}^{*n+1} + B_s^* T_{j-1}^{*n+1}) \right] \Delta F_o + \\
& \tau \left[ \zeta^2 (B_f^* T_{k+1}^{*n+1} + B_b^* T_{k-1}^{*n+1}) \right] \Delta F_o - \left[ \tau B_{tot}^* \Delta F_o + \{\rho^* \Delta V^* c_{p_c}^*\}^{n+1} \right] T_{ijk}^{*n+1} = \\
& -(\tau-1) \left[ \xi^2 (B_e^* T_{i+1}^{*n} + B_w^* T_{i-1}^{*n}) + \gamma^2 (B_n^* T_{j+1}^{*n} + B_s^* T_{j-1}^{*n}) \right] \Delta F_o - \\
& (\tau-1) \left[ \zeta^2 (B_f^* T_{k+1}^{*n} + B_b^* T_{k-1}^{*n}) \right] \Delta F_o - \left[ (\tau-1) B_{tot}^* \Delta F_o + \{\rho^* \Delta V^* c_{p_c}^*\}^n \right] T_{ijk}^{*n} + \\
& \Delta V^* \left[ \{\rho^* (h_{f_c}^* - c_{p_c}^* T_{f_c}^*)\}^{n+1} - \{\rho^* (h_{f_c}^* - c_{p_c}^* T_{f_c}^*)\}^n \right]
\end{aligned} \tag{2.24}$$

$$\begin{aligned}
& \left[ \xi^2 (B_e^* T_{i+1,j,k}^{*n+1} + B_w^* T_{i-1,j,k}^{*n+1}) + \gamma^2 (B_n^* T_{ij+1,k}^{*n+1} + B_s^* T_{ij-1,k}^{*n+1}) \right] \Delta F_o + \\
& \left[ \zeta^2 (B_f^* T_{ij,k+1}^{*n+1} + B_b^* T_{ij,k-1}^{*n+1}) \right] \Delta F_o - \left[ B_{tot}^* \Delta F_o + \{\rho^* \Delta V^* c_{p_c}^*\}^{n+1} \right] T_{ijk}^{*n+1} = \\
& - \left[ \{\rho^* \Delta V^* c_{p_c}^*\}^n \right] T_{ijk}^{*n} + \Delta V^* \left[ \{\rho^* (h_{f_c}^* - c_{p_c}^* T_{f_c}^*)\}^{n+1} - \{\rho^* (h_{f_c}^* - c_{p_c}^* T_{f_c}^*)\}^n \right]
\end{aligned} \tag{2.25}$$

To improve the convergence for each time step, two simple rules [5] will be employed. In the first, a control volume can change state by only one state in a single iteration. That is to say that a control volume changing phase from a solid or a liquid can only take on the value of the phase transition -- the control volume can not change phase from the solid to the liquid without first charging through the phase transition region. The second rule considers that neighboring control volumes of the CV undergoing phase transition must have gone through a phase transition in the last iteration before the CV of the present iteration can change phase.

The heat diffusion equation is a modified approach to evaluating three dimensional phase change problems including canister geometries. The equation does not take convection terms resulting from buoyancy and density gradient into account for reasons explained in Chapter 1. As a result, the problem of phase change is modelled via conduction only.

## 2.3 Boundary Conditions

The boundary conditions of the TES unit can take on two forms:

- 1)  $q = \text{constant}$  {Neumann}
- 2)  $T = f(F_o)$  {Dirichlet}

Each condition is evaluated at each time interval and becomes an integral part of the solution. For both the Neumann and Dirichlet case, the reference temperature associated with each normalization is a result of the largest prescribed temperature gradient, which is boundary condition dependent. From a geometric standpoint,  $q_b$  represents the prescribed heat flux of either a point in one dimension, a line in two, or a surface in three and is associated with the length in the direction of the flux. Similarly,  $T_b$  takes on either a constant temperature value or the amplitude of the surface temperature excitation as in the case of periodic or other functional Dirichlet conditions. The largest reference temperature difference resulting from either the Neumann or Dirichlet boundary condition is then used throughout the phase change evaluation.

$$\begin{aligned} \Delta T_{ref} &= \frac{q_b D}{k_{can}} && \text{Neumann} \\ \Delta T_{ref} &= T_b - T_f && \text{Dirichlet} \end{aligned} \tag{2.26}$$

Constant temperature surfaces represent an easy application to the canister geometry; however, flux prescribed surfaces are temperature dependent and require a set of separate equations coupled with the interior nodes of the enthalpy formulation. Accordingly, a three-dimensional application will be developed which can easily be reduced to one dimension.

Beginning with the conservation of energy, an energy balance centered around node (0,j,k) of Figure 2.4 can be considered in eqn. (2.27). In this case, canister properties are assumed to be independent of temperature and uniform throughout the control volume so that a finite difference approximation to the partial derivatives may be applied. The solution assumes a three dimensional control volume that experiences a constant heat flux entering through the west face and heat transfer leaving and entering the CV via conduction.

A first order Taylor series approximation for the diffusion and energy storage terms applies a forward finite difference implicit solution for both the spatial and temporal domain.

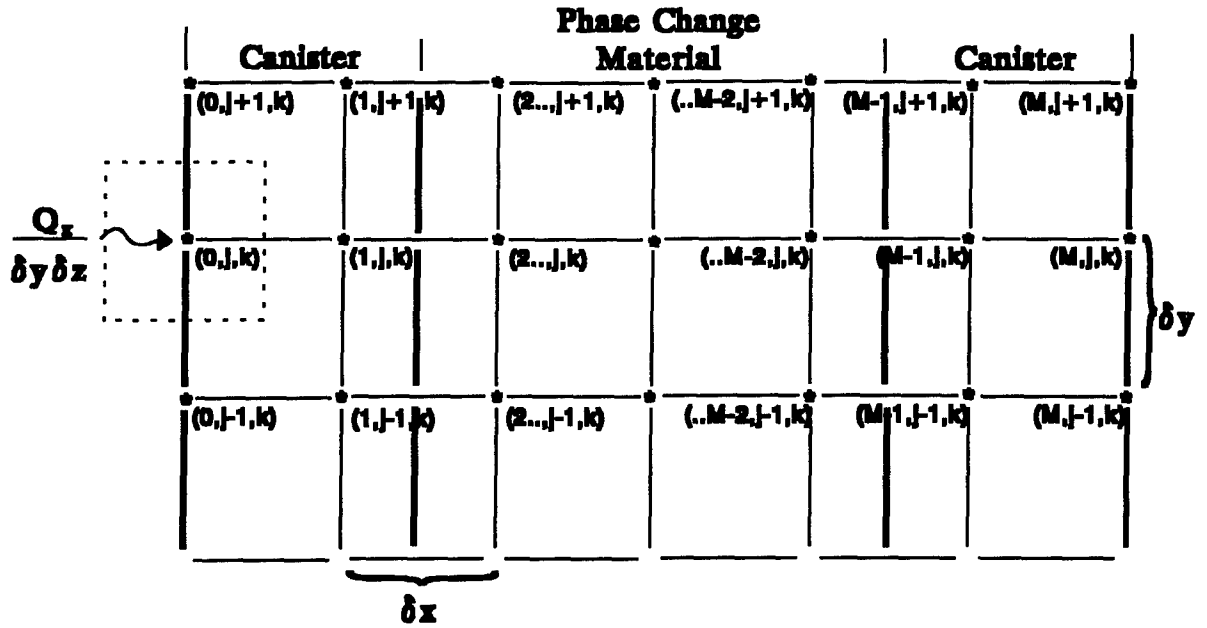


Figure 2.4 Evaluation of exterior boundary nodes for edges, surfaces, and corners given both Neumann and Dirichlet prescribed boundary conditions

$$\left[ q_x|_w + k \frac{\partial T}{\partial x} \Big|_e \right] \delta y \delta z + k \left[ \frac{\partial T}{\partial y} \Big|_n + \frac{\partial T}{\partial y} \Big|_s \right] \frac{\delta x}{2} \delta z + k \left[ \frac{\partial T}{\partial y} \Big|_f + \frac{\partial T}{\partial y} \Big|_b \right] \frac{\delta x}{2} \delta y = \rho c_p \left( \frac{\delta x}{2} \delta y \delta z \right) \frac{\partial T}{\partial t} \quad (2.27)$$

The solution to eqn. (2.27) after substitution of the proper spatial terms and temporal term along with the consideration of an implicit solution results in eqn. (2.28).

$$\begin{aligned} & q_x \delta y \delta z + k \frac{(T_{1,j,k}^{n+1} - T_{0,j,k}^{n+1})}{\delta x} \delta y \delta z + k \frac{(T_{0,j+1,k}^{n+1} - T_{0,j,k}^{n+1})}{\delta y} \frac{\delta x}{2} \delta z \\ & + k \frac{(T_{0,j-1,k}^{n+1} - T_{0,j,k}^{n+1})}{\delta y} \frac{\delta x}{2} \delta z + k \frac{(T_{0,j,k+1}^{n+1} - T_{0,j,k}^{n+1})}{\delta z} \frac{\delta x}{2} \delta y \\ & + k \frac{(T_{0,j,k-1}^{n+1} - T_{0,j,k}^{n+1})}{\delta z} \frac{\delta x}{2} \delta y = \rho c_p \left( \frac{\delta x}{2} \delta y \delta z \right) \frac{(T_{0,j,k}^{n+1} - T_{0,j,k}^n)}{\delta t} \end{aligned} \quad (2.28)$$

Although presently evaluated for a heat flux entering through the west surface, eqn. (2.28) can be modified to evaluate the surface temperature  $T_{i,j,k}^{n+1}$  of a flux prescribed boundary whether the



prescribed heat flux is entering through the east, west, north, south, front, or back control surface.

Simplification of eqn. (2.28) results from dividing through by both the incremental control volume and the thermal conductivity and normalizing with respect to temperature and time. The energy balance can then be resolved in eqn. (2.29) by its implicit surface temperatures  $T_{0,j,k}^{*(n+1)}$  which represent any node on the east face with exception to the edges and corners associated with the control surface.

$$T_{0,j,k}^{*(n+1)} = \frac{D^2 \Delta F_o \left[ (x\text{-term}) + (y\text{-term}) + (z\text{-term}) \right] + \frac{1}{\alpha_c^*} T_{0,j,k}^{*n}}{\left[ \frac{1}{\alpha_c^*} + 2D^2 \Delta F_o \left( \frac{1}{\Delta x^2} + \frac{1}{\Delta y^2} + \frac{1}{\Delta z^2} \right) \right]}$$

$$\begin{cases} \frac{2}{\Delta x^2} (T_{1,j,k}^{*(n+1)} + \frac{q_x \Delta x}{k \Delta T_{ref}}) & x\text{-term} \\ \frac{1}{\Delta y^2} (T_{0,j+1,k}^{*(n+1)} + T_{0,j-1,k}^{*(n+1)}) & y\text{-term} \\ \frac{1}{\Delta z^2} (T_{0,j,k+1}^{*(n+1)} + T_{0,j,k-1}^{*(n+1)}) & z\text{-term} \end{cases} \quad (2.29)$$

Similar solutions can be obtained for the west, north, south, front, and back control surfaces by altering the flux's location in either the x, y, or z term, placing a factor of two on the appropriate term corresponding to the flux's direction, and adjusting the local temperature nodes under consideration. To evaluate the edges and corners, a similar approach to the eqn. (2.27) must be considered. Note that only a fraction of the control volume is accounted for along a surface as seen by  $(\delta x/2)$  in eqn. (2.27), an edge  $(\delta x/2 \delta y/2)$ , and a corner  $(\delta x \delta y \delta z/8)$ .

Adjacent flux surfaces such as an x-y edge need the flux evaluation for both the x and y terms, a multiplication factor of 2, and the appropriate neighboring CV temperatures to consider the temperature of  $T_{i,j,k}^{n+1}$ . A corner having three adjacent flux surfaces requires a flux evaluation for each term along with the other considerations. Keep in mind that three dimensions requires 6 equations describing the control surfaces, 12 equations describing the control surface edges, and 8 equations describing the corners.

The edges can have three different types of boundary combinations: flux/flux, flux/temperature, and temperature/temperature. Two flux prescribed adjacent surfaces have

already been considered above. In the case where a temperature prescribed surface lies adjacent to a flux prescribed surface, the edge temperature takes on the value of the temperature of the adjacent surface. Adjacent walls having different surface temperature excitations will be considered by an average value located along the edge.

The corners can have four boundary combinations: flux/flux/flux, flux/flux/temperature, flux/temperature/temperature, and temperature/temperature/temperature. The adjacent fluxes have already been considered above. In the case where two flux surfaces lie adjacent to a temperature prescribed surfaces, the corner temperature takes on the value of the temperature excitation at that time step. The evaluation of the flux and two temperature surfaces will involve an averaging of the two surfaces. The three temperature prescribed surface combination results in an averaging of the three surface excitations for each time step.

## Chapter 3. Numerical Results

The representation of numerical models appears in three forms: normalized isotherms in the spatial and temporal domain, percent melt in the temporal domain, and heat storage in the temporal domain. Although many different scenarios have been evaluated, only specific cases involving direct comparisons between two dimensional evaluations are considered with fin enhancement included.

Evaluating phase change material canisters begins with the simple case of melting a zero-subcooled solid in a semi-infinite region. The exact solution of eqns. (1.1 and 1.2) results in a similarity transform shown in eqn. (3.1) where the Stefan number represents the specific to latent heat ratio and characterizes heat transfer during phase change.

$$T^* = \frac{\operatorname{erf}\left(\frac{x}{(4\alpha t)^{0.5}}\right)}{\operatorname{erf}\left(\left(\frac{1}{Ste}\right)^{0.5}\right)} \quad (3.1)$$

The solution is only valid for small Stefan values and can be modelled numerically by applying an adiabatic boundary constraint at a distance greater than the interface location at any period. Figure 3.1 illustrates a comparison between the similarity transform and numerical model using initially zero-subcooled ice subjected to a constant wall temperature of 10°C, and Stefan number of 0.125. Since the similarity solution does not take into account the wall's thickness, the numerical solution must be offset by the wall thickness to provide an accurate comparison between the two solutions. As expected, the largest error occurs near the wall and the phase change interface because the normalized temperature profile of eqn. (3.1) does not take into account the wall's density, specific heat, and thermal conductivity and is continuous at the interface while the enthalpy approach of the numerical model is piece-wise linear and accounts for the material properties of every phase state including the canister.

Although multi-dimensional phase change modelling relies heavily on many parameters such as material properties, boundary types, canister shape and size, and fin enhancement, parameter requirements for one dimension are less demanding. One dimensional solutions, require only the material properties and boundary constraints imposed on the side walls because the boundary constraints at any height and width are adiabatic in the y and z direction.

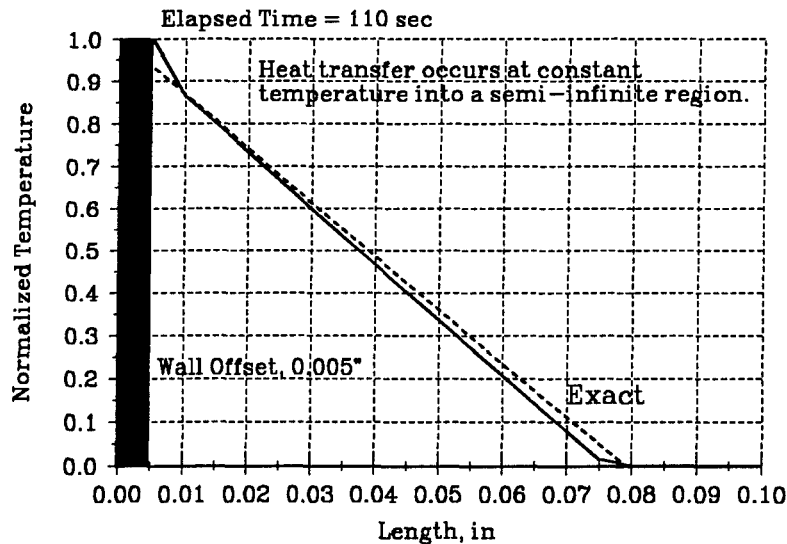


**Figure 3.1** Similarity Solution vs Numerical Model

For most of the numerical studies, the PCM is water housed in a brass container. The material combination, although not suited for space power applications because of the large density of brass and high sensible heat associated with water, is used because the large thermal conductivity of brass magnifies the heat transfer penetration into the system and the effects from sensible heating can be observed. The properties for a water/brass combination are listed in Table 3.1 and unless otherwise stated, uses a reference temperature difference of  $60^{\circ}\text{C}$  which corresponds to a Stefan number of 0.75. The phase change region and canister walls are initially zero-subcooled to demonstrate the melting process of the numerical model but can be set at a below fusion temperature. Freezing processes with an initial temperature above the fusion, require a separate set of enthalpy reference coefficients. An approach similar to that of melting (see Section 2.2) is used to describe the freezing process.

Although the enthalpy formulation accounts for the canister's sensible heat, the output information specifically omits the canister's sensible heat from the PCM's total sensible and latent heat storage so that PCM and canister combinations can be compared with various PCM behavior and TES units. Consequently, adding fins to a canister reduces the PCM volume and total latent heat capacity but increases the melting and heat penetration rates. The trade-off will determine which design best meets mission criteria.

**Table 3.1** Material properties for water and brass canister combination [10].

Material Properties/State	Solid	Liquid	Canister
Conductivity [W / m·°C]	2.215	0.6084	109.0
Specific Heat [kJ / kg·°C]	2.100	4.177	0.385
Density [kg / m <sup>3</sup> ]	917.0	999.8	8522
Latent Heat of Fusion [kJ / kg]	333.7	Ste = 0.75	-----

The melt fraction is based on the total number of control volumes which have undergone a phase change from solid to liquid divided by the total volumes of phase change material. Since the phase change interface is only tracked within one mesh spacing, the accuracy of the percent melt relies on the number of capable phase change volumes. For example, if a two-dimensional canister is considered to have a LH in<sup>2</sup> configuration with a control volume size of  $\Delta x \Delta y$  in<sup>2</sup> then the total number of control volumes capable of changing phase becomes:

$$NCV = \left( \left( \frac{L}{\Delta x} + 1 \right) - 2 \right) \cdot \left( \left( \frac{H}{\Delta y} + 1 \right) - 2 \right) \quad (3.2)$$

In eqn. (3.2), one represents the domain evaluation from  $I$  equal 0 to  $L/\Delta x$  while two takes into account that the walls are not phase change volumes. This type of melt fraction analysis may result in irregular percent melt curves which can be remedied using curve fits. The output format of two and three dimensional analyses evaluates a selected time modulus and depth (3D only). The output columns show the normalized length, height, and temperature, heat transfer vectors having an angle (Deg) and magnitude (Watts), and normalized time versus the melt fraction (%Melt) and heat stored (Joules). The results are easily plotted with either a spreadsheet such as QuatroPro or graphics and analysis package such as Axum. The accompanying phase change program PCM\_Anal.EXE applies simple graphing to provide quick evaluations.

## Chapter 4. Discussion

Chapter 3 compared the accuracy of the enthalpy solution with a similarity transform that evaluated the normalized temperature for a semi-infinite phase change media. It demonstrated the method's flexibility for evaluating TES canisters having a complex set of boundary conditions, and successfully predicted TES performance based on percent melt and heat storage. Now consider a thermal canister *effectiveness* that can be used to quantify the amount of both latent and sensible heat that actually effects the energy storage capability.

The effectiveness can be defined as a ratio of the average heat stored to the maximum theoretical amount of heat stored. Since the energy storage rate is not constant, the thermal effectiveness will vary with time as in eqn. (4.1).

$$\eta (Fo) = \frac{\bar{U}}{U_{\max}} = \frac{\frac{\int_0^{Fo} U(Fo) \cdot d(Fo)}{Fo}}{m_{PCM}(C_{ps}(T_f - T_{init}) + \lambda + C_{pl}(T - T_f))} \quad (4.1)$$

Since all the solutions previously considered a zero-subcooled solid in a state of melt, the sensible heat stored in the solid is equal to zero.

The analysis of canisters with and without fins includes the thermal effectiveness for a canister subjected to a normal heat load of 60°C at the north and south boundaries and adiabatic side walls. The evaluation extends a base solution having no fins to consider TES canisters with the addition of 1, 2, 4, and 6 fins protruding into the domain to demonstrate that the thermal effectiveness increases considerably with the addition of fins but must be balanced by other considerations such as canister mass, PCM melt fraction, and the total heat storage capability.

The base and enhanced canisters included in Table 4.1 list the major parameters used to develop a typical TES trade study. The study evaluates the average percent melt and heat storage at a Fourier modulus of 0.1 and determines the time required to melt the initially zero-subcooled solid. Recall that some solid PCM margin should be maintained to facilitate freezing of the next freeze cycle and avoid possible subcooling. As a result, the time required for 100 percent melt represents the maximum amount of time that a TES canister should be subjected to the boundary conditions. Exceeding the critical heating period is a result of poor design practice.

The design trade-off for a canister lies primarily with the percent melt and the thermal effectiveness, Figure 4.1, and the establishment of a suitable PCM safety margin that will tend to decrease the effectiveness of the canister. Another consideration includes the mass of the canister. Fins added to improve the thermal effectiveness increase the canister mass considerably, especially when they are made of dense materials such as brass, copper, and steel.

**Table 4.1** Thermal Storage Unit - Trade Study of Two-Dimensional Canister

Phase Change Material	Water				
Canister Type	Rectangular				
Canister Size	(2.1·2.1·2.0) in <sup>3</sup>				
Latent Heat of Fusion	333.7 Joules/gram				
Density	---	Specific Heat	1 g/cm <sup>3</sup>	---	4.20 J/g·°C
Number of Rectangular Fins	0	1	2	4	6
Fin Thickness, [in]	0.05	0.05	0.05	0.07	0.05
Fin Spacing, [in]	N/A	1.05	0.70	0.42	0.3
Wall Thickness, [in]	0.025	0.025	0.025	0.035	0.025
PCM Mass, [grams]	134.4	131.1	127.8	116.02	114.7
Theoretical Latent Capacity, [kJ]	44.8	43.7	42.6	38.7	38.3
Theoretical Sensible Capacity, [kJ]	33.9	33.0	32.2	29.2	28.9
Canister Total Mass, [grams]	253.2	277.8	302.5	415.0	401.1
Percent PCM by Volume, [%]	100	97.6	95.1	86.2	85.3
Avg Percent Melt @ (t = 32.55 min), [%]	47.1	66.6	80.3	92.0	93.71
Avg Heat Stored @ (t = 32.55 min), [kJ]	28.5	40.9	50.9	57.6	59.5
Time to 100 Percent Melt [min]	56.96	39.82	26.04	9.76	6.51
Canister Effectiveness @ (t = 32.55 min)	36.2	53.3	68.0	84.8	88.5

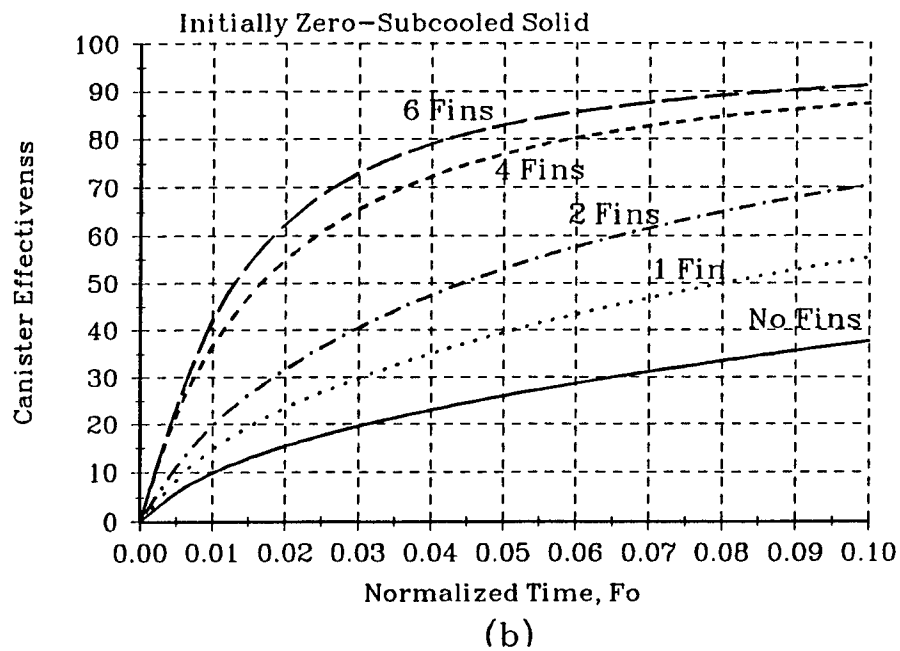
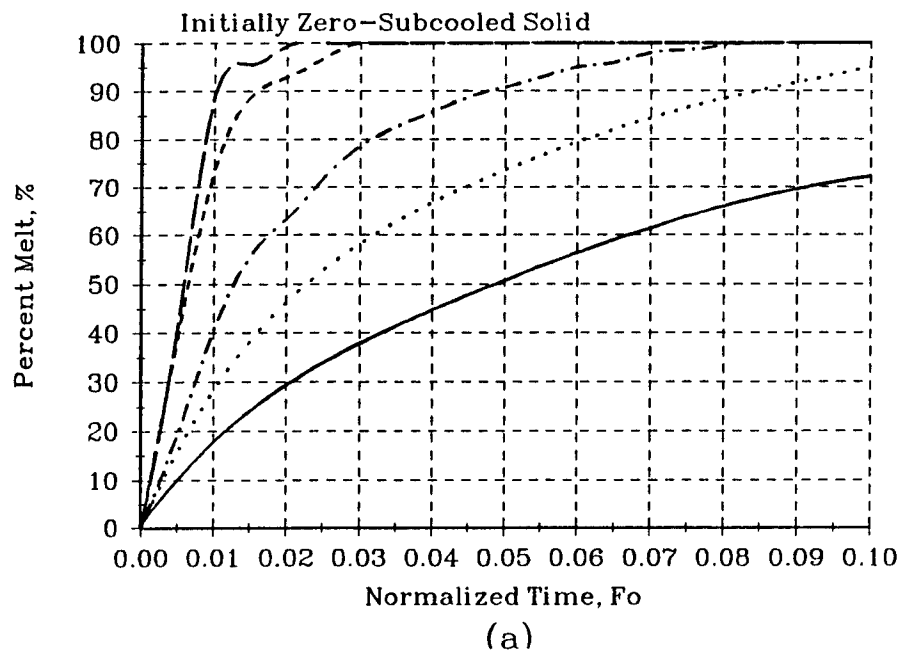
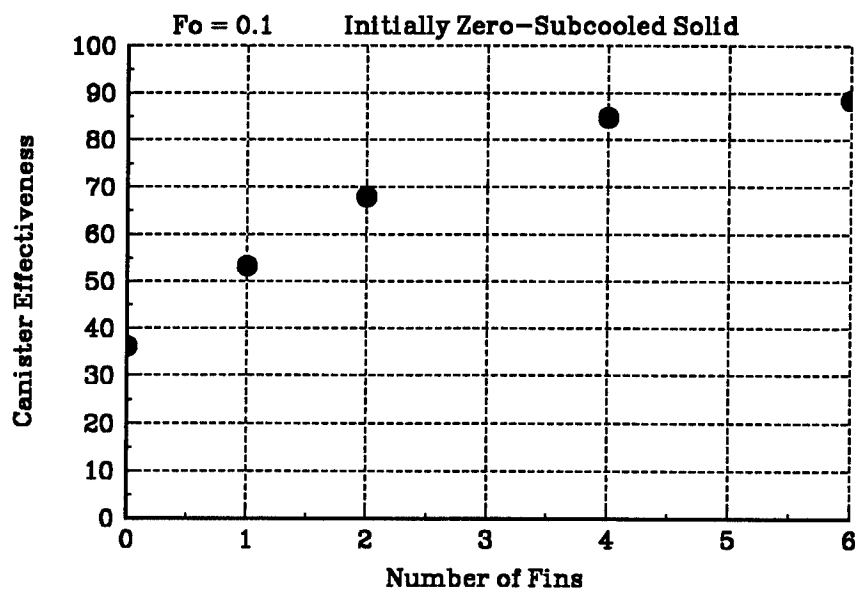


Figure 4.1 Comparison of a) Percent Melt and b) Canister Effectiveness



The canister effectiveness can be considered for a base solution having no fins, and the effect of adding consecutive number of fins, spaced evenly, to enhance the performance of a TES canister can be examined. Figure 4.2 demonstrates this type of comparison for  $Fo = 0.1$ . Although it is strongly agreed throughout phase change studies that a combination of thin fins provides better performance than a few thick ones, research into the convective influence on the open regions should be considered to truly ascertain the difference in performance. Eventually, the addition of fins provides negligible differences in the melting and heating rates but reduces the amount of energy storage capability of the PCM.

Aspects of thermal control systems require stable or small temperature excursions which can be achieved with TES units having highly conductive enhancement fins, high latent PCMs, and designs to provide short response time and high energy absorbing capabilities for future spacecraft. Using similar analysis to that of Table 4.1, Figure 4.1, and Figure 4.2, several latent thermal energy storage canisters can now be considered as viable alternatives for removing waste heat from systems experiencing melt/freeze cycles. Heat can be removed using refrigeration or cryogenic coolers, heat transfer loops, or naturally via environmental heating.



**Figure 4.2** Canister Effectiveness,  $\eta(Fo = 0.1)$ , vs Number of Fins

Dispersion of metal fins in the PCM reduces the thermal time constant and provides more uniform heating and freezing of the PCM where the melt front propagates perpendicular to the baseplate. The heat flow is largely two-dimensional and the melt front is shaped like a semi-circle. Optimum performance is obtained when the foils/fins are sufficiently thin and closely spaced so that the thermal resistance along the foils is equal to or greater than the thermal resistance across the PCM between the foils. For small spacing and thickness, the PCM/metal performs as a homogeneous material conducting heat in one dimension. The TES canister can be considered to have uniform thermal properties with volumetric averages for the thermal conductivity and specific heat.

Two primary difficulties with the enthalpy model exist. The first concerns the void volumes which develop from phase change materials whose variation in density during contraction and expansion is large. The present model does not take into account that the PCM mass must remain constant and is dependent upon initial conditions (i.e. solid or liquid). The numerical procedure simply omits the volume change from solid to liquid and vice versa. For example, water housed in the container of Table 4.1 actually has a mass of 123.22 grams for an initially subcooled ice having a PCM volume of  $134.4 \text{ cm}^3$ . After all the ice melts, the volume occupied by the liquid PCM is  $123.2 \text{ cm}^3$  which corresponds to a void volume of approximately 9 percent. Clearly the void volume does not contribute to the canister's or the PCM's ability to transfer heat. Other PCMs exhibit similar development of void volumes as they undergo phase transition and must be evaluated appropriately for both solidification and melting.

Although the Stefan problem has been simplified considerably through assumptions, a considerable amount of computer memory allocations for both the two and three dimensional canister is required. As a shortcoming of the enthalpy solution, the memory requirements of a temperature time history for the three dimensional canister severely limits the size that can be evaluated. The numerical model uses dynamic memory allocation in the form of a four dimensional pointer, but is limited in size to the heap (640 kbytes) on personal computers.

## Chapter 5. Conclusion

Latent thermal energy storage represents an attractive solution to waste heat removal from space power thermal control systems. Past evaluations have been extremely difficult and required extensive testing to quantify a canister's effectiveness for a single application. Using the modified enthalpy solution, canisters were evaluated numerically to determine an optimum design based on weight, heat storage, percent melt, and other performance requirements.

The modified enthalpy solution successfully predicts the solidification and melt performance of every boundary condition and canister size with and without fins. Furthermore, the enthalpy method successfully evaluates canisters that have multiple phase fronts and interactions from phase fronts that couple into a single interface. However, some solutions experienced convergence problems which may be associated with the interface region since the convergence error must resolve a precise solution of at least one decimal more accurate than the value of  $2\varepsilon$ . Explicit solutions are not considered in this paper, but can be derived from eqn. (2.24) by substituting  $\tau = 0$ . Such a solution would require an analysis of a stability criterion based on the time step of the Fourier modulus.

Although the model includes TES contributions of sensible heating, satellite applications require small temperature excursions near the base plate or mounting surface which tend to reduce the effects of sensible heat. Canisters of this type require a design based primarily on the high energy storage densities of the phase change material in terms of its latent heat of fusion and the effectiveness with which heat is transferred into the PCM via conduction enhancement fins. Enhanced TES canisters have shown increases in the capability for rapid absorption of thermal energy to accommodate pulsed or periodic loads. The TES canister can be attached directly to equipment packages or used with a heat transfer loop to permit components to be sized for average rather than peak loads.

The moving boundary problem is not limited to a fusion temperature of any phase change material unless the material experiences subcooling or freezing over a specific range. Solutions in the cryogenic range (i.e. below 120 K), require careful selection of the material properties of the solid and liquid. Quite often, these values are very different and can change significantly

over several degrees centigrade. As a result, a modification to the solution could include relationships in the form of a quadratic equation used to determine properties such as thermal conductivity and specific heat as a function of temperature.

Additional work should consider rectangular canisters with staggered fin arrangements and cylindrical canisters with various fin types such as concentric cylinders, cylindrical rods, and rectangular fins. More complex solutions including the expansion and contraction of the phase change material which creates void volumes that reduce the total effectiveness and thermal storage capacity of the phase change canister should be considered. Furthermore, solutions including buoyancy and natural convection represent an extremely challenging task for canisters containing fin enhancement methods. Accounting for convection may provide a general TES canister size which may determine where heat transfer via conduction is overshadowed by convection.

Thermal degradation of the PCM and thermal stresses in the storage container after extensive periodic thermal loads requires a significant amount of design. The TES canister analysis must be expanded to include structural as well as thermal effects from stresses during lift-off and critical mission conditions which can fatigue connections, and ultimately rupture the canister. Only a complete and thorough investigation of the phase change canister will assure adequate performance of latent thermal storage modules in a space environment.

## APPENDIX

Diskette includes:

a) Executable Files:

- 1) PCM\_Anal.EXE -- executes the program

b) Turbo Pascal Units:

- 1) PCM\_Anal.OVR -- Overlay File
- 2) InitOvr.TPU -- Initializes the overlay file
- 3) Global3D.TPU -- Declares global variables and sets up an array of pointers
- 4) Wait.TPU -- Pauses the program and waits for a response
- 5) Credit.TPU -- University of Texas at San Antonio
- 6) Intro.TPU -- Introduces the program and operation
- 7) Input3D.TPU -- Request specific phase change parameters
- 8) Apply\_3D.TPU -- Applies the boundary condition of Input3D.TPU
- 9) Output3D.TPU -- Provides both graphical and file data
- 10) StEnergy.TPU -- Evaluates the energy stored and percent melt
- 11) Crt.TPU -- Turbo Pascal Unit
- 12) Printer.TPU -- Turbo Pascal Unit

## BIBLIOGRAPHY

- [1] Edelstein, F., "The Behavior of Cryogenic Phase Change Materials Used for IR Sensor Thermal Control in Space," SAE Technical Paper, # 911555, 1991.
- [2] Busby, M.S. and Mertesdorf, S.J., "The Benefit of Phase Change Thermal Storage for Spacecraft Thermal Management," AIAA Journal.
- [3] "Some Aspects of Spacecraft Equipment Heat Transfer Technology," AIAA Journal.
- [4] Shamsundar, N. and Sparrow E.M., "Analysis of Multidimensional Conduction Phase Change Via the Enthalpy Method," ASME Journal of Heat Transfer, Vol 97, 1975, pp. 333 - 340.
- [5] Shamsundar, N. and Sparrow E.M., "Effects of Density Change on Multidimensional Conduction Phase Change," ASME Journal of Heat Transfer, Vol 98, 1976, pp. 550 - 557.
- [6] Schneider, G.E. and Raw, M.J., "An Implicit Solution Procedure for Finite Difference Modeling of the Stefan Problem," AIAA Journal, Vol 22, 1984, pp. 1685 - 1690.
- [7] Schneider, G.E., "Computation of Heat Transfer with Solid/Liquid Phase Change Including Free Convection," Journal of Thermophysics and Heat Transfer, Vol 1, No 2, 1987, pp. 136 - 145.
- [8] Hunter, L.W. and Kuttler, J.R., "The Enthalpy Method for Moving Boundary Problems," The Johns Hopkins University Applied Physics Laboratory, Memo BBP 87-47, 1987.

- [9] Hunter, L.W. and Kuttler, J.R., "The Enthalpy Method for Heat Conduction Problems With Moving Boundaries," ASME Journal of Heat Transfer, Vol 111, 1989, pp. 239 - 242.
- [10] Lienhard, J. H., A Heat Transfer Textbook, Prentice-Hall, Englewood Cliffs NJ, 1987, pp. 220 - 267.
- [11] Werner F., Turbo Pascal 6 - DISKTUTOR, Osborne McGraw-Hill, Berkeley CA, 1991, pp. 415 - 466.
- [12] O'Brien, S.E. and Nameroff, S., Turbo Pascal 7 - the Complete Reference, McGraw-Hill, Berkeley, CA, 1993.
- [13] Tong, W., "Cryogenic Heat Transfer Model Involving Phase Change," ASME Heat Transfer Design, Vol 167, 1991.
- [14] Viswanath, R. and Jaluria, Y., "Numerical Simulation of Phase Change Problems In Enclosures: A Comparison of Different Approaches," ASME Heat Transfer Design, Vol 205, 1992.
- [15] Zeng, X. and Xin, M.D., "An Implicit Finite Difference Solution of Phase Change Problems Via Coupling the Enthalpy and Moving Boundary," ASME Heat Transfer Design, Vol 159, 1991.
- [16] Chow, L.C. and Zhong, J.K., "Thermal Conductivity Enhancement for Phase Change Storage Media," AIAA Journal, 1989, pp. 1743 - 1747.
- [17] Wen, C., Sheffield, J.W., and O'Dell, M.P., "An Analytical and Experimental Investigation of Melting Heat Transfer," Journal of Thermophysics and Heat Transfer, Vol 3, No 3, 1989, pp. 330 - 339.

- [18] Sheffield, J.W. and Wen, C., "Phase Change Material for Spacecraft Thermal Management," Contract WRDC-TR-90-2029, 1989..
- [19] Knowles, T., "Cryogenic PCM Database," Grumman Space & Electronics Division, Bethpage, NY, 1993.
- [20] Rubenstein, L.I., "Transaction of Mathematical Monographs," The Stefan Problem, American Mathematical Society, Providence, RI, Vol 27, 1971, pp. 1 - 38.
- [21] CRC Handbook of Chemistry and Physics, CRC Press, Boca raton, FL, 1990..
- [22] "I-DEAS TMG Notebook", Phase Change Modeling, 1992. ,



AN INTRODUCTION TO WIDEBAND RANGE  
AND DOPPLER CROSS RANGE RADAR  
IMAGERY OF ROTATING OBJECTS

Dr. J.M. Henson  
Assistant Professor  
Department of Electrical Engineering

University of Nevada/260  
Reno, NV 89557-0153

Final Report for:  
Summer Research Extension Program

Sponsored by:  
Air Force Office of Scientific Research  
Bolling Air Force Base, Washington, D.C.

and

University of Nevada, Reno

December 1993

AN INTRODUCTION TO WIDEBAND RANGE  
AND DOPPLER CROSS RANGE RADAR  
IMAGERY OF ROTATING OBJECTS

Dr. J.M. Henson  
Assistant Professor  
Department of Electrical Engineering  
University of Nevada, Reno

Abstract

The following paper is essentially a detailed tutorial discussion of the physical mechanisms and underlying mathematics that facilitate high resolution ISAR range and cross range imaging of rotating space objects. Specifically, it addresses those concepts necessary for a thorough understanding of the key image simulation algorithms that form the Lincoln Laboratories RCS Toolbox. The report is divided into three primary Sections as follows: 1) Range Resolution and Signal Bandwidth, 2) Cross Range Resolution and Doppler Frequency Processing and 3) Cross Range Resolution and ISAR Image Focusing.

AN INTRODUCTION TO WIDEBAND RANGE  
AND DOPPLER CROSS RANGE RADAR  
IMAGERY OF ROTATING OBJECTS

Dr. J.M. Henson

1.0 Introduction

This paper is a result of an AFOSR sponsored SFRP follow on contract at the University of Nevada, Reno, NV, funded through Phillips Laboratories Advanced Weapons Directorate WSAI group. It is the purpose of the exposition that follows to provide for WSAI personnel a succinct yet tutorial discussion of high resolution Inverse Synthetic Aperture Radar (ISAR) imaging concepts and signal processing techniques suitable for the description and analysis of real or synthetic imagery of rotating space objects. More specifically, we have addressed those concepts necessary for a thorough understanding of the key image simulation algorithms that underlie the Lincoln Laboratories RCS Toolbox software.

In addition to the current introduction the report is divided into four primary sections that treat the following topics. Section 2.0, Range Resolution and Signal Bandwidth, establishes the basic relations between range resolution and the bandwidth of a transmitted radar signal. Additionally, the similarity between the impulse and frequency responses of a linear system and the range and frequency responses of objects illuminated by stepped frequency radar signals is considered with respect to Fourier Transform methods.

Section 3.0, Cross Range Resolution and Doppler Frequency Processing, defines the Doppler frequency of a rotating radar scattering center and provides bounds on certain cross range resolution related quantities such as processing interval duration and sampling rate. This section also provides the intuitive, physical connection between Doppler and cross range resolution and serves as a bridge between time/Doppler processing and beam steering concepts.

Section 4.0, Cross Range Resolution and ISAR Image Focusing, revisits the topic of cross range resolution of rotating objects and casts the problem in

terms of steering a synthetically formed radar beam to particular points on an object of interest. The exact nature and effect of the Fast Fourier Transform (FFT) of a sequence of aspect variant magnitude and phase data at a fixed range is made clear. Specifically, the transform is shown to approximately steer or focus the synthetic beam in the cross range dimension. The final summary section reviews basic results and provides a recommendation for continuing efforts in the area of radar imaging, analysis and evaluation of rotating space objects.

The reader is assumed to have only a casual familiarity with array and synthetic array antenna and radar systems. In particular, the concepts that (a) long linear arrays act to decrease the real antenna beamwidth in the cross range direction and (b) that beam steering (focusing) is accomplished by adjusting the phases of individual antenna array elements based on focal point path length differences constitute an adequate technical background. We have attempted to initiate all analyses based on first principles. It should, however, be understood that a significant effort on the part of the reader may still be required.

## 2.0 Range Resolution and Signal Bandwidth

As shown in *Figure 2-1*, if a pulse of width  $\tau$  is transmitted by a radar, the received signal,  $V_r(t)$ , due to a collection of point scatterers, is a series of delayed versions of the transmitted pulse. As shown in 2-1(c) the time difference,  $t_2 - t_0$ , between the leading edge (LE) of the transmitted pulse and the leading edge of the return pulse from scattering center  $S_1$  is a measure of the distance of  $S_1$  from the radar,

$$r_{s_1} = \frac{c(t_2 - t_0)}{2} \quad (2.1)$$

where  $\frac{t_2 - t_0}{2}$  is the one way travel time to  $S_1$ . In order for two of the return pulses to be clearly separated (resolved in range) it is necessary that the radial distance between scattering centers correspond to at least the pulse

width  $\tau$ . That is, the separation distance which we define as the range resolution must take the form

$$\Delta r = \frac{C\tau}{2} \quad (2.2)$$

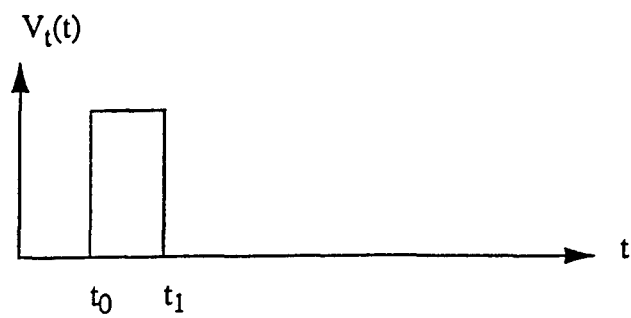
where the factor of  $1/2$  is necessary to convert  $\Delta r$  to a one way distance increment. In other words, the time,  $\frac{\tau}{2}$ , is the amount of time necessary for a wave to travel the distance  $\Delta r$ . If two scattering centers are located at ranges  $R$  and  $R + \Delta r$ , the leading edge of a transmitted pulse will be received from Range  $R$  after  $t = \frac{2R}{C}$  seconds. The trailing edge will be received at  $t = \tau + \frac{2R}{C}$ . The leading edge of the pulse received from the scatterer at range  $R + \Delta r$  will be received after  $t = \frac{2(R + \Delta r)}{C} = \frac{2R}{C} + \frac{2\Delta r}{C} = \frac{2R}{C} + \tau$ . Thus the trailing edge of the echo from range  $R$  and the leading edge of the echo from range  $R + \Delta r$  occur at the same time. In this way the two echo pulses are exactly separated in time.

With respect to part (c) of the figure, note that the return from  $S_3$  is of greater duration than that from  $S_1$  or  $S_2$ . The duration of the pulse is a measure of the range extent of a scattering element, while the height of the pulse is a measure of the ability of the element to scatter energy in the direction of the radar. In terms of bandwidth,  $B$ , the range resolution can be written

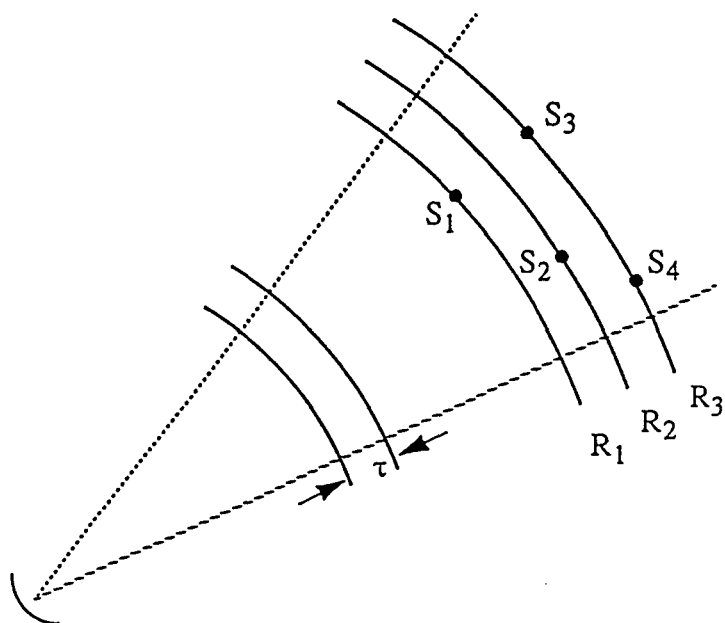
$$\Delta r = \frac{C}{2B} \quad (2.3)$$

where the approximation  $\tau \approx \frac{1}{B}$  derives from the fact that the first zero crossing (in frequency) of the Fourier Transform of a pulse of width  $\tau$  centered on the time origin occurs at  $f = \frac{1}{\tau}$  Hertz.

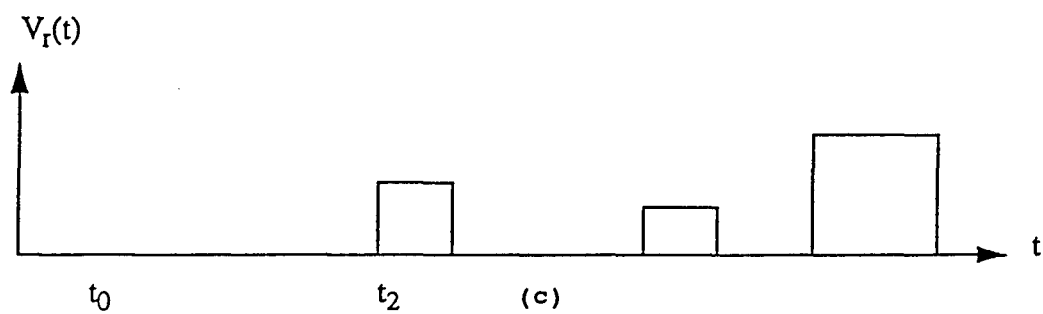
It is clear from Equation 2.2 that enhanced range resolution can be achieved by decreasing the width of the transmitted pulse. Equivalently,



(a)



(b)



(c)

Figure 2-1

Equation 2.3 indicates that resolution can be increased by increasing the bandwidth,  $B$ , of the pulse. In other words, the required range resolution can be obtained when an object (modeled as a collection of scattering elements in Figure 2-1) can be illuminated and its response measured over a wide band of frequencies. Any waveform that possesses the required bandwidth can be used. The specific form of the transmitted signal dictates the nature of the necessary signal processing.

In the language of Linear Systems Theory we note that as the pulse width approaches zero the transmitted signal approaches a delta function and the temporal impulse response,  $h(t)$ , of the object to the impulse,  $\delta(t)$ , is related to the frequency response,  $H(f)$  by the Fourier Transform.

$$H(f) = F\{h(t)\} \quad (2.4)$$

$$h(t) = F^{-1}\{H(f)\} \quad (2.5)$$

If the frequency response of a linear system (circuit) is desired, it is entirely feasible to simply input a set of sinusoids of varying frequency one at a time and to measure the system output (response) for each frequency. Due to the linear nature of the system, each response will be a sinusoid of modified magnitude and phase at a frequency identical to that of the input signal. The system frequency response,  $H(f)$ , is then simply the superposition of the individual responses and can be written as a set of magnitude and phase angles,  $(E(f_i), \text{Angle}(f_i))$  or equivalently as a set of complex values,  $a(f_i) + jb(f_i)$  where

$$E(f_i) = [a^2(f_i) + b^2(f_i)]^{1/2} \quad (2.6)$$

$$\text{Angle}(f_i) = \text{Tan}^{-1} \left[ \frac{b(f_i)}{a(f_i)} \right] \quad (2.7)$$

If  $H(f)$  can be measured over a large enough frequency band the system impulse response may be found approximately as the DFT of  $H(f)$ ,

$$h(n) \approx \frac{1}{2\pi} \sum_{-\infty}^{\infty} H(f) e^{j2\pi fn} \quad (2.8)$$

where  $h(n)$  is discrete.

In terms of an  $N$  point FFT

$$h(n) \approx \frac{1}{N} \sum_{k=0}^{N-1} H(k) e^{j2\pi kn/N} \quad (2.9)$$

for  $N$  discrete frequencies,  $k=0, 1, \dots, N-1$ , and  $N$  discrete times  $n=0, 1, \dots, N-1$ .

Because electromagnetic fields are also linear in nature the described procedure can be used to generate a time (range) resolved signal from an object frequency response,  $H(f)$ , as follows. This procedure, sometimes termed synthetic range resolution, is applicable for use in connection with RCS instrumentation range measurement systems or software simulation techniques.

Specifically, assume that an object of interest is placed on a high precision turntable and rotated to some initial position  $\phi_0$ . In this position a cw radar tuned to frequency  $f_1$  illuminates the entire object. The return signal (also at  $f_1$ ) is received, and phase and magnitude are recorded. The process is repeated for a discrete set of frequencies  $f_1, f_2, \dots, f_N$ .

In this way the frequency response is formed

$$H(f_k) = \sum_{n=0}^{N-1} a(r_n, f_k) e^{-j2\pi \left( \frac{2r_n}{c} \right) f_k/N}, \quad (2.10)$$

for  $k=0, 1, \dots, N-1$  discrete frequencies, as an  $N$  point FFT of the function  $a(r_n, f_k)$ . We interpret  $a(r_n, f_k)$  as the scattered signal received



from all object scattering elements at range  $r_n$  due to frequency  $f_k$ . With respect to the Lincoln Laboratories simulation,  $a(r_n, f_k)$  is calculated as a physical optics approximation for each scattering element at the prescribed range and frequency. The required range return is then formed quite simply as the inverse FFT of the measured or computed frequency response.

$$a(r_n) = \sum_{k=1}^N H(f_k) e^{j2\pi \left(\frac{2r_n}{c}\right) f_k / N} \quad (2.11)$$

for  $n=0$  to  $N-1$ .

Suppose, for example, that a range resolution of 25 cm is required. Then from Equation 2.3  $B = 600$  MHz. If the object is assumed to have a maximum range extent of 10 m, 40 range bins, each of length  $\Delta r = 0.25$  m will be required. Then, due to the nature of the  $N$  point FFT,  $N = 40$  frequency responses in the range  $\left(f_c - \frac{B}{2}, f_c + \frac{B}{2}\right)$  must be computed. This corresponds to a frequency separation increment of  $\frac{B}{40} = 15$  Mhz. Because the range response of Equation 2.11 is formed from a sampled version of the continuous frequency response, range ambiguities may result if the increment  $\Delta f$  is chosen incorrectly. The relation between range ambiguity and a stepped frequency response is discussed in the following section.

## 2.1 Discrete Frequency Sampling

The effect of illuminating an object with a set of discrete frequencies is best illustrated as follows. If a group of frequencies,  $f_0, f_1, f_2, \dots, f_N$ , with constant spacing,  $\Delta f$ , are used to illuminate an object one at a time in order to measure the frequency response  $H(f_k)$ , the effect is the same as transmitting the signal

$$V_t(t) = \cos(2\pi f_0 t) + \cos(2\pi f_1 t) + \dots + \cos(2\pi f_N t) \quad (2.12)$$

The Fourier Transform of this signal is shown in Figure 2-2(a) for  $N=3$ .

$V_t(t)$  can be sketched as the inverse transform of (a) if we note that  $V_t(f)$  can be formed as the product of an impulse train with frequency spacing  $\Delta f = \frac{B}{N}$  and a rectangular window of bandwidth,  $B$  as shown in 2.2(b).

$V_t(t)$  must then take the form of the convolution of the inverse transforms of these two frequency functions. The operation and its result is shown in 2.2(c) and (d). We see that  $V_t(t)$  is a periodic set of sync like pulses extending from positive to negative infinity with period  $N/B$ , which is the effective Interpulse Period (IPP) for the transmitted signal. If an echo returns from the pulse centered on  $t = 0$  but arrives after the pulse at  $t = \frac{N}{B}$ , it will mistakenly be interpreted as an echo due to the second pulse. Therefore, the range associated with this echo will also be in error. A received echo must occur before the next pulse is transmitted if ambiguous range returns are to be avoided. That is, the echo must be received approximately at  $t = \frac{N}{B}$ . An echo occurring at  $t = \frac{N}{B}$  corresponds to a scattering center at range

$$\begin{aligned} R_u &= \frac{c\left(\frac{N}{B}\right)}{2} \\ &= \frac{c}{2\Delta f} \end{aligned} \quad (2.13)$$

The range,  $R_u$ , is called the maximum unambiguous range. In order to avoid ambiguous range returns  $R_u$  should be made large. As indicated by Equation 2.13, this corresponds to decreasing  $\Delta f$ . As  $\Delta f \rightarrow 0$   $R_u \rightarrow \infty$  and  $V_t(t)$  becomes a single pulse.

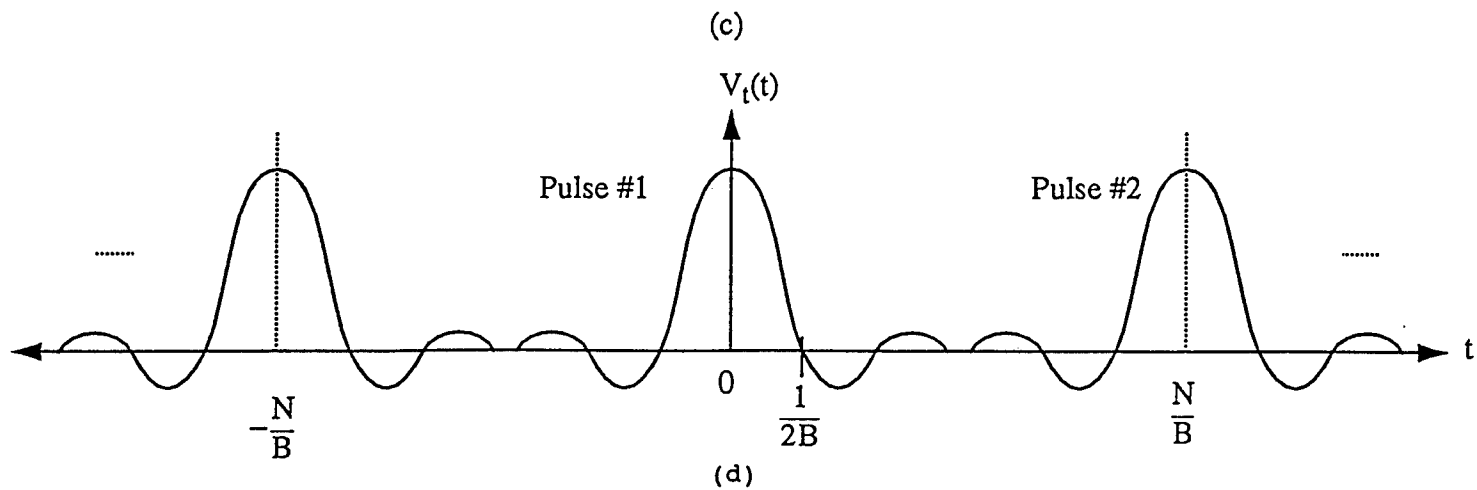
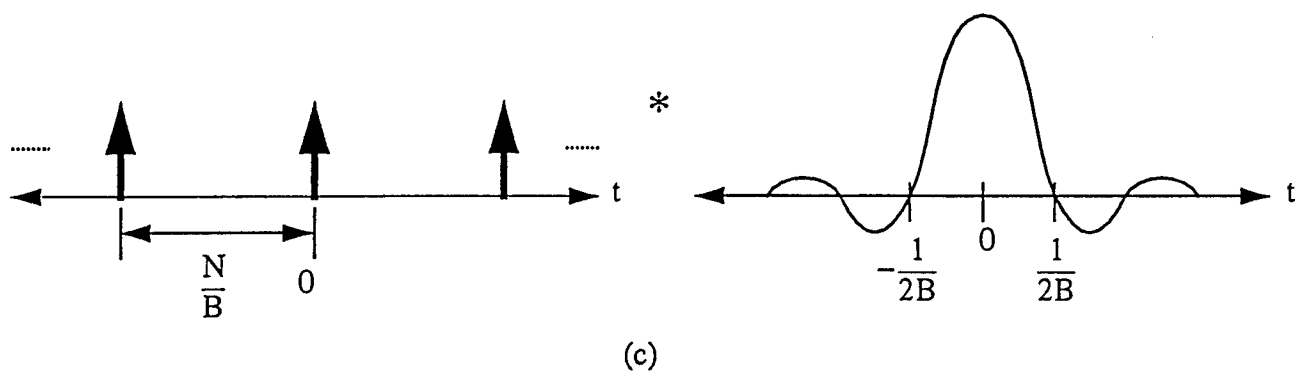
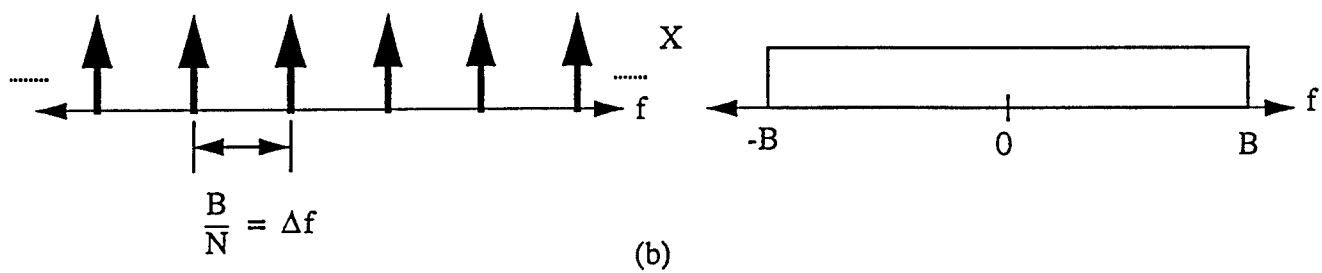
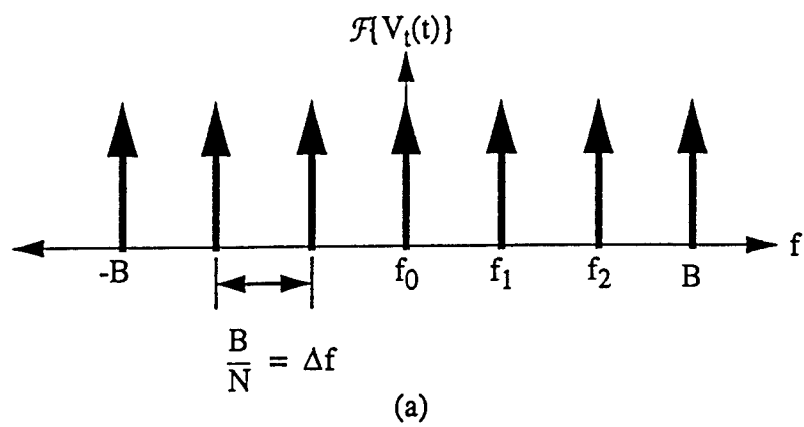


Figure 2-2

Consider an object with a total range extent of  $L$  meters which has scattering centers located at ranges  $R$  and  $R + L$  as shown in Figure 2-3.

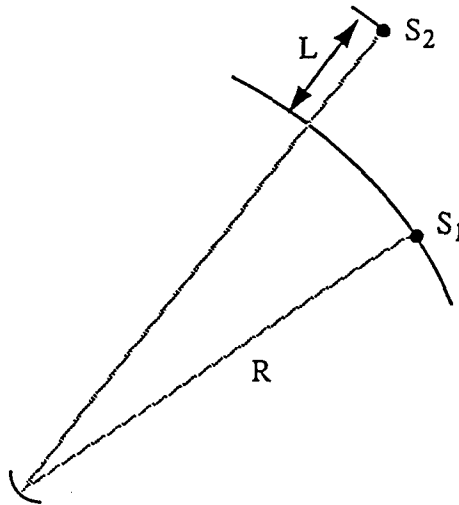


Figure 2-3

To insure that an echo from  $S_2$  due to pulse 1 will not be received after pulse 2 has been transmitted we must fix the interpulse period,  $IPP = \frac{N}{B} = \frac{1}{\Delta f}$ , such that  $R_u = L$ . That is, we simply set  $R_u = L$  in Equation 2.13 and solve for  $\Delta f$ .

$$\Delta f = \frac{c}{2L} \quad (2.14)$$

If  $\Delta f$  is chosen according to Equation 2.14 to avoid range ambiguity, and the total bandwidth is chosen based on the desired  $\Delta r$  with the aid of Equation 2.3 as

$$B = \frac{c}{2\Delta r}, \quad (2.15)$$

then the number of frequency increments becomes

$$N = \frac{B}{\Delta f} = \frac{\frac{c}{2\Delta r}}{\frac{c}{2L}} = \frac{L}{\Delta r}. \quad (2.16)$$

The result is satisfying intuitively as well as with respect to the form of the  $N$  point FFT. Note that the resolution can be increased (i.e.  $\Delta r$  decreased) by increasing  $B$ , and hence  $N$ , without modifying  $\Delta f$ .

### 3.0 Cross Range Resolution and Doppler Frequency Processing

In the case of a rotating three dimensional reflecting object and a stationary radar platform the doppler shift of the return signal may be exploited to enhance the cross range (azimuth) resolution - that is, the resolution in a direction normal to both the axis of rotation and the radar line of sight (RLOS). The situation is shown for a two dimensional object in Figure 3-1. Note that for purposes of analysis the object is modeled as a set of rigidly connected scattering centers in the  $x/y$  plane and that the real antenna beamwidth,  $\alpha$ , is shown only in one dimension.

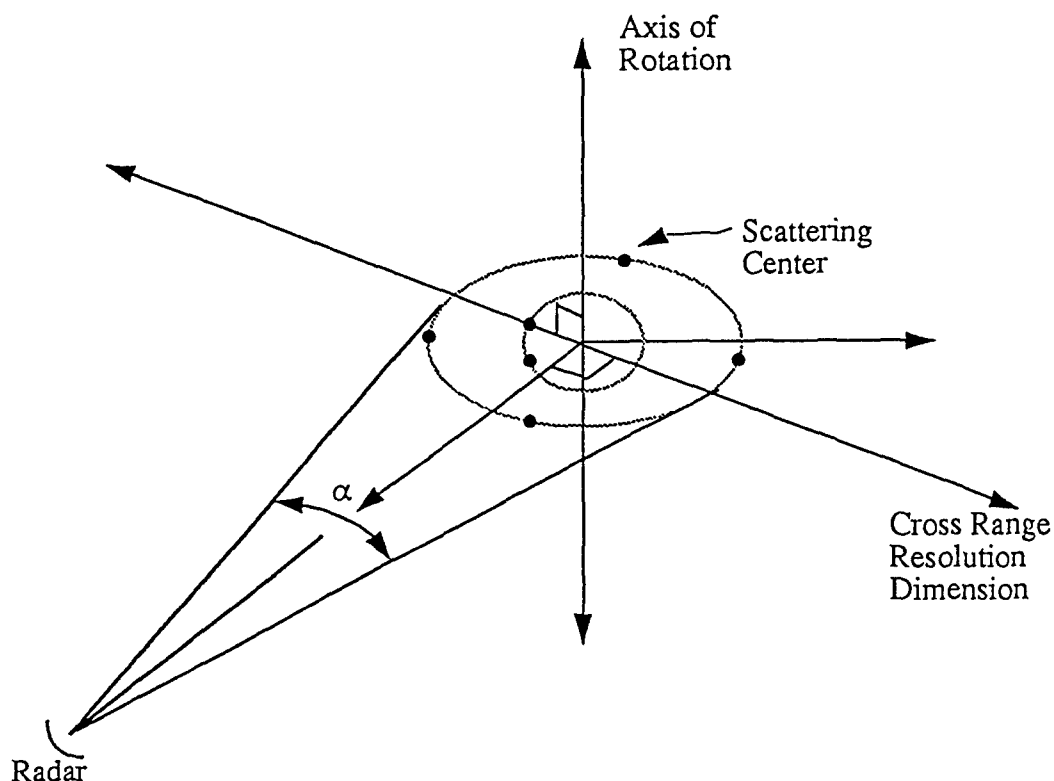


Figure 3-1

Spectral analysis of the signal returned from such a rotating target will exhibit distinct components at frequencies proportional to the radial components of velocity between the scattering centers and the radar. See Figure 3-2 where the velocity vectors of several scattering centers have been resolved into components tangential and orthogonal to directions of wave propagation.

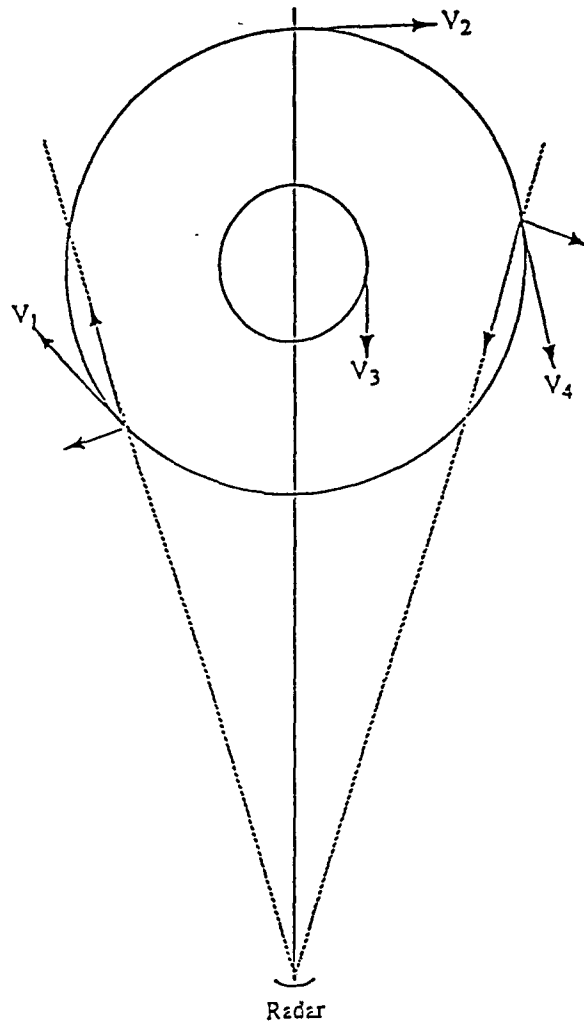


Figure 3-2

The relations between scattering center locations and scattering center doppler frequencies due to varying velocity components in the direction of propagation are developed as follows. Let the object rotate at constant angular rate  $\Omega$ , and let  $d$  be the radial distance from a scattering center to the center of the object as shown in Figure 3-3.

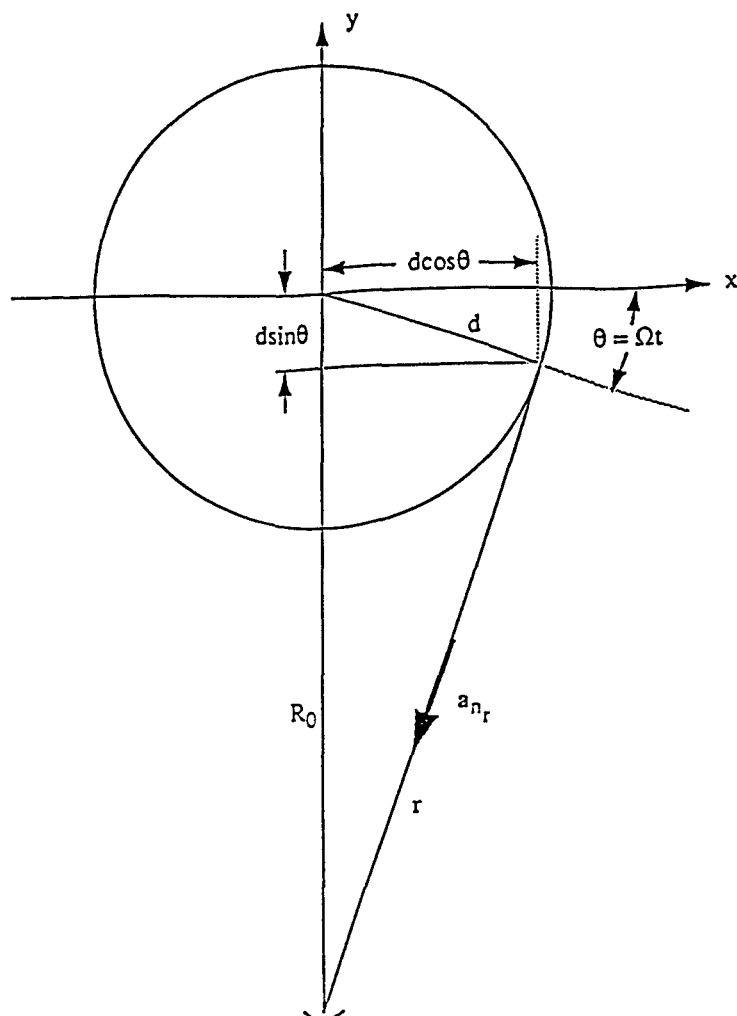


Figure 3-3

Ignoring polarization of the wave, let the transmitted signal take the form  $E_t(t) = RE\{e^{j\omega_0 t}\}$ .

At time  $t$ , the distance  $r$  shown in Figure 3.3 is approximately

$$\begin{aligned} r &= R_0 - d \sin \Omega t \\ &= R_0 - d \sin \theta \end{aligned} \quad (3.1)$$

This approximation is valid for small rotation angles,  $\theta = \Omega t$ , and for  $R_0 \gg d$ . For illustration purposes the received signal may be considered a replica of the transmitted signal delayed by the round trip travel time,  $T = \frac{2r}{c}$ :

$$\begin{aligned}
E_r(t) &= RE\{e^{j\omega_o t - j2k_o r}\} \\
&= RE\left\{e^{j(\omega_o t - j2(\frac{2\pi}{\lambda})r)}\right\} \\
&= RE\left\{e^{j\left(\omega_o t - \frac{4\pi}{\lambda}(R_o - d\sin\Omega t)\right)}\right\} \\
&= RE\left\{e^{j\left(\omega_o t - \frac{4\pi R_o}{\lambda} + \frac{4\pi d\sin\Omega t}{\lambda}\right)}\right\}
\end{aligned} \tag{3.2}$$

where  $k_o = \frac{2\pi}{\lambda}$  is the free space wave number and the factor  $2k_o r$  is the two way travel distance in radian wavelengths.

The first term in the argument of the exponential is the carrier phase. The second term is constant (for a given  $\lambda$  and  $R_o$ ). The third term is a variable phase shift and depends on both the distance,  $d$ , of the scattering center from the axis of rotation and the angular rate of rotation  $\Omega$  - or equivalently on the total angle of rotation,  $\theta = \Omega t$ . We define the cyclic doppler frequency of an individual scattering center as the time rate of change of phase of the received waveform,

$$\begin{aligned}
f_d &= \frac{1}{2\pi} \frac{d}{dt} \left[ \frac{-4\pi R_o}{\lambda} + \frac{4\pi d\sin\Omega t}{\lambda} \right] \\
&= \frac{1}{2\pi} \left[ \frac{4\pi d}{\lambda} (\Omega \cos\Omega t) \right]
\end{aligned} \tag{3.3}$$

or with  $x = d\cos\Omega t$  as shown in Figure 3-3.

$$f_d = \frac{2\Omega x}{\lambda} \tag{3.4}$$

Thus, we see that points  $x$  in the cross range direction (along the  $x$  axis) are related to  $f_d$  according to

$$x = \frac{\lambda f_d}{2\Omega} \tag{3.5}$$



The doppler frequency can also be written in terms of  $\theta = \Omega t$ , in which case we define the doppler phase as

$$\begin{aligned}
 f_{dp} &= \frac{1}{2\pi} \frac{d}{d\theta} \left[ \frac{-4\pi R_o}{\lambda} + \frac{4\pi d \sin\theta}{\lambda} \right] \\
 &= \frac{1}{2\pi} \left[ \frac{4\pi d \cos\theta}{\lambda} \right] \\
 &= \frac{2d \cos\theta}{\lambda} \\
 &= \frac{2x}{\lambda}
 \end{aligned} \tag{3.6}$$

In this case we find 
$$x = \frac{\lambda f_{dp}}{2}. \tag{3.7}$$

This direct relation between  $f_d$  (or  $f_{dp}$ ) and cross range position,  $x$ , permits separation of scattering points in the cross range dimension. The resolving power of any doppler processing system depends in one way or another on the ability to distinguish between frequencies  $f_d$  and  $f_d + \Delta f_d$ . We call  $\Delta f_d$  the system doppler resolution (frequency). The time period of a sinusoid of this frequency is  $T = \frac{1}{\Delta f_d}$ . Thus, as  $\Delta f_d$  decreases (better resolution),  $T$  increases. In order to detect a frequency difference,  $\Delta f_d$ , a system must observe (process) the signals for at least  $T = \frac{1}{\Delta f_d}$  seconds. This provides a lower bound on the processing or observation interval,  $T$ . In order to find an upper bound for the processing interval  $T$ , and hence  $\theta = \Omega T$ , we proceed as follows. Beginning with our expression for cross range position

$$x = \frac{\lambda f_d}{2\Omega}, \tag{3.8}$$

we find  $\Delta x$ , the cross range resolution quite simply as

$$\begin{aligned}
 \Delta x &= \frac{\lambda \Delta f_d}{2\Omega} \\
 &= \frac{\lambda}{2\Omega T} \\
 &= \frac{\lambda}{2\theta}
 \end{aligned} \tag{3.9}$$

Unfortunately  $\Delta X$  cannot be made arbitrarily small by arbitrarily increasing the processing interval,  $T$ , since over large processing intervals the "instantaneous" frequency of an individual scattering center will change as a function of position. That is, the velocity of the rotating scatterer is position dependent and may vary greatly over the processing period  $T$ . This means that during a processing interval sufficiently long to give the desired cross range resolution, points on the rotating object may move through several resolution cells ( $\Delta x$  or  $\Delta f_d$ ) [Brown], [Mensa], [Walker], [Linear Periodogram Imagery Part I]. Mensa, 1991, bounds  $T$  and thus  $\theta$  by pointing out that a scatterer will remain in a single cross range resolution cell,  $\Delta X$ , during the processing interval if the arc length  $R\Omega T = R\theta$  is less than the distance  $\Delta X$ .

Figure 2-4 indicates the general situation for scatters at various positions. From the figure it is clear that  $R\theta$  is in general greater than  $\Delta X$ . The condition (engineering approximation)  $R\theta \leq \Delta X$  appears then to be a conservative bound on both  $\Delta X$  and  $T$ . Taking  $\Delta X \geq R\Omega T = R\theta$  and substituting the equality in our expression  $\Delta X = \frac{\lambda}{2\Omega T}$ , we find,  $\frac{\lambda}{2\Omega T} = R\Omega T$ ,

or equivalently

$$1) \quad T \leq \sqrt{\frac{\lambda}{2R\Omega^2}} = \frac{1}{\Omega} \sqrt{\frac{\lambda}{2R}} \quad (3.10)$$

$$2) \quad \theta \leq \sqrt{\frac{\lambda}{2R}}. \quad (3.11)$$

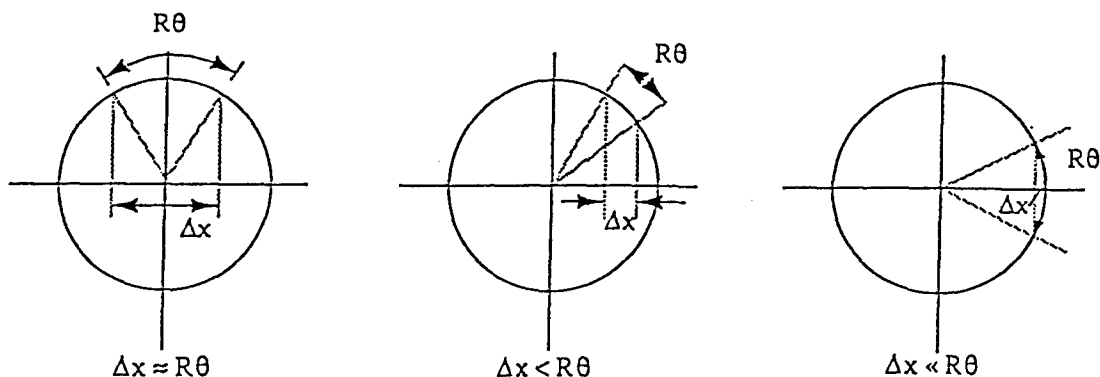


Figure 3-4

Substituting the above expression for  $\theta$  in  $\Delta x \geq R\theta$  we also find

$$3) \quad \Delta x \geq \sqrt{\frac{\lambda R}{2}} \quad (3.12)$$

which is a well known bound on the cross range resolution, [Mensa], [Brown], [Walker], in terms of wavelength and the radius of the rotating body. The Lincoln Laboratories report, "Linear Periodogram Imaging", does not provide this important result. It does, however, provide variations of (1) and (2) in the form of equation (36). This equation is somewhat more complex than 1) and 2) above and less useful - particularly from the point of view of the RCS Toolbox end user. That is, (2) provides an upper bound on the processing interval,  $\theta$ , such that a scattering center will be confined to a single cross range resolution cell,  $\Delta x$ . It should be noted that the same bounds on  $\Delta x$ ,  $T$ , and  $\theta$  can be derived in terms of quadratic phase error tolerance [Walker].

If these equivalent conditions on  $\theta$  and  $T$  are violated, doppler frequency analysis will produce degraded imagery [Mensa] - unless techniques for compensation of scattering center movement through resolution cells are applied. While such techniques have been documented [Brown, Mensa, Walker], they are not a part of the LL RCS Toolbox.

Returning to our expressions for  $x$  and  $\Delta x$ ,

$$x = \frac{\lambda f_d}{2\Omega} \quad (3.13)$$

$$\begin{aligned} \Delta x &= \frac{\lambda \Delta f_d}{2\Omega} \\ &= \frac{\lambda}{2\Omega T} \\ &= \frac{\lambda}{2\theta} \end{aligned} \quad (3.14)$$

it is clear that if the return signal from a single range bin is processed over a period of time,  $T = \frac{1}{\Omega} \sqrt{\frac{\lambda}{2R}}$ , in such a way that the doppler frequency is extracted as a function of time,  $f_d(t)$  can be used to map the voltages of the received signal into cross range(x direction) resolution increments (bins) of width  $\Delta x$ .

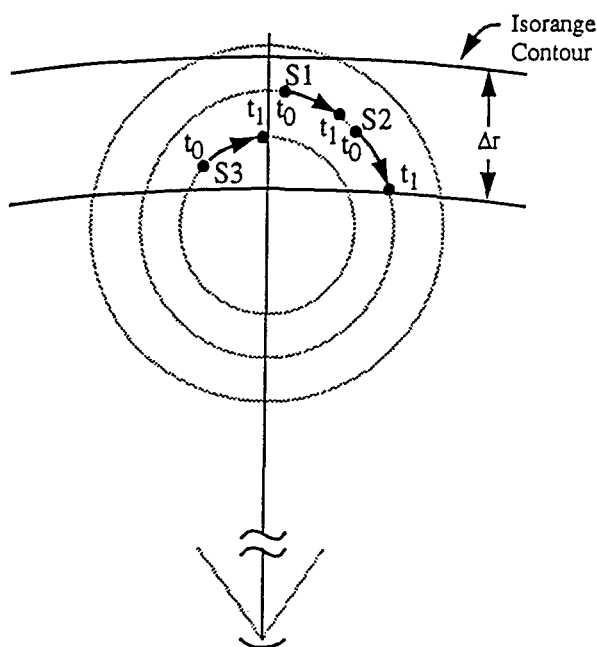


Figure 3-5

At time  $t_0$  the signal returned from the range bin pictured in Figure 3-5 is composed of the sum of the scattered energy (signals) from three scattering elements. Corresponding to the received signal at  $t_0$  there is a single doppler frequency due to the sum of all three doppler shifted signals. At time  $t_1$  the object, and hence each scattering center, will have rotated by the angular amount  $\Delta\theta = \Omega t_1 - \Omega t_0$ . The signal returned from the range bin is again the sum of three scattered signals. Corresponding to this signal,  $V(t_1)$ , there is yet another doppler frequency. If the object is allowed to rotate at a constant angular rate,  $\Omega$ , for a period of  $T$  seconds, it is clear that the radar, in receive mode, can collect a signal  $V(t)$  of duration  $T$ . It is critical

that  $T$  and hence  $\theta = \Omega T$  be taken small enough so that the doppler frequency from any one scattering center does not change "significantly" over the rotation interval,  $\theta$ . This is our condition  $\theta \leq \sqrt{\frac{\lambda \Omega}{2}}$ . If this condition is met we can associate a single doppler frequency,  $f_{d_i}$ , with each scattering center during the processing period  $T$  - or, equivalently, over the rotation interval,  $\theta$ . That is,  $V(t)$  can be written,

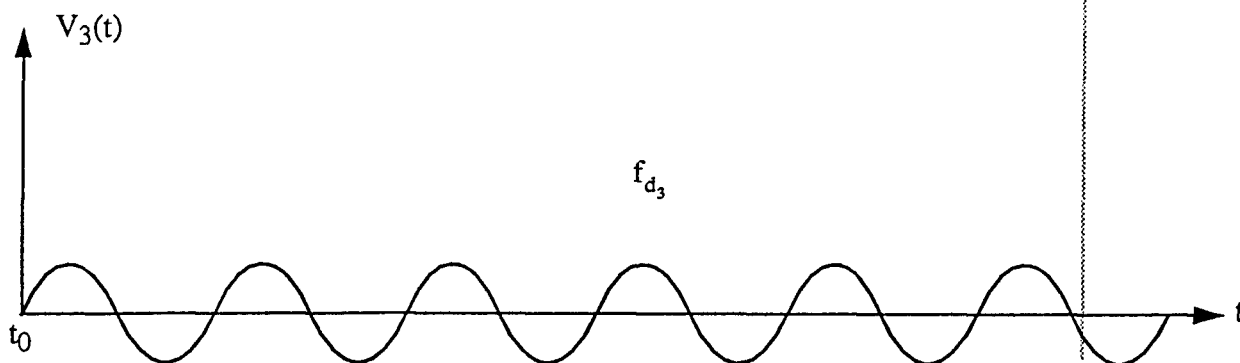
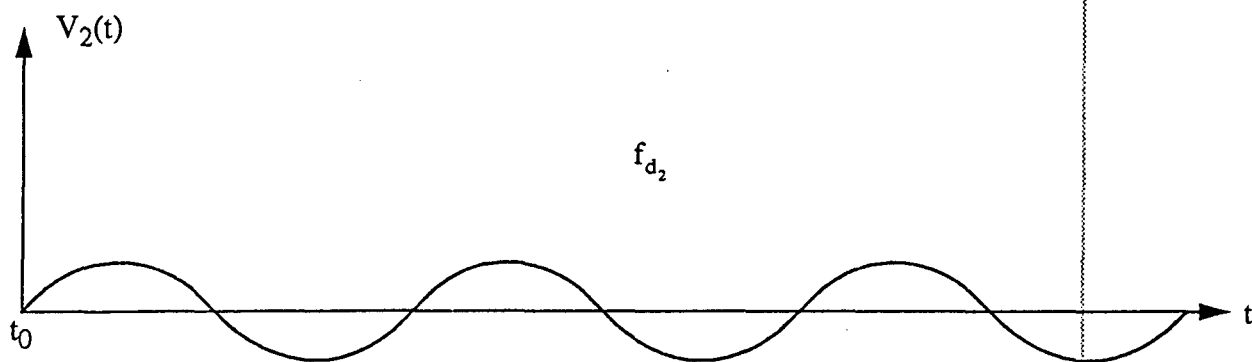
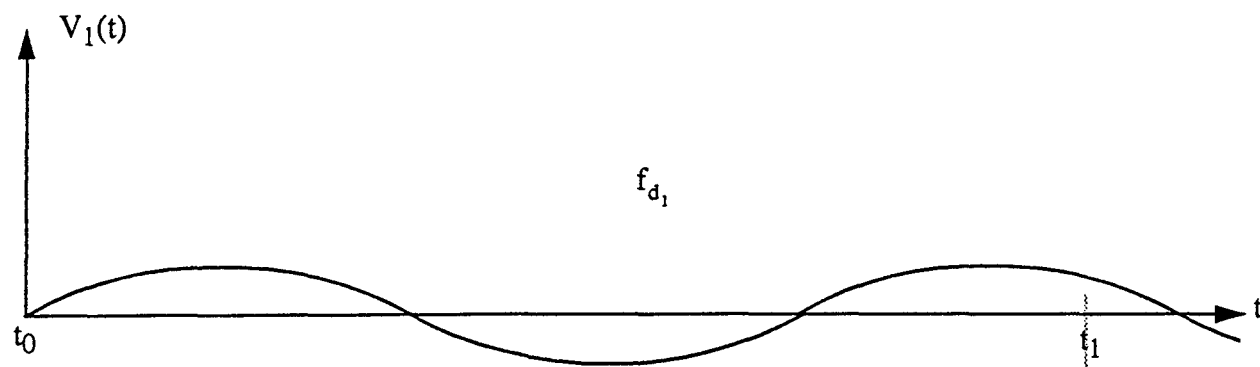
$$V(t) = \sum_{i=1}^N V_i(t) , \quad (3.15)$$

where  $N$  = the constant number of scattering centers in a particular range bin at any time  $0 \leq t \leq T$ . In other words, we assume (require) that scattering centers will not migrate between range or cross range bins during the processing interval,  $T$ . The result of scattering centers "walking" between resolution cell bins manifests itself as focusing error which results in blurred imagery.

Figure 3-6 depicts signals returned from the three scattering centers of Figure 3-5 over a processing interval  $T$  after doppler frequency extraction.

Notice that the amplitude of the signal for any one scatterer is shown as constant. This is an idealized case. In fact, scattering signals may disappear completely during  $T$  due to aspect sensitivity of the scatterer.

Taking the Fourier Transform of  $V(t)$  will resolve the scattered signals  $V_1(t), V_2(t), \dots, V_N(t)$ , in frequency space as shown in Figure 3-7. This is because each of the  $V_i(t)$  corresponds to a particular doppler frequency that is a function of the position of the scattering center,  $S_i$ , along the  $X$  direction within the single range bin.



$T = t_1 - t_0$   
 No doppler frequency variation  
 over  $\theta = \Omega T$

Figure 3-6

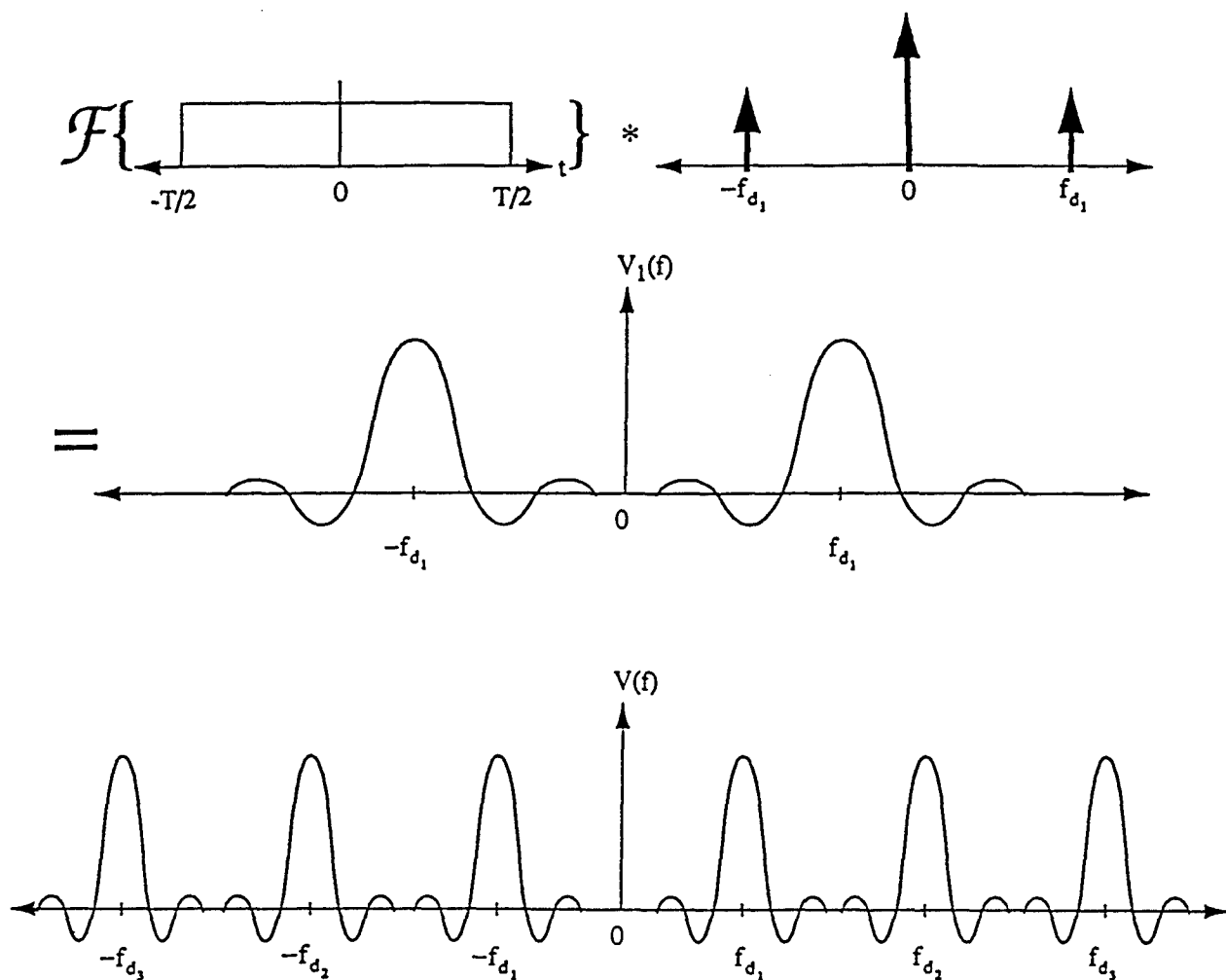


Figure 3-7

If the Fourier Transform  $V(f)$  is generated via a FFT from (discrete) sampled data,  $V_s(t)$ , the signal  $V(t)$  must be sampled at a rate consistent with the Nyquist criterion -- that is, twice the maximum frequency content of  $V(t)$ . Taking  $f_{d_i} = \frac{2\Omega x}{\lambda}$  (see Figure 3-3 where  $x=d$ ) and setting  $x=R$  (the maximum radius of the object) we find  $f_{d_{\max}} = \frac{2\Omega R}{\lambda}$ . Thus the Nyquist rate is

$$2f_{d_{\max}} = \frac{4\Omega R}{\lambda} \text{ samples/sec.} \quad (3.16)$$

or

$$\Delta t = \frac{\lambda}{4\Omega R} \quad (3.17)$$

If the processing interval is  $T$  seconds  $n = \frac{T}{\Delta t} = \frac{4R\theta}{\lambda}$  samples will be required. The angular sampling increment,  $\Delta\theta$ , is found as

$$\Delta\theta = \frac{\theta}{n} = \frac{\theta}{\frac{4R\theta}{\lambda}} = \frac{\lambda}{4R} \quad (3.18)$$

With the introduction of sampled signals the transform operations shown in Figure 3-7 must be modified somewhat. That is,  $V(f)$  must be convolved with the transform of a windowed version of an infinite pulse train where pulse spacing (in the time domain) is determined by the sampling rate and given by Equation 3.17.

The shape of the window function (of length  $T$ ) will, of course, influence the transform,  $F\{V(t)\}$ .

Thus far the discussion of cross range resolution enhancement and Fourier Transform analysis has been intentionally somewhat heuristic. Section 4.0 which takes up the topic of ISAR focusing will make the relation between cross range resolution and the Fourier Transform exact.

Before preceding to the next section we would also point out that cross-range profiles and hence range/cross-range imagery generated from this type of processing cannot be uniquely associated with a particular object aspect, but only with a range of aspect angles between 0 and  $\theta$  degrees.



#### 4.0 Cross Range Resolution and ISAR Image Focusing

The primary results from Section 3 are listed for convenience in Table 4.1 below.

Table 4.1

$f_d = \frac{2\Omega x}{\lambda}$	Cyclic Doppler Frequency	Eqn. (3.4)
$x = \frac{\lambda f_d}{2\Omega}$	Cross Range Position	Eqn. (3.5)
$T \geq \frac{1}{\Delta f_d}$	Minimum Processing Interval	
$\Delta x = \frac{\lambda}{2\theta}$	Cross Range Resolution	Eqn. (3.9)
$T \leq \frac{1}{\Omega} \sqrt{\frac{\lambda}{2R}}$	Maximum Processing Interval	Eqn. (3.10)
$\theta \leq \sqrt{\frac{\lambda}{2R}}$	Maximum Rotation Period	Eqn. (3.11)
$\Delta x \geq \sqrt{\frac{\lambda R}{2}}$	Optimal Cross Range Resolution	Eqn. (3.12)
$\Delta \theta = \frac{\lambda}{4R}$	Angular Processing Increment	Eqn. (3.17)
$\Delta t = \frac{\lambda}{4\Omega R}$	Temporal Processing Increment	Eqn. (3.18)

For purposes of the present discussion we begin by pointing out that the geometry of Figure 3-1 in which the target rotates with respect to a stationary radar antenna is completely equivalent to the geometry of Figure 4-1 in which the object is stationary (no rotation) and the radar travels along a circular arc centered on the target center. Therefore, the results of Table 4.1 remain valid for the discussion that follows.

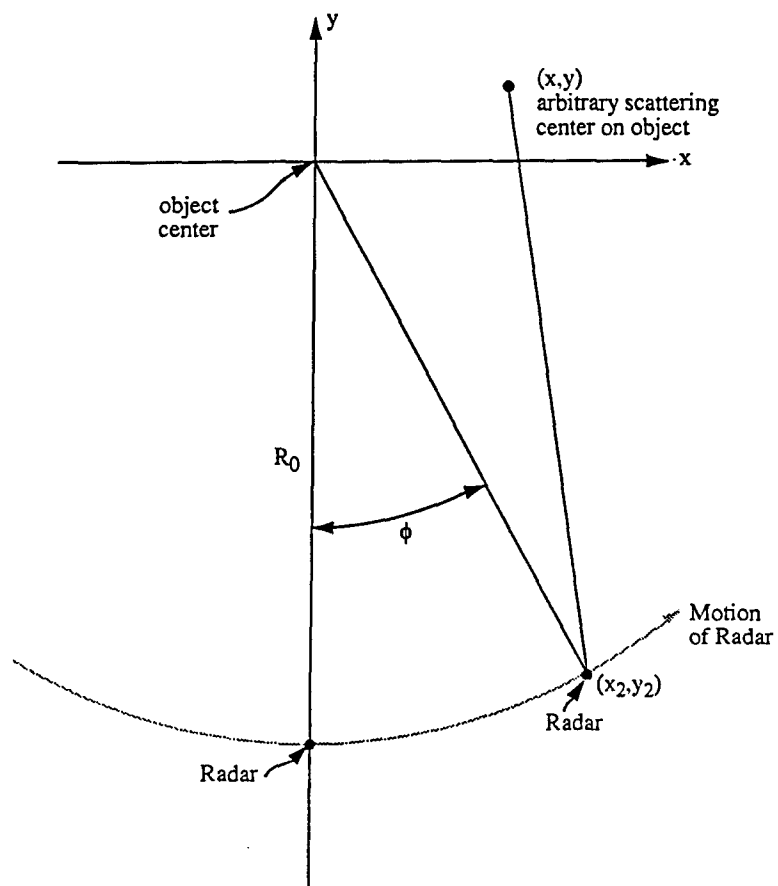


Figure 4-1

Notice that  $\phi$ , in this figure locates the position of the radar, at Range  $R_0$  from the object center, at a particular point on the circular arc. Thus, this  $\phi$  does not correspond to the  $\theta$  of Table 4-1 which, with respect to Figure 4-1, should be thought of as the allowable travel (in radians) of the radar along the circular arc.

If the full path (of length  $R_0\theta$ ) of the radar along this arc is thought of as an optical lens, it becomes apparent that the data (return signal) collected from scattering center  $(X,y)$  by the radar at each point along this arc should be processed (somehow) exactly as a lens would process the data in order to "focus" all the signals entering the lens from point  $(X,y)$  at a particular point on the image plane.

Figure 4-2 shows the idealized operation of focusing the signals scattered by point  $(X,y)$ .

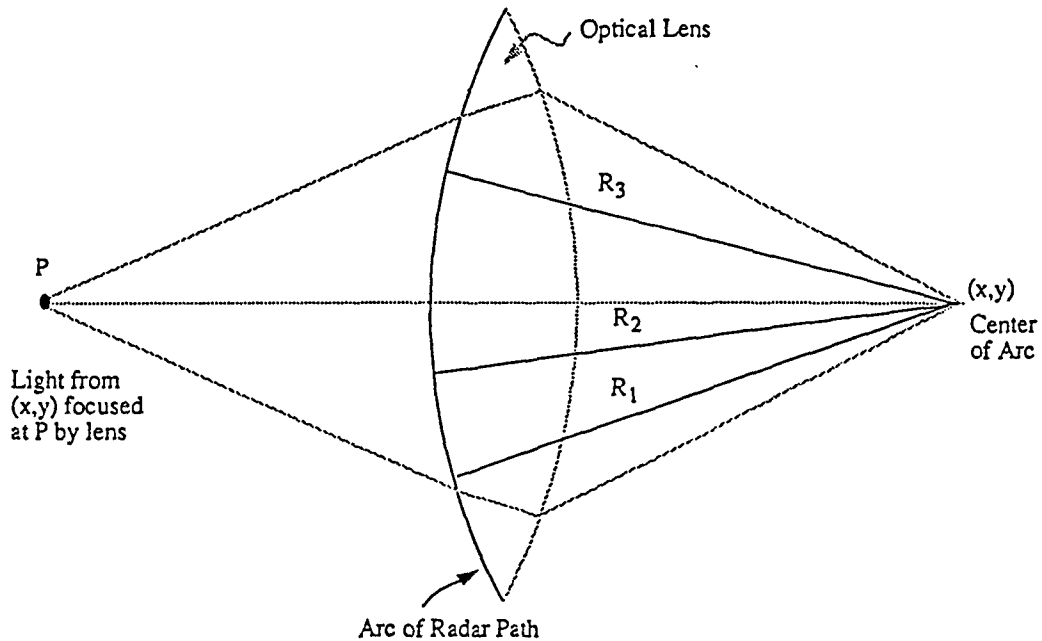


Figure 4-2

Notice that the point  $(X,y)$  has been relocated to the center of the circular arc. In this way the signals collected by the radar at  $R_1, R_2$  and  $R_3$  are all in phase. This is because the path lengths (Radi)  $R_1, R_2$  and  $R_3$  are all equal. Thus, the two way travel distance of each radar signal is the same. In terms of the optical lens, it is the purpose of the lens curvature, thickness and permittivity to adjust the various optical paths such that they are of equal length.

Unfortunately, arbitrary points  $(X,y)$ , as shown in Figure 4-1, are not at the center (focus point) of the circular arc along which the radar operates. Hence, the received signals at various points  $\phi_n = n\Delta\theta$  along the "synthetic aperture" must be processed in order to correct for focusing error (path length

differences). In the language of radar engineering, we say the aperture must be "steered" to various points  $(X, y)$  in order to achieve proper focusing.

The distance,  $d[(X, y), (x_2, y_2)]$  between an arbitrary point on the circular aperture and an arbitrary scattering center is found as follows:

$$\begin{aligned}
 x_2 &= R_o \sin \phi \\
 y_2 &= -R_o \cos \phi \\
 d(\phi, x, y) &= \sqrt{(x-x_2)^2 + (y-y_2)^2} \\
 &= \sqrt{x^2 - 2xR_o \sin \phi + R_o^2 \sin^2 \phi + y^2 + 2yR_o \cos \phi + R_o^2 \cos^2 \phi} \quad (4.1) \\
 &= \sqrt{R_o^2 - 2R_o(x \sin \phi - y \cos \phi) + x^2 + y^2} \\
 &= R_o \sqrt{1 + \frac{2}{R_o}(-x \sin \phi + y \cos \phi) + \frac{1}{R_o^2}(x^2 + y^2)}
 \end{aligned}$$

The two way path length is then  $2d(\phi, x, y)$ , and we can write the received field at  $\phi$  due to a scattering center at point  $(X, y)$  as

$$\begin{aligned}
 V(\phi, x, y) &= E_o e^{-j2k\hat{a}_{n_r} \cdot \bar{R}} \\
 &= E_o e^{-j \frac{4\pi}{\lambda R_o} \left[ 1 + \frac{2}{R_o}(-x \sin \phi + y \cos \phi) + \frac{1}{R_o^2}(x^2 + y^2) \right]^{1/2}} \quad (4.2)
 \end{aligned}$$

where  $k\hat{a}_{n_r} \cdot \bar{R} = 2d(\phi, x, y)$ , and  $E_o$  is a scalar value proportional to the strength of the scattered signal. The argument of this exponential gives the phase variation of the received signal (from any  $(X, y)$ ) across the circular aperture as a function of  $\phi$ . In order to fully focus the aperture on a given point  $((X, y))$  we must process each received signal (at each  $\phi$ ) such that there is zero phase variation in the received signals across the aperture. In this way

the result of the coherent summation of the signals will be a maximum. This can be accomplished if the quantity:

$$e^{j4\pi \frac{R_o}{\lambda} \left[ 1 + \frac{2}{R_o} (-x \sin \phi_i + y \cos \phi_i) + \frac{1}{R_o^2} (x^2 + y^2) \right]^{1/2}} \quad (4.3)$$

is added to each of the responses,  $V_i(x, y, \phi) = V(x, y, \phi_i)$ . That is, the focused response of the synthetic aperture steered to the point  $(x, y)$  is

$$G(x, y) = \sum_{\phi_i} V_i(x, y, \phi) e^{j4\pi \frac{R_o}{\lambda} \left[ 1 + \frac{2}{R_o} (-x \sin \phi_i + y \cos \phi_i) + \frac{1}{R_o^2} (x^2 + y^2) \right]^{1/2}} \quad (4.4)$$

In terms of the rotating object described in Section 3, this operation must be carried out for each scattering center (point  $(x, y)$  in a given range bin) with the number of terms in each sum given by  $\frac{\theta}{\Delta\theta}$ .

In order to reduce the computational overhead of this operation we begin by expanding the argument of the exponential in a binomial series,

$$(1+x)^k = 1 + kx + \frac{k(k-1)x^2}{2!} + \dots \quad (4.5)$$

Using only the first two terms in the series we find

$$\left[ 1 + \frac{2}{R_o} (-x \sin \phi + y \cos \phi) \right]^{1/2} = 1 + \frac{1}{R_o} [-x \sin \phi + y \cos \phi] \quad (4.6)$$

where the term  $\frac{1}{R_0} (x^2 + y^2)$  has been neglected (i.e., assume  $R_0 \gg x, y$ ) prior to expansion.

The further assumption that  $\phi_{\max} = \theta$  is very small implies

$$\begin{aligned} \sin \phi &\approx \phi \\ \cos \phi &\approx 1. \end{aligned} \quad (4.7)$$

The expression may then be approximated as

$$\left[ 1 + \frac{2}{R_0} (-x \sin \phi_i + y \cos \phi_i) + \frac{1}{R_0^2} (x^2 + y^2) \right]^{1/2} \approx 1 + \frac{1}{R_0} [y - x \phi] \quad (4.8)$$

With this approximation, the "phase corrected" aperture response  $G(x, y)$ , becomes

$$\begin{aligned} G(x, y) &\approx \sum_{\phi_i} V_i(x, y, \phi) e^{\frac{-j4\pi R_0}{\lambda} \left[ 1 + \frac{1}{R_0} (y - x \phi_i) \right]} \\ &= \sum_{\phi_i} V_i(x, y, \phi) e^{\frac{j4\pi R_0}{\lambda}} e^{\frac{-j4\pi x \phi_i}{\lambda}} e^{\frac{j4\pi y}{\lambda}} \\ &= e^{\frac{j4\pi}{\lambda} [R_0 + y]} \sum_{\phi_i} V_i(x, y, \phi) e^{\frac{-j4\pi x \phi_i}{\lambda}} \end{aligned} \quad (4.9)$$

For a fixed scattering center  $(x, y)$  the first exponential represents a constant phase factor which does not vary with  $\phi_i$  and hence has no effect on the sum. Omitting this term or taking the magnitude of  $G(x, y)$  we find

$$|G(x, y)| = \left| \sum_{\phi_i} V_i(x, y, \phi) e^{-j\omega \phi_i} \right| \quad (4.10)$$

where  $\Omega = \frac{4\pi x}{\lambda}$ .

We recognize the summation as the discrete Fourier Transform of  $V_i(x, y, \phi)$  the received field from scattering center  $(x, y)$  at position  $\phi_i$  on the circular arc traversed by the radar. This is an entirely non-intuitive result based on phase considerations and is valid only under the following conditions:

1.  $R_0 \gg x, y$
2.  $\theta = \phi_{i_{\max}} - \phi_{i_{\min}}$  small enough

Such that

a)  $\sin \theta \approx \theta$

b)  $\cos \theta \approx 1$

Even under these conditions, the result is only an approximation.

We interpret  $|G(x, y)|$  as an approximate two dimensional image (in the  $x/y$  plane) of the object. This image is constructed as a phase corrected sum of responses  $V_i(x, y, \phi_i)$ , where each  $V_i(x, y, \phi)$  is the instantaneous quadrature and phase return (sum) from all scattering centers on target (in a given range bin) arriving at the radar position,  $(R_0, \phi_i)$ . The situation is shown in Figure 4.3 for 4 scattering centers.

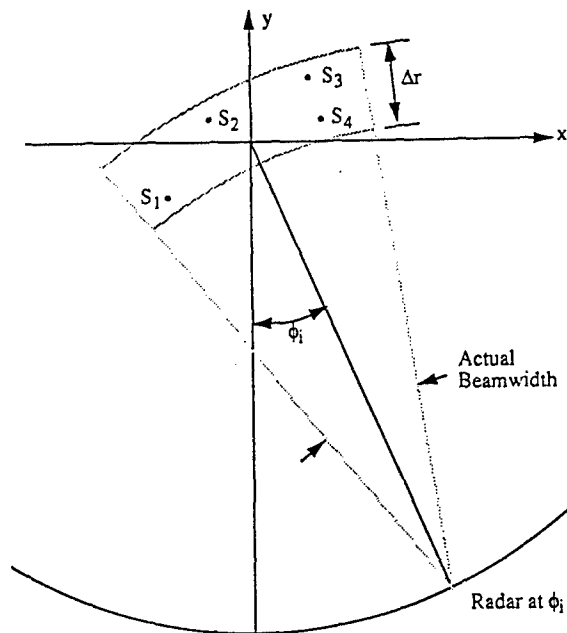


Figure 4-3

Comparing

$$|G(x, y)| = \left| \sum_{\phi_i} V_i(x, y, \phi) e^{\frac{-j4\pi x \phi_i}{\lambda}} \right| \quad (4.11)$$

to the standard form of the DFT,

$$F(\omega) = \sum_{n=0}^{N-1} f(n) e^{-j\omega n} \quad (4.12)$$

we see that  $x$  corresponds to  $\omega$ , and that  $\phi_i$  corresponds to  $n$ , while  $N$  is the total number of discrete positions along the arc of the radar at which the signal  $V_i(x, y, \phi)$  is received. The factor,  $\frac{4\pi}{\lambda}$ , in the exponential is simply a constant. We also notice that  $G(x, y)$  will be continuous in the variable  $x$  and that  $y$  is constant and corresponds to a fixed range or range bin. If an  $N$  point FFT of the form,

$$F(k) = \sum_{n=0}^{N-1} f(n) e^{-j2\pi kn/N} \quad (4.13)$$

for  $k=0$  to  $N-1$ ,

is used to compute  $|G(x, y)|$ , a single row of the image corresponding to scatter at range  $y$  takes the form

$$G(x_k) = \sum_{n=0}^{N-1} V(x, y, \phi_n) e^{-j4\pi kn/N} \quad (4.14)$$

for  $k=0$  to  $N-1$ .

In this way one can generate  $N$  cross range grey level values which correspond to resolution points  $x_1, x_2, \dots, x_N$ . The sum (Transform) must be computed for each point,  $x_k$ , at which a grey level is desired. The maximum number of points (pixels) for which cross range grey levels can be computed is given by  $N = \frac{\theta}{\Delta\theta}$  where  $\theta$  and  $\Delta\theta$  are as shown in Table 4.1. In order to compute a



single grey level at point/pixel  $X_k$  the synthetic beam formed by the synthetic aperture is steered (in an approximate fashion) by the FFT operation to a point  $(X_k, y)$  as shown in Figure 4-4. The actual shape and width of the beam is determined by the length of the aperture (i.e. the extent of  $\theta$ ). As  $\theta$  is increased the beam width is decreased. The beam is steered to various  $X_k$  in the single range bin by the FFT operation which is simply a convenient (and approximate) method of adjusting the phases of the signals received from the scattering center at  $(X_o, y_o)$  at each point  $\phi_1, \phi_2, \dots, \phi_N$  along the aperture to an in phase condition.

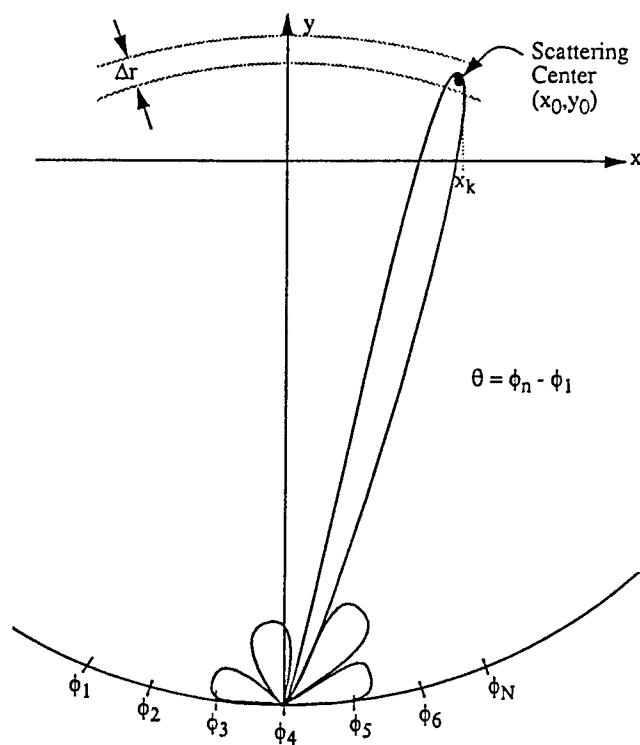


Figure 4-4

The side lobes and beam width of the synthetically generated antenna pattern shown in Figure 4-4 represent focusing errors due to the approximations introduced by the FFT phase collection as well as the finite extent of the aperture itself.

In practical image/signal processing terms, an approximate two dimensional image of a rotating object may be generated as described in steps 1 through 5 below. The angular rotation rate,  $\Omega$ , is assumed to be known apriori or to have been estimated using narrow band RTI plots.

- 1) The allowable rotation is computed as  $\theta = \sqrt{\frac{\lambda}{2R}}$  where  $R$  is the estimated radius of the object in a plane orthogonal to the axis of rotation.
- 2) The rotational increment  $\Delta\theta$  is computed as  $\Delta\theta = \frac{\lambda}{4R}$ .
- 3) As the object rotates from an initial position  $\phi_0$ , through the angle  $\Delta\theta$  a wide band return signal (from the entire object) is collected as a function of time. This signal is processed as described in Section 2 to resolve the object in the range direction into  $M$  range bins. The process is repeated for each of the  $N = \frac{\theta}{\Delta\theta}$  rotation increments. The result of this process which may take the form of  $N$  one dimensional Fourier transforms is an  $N \times M$  array of quadrature and phase (I/Q) data as shown in Figure 4-5. Each row corresponds to a range resolved return over a particular resolution increment,  $\phi_i + \Delta\theta$ . The data at any point along such a row gives the quadrature and phase of the return signal from a particular range increment of extent  $\Delta r = \frac{c\tau}{2} = \frac{c}{2B}$ .
- 4) Each column shown in Figure 4-5 represents I/Q data versus rotation angle at a specific range. The one dimensional Fourier Transform (FFT) of each column of I/Q data has the effect of resolving each column into  $N$  cross range resolution bins of width  $\Delta x$ . Note that  $N$  transform sums (one for each for each  $k=0$  to  $N-1$ ) must be computed to generate a single column of data.

- 5) Finally, taking the magnitude of each complex data point in the resultant array converts the data to scalar values that may be used for grey level intensity mapping purposes.

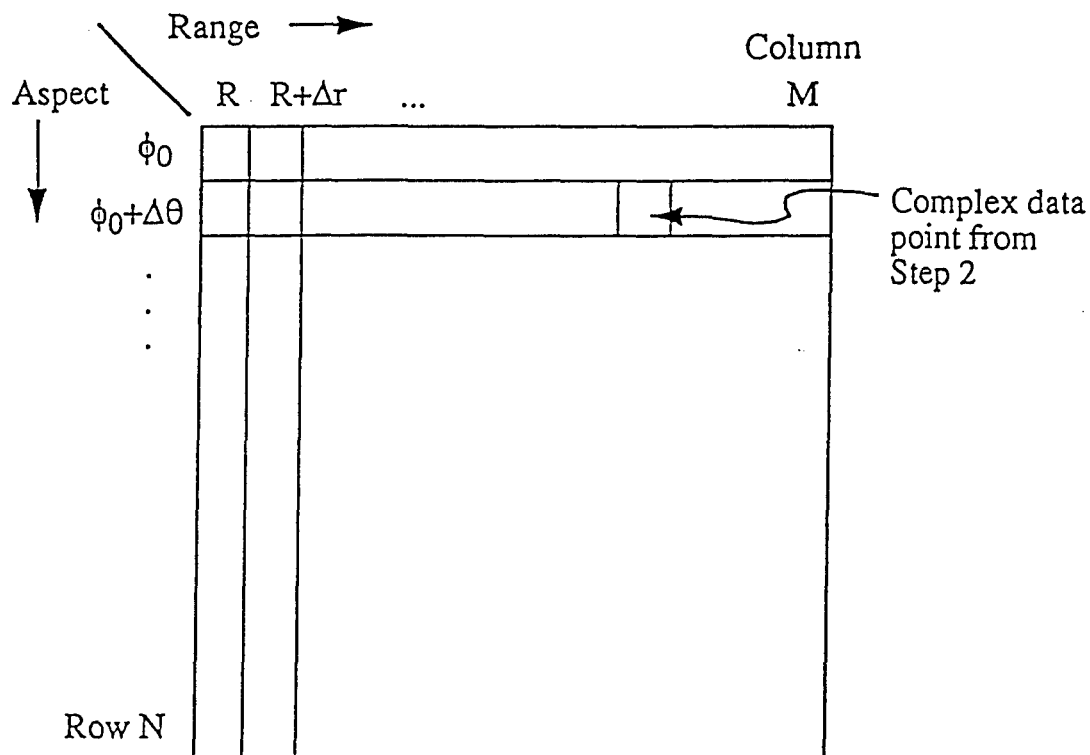


Figure 4-5

#### 5.0 Summary and Recommendations

A single  $M \times N$  high resolution radar image consisting of  $M = \frac{B}{\Delta f} = \frac{L}{\Delta r}$  range pixels and  $N = \frac{\theta}{\Delta\theta}$  cross range pixels can be constructed from the wideband radar echo of a rotating object as described in the previous section. As indicated in Section 3.0, such an image cannot be associated with a particular aspect. Rather, the image is formed in the cross range dimension as a function of illuminating the object from a series of varying aspect sensitive positions. If, as shown in Figure 5-1, a set of such imagery is generated for a single object, the individual images can be rotated and transposed to create a single image that represents scatter from all aspect positions.

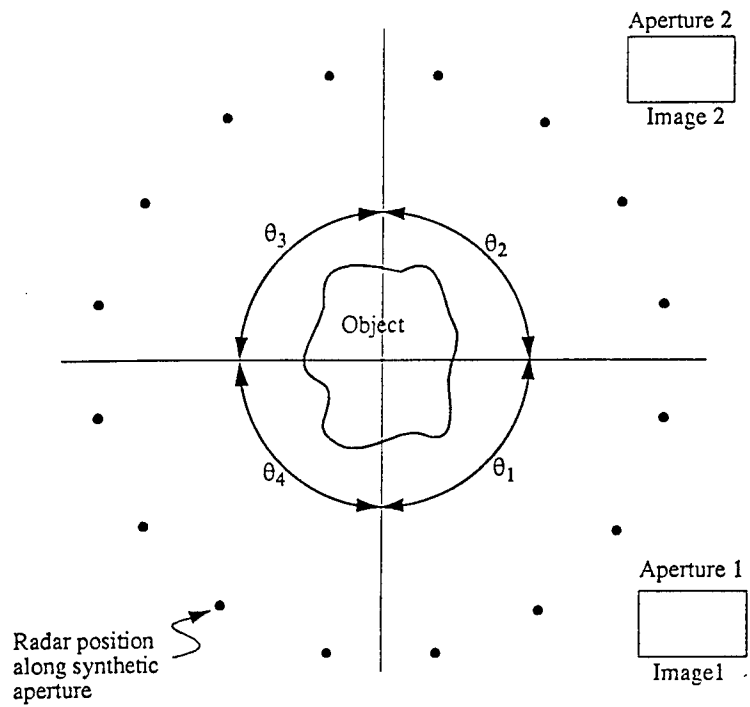


Figure 5-1

Figure 5-2 [Auscherman] shows an actual composite image and the related optical photograph.

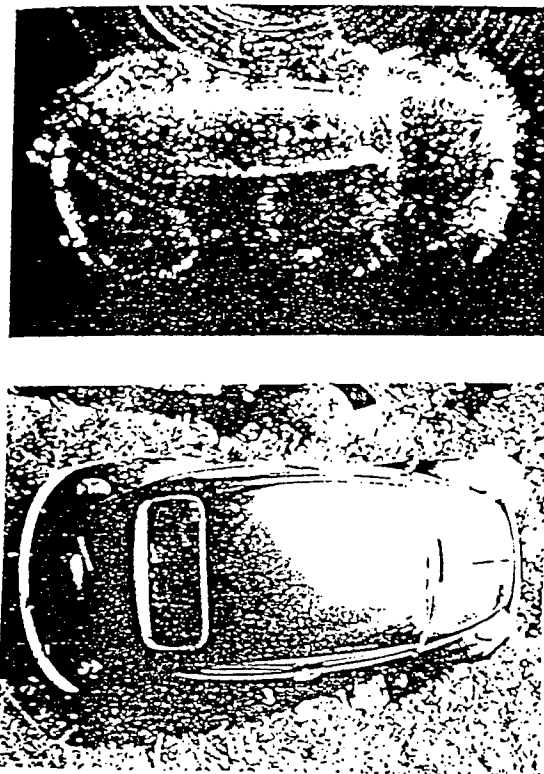


Figure 5-2

Such imagery can provide a valuable visualization aid if interpreted correctly. Depending on the nature of the object (shape, scattering characteristics, and axis of rotation), it can also be misleading.

With respect to range imagery we have shown that resolution in this dimension is directly proportional to the bandwidth of the transmitted signal and that wide bandwidths can be achieved by consecutively illuminating an object with a series of sinusoids - each of a different but constant frequency.

The superposition of the object responses to these signals defines the object frequency response which can be Fast Fourier Transformed to generate a range resolved response.

With respect to the cross range image dimension, we have seen that resolution in this dimension is possible by virtue of the variance in the Doppler frequency of signals from scattering centers at varying cross range positions on rotating objects. In Section 4 we investigated the cross range imaging process from the equivalent standpoint of a stationary object and a synthetic antenna array formed along a circular arc. In this case it was shown that approximated focusing of the synthetic beam is accomplished through the FFT of constant range magnitude and phase data that varies as a function of antenna position along the circular arc.

Related topics that have not been addressed and which may be of interest to Phillips personnel include:

- (1) Focusing corrections through use of a two dimensional Polar Fourier Transform. While this technique is not currently available as part of the LL RCS Toolbox, it is, according to Lincoln Laboratories personnel, frequently used when processing real data.
- (2) Three Dimensional Image generation
- (3) The relation of ISAR imaging to Computer Axial Tomographic (CAT-SCAN) imaging theory and practice. It is possible that continued research efforts in one area may lead to developments in the other.
- (4) Alternate Image presentation/visualization methods

- (5) Radar object modeling issues including model complexity and model resolution scale as these may affect resultant two dimensional imagery.

### 5.1 Recommendations

As a result of the current effort we are confident that involved personnel at both the University of Nevada and WSAI will have been brought "up to speed" in the area of wideband range and doppler cross range image simulation of rotating objects. This has been a critical and necessary task; it is impossible to analyze/interpret imagery whose most basic information content is not well understood.

Based on our understanding of current and anticipated WSAI goals and requirements, we suggest the following continued effort. With respect to the microwave (10 GHz center frequency) information spectrum, data is available in two basic forms:

- 1) Wideband doppler imagery as described herein
- 2) Narrowband range time intensity signature data.

Both information sources are important and may be utilized as part of a robust automatic object analysis, object mission assessment system. Currently, analyses of real imagery are carried out (in the image domain) using the RCS Toolbox to generate synthetic imagery in an attempt to match observed imagery or particular observed scattering phenomena. These phenomena may be confined to single time static images, time sequences of imagery or composite images. As a First Task, we suggest that the RCS Toolbox be utilized intensively by University of Nevada/WSAI personnel to accomplish as many practical analysis tasks as possible. These analyses may take the form of "experiments" designed to test the utility/scope of the tool in an analysis mode and must include analysis and modeling of actual high resolution imagery. In this way we will begin to become knowledgeable with respect to the sorts of information that can be extracted from

the imagery - real or simulated. It is anticipated that this task can be accomplished during a continuous 4-6 week effort at Phillips Laboratories by University of Nevada personnel.

As a major part of Task Area 2, we would advise the initial development of a set of basic algorithms that would operate on time series imagery (combinations of real and simulated) to extract information as deemed possible based on Task 1 efforts. The primary purpose here is to define (and test) ways to automate the analysis process.

As a third general task area we suggest a careful study of narrowband signature data, its information content and the specific types of object features that can be extracted from these one dimensional waveforms. A large part of this task would be devoted to developing automated signal processing tools to extract such information as object shape, object motion, maximum, minimum, and average radar cross section, and object component (scattering element) analysis. Correlation of narrowband RCS data of the same satellite over repeated observation periods may also prove to be an extremely useful tool for detecting changes (damage, antenna deployment, etc.) in satellite status and condition.

Finally (Task Area 4), it will be desirable to devise techniques to merge (fuse) the analysis strategies and results as they emerge as a function of Tasks 2 and 3.

## 6.0 Bibliography

- [1] Ausherman, D.A., Kozma, A., Walker, J.L., Jones, H.M., and E.C. Poggio, Developments in Radar Imaging, *IEEE Transactions on Aerospace and Electronic Systems*, Vol. AES-20, No. 4, July, 1984.
- [2] Brown, W.M. and R.J. Fredricks, Range-Doppler Imaging Motion Through Resolution Cells, *IEEE Transactions on Aerospace and Electronic Systems*, Vol. AES-5, No. 1, Jan., 1969.
- [3] Burt, E.C., and T.G. Moore, High Frequency RCS Prediction Theory, *Project Report PSI-172*, Lincoln Laboratories, Jan., 1991.
- [4] Carey, M.O., and C.M. DeRidder, Linear Periodogram Imaging, *Project Report PSI-19*, Lincoln Laboratories, April, 1994.
- [5] Mensa, D.L., High Resolution Radar Cross-Section Imaging, Artech House, MA, 1991.
- [6] Mensa, D. and K. Vaccaro, Two-Dimensional RCS Image Focusing, *Proceedings of the 1987 Meeting of the Antenna Measurement Techniques Association*, Seattle.
- [7] Rihaczek, A.W., Principles of High Resolution Radar, Peninsula Publishing, Los Altos, CA, 1985.
- [8] Syracuse Research Corp., Coherent and Wideband Imaging Analysis Workbook, Prepared for USAF Air Training Command, 1979.
- [9] Walker, J.L., Range-Doppler Imaging of Rotating Objects, *IEEE Transactions on Aerospace and Electronic Systems*, Vol. AES-16, No. 1, Jan., 1980.



## OPTICAL AND CLEAR AIR TURBULENCE

Mayer Humi  
Professor  
Department of Mathematical Sciences

Worcester Polytechnic Institute  
100 Institute Road  
Worcester, MA 01609-2280

Final Report for:  
Research Initiation Program  
Philips Laboratory, Hanscom AFB

Sponsored by:  
Air Force Office of Scientific Research  
Bolling Air Force Base, Washington, D.C.

December 1993

## OPTICAL AND CLEAR AIR TURBULENCE

Mayer Humi  
Professor  
Department of Mathematical Sciences  
Worcester Polytechnic Institute

### Abstract

The paper explores different paradigms for detrending the meteorological data which was collected on the ER2 NASA mission of Jan–Feb, 89. In particular we describe a new wavelet based algorithm for this purpose. In this algorithm the wavelets used conform to the global features of the data. The paper explores also the possible characterization of the "atmospheric state" (in the region where the data was collected) by estimating the Lyaponouv exponents and the fractal dimension of the "atmospheric signal".

\* Research sponsored in part by AFOSR under grant #F49620–90–C–09076

# OPTICAL AND CLEAR AIR TURBULENCE

Mayer Humi

## I. INTRODUCTION

The analysis of meteorological data requires in many instances [1,2,3,4] the separation of the large (slow) scales from the turbulent residuals. That is if  $A(x,t)$  is a meteorological observable and  $A_{obs}$  is a time-series of measurements of  $A$  then a proper algorithm (or filter) is needed to decompose

$$A_{obs} = A_L + A_T$$

where  $A_L$  and  $A_T$  are the large and turbulent components of  $A_{obs}$ . Such a decomposition is needed, for example, in the modeling and analysis of optical turbulence [5,6]. In this particular case the resulting statistics of the turbulent residuals has significant implications for any attempt to compensate for the effects that atmospheric turbulence has on the optical signal.

Common techniques that are used to obtain this decomposition include Fourier transform least squares and ARMA models (to name a few) [7,8]. Recently, however, wavelets were introduced and used in many applications especially for signal processing and image smoothing [9,10]. The advantage that wavelets have in these contexts is their ability to detect, at least in principle, localized signal. Many wavelet bases were constructed in the literature in the last few years. However, we felt that the analysis of meteorological data requires a new type of wavelets. These should be "data fitted" and as a result better suited to capture the scale invariance that might be present in the data. To accomplish this objective we construct in this paper a mother wavelet that has the same "global structure" as the raw data and use it to generate a wavelet basis for data decomposition.

In this paper we use and compare the "classical" detrending algorithms with those using wavelets in general and "data fitted wavelets" in particular. Moreover we apply currently

available algorithms to evaluate the Lyapunov exponents and fractal dimension [11] of the raw meteorological data in an attempt to characterize the nature of the chaotic attractor that is represented by it.

The plan of the paper is as follows: In section 2 we present a short introduction to wavelets and their basic properties. In section 3 we introduce the concept of data fitted wavelets and detail an algorithm for their computation. Section 4 describes the principal component analysis that has been applied to the data in order to eliminate measurements errors. Section 5 we apply and compare different detrending algorithms to the data set collected by "NASA arctic stratospheric expedition" on Jan–Feb 1989 [21]. Section 6 attempts to characterize the "atmospheric state" in terms of chaotic and fractal invariants. We end in section 7 with some conclusions.

## II. WAVELETS [12,13,14]

Fourier series expansions in  $L^2(\mathbb{R})$  use basis functions  $\{e^{ikt}\}$  which have a unique wave number. However these functions are not localized in time and their support consists of the whole real line. "Wavelet philosophy" is to give up the sharp spectral contents of the basis functions in favor of functions which have compact support in both time and frequency domains.

To construct an orthogonal wavelet basis one has to find a function  $\varphi(x)$  – which is called the scaling function – which satisfies the dilation–difference equation

$$\varphi(x) = \sum_n c_n \varphi(2x - n) \quad (2.1)$$

subject to the following requirements;

1.  $\int \varphi(x) dx = 1.$
2. Using suitable coefficients  $\{a_n\}$  one can approximate smooth function in  $L^2(\mathbb{R})$  so that for some fixed  $p$

$$\|f - \sum_n a_n \varphi(2^m x - n)\| \leq C 2^{-mp} \|f^{(p)}\| \quad (2.2)$$

where  $f^{(p)}$  is the  $p$ -th derivative of  $f$ .

### 3. Orthogonality

We require that

$$\varphi_j(x) = \sum_n c_n \varphi(2^j x - n) \quad (2.3)$$

and its translates  $\varphi_j(x - m)$  are orthogonal. That is

$$\int \varphi_j(x - k) \varphi_j(x - m) = \delta_{km}. \quad (2.4)$$

Together these conditions imply the following

$$1. \quad \sum c_k = 2 \quad (2.5)$$

$$2. \quad \sum (-1)^k c_k = 0, \quad m = 0, 1, \dots, p-1 \quad (2.6)$$

$$3. \quad \sum c_k c_{k-2m} = 2\delta_{0m}. \quad (2.7)$$

As an example we point out that the Haar function

$$\varphi_0(x) = \begin{cases} 1, & 0 \leq x \leq 1 \\ 0, & \text{otherwise} \end{cases} \quad (2.8)$$

satisfies these conditions with  $p = 1$  and  $c_0 = c_1 = 1$ .

Another family of scaling functions is due to Daubechies. One of the functions in this family,  $D_4(x)$ , satisfies eq. (2.1) with

$$c_0 = \frac{1}{4}(1 + \sqrt{3}), c_1 = \frac{1}{4}(3 + \sqrt{3}), c_2 = \frac{1}{4}(3 - \sqrt{3}), c_3 = \frac{1}{4}(1 - \sqrt{3}). \quad (2.9)$$

Once a solution of the scaling equation is known a wavelet mother function can be defined as

$$\psi(x) = \sum (-1)^k c_{1-k} \varphi(2x - k) \quad (2.10)$$

and a wavelet basis of  $L^2(\mathbb{R})$  is defined by  $\{\psi_{jk}\}$  where

$$\psi_{jk}(x) = 2^{j/2} \psi(2^j x - k) \quad (2.11)$$

Using such an orthogonal wavelet basis we can expand a function  $f(x)$  in  $L^2(\mathbb{R})$  as

$$f(x) = \sum_{j=-\infty}^{\infty} \sum_{k=-\infty}^{\infty} a_{jk} \psi_{jk}(x) \quad (2.12)$$

with

$$a_{jk} = \int_{-\infty}^{\infty} f(x) \psi(x - 2^{-j}k) dx. \quad (2.13)$$

In practice, when the wavelet transform is applied to a discrete time series, the application requires only the coefficients  $\{c_i\}$  which are referred to as the wavelet filter coefficients. As a first step in this analysis one generates the transform matrix

$$C = \begin{bmatrix} c_0, & c_1, & & c_n & \dots & & \\ c_n, & -c_{n-1} & \dots & -c_0 & & & \\ & c_0, & c_1 & \dots & c_n & & \\ & c_n, & -c_{n-1} & \dots & -c_0 & & \\ & & & & \dots & & \\ c_2, & \dots & & c_n & & c_0, & c_1 \\ c_{n+2}, & \dots & & -c_0 & & c_n, & -c_{n-1} \end{bmatrix}$$

(Here the number of coefficients is assumed to be even).

In this context  $\{c_0, \dots, c_n\}$  is a smoothing filter while the mirror filter  $\{c_n, -c_{n-1}, \dots, -c_0\}$  is the "detail" filter. Together these filters are referred to as "quadrature mirror filters".

When the filter matrix  $C$  is applied to a data vector of length  $2^n$

$$x = \begin{bmatrix} x_1 \\ \vdots \\ x_{2^n} \end{bmatrix}$$

it decomposes it into a smooth part and a detail

$$Cx = \begin{bmatrix} s_1 \\ d_1 \\ \vdots \\ s_m \\ d_m \end{bmatrix}, \quad m = 2^{n-1} \quad (2.15)$$

We can now retain only the smooth part of the data  $\begin{bmatrix} s_1 \\ \vdots \\ s_m \end{bmatrix}$  and iterate the process to obtain the

smooth-smooth part of the data and so on. Thus from this point of view wavelets form a natural

methodology to detrend meteorological data by retaining only the smooth part that is left after  $m$  iterations of the filter. In fact after each iteration of the wavelet filter the smooth part represents the data at a larger (coarser) scale.

By applying the inverse wavelet transform  $m$  times on the smooth part of the data to obtain  $x_{\text{smooth}}$  and taking the difference  $x - x_{\text{smooth}}$  we obtain the turbulent residuals of the flow.

### III. DATA FITTED WAVELETS

In the literature of the last few years several authors constructed a large number of wavelet bases. Each of these was found by imposing additional constraints on the properties of the desired basis beside those enumerated in section II. As explained above these can be used as filters to detrend time series of meteorological observations. The fact remains however that each of these filters bears no intrinsic relationship to the data and its properties. In particular since meteorological data is assumed to be "scale invariant" (at least for some range of wave numbers) it is appropriate to try to use wavelet filters that are "data fitted". By this we mean that in constructing these wavelets the actual gross features of the data are taken into account. With these built in properties these filters should be better suited to identify any spectral—spikes which are due to turbulence effects.

To accomplish this objective we observe that from an algorithmic point of view the construction of a wavelet filter with  $n$  coefficients  $c_1, \dots, c_n$  requires  $n$  independent equations (For reasons that will become clear later we let  $n = 2^k$ ). The constraints given by eqs (2.5)–(2.7) with (let's say)  $p = 1$  yield only  $\frac{n}{2} + 2$  (nonlinear) equations. The remaining  $\frac{n}{2} - 2$  equations should come from the imposition of additional "mathematical properties" or from the data.

To construct these additional equations from the data we first create a sample of  $n$  representative points  $x_i = x(t_i)$ ,  $i = 1, \dots, n$ . The application of the yet to be found smoothing filter  $S$  (without the mirror filter) on  $x = (x_1, \dots, x_n)$  yields a vector  $s$  of length  $n/2$  which is



representative of the smoothed data.

$$Sx = s$$

$$S = \begin{bmatrix} c_1 & \dots & c_n \\ c_{n-1} & c_n & c_1 & \dots & c_{n-2} \\ & & \dots & & \\ c_3 & \dots & c_n & c_1 & c_2 \end{bmatrix}, \quad s = \begin{bmatrix} s_1 \\ \vdots \\ s_{n/2} \end{bmatrix}$$

Some "generic" strategies can be used to obtain a representation of  $s$ .

(1) We can compute  $s_i$  by some data-smearing-smoothing algorithm. E.g. we can let

$$s_i = \frac{x_{2i-1} + x_{2i}}{2}$$

(2) Compute the least squares curve  $f(t)$  (of appropriate order) to the vector  $x$  and let

$$s_i = \frac{f(t_{2i-1}) + f(t_{2i})}{2}$$

(3) Apply a known wavelet filter to the whole data several times until the number of components in the smooth representation of this data is  $\frac{n}{2}$  and use these values as a representation of  $s$ .

Remark: All these strategies yield  $\frac{n}{2}$  equations for the filter coefficients. However we can reduce these to  $\frac{n}{2} - 2$  by leaving out the two end point equations.

Of the strategies mentioned above the second and the third seems to be more robust and successful. However even for these implementations one has to be careful about the choice of  $n$ . Small  $n$  leads to "small data input". That is the number of equations that are data dependent is small e.g. for  $n = 8$  only 2 equations originate from the data. On the other hand when  $n$  is

large (e.g.  $n = 128$ ) the influence of the data on the filter coefficients is strong but we have to solve a large number of nonlinear equations. Furthermore the set of equations becomes ill posed (due to the nature of eq. (3.1)) especially if the data contains large errors. Nevertheless in "mid-range" we were able to solve the resulting set of equations to obtain appropriate filter coefficients.

#### IV. PRINCIPAL COMPONENT ANALYSIS

The measurement and collection of meteorological data is subject to various types of errors. The goal of principal component analysis (PCA) is to identify and subtract these errors by the use of statistical analysis. We give here an overview of the algorithm used in this analysis and refer the reader to the literature for more details [15].

Suppose we have a set of (atmospheric) measurements  $z(i,j)$ ,  $i = 1, \dots, n$ ,  $j = 1, \dots, nvar$ . Here  $i$  stands (typically) for the time variable while  $j$  may refer to different atmospheric variables (pressure, temperature, etc.) or different sets of measurements of the same variable.

To apply PCA to this data set we first arrange it in a matrix of  $n$  rows and  $nvar$  cols. The algorithm then consists of the following steps.

1. Center and normalize the data

$$y(i,j) = \frac{z(i,j) - \bar{z}(j)}{\sqrt{n}} \quad (4.1)$$

where  $\bar{z}(j)$  represents the average of the measurements  $z(i,j)$ ,  $i = 1, \dots, n$ .

2. Generate the covariance matrix of the data.

$$S = y^T \cdot y \quad (4.2)$$

(Note that  $S$  is  $nvar \times nvar$  matrix.)

3. Find the eigenvalues and eigenvectors of  $S (\lambda_k, e_k)$ ,  $k = 1, \dots, nvar$ .

$$e_i \cdot e_j = \delta_{ij} \quad (4.3)$$

The eigenvectors  $e_i$  thus provide an intrinsic frame for the decomposition of the measurements  $y(i,j)$

$$y(i,*) = \sum_{k=1}^{nvar} x(i,k)e_k \quad (4.4)$$

where  $y(i,*) = (y(i,1), \dots, y(i,nvar))$ .

In many cases some of the eigenvalues of  $S$  are small as compared to the leading one e.g.

$$|\lambda_1| < |\lambda_2| < \dots < |\lambda_{nvar}| \quad (4.5)$$

and

$$\left| \lambda_k / \lambda_{nvar} \right| < \epsilon < 1, \quad k = 1, \dots, m-1 \quad (4.6)$$

The basic premise of PCA is that one can attribute the components of  $y(i,x)$  along  $k = 1, \dots, m-1$  to measurement errors rather than physical causes. We can therefore reconstruct the "error free" scaled measurements in the form

$$y(i,j) = \sum_{k=m}^{nvar} x(i,k)e_k(j) \quad (4.7)$$

PCA can be applied to the meteorological data set obtained from the ER2 mission in two ways.

The first is to use this analysis on the data obtained in one flight. (Thus we attempt to eliminate errors due to airplane vibrations and similar in flight errors). In this context the index  $j$  in the analysis refers to the six atmospheric variables which were measured viz. pressure, temperature, true air speed and the three velocity components  $(u,v,w)$ . We found that the ratio of the first two eigenvalues of  $S$  to the leading one was  $10^{-3}$  and the data was reconstructed accordingly. As a second application of PCA we used the data collected for the temperature on eight daily missions. (The hope was to eliminate in this way possible instrument errors). We found that the ratio of the first three eigenvalues to the leading one was  $10^{-2}$  and the data was reconstructed accordingly.

## V. PARADIGMS FOR DETRENDING

There exist in the literature a wide range of methods to detrend stochastic time series which are based on the Box—Jenkins ARMA models. However the global ( $\equiv$  "smooth") structure of the mean quantities remains obscured by this method. Furthermore it is questionable whether such stochastic approach is suitable in the context of meteorological data which represents the state or evolution of a deterministic system (at least in principle). Also as the spectral distinction between the large and turbulent scales is not sharp it is not appropriate to use a "frequency filter" which will eliminate all the low frequencies from the spectral representation of the flow.

With these constraints in mind one has to use the "large scale pattern" of the flow to detrend the local data and compute the turbulent residuals. The following strategies were used by us in an attempt to achieve this goal:

1. "Global" least squares algorithm.

In this approach we divide the data into subsets ( $\equiv$  windows) of 1000–5000 data points. For each window we compute the least squares curve  $f(t)$  of appropriate order (usually 1 or 2) to the data. The turbulent residuals are then given by

$$r_i = x_i - f(t_i) \quad (5.1).$$

To avoid sharp discontinuities on the edges of these windows we allowed an overlap of 256 data points on each side of these subsets.

## 2. Local least squares algorithm.

In this algorithm (which was inspired by the Kalman filter) we open a window of 50–100 points on each side of  $x_i$  and compute the least squares curve (of appropriate order) for this data window. The turbulent residual at  $x_i$  (only) is then given by (5.1). The difference between this and the previous algorithm is that here a new least squares curve is computed for each data point. This requires a fairly extensive resource.

## 3. Detrending by the FFT transform

Here we apply the FFT transform to the data and then compute the inverse transform  $\bar{x}_i$  from the first few coefficients (usually 3–9) which represent the slow frequencies in the flow. The turbulent residuals are then given naturally by  $r_i = x_i - \bar{x}_i$ .

## 4. Spline Smoothing Filter

To produce this filter we use a natural cubic spline  $S(t)$  for the data set  $(t_i, x_i)$  with knots at all  $t_i$ . However the smoothing spline does not interpolate for the  $x_i$ 's. Instead it minimizes

$$\int_a^b S''(t)^2 dt \quad (5.2)$$

subject to the constraint

$$\sum \left| \frac{S(t_i) - x_i}{\omega_i} \right| < \sigma \quad (5.3)$$

where the  $\omega_i$ 's are proper "data weights" (we used  $\omega_i \equiv 1$ ) and  $\sigma$  a "smoothing parameter".

As a refinement one can use various strategies to estimate the value of  $\sigma$  that is appropriate for a given data set. As before the turbulent residuals are given by  $r_i = x_i - S(t_i)$ .

## 5. Convolution Transform.

It is well known that

$$(f * x)^\wedge(s) = \hat{f}(s)\hat{x}(s) \quad (5.4)$$

where  $*$  is the convolution operator and  $\hat{\phantom{x}}$  stands for the Fourier transform. It follows then that if one wanted to eliminate from the spectrum of a signal  $x(t)$  all the frequencies greater than  $\omega$  then  $\hat{f}(s)$  must be of the form

$$\hat{f}(s) = \begin{cases} 1 & 0 < s < \omega \\ 0 & s \geq \omega \end{cases} \quad (5.5).$$

The filtered data will be given then by the convolution

$$(f * x)(s) = \int_{-\infty}^{\infty} f(s-t)x(t)dt. \quad (5.6)$$

However as explained earlier filters of the form (5.5) are not appropriate in the context of meteorological analysis. To motivate the choice of an appropriate filter we observe that the simulation of fluid flow using large eddy simulation methodology [16] requires a subgrid filter (to eliminate and model the fast modes in the flow). An optimal choice for such a filter was shown to have the form of a normal distribution [17]. We used therefore such a filter (with different standard deviations) to detrend the meteorological data using (5.4), (5.6).

## 6. Wavelet Transform

The use of this transform with appropriate wavelet basis has been discussed at length in previous sections. Besides the choice of the basis one has to determine the appropriate number of data smoothing iterations to be applied to the data. This was found to be between 4 and 6. As

mentioned earlier we used "general purpose" wavelets as well as data fitted wavelets to detrend the meteorological data.

We used all the methods enumerated above to detrend the meteorological data that was obtained in the ER2 mission. The most successful to these methods were (1), (2) and (6). Figs. 1-3 represent part of the detrended data for  $u$  on Feb. 9, 89 using these methods (respectively). The spectral analysis for the temperature and  $u, v$  on this date using method (1) is given in Figs 4-6. Note that rather unexpectedly the spectral curve for  $v$  contains a plateau in the range of 10 rads/sec. The physical origin of this plateau is not clear. However it seems to indicate that the measured flow is strongly non-isotropic.

We present also some statistical analysis pertaining to the data of Feb. 9, 89. Figs 7,8 contain the autocorrelation curves for the temperature and  $u$  while fig. 9 represents the cospectrum of  $w$  and the temperature.

## VI. CHARACTERIZATION OF THE ATMOSPHERIC STATE

How one can characterize the fundamental difference between the state of the (upper) atmosphere on a "regular" day and another in which there exists a mesoscale disturbance? Furthermore can we characterize these differences in terms of some appropriate "global" invariants?

In an attempt to answer these questions we introduce two tools from dynamical system theory. These are Lyapunov exponents and the fractal dimension of the data. A formal definition of these quantities will not be given here (we refer the reader to the literature on chaotic systems [11]). It is enough to say however that Lyapunov exponents characterize the divergence of trajectories with similar initial conditions. The dominant Lyapunov exponent  $\lambda$  quantifies this divergence rate. Thus if  $\lambda > 0$  the trajectories will diverge and the system is referred to as chaotic (larger values of  $\lambda$  lead to a faster divergence). In the same manner the fractal dimension of a time series gives some indication of the underlying chaotic system. (Although there exist several competing definitions of this number). This dimension reflect the "strength"

and frequency of the small scale (turbulent) fluctuations in the data.

In the data collected by the ER2 mission large scale mesoscale disturbance was present in the atmosphere on two days (Jan. 30 and Feb. 10, 89). Two "regular" days are Feb. 8 and 9, 89. To compute and compare the Lyapunov exponents and fractal dimensions on these four days we used (with some enhancements) the programs written by Kruehl and Eisinger [18] (for the Lyapunov exponents) and J.J. Sarraile [19] (for the fractal dimension). These programs are based on algorithms which appeared previously in the literature [20].

Table 1 which summarizes these estimates shows that there exist little difference in the leading Lyapunov exponents and the fractal dimensions of these dates. Thus while these results reflect the chaotic state of the atmosphere they fail (at least in this instance) to yield a reliable distinction between the state of the atmosphere on these dates.

We wish to point out however that the current version of the programs to estimate the Lyapunov exponents of the flow is based on linear fits for the approximation of the local Jacobians. A more sophisticated algorithm for this purpose might be based on local polynomial approximations for the Jacobians. In this respect the use of Lyapunov exponents to characterize the "atmospheric state" remains an open question.

## VII. CONCLUSIONS

The paper explored different paradigms for the detrending of meteorological data. The most successful of these were found to be based on least squares and wavelet transform. Using these techniques we carried out statistical and spectral analysis of the turbulent residuals.

As to the characterization of the "atmospheric signal" further research is needed. In particular we wish to point out that the meteorological data that was collected on the ER2 mission does not constitute a time series per se. In fact it represents a space-time series of measurements. As such it provides only a one-dimensional cross section of a 4-dimensional set of data points. To ameliorate this situation accurate modeling and simulations of the atmospheric



conditions in the stratosphere are needed. In these efforts proper attention must be paid to the mechanisms that underlie the creation of turbulence in these heights.

### Acknowledgement

We would like to express our gratitude to K. Roland Chan of NASA-Ames and Stuart W. Bowen of San Jose State University for providing the CDRM of ER2-MMS 5Hz data for the ER2 Artic Stratosphere Measurements.

### REFERENCES

1. E. F. Danielsen et al — Irreversible Transport in the Stratosphere by Internal Waves of Short Vertical Wavelength, J. Geo Res. 96D p. 17433–17452 (1991).
2. P. J. Kennedy and M. A. Shapiro — Further Encounters with Clear Air Turbulence in Research Aircraft, J. Atmos. Sci. 37 p. 986–993 (1980).
3. C. Cot and J. Barat — Wave-Turbulence Interaction in the Stratosphere, J. Geo Res. 91D p. 2749–2756 (1986).
4. L. Kristensen and P. Kirkegaard — Comments on effects of finite sampling on atmospheric spectra, Boundary Layer Metes 48 p. 205–210 (1989).
5. R. L. Fante — Wave Propagation in Random Media, Prog. In Optics 21 p. 341–401 (1985).
6. E. M. Dewan — Optical Turbulence Forecasting, AFGL-TR-80-0300 (1980).
7. C. F. Gerald — Applied Numerical Analysis, Addison Wesley, Reading, MA 1989.
8. G. Box and G. M. Jenkins — Time Series Analysis, Holden Day 1976.
9. J. Morlet et al — Wave Propagation and Sampling Theory, Geophysics 47 p. 202 (1982).
10. R. Coifman et al — Wavelet Analysis and Signal Analysis, IEEE Trans. Inform. Theory 38 p. 713–718 (1990).
11. F. C. Moon — Chaotic and Fractal Dynamics, J. Wiley, New York, 1992.
12. I. Daubechies — Ten Lectures on Wavelets, SIAM, Philadelphia, PA 1992.

13. G. Strang — Wavelets and Dilation Equations, SIAM Rev. 31 p. 614–622 (1989).
14. M. Farge — Wavelet Transforms and Their Applications to Turbulence, Ann. Rev. Fluid Mech. p. 395–457 (1992).
15. J. F. Jackson — A User's Guide to Principal Components, J. Wiley, New York, 1991.
16. M. Lesieur and R. Rogallo — Large Eddy Simulation of Passive Scalar Diffusion in Isotropic Turbulence, Phys. Fluids A 1 p. 718–731 (1989).
17. M. Humi — Optimal Large Eddy Simulation in One Dimension, Phys. Fluids A 2 p. 1046–1048 (1990).
18. Th. M. Kruel — Computation of Lyapunov Spectra, Physica D p. 117–131 (1993).
19. Liebovitch and Toth — A Fast Algorithm to Determine Fractal Dimensions by Box Counting, Phys. Letts. A 141 p. 386–390 (1989).
20. R. Stoop and R. F. Meier — Evaluation of Lyapunov Exponents and Scaling Functions From Time Series, J. Opt. Soc. Am. B5 p. 1037 (1987).
21. S. Hipskind and S. Gaines, May 1990, Airborne Arctic Stratospheric Expedition, NASA/VARP-003, Appendix A: ER2 Meteorological Measurement Supplement, 5Hz Data, 5530 — CDRM 283000.

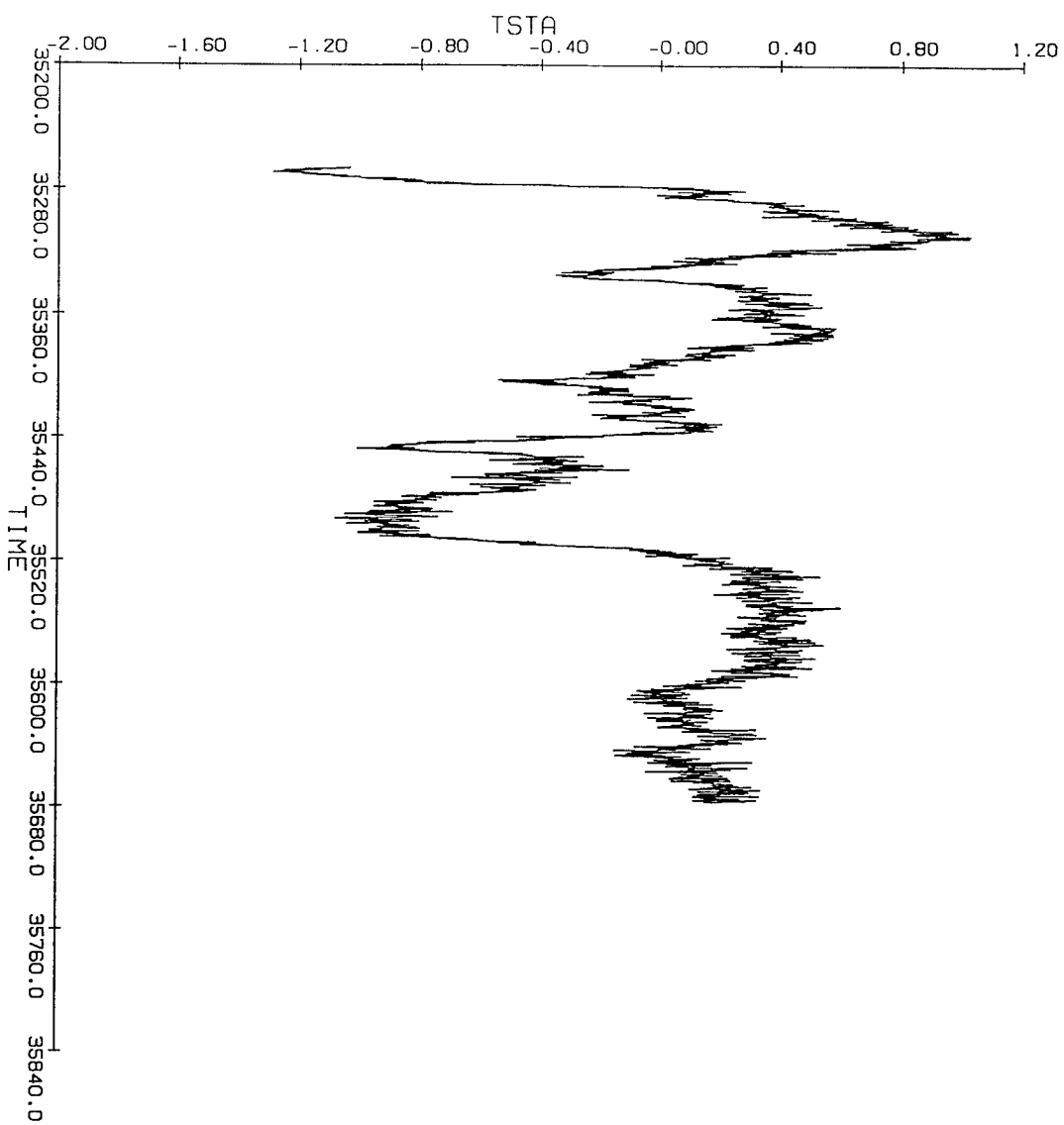


Fig 1

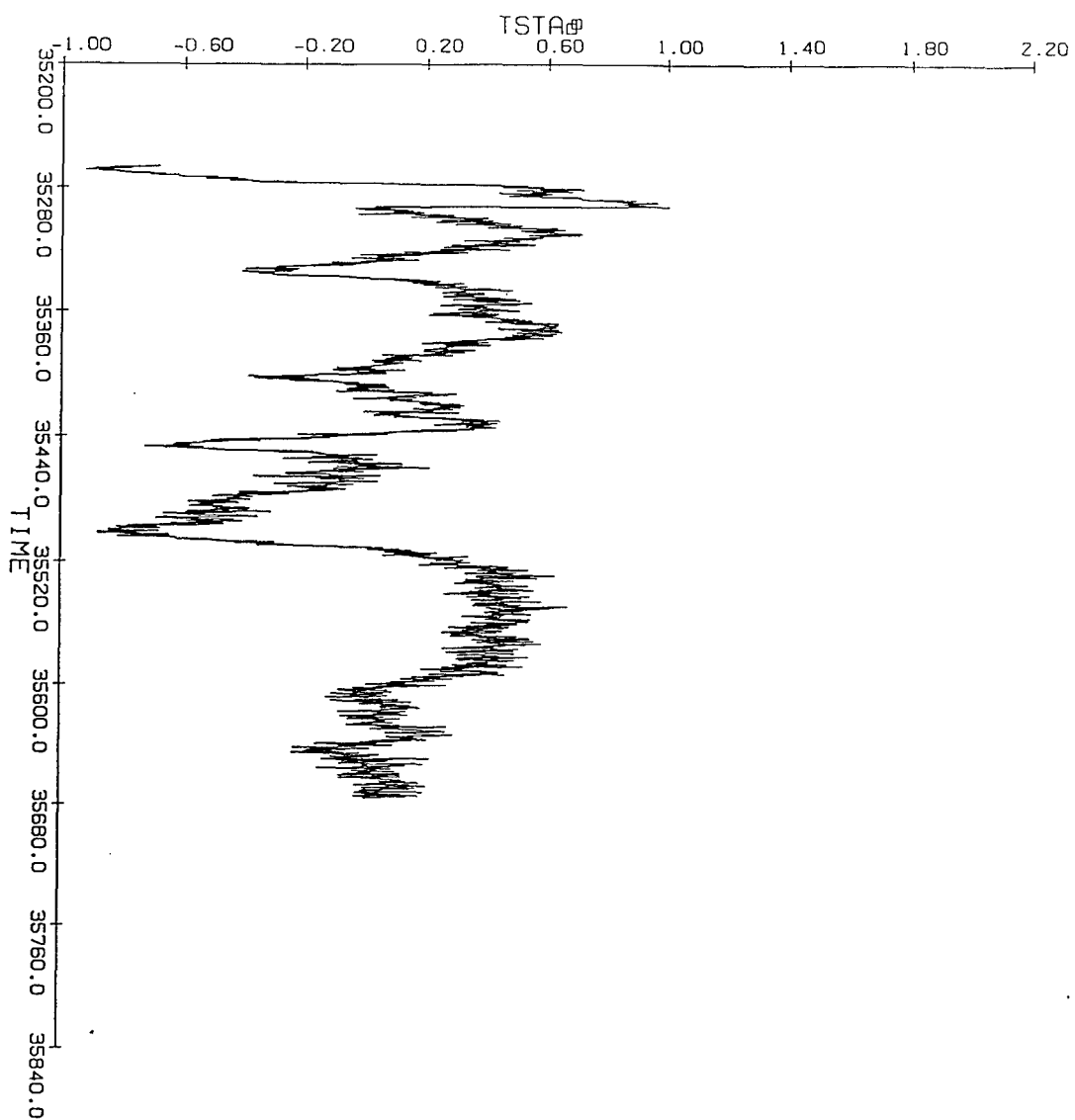


Fig 2

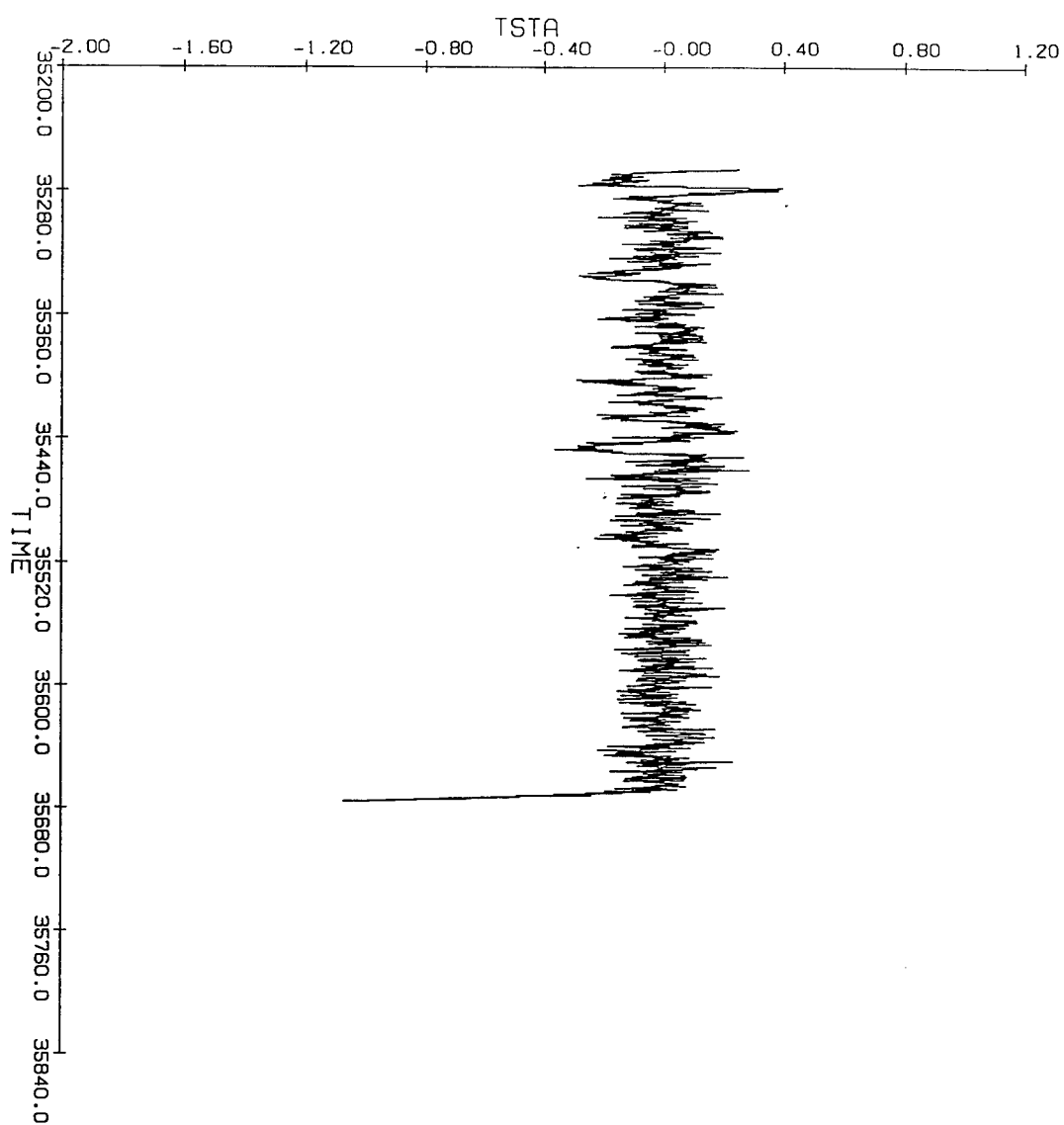
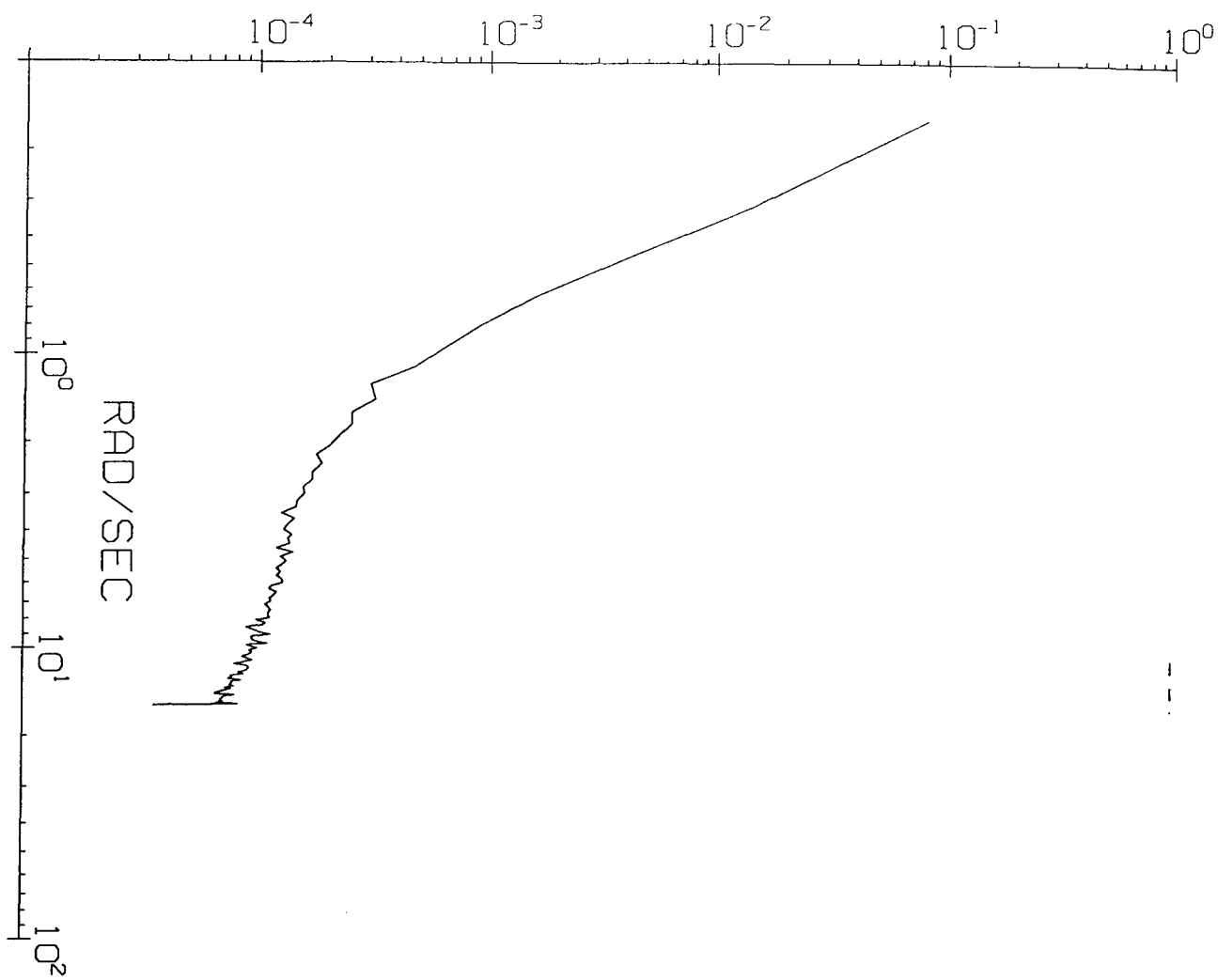


Fig 3

16TA<sub>0</sub>



RAD/SEC

Fig 4

Fig 5

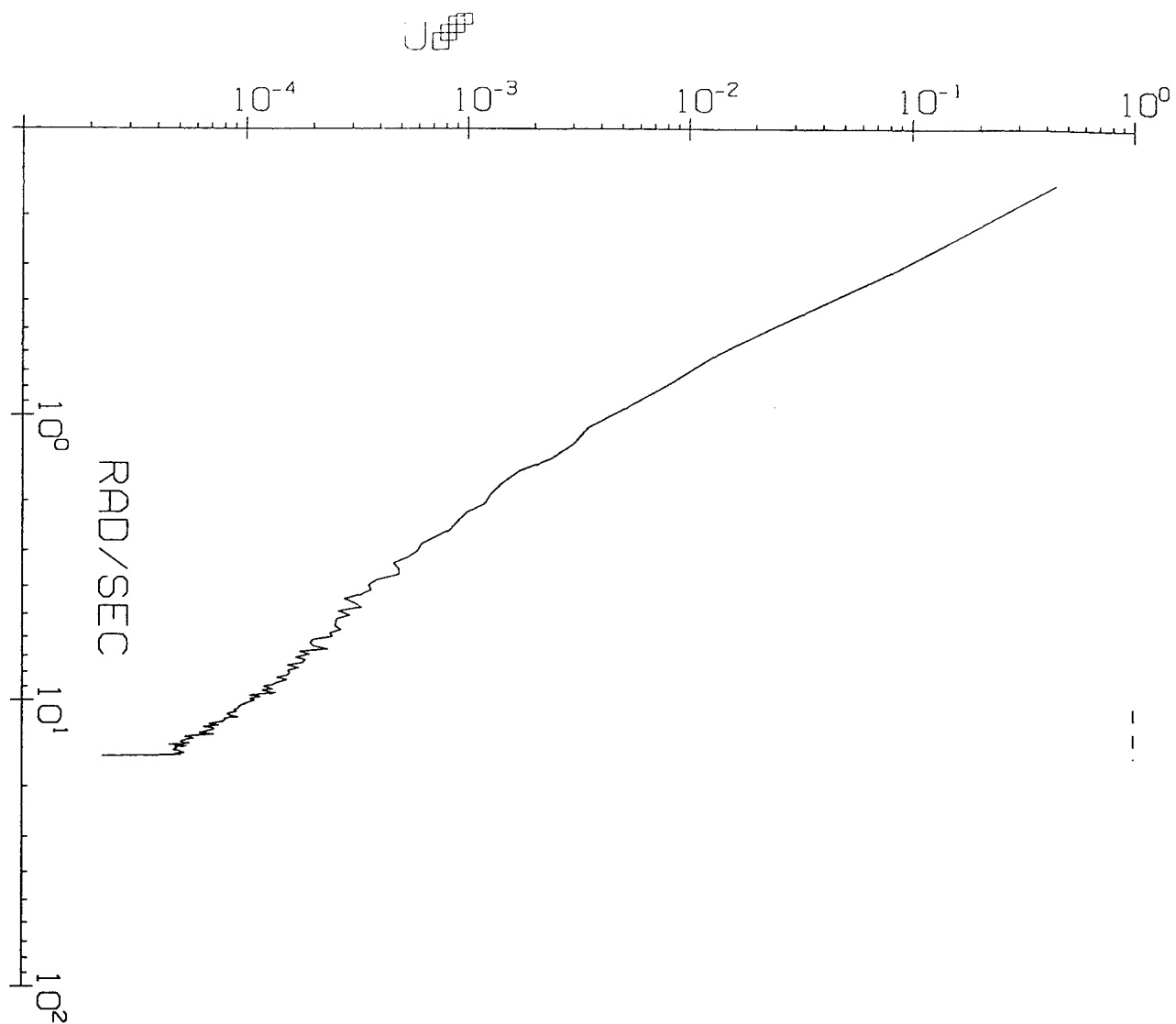
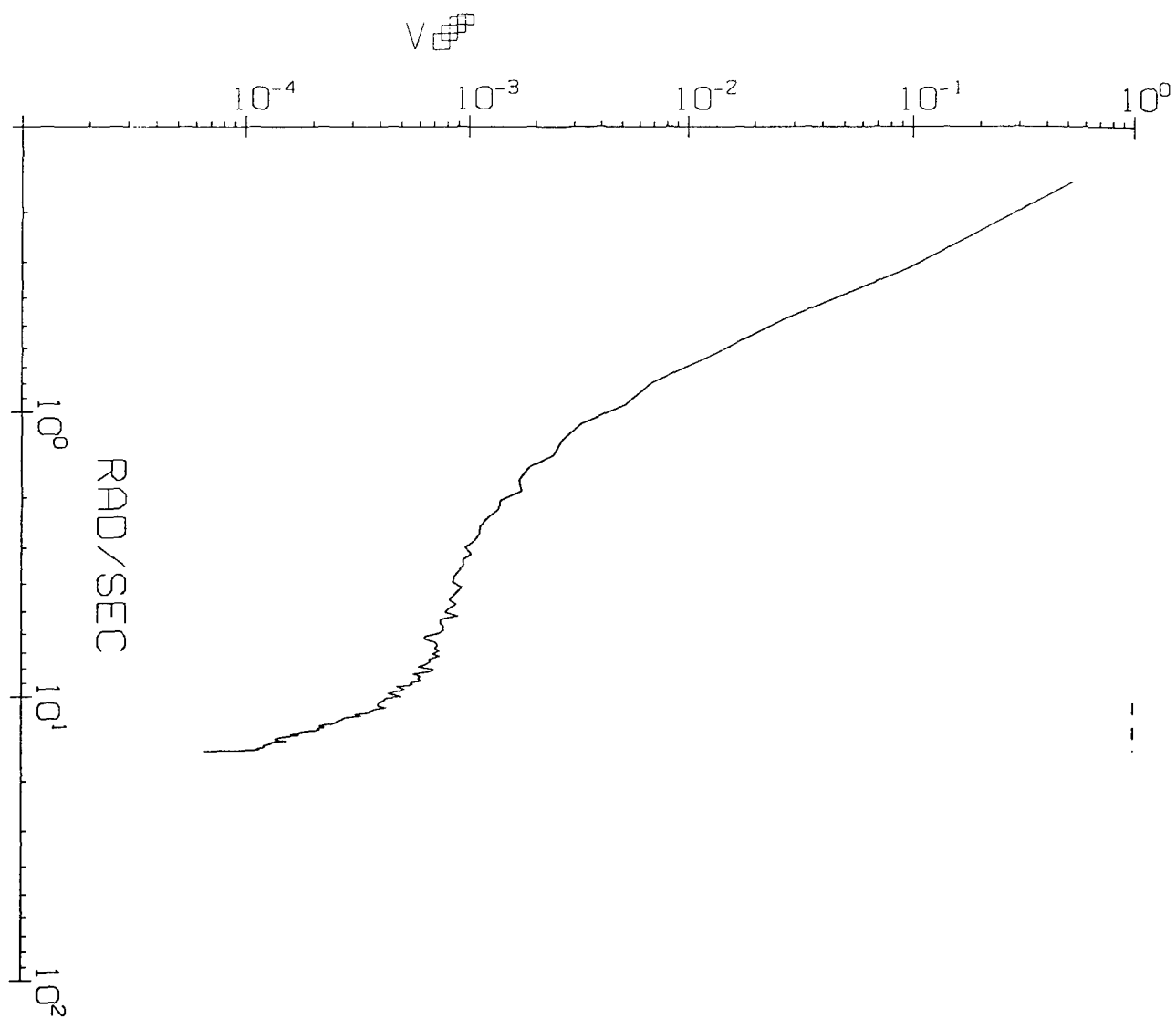
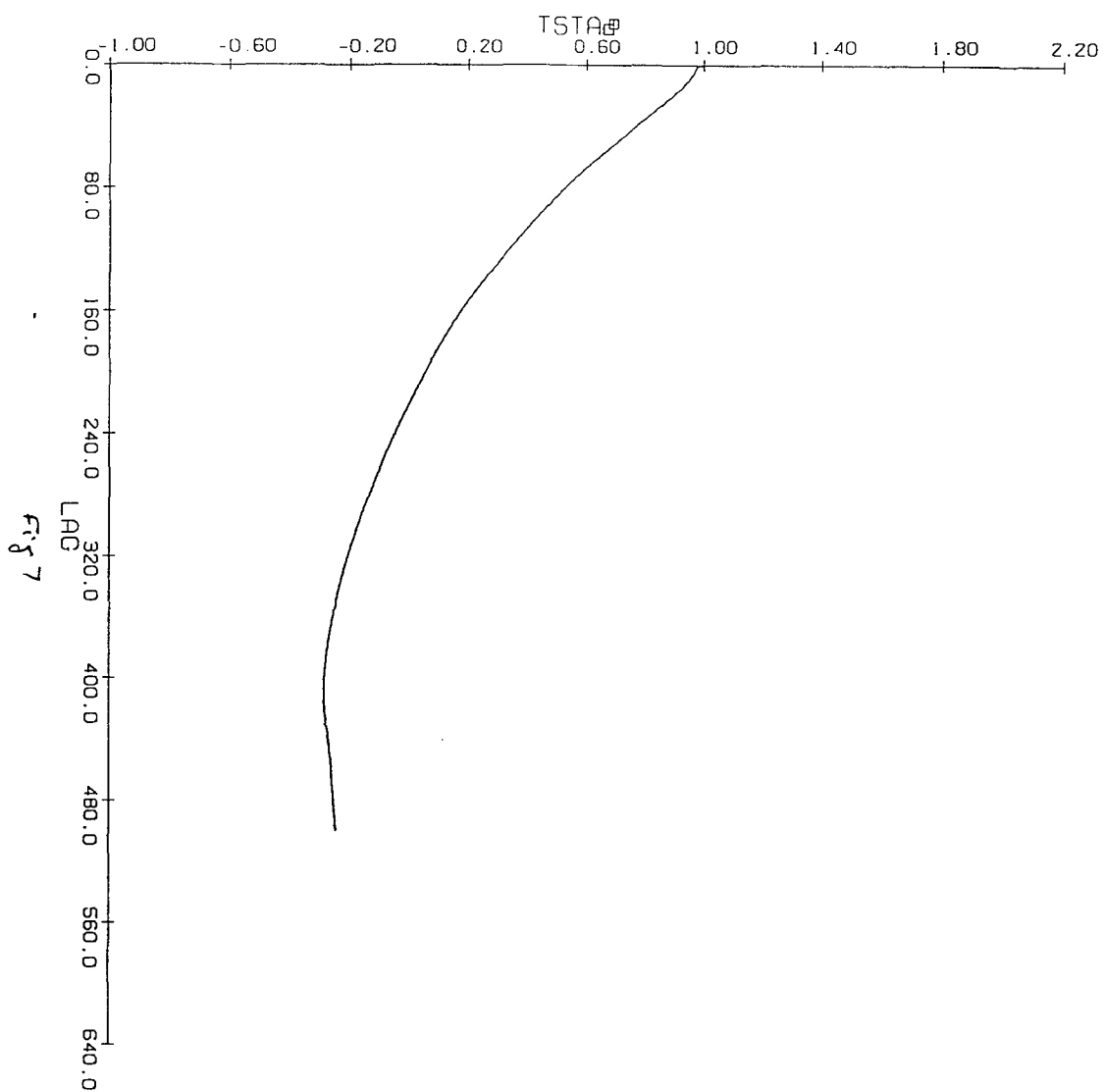


Fig 6







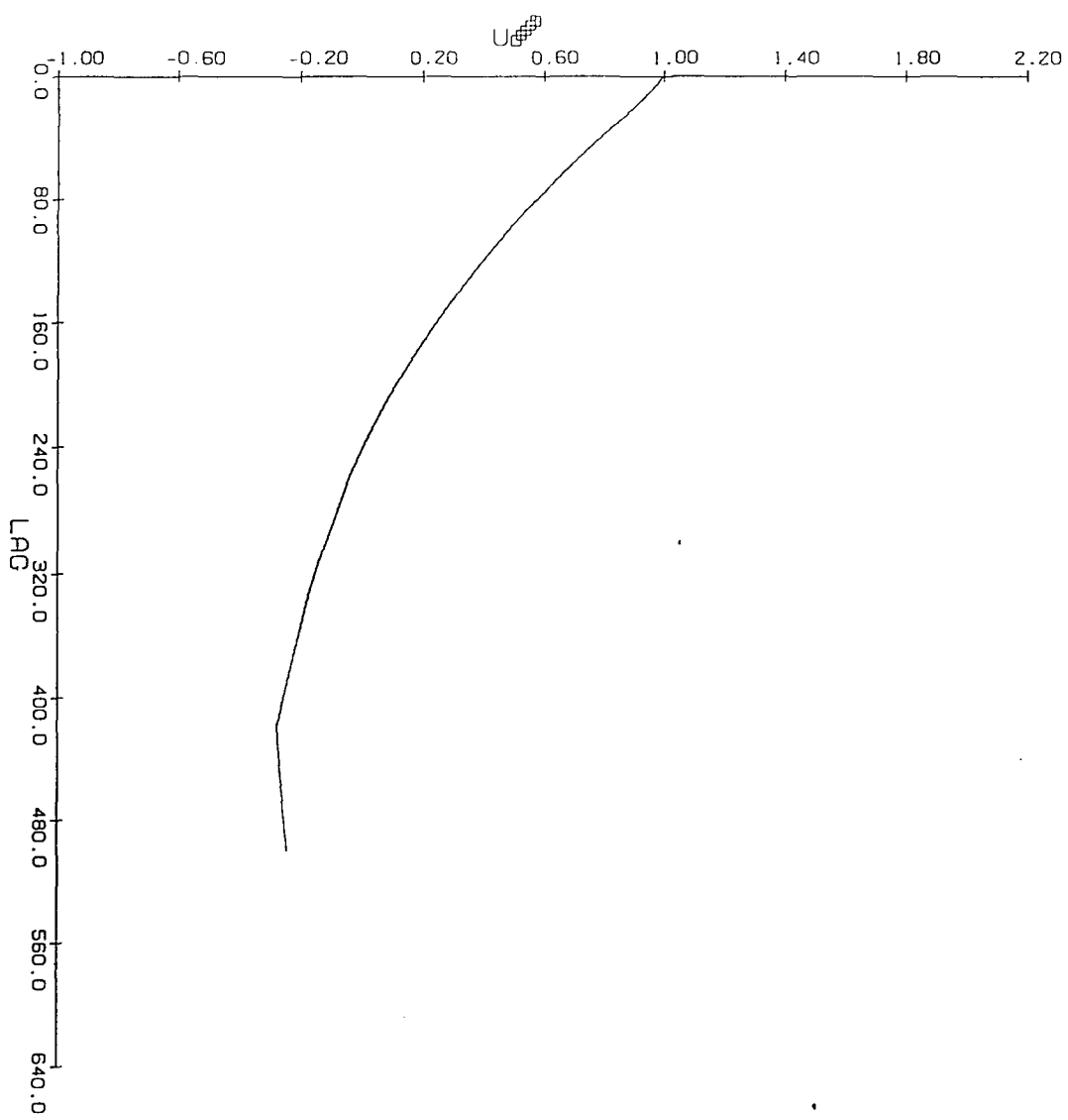


Fig 8

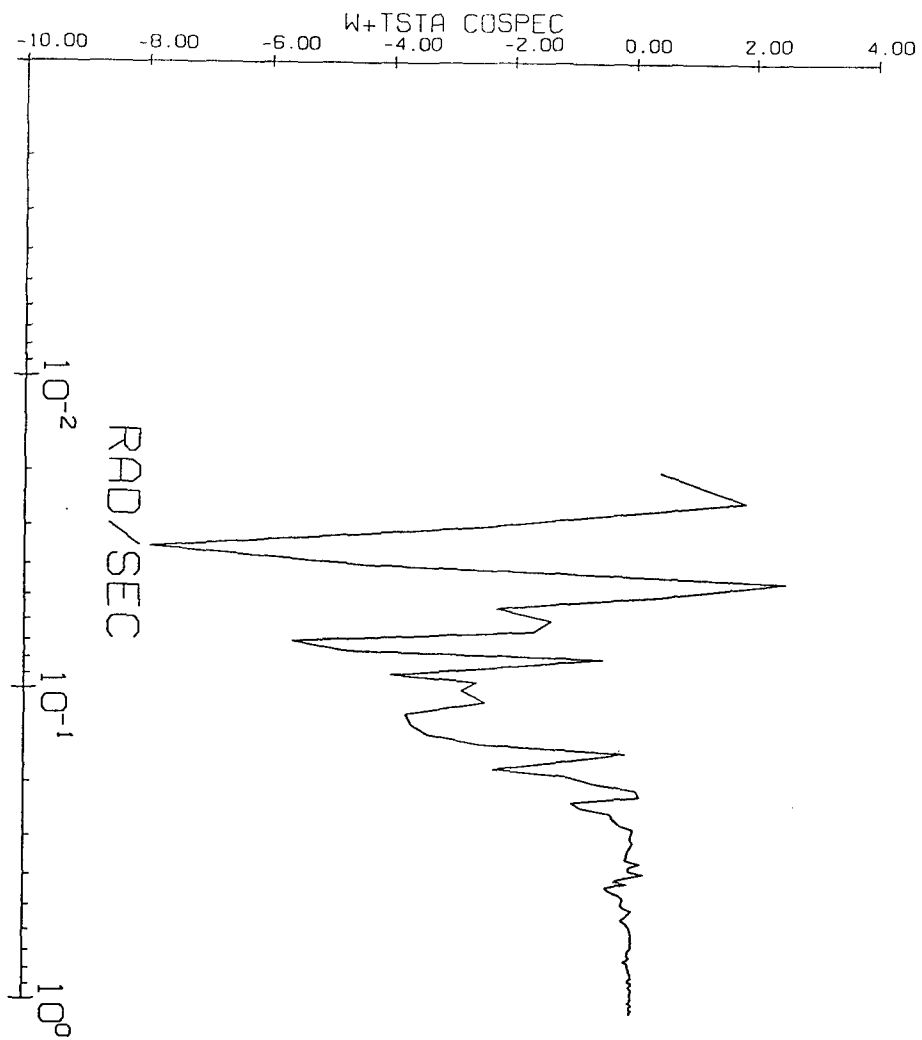


Fig 8.

**ROTATIONAL DYNAMICS OF LAGEOS SATELLITE**

**Arkady Kheyfets  
Assistant Professor  
Department of Mathematics**

**North Carolina State University  
Raleigh, NC 27695-8205**

**Final Report for:  
Summer Research Extension Program  
Phillips Laboratory**

**Sponsored by:  
Air Force Office of Scientific Research  
Bolling Air Force Base, Washington, D.C.  
and  
North Carolina State University**

**December 1993**

## ROTATIONAL DYNAMICS OF LAGEOS SATELLITE

Arkady Kheyfets  
Assistant Professor  
Department of Mathematics  
North Carolina State University

### Abstract

LAGEOS (LAsEr-ranged GEOdynamic Satellite) is a dense spherical satellite covered with a total of 426 corner-cube LASER retroreflectors, which allow its tracking to extremely high accuracy. Such accuracy yields a medium term (years to decades) inertial reference frame, which may be determined via relatively inexpensive observations and which can be used as an adjunct to more difficult and more data intensive absolute frame measurements via VLBI (Very Long Baseline Interferometry). LAGEOS will lead to significantly better position determination and timing accuracy. It will allow bench marking of a global-positioning system against a surface-based coordinate system. There is a substantial secular precession of the satellite line of nodes consistent with the classical, Newtonian precession from the non spherical Earth. There has been a suggestion (Ciufolini) of launching an additional satellite (LAGEOS-3) that would experience equal and opposite classical precession than LAGEOS-1. LAGEOS-3, besides providing a more accurate real-time measurement of the rotation rate of the earth and its orientation parameters, it will provide the first direct measurement of the magnetic component of gravity (*the gravitomagnetic or frame-dragging force*) predicted by Einstein's 1915 and still standard theory of gravitation. Of the five dominant error sources in this experiment, the largest one (potentially) involves surface forces on the satellite and its consequent impact on the orbital nodal precession. The surface forces depend on the orientation and spin rate of the satellite. Consequently, we have undertaken an analytic and numerical effort to model the spin dynamics of the LAGEOS satellite. This report presents our results. The analytic results are valid only under the assumption that the body axis of the satellite coincides with its spin axis. This assumption is violated at very low values of the spin rate. The analytic treatment of the problem becomes intractable under this conditions and we resort to the numerical analysis to augment our investigation.

# ROTATIONAL DYNAMICS OF LAGEOS SATELLITE

Arkady Kheyfets

## I. INTRODUCTION

The Laser Geodynamic Satellite Experiment (LAGEOS-3) is a joint USAF, NASA and ASI proposed program to measure, for the first time, a new quasi-stationary property of the earth — the gravitational magnetic dipole moment of the earth (gravitomagnetism) predicted by Einstein's theory of general relativity. Just as an electrical current of mass (e.g. the spinning motion of the earth) gives rise to a gravitational dipole field. This gravitomagnetic field causes the local inertial frames to be dragged around with the earth at a rate proportional to the angular momentum of the earth and inversely proportional to the cube of the distance from the center of the earth. This will cause the line of nodes of LAGEOS-3 to precess eastward at  $32 \text{ mas/yr}$ . Although this frame dragging effect is small compared to the torque on the orbital plane due to the oblateness of the earth, it is an essential ingredient in the dynamics of accretion disks, binary systems and other astrophysical phenomena.

Today, almost eighty years after Einstein introduced his geometric theory of gravity, we have just begun to measure — to verify — his gravitation theory. Of no less stature than the "tide producing"  $-M/r^2$  "electric component" of gravity is the inertial-frame defining "magnetic component" of gravitation  $-J/r^3$ . To see this force in action; first, inject a satellite into a polar orbit about an earth-like mass idealized as not spinning with respect to the distant quasars. The satellite will remain in orbit in a continuous acceleration towards the center-of-mass of the attracting body under the influence of the Newtonian  $1/r^2$  force, and its orbital plane will remain fixed in orientation with respect to distant quasars. Second, spin this central body, give it angular momentum and follow the trajectory of the satellite. Its orbital plane will experience a torque along the body's rotation axis. The orbital plane will undergo a precessional motion in the direction of the central body's rotation. The mass in motion of the central body or "mass current" produces a magnetic field of gravity — the gravitomagnetic field. In the case of a satellite orbiting at two earth radii, the orbital plane will precess about the body axis of the earth at approximately  $28 \text{ mas/yr}$ .

This force has never been directly measured. A measurement of this gravitomagnetic force can be cast in parallel to the pioneering work of Michael Faraday on the measurement of a magnetic force

between two current-carrying wires. However, the laboratory setting for this gravity measurement will be the 4-dimensional curved spacetime (Kerr) geometry enveloping the earth. The idea behind this gravity measurement is simple. The Everett-Fairbanks experiment (Gravity Probe-B) proposes a polar orbiting gyroscope. The Ciufolini LAGEOS-3 experiment<sup>1</sup> uses the orbital plane as a gyroscope. In particular, in 1976 NASA launched the LAGEOS-1 satellite. It is a totally passive satellite, a 60cm diameter ball of aluminum with 426 retro-reflecting mirrors embedded in its surface. There are 25 globally-located laser tracking stations to observe LAGEOS-type satellites. LAGEOS-1 was injected into a two earth-radii circular orbit at an inclination of 110 deg. The orbital plane rotates due to the oblateness of the earth at a rate of 126 deg/yr. This torque can only be modeled to 450 mas/yr — which is not accurate enough to measure the 32 mas/yr gravitomagnetic force. The idea of Ciufolini: launch another LAGEOS satellite (LAGEOS-3) into an orbit identical to that of LAGEOS-1 except that its inclination is supplementary (70 deg = 180 deg - 110 deg). This proposed orbital plane will rotate in the opposite direction, -126 deg/yr. The intersection of the two (LAGEOS-1, LAGEOS-3) orbital planes will sweep out a "tandem-generated gyro plane" — a plane inertial enough to provide a measurement, accurate to five percent, of the "magnetic component" of gravity.

In this report we discuss the motion of an oblate spheroidal metallic satellite in orbit about the earth. In particular, we are concerned with the effects of the earth's gravitational and magnetic field upon the spin vector of the satellite. The motivation behind this study is the LAGEOS-3 satellite experiment mentioned above. The success of this experiment depends upon the detection of a 32 milliarcsecond per year eastward drift of the line of nodes of the two satellites. The utilization of two satellites forms what we refer to as a tandem-generated gyroscope (see Fig. 1), canceling out many of the much larger precessional effects due to mass eccentricities of the earth. A strong effort is under way to model the orbital and spin dynamics of these satellites, and make an assessment of the uncertainties these will add to the desired measurements. There are five major classes of errors in this experiment: geopotential (other than even zonals) & tides, earth radiation pressure, uncertainty in other relativistic effects, earth and solar-induced thermal forces, and even zonal geopotentials (per 0.1 deg inclination injection error). Due to the recent GEM-T1 improvements in the earth's zonal harmonics, the errors due to solid-earth tides are now smaller than those due to surface effects. The largest source of error on the satellite such as Yarkowsky thermal drag, neutral and charge particle drag, and others<sup>2,3,4</sup>, depend crucially upon the orientation and spin rate of the satellite<sup>4,5</sup>. It is

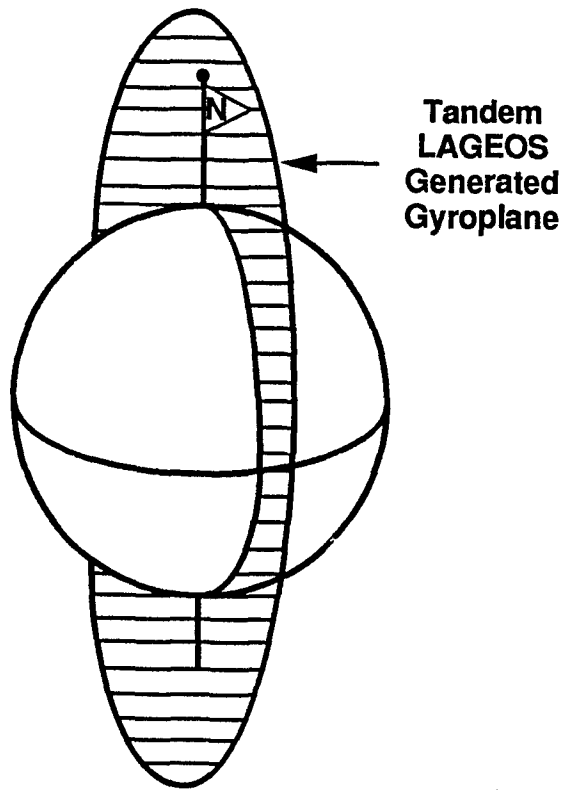


**Fig. 1: The tandem-generated gyro plane and the LAGEOS-3 satellite experiment:** The idea is to launch another LAGEOS satellite (LAGEOS-3) into an orbit identical to that of LAGEOS-1 except that its inclination is supplementary ( $70 \text{ deg} = 180 \text{ deg} - 110 \text{ deg}$ ). This proposed orbital plane will rotate in the opposite direction,  $-126 \text{ deg/yr}$ . The intersection of the two (LAGEOS-1, LAGEOS-3) orbital planes will sweep out a "tandem-generated gyro plane" — a plane inertial enough to provide a measurement, accurate to five percent, of the "magnetic component" of gravity.



the surface forces, in particular the Yarkowsky thermal drag, also referred to as the Rubincam effect, that cause a change in the nodal precession of the satellite, thus contributing to the largest error source in the LAGEOS-3 measurement of the gravitomagnetic effect. It is for this reason that we undertake in this report a theoretical model of the spin dynamics of the LAGEOS-type satellites, and compare it with observational results. One of the important effects considered is the Yarkowsky thermal drag, caused by differential heating and delayed reradiation. This effect is fundamentally related to the nature of the spin vector of the satellite.

Previous studies on the spin dynamics of the LAGEOS satellite<sup>6</sup> were valid only for spins much larger than the orbital period. However, today the spin of the satellite, decaying with a three-year time constant, is rapidly approaching the orbital period. Therefore, we require a low-frequency regime analysis. This low frequency regime, we show, exhibits complex behavior, and the asymptotic state of this forced, damped system, appears to be robust. In this report, we will examine the spin-orbit resonance phase, discuss the asymptotic state of the spin of the satellite, and examine the Aponov exponents. It is the goal of this research to provide an optimum strategy for the measurement of the spin dynamics of the LAGEOS satellites in support of the proposed gravity measurement. In addition, we use our theoretical model to propose an optimum orbital injection procedure for LAGEOS-3. It is our opinion that the LAGEOS-3 satellite should be injected into the orbital plane with as large a spin rate as possible. We demonstrate in this report that the LAGEOS-1 satellite will be sufficiently predictable to support the gravitomagnetic measurement. The results in this report provide the first analysis of the asymptotic spin dynamics of the LAGEOS satellite. Previous calculations were unable to analyze the spin-orbit resonances of the satellite, which will play a crucial role in the experiment.

It is rather interesting that after 36 years the spin dynamics of satellites are once again important in the field of astrodynamics. In 1957 Vinti<sup>7</sup> analyzed the spin dynamics of a non-ferromagnetic spherical satellite in the earth's magnetic field which was of critical importance to the alignment of antennas. Today, we perform the same analysis on a slightly oblate satellite, of critical importance to the first measurement of the magnetic component of gravity, as predicted by Einstein. That the uncertainties induced by the surface forces on LAGEOS are on the order of 4% percent out of a 6% experiment make the theoretical modeling paramount.

In sections II-IV of this report we provide a brief review of the two principal driving forces of the LAGEOS rotational dynamics — magnetic torques caused by the action of the Earth magnetic field on Eddy

currents induced in the conducting structure of the satellite, and gravitational torques caused by the action of Earth's inhomogeneous gravitational field on the oblate satellite. We, also, briefly describe the state of studies on the LAGEOS rotational dynamics preceding our work.

In section V we provide a critical analysis of the approximations used in describing the LAGEOS spin dynamics in previous research. We note that some of the approximations were not realistic, could lead to incorrect predictions, and need to be discarded. In particular, we discard the assumption of the fast spinning rate of the satellite. The long term predictions of the satellite rotational dynamics change considerably. We have been able to investigate the LAGEOS spin dynamics analytically if we assume that the spin axis of the satellite coincides with the frame body axis, which is good only for moderately low spin rates. The results of this analysis are described in sections VI and VII of the report.

At very low spin rates the assumption of the fixed spin axis cannot be retained. An analytic investigation of the Lagrange equations of the satellite spin dynamics becomes intractable. For this reason, we have switched to numerical methods. Under these conditions Lagrange approach does not present any advantages, and in sections VIII–XI we use the Euler equations. The results are briefly discussed in section XII.

## II. MAGNETIC TORQUE ON LAGEOS

As it has been mentioned above, the model<sup>6</sup> of LAGEOS spin dynamics takes into account the influence of the eddy currents induced in the aluminum core of LAGEOS by the Earth's magnetic field and the precession caused by the influence of gravitational gradient on the oblate spinning satellite. The main acting torques in this model are due to (1) the eddy currents generated in the conducting body of the LAGEOS satellite by the  $\vec{v} \times \vec{B}$  force due to the rotational velocity and (2) the gradient of the gravitational field of the Earth acting on the oblate distribution of LAGEOS's mass.

In this section we discuss the origin of the magnetic torques acting on LAGEOS.

In a rotating frame of the satellite the Earth's magnetic field is changing with the rotation frequency  $\omega$  and induces in the body of the satellite eddy currents to a depth of the order of

$$\delta = \frac{c}{\sqrt{2\pi\omega\sigma}} \quad (1)$$

where  $c$  is the speed of light, and  $\sigma$  is the electrical conductivity ( $\sigma = 2.2 \times 10^{17} \text{ s}^{-1}$ )<sup>8</sup>. The induced current interacts with the Earth's magnetic field and produces the magnetic torque. In this report, when calculating magnetic effects, we assume that LAGEOS has the shape of a sphere. We neglect subtle details related to the complex internal structure of the satellite because it does not seem to contribute to the drastic difference between our predictions and these of the previously established model. The magnetic torque exerted on the spherical conductor rotating with the angular velocity  $\vec{\omega}$  is expressed by

$$\vec{\Gamma} = V\alpha'\vec{\omega} \times \vec{B}(\vec{\omega} \cdot \vec{B}) - V\alpha''(\vec{B} \times \vec{\omega}) \times \vec{B} = \vec{\Gamma}' + \vec{\Gamma}'' \quad (2)$$

where  $\hat{\omega}$  is the unit vector pointing in the direction of  $\vec{\omega}$ , and  $\alpha' + i\alpha'' = \alpha$  is the complex polarizability per unit volume (dimensionless), and  $V$  is the volume of the satellite. For the conducting sphere of radius  $\rho$  functions  $\alpha'$  and  $\alpha''$  are given by<sup>8</sup>

$$\begin{aligned} \alpha' &= -\frac{3}{8\pi} \left[ 1 - \frac{3}{x} \frac{\sinh x - \sin x}{\cosh x - \cos x} \right] \\ \alpha'' &= -\frac{9}{4\pi} \frac{1}{x^2} \left[ 1 - \frac{1}{2} x \frac{\sinh x + \sin x}{\cosh x - \cos x} \right] \end{aligned} \quad (3)$$

where  $x = \frac{2\rho}{\delta} = \frac{2\rho}{c} \sqrt{2\pi\omega\sigma}$ . Two particular cases are of special importance, (1) the low frequency approximation ( $x \ll 1$ , or, equivalently,  $\omega$  small) and the limit  $\omega \rightarrow 0$  ( $x \rightarrow 0$ ), and (2) the high frequency approximation ( $x \gg 1$ , or, equivalently,  $\omega$  large) and the limit  $\omega \rightarrow \infty$  ( $x \rightarrow \infty$ ). For the low frequency approximation  $\alpha'$  and  $\alpha''$  can be represented by series

$$\begin{aligned} \alpha' &= -\frac{1}{1680\pi} x^4 + \frac{1}{665280\pi} x^8 + \dots \\ \alpha'' &= -\frac{1}{80\pi} x^2 + \frac{1}{33600\pi} x^6 + \dots \end{aligned} \quad (4)$$

so that in the limit  $\omega \rightarrow 0$  ( $x \rightarrow 0$ ) both  $\alpha' \rightarrow 0$  and  $\alpha'' \rightarrow 0$ . It is easy to figure out corresponding expressions for the high frequency approximation, particularly it is clear that, as  $\omega \rightarrow \infty$  ( $x \rightarrow \infty$ ),  $\alpha' \rightarrow -\frac{3}{8\pi}$  and  $\alpha'' \rightarrow 0$ .

Bertotti and Iess<sup>6</sup> perform the magnetic torque analysis in the low frequency approximation. They argue that in this approximation the real part of polarizability  $\alpha'$  is much smaller than its imaginary part  $\alpha''$  (cf. expressions (4)) and can be neglected, in which case the torque  $\vec{\Gamma}$  can be approximated by

$$\vec{\Gamma} \approx \vec{\Gamma}'' = -V\alpha''\vec{\omega} \cdot (\vec{B}\vec{B} - \mathbf{I}B^2) \quad (5)$$

where  $\mathbf{I}$  is the unit dyadic. This torque obviously causes the decay of the satellite spin rate. More detailed analysis by Bertotti and Iess indicates that the direction of the spin also evolves and that the picture of the spin evolution can be rather involved.

### III. MAGNETIC SLOWING DOWN OF LAGEOS

The magnetic field experienced by LAGEOS along its orbit is not constant. A reasonable suggestion<sup>6</sup> is to approximate the Earth's magnetic field by a dipole magnetic field

$$\vec{B} = \nabla \frac{\vec{d} \cdot \vec{r}}{r^3} = \frac{r^2 \vec{d} - 3\vec{r}(\vec{r} \cdot \vec{d})}{r^5} \quad (6)$$

where  $\vec{d}$  is the Earth's magnetic dipole vector. Since the angular velocity changes very little in an orbital period it is reasonable to average the torque (5) over the orbit. In the frame where the node is at rest and the components of the unit vector parallel to the Earth's axis are  $(0, 0, 1)$  while the components of the unit vector orthogonal to the orbit plane are  $(\sin I, 0, \cos I)$  (where  $I$  is the orbital inclination) the averaging procedure leads to the positive definite matrix

$$\langle B^2 \delta_{ij} - B_i B_j \rangle = \frac{d^2}{a^6} \beta_{ij} \quad (7)$$

where  $a$  is the orbital radius, and  $\beta_{ij}$  is the matrix

$$\beta_{ij} = \begin{pmatrix} b_1 & 0 & b_2 \\ 0 & b_3 & 0 \\ b_2 & 0 & b_4 \end{pmatrix} \quad (8)$$

with

$$\begin{aligned} b_1 &= \frac{1}{8}(20 - 39 \cos^2 I + 27 \cos^4 I) \\ b_2 &= \frac{3}{8}(5 - 9 \cos^2 I) \cos I \sin I \\ b_3 &= \frac{1}{8}(11 - 3 \cos^2 I) \\ b_4 &= \frac{3}{8}(3 - 4 \cos^2 I - 9 \cos^4 I) \end{aligned} \quad (9)$$

The averaged magnetic torque causes the mean rotation vector  $\omega_i$  to evolve according to the equation

$$\frac{1}{\nu_m} \frac{d\omega_i}{dt} = -\beta_{ij} \omega_j \quad (10)$$

where

$$\nu_m = V \frac{\alpha''}{I_3} \frac{a^2}{d^6} \quad (11)$$

is the value of the magnetic spin decay frequency ( $I_3$  is the moment of inertia with respect to the principal axis parallel to  $\vec{\omega}$ ). The  $\nu_m$  is the measure of how fast the LAGEOS's spin decays. One has to keep in mind that, in such a description, the actual evolution of spin (including its direction) can be rather involved and depends crucially on the eigenvalues and eigenvectors of the matrix  $\beta_{ij}$ . One can find a rather detailed description of the different possibilities in the paper by Bertotti and Iess<sup>6</sup>. We are not considering these details here. Although it is an interesting subject, it has nothing to do, in our opinion, with the long term prediction of LAGEOS's spin dynamics. Any attempt to extrapolate this technique to the case of small spin will fail. The breakdown will take place long before the averaging procedure will lose its meaning. As we will see the basic procedures can be applied for the small value of spin. The main problem with the described technique is an implicit assumption of a rigid split of rotation into the spin itself and precession that cannot be sustained at small values of the spin rate. However this assumption can be dropped without essential losses if the goal is restricted to asymptotic predictions.

#### IV. GRAVITATIONAL PRECESSION: FAST SPINNING SATELLITE

Gravitational precession is caused by the influence of gravitational gradient on the oblate spinning satellite. The oblateness of the satellite is determined by the combination

$$\Delta = \frac{I_3 - I_1}{I_3} \quad (12)$$

where  $I_3$  and  $I_1 = I_2$  are the principal moments of inertia (the principal direction corresponding to  $I_3$  is assumed to be that of  $\vec{\omega}$  (coinciding with the direction of the symmetry axis of the oblate satellite). The gradient of the Earth's gravitational field acts on the oblate mass distribution of LAGEOS and produces a precession of its spin vector around the normal to the orbital plane at a rate  $\omega_p$  given by the formula

$$\omega_p = \frac{3}{2} \Delta \frac{\omega_0^2}{\omega_3} \cos \theta \quad (13)$$

for  $\omega_p \ll \omega_0 \ll \omega$ , where  $\omega_0$  is the orbital angular velocity,  $\omega_3$  is the satellite spin, and  $\theta$  is the obliquity angle of spacecraft (the angle between  $\vec{\omega}$  and the normal to the orbital plane). This gravitational precession has the same mechanism as the lunisolar Hipparchos precession of the Earth<sup>9</sup>. The value of the LAGEOS's oblateness is  $\Delta \approx 3.35\%$ <sup>1</sup>. The initial gravitational precession period was of the order of hundreds of years but should decrease rapidly as spin motion of the satellite slows down.

It is argued by Bertotti and Iess<sup>6</sup> that, since  $\omega_p \propto 1/\omega$  the gravitational precession in the asymptotic limit dominates and may make the spin dynamics chaotic. According to their original prediction the first signs of such a behavior should show up by now. This prediction has not been confirmed by observations and, as we will argue, is not likely to be observed in far future, in any case not at spin rates satisfying the assumption of separability of the LAGEOS spin, precessional and nutational components in its total rotational motion. It is based on the equation (13) which can be applied only if the spin rate  $|\omega_3|$  is large. It is assumed that eventually the period of gravitational precession will become very short and it is concluded<sup>6</sup> that LAGEOS, like a very slow top, will start tumbling faster and faster, with a chaotic dynamics until eventually the scale of variations of  $\vec{\omega}$  will become shorter than the orbital period of the satellite and the original model of Bertotti and Iess will be no longer applicable.

We believe that the latter prediction of Bertotti and Iess is too pessimistic. Their model, with minor improvements, is much more viable than it might appear. It is not quite clear what, within their model, is the nature of the predicted tumbling. Perhaps, it is nutation. If so, it can be included in the model without too much trouble and analyzed by relatively simple means. As about breaking the averaging approximation because of fast precession and nutation, the situation is also not so desperate. As we will see later it simply does not happen. The model is breaking down only when the split of the satellite total rotational motion into its spin, precessional and nutational components cannot be sustained, and when the satellite rate of rotation becomes comparable to its rate of orbital motion.

## V. APPROXIMATIONS IN LAGEOS SPIN DYNAMICS

A discrepancy between the theoretical predictions concerning gravitational precession<sup>6</sup> and the recent observational evidence presents us with a strong motivation to reconsider carefully approximations made in the process of deriving basic equations describing LAGEOS's spin dynamics and the adequacy of these approximations in the case of LAGEOS. These approximations are necessary not only to make the problem tractable but also, and this is much more important, to make sure that a model captures sufficient features of the phenomenon under consideration and ignores the unimportant aspects of the problem, the ones that seem to be important to provide a better fit with available experimental data but in fact are unnecessary and eventually prevent the model from making correct predictions on the future evolution of the system. The issue of correct approximations is especially important in problems demanding long term predictions, like the LAGEOS's spin dynamics.

The assumptions in modeling the LAGEOS's spin dynamics can be subdivided in several different classes. These are:

(1) Assumptions on the nature of forces acting on the satellite.

These are the assumptions that enable one to write down the expressions for potential functions, Lagrangians, torques, etc. Ordinarily, they include some assumptions concerning the properties of the materials, shapes of the objects, influence of motions of the objects on these properties. Any change in these assumptions usually implies a very extensive effort. We are going to avoid doing it for as long as it does not appear absolutely necessary.

(2) Assumption concerning the independence of degrees of freedom.

This assumption is present implicitly in the Bertotti-Iess model and expresses itself in neglecting the nutations. It prevents the model from analyzing the transition to the regime of tumbling. We will discard this assumption eventually. This requires introduction of the full system of Lagrange or Euler equations and leads to some complications but the problem appears to be tractable for the asymptotic analysis, at least numerically. Neglecting the nutations can also lead to incorrect conclusions concerning precessions because nutations and precessions are coupled.

(3) Assumptions on the relative rates of the orbital angular velocity, spin, and precession.

The model of Bertotti and Iess uses the standard assumption that the rate of precession is much smaller than the orbital angular velocity. This assumption allows the to use the averaging procedure (averaging over the orbit) for the magnetic torque and, implicitly, for the Earth's gravitational field gradient. This assumption appears to lead to breakdown of the model as soon as the satellite spin slows down sufficiently (cf. equation (13)) and the rate of precession exceeds the orbital angular velocity, which would make the averaging procedure meaningless. It is interesting that the potentially troublesome averaging procedure turns out to be rather harmless. The reason for this is that formula (13) is correct only for large values of spin. At small values of spin the rate of precession is given by a different expression (cf. next section) according to which the rate of precession is bounded by the value much smaller than the orbital angular velocity. The assumption in question, and together with it

the orbital averaging procedure, can be, unexpectedly, retained with no severe penalty for as long as the rate of precession is being calculated (but should be dropped when discussing nutations). The assumption of the spin being large compared to the orbital angular velocity is completely different matter. It is a very common assumption in the rigid body mechanics. It is used in the theory of the equinoxes precession, and, in particular, in deriving expression (13). It is absolutely unnecessary, cannot be satisfied in the study of asymptotic behavior of LAGEOS's spin, and dropping it only improves the physics of the model. We will illustrate this point in the next section.

In conclusion of this section a few general remarks are in order. It is very hard to believe predictions of the previously established model<sup>6</sup> concerning asymptotic behavior of the LAGEOS's spin dynamics at  $t \rightarrow \infty$  ( $\omega_3 \rightarrow 0$ ).

- (i) For any mechanism of spin dissipation it seems hardly possible that the precession frequency can grow too much. Energy associated with the precession motion is coming from the potential energy of the oblate mass distribution of the satellite in the inhomogeneous gravitational field of Earth and is bounded which implies that the precession rate should be bounded too.
- (ii) The same mechanism as that of spin dissipation (eddy currents) should also dissipate motions associated with precession and nutation. Admittedly, in the beginning the rate of precession is very small compared with the spin. However this cannot be told about nutation. A rough estimate of the nutation frequency (using the formulae derived for the fast top) at large values of spin leads to

$$a = \frac{I_3}{I_1} \omega_3 \approx \omega_3 \quad (14)$$

which means that the nutation frequency is of the same order of magnitude as the spin rate and, as a consequence, the rate of decay of nutation should be about the same as that of spin. Under these conditions one cannot expect the satellite to tumble eventually like a very slow top. As about the decay of precessions, it should eventually occur, too, although the time scale of this decay might be different.

More generally, it should be, probably, expected that all spin related motions will be eventually decayed except those that are sustained by some constantly present torque. Roughly speaking, the situation should



be like in the case of Moon orbiting around Earth, although the decay mechanism in the latter case is quite different from this of LAGEOS.

Finally, it should be noted that all these conclusions do not take into account the resonance type phenomena that occur when the satellite spin frequency approaches its orbital frequency. These phenomena are hard to investigate analytically. We present the results of our numerical analysis in sections VIII – XII of this report.

## **VI. GRAVITATIONAL PRECESSION: ARBITRARY SPIN OF THE SATELLITE**

In this section we are going to analyze the procedure of calculating the gravitational precession of LAGEOS dropping the assumption of the fast rate of spin, but retaining the assumption of the rate of precession being slow compared to the orbital angular velocity. This analysis is much simpler than the analysis of the full system of Lagrange equations describing the spin dynamics of LAGEOS interacting with both magnetic and gravitational field of the Earth, it gives an idea on the origin of the bounds imposed on the parameters of the spinning satellite, and motivate the further study of the complete system of equations. In the next section we describe briefly the most important results of our study of asymptotics of the LAGEOS's spin dynamics.

The equations governing the LAGEOS's gravitational precession are the same as those describing the Earth's precession about the normal to the ecliptic, a motion known in astronomy as the precession of equinoxes, or Hipparchos precession<sup>9</sup>. In our case this precession is caused by the action of the Earth's gravitational field on the slightly oblate LAGEOS. To calculate the rate of this precession one needs to calculate the mutual gravitational potential of the Earth, approximated in the standard procedure of derivation<sup>9</sup> by a mass point  $M$ , and a nonspherical distribution of matter representing LAGEOS. Approximating the Earth by a mass point is equivalent to neglecting the Earth's oblateness which appears quite adequate in matters concerning the satellite spin dynamics, as simple considerations indicate that the Earth's oblateness coupled only to orbital parameters in the lowest order approximation.

Evaluation of potential energy is performed via expansion of energy in a power series with coefficients proportional to appropriate Legendre polynomials and subsequent truncation neglecting the terms of higher than the second power. It is assumed in calculations that the axis of symmetry is the third principal axis

of the LAGEOS's inertia tensor, so that  $I_1 = I_2 \neq I_3$ . If  $\alpha, \beta, \gamma$  are the direction cosines of the radius vector from the LAGEOS's center to the Earth with respect to the principal axes, then the expression for the potential is given by

$$V = -\frac{GMm}{r} + \frac{GM(I_3 - I_1)}{2r^3} [3\gamma^2 - 1], \quad (15)$$

or

$$V = -\frac{GMm}{r} + \frac{GM(I_3 - I_1)}{r^3} P_2(\gamma). \quad (16)$$

where  $P_2(x)$  is the second Legendre polynomial determined by

$$P_2(x) = \frac{1}{2}(3x^2 - 1). \quad (17)$$

In what follows we assume LAGEOS to be rigid. In particular, we require that the principal axes be fixed in LAGEOS and the associated moments of inertia be constant in time.

In expression (16) for the potential only the second term

$$V_2 = \frac{GM(I_3 - I_1)}{r^3} P_2(\gamma) \quad (18)$$

depends on the orientation of LAGEOS and thus could give rise to torques. It was mentioned above that  $\gamma$  is the direction cosine between the LAGEOS axis and the radius vector from the LAGEOS's center to the Earth. As the Earth goes around its apparent orbit  $\gamma$  is changing. It is customary to express  $\gamma$  in terms of functions of two angles, the first one ( $\theta$ ) being the angle between the axis of LAGEOS and the normal to the LAGEOS's orbit plain (also called the obliquity of the LAGEOS's axis), the second one ( $\eta$ ) being the angular position of the Earth on its apparent orbit. The relation between  $\gamma, \theta$ , and  $\eta$  is

$$\gamma = \sin \theta \cos \eta. \quad (19)$$

Hence,  $V_2$  can be written

$$V_2 = \frac{GM(I_3 - I_1)}{2r^3} [3 \sin^2 \theta \cos^2 \eta - 1]. \quad (20)$$

In typical applications the orbital motion is very rapid compared to the precessional motion. The usual practice is to average  $V_2$  over a complete orbital period for the purpose of obtaining the mean precession rate. The orbit of LAGEOS has very low eccentricity, which implies that  $r$  can be assumed constant and the only variation is in  $\cos \eta$  (with  $\overline{\cos^2 \eta} = \frac{1}{2}$ ), so that

$$\overline{V_2} = \frac{GM(I_3 - I_1)}{2r^3} \left[ \frac{3}{2} \sin^2 \theta - 1 \right] = \frac{GM(I_3 - I_1)}{2r^3} \left[ \frac{1}{2} - \frac{3}{2} \cos^2 \theta \right]. \quad (21)$$

Finally, the expression for  $\overline{V}_2$  takes form

$$\overline{V}_2 = \frac{GM(I_3 - I_1)}{2r^3} P_2(\cos \theta). \quad (22)$$

The torque derived from equation (22) is perpendicular to both LAGEOS's axis and the normal to the orbit (which plays the same role as the vertical axis for the heavy top). Hence the precession is about the direction of the orbit normal vector. The magnitude of the precession rate can be obtained in several different ways. We choose to use Lagrange equations approach because it makes assumptions of an accepted approximation transparent.

For a symmetric body in which the potential is a function of  $\cos \theta$  only, as it is the case with LAGEOS, the Lagrangian can be written as

$$L = \frac{I_1}{2}(\dot{\theta}^2 + \dot{\phi}^2 \sin^2 \theta) + \frac{I_3}{2}(\dot{\psi} + \dot{\phi} \cos \theta)^2 - V(\cos \theta). \quad (23)$$

At this point we are not going to write the full Lagrangian equation corresponding to  $\theta$ . Instead, as it is done ordinarily, we assume only uniform precession and do not concern ourselves about the necessary initial conditions. We simply take  $\dot{\theta} = 0$  and  $\ddot{\theta} = 0$  in the equations of motion. The simplified Lagrangian equation corresponding to  $\theta$  is then

$$\frac{\partial L}{\partial \theta} = I_1 \dot{\phi}^2 \sin \theta \cos \theta - I_3 \dot{\phi} \sin \theta (\dot{\psi} + \dot{\phi} \cos \theta) - \frac{\partial V}{\partial \theta} = 0. \quad (24)$$

Taking into account that

$$\omega_3 = \dot{\psi} + \dot{\phi} \cos \theta, \quad (25)$$

and, for  $V = V(\cos \theta)$ ,

$$\frac{\partial V}{\partial(\cos \theta)} = -\frac{1}{\sin \theta} \frac{\partial V}{\partial \theta}, \quad (26)$$

we can rewrite equation (24) in the form

$$I_3 \omega_3 \dot{\phi} - I_1 \dot{\phi}^2 \cos \theta = \frac{\partial V}{\partial(\cos \theta)}. \quad (27)$$

In our case

$$\frac{\partial V}{\partial(\cos \theta)} = \frac{\partial \overline{V}_2}{\partial(\cos \theta)} = -\frac{3}{2} \frac{GM(I_3 - I_1)}{r^3} \cos \theta. \quad (28)$$

Using Kepler's law

$$\omega_0^2 = \left(\frac{2\pi}{\tau}\right)^2 = \frac{GM}{r^3}, \quad (29)$$

where  $\omega_0$  the angular velocity of the orbital motion and  $\tau$  is the orbital period, we can write instead of (28)

$$\frac{\partial V}{\partial(\cos \theta)} = \frac{\partial \bar{V}_2}{\partial(\cos \theta)} = -\frac{3}{2} \omega_0^2 (I_3 - I_1) \cos \theta. \quad (30)$$

Hence, the Lagrange equation (27) takes the following final form

$$I_3 \omega_3 \dot{\phi} - I_1 \dot{\phi}^2 \cos \theta = -\frac{3}{2} \omega_0^2 (I_3 - I_1) \cos \theta. \quad (31)$$

Standard applications of equation (31), such as, for instance, the precession of the Earth's equinoxes, assume also that the precession rate  $\dot{\phi}$  is small. It is usually stated<sup>9</sup> that for the case  $\dot{\phi} \ll \omega_3$  the  $\dot{\phi}^2$  term in equation (31) can be dropped. As we will see later this procedure (dropping the term quadratic in  $\dot{\phi}$ ) is not as innocent as it might look from the first sight. But for the time being we will go along with the standard line of reasoning. Neglecting this quadratic term immediately leads to the following expression for the rate of precession

$$\dot{\phi} = -\frac{3}{2} \frac{\omega_0^2}{\omega_3} \frac{I_3 - I_1}{I_3} \cos \theta = -\frac{3}{2} \frac{\omega_0^2}{\omega_3} \Delta \cos \theta, \quad (32)$$

where  $\Delta = (I_3 - I_1)/I_3$  determines the oblateness of LAGEOS. This expression is used to conclude<sup>1</sup> that the rate of gravitational precession is proportional to the period of spin motion of the satellite  $T = \frac{2\pi}{\omega_3}$ . Furthermore, it is stated that when the period  $T$  increases exponentially under the influence of the Earth's magnetic field, so does the rate of gravitational precession, and that this rate of precession can become very large threatening to lead the spin dynamics of LAGEOS to chaos ( $|\dot{\phi}| \rightarrow \infty$  when  $\omega_3 \rightarrow 0$ ).

A rather simple analysis shows that this conclusion is wrong<sup>10</sup>. A misunderstanding emerges entirely due to an attempt to use equation (32) in the domain where it is not applicable. The expression is appropriate only for small magnitudes of  $\dot{\phi}$  (which is indeed the case in describing, say, the precession of the Earth's equinoxes, but not in analyzing the LAGEOS's spin dynamics). More precisely, it can be used only when the term quadratic in  $\dot{\phi}$  can be dropped from the Lagrange equation (31). To see what is involved in such an assumption, we return to equation (31) and rewrite it in the following form

$$\dot{\phi}^2 - \frac{I_3 \omega_3}{I_1 \cos \theta} \dot{\phi} - \frac{3}{2} \omega_0^2 \frac{I_3 - I_1}{I_1} = 0, \quad (33)$$

or

$$\dot{\phi}^2 - C_1 \dot{\phi} - C_2 = 0, \quad (34)$$

where

$$\begin{aligned} C_1 &= \frac{I_3}{I_1} \frac{\omega_3}{\cos \theta} \approx \frac{\omega_3}{\cos \theta} \\ C_2 &= \frac{3}{2} \omega_0^2 \frac{I_3 - I_1}{I_1} \approx \frac{3}{2} \omega_0^2 \Delta \end{aligned} \quad (35)$$

The solution of the quadratic equation (34) is

$$\dot{\phi} = \frac{C_1 \pm \sqrt{C_1^2 + 4C_2}}{2} = \frac{1}{2} \left( \frac{\omega_3}{\cos \theta} \pm \sqrt{\frac{\omega_3^2}{\cos^2 \theta} + 6\omega_0^2 \Delta} \right). \quad (36)$$

A simple reasoning (no oblateness, no precession) resolves the ambiguity of the sign in front of the square root (the minus sign should be taken), which leaves us with the solution

$$\dot{\phi} = \frac{1}{2} \left( \frac{\omega_3}{\cos \theta} - \sqrt{\frac{\omega_3^2}{\cos^2 \theta} + 6\omega_0^2 \Delta} \right). \quad (37)$$

This solution has finite limits in both cases when  $\omega_3 \rightarrow \infty$  and when  $\omega_3 \rightarrow 0$

$$\begin{aligned} \lim_{\omega_3 \rightarrow \infty} \dot{\phi} &= 0, & \lim_{\omega_3 \rightarrow 0} \dot{\phi} &= -\omega_0 \sqrt{\frac{3}{2} \Delta}, \\ \Delta \ll 1 &\Rightarrow \left| \lim_{\omega_3 \rightarrow 0} \dot{\phi} \right| \ll |\omega_3|. \end{aligned} \quad (38)$$

and at any value of  $0 < \frac{1}{\omega_3} < \infty$  the value of the solution belongs to the interval determined by (38). When  $T$  increases exponentially the rate of precession  $\dot{\phi}$  does not follow it.

It is instructive to rewrite equation (37) in form

$$\dot{\phi} = \frac{1}{2} \frac{\omega_3}{\cos \theta} \left( 1 - \sqrt{1 + \frac{6\omega_0^2 \Delta \cos^2 \theta}{\omega_3^2}} \right), \quad (39)$$

and look at it approximation when  $\frac{6\omega_0^2 \Delta \cos^2 \theta}{\omega_3^2}$  is small. It is easy to see that in this case

$$\dot{\phi} \approx \frac{1}{2} \frac{\omega_3}{\cos \theta} \left( 1 - 1 - \frac{1}{2} \frac{6\omega_0^2 \Delta \cos^2 \theta}{\omega_3^2} \right) \approx -\frac{3}{2} \frac{\omega_0^2}{\omega_3} \Delta \cos \theta, \quad (40)$$

and we recover expression (32). However, the expansion of the square root that we use to recover this expression explicitly demands smallness of the ratio

$$\frac{6\omega_0^2 \Delta \cos^2 \theta}{\omega_3^2}. \quad (41)$$

A careful look at (41) uncovers that the procedure of dropping the term proportional to  $\dot{\phi}^2$  in equation (31) not only demands smallness of  $\dot{\phi}$  but also, at fixed values of  $\theta$ ,  $\Delta$ , and  $\omega_0$ , imposes the lower limit on the magnitude of  $\omega_3$ . In other words, in order for (32) to work the satellite should have enough spin. Equations (37), (38) also indicate that at small values of  $\omega_3$  neglecting  $\omega_1$  and  $\omega_2$  would not be appropriate. However, an assumption of smallness of  $\omega_1$  and  $\omega_2$  still can be used in neglecting their higher powers, provided that it is done carefully.

## VII. LAGRANGE EQUATIONS FOR THE LAGEOS SPIN DYNAMICS

The results of the previous section indicate that the LAGEOS's spin dynamics at slow spin rate might look quite different from what one expects making intuitive assumptions coming from experience in high spin frequency domain. A safer approach would be to obtain first the full system of equations governing the spin dynamics and to introduce simplifying assumptions on the later stage, depending on the question asked. As in previous section, we are going to use the Lagrange formulation of the problem. Restrictions on the length of this report prevent us from providing most of the details of the calculations. We are going to review only the basic principles and some of the preliminary conclusions. Some additional details can be found in the report of C. Fuchs<sup>11</sup>.

As in previous section, we introduce the frame of principal axes of inertia (the body-fixed frame) rotation of which with respect to space-fixed frame is described by the Euler angles  $\theta$ ,  $\phi$ , and  $\psi$ . The components of the angular velocity  $\vec{\omega}$  in the body-fixed frame are

$$\begin{aligned}\omega_1 &= \dot{\phi} \sin \theta \sin \psi + \dot{\theta} \cos \psi \\ \omega_2 &= \dot{\phi} \sin \theta \cos \psi - \dot{\theta} \sin \psi \\ \omega_3 &= \dot{\phi} \cos \theta + \dot{\psi}\end{aligned}\tag{42}$$

To include in the dynamic picture the action of the Earth's magnetic field on the satellite one needs to add to the gravitational Lagrangian

$$L_g = \frac{I_1}{2}(\dot{\theta}^2 + \dot{\phi}^2 \sin^2 \theta) + \frac{I_3}{2}(\dot{\psi} + \dot{\phi} \cos \theta)^2 - V\tag{43}$$

the term  $L_m = \vec{M} \cdot \vec{B}$ , where  $\vec{B}$  is the external magnetic field and  $\vec{M}$  is the magnetic moment induced by  $\vec{B}$  in the satellite ( $V$  in equation (43) represents gravitational potential energy determined by either expression

(20) or (22) depending on whether one tries to evaluate instantaneous quantities or the ones averaged over the orbital period). In other words the full Lagrangian for the LAGEOS's spin dynamics is

$$L = L_g + L_m = \frac{I_1}{2}(\dot{\theta}^2 + \dot{\phi}^2 \sin^2 \theta) + \frac{I_3}{2}(\dot{\psi} + \dot{\phi} \cos \theta)^2 - V + \vec{M} \cdot \vec{B}. \quad (44)$$

To calculate the  $L_m$  one needs to use the relation between the components of magnetic field  $B_1, B_2, B_3$  in the body-fixed frame and  $\tilde{B}_1, \tilde{B}_2, \tilde{B}_3$  in the space-fixed frame

$$\begin{aligned} B_1 &= (\cos \psi \cos \phi - \cos \theta \sin \phi \sin \psi) \tilde{B}_1 + (\cos \psi \sin \phi + \cos \theta \cos \phi \sin \psi) \tilde{B}_2 + (\sin \psi \sin \theta) \tilde{B}_3 \\ B_2 &= (-\sin \psi \cos \phi - \cos \theta \sin \phi \cos \psi) \tilde{B}_1 + (-\sin \psi \sin \phi + \cos \theta \cos \phi \cos \psi) \tilde{B}_2 + (\cos \psi \sin \theta) \tilde{B}_3 \\ B_3 &= (\sin \theta \sin \phi) \tilde{B}_1 - (\sin \theta \cos \phi) \tilde{B}_2 + (\cos \theta) \tilde{B}_3 \end{aligned} \quad (45)$$

and the relation between the magnetic field  $\vec{B}$ , polarizability<sup>8</sup>  $\alpha$  (cf. equation (3)), and the induced magnetic moment  $\vec{M}$ . Equation (3) indicates that  $\alpha$  is a function of the frequency  $\omega$ . The equations below will depend on three frequencies  $\omega_1, \omega_2, \omega_3$ . The notation  $\alpha_k$  will refer to  $\alpha(\omega_k)$  for  $k = 1, 2, 3$ . The resulting expression for  $L_m$  is

$$L_m = \vec{M} \cdot \vec{B} = V [\alpha'_1(B^2 - B_1^2) + \alpha'_2(B^2 - B_2^2) + \alpha'_3(B^2 - B_3^2)], \quad (46)$$

where  $B^2 = B_1^2 + B_2^2 + B_3^2 = \tilde{B}_1^2 + \tilde{B}_2^2 + \tilde{B}_3^2$ .

One could write now the full system of Lagrange equations of the satellite spin dynamics

$$\frac{d}{dt} \frac{\partial L}{\partial \dot{\theta}} - \frac{\partial L}{\partial \theta} = 0, \quad \frac{d}{dt} \frac{\partial L}{\partial \dot{\phi}} - \frac{\partial L}{\partial \phi} = 0, \quad \frac{d}{dt} \frac{\partial L}{\partial \dot{\psi}} - \frac{\partial L}{\partial \psi} = 0. \quad (47)$$

An investigation of such equations (both analytically and numerically) is under way at present time but can be completed only in course of the follow-up research. In any case, the full discussion of the results (even those available now) would be beyond the scope of this report. Instead, we are going to describe a qualitative result similar to the one of the previous section.

We are going to obtain expressions for precession, averaged over the orbit, extending the results of previous section to the combined effect of both magnetic and gravitational forces. Exactly as in previous section, we assume  $\dot{\theta} = 0$  and  $\ddot{\theta} = 0$  (this assumption will be discussed later). The resulting Lagrange equation for  $\theta$  takes form (compare to equation (31))

$$I_1 \dot{\phi}^2 \sin \theta \cos \theta - I_3 \omega_3 \dot{\phi} \sin \theta - \frac{3}{2} \omega_0^2 (I_3 - I_1) \sin \theta \cos \theta + \frac{\partial}{\partial \theta} (\vec{M} \cdot \vec{B}) - \frac{d}{dt} \frac{\partial}{\partial \dot{\theta}} (\vec{M} \cdot \vec{B}) = 0 \quad (48)$$

The last two terms of this equation describe coupling of spin degrees of freedom to the Earth's magnetic field. For their evaluation or estimate it is necessary to be able to calculate the expressions (cf. previous sections for notations)

$$\begin{aligned}\frac{\partial \alpha'_k}{\partial \theta} &= \frac{\partial \alpha'_k}{\partial x_k} \frac{\partial x_k}{\partial \omega_k} \frac{\partial \omega_k}{\partial \theta} = \frac{\rho}{c} \sqrt{2\pi\sigma} \frac{1}{\omega_k} \frac{\partial \alpha'_k}{\partial x_k} \frac{\partial \omega_k}{\partial \theta} = f(x_k) \frac{\partial \omega_k}{\partial \theta} \\ \frac{\partial \alpha'_k}{\partial \dot{\theta}} &= \frac{\partial \alpha'_k}{\partial x_k} \frac{\partial x_k}{\partial \omega_k} \frac{\partial \omega_k}{\partial \dot{\theta}} = \frac{\rho}{c} \sqrt{2\pi\sigma} \frac{1}{\omega_k} \frac{\partial \alpha'_k}{\partial x_k} \frac{\partial \omega_k}{\partial \dot{\theta}} = f(x_k) \frac{\partial \omega_k}{\partial \dot{\theta}}\end{aligned}\quad (49)$$

where

$$f(x) = \frac{4\pi\rho^4}{c^2} \sigma \frac{1}{x} \frac{\partial \alpha'}{\partial x} = \frac{9\rho^2\sigma}{c^2} \frac{1}{x^2} \left[ 2 \frac{1 - \cosh x \cos x}{(\cosh x - \cos x)^2} - \frac{1}{x} \frac{\sinh x - \sin x}{\cosh x - \cos x} \right] \quad (50)$$

Since we are planning to investigate the domain of small  $\omega$  it is useful to stress that, for small  $\omega$

$$\alpha' \sim \omega^2, \quad \frac{d\alpha'}{dx} \sim \omega^{\frac{3}{2}}, \quad \frac{d\alpha'}{d\omega} \sim \omega, \quad f(x) \sim \omega \quad (51)$$

Computations for  $\frac{\partial}{\partial \theta}(\vec{M} \cdot \vec{B})$  and  $\frac{\partial}{\partial \dot{\theta}}(\vec{M} \cdot \vec{B})$  yield

$$\begin{aligned}\frac{\partial}{\partial \theta}(\vec{M} \cdot \vec{B}) &= V [(B^2 - B_1^2)f(x_1)\dot{\phi} \cos \theta \sin \psi + (B^2 - B_2^2)f(x_2)\dot{\phi} \cos \theta \cos \psi \\ &\quad - (B^2 - B_3^2)f(x_3)\dot{\phi} \sin \theta - 2(\alpha'_1 \frac{\partial B_1}{\partial \theta} + \alpha'_2 \frac{\partial B_2}{\partial \theta} + \alpha'_3 \frac{\partial B_3}{\partial \theta})]\end{aligned}\quad (52)$$

and

$$\begin{aligned}\frac{\partial}{\partial \dot{\theta}}(\vec{M} \cdot \vec{B}) &= V \left[ (B^2 - B_1^2) \frac{\partial \alpha'_1}{\partial \dot{\theta}} + (B^2 - B_2^2) \frac{\partial \alpha'_2}{\partial \dot{\theta}} + (B^2 - B_3^2) \frac{\partial \alpha'_3}{\partial \dot{\theta}} \right] \\ &= V [(B^2 - B_1^2)f(x_1) \cos \psi - (B^2 - B_2^2)f(x_2) \sin \psi]\end{aligned}\quad (53)$$

At this point we undertake a shortcut. Keeping in mind that we are trying to compute the rate of the satellite precession when the satellite rotates slowly and spins around its axis of symmetry even slower we drop in the Lagrange equation (48) the terms of the first order with respect to  $\omega_3$  (and higher orders), and the terms of the second order (and higher) with respect to  $\omega_2, \omega_3$ . Furthermore, as we are trying to compute only the (quasi)stationary part of precession, we drop all the terms proportional to the angular accelerations  $\dot{\omega}_k$ . The final form of the Lagrange equation under these assumptions is

$$\dot{\phi}^2 - C \dot{\phi} - \frac{3}{2} \omega_0^2 \Delta = 0 \quad (54)$$

where

$$C = -\frac{V}{I_1 \sin \theta} [(B^2 - B_1^2)f(x_1) \sin \psi + (B^2 - B_2^2)f(x_2) \cos \psi] \quad (55)$$



so that the mean value of the satellite precession rate is given by

$$\dot{\phi} = \frac{1}{2}C - \sqrt{\frac{C^2}{4} + \frac{3}{2}\omega_0^2\Delta} \quad (56)$$

The solution for  $\dot{\psi}$  has some attractive features: (i) it has the correct limit coinciding with (38) when the magnetic field is switched off, and (ii) it predicts that the mean precession rate is slower in presence of magnetic field than it would be without it. However, the solution is not quite stationary (which shows up in the dependence of  $C$  on  $\psi$ ). This indicates that the demand to have a stationary solution might be not quite compatible with dynamics determined by the total Lagrangian (44) of the system, or that a more sophisticated averaging procedure for the magnetic part of the Lagrangian is needed. In any case, exactly like in previous section, all indications are that the precession rate of the satellite is bounded by the limit well under the orbital angular velocity of the satellite. It is hardly probable that the chaotic spin dynamics can emerge through this mechanism. Another possibility of transition to the chaotic dynamical regime, namely through the growth of the satellite nutation, requires more numerical treatment and will be described in subsequent sections of the report.

## VIII. ROTATIONAL DYNAMICS OF THE LAGEOS SATELLITE. NUMERICAL APPROACH.

The analytic results described above do not represent adequately what happens at very slow spin rates. Accordingly we have undertaken a numerical investigation. In what follows we do not assume that the spin axis coincides with the body axis. Also, we do not apply the averaging procedure (averaging over the satellite orbital period). This means that we are not restricted anymore to the spin rates higher than the frequency of the orbital motion of the satellite. The Lagrange equations used in previous sections do not provide any advantages in the numerical approach. Therefore, we are going to use Euler equations from now on. In this section we summarize the results of the previous sections and describe the general facts used in our numerical investigation.

There are many factors to consider when analyzing the dynamics of the spin vector of an oblate, metallic satellite. The most prominent effect is the torqueing due to the gravitational field of the earth. This arises due to the oblateness of the satellite, with the oblateness of the earth producing negligible contributions than can be added to our calculations as an adiabatic correction. If the satellite's (bulging) equatorial plane lies in the plane of orbit, no such torques are possible. However, when the satellite is not placed exactly in

such a position, gravitational torques will arise. In an effort to model these torques, we consider the situation of an oblate spheroid in orbit around a point mass. As was done by Bertotti, we parallel the development in Goldstein<sup>9</sup>.

However, we note that the Bertotti and Iess analysis of the effects of gravity on the spin dynamics of the oblate satellite, that resulted in predicting the chaotic spin dynamics in the future, is not appropriate for small rates of spin (when the spin frequency is of the order of the orbital frequency). Their prediction is based on the "Hipparcos" formula for the rate of precession  $\omega_p$  of the oblate satellite in the inhomogeneous gravity field of the Earth

$$\omega_p = \frac{3}{2} \Delta \frac{\omega_0^2}{\omega_3} \cos \theta \quad (57)$$

where  $\omega_0$  is the orbital angular velocity,  $\omega_3$  is the satellite spin rate,  $\theta$  is the obliquity angle of the satellite (the angle between  $\vec{\omega}$  and the normal to the orbital plane) and

$$\Delta = \frac{I_3 - I_1}{I_3} \quad (58)$$

is the satellite oblateness. Here  $I_3$  and  $I_1 = I_2$  are the principal moments of inertia (the principal direction corresponding to  $I_3$  is assumed to be that of  $\vec{\omega}$  and coincides, by an assumption, with the symmetry axis of the oblate satellite).

It is argued by Bertotti and Iess that, since  $\omega_p \propto 1/\omega_3$ , the gravitational precession in the asymptotic limit of small  $\omega$  (when  $\omega_3$  becomes of the order of  $\omega_0$ ) becomes very fast and may make the spin dynamics chaotic.

The latter conclusion is based on a misunderstanding. It has been shown by us<sup>10</sup> via a careful analysis of assumptions underlying the "Hipparcos" formula that even in the approximation commonly used in deriving the formula (averaging of the gravitational potential over the satellite orbit, dipole cutoff of the multipole decomposition, etc.) a care should be exercised. Equation (57) can be used only when

$$\frac{6\omega_0^2 \Delta \cos^2 \theta}{\omega_3^2} \sim \frac{\omega_0^2}{\omega_3^2} \ll 1 \quad (59)$$

i. e. when the spin rate of the satellite is much greater than its orbital angular velocity. The latter restriction is very easy to overcome. The corrected equation for  $\omega_p$  is

$$\omega_p = \frac{1}{2} \frac{\omega_3}{\cos \theta} \left( 1 - \sqrt{1 + \frac{6\omega_0^2 \Delta \cos^2 \theta}{\omega_3^2}} \right) \quad (60)$$

This equation obviously imposes a bound on  $|\omega_p|$

$$|\omega_p| < \omega_0 \sqrt{\frac{3}{2} \Delta} \quad (61)$$

which makes it clear that the rate of precession cannot grow enough to cause the chaoticity of the satellite spin dynamics. The subsequent qualitative investigation<sup>11</sup> has shown that when magnetic forces are included in the picture the precession rate remains bounded and should be much smaller than  $\omega_0$ . Another conclusion reached in the course of this analysis<sup>10</sup> has been that, when both gravitational and magnetic forces are taken into account, the nutation, although bounded in its amplitude, does not disappear completely even in the asymptotical limit. The value of these results, however, is limited by the fact that they do not tell one what are the bounds exactly. Neither they provide any information on the time scale of reaching the asymptotic limit. However, they show clearly that the chaoticity of the LAGEOS spin dynamics caused by an unbounded growth of gravitationally induced precession cannot occur.

Another important factor governing the evolution of the spin vector is the interaction of the metallic core of the satellite with the magnetic field of the earth. The LAGEOS satellite is composed of two aluminum hemispheres bolted together, with a brass cylindrical core along an axis (the original axis of spin)<sup>12</sup>. The spinning of the metallic object in the magnetic dipole field of the earth (and the motion through that field) will cause eddy currents within the satellite, which will in turn cause dissipation (through Joule heating) and a slowdown of the spin, and furthermore will cause torques on the spin vector. These torques can be understood as the interaction of the magnetic dipole caused by the induced eddy currents with the magnetic field of the earth. In modeling this effect, we have treated a uniform, spherical object in the orbit of a perfect magnetic dipole (as the reader will recall, we are concerned with qualitative results). We have allowed the orbit to be placed at an arbitrary inclination and our results in this report correspond to  $I \sim 78$  deg. The problem of a spinning metallic sphere in a constant magnetic field has been treated by Landau and Lifshitz, and we avail ourselves of their results. For our purposes, we ignore the torques caused by the changing magnetic field due to the orbit (as opposed to spin) of the satellite. These torques can be shown to be negligible until asymptotically late stages of motion, and have no qualitative effects upon the dynamics.

The source of many of the difficulties in doing analyses of such orbiting, spinning bodies lies in the involved coordinate systems needed to describe their motion. Thus, it is important at this point to give a

brief description of the coordinates we will use in this report. In our analysis of the spin dynamics of the LAGEOS satellite we found it convenient to introduce the following four coordinate systems:

- 1) *The earth-centered inertial (ECI) reference frame*  $\{x_2, y_2, z_2\}$ . Here the  $z_2$ -axis is aligned with the body axis of the earth. The  $x_2$ -axis lies in the earth's equatorial plane at zero degrees longitude, and the origin coincides with the center of the earth.
- 2) *The orbit-centered inertial frame (OCI)*  $\{x_1, y_1, z_1\}$ . Here the  $z_1$ -axis is oriented along the normal to the orbital plane of the satellite with its  $\sim 22$  deg coinclination. The  $x_1$ -axis is defined to be the intersection of the orbital plane and the equatorial plane of the earth, and the origin is the center of mass of the earth. We have assumed here that this frame is inertial as we have not included the secular drag of the line-of-nodes of the orbital plane due to the oblateness of the earth. This  $\sim 126$  deg /yr precession can be included at the end of our analysis as an adiabatic correction.
- 3) *The body frame (non-inertial)*  $\{x_b, y_b, z_b\}$ . Here the  $z_b$ -axis is aligned along the body axis of the satellite which is assumed here to be a slightly oblate ( $\sim 3\%$ ) spheroid of brass. The origin is at the center of the satellite. In our calculations, the body axis is related to the orbit-centered frame through the three Euler angles  $\theta$ ,  $\phi$  and  $\psi$ . The nutation angle  $\theta$  is the angle between  $z_b$  and  $z_1$ , while the angle of precession  $\phi$  is the angle between the  $x_1$  - *axis* and the line of nodes. Finally, the spin angle  $\psi$  is the angle between the line of nodes and the  $x_b$ -axis.
- 4) *The Landau-Lifshiz (non inertial) coordinate system*  $\{x'', y'', z''\}$ . The  $x''$ -axis is aligned along the instantaneous angular momentum vector of the satellite ( $\vec{\omega}$ ), and the instantaneous magnetic field ( $\vec{B}$ ) at the satellite lies in the  $x'' - z''$  plane. Note that  $z''$  need not be aligned with the body axis of the satellite, and in fact the asymptotic behavior of the satellite they are vastly different.

## IX. EULER'S EQUATIONS OF THE LAGEOS SPIN DYNAMICS

Spin dynamics of the axially symmetric satellite is determined by Euler's equations

$$\begin{aligned} I_1 \dot{\omega}_1 - \omega_2 \omega_3 (I_1 - I_3) &= N_1 \\ I_1 \dot{\omega}_2 - \omega_3 \omega_1 (I_3 - I_1) &= N_2 \\ I_3 \dot{\omega}_3 &= N_3 \end{aligned} \quad (62)$$

where  $\omega_1, \omega_2, \omega_3$  are the components of the satellite angular velocity in the body frame,  $I_1 = I_2$ , and  $I_3$  are principal moments of inertia, and  $N_1, N_2, N_3$  are the components of the torques in the direction of the satellite principal axes. After substituting the expressions for  $\omega_1, \omega_2, \omega_3$  in terms of the Euler angles

$$\begin{aligned} \omega_1 &= \dot{\phi} \sin \theta \sin \psi + \dot{\theta} \cos \psi \\ \omega_2 &= \dot{\phi} \sin \theta \cos \psi - \dot{\theta} \sin \psi \\ \omega_3 &= \dot{\phi} \cos \theta + \dot{\psi} \end{aligned} \quad (63)$$

the Euler equations become

$$\begin{aligned} \ddot{\theta} &= \ddot{\theta}_{free} + \frac{N_1 \cos \psi - N_2 \sin \psi}{I_1} \\ \ddot{\theta}_{free} &= \left( \frac{I_1 - I_3}{I_1} \right) \dot{\phi}^2 \cos \theta \sin \theta - \frac{I_3}{I_1} \dot{\psi} \dot{\phi} \sin \theta \\ \ddot{\phi} &= \ddot{\phi}_{free} + \frac{N_1 \sin \psi + N_2 \cos \psi}{I_1 \sin \theta} \\ \ddot{\phi}_{free} &= \left( \frac{I_3 - 2I_1}{I_1} \right) \frac{\cos \theta}{\sin \theta} \dot{\theta} \dot{\phi} + \frac{I_3}{I_1} \frac{\dot{\theta} \dot{\psi}}{\sin \theta} \\ \ddot{\psi} &= \ddot{\psi}_{free} + \frac{N_3}{I_1} - \frac{N_1 \sin \psi + N_2 \cos \psi \cos \theta}{I_1 \sin \theta} \\ \ddot{\psi}_{free} &= - \left( \frac{I_3 - I_1}{I_1} \right) \frac{\cos^2 \theta}{\sin \theta} \dot{\theta} \dot{\phi} + \frac{\dot{\theta} \dot{\phi}}{\sin \theta} - \frac{I_3 \cos \theta}{I_1 \sin \theta} \dot{\theta} \dot{\psi} \end{aligned} \quad (64)$$

The torque components  $N_1, N_2, N_3$  are due to gravitational and magnetic forces acting on the satellite

$$N_i = N_i^{(g)} + N_i^{(m)}, \quad i = 1, 2, 3 \quad (65)$$

Gravitational torques in the body frame are given by

$$\begin{aligned} N_1^{(g)} &= -\cos \psi \frac{\partial V}{\partial \theta} - \frac{\sin \psi}{\sin \theta} \frac{\partial V}{\partial \phi} + \frac{\cos \theta \sin \psi}{\sin \theta} \frac{\partial V}{\partial \psi} \\ N_2^{(g)} &= \sin \psi \frac{\partial V}{\partial \theta} - \frac{\cos \psi}{\sin \theta} \frac{\partial V}{\partial \phi} + \frac{\cos \theta \cos \psi}{\sin \theta} \frac{\partial V}{\partial \psi} \\ N_3^{(g)} &= -\frac{\partial V}{\partial \psi} \end{aligned} \quad (66)$$

The gravitational potential  $V$  is (the standard dipole approximation is used)

$$V = \frac{GM(I_3 - I_1)}{2R^3} (3\gamma^2 - 1) \quad (67)$$

where  $\gamma$  is the direction cosine between (1) the radial vector from the satellite center of mass to the center of the Earth, and (2) the symmetry axis of the satellite. It is related to Euler's angles via

$$\gamma = \sin \theta \sin(\eta - \eta_0 - \phi) \quad (68)$$

so that

$$V = \frac{GM(I_3 - I_1)}{2R^3} (3 \sin^2 \theta \sin^2(\eta - \eta_0 - \phi) - 1) \quad (69)$$

and

$$\begin{aligned} -\frac{\partial V}{\partial \theta} &= -\frac{3GM(I_3 - I_1)}{R^3} \sin \theta \cos \theta \sin^2(\eta - \eta_0 - \phi) \\ -\frac{1}{\sin \theta} \frac{\partial V}{\partial \phi} &= \frac{3GM(I_3 - I_1)}{R^3} \sin \theta \sin(\eta - \eta_0 - \phi) \cos(\eta - \eta_0 - \phi) \end{aligned} \quad (70)$$

$$\frac{\partial V}{\partial \psi} = 0$$

Equations (66) and (70) lead to the following final expressions for the components of the gravitational torque in the body frame

$$\begin{aligned} N_1^{(g)} &= \frac{3GM(I_3 - I_1)}{R^3} \sin \theta \sin(\eta - \eta_0 - \phi) \left\{ \begin{array}{l} -\cos \theta \cos \psi \sin(\eta - \eta_0 - \phi) \\ + \sin \psi \cos(\eta - \eta_0 - \phi) \end{array} \right\} \\ N_2^{(g)} &= \frac{3GM(I_3 - I_1)}{R^3} \sin \theta \sin(\eta - \eta_0 - \phi) \left\{ \begin{array}{l} \cos \theta \sin \psi \sin(\eta - \eta_0 - \phi) \\ + \cos \psi \cos(\eta - \eta_0 - \phi) \end{array} \right\} \\ N_3^{(g)} &= 0 \end{aligned} \quad (71)$$

The components of the magnetic torque in the body frame  $N_1^{(m)}$ ,  $N_2^{(m)}$ , and  $N_3^{(m)}$  can be figured out starting from the torque components acting on a conducting ball of radius  $a$  spinning with the angular velocity  $\vec{\omega}$  in an external magnetic field  $\vec{B}$  in the Landau-Lifshitz frame<sup>8</sup>.

The Landau-Lifshitz frame is determined by vectors  $\vec{\omega}$  and  $\vec{B}$ . Its axis  $z''$  is picked to coincide in its direction with  $\vec{\omega}$ , its axis  $y''$  is oriented in the direction of  $\vec{\omega} \times \vec{B}$ , and the axis  $x''$  is orthogonal to both  $y''$  and  $z''$  with its direction chosen so that  $x''y''z''$  forms a left-handed coordinate system. We introduce notations  $\hat{x}''$ ,  $\hat{y}''$ ,  $\hat{z}''$  for the vectors of the orthonormal frame associated with these axes. These vectors form

the Landau-Lifshitz frame. If we introduce an arbitrary rectangular coordinates  $x, y, z$  with its associated orthonormal frame formed by unit vectors  $\hat{x}, \hat{y}, \hat{z}$  such that in this frame  $\vec{\omega}$  and  $\vec{B}$  are represented as

$$\begin{aligned}\vec{\omega} &= \omega_x \hat{x} + \omega_y \hat{y} + \omega_z \hat{z} = \langle \omega_x, \omega_y, \omega_z \rangle \\ \vec{B} &= B_x \hat{x} + B_y \hat{y} + B_z \hat{z} = \langle B_x, B_y, B_z \rangle\end{aligned}\quad (72)$$

then the transition between the two frames is given by

$$\begin{pmatrix} \hat{x}^{\parallel} \\ \hat{y}^{\parallel} \\ \hat{z}^{\parallel} \end{pmatrix} = \begin{pmatrix} \frac{[(\vec{\omega} \times \vec{B}) \times \vec{\omega}]_x}{\omega |\vec{\omega} \times \vec{B}|} & \frac{[(\vec{\omega} \times \vec{B}) \times \vec{\omega}]_y}{\omega |\vec{\omega} \times \vec{B}|} & \frac{[(\vec{\omega} \times \vec{B}) \times \vec{\omega}]_z}{\omega |\vec{\omega} \times \vec{B}|} \\ \frac{(\vec{\omega} \times \vec{B})_x}{|\vec{\omega} \times \vec{B}|} & \frac{(\vec{\omega} \times \vec{B})_y}{|\vec{\omega} \times \vec{B}|} & \frac{(\vec{\omega} \times \vec{B})_z}{|\vec{\omega} \times \vec{B}|} \\ \frac{\omega_x}{\omega} & \frac{\omega_y}{\omega} & \frac{\omega_z}{\omega} \end{pmatrix} \begin{pmatrix} \hat{x} \\ \hat{y} \\ \hat{z} \end{pmatrix} \quad (73)$$

where  $\omega = |\vec{\omega}|$ .

The components of the magnetic torque in this frame is given by

$$\begin{aligned}N_x^{\parallel} &= V \alpha'' B_x^{\parallel} B_z^{\parallel} \\ N_y^{\parallel} &= V \alpha' B_x^{\parallel} B_z^{\parallel} \\ N_z^{\parallel} &= V \alpha'' (B_x^{\parallel})^2\end{aligned}\quad (74)$$

where  $V = \frac{4\pi}{3} a^3$  is the volume of the ball,  $B_x^{\parallel}, B_y^{\parallel}, B_z^{\parallel}$ , are components of the magnetic field in Landau-Lifshitz frame, and the coefficients of magnetization are,

$$\begin{aligned}\alpha' &= -\frac{3}{8\pi} \left[ 1 - \frac{\delta \sinh(2\frac{a}{\delta}) - \sin(2\frac{a}{\delta})}{a \cosh(2\frac{a}{\delta}) - \cos(2\frac{a}{\delta})} \right] \\ \alpha'' &= -\frac{9\delta^2}{16\pi a^2} \left[ 1 - \frac{a \sinh(2\frac{a}{\delta}) - \sin(2\frac{a}{\delta})}{\delta \cosh(2\frac{a}{\delta}) - \cos(2\frac{a}{\delta})} \right] \\ \delta &= \frac{c}{\sqrt{2\pi\sigma\omega}}\end{aligned}\quad (75)$$

Here  $c$  is the speed of light and  $\sigma$  is the specific conductivity of the material forming the ball. At small values of  $\omega$ ,  $\alpha'$  and  $\alpha''$  can be approximated by the expressions

$$\begin{aligned}\alpha' &\approx -\frac{4\pi}{105} \frac{a^4 \sigma^2 \omega^2}{c^4} \\ \alpha'' &\approx \frac{a^2 \sigma \omega}{10c^2}\end{aligned}\quad (76)$$

Components of the magnetic field can be evaluated easily in ECI in the dipole approximation. In the spherical coordinate representation of the ECI frame the magnetic field components are

$$\begin{aligned}B_{r_1} &= -\frac{d}{R^3} \cos \theta_1 \\ B_{\theta_1} &= \frac{d}{R^3} \sin \theta_1 \\ B_{\phi_1} &= 0\end{aligned}\quad (77)$$

In the rectangular coordinate representation of the ECI frame (index 1 is used everywhere for quantities in ECI)

$$\begin{aligned} B_{x_1} &= B_{r_1} \sin \theta_1 \cos \phi_1 + B_{\theta_1} \cos \theta_1 \cos \phi_1 \\ B_{y_1} &= B_{r_1} \sin \theta_1 \sin \phi_1 + B_{\theta_1} \cos \theta_1 \sin \phi_1 \\ B_{z_1} &= B_{r_1} \cos \theta_1 - B_{\theta_1} \sin \theta_1 \end{aligned} \quad (78)$$

The magnetic field components in OCI frame are

$$\begin{aligned} B_{x_2} &= (B_{r_1} \sin \theta_1 + B_{\theta_1} \cos \theta_1) \cos \phi_1 \\ B_{y_2} &= (B_{r_1} \sin \theta_1 + B_{\theta_1} \cos \theta_1) \sin \phi_1 \cos \xi + (B_{r_1} \cos \theta_1 - B_{\theta_1} \sin \theta_1) \sin \xi \\ B_{z_2} &= -(B_{r_1} \sin \theta_1 + B_{\theta_1} \cos \theta_1) \sin \phi_1 \sin \xi + (B_{r_1} \cos \theta_1 - B_{\theta_1} \sin \theta_1) \cos \xi \end{aligned} \quad (79)$$

where  $\xi$  is the colatitude angle and index 2 is used for the quantities in the OCI.

The angles  $\theta_1$  and  $\phi_1$  are determined by the satellite position on its orbit. Indeed, the satellite coordinates in OCI are

$$\begin{aligned} x_2 &= r \cos(\eta - \eta_0) \\ y_2 &= r \sin(\eta - \eta_0) \\ z_2 &= 0 \end{aligned} \quad (80)$$

where

$$\eta = -\frac{2\pi}{T_{\text{orbit}}} t \quad (81)$$

In ECI we have

$$\begin{aligned} x_1 &= R \cos(\eta - \eta_0) \\ y_1 &= R \sin(\eta - \eta_0) \cos \xi \\ z_1 &= -R \sin(\eta - \eta_0) \sin \xi \end{aligned} \quad (82)$$

Hence,

$$\begin{aligned} \sin \theta_1 &= \sqrt{\cos^2(\eta - \eta_0) + \sin^2(\eta - \eta_0) \cos^2 \xi} \\ \cos \theta_1 &= -\sin(\eta - \eta_0) \sin \xi \\ \cos \phi_1 &= \frac{\cos(\eta - \eta_0)}{\sin \theta_1} \\ \sin \phi_1 &= \frac{\sin(\eta - \eta_0) \cos \xi}{\sin \theta_1} \end{aligned} \quad (83)$$

The three Euler equations (equation 64) with the magnetic and gravitational torques included give us the vehicle to analyze qualitatively the spin dynamics of the LAGEOS-1 satellite. We present our numerical results of integrating the Euler equations in the next two sections.



## X. SPIN DYNAMICS OF LAGEOS: THE INITIAL-VALUE DATA

We solved the Euler equations (equation 64) using a fourth-order Bulirsch-Stoer algorithm. We integrated the equations for  $2 \times 10^9$  seconds as we wanted to (1) reproduce the experimentally-measured spin rates (launch through 17 yrs.), (2) examine the spin-orbit resonance ( $\sim 29$  yrs. after launch), and (3) reveal the asymptotics of the spin dynamics ( $\sim 41$  yrs. after launch). The experimentally-measured exponential decrease in the spin rate imposed a constraint on our theoretical model linking the "effective" radius of the satellite ( $a$ ) with the satellites "effective" conductivity ( $\sigma$ ).

$$\sigma a^5 \sim 2.685 \times 10^{22} \text{cm}^5/\text{s} \quad (84)$$

The satellite was modeled as an  $11.9591 \text{cm}$  radius spheroid of brass ( $\sigma = 1.098 \times 10^{17} 1/\text{s}$ ). The moments of inertia of the satellite's body axis was chosen to be  $I_{z_b} = 1.1516 \times 10^6 \text{g} - \text{cm}^2$ , while the moment of inertia perpendicular to the body axis was  $I_{x_b} = I_{y_b} = 1.084 \times 10^6 \text{g} - \text{cm}^2$  which corresponds to approximately 4% deviation from sphericity.

We started the integration at  $t = 0$  with the satellite in a  $68^\circ$  inclination orbit at a radius of  $1.227 \times 10^7 \text{cm}$ . The satellite was initially over the equator at  $0^\circ$  longitude ( $\eta = 0$ ). We inserted the body axis of the satellite into the orbital plane with the angular momentum vector parallel to the OCI  $Y_1$ -axis. The initial spin of the satellite was determined by the best fit to the experimental measurements and was set to  $10.472 \text{ rad/sec}$ :

$$\begin{aligned} \psi(t=0) &= 0, & \theta(t=0) &= \frac{\pi}{2}, & \phi(t=0) &= 0 \\ \dot{\theta}(t=0) &= 0, & \dot{\phi}(t=0) &= 0, & \dot{\psi}(t=0) &= 10.472 \end{aligned} \quad (85)$$

Finally, our magnetic field was assumed to be a perfect dipole field of moment  $M = 7.9 \times 10^{25} \text{gauss/cm}^3$  and aligned along the  $z_2$ -axis of the ECI frame.

## XI. SPIN DYNAMICS OF LAGEOS: NUMERICAL RESULTS

We have identified three distinct phases in the spin dynamics of the lageos satellite (Fig. 2). The first phase is characterized by an exponential decline in the spin rate ( $\dot{\psi}$ ) of the satellite (Fig.3) with nutation and precession evolving as a small amplitude bobbing of the body axis in and out of the orbital plane. Our

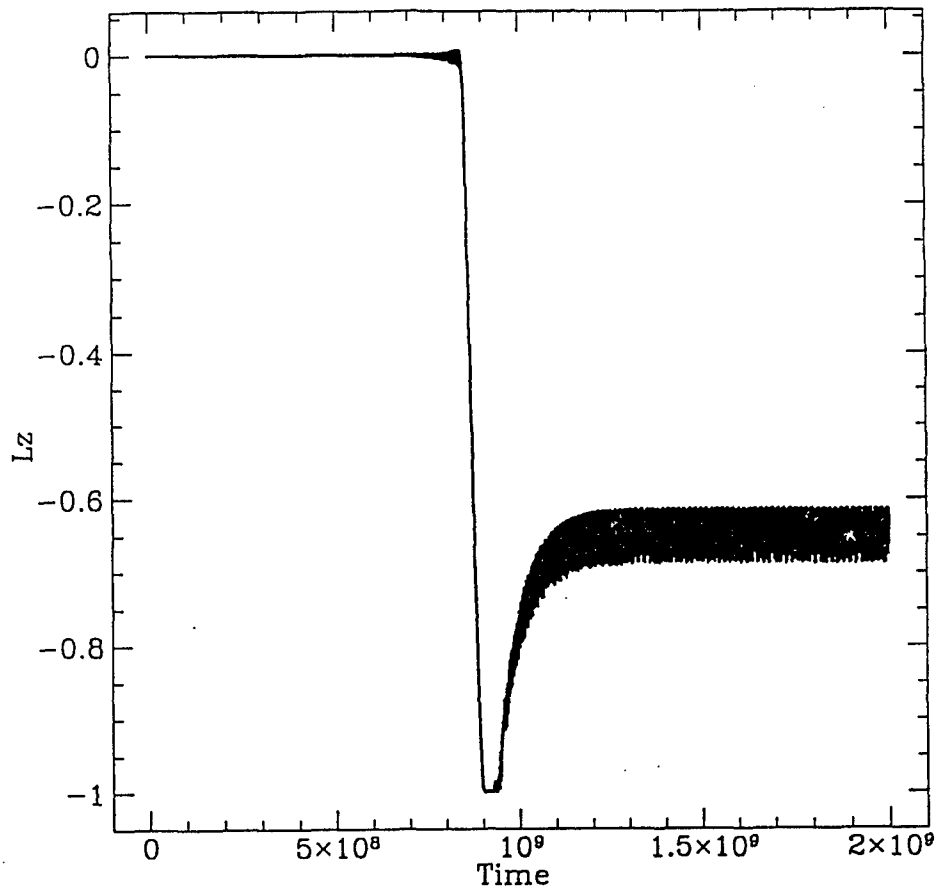


**Fig. 2: The spin dynamics of LAGEOS: Numerical Results:** We present here results from our numerical simulation of the dynamic evolution of the LAGEOS satellite. The evolution of the satellite's angular momentum reveals three unique phases as demonstrated in the plot of the component of angular momentum orthogonal to the orbital plane. The first phase is characterized by an exponential decrease in spin of the satellite with negligible nutation and precession. In the first phase, the decay in spin for a 17 cm radius sphere of brass agrees with the data. When the angular velocity decays to a value comparable to the orbital angular velocity the nutation and precession increase and the angular momentum vector lifts off the orbital plane and settles down orthogonal to the orbital plane. The third phase is characterized by a drift of the angular momentum vector  $\approx 40$  deg off the orbital plane. It sweeps out a cone centered on the orthogonal to the orbital plane with an opening angle of 100 deg. All characteristic angular velocities are of the order of the orbital angular velocity.

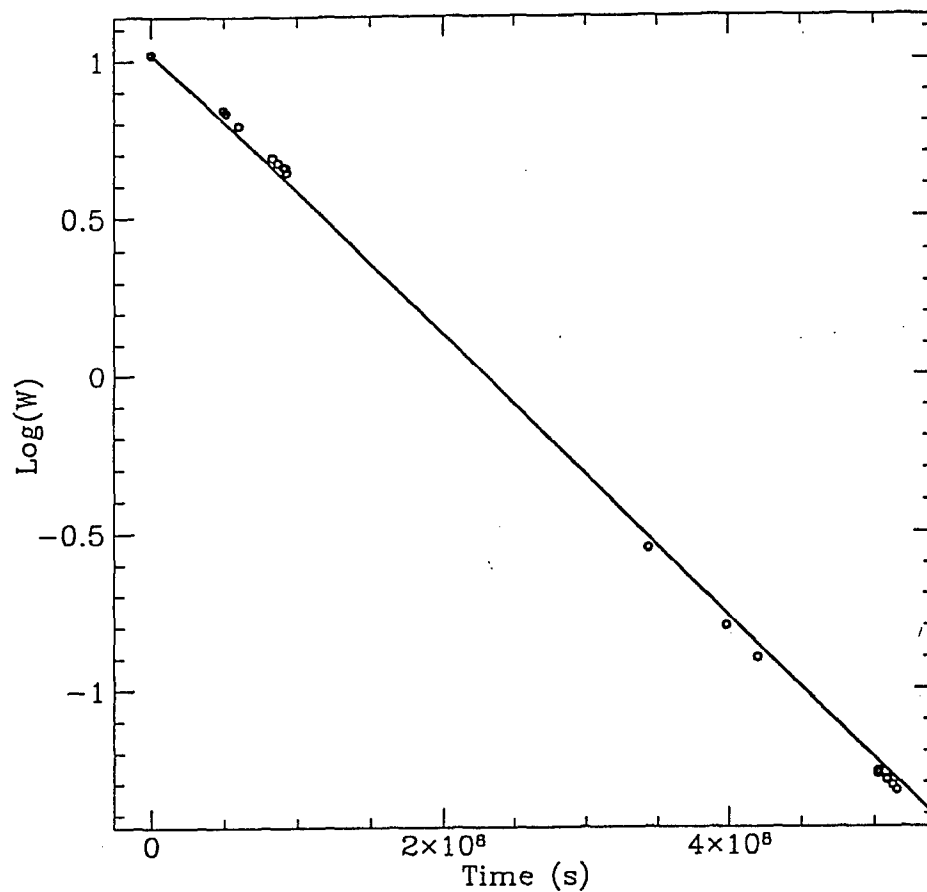
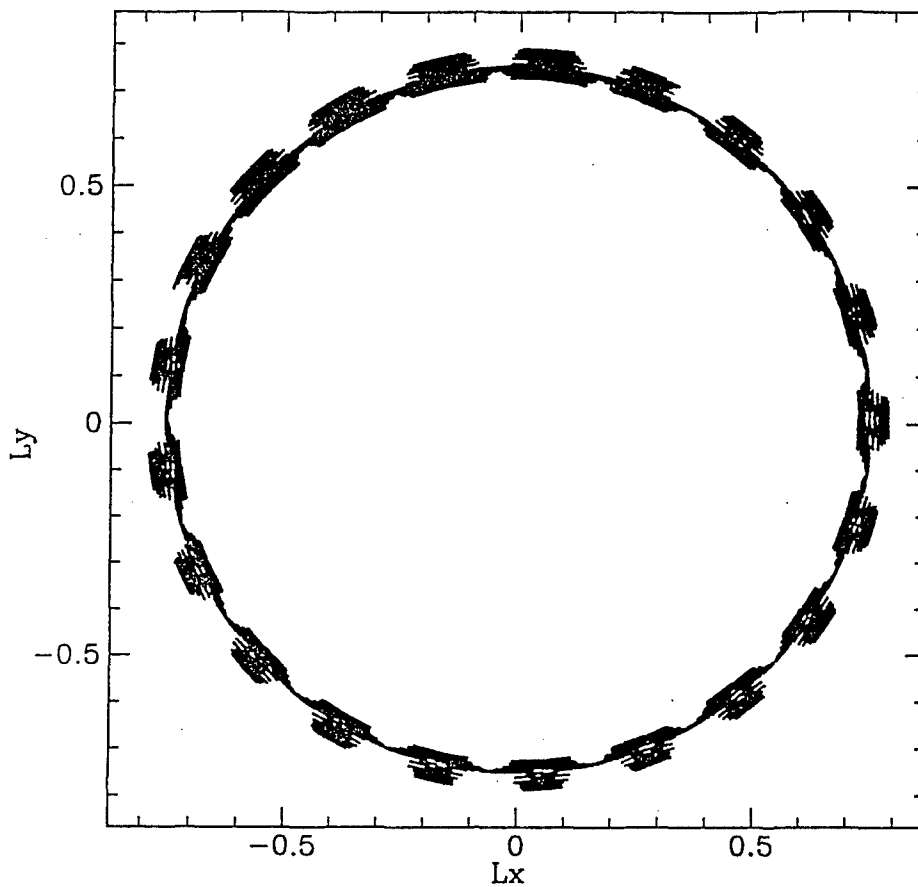


Fig. 3: The spin dynamics of LAGEOS: The first phase: The first phase is characterized by an exponential decrease in spin of the satellite with negligible nutation and precession. In the first phase, the decay in spin for a 17 cm radius sphere of brass agrees with the data.

analytic results apply quite well to this phase. This persists until the angular velocity approaches the orbital angular velocity ( $t \approx 8 \times 10^8 \text{ sec}$ ). The onset of the spin-orbit phase is preceded by an exponential increase in amplitude of the nutation and precession oscillation. The resonance drives the spin of the satellite out of the orbital plane. This transition occurs rather abruptly taking only  $\approx 1$  year. The angular momentum of the satellite remains orthogonal to the orbital plane for only  $\approx 1$  year and then transits to the third phase — the asymptotic phase. This third phase is characterized by a drift of the angular momentum vector  $\approx 40$  deg off the orbital plane. The nutation amplitude increases in this transition. The asymptotic state of the spin vector is rather interesting (Fig. 4). The angular momentum vector sweeps out a cone centered on orthogonal to the orbital plane. The cone has an opening angle of  $\approx 100$  deg and is swept out every eighteen orbits. However, the nutation has an amplitude of  $\approx 5.2$  deg. The period of this nutational motion is close to the orbital period. In this asymptotic phase the body axis is quite independent from the angular momentum vector. We were rather surprised that the angular momentum vector is so well behaved as the body axis is much less predictable. Although we have not performed a complete survey of phase space for the robustness of this asymptotic state, we have reproduced this state using a substantially different initial condition — an initial condition where the initial spin vector was directed  $\approx 45$  deg out of the orbital plane. This deserves a more detailed investigation.

## XII. CONCLUSIONS

Of the five largest sources of error identified in the LAGEOS-3 experiment, the earth and solar-induced surface forces are the largest. The anisotropic heating of the satellite and subsequent reradiation gives the satellite a thermal rocketing perturbation (referred to as the Rubincam effect or the Yarkowski thermal drag) which tends to degrade the experiment. To model this effect requires, in part, a detailed knowledge of the behavior of the angular momentum of the satellite. Toward this end, we derived and solved numerically a simplified set of Euler equations that evolves the angular momentum vector for a slightly oblate spheroid of brass orbiting an earth-like mass idealized as being a perfect sphere and having a perfect polar-oriented dipole magnetic field. The Euler equations included both the tidal gravitational torques, the eddy-current torques as well as the resistive damping torques modeled by complex magnetization coefficients<sup>8</sup>. Using this rather simplified model we identified here three phases of the rotational dynamics — an exponential damping phase, a locking phase and a forced oscillation phase (Fig. 2). Our analytic results describe well only the first phase. We also identified an error in the previously established model<sup>6</sup>. The error has led to confusion



**Fig. 4: The spin dynamics of LAGEOS: Asymptotics:** When the angular velocity decays to a value comparable to the orbital angular velocity the nutation and precession increase and the angular momentum vector lifts off the orbital plane and settles down orthogonal to the orbital plane. The third phase is characterized by a drift of the angular momentum vector  $\approx 40$  deg off the orbital plane. It sweeps out a cone centered on the orthogonal to the orbital plane with an opening angle of 100 deg. All characteristic angular velocities are of the order of the orbital angular velocity.

and, in an attempt to reconcile the data with the model, has led others to hypothesize an erroneous model for the moments of inertia of LAGEOS-1<sup>13</sup>.

Our results have led us to formulate the following unresolved questions: (1) Why are the eddy currents damped primarily in the cylindrically-shaped brass core of the satellite and not in the aluminum shell?; and (2) What is the physics behind the three distinct phases of the LAGEOS spin dynamics? We are addressing these questions by (1) introducing a more realistic model of the satellite and earth into our simplified calculations<sup>14</sup>, and (2) by exploring more of phase space by way of Poincare sections. Our results presented here provide us with clues, now we must piece them together to reveal the physics behind the complex motion we observe.

### **Acknowledgments**

All work presented in this report was accomplished in a close cooperation with Warner Miller. Both of us wish to thank Stirling Colgate, Christopher Fuchs, Richard Matzner, John Ries, and James Thorne for many helpful discussions. We also wish to acknowledge the hospitality of the Astrodynamics Group at the Phillips Laboratory (PL/VTa) where part of this research was performed.

## REFERENCES

- <sup>1</sup> Ciufolini I., Measurement of the Lense-Thirring drag effect on LAGEOS and another high altitude laser ranged satellite, *Phys. Rev. Lett.*, **56**, 278 (1986).
- <sup>2</sup> Rubincam D. P., Drag on the LAGEOS satellite, *J. Geophys. Research*, **95**, 4881 (1990).
- <sup>3</sup> Rubincam D. P., LAGEOS orbit decay due to infrared radiation from earth, *J. Geophys. Res.*, **92**, 1278-1294 (1987).
- <sup>4</sup> Rubincam D. P., The LAGEOS along track acceleration: a review, Paper presented at the First William Fairbanks meeting on relativistic gravity experiments in space, Rome, Italy, September 10-14, (1990).
- <sup>5</sup> Rubincam D. P., Yarkovski thermal drag on LAGEOS, *J. Geophys. Research*, **93**, 13805 (1988).
- <sup>6</sup> Bertotti B., Iess L., The rotation of LAGEOS, *J. Geophys. Research*, **96**, 2431 (1991).
- <sup>7</sup> Vinti J. P., Theory of the Spin of a Conducting Satellite in the Magnetic Field of the Earth, Defense Technical Information Center, BRL-1020, 1957.
- <sup>8</sup> Landau L.D., Lifshitz E. M., *Electrodynamics of continuous media*, Pergamon Press, Oxford (1984).
- <sup>9</sup> Goldstein H., *Classical mechanics*, Addison-Wesley Publ. Co., Reading, MA (1981).
- <sup>10</sup> Kheyfets A., Spin Dynamics of Lageos Satellite, Final Report, 1992 Air Force Summer Research Program, July 1992.
- <sup>11</sup> Fuchs C., Lagrangian formulation of LAGEOS's spin dynamics, Final Report, 1992 Air Force Summer Research Program, August 1992.
- <sup>12</sup> Johnson C. W., Lundquist C. A., Zurasky J. L., The LAGEOS satellite, Paper presented at International Astronautical Federation XXVII Congress, Anaheim, CA, October 10-16, (1976).
- <sup>13</sup> Scharroo, R., Wakker, K. F., Ambrosius, B. A. C., and Noomen, R., On the along-track acceleration of the LAGEOS satellite, *J. Geophys. Res.*, **96** 729-40 (1991).
- <sup>14</sup> Halverson, R. P. and Cohen H. Torques on a spinning hollow sphere in a uniform magnetic field, *IEEE Trans. Aerosp. Navig. Electron.*, ANE-11 118-22 (1964).

**CASCADING OF THE UPPER HYBRID/ELECTRON BERNSTEIN WAVE IN  
THE IONOSPHERIC HEATING EXPERIMENTS**

(Final Report for AFOSR Research Initiation Program Subcontract 93-59 from the R&D  
Laboratory)

H. L. Zhou and J. Huang  
S. P. Kuo, Principal Investigator

Weber Research Institute and Department of Electrical Engineering  
Polytechnic University, Route 110, Farmingdale, NY 11735



## Summary

Parametric decay of an upper hybrid/electron Bernstein pump wave into an upper hybrid/electron Bernstein sideband wave and a lower hybrid decay wave in the long wave length regime is studied. It is found that the process associated with the electron Bernstein pump wave has a lower threshold field than that of a similar decay process of the upper hybrid pump wave when the instability is excited in the region away from the double resonance layer. Their threshold fields approach each other as the instability region is moved toward the double resonance layer where the upper hybrid resonance frequency equals a harmonic of the electron cyclotron frequency. Near the double resonance layer, the upper hybrid wave and the electron Bernstein wave become linearly coupled, the threshold field of the parametric decay process changes back to a similar functional dependence as that of the upper hybrid decay process. When incorporated with the appropriate nonlinear scattering processes, this instability process along with its cascading is proposed to be the generation mechanism for the DM, 2DM, 3DM...etc. features as well as the UM feature in the stimulated electromagnetic emission spectrum observed in the ionospheric heating experiments.

## I. Introduction

Heating and modification of the ionosphere by powerful radio waves transmitted from the ground heating facilities have revealed a large number of new phenomena related to wave-plasma interaction. Most of these phenomena are believed to be attributed to the plasma turbulence excited by the high frequency (HF) heaters via parametric instabilities. In the mid-latitude region, e.g., Arecibo, Puerto Rico, the sideband and decay modes of the parametric instabilities are dominated by Langmuir wave and ion acoustic wave/field-aligned density irregularities, respectively. On the other hand, in the high latitude region, e.g., Tromsø, Norway, and Gorby, Russia, upper hybrid wave/electron Bernstein wave and lower hybrid wave/ion Bernstein wave as the candidates of the instability products can be at least as important as those involved in the mid-latitude dominant processes. In addition to the electrostatic waves detected by the remote sensing technique, such as backscatter radar, some "secondary electromagnetic waves" which cover a frequency band of the order of 100 KHz around the pump frequency has also been measured directly on the ground. The spectrum of these waves, so called stimulated electromagnetic emissions (SEEs), is shown experimentally to be richly structured. A classification of these spectral features is given in detail by Stubbe et al.<sup>1</sup>

A most commonly observed feature in the SEE spectrum is the so called downshifted maximum (DM)<sup>1,2,3,4</sup>. It is a spectral peak about 10 KHz below the heater wave frequency. Sometimes a second (2DM) and third (3DM) downshifted maximum develop in the SEE spectrum with the downshifted frequency approximately twice and three times that of the DM. This cascading spectrum develops most strongly when the heater wave frequency  $f_0$  is near but not very close to a harmonic of the electron cyclotron frequency  $f_c$  of the ambient ionosphere. Moreover, an upshifted maximum (UM) with a spectral peak upshifted from  $f_0$  about the same amount as that of the DM feature is also

detected. When  $f_0$  is very close to the cyclotron harmonic frequency  $lf_c$  ( $l = 3, 4, 5, 6, 7$ ), the whole family of the DM feature is quenched<sup>2,5,6</sup>.

Several theoretical model for the generation of the DM emission have been proposed. Stubbe et al.<sup>1</sup> suggested that the Langmuir wave generated near reflection height by the parametric decay instability along the geomagnetic field can scatter off the ion acoustic wave generated through a similar mechanism to produce the DM emission. On the other hand, it is observed in the experiments that this DM feature has a cutoff frequency near the lower hybrid resonance frequency and that, for the Tromso heating experiments, most of the heater power is dumped into the height region near the upper hybrid resonance layer after the formation of the heater induced field-aligned short scale irregularities. Leyser<sup>7</sup> then suggested that the parametric decay of the upper hybrid pump wave into a lower hybrid wave and a frequency downshifted o-mode electromagnetic emissions could be responsible for the observed DM feature. The upper hybrid pump wave was generated through a direct conversion process facilitated by the field-aligned density irregularities. He also suggested that the observed 2DM feature be attributed to a two step emission process<sup>7</sup>. The HF heater wave first decayed into an upper hybrid wave and a lower hybrid wave, and the excited upper hybrid wave subsequently decayed into another lower hybrid wave and an o-mode emission with a downshifted frequency of twice the lower hybrid frequency. However, the proposed mechanisms can not explained the presence of 3DM as well as the UM lines observed in the SEE spectrum<sup>8</sup>. Therefore, in the present work, an alternative process similar to that proposed by Grach and Shvarts<sup>9</sup> is investigated. The corresponding threshold fields will be shown to be less than those of the processes suggested by Leyser<sup>7</sup>.

As evidenced by the experimental results, the electron Bernstein wave should be involved in the DM generation process when the  $f_0$  is near but not very close to  $\eta f_c$ . Thus

in the present work, we study the parametric decay of the upper hybrid/electron Bernstein pump wave  $(\bar{k}_0, f_0)$  into an upper hybrid/electron Bernstein sideband  $(\bar{k}_1, f_1 = f_0 - f_{LH})$  and a lower hybrid decay mode  $(\bar{k}_s, f_{LH})$ . The upper hybrid/electron Bernstein wave having the same frequency as that of the HF heater wave is produced through a thermal oscillating two stream instability (OTSI)<sup>6,10,11</sup> in which the short scale field-aligned density irregularity  $(\bar{k} = \bar{k}_0)$  is the decay mode. The scattering of the frequency downshifted upper hybrid/electron Bernstein sideband  $(\bar{k}_{1\perp} \cong -\bar{k}_0)$  off the field-aligned density irregularity is then suggested to be an additional generation mechanism of the DM lines. Moreover, the scattering of the oppositely propagating upper hybrid/electron Bernstein wave  $(-\bar{k}_0, f_0)$  excited via the OTSI process off the lower hybrid decay mode (with  $\bar{k}_s \cong 2\bar{k}_0$ ) produce a frequency upshifted high frequency sideband  $(\bar{k}_2 \approx \bar{k}_0, f_0 + f_{LH})$  which can subsequently scatter off the field-aligned density irregularity to excite the UM emission. The frequency downshifted high frequency sideband, once fully developed, can act as a secondary pump wave to decay into a lower hybrid decay mode and another high frequency sideband  $(\bar{k}'_{1\perp} \cong -\bar{k}_{1\perp} \cong \bar{k}_0, f_1' = f_0 - 2f_{LH})$ . The 2DM emission can then be produced through the scattering of the secondary high frequency sideband off the field aligned density irregularity. As the parametric decay and scattering processes continue, a cascading spectrum of the DM lines (ie., DM, 2DM, 3DM...etc) can thus be formed. The purpose of the present work is to show that the upper hybrid/electron Bernstein pump wave can indeed cascade its frequency downward through the proposed parametric instability. Therefore, along with the above mentioned nonlinear scattering processes, the SEE lines bearing the nDM features as well as the UM feature are generated as observed in the HF heating experiments.

Parametric instability involving three electrostatic waves in a magnetized plasma has been studied from a kinetic approach by Tataronis and Teichmann<sup>12</sup>. However, the resultant coupled mode equations involved the integration of the product of three Bessel

functions over the distribution function. Due to this complexity, the derived equations were not analyzed to determine the threshold field and growth rate of the instability. On the other hand, in the long wavelength regime of the present interest, the Bessel function can be expanded into a perturbation series. Thus, only the first few terms have to be kept, and the integration can be performed analytically. It leads to an explicit expression for the dispersion relation which can then be solved analytically to determine the threshold field and growth rate of the instability. Moreover, a general formulism for the electrostatic wave interactions based on a fluid-kinetic hybrid approach has also been developed<sup>13</sup>. In this approach, the coupled mode equations developed from the fluid equations is first formulated, and the kinetic effect can be included by replacing the fluid susceptibilities with the kinetic ones. One can also start from the Vlasov equation and calculate the nonlinear coupling terms from the fluid point of view and obtain the same result<sup>14</sup>. It will be shown in sections II and III, however, that this hybrid formulism which does not take into account the finite Larmor radius effect in the coupling terms properly is not suitable for the analysis of the electron Bernstein wave decay process.

The organization of this paper is as follows: The theory of the proposed parametric coupling process is formulated in Sec. II. In Sec. III, the dispersion relation obtained from the derived coupled mode equations is analyzed for the threshold field and growth rate for three cases: (1) upper hybrid pump and upper hybrid sideband; (2) electron Bernstein pump and electron Bernstein sideband; and (3) upper hybrid-electron Bernstein pump and upper hybrid-electron Bernstein sideband. In all three cases, the decay modes are lower hybrid waves. In Sec. IV, the results of the analysis are discussed in relevance to the DM cascading feature and the UM line in the SEE spectrum observed in the heating experiments. Summary and conclusion of the work are finally drawn in Sec. V.

## II. Formulation

A parametric coupling process considering the decay of an upper hybrid/electron Bernstein pump  $(\omega_0, \bar{k}_0)$  into an upper hybrid/electron Bernstein sideband  $(\omega_1, \bar{k}_1)$  together with a lower hybrid decay mode  $(\omega_s, \bar{k}_s)$  is studied in the following. The parametric coupling is imposed by the frequency and wave vector matching conditions:  $\omega_0 = \omega_1 + \omega_s^*$  and  $\bar{k}_0 = \bar{k}_1 + \bar{k}_s$ .

### A. Coupled mode equation for the upper hybrid/electron Bernstein sideband

The electron Bernstein wave oscillates near one of the harmonics of electron cyclotron frequency and couples resonantly with the electron plasma through the finite Larmor radius effect. Thus, it is necessary to use the kinetic equation to determine its linear dispersion relation in the plasma. Likewise, the kinetic equation should also be used to formulate the coupled mode equations of the considered parametric decay process. A transformation of the Vlasov equation to the guiding center coordinate  $\bar{x}_g$  is introduced to assist the analysis. The detail of the transformation is presented in appendix A. The transformed Vlasov equation is then analyzed by a perturbation expansion procedure which is described in appendix B. The relevant first and second order kinetic equations (B2) and (B3) derived in appendix B are then employed for the following formulation. They are solved by first expanding the perturbed physical quantities  $f_e^{(i)}$ ,  $\bar{E}^{(i)}$ , and  $n_e$ ,  $i = 1, 2$ , in terms of the guiding center coordinate  $\bar{x}_g$  in the forms of (B4). Substituting (B4) into (B2), it is straightforward to obtain  $f_e^{(1)}$  as

$$f_e^{(1)} = \exp[-i(\omega t - \vec{k} \cdot \vec{x}_g)] \sum_l \frac{(l\Omega_e + k_z v_z)(\frac{-e}{T_e}) \hat{\phi}^{(1)} + i\nu_e(\frac{\hat{n}_e^{(1)}}{n_0})}{\bar{\omega} - k_z v_z - l\Omega_e} J_l(\alpha) f_e^0 e^{il(\varphi - \delta)} \quad (1)$$

where  $\bar{\omega} = \omega + i\nu_e$ ,  $\nu_e = \nu_{ei}$  being the electron-ion collision frequency (the electron-neutral collision frequency  $\nu_{en} \ll \nu_{ei}$  in the F region of the ionosphere and is neglected);  $\hat{\phi}^{(1)} = i\vec{k} \cdot \hat{\vec{E}}^{(1)} / k^2$ .

In the present work,  $f_e^0$  is assumed to be a Maxwellian distribution function

$$f_e^0 = \frac{n_{e0}}{(2\pi)^{3/2} v_e^3} \exp\{-(v_\perp^2 + v_\parallel^2) / 2v_e^2\}$$

where  $v_e = (T_e / m_e)^{1/2}$  is the electron thermal speed.

To construct the coupled mode equation for the upper hybrid/electron Bernstein sideband wave, (B3) is used. It is also solved by, again, using the expansion expressions (B4) for the perturbations. With the aid of (1) and the matching conditions, the result is found to be

$$\begin{aligned} \hat{f}_{e1} = & -\frac{e}{T_e} \hat{\phi}_1 \frac{l'\Omega_e + k_{1z}v_z + i\nu_e(k_1^2 / k_D^2)}{\bar{\omega}_1 - k_{1z}v_z - l'\Omega_e} J_{l'}(\alpha_1) f_e^0 \\ & -\frac{e}{m_e} \hat{\phi}_s^* \sum_l \frac{1}{\bar{\omega}_1 - k_{1z}v_z - l'\Omega_e} \{J_{l-l'}(\alpha_s) [\frac{(l-l')\Omega_e}{v_\perp} \frac{\partial}{\partial v_\perp} + k_{sz} \frac{\partial}{\partial v_z} - i \frac{\vec{k}_s \times \hat{z} \cdot \vec{k}_0}{\Omega_e} \\ & + \frac{lk_{s\perp}}{v_\perp} J_{l-l'}(\alpha_s)] \frac{(l\Omega_e + k_{0z}v_z)(\frac{-e}{T_e}) \hat{\phi}_0}{\omega_0 - k_{0z}v_z - l\Omega_e} J_l(\alpha_0) f_e^0 e^{i[l\delta_1 + (l-l')\delta_s - l\delta_0]} \\ & + \frac{e}{m_e} \hat{\phi}_0 \sum_l \frac{1}{\bar{\omega}_1 - k_{1z}v_z - l'\Omega_e} \{J_{l+l'}(\alpha_0) [\frac{(l+l')\Omega_e}{v_\perp} \frac{\partial}{\partial v_\perp} + k_{0z} \frac{\partial}{\partial v_z} + i \frac{\vec{k}_0 \times \hat{z} \cdot \vec{k}_s}{\Omega_e} \end{aligned}$$

$$+\frac{lk_{0\perp}}{v_{\perp}}J'_{l+l'}(\alpha_0)]\frac{(l\Omega_e+k_{sz}v_z)(-\frac{e}{T_e})\hat{\phi}_0-i\nu_e(\frac{\hat{n}_{e1}}{n_0})}{\bar{\omega}_s^*-k_{sz}v_z-l\Omega_e}J_l(\alpha_s)f_e^0e^{i[l'\delta_1-(l+l')\delta_0+l\delta_s]} \quad (2)$$

where the formal superscripts of all the perturbation quantities have been dropped;  $\alpha_i = k_{i\perp}v_{\perp}/\Omega_e$ ,  $i = 0, 1$ , and  $s$ ; where the relations  $k_1^2\hat{\phi}_1^{(1,2)} = -4\pi e\hat{n}_e^{(1,2)}$  of the first and second order iteration of the Poisson equation have been used.

With the aid of (2) and (B4), the perturbed electron distribution function in the original coordinate  $\bar{x}$  can be expressed as

$$f_{e1} = \exp[-i(\omega_1 t - \bar{k}_1 \cdot \bar{x})] \sum_{m,l'} J_m(\alpha_1) \hat{f}_{e1} e^{i(l'-m)(\varphi - \delta_1)} \quad (3)$$

where  $\hat{f}_{e1}$  is given by (2). Integrating (3) over the velocity space, the total electron density perturbation  $n_{e1}$  of the sideband wave is obtained. The result is then substituted into the Poisson equation to form the coupled mode equation for the upper hybrid/electron Bernstein sideband wave. However, it is found that the resultant equation is too complicated to be analyzed analytically. Thus, two conditions: (1)  $k_z = k_y = 0$ , i.e. all waves propagate in  $\bar{x}$  direction; and (2)  $k^2 v_e^2 \ll \omega_{pe}^2$  and  $\nu_e \ll \Omega_e$ , are introduced to simplify the nonlinear distribution function  $f_{e1}$ . Even so, the integrands of the velocity integrals still contain the product of three Bessel functions. In order to carry out the integrations, the Bessel functions are expanded by

$$J_l(x) \cong \frac{1}{l!} \left(\frac{x}{2}\right)^l \left[1 - \frac{x^2}{2(2n+2)} + \dots\right]$$

After some manipulation and keeping only the dominant terms, the coupled mode equation for the upper hybrid/electron Bernstein sideband in the explicit form is derived to be



$$\begin{aligned}
& \left\{ \frac{\omega_1}{\bar{\omega}_1} - \frac{\omega_{pe}^2}{\bar{\omega}_1^2 - \Omega_e^2} \left( 1 + \frac{3k_1^2 v_{te}^2}{\bar{\omega}_1^2 - 4\Omega_e^2} \right) - \frac{l\omega_{pe}^2}{\bar{\omega}_1^2 - l^2\Omega_e^2} K_{l-1}(\beta_1) \right\} \hat{\phi}_1 \\
&= \frac{k_0 k_s}{k_1} \left\{ \frac{\omega_{pe}^2}{\bar{\omega}_1^2 - \Omega_e^2} \left( \frac{k_s}{\omega_0^2 - \Omega_e^2} - \frac{k_0}{\bar{\omega}_s^{*2} - \Omega_e^2} \right) - \frac{k_1 \omega_{pe}^2}{2\bar{\omega}_1 \Omega_e^2} \left( \frac{\omega_0}{\omega_0^2 - \Omega_e^2} - \frac{\bar{\omega}_s^*}{\bar{\omega}_s^{*2} - \Omega_e^2} \right) \right. \\
&+ \frac{k_1 \omega_{pe}^2}{2\Omega_e^2 (\bar{\omega}_1^2 - 4\Omega_e^2)} \left( \frac{\bar{\omega}_1 \omega_0 + 2\Omega_e^2}{\omega_0^2 - \Omega_e^2} - \frac{\bar{\omega}_1 \bar{\omega}_s^* - 2\Omega_e^2}{\bar{\omega}_s^{*2} - \Omega_e^2} \right) \\
&\left. + \frac{k_s \omega_{pe}^2}{2\Omega_e^2} \frac{l(\bar{\omega}_1 \omega_0 + l^2 \Omega_e^2)}{(\bar{\omega}_1^2 - l^2 \Omega_e^2)(\omega_0^2 - l^2 \Omega_e^2)} K_{l-1}(\beta_{01}) \right\} \frac{e}{m_e} \hat{\phi}_s^* \hat{\phi}_0 \quad (4)
\end{aligned}$$

where  $\Lambda_1(x) \equiv \frac{x}{2}(1-x)$  has been used and only  $l \geq 3$  cases are considered with  $\beta_{01} = k_0 k_1 v_e^2 / \Omega_e^2$  and  $K_l(x) \equiv \frac{1}{l!} \left( \frac{x}{2} \right)^l$ .

Equation (4) is the coupled mode equation of the upper hybrid/electron Bernstein sideband wave. The upper hybrid/electron Bernstein sideband is coupled to the lower hybrid wave through the pump as manifested by the dependence of the right hand side (RHS) terms of (4).

#### B. Coupled mode equation for the lower hybrid decay wave.

Using a similar procedure, the perturbed electron distribution function responding to the lower hybrid decay mode is obtained to be

$$f_{es} = \exp[-i(\omega_s t - \bar{k}_s \cdot \bar{x})] \left\{ \sum_{m,l} \frac{l\Omega_e \left( -\frac{e}{T_e} \right) \hat{\phi}_s + i v_e \left( \frac{\hat{n}_{es}}{n_0} \right)}{\bar{\omega}_s - l\Omega_e} J_m(\alpha_s) J_l(\alpha_s) f_e^0 e^{i(l-m)\varphi} \right.$$

$$\begin{aligned}
& -\frac{e}{m_e} \hat{\phi}_1^* \sum_{m,l',l} \frac{l\Omega_e(-\frac{e}{T_e})\hat{\phi}_0}{(\bar{\omega}_s - l'\Omega_e)(\omega_0 - l\Omega_e)} \\
& J_m(\alpha_s) \left[ \frac{(l-l')\Omega_e}{v_\perp} J_{l-l'}(\alpha_1) \frac{\partial}{\partial v_\perp} + \frac{lk_1}{v_\perp} J'_{l-l'}(\alpha_1) \right] J_l(\alpha_0) f_e^0 e^{i(l-m)\varphi} \\
& + \frac{e}{m_e} \hat{\phi}_0 \sum_{l',l} \frac{l\Omega_e(-\frac{e}{T_e})\hat{\phi}_1^*}{(\bar{\omega}_s - l'\Omega_e)(\bar{\omega}_1^* - l\Omega_e)} \\
& J_m(\alpha_s) \left[ \frac{(l+l')\Omega_e}{v_\perp} J_{l+l'}(\alpha_0) \frac{\partial}{\partial v_\perp} + \frac{lk_0}{v_\perp} J'_{l+l'}(\alpha_0) \right] J_l(\alpha_1) f_e^0 e^{i(l-m)\varphi} \Bigg\} \quad (5)
\end{aligned}$$

where  $\bar{\omega}_s = \omega_s + i\nu_e$ , and  $\hat{n}_{es} = \int f_{es} d\mathbf{v}$  is the linear part of the electron density perturbation responding to the lower hybrid wave field.

For the ion component, the coupling terms can be neglected, and the perturbed distribution function is obtained to be

$$f_{is} = \exp[-i(\omega_s t - \bar{k}_s \cdot \bar{x})] \sum_{m,l} \frac{l\Omega_i(\frac{e}{T_i})\hat{\phi}_s}{\omega_{si} - l\Omega_i} J_m(\alpha_{is}) J_l(\alpha_{is}) f_i^0 e^{i(l-m)\varphi} \quad (6)$$

where  $\Omega_i = eB_0 / m_i c$  is the ion cyclotron frequency,  $\alpha_{is} = k_s v_\perp / \Omega_i$ , and  $\hat{n}_{is} = \int f_{is} d\mathbf{v}$ .

The corresponding electron and ion density perturbations,  $\hat{n}_{es}$  and  $\hat{n}_{is}$  respectively, are obtained by integrating (5) and (6) over the velocity space, and are then substituted into the Poisson equation  $k_s^2 \hat{\phi}_s = 4\pi e(\hat{n}_{is} - \hat{n}_{es})$ . Replacing again the Bessel functions in the velocity integrals by their first few expansion terms, the integrations can be carried out. It leads to the following coupled mode equation for the lower hybrid wave

$$\begin{aligned}
& \left\{ 1 - \frac{\bar{\omega}_s}{\omega_s} \frac{\omega_{pe}^2}{\bar{\omega}_s^2 - \Omega_e^2} \left( 1 + \frac{3k_s^2 v_e^2}{\bar{\omega}_s^2 - 4\Omega_e^2} \right) + \frac{k_{di}^2}{k_s^2} \text{PW} \left( \frac{\omega_s}{k_s v_i} \right) \right\} \hat{\phi}_s \\
&= \frac{k_0 k_1}{k_s} \left\{ \frac{\omega_{pe}^2}{\bar{\omega}_s^2 - \Omega_e^2} \left( \frac{k_1}{\omega_0^2 - \Omega_e^2} - \frac{k_0}{\bar{\omega}_1^{*2} - \Omega_e^2} \right) - \frac{k_s \omega_{pe}^2}{2\bar{\omega}_s \Omega_e^2} \left( \frac{\omega_0}{\omega_0^2 - \Omega_e^2} - \frac{\bar{\omega}_1^*}{\bar{\omega}_1^{*2} - \Omega_e^2} \right) \right. \\
&\quad + \frac{k_s \omega_{pe}^2}{2\Omega_e^2 (\bar{\omega}_s^2 - 4\Omega_e^2)} \left( \frac{\bar{\omega}_s \omega_0 + 2\Omega_e^2}{\omega_0^2 - \Omega_e^2} - \frac{\bar{\omega}_s \bar{\omega}_1^* - 2\Omega_e^2}{\bar{\omega}_1^{*2} - \Omega_e^2} \right) \\
&\quad \left. - \frac{k_s l \omega_{pe}^2}{2\bar{\omega}_s \Omega_e^2} \left( \frac{\omega_0}{\omega_0^2 - l^2 \Omega_e^2} - \frac{\bar{\omega}_1^*}{\bar{\omega}_1^{*2} - l^2 \Omega_e^2} \right) K_{l-1}(\beta_{01}) \right\} \frac{e}{m_e} \hat{\phi}_1^* \hat{\phi}_0 \quad (7)
\end{aligned}$$

where  $\text{PW}(Z) = (2\pi)^{-1/2} \mathbf{P} \int_{-\infty}^{\infty} \frac{x}{x - Z - i\eta} \exp(-\frac{x^2}{2}) dx \approx -\frac{1}{Z^2} - \frac{3}{Z^4} - \dots$  for  $|Z| \gg 1$ .

Note that  $(k_{di}^2 / k_s^2) \text{PW}(\omega_s / k_s v_i) = \chi_e(k_s, \omega_s)$  with  $\mathbf{P}$  denoting the principal part is equivalent to the unmagnetized ion susceptibility except for the ion Landau damping effect. This term is obtained formally from the exact ion susceptibility of the magnetized plasma using asymptotics for the large argument  $k_s \rho_i$ <sup>15</sup>. Unless the gyro motion of the ions is broken down through collisions, the effect of the ion Landau damping is averaged out. This point is evident in the exact magnetized ion susceptibility from which there is no collisionless damping in the direction perpendicular to the magnetic field. In the *F*-region of the ionosphere,  $\Omega_i = 2\pi \times 50\text{Hz}$ ,  $\nu_{in} = 2.5\text{s}^{-1}$ ,  $\nu_{ie} = (m_e / m_i) \nu_{ei} = 0.017\text{s}^{-1}$  with  $\nu_{ie}$  being the ion-electron collision frequency and  $\nu_{in}$  being the ion-neutral collision frequency, it is clear that  $\Omega_i \gg \nu_i = \nu_{ie} + \nu_{in}$ . That is, ion gyro motion can be completed. Therefore, we do not expect that the ion Landau damping has a significant effect on a wave propagating nearly perpendicular to the magnetic field as the lower hybrid wave in the considered parametric process. It is also noted that the effect of the collisional

damping of ions on the lower hybrid wave is small and has been neglected. This point will be further elaborated in the appendix A.

Equations (4) and (7) form a set of coupled equations describing the considered parametric decay process, namely, decay of an upper hybrid/electron Bernstein pump into another upper hybrid/electron Bernstein sideband and a lower hybrid decay mode.

### III. Dispersion relation and analysis

Combining (4) and the complex conjugate of (7), a dispersion relation is obtained. This dispersion relation is simplified and analyzed for the following three cases.

(1) Decay of an upper hybrid pump wave into a lower hybrid decay wave and an upper hybrid sideband wave:

In this case, only the first three terms on the RHS of (4) are dominant. The remaining term attributed to the finite Larmor radius effect can be neglected. Considering the fact that  $\omega_2 \ll \omega_0$ ,  $\omega_1$ ,  $\Omega_e$ , and employing the linear dispersion relation of the upper hybrid wave to reexpress the coefficients of the coupling terms, (4) is simplified to be

$$\begin{aligned} & \{\omega_1^2 + i\Gamma_{uh}\omega_1 - \omega_{uk_1}^2\} \hat{\phi}_1 \\ &= -\frac{k_0 k_s}{k_1} \frac{\omega_{pe}^2}{(\omega_0^2 - \Omega_e^2)(\bar{\omega}_s^{*2} - \Omega_e^2)} [k_0 \bar{\omega}_1 \bar{\omega}_s^* + k_1 \bar{\omega}_s^* \omega_0 + k_s \bar{\omega}_1 \omega_0] \frac{e}{m_e} \hat{\phi}_s^* \hat{\phi}_0 \\ &\cong \frac{k_0 k_s^2}{k_1} \left(1 + \frac{\omega_{pe}^2}{\Omega_e^2}\right) \frac{e}{m_e} \hat{\phi}_s^* \hat{\phi}_0 \end{aligned} \quad (8)$$

where  $\omega_{uk_1}^2 = \omega_{UH}^2 + 3k_1^2 v_{te}^2 \omega_{pe}^2 / (\omega_{pe}^2 - 3\Omega_e^2) \cong \omega_{UH}^2$  is the upper hybrid wave frequency with  $\omega_{UH}^2 = \omega_{pe}^2 + \Omega_e^2$  being the upper hybrid resonance frequency; and  $\Gamma_{uh} = v_e (1 + \Omega_e^2 / \omega_{UH}^2)$ .

Again, with the aid of the linear dispersion relation of the upper hybrid wave, the coupling terms on the RHS of (7) can be combined. Keeping only the dominant contributions, (7) is reduced to

$$\begin{aligned}
& \{\omega_s^2 + i\Gamma_{lh}\omega_s - \omega_{lk}^2\} \hat{\phi}_s \\
&= \frac{\omega_s^2}{\omega_{UH}^2} \frac{k_0 k_1}{k_s} \frac{\omega_{pe}^2}{(\omega_0^2 - \Omega_e^2)(\bar{\omega}_1^{*2} - \Omega_e^2)} [k_0 \bar{\omega}_s \bar{\omega}_1^* + k_s \bar{\omega}_1^* \omega_0 + k_1 \bar{\omega}_s \omega_0] \frac{e}{m_e} \hat{\phi}_1^* \hat{\phi}_0 \\
&\cong \frac{\omega_s^2}{\omega_{pe}^2} k_0 k_1 \frac{e}{m_e} \hat{\phi}_1^* \hat{\phi}_0
\end{aligned} \tag{9}$$

where  $\omega_{lk}^2 \cong \Omega_e \Omega_i [1 + m_i / m_e (k_z / k_s)^2] + k_s^2 c_s^2 \approx \omega_{LH}^2$  is the lower hybrid wave frequency with  $\omega_{LH}^2 = \omega_{pi}^2 / (1 + \omega_{pe}^2 / \Omega_e^2) \approx \Omega_e \Omega_i$  being the lower hybrid resonance frequency and  $c_s = \sqrt{(3T_e / 4 + 3T_i) / m_i}$ ;  $\Gamma_{lh} = \nu_e (1 - \Omega_e^2 / \omega_{UH}^2)$ . Note that the effect of finite  $k_z$  has been taken into account phenomenologically into the present formulation. For the perpendicularly propagating pump electrostatic wave,  $k_z = [\omega_0^2 - \omega_{pe}^2 \omega_0 / (\omega_0 + \Omega_e)] / c$  which is obtained from the linear dispersion relation of the o-mode electromagnetic wave is chosen for the lower hybrid wave. Here  $c$  is the speed of light. On the other hand, the effect of Landau damping associated the wave-particle (electron) interaction along the magnetic field (due to the presence of finite  $k_z$ ) is found to be negligible.

Combining (8) and (9), and setting  $\omega_s = \omega_{lk} + i\gamma$ , an equation for growth rate  $\gamma$  of the instability is obtained as

$$\left(\gamma + \frac{\Gamma_{uh}}{2}\right) \left(\gamma + \frac{\Gamma_{lh}}{2}\right) = \frac{\omega_{LH} \omega_{UH}}{4 \omega_{pe}^2 \Omega_e^2} (k_0 - k_1)^2 \left(\frac{e}{m_e}\right)^2 |E_0|^2 \tag{10}$$

Setting  $\gamma = 0$  in (10), the threshold field of the instability is obtained

$$|E_{th}| = \left(\frac{m_e}{e}\right) \left(\frac{\Gamma_{uh} \Gamma_{lh}}{\omega_{LH} \omega_{UH}}\right)^{1/2} \frac{\omega_{pe} \Omega_e}{|k_0 - k_1|} \tag{11}$$

where the relationship between  $k_1$  and  $k_0$  determined from the dispersion relation of the upper hybrid waves and the frequency matching condition is found to be

$$k_1 = \pm k_0 \left( 1 - \frac{2\omega_{UH}\omega_{LH}}{3k_0^2 v_{te}^2 \omega_{pe}^2 / (\omega_{pe}^2 - 3\Omega_e^2)} \right)^{1/2} \quad (12)$$

The dependence of the threshold field on  $k_0 \rho_e$  ( $\rho_e = v_e / \Omega_e$ ) is plotted in Fig. 1. with the following ionospheric  $F$ -region parameters:  $\Omega_e = 2\pi \times 1.35$  MHz,  $v_e = 10^5$  m/s,  $v_e \cong v_{ei} = 500$  s $^{-1}$ ,  $m_e/m_i(O^+) = 3.4 \times 10^{-5}$ ,  $T_i/T_e = 0.75$ . The growth rate of the instability as a function of  $|E_0/E_{th}|$  is determined from (10) to be

$$\gamma = -\frac{(\Gamma_{uh} + \Gamma_{lh})}{4} + \frac{1}{2} \left[ \frac{(\Gamma_{uh} + \Gamma_{lh})^2}{4} - \Gamma_{uh}\Gamma_{lh} \left( 1 - \left| \frac{E_0}{E_{th}} \right|^2 \right) \right]^{1/2} \quad (13)$$

(2) Decay of an electron Bernstein wave into a lower hybrid decay wave and an electron Bernstein sideband wave:

In this case, the last term on the RHS of (4) becomes dominant. It should be pointed out that this term arises from the finite Larmour radius effect and thus appears only when a kinetic approach is employed in the analysis. With the aid of the linear dispersion relation of the electron Bernstein pump wave

$$\omega_0^2 - l^2 \Omega_e^2 = \frac{l \omega_{pe}^2 (\omega_0^2 - \Omega_e^2)}{\omega_0^2 - \Omega_e^2 - \omega_{pe}^2} K_{l-1}(\beta_0)$$

where  $\beta_0 = k_0^2 v_e^2 / \Omega_e^2$ , (4) is reduced to

$$[\omega_1^2 + i\Gamma_{eb}\omega_1 - \omega_{EB}^2] \hat{\phi}_1 = \frac{l^2 k_0 k_s^2}{k_1} \left( \frac{k_1}{k_0} \right)^{l-1} \frac{e}{m_e} \hat{\phi}_s^* \hat{\phi}_0 \quad (14)$$

where  $\omega_{EB} \cong l\Omega_e$  and  $\Gamma_{eb} = 2 v_e$ .

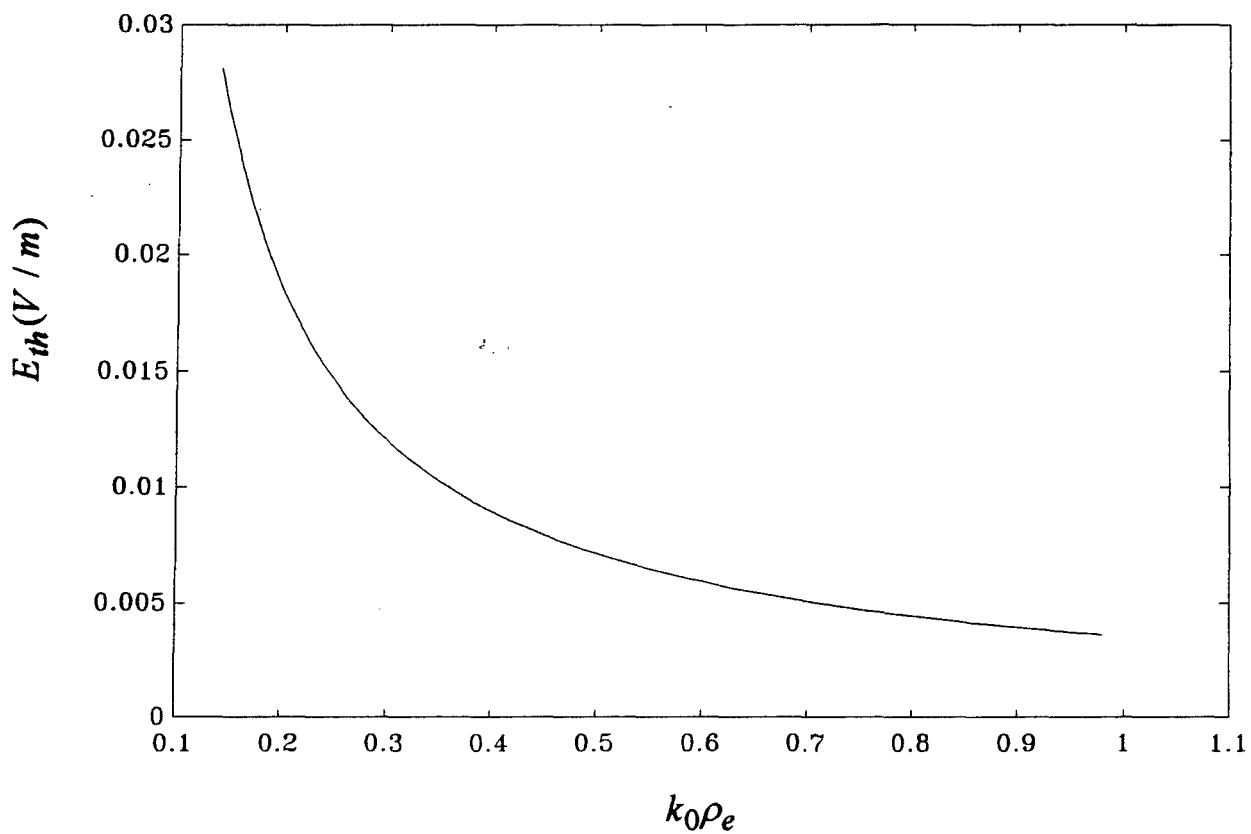


Fig. 1. Threshold field and vs.  $k_0 \rho_e$  for the parametric decay of the upper hybrid wave into a backscattered upper hybrid wave and a lower hybrid decay mode below the double resonance layer (with  $\omega_s = 9$  KHz and  $\eta = 2.65$ ).



Correspondingly, taking only the resonant term, (7) is also reduced to

$$\begin{aligned}
 & (\omega_s^2 + i\Gamma_{lh}\omega_s - \omega_{lk}^2)\hat{\phi}_s \\
 &= \frac{\omega_s}{1 + \omega_{pe}^2/\Omega_e^2} \frac{lk_0k_1}{2\Omega_e} \left[ \left(\frac{k_0}{k_1}\right)^{l-1} - \left(\frac{k_1}{k_0}\right)^{l-1} \right] \left(1 - \frac{\omega_{pe}^2}{(l^2-1)\Omega_e^2}\right) \frac{e}{m_e} \hat{\phi}_1^* \hat{\phi}_0
 \end{aligned} \quad (15)$$

From the frequency matching condition and the linear dispersion relations for the pump and sideband electron Bernstein waves, one can obtain a relation between  $k_0$  and  $k_1$  as

$$2\Omega_e\omega_s = \frac{(l^2-1)\Omega_e^2\omega_{pe}^2}{[(l^2-1)\Omega_e^2 - \omega_{pe}^2]} \left\{1 - \left(\frac{k_1}{k_0}\right)^{2(l-1)}\right\} K_{l-1}(\beta_0) \quad (16)$$

(14) and (15) are then combined with the aid of (16) to obtain the dispersion relation

$$\begin{aligned}
 & (\omega_1^{*2} - i\Gamma_{eb}\omega_1 - \omega_{EB}^2)(\omega_s^2 + i\Gamma_{lh}\omega_s - \omega_{lk}^2) \\
 &= \frac{\omega_s^2\Omega_e^2}{\omega_{pe}^2\omega_{UH}^2} \frac{l^3(k_0-k_1)^2}{K_{l-1}(\beta_0)} \left[1 - \frac{\omega_{pe}^2}{(l^2-1)\Omega_e^2}\right]^2 \left(\frac{e}{m_e}\right)^2 |E_0|^2
 \end{aligned} \quad (17)$$

The threshold field of the instability in this case is found to be

$$|E_{th}| = \left(\frac{m_e}{e}\right) \frac{1}{\omega_{LH}^{1/2}} \frac{\omega_{pe}\omega_{UH}(l^2-1)\Omega_e^{3/2}}{|(l^2-1)\Omega_e^2 - \omega_{pe}^2|} \frac{(\Gamma_{eb}\Gamma_{lh})^{1/2}}{l|k_0-k_1|} K_{l-1}^{1/2}(\beta_0) \quad (18)$$

The growth rate  $\gamma$  has the same functional dependence on  $|E_0/E_{th}|$  as (13) except that the subscript of the damping term  $\Gamma$  should be changed from  $uh$  to  $eb$ .

Based on (16), (18) is examined for two cases:

(i)  $l^2 \Omega_e^2 > \omega_{pe}^2 + \Omega_e^2$  (below the double resonance layer)

As indicated by (16),  $|k_1| < k_0$ . Thus,  $k_0$  has a minimum value which corresponds to  $|k_1| = 0$ . This minimum value is obtained to be

$$k_{0\min} = \frac{\Omega_e}{v_e} [2(l-1)! \omega_s \Omega_e \frac{(l^2-1)\Omega_e^2 - \omega_{pe}^2}{(l^2-1)\Omega_e^2 \omega_{pe}^2}]^{\frac{1}{2(l-1)}} \quad (20)$$

The threshold field (18) at  $k_0 = k_{0\min}$  is found to be

$$|E_{th}|_{\min} = \sqrt{2} \left( \frac{m_e}{e} \right) \frac{(l^2-1)^{1/2} \Omega_e \omega_{UH}}{l [(l^2-1)\Omega_e^2 - \omega_{pe}^2]^{1/2}} \frac{(\Gamma_{eb} \Gamma_{lh})^{1/2}}{k_{0\min}} \quad (21)$$

(21) is a good estimation of the lower bound of the threshold field for all possible  $k_0$  and  $k_1$ . Using (16) to express  $k_1$  in terms of  $k_0$ , the dependence of the threshold field (18) on  $k_0 \rho_e$  ( $\rho_e = v_e / \Omega_e$ ) in this case (for  $l = 3$ ) is plotted in Fig. 2. Note that  $k_0$  can not be too large, otherwise the series expansion of the Bessel functions adopted in the present work becomes invalid.

(ii)  $l^2 \Omega_e^2 < \omega_{pe}^2 + \Omega_e^2$  (above the double resonance layer)

In this case,  $|k_1| > k_0$ , and as  $k_0$  decreases,  $|k_1|$  increases while the threshold field decreases. When  $k_0$  is very small,  $|k_1| \approx |k_s| \gg k_0$ , and the threshold field of the instability becomes very small. On the other hand,  $k_0$  can not be too small, so the electrostatic approximation used in the formulation can still hold. The threshold field versus  $k_0 \rho_e$  in this case ( $l = 3$ ) is plotted in Fig 3.

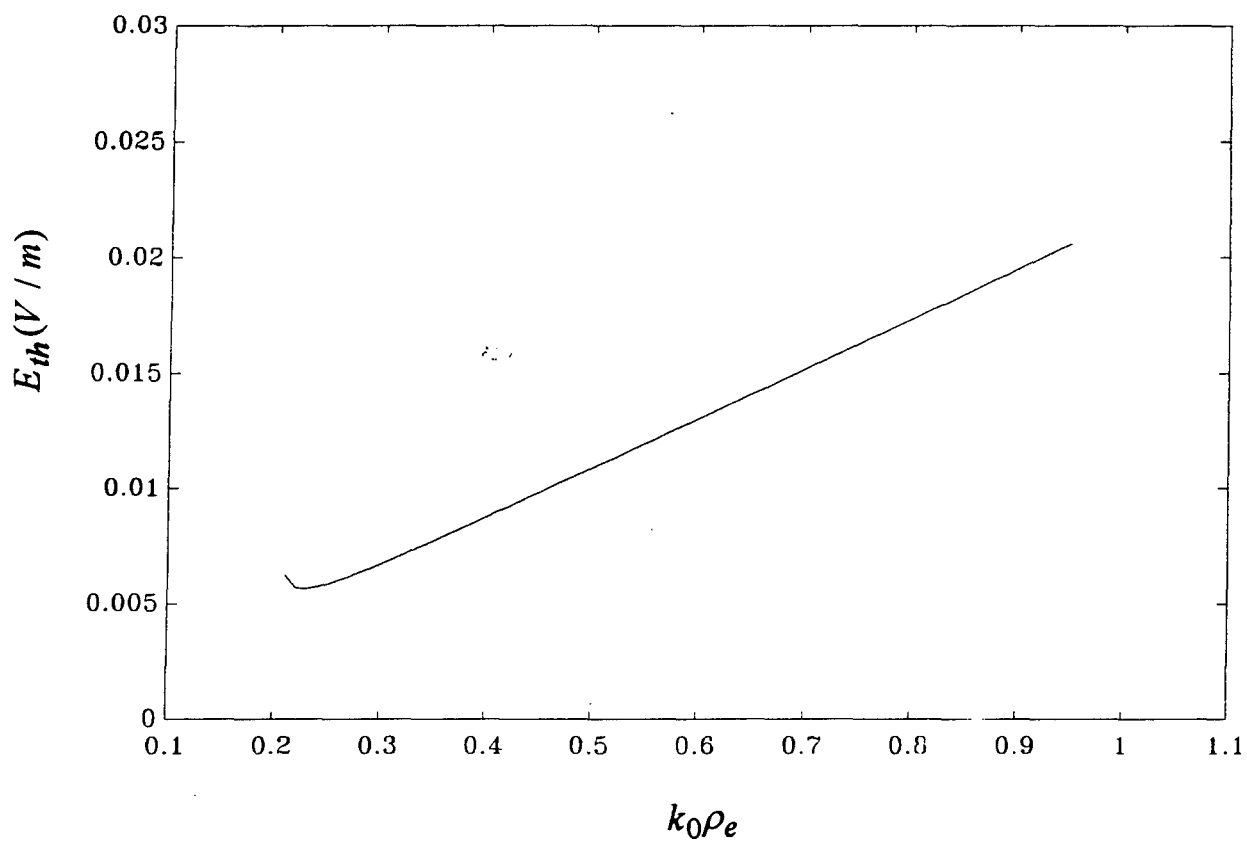


Fig. 2. Threshold field vs.  $k_0 \rho_e$  for the parametric decay of the electron Bernstein wave into a backscattered electron Bernstein wave and a lower hybrid decay mode below the double resonance layer (with  $l = 3$ ,  $\omega_s = 9$  KHz and  $\eta = 2.65$ ).

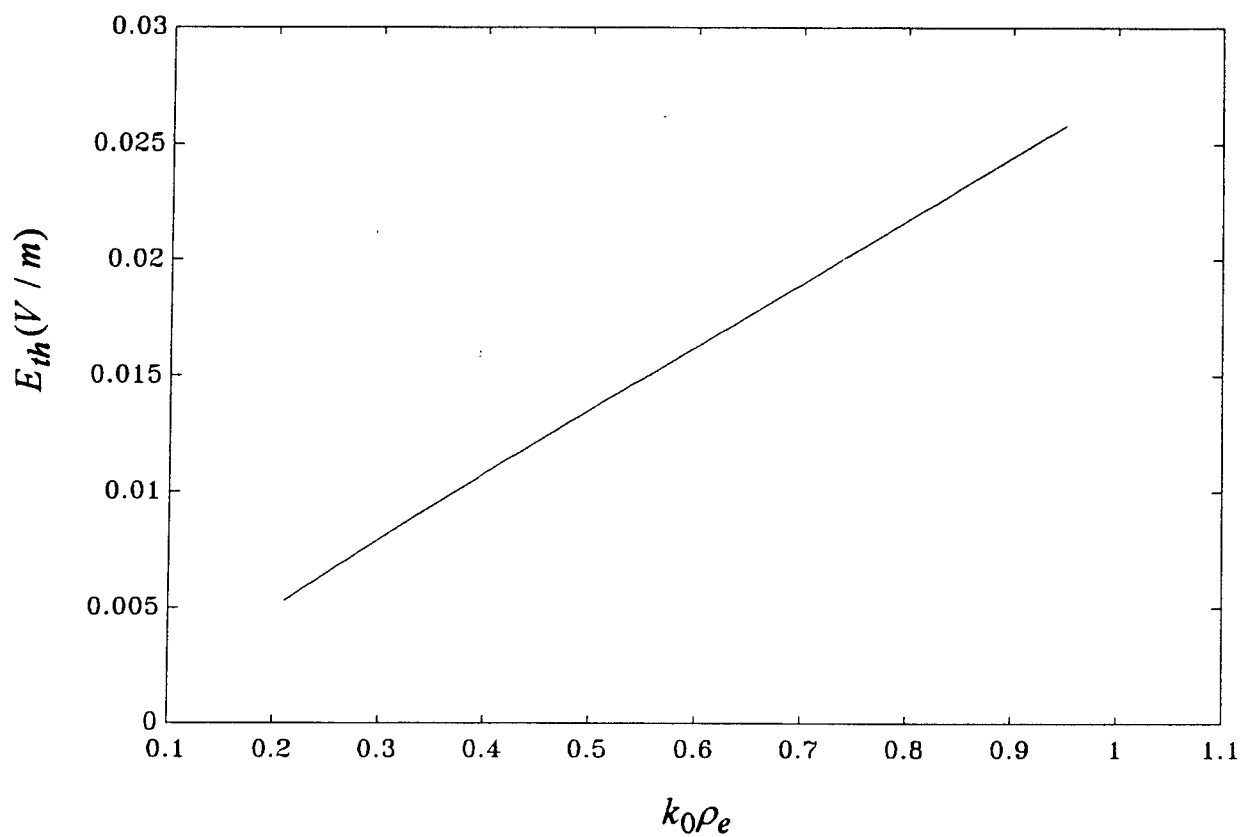


Fig. 3. Threshold field vs.  $k_0 \rho_e$  for the parametric decay of the electron Bernstein wave into a backscattered electron Bernstein wave and a lower hybrid decay mode above the double resonance layer (with  $l = 3$ ,  $\omega_s = 9$  KHz and  $\eta = 3$ ).

Moreover, the threshold field versus  $\eta$  ( $\eta = \omega_{pe} / \Omega_e$ ) for a given  $k_0 \rho_e$  is plotted in Fig 4. It is noted from (18) that  $|E_{th}|$  becomes very large as  $\eta^2 \rightarrow (l^2 - 1)$  (i.e. near the double resonance layer,  $\omega_{pe}^2 + \Omega_e^2 \rightarrow l^2 \Omega_e^2$ ). In this parameter regime, the upper hybrid wave and electron Bernstein wave are linearly coupled (and hence termed upper hybrid-electron Bernstein wave), a more careful treatment of the instability process is required. This is given in the following.

(3) Decay of an upper hybrid-electron Bernstein pump wave into a lower hybrid wave and an upper hybrid-electron Bernstein sideband wave

Considering a special case that  $\omega_{pe}^2 + \Omega_e^2 = l^2 \Omega_e^2$  (i.e. on the double resonance layer), then the linear dispersion relation of the upper hybrid-electron Bernstein pump is simplified to be

$$(\omega_0^2 - l^2 \Omega_e^2)^2 = l \omega_{pe}^4 K_{l-1}(\beta_0)$$

$$\text{or} \quad [\omega_0^2 - \omega_+^2(k_0)][\omega_0^2 - \omega_-^2(k_1)] = 0$$

where  $\omega_{\pm}^2(k_0) = l^2 \Omega_e^2 \pm \omega_{pe}^2 \sqrt{l K_{l-1}(\beta_0)}$  and the relation  $\omega_0^2 \equiv l^2 \Omega_e^2 = \omega_{UH}^2$  has been used.

The high frequency coupled mode equation (4) is reduced for the upper hybrid electron Bernstein sideband wave to

$$\{[\tilde{\omega}_1^2 - \omega_+^2(k_1)][\tilde{\omega}_1^2 - \omega_-^2(k_1)]\} \hat{\phi}_1$$

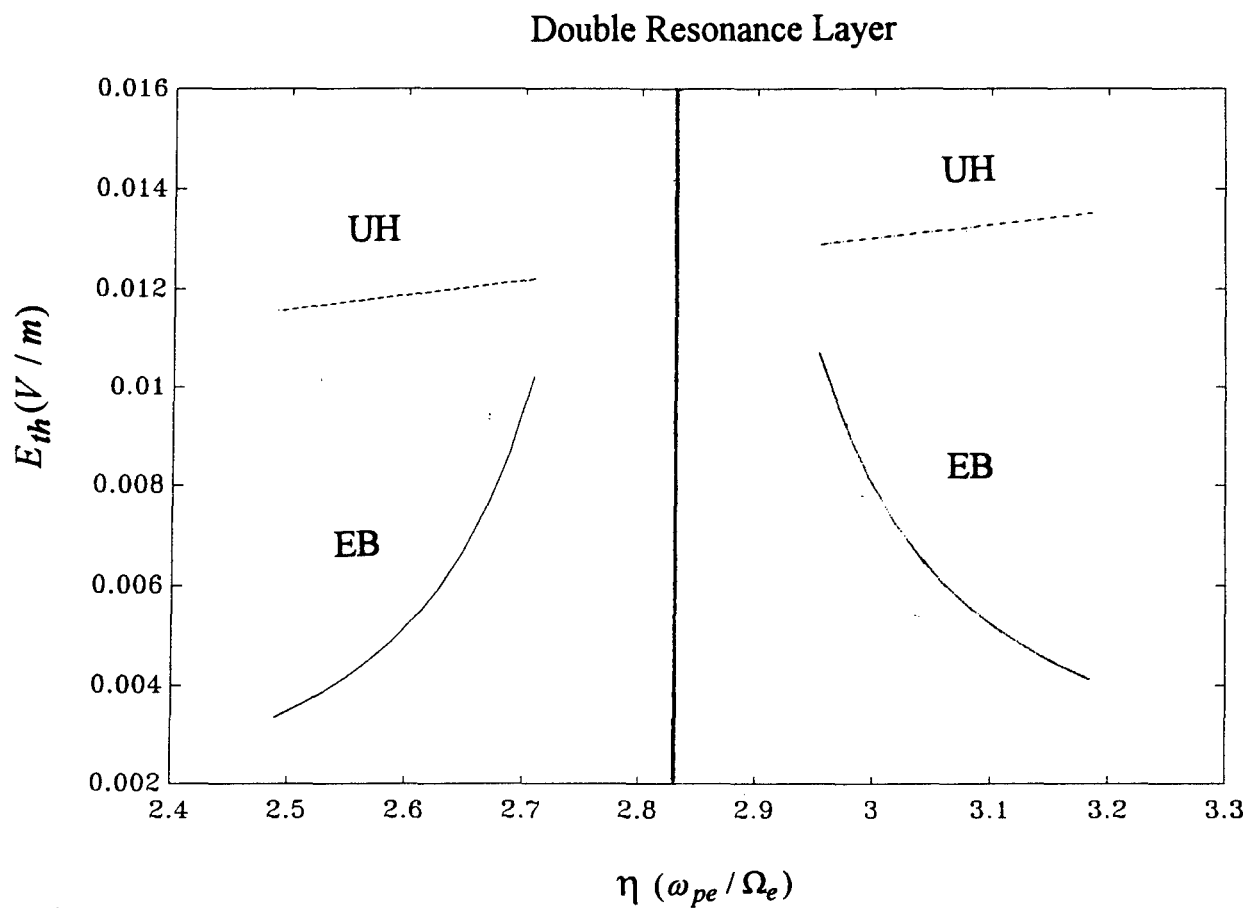


Fig. 4. Threshold field vs.  $\eta$  for both the backscattering parametric decay process for the upper hybrid pump and the electron Bernstein pump waves (with  $l = 3$ ,  $\omega_s = 9$  KHz and  $k_0 \rho_e = 0.3$ ). It is seen that the electron Bernstein decay process has a much lower threshold field away from the double resonance layer.

$$\begin{aligned}
&= \frac{k_0 k_s}{k_1} \left\{ \frac{-\omega_{pe}^2 (\bar{\omega}_1^2 - l^2 \Omega_e^2)}{(\omega_0^2 - \Omega_e^2)(\bar{\omega}_s^{*2} - \Omega_e^2)} [k_0 \bar{\omega}_1 \bar{\omega}_s^* + k_1 \bar{\omega}_s^* \omega_0 + k_s \bar{\omega}_1 \omega_0] \right. \\
&\quad \left. + \frac{k_s \omega_{pe}^2}{2 \Omega_e^2} (\bar{\omega}_1^2 - \Omega_e^2) \frac{l(\bar{\omega}_1 \omega_0 + l^2 \Omega_e^2)}{(\omega_0^2 - l^2 \Omega_e^2)} K_{l-1}(\beta_{01}) \right\} \frac{e}{m_e} \hat{\phi}_s^* \hat{\phi}_0
\end{aligned} \tag{19}$$

where  $\tilde{\omega}_1 = \omega_1 + i\Gamma_{ub}/2$ ,  $\Gamma_{ub} = (\Gamma_{uh} + \Gamma_{eb})/2$ , and the approximation

$$(\omega_1^2 + i\Gamma_{uh}\omega_1 - l^2\Omega_e^2)(\omega_1^2 + i\Gamma_{eb}\omega_1 - l^2\Omega_e^2) \cong (\omega_1^2 + i\Gamma_{ub}\omega_1 - l^2\Omega_e^2)^2$$

has been used.

Correspondingly, the coupled mode equation (7) for the lower hybrid decay wave becomes

$$\begin{aligned}
&\{\omega_s^2 + i\Gamma_{lh}\omega_s - \omega_{lk}^2\} \hat{\phi}_s \\
&= \frac{\omega_s^2}{\omega_{UH}^2} \frac{k_0 k_1}{k_s} \left\{ \frac{\omega_{pe}^2}{(\omega_0^2 - \Omega_e^2)(\bar{\omega}_1^{*2} - \Omega_e^2)} [k_0 \bar{\omega}_s \bar{\omega}_1^* + k_s \bar{\omega}_1^* \omega_0 + k_1 \bar{\omega}_s \omega_0] \right. \\
&\quad \left. + \frac{k_s l \omega_{pe}^2}{2 \omega_s} \left( \frac{\bar{\omega}_1^*}{\bar{\omega}_1^{*2} - l^2 \Omega_e^2} - \frac{\omega_0}{\omega_0^2 - l^2 \Omega_e^2} \right) K_{l-1}(\beta_{01}) \right\} \frac{e}{m_e} \hat{\phi}_1^* \hat{\phi}_0
\end{aligned} \tag{20}$$

Two different cases are examined in the following:

$$(i) \omega_0 = \omega_+(k_0), \omega_1 = \omega_+(k_1)$$

The coupled mode equations (19) and (20) become, respectively

$$[\omega_1^2 + i\Gamma_{ub}\omega_1 - \omega_+^2(k_1)] \hat{\phi}_1$$

$$\begin{aligned}
&\cong \frac{k_0 k_s}{k_1} \left\{ k_s l^2 \frac{\bar{\omega}_1^2 - l^2 \Omega_e^2}{\bar{\omega}_1^2 - \omega_-^2(k_1)} + k_s l^2 \frac{l \omega_{pe}^4 K_{l-1}(\beta_{01})}{[\bar{\omega}_1^2 - \omega_-^2(k_1)](\omega_0^2 - l^2 \Omega_e^2)} \right\} \frac{e}{m_e} \hat{\phi}_s^* \hat{\phi}_0 \\
&\cong \frac{k_0 k_s^2}{k_1} l^2 \frac{e}{m_e} \hat{\phi}_s^* \hat{\phi}_0 \cong \frac{k_0 k_s^2}{k_1} \left( 1 + \frac{\omega_{pe}^2}{\Omega_e^2} \right) \frac{e}{m_e} \hat{\phi}_s^* \hat{\phi}_0
\end{aligned} \tag{21}$$

and

$$\begin{aligned}
&\{\omega_s^2 + i\Gamma_2 \omega_s - \omega_{lk}^2\} \hat{\phi}_s \\
&= \frac{\omega_s^2}{\omega_{UH}^2} k_0 k_1 \left\{ \frac{\omega_{UH}^2}{\omega_{pe}^2} + \frac{1}{2\omega_{pe}^2} \frac{l \omega_{pe}^4 K_{l-1}(\beta_{01})}{(\bar{\omega}_1^{*2} - l^2 \Omega_e^2)(\omega_0^2 - l^2 \Omega_e^2)} (l^2 \Omega_e^2 - \bar{\omega}_1^* \omega_0) \right\} \left( \frac{e}{m_e} \right) \hat{\phi}_1^* \hat{\phi}_0 \\
&\cong \frac{\omega_s^2}{\omega_{pe}^2} k_0 k_1 \frac{e}{m_e} \hat{\phi}_1^* \hat{\phi}_0
\end{aligned} \tag{22}$$

where the linear dispersion relation  $\omega_{\pm}^2(k_{0,1}) = l^2 \Omega_e^2 \pm \omega_{pe}^2 \sqrt{l K_{l-1}(\beta_{0,1})}$  has been used.

It is interesting to note that the set of coupled mode equations obtained here is approximately equal to that obtained for the upper hybrid pump case. Therefore, the threshold field and growth rate are similar to (11) and (13) respectively for the upper hybrid pump case.

$$(ii) \omega_0 = \omega_-(k_0), \omega_1 = \omega_-(k_1)$$

Following the same procedure, it can be shown that the coupled mode equations in this case have the same forms as (21) and (22) of the first case. The only difference between these two cases is that  $|k_1| < k_0$  in the first case while  $|k_1| > k_0$  in the second case as can be seen from the linear dispersion relations  $\omega_{0,1} = \omega_{\pm}(k_{0,1})$  and the matching conditions  $\omega_s = \omega_0 - \omega_1^*$ .



#### IV. Discussion

The threshold fields of the parametric decay instability of the upper hybrid/electron Bernstein wave considered in the present work are given by (11) and (18) respectively. This simple relation is obtained by keeping only the leading order contributions of the Bessel functions in integrating the distribution functions over the velocity space. The threshold field of the instability depends on the electron harmonic number  $l$ , pump wavelength  $\lambda_0$  ( $\lambda_0 = 2\pi/k_0$ ), and the ionosphere conditions including electron density, temperature and collision frequency. The dependence of the threshold field on pump wavelength  $\lambda_0$  is found to be

$$E_{th} \sim \lambda_0^{2-l} \quad \text{for EB decay process}$$

or

$$E_{th} \sim \lambda_0 \quad \text{for UH decay process}$$

The electron Bernstein wave decay process has been considered before by Asthana<sup>16</sup>. In his treatment, however, lower hybrid decay mode was analyzed from a fluid approach and the ponderomotive force for the nonlinear coupling was derived in the unmagnetized plasma. Moreover, his approach did not include the contribution of the finite Larmor radius effect to the coupling coefficient of the low frequency decay mode, which is shown in Sec III.(2) to give the dominant coupling term in the present case. The coupled mode equation of the high frequency sideband used in his analysis also appears suitable only for the fundamental cyclotron resonance case (as can be seen from his equation (11) and the following two equations). The present work gives a more general treatment of the decay process and becomes applicable for the ionospheric heating experiments.

It is suggested that the scattering of the backscattered upper hybrid/electron Bernstein sideband wave off the short scale irregularities excited through the thermal oscillating two stream instability<sup>6</sup> be a potential mechanism for the generation of the DM lines. This nonlinear scattering process is elucidated as follows. Considering an upper hybrid/electron Bernstein wave with a potential function  $\phi_1 = \hat{\phi}_1 e^{i(k_1 x - \omega_1 t)}$  propagates in a density layer at  $z = z_0$ . When this wave is scattered by a density irregularity characterized by  $\delta n_e = \delta \tilde{n}_e e^{-ik_1 x}$ , a nonlinear beating current density is produced in this layer and given by  $\delta \vec{J} = -e \delta n_e \vec{v}_{e1} = [\hat{x} + i(\Omega_e / \omega_1) \hat{y}] [\omega_{pe}^2 / 4 \pi \omega_1 (1 - \Omega_e^2 / \omega_1^2)] (\delta \tilde{n}_e / n_0) k_1 \hat{\phi}_1 e^{-i\omega_1 t} \delta(z - z_0)$ . It contains both right-hand and left-hand circularly polarized components which become the source of x-mode (R-wave) and o-mode (L-wave) emissions respectively. Since only the o-mode emission can effectively propagate down to the ground (x-mode wave will be effectively reabsorbed by the plasma), its generation is analyzed. Let  $\vec{A} = (\hat{x} - i\hat{y}) A(z) e^{-i\omega_1 t}$  be the vector potential of the o-mode emission generated by the beating current, then its governing wave equation is derived from the Maxwell's equations as

$$\left( \frac{\partial^2}{\partial z^2} + \kappa^2 \right) A(z) = -[\omega_{pe}^2 / 2c(\omega_1 + \Omega_e)] (\delta \tilde{n}_e / n_0) k_1 \hat{\phi}_1 \delta(z - z_0) \quad (23)$$

where  $\kappa^2 = (\omega^2 / c^2) [1 - \omega_{pe}^2 / \omega(\omega + \Omega_e)]$ .

Equation (23) is solved to be

$$A(z) = i[\omega_{pe}^2 / 4\kappa c(\omega_1 + \Omega_e)] (\delta \tilde{n}_e / n_0) k_1 \hat{\phi}_1 [e^{i\kappa(z-z_0)} + e^{-i\kappa(z-z_0)}] \quad (24)$$

where the two terms in the bracket of the right hand side of (24) represent down-propagating and up-propagating components respectively. Hence, the wave fields of the down-propagating o-mode emission are obtained to be

$$\bar{E} = -\frac{1}{c} \frac{\partial}{\partial t} \bar{A} = -(\hat{x} - i\hat{y}) [\omega_1 \omega_{pe}^2 / 4 \kappa c (\omega_1 + \Omega_e)] (\tilde{n}_e / n_0) k_1 \hat{\phi}_1 e^{i\kappa(z-z_0)} e^{-i\omega_1 t}$$

$$\bar{B} = \nabla \times \bar{A} = -i(\hat{x} - i\hat{y}) [\omega_{pe}^2 / 4c (\omega_1 + \Omega_e)] (\tilde{n}_e / n_0) k_1 \hat{\phi}_1 e^{i\kappa(z-z_0)} e^{-i\omega_1 t}$$

Moreover, since the upper hybrid/electron Bernstein pump wave excited by the thermal oscillating two-stream instability (OTSI) process is a standing wave in nature, the backward propagating upper hybrid/electron Bernstein wave can scatter off the lower hybrid decay mode excited parametrically by the forward propagating upper hybrid/electron Bernstein wave to produce a frequency upshifted upper hybrid/electron Bernstein wave. The subsequent scattering of this frequency upshifted upper hybrid/electron Bernstein wave off the field-aligned density irregularity generated from the thermal OTSI process is proposed to be the generation mechanism for the UM lines. Thus the generation of the UM lines does not require  $f_0 \approx lf_c$ . It is consistent with the experimental observations.

As can be seen from Fig. 4, the threshold field of the electron Bernstein wave decay process is lower than that of the upper hybrid wave decay process except in the region near the double resonance layer. Thus the cascading features of the DM lines (i.e., 2DM 3DM...etc.) are suggested to be produced through the cascading of the electron Bernstein wave parametric decay process. Moreover, it has been shown in the experiments<sup>17</sup> that the cascading feature of the DM lines starts to develop when

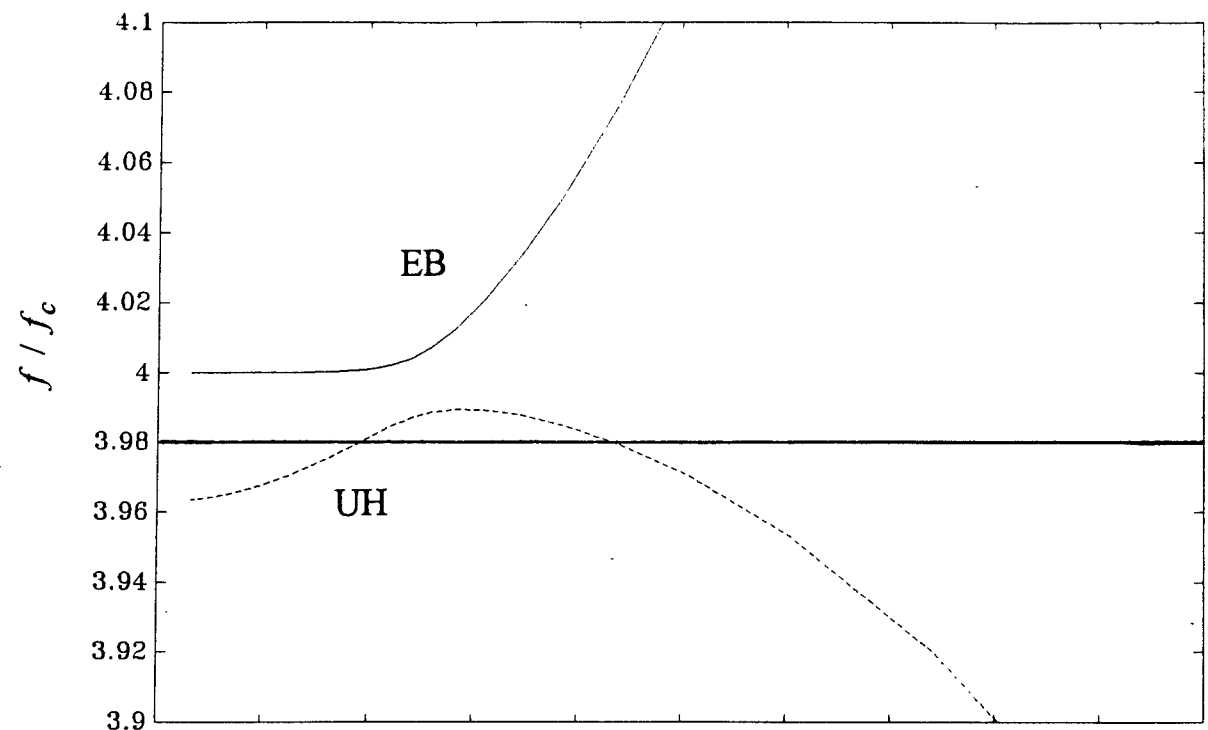
$f_0 \approx lf_c + 30$  KHz, and appears most strongly when  $f_0 \approx lf_c + 60$  KHz. Our theory also shows the same trend since the cascading process of the electron Bernstein wave can not proceed when  $f_0$  is below  $lf_c + 2f_{LH} \sim lf_c + 20$  KHz. It is worth noting that even though the numerical results in Figs. 1 - 4 are presented for the case of  $l = 3$ , their qualitative properties have been found to be similar for all  $l \geq 3$ .

In the frequency range  $lf_c < f_0 < lf_c + f_{LH} \sim lf_c + 10$  KHz, the proposed cascading process can not occur (except for the possibility of parametric decay of the electron Bernstein wave into an upper hybrid wave and a lower hybrid wave in the appropriate height region, which is outside the scope of the present work). Therefore, in this frequency range, only the parametric process proposed by Leyser<sup>7</sup> is operative. Correspondingly, the experimental results also show that the DM feature is weakened within this frequency range. On the other hand, one may argue that after the parametric decay of the upper hybrid/electron Bernstein wave, its sideband upper hybrid /electron Bernstein wave could also further decay into a lower hybrid wave and the o-mode emission (i.e. 2DM line) directly. This is unlikely because the threshold field ( $\sim 0.5$  V/m) required for this emission excitation process is much larger than that for the further cascading process considered in the present work.

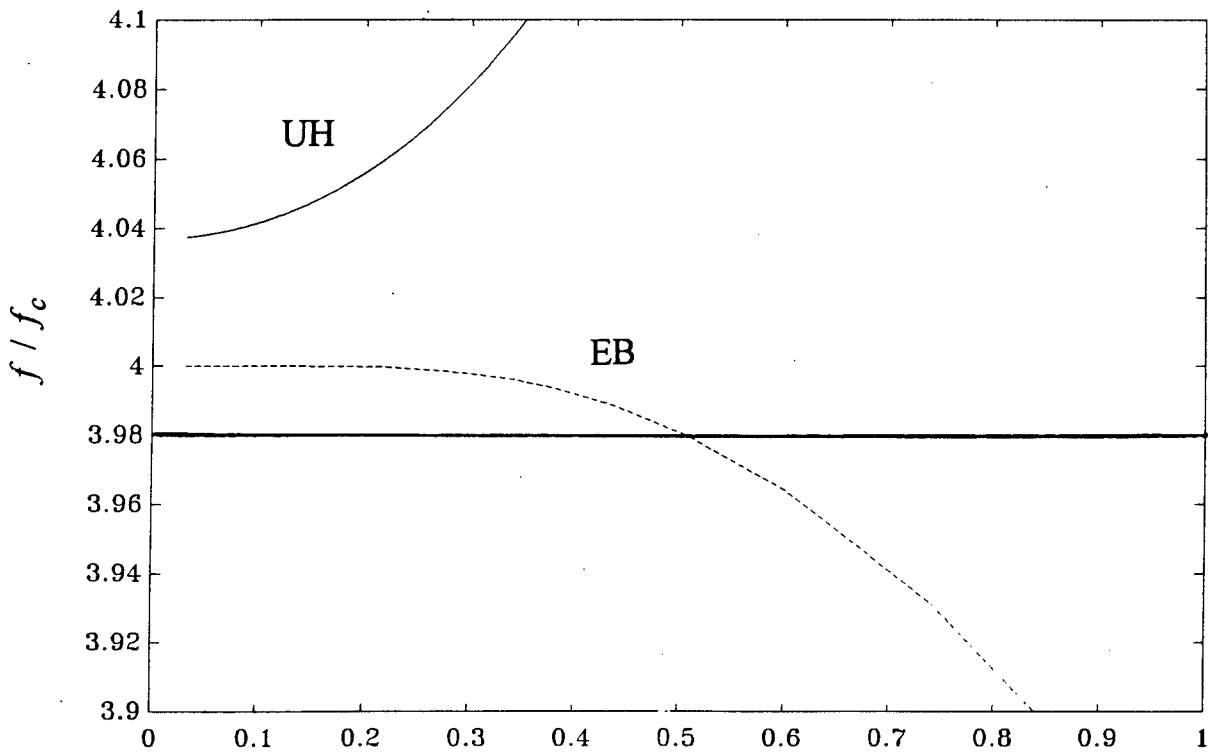
Most of the SEE spectra with DM cascading feature were observed when  $f_0$  was slightly larger than  $lf_c$ <sup>17</sup>, however, such a spectral feature was also observed when  $f_0$  was slightly below  $lf_c$  and when the continuum feature was weak (see Fig.4 of Ref. 2). In that case, the 2DM line was found to quench when  $4f_c < f_0 < 4f_c - 20$  Hz but the DM line persisted until  $f_0 \approx 4f_c$ . The explanation of this observation based on the present theory is given as follows. When the HF heater wave frequency  $f_0$  is slightly less than  $4f_c$ , both upper hybrid waves (below the double resonance layer) and electron Bernstein waves (above the double resonance layer) can be excited through the thermal OTSI process.

This fact can be demonstrated qualitatively from their dispersion relations plotted in Fig. 5 together with the general criterion of the OTSI instability region given by Huang and Kuo<sup>6</sup>. The upper hybrid wave can then undergo either the parametric decay process discussed in this paper or that proposed by Leyser to generate the DM emission. The electron Bernstein wave decay process (case (ii) of Sec. III part 2), on the other hand, proceeds to form a cascading spectrum which leads to the 2DM emission.

Moreover, anomalous absorption experiments<sup>18</sup> have demonstrated that the level of field-aligned density irregularity was reduced in two stages as  $f_0$  approaches  $4f_c$ . The associated frequency ranges of the reduction of anomalous absorption around cyclotron harmonics were correlated with the quenching frequency ranges of the DM and 2DM respectively<sup>19</sup>. This implies that the pump electrostatic wave strength was reduced accordingly. Since the occurrence of the cascading process requires the sideband of the first step parametric decay process to be fully developed, the 2DM line should quench before the DM line as the pump strength is reduced due to the cyclotron harmonic effect. This interpretation is consistent with the experimental observations. Lastly, it has been shown that the electron Bernstein wave is more strongly excited through the thermal OTSI processes below the upper hybrid resonance layer (when the heater wave frequency  $f_0 > lf_c$ ) than above the upper hybrid resonance layer (when  $f_0 < lf_c$ )<sup>6</sup>. This explains why the DM cascading lines are observed more often in the case of  $f_0 > lf_c$  than that of  $f_0 < lf_c$ .



(a)



(b)

Fig. 5. Dispersion relations of the electron Bernstein wave and upper hybrid wave in the regions (a) below the double resonance layer and (b) above the double resonance layer for their frequencies near the forth harmonic of the electron cyclotron frequency. The OTSI process is expected to be excited most favorably near the intersection points between the horizontal line denoting the HF heater wave frequency (slightly smaller than  $4f_c$ ) and the dashed dispersion curve.

## V. Conclusion

The process concerning the parametric decay of an upper hybrid/electron Bernstein pump wave into an upper hybrid/electron Bernstein sideband wave and a lower hybrid decay wave is studied. A new generation mechanism for the DM and UM lines has been proposed based on the coupling of the products of the considered parametric decay process with those of the thermal OTSI via nonlinear scattering processes. Moreover, it has been found that the decay process associated with the electron Bernstein wave has a much smaller threshold field than that of the upper hybrid wave. Thus the cascading of the electron Bernstein wave along with the appropriate nonlinear scattering process is suggested to be responsible for the observed 2DM and 3DM lines...etc in the SEE spectrum. The proposed theory has provided a physical interpretation of the experimental observations.

## Acknowledgments

Part of this work was performed at the Geophysics Directorate of the U. S. Air Force's Phillips Laboratory (PL/GP), Hanscome AFB, Massachusetts. The authors would like to thank PL for its hospitality. He also wishes to acknowledge the frequent and useful discussions with Dr. Paul Kossey, Dr. Keith Groves, and Mr. John He<sup>z</sup>kscher of the PL/GP, and <sup>P</sup>rofessor M. C. Lee of the Massachusetts Institute of Technology.

This work was supported by the AFOSR Research Initiation Program subcontract 93-59 from the Research and Development Laboratory, Culver City, CA.



## Appendix A Transformation of the Vlasov equation

In analyzing electron Bernstein waves, ions are too heavy to respond and only electron plasma is involved. Thus, the Vlasov equation of the electron plasma with an appropriate collision term is given by

$$\frac{\partial}{\partial t} f_e + \bar{v} \cdot \nabla f_e - \frac{e}{m_e} \left( \bar{E} + \frac{1}{c} \bar{v} \times \bar{B} + \frac{1}{c} \bar{v} \times \bar{B}_0 \right) \cdot \frac{\partial}{\partial \bar{v}} f_e = -\nu_e \left[ f_e - \left( \frac{n_e}{n_{e0}} \right) f_e^0 \right] \quad (A1)$$

where  $\nu_e = \nu_{ei}$  is the electron ion collision frequency,  $f_e^0$  is the equilibrium distribution and  $n_e$  and  $n_{e0}$  are the perturbed and unperturbed electron density which are defined to be

$$n_e = \int d\bar{v} (f_e - f_e^0) \quad \text{and} \quad n_{e0} = n_0 = \int d\bar{v} f_e^0.$$

On the other hand, when lower hybrid waves are considered, both electron and ion plasmas are involved in the interaction. Thus, the collisional term on the right hand side (RHS) of (A1) is not appropriate and should be replaced by  $-\nu_e [f_e - f_i - (n_e f_e^0 - n_i f_i^0) / n_0]$ . In this case, the collisional term of the ion Vlasov equation takes the form  $-\nu_{ie} [f_i - f_e - (n_i f_i^0 - n_e f_e^0) / n_0] - \nu_{in} [f_i - (n_i / n_0) f_i^0]$  where  $\nu_{ie} = (m_e / m_i) \nu_{ei}$  and  $\nu_{in}$  are the ion-electron and ion-neutral collision frequencies respectively;  $n_i = \int d\bar{v} f_i$ . These collision terms assure the momentum conservation, however, also complicate the analysis. On the other hand, it is noted that the ratio of ion to electron velocity response to the lower hybrid wave field is about  $|\delta \bar{v}_i / \delta \bar{v}_e| \approx (m_e \Omega_e / m_i \omega_s) \cong \sqrt{m_e / m_i}$ , which is much less than one. It suggests that  $f_i$  and  $f_i^0$  in the electron and ion collision terms reduces to the same form as that on the RHS of (A1). The ion collision term then becomes  $\nu_{ie} [f_e - n_e f_e^0 / n_0]$ . This term has been included in the ion Vlasov equation in the analysis, but the result turns out to have a negligible contribution. It is because  $\nu_{ie} \ll \nu_{ei}$ . This

conclusion also agrees with that drawn from the fluid approach. Therefore, in dealing with the lower hybrid wave, (A1) together with a collisionless ion Vlasov equation are employed in the analysis.

We proceed to transform the Vlasov equation (1) from the original variables  $(\bar{x}, \bar{v}, t)$  to the new variables  $(\bar{x}_g, \bar{v}, t)$  of the guiding center coordinates by the guiding center transformation

$$\bar{x}_g = \bar{x} - \frac{1}{\Omega_e} \bar{v} \times \hat{z} \quad (\text{A2})$$

The associated differential operators in the transformed frame can then be found from the chain rule to be (o denotes original frame and g denotes guiding center frame)

$$\left. \frac{\partial}{\partial \bar{x}} \right|_o \rightarrow \left. \frac{\partial}{\partial \bar{x}} \right|_g, \quad \nabla_o \rightarrow \nabla_g \quad \text{and} \quad \nabla_{\bar{v}}|_o \rightarrow \nabla_{\bar{v}}|_g - \frac{1}{\Omega_e} \hat{z} \times \nabla_g \quad (\text{A3})$$

where  $\nabla_g$  is the spatial gradient operator in the guiding center coordinates and  $\Omega_e = eB_0/m_e c$  is the electron cyclotron frequency. Using these transformation relations, and the following expressions in the cylindrical coordinate system (with  $\varphi$  the gyrophase angle)

$$\bar{v} = v_{\perp} (\hat{x} \cos \varphi + \hat{y} \sin \varphi) + v_{\parallel} \hat{z}$$

$$\nabla_{\bar{v}} = \frac{\bar{v}_{\perp}}{v_{\perp}} \frac{\partial}{\partial v_{\perp}} + \hat{z} \frac{\partial}{\partial v_{\parallel}} + \frac{\hat{z} \times \bar{v}}{v_{\perp}^2} \frac{\partial}{\partial \varphi}$$

the Vlasov equation (1) in the guiding center frame becomes

$$\frac{\partial f_e}{\partial t} + v_{\parallel} \hat{z} \cdot \nabla_g f_e + \Omega_e \frac{\partial f_e}{\partial \varphi} = \frac{e}{m_e} \left( \bar{E} + \frac{1}{c} \bar{v} \times \bar{B} \right) \cdot \left\{ \nabla_{\bar{v}} f_e - \frac{1}{\Omega_e} \hat{z} \times \nabla_g f_e \right\} - \nu_e \left\{ f_e - \left( \frac{n_e}{n_{e0}} \right) f_e^0 \right\} \quad (\text{A4})$$

## Appendix B Formal expansion of Eq (A4)

We adopt a formal parameter  $\delta$  ( $= 1$ ) to find a general procedure of nonlinear problem. According to Eq. (A4), we write

$$\begin{aligned}
 f_e &= f_e^0 + \delta^1 f_e^{(1)} + \delta^2 f_e^{(2)} + \delta^3 f_e^{(3)} + \dots \\
 \bar{E} &= \delta^1 \bar{E}^{(1)} + \delta^2 \bar{E}^{(2)} + \delta^3 \bar{E}^{(3)} + \dots \\
 \bar{B} &= \delta^1 \bar{B}^{(1)} + \delta^2 \bar{B}^{(2)} + \delta^3 \bar{B}^{(3)} + \dots \\
 n_e &= n_{e0} + \delta^1 n_e^{(1)} + \delta^2 n_e^{(2)} + \delta^3 n_e^{(3)} + \dots
 \end{aligned} \tag{B1}$$

Substituting (B1) into (A4), and collecting  $\delta^1$  order terms, we have

$$\begin{aligned}
 \frac{\partial f_e^{(1)}}{\partial \alpha} + v_{||} \hat{z} \cdot \nabla_g f_e^{(1)} + \Omega_e \frac{\partial f_e^{(1)}}{\partial \varphi} \\
 = \frac{e}{m_e} \left( \bar{E} + \frac{1}{c} \bar{v} \times \bar{B} \right) \cdot \left\{ \nabla_{\bar{v}} - \frac{1}{\Omega_e} \hat{z} \times \nabla_g \right\} f_e^0 - v_e \left\{ f_e^{(1)} - \left( \frac{n_e}{n_{e0}} \right) f_e^0 \right\}
 \end{aligned} \tag{B2}$$

Similarly,  $\delta^2$  order equation is obtained to be

$$\begin{aligned}
 \frac{\partial f_e^{(2)}}{\partial \alpha} + v_{||} \hat{z} \cdot \nabla_g f_e^{(1)} + \Omega_e \frac{\partial f_e^{(2)}}{\partial \varphi} \\
 = \frac{e}{m_e} \left( \bar{E}^{(2)} + \frac{1}{c} \bar{v} \times \bar{B}^{(2)} \right) \cdot \left\{ \nabla_{\bar{v}} - \frac{1}{\Omega_e} \hat{z} \times \nabla_g \right\} f_e^0 \\
 + \frac{e}{m_e} \left( \bar{E}^{(1)} + \frac{1}{c} \bar{v} \times \bar{B}^{(1)} \right) \cdot \left\{ \nabla_{\bar{v}} - \frac{1}{\Omega_e} \hat{z} \times \nabla_g \right\} f_e^{(1)} \\
 - v_e \left\{ f_e^{(1)} - \left( \frac{n_e}{n_{e0}} \right) f_e^0 \right\}
 \end{aligned} \tag{B3}$$

(B2) and (B3) can be solved by first expanding the perturbed physical quantities in terms of the guiding center coordinate  $\bar{x}_g$  as

$$\begin{aligned}
 f_e &= \exp[-i(\omega t - \bar{k} \cdot \bar{x}_g)] \sum_l \hat{f}_e e^{il(\varphi - \delta)} \\
 \bar{E} &= \hat{\bar{E}} \exp[-i(\omega t - \bar{k} \cdot \bar{x}_g)] \sum_l J_l(\alpha) e^{il(\varphi - \delta)} = -i\bar{k}\phi \\
 n_e &= \hat{n}_e \exp[-i(\omega t - \bar{k} \cdot \bar{x}_g)] \sum_l J_l(\alpha) e^{il(\varphi - \delta)} \tag{B4}
 \end{aligned}$$

where  $\alpha = k_{\perp} v_{\perp} / \Omega_e$ ,  $\delta$  is the angle between  $\bar{k}_{\perp}$  and the x axis, and  $J_l(\alpha)$  is the Bessel function of the order  $l$ .

## References

1. P. Stubbe, H. Kopka, B. Thide' and H Derblom, J. Geophys. Res. **89**, 7523 (1984).
2. T. B. Leyser, B. Thide, H. Derblom, A. Hedberg, B. Lundborg, P. Stubbe, and H. Kopka, J. Geophys. Res., **95**, 17233 (1990).
3. B. Thide, Ake Hedberg, J. A. Fejer, and M. P. Sulzer, Geophys. Res. Lett., **16**, 369 (1989).
4. P. A. Bernhardt, L. S. Wagner, J. A. Goldstein, V. Yu. Trakhtengerts, E. N. Ermakova, V. O. Rapoport, G. P. Komrakov, A. M. Babichenko, submitted to Phys. Rev. Lett., 1993.
5. T. B. Leyser, B. Thide, S. Goodman, M. Waldenvik, and E. Veszelei, S. M. Grach, A. N. Karashtin, G. P. Komrakov, and D. S. Kotik, Phys. Rev. Lett., **68**, 3299 (1992).
6. J. Huang and S. P. Kuo, J. Geophys. Res., **99**, 2173 (1994).
7. T. B. Leyser, Geophys. Res. Lett., **18**, 408 (1991).
8. T. B. Leyser, Ph. D dissertation (Figure 3-12).
9. S. M. Grach and M. M. Shvarts, Proc. III Suzdal URSI Symposium (ISIM - 3), 89 - 90, 1991.
10. S. P. Kuo and M. C. Lee, Phys. Lett., **91A**, 444 (1982).
11. M. C. Lee and S. P. Kuo, **30**, 463 (1983).
12. J. A. Tataronis and J. Teichmann, J. Plasma Phys., **6**, 325 (1971).
13. K. Akimoto, Phys. Fluids B, **1** (1989).
14. J. F. Drake, P. K. Kaw, Y. C. Lee, G. Schmidt, C. S. Liu and Marshall N. Rosenbluth, Phys. Fluids, **17**, 4 (1974).
15. D. G. Swanson, *Plasma Waves*, Academic Press (1989).
16. M. Asthana, Phys. Fluids B, **3**, 2510 (1991).

17. T. B. Leyser, B. Thide, M. Waldenvik, S. Goodman, V. L. Frolov, S. M. Grach, A. N. Karashtin, G. P. Komrakov, and D. S. Kotik, *J. Geophys. Res.*, **98**, 17,597 (1993).
18. A. J. Stocker, F. Honary, T. R. Robinson, and T. B. Jones, *J. Geophys. Res.*, **98**, 13,627 (1993).
19. P. Stubbe, A. Stocker and F. Honary, Santa Fe work shop on the nonlinear RF excitation of the ionosphere, Jan. 11-14, 1993.

PARTICLE SIMULATIONS OF PLASMAS

R. D. Murphy  
Professor  
University of Missouri - Kansas City  
Kansas City, Missouri 64110

Final Report for:  
Summer Research Extension Program  
Phillips Laboratory

Sponsored by:  
Air Force Office of Scientific Research  
Bolling Air Force Base, Washington, D.C.

and  
University of Missouri - Kansas City

December 1993

## PARTICLE SIMULATIONS OF PLASMAS

R. D. Murphy  
Professor  
Department of Physics  
University of Missouri - Kansas City

### Abstract

Computational problems of interest to the Phillips Laboratory were studied. A Direct Simulation Monte Carlo method was applied to the aerodynamics of the injection of neutral argon through a nozzle and a Monte Carlo method was used to study the structure of molten aluminum. Preliminary work on the production of a hybrid code incorporating Direct Simulation Monte Carlo and molecular dynamics methods was undertaken.



## PARTICLE SIMULATIONS OF PLASMAS

R. D. Murphy

### INTRODUCTION

The High Energy Plasma Physics Division of the Phillips Laboratory is a leading center in the investigation of the physics of dense, hot plasmas, an area of considerable importance to the Air Force. A major reason for this preeminent position is the Laboratory's SHIVA Star 9.5 Megajoule fast capacitor bank, which has made possible a number of experimental studies of plasma phenomena. Of particular importance for present purposes are two current investigations: Magnetically Accelerated Rings for the Achievement of Ultra-high Density, Energy and Radiation (MARAUDER) and a project to achieve ultrahigh compression using electromagnetically imploded aluminum liners.

Another important reason for the Laboratory's preeminence in plasma physics investigations is the existence of a Computational Plasma Physics group and the accessibility to this group of state-of-the-art computer facilities at the Air Force Supercomputer Center as well as access to massively parallel machines. The collaboration and close interaction between theory and experiment has greatly benefitted both.

This report is a summary of work begun during the summer of 1992 and previously reported<sup>1</sup> and of the continuation of these efforts under the Summer Research Extension Program (SREP) during 1993. These efforts were continued part-time at UMKC during the academic years 1992-93 and 1993-94 and full-time during the summer of 1993.

### DISCUSSION AND METHODOLOGY

Plasma physics is characterized by a considerable variety of phenomena which operate at very different densities and on very different time scales<sup>2</sup> which range from sub-picosecond to greater than microsecond times. This diversity has necessitated a wide variety of computational

approaches, which can be roughly divided into "continuum" approaches, e.g. magnetohydrodynamics (MHD), and "particle" approaches, e.g. particle-in-cell (PIC), molecular dynamics (MD) and Monte Carlo methods.<sup>3</sup> As previously reported,<sup>1</sup> the PI studied the feasibility of applying particle approaches to problems of interest to the Phillips Laboratory. This choice was made for two reasons: first, state-of-the-art MHD codes were already in use at the Laboratory and second, the PI has considerable experience with particle-based codes. The calculations done and those to be proposed shortly are intended to complement the existing efforts at the Phillips Laboratory.

A number of interesting problems were identified. They are of considerable complexity in that each is cross-disciplinary and will require study of, in addition to plasma phenomena, such areas as intermolecular potentials and atomic, molecular, solid-state and liquid-state physics. The areas are as follows:

- 1) Wall effects. The MARAUDER experiments produce an argon plasma toroid which accelerates past the metal containing walls. Spectroscopic evidence<sup>4</sup> indicates that the argon plasma contains silicon, carbon and hydrogen contaminants. This suggested two interesting lines of investigation: a) the interaction of the plasma with the contaminants (a plasma and molecular physics problem) and b) the physics of the absorption, desorption, etc. of the contaminants under bombardment by the plasma (a solid-state and surface-science problem).

- 2) Properties of liquid and solid aluminum: the interaction of the imploding aluminum liners with a) plasma and b) metal walls.

At least part of each of the above areas requires development of new computational approaches; in addition, it must be stressed that implementation of particle approaches will be extremely computationally-intensive and will require substantial computer resources. In essence, a hybrid code, which combines PIC or MD methods with methods like the Direct

Simulation Monte Carlo Method (DSMC)<sup>5</sup>, is needed. The DSMC is a probabilistic procedure for solving the Boltzmann equation which was originally developed for the study of rarefied neutral gas flows; in most such applications, the collisions were treated as hard spheres. But the method has been generalized<sup>6,7</sup> to include other kinds of events, e.g. ionization, molecular excitation, charge attachment, charge exchange, etc. Birdsall<sup>7</sup> has emphasized that this generalization and the merger of these codes into a viable plasma code is a developing art which relies heavily on experimental cross-section data. A major accomplishment of the PI's work during the summer of 1992 was the development and testing of a DSMC code which can be used on a "stand-alone" basis to study rarefied gas dynamics and which can also be integrated with MD or PIC codes to produce a hybrid code.

#### RESEARCH ACCOMPLISHMENTS

While substantial progress was made during the contract period, the work was slowed somewhat by the heavy demands on UMKC's computing facilities and by the lack of an adequate, convenient graphics capability. This problem, however, will be solved shortly: the PI is the recipient of an equipment grant from the DEPSCOR (Defense Program to Stimulate Competitive Research) program. Funds from this grant are committed to purchase of a Digital Equipment Corporation Alpha workstation, ancillary hardware, and powerful graphics software. This machine, while will be installed in February, 1994, will be entirely dedicated to DoD research, with the immediate priority being completion of the production runs required (see below) to produce publishable results.

The PI studied three problems during the course of the SREP grant, as follows:

1) Aerodynamics of the injection through nozzles of neutral argon. This is a straightforward application of the DSMC code, and the results which have been obtained are quite interesting in that they show such phenomena as shock waves and vorticity. But the DSMC is a Monte Carlo, i.e. a statistical procedure, and considerably better statistics and graphical analysis are needed in order to permit more definitive conclusions to be drawn. The DEC Alpha workstation will be used for this purpose.

2) Characteristics of aluminum in molten and nonequilibrium phases by Monte Carlo methods. This effort built on previous work by the author on molten sodium<sup>8,9</sup> and potassium<sup>9,10</sup> and, as before, relied on tested interionic potentials. Results obtained for the structure by using the potentials of Dagens et al.<sup>11</sup> are quite accurate, and it appears that it will be possible to calculate resistivity by the Ziman formula, as was done previously.<sup>10</sup> Other pseudopotentials, e.g. that of Bretonnet and Regnault<sup>12</sup>, will also be considered.

3) Efforts began on a hybrid code, as discussed above, which will integrate DSMC (for a probabilistic treatment of collisions, etc.) and MD methods (for exact treatment of the particle dynamics). This problem is at the frontiers of computational plasma physics and is obviously a long-range project which will require development of new computational approaches. Development of such codes is the subject of a proposal to be submitted by the PI to DEPCOR in January, 1994. It will involve entirely new codes, which will include: integration of the equations of motion by symplectic (Hamiltonian) methods; use of multiple time steps in order to permit study of the plasma over times long enough to be of experimental interest; and ultimately (as even the power of the DEC Alpha workstation becomes inadequate) movement to massively parallel machines.

#### PUBLICATIONS

One publication<sup>13</sup> has already resulted from the SREP grant. It is expected that two others will be ready for submission shortly after the arrival of the DEC Alpha workstation: one on the structure and resistivity of liquid aluminum and the other on the aerodynamics of argon flow through a nozzle.

## REFERENCES

1. "Particle Simulations of Plasmas," by R. D. Murphy: Final Report to AFOSR for Summer 1992.
2. See, for example, T. Tajima, Computational Plasma Physics, Addison-Wesley, New York (1989).
3. See, for example, Liquid State Chemical Physics, by R. O. Watts and I. J. McGee, Wiley, New York (1976).
4. T. Englert, D. W. Price and G. F. Kiuttu, "Temporal and Spatial Distribution of Contaminant Plasma in Compact Toroid Formation at the Phillips Laboratory," paper presented at ICOPS 92.
5. G. A. Bird, Molecular Gas Dynamics, Clarendon Press, Oxford (1976).
6. C. Borgnakke and P. S. Larsen, J. Computational Phys. 18, 405 (1976).
7. C. K. Birdsall, IEEE Trans. on Plasma Sci. 19, 65 (1991).
8. R. D. Murphy and M. L. Klein, Phys. Rev. A 8, 2640 (1973).
9. W. Lotko and R. D. Murphy, Fluid Phase Eq. 1, 277 (1978).
10. R. D. Murphy, Phys. Rev. A 15, 1188 (1977).
11. L. Dagens, M. Rasolt and R. Taylor, Phys. Rev B 11, 2725 (1975).
12. J. Bretonnet and C. Regnault, Phys. Rev. B 31, 5071 (1985).
13. R. D. Murphy, Physics of Fluids B (Plasma Physics), 5, 2337 (1993).

# **UNIVERSAL SLOPE OF THE SHOCK VELOCITY EQUATION FOR HOMOGENEOUS MATERIALS**

by

**Jon H. Shively**  
**Civil and Industrial Engineering and Applied Mechanics Department**

**School of Engineering and Computer Science**  
**California State University at Northridge**  
**18111 Nordhoff Street**  
**Northridge California 91330-8295**

**Final Report for:**  
**Summer Research Extension Program**  
**Phillips Laboratory**  
**Kirtland Air Force Base**

**Sponsored by:**  
**Air Force Office of Scientific Research**  
**Bolling Air Force Base, Washington, D.C.**  
**and**  
**California State University at Northridge**

**December 30, 1992**

# UNIVERSAL SLOPE OF THE SHOCK VELOCITY EQUATION FOR HOMOGENEOUS MATERIALS

by

Jon H. Shively  
Civil and Industrial Engineering and Applied Mechanics Department  
California State University Northridge

## Abstract

It has long been known that the shock velocity in most materials can be written as a power series in particle velocity,  $U_p$ , with only the linear form being needed for most materials, in the range of shock pressures thus far studied, namely,  $U_s = C + sU_p$  where  $U_s$  is the shock velocity and  $C$  is the ambient bulk sound velocity. When the shock velocity equation is combined with the "jump" equations, the available, open-literature shock-data can be compared through a "master" equation which contains reduced variables for pressure and particle velocity, namely,  $P/\rho_0 C^2 = (U_p/C)(1 + sU_p/C)$  where  $\rho_0$  is initial density. This master equation has been applied to a large number of condensed homogeneous materials including both solids and liquids and metals, polymers, and ceramics. Comparisons of the slopes derived from the master equation have revealed that a single value of  $s$  seems to universally fit all homogeneous materials.

A simple explanation is provided for the universal slope observation in terms of the molecular potentials, written in terms of scaled variables. Expressing the potential as a power series, we have been able to show a relationship between the shape of the potential function equation in the compressive region to the slope of the shock velocity equation. Values of  $C$  and  $s$  derived from commonly-used analytic forms of the potentials, are given along with comments on the expected range of validity and accuracy of these results. Future developments are suggested.



## 1.0 INTRODUCTION

### 1.1 Hypervelocity Collisions of Space Debris and Shock

Hypervelocity collisions of space debris and micro meteorites with spacecraft materials produce shock waves in these materials. The resultant shock phenomena have been the subject of numerous investigations and theoretical studies. Most notable has been the extensive studies of shock by Los Alamos National Laboratory which has been a leader in this field for more than 40 years.( 1, 2 ) Hypervelocity shock data have been compiled by Los Alamos ( 3 ), by the Air Force Weapons Laboratory (now the Phillips Laboratory)( 4 ), and by Sandia National Laboratory ( 5 ).

Attempts have been made by individual researchers to relate the observations from shock experiments to theory ( 6-11 ). Several attempts have been made to establish a universal equation of state describing the thermodynamics of shock ( 6-11 ). The equations developed, to date, contain at least two empirical material parameters, the Gruneisen constant and the slope of the shock velocity versus particle velocity curve. Thus the equation of state is not universal for all materials but contains constants for each material.

The quest for a universal equation for shock, while elusive, has value in predicting shock behavior. The open literature data on shock of condensed materials are limited in applicability to the space debris problem because the upper bound on the data lie in the range of 3 to 5 km/s. The space debris particles are expected to travel at velocities up to 10 -15 km/s. In addition, much of the data is limited to materials not in use in space vehicles. Therefore, data are missing on the shock behavior of many important space craft materials. However, if a universal equation for all materials could be established, then the shock behavior in low-end of the hypervelocity regime (1 to 5 km/s) could be used to predict shock behavior for other materials for which the data are absent or scarce. Moreover the need for extrapolation of existing data into the high-end of the hypervelocity regime ( 5 to 15 km/s) could be validated with the results of just a few critical experiments rather than a whole series of expensive experiments at extreme hypervelocities. Therefore, a theoretical study was undertaken this year with the hope that a single universal equation of state for shock in the regime of 1 to 15 km/s could be established and that this equation would describe the phenomena of shock wave propagation in homogeneous solids.

One of the key relationships describing shock impact is the relationship between the shock velocity and the particle velocity. Most researchers have reported that this relationship is linear with empirical constants corresponding to the intercept and the slope. The intercept appears to correspond very closely with the bulk sound velocity (9). However, the slope is still viewed as empirical. This purpose of this grant is to establish a universal slope of the shock velocity equation through data analysis and theoretical derivations and analysis.

## 1.2 Review of Shock Physics

A collision of a hypervelocity projectile with a target produces shock waves in the target material. The relationship between the pressure induced by the shock, the volume, and the energy is called the Hugoniot ( 1, 2 ). The most common expression for the Hugoniot is the so-called Mie-Gruneisen compression equation of state:

$$P - P_H(V_H) = [(\Gamma(V)/V)][(E - E_H(V_H))] \quad (1)$$

where  $P_H$ ,  $V_H$ , and  $E_H$  are pressure, volume, and energy, respectively, along the Hugoniot and  $\Gamma(V)$  is the Gruneisen constant for the material (13 ).

Assuming that the shock wave propagates as a plane wave, the Hugoniot can be expressed in measurable terms of mass, momentum, and energy as in the following conservation equations:

$$\rho U_S = \rho_0(U_S - U_p) \quad \text{Conservation of Mass} \quad (2)$$

$$P - P_0 = \rho_0 U_S U_p \quad \text{Conservation of Momentum} \quad (3)$$

$$P U_p = \frac{1}{2} \rho_0 U_S U_p^2 + \rho_0 U_S (E - E_0) \quad \text{Conservation of Energy} \quad (4)$$

where

$\rho$  = density  
 $U_S$  = shock velocity  
 $U_p$  = particle velocity  
 $P$  = pressure  
 $E$  = energy

and subscript, o, refers to the initial state (undisturbed).

Substituting Equations 1, 2, and 3 into Equation 4 yields

$$E_H - E_0 = \frac{1}{2} (P_H - P_0)(V_0 - V_H) \quad (5)$$

The experimental determination of the Hugoniot requires measuring any two of the following three quantities:  $U_s$ ,  $U_p$ , or  $P$  (see Equations. 2 and 3).

There are several other important relationships which define various aspects of the shock phenomena. For example, most materials exhibit a linear relationship between the shock velocity and the particle velocity, although the reason for this behavior is not understood;

$$U_s = C + sU_p \quad (6)$$

where  $C \approx$  bulk sound velocity = shock velocity at zero pressure. The bulk sound velocity can be determined from a  $U_s - U_p$  plot where  $C$  is the intercept. The bulk sound velocities in solids are calculated using Equation 7 below and are given in References 3 and 4 for numerous materials.

$$C^2 = C_L^2 - (4/3) C_S^2 \quad (7)$$

where

$C$  = bulk sound velocity

$C_L$  = longitudinal speed of sound

$C_S$  = shear speed of sound

The shear velocity in liquids is zero, or  $C = C_L$ . However, for solids the shear velocity is significant and Equation 7 applies. Extrapolations to  $U_s$  for  $U_p = 0$  correspond closely to the bulk sound velocity. If the shock velocity is linearly related to the particle velocity, then the following equation is obtained which is convenient for representing shock data:

$$P/(\rho_0 C^2) = (U_p/C)(1 + sU_p/C) \quad (8)$$

In the past, many workers in shock testing have associated the slope,  $s$ , with the Gruneisen constant,  $\Gamma$ , which is used in Equation 1. The works of Slater (13) and Dugdale and MacDonald (14) lead to equations for  $\Gamma$  in terms of the slope,  $s$ . The prediction in Reference 13 is  $s = (\Gamma/2) + 1/2$  and the prediction in Reference 14 is  $s = (\Gamma/2) + 1/3$ . The validity of these relations between the slope and the Gruneisen constant are yet to be established.

## 2.0 REVIEW OF SHOCK DATA CORRELATIONS

### 2.1 Literature Review of Data Correlations

Jeanloz (9) recently reviewed some selected equations of state currently published for shock in materials. The equations developed by Rose, et.al,(15,16), Grover, et al, (17), and Jeanloz et.al (9), seem to fit the data on shock better than others developed by Slater(13) and Birch.(7) The equations developed by Prieto et.al., (6), while not included in Jeanloz comparisons, have been shown by Prieto (19) to be equivalent to both the Rose and the Jeanloz equations of state. All of the above attempts to develop equations of state are semiempirical and depend upon measured isothermal bulk quantities. They are intended to apply to both isothermal and adiabatic thermodynamic processes such as shock.

Prieto et.al., developed their equations based upon The Principle of Corresponding States which broadly states that fluids behave alike when in corresponding states; i.e., when  $n$  thermodynamic variables bear a constant ratio to  $n$  critical values of those same thermodynamic variables. Consider as an example, the Van der Waal's equation of state for a gas. The  $p, v, T$  relation for a given gas can be represented in terms of reduced variables  $p_r, v_r$ , and  $T_r$ , which are ratios of  $p, v$ , and  $T$  to  $p_c, v_c$ , and  $T_c$ , respectively, and where the subscript  $c$  refers to a critical value of the variable for a particular gas. However, any gas can be represented by the reduced form of the Van der Waal's equation of state as long as  $p_c, v_c$ , and  $T_c$  are known for that gas.

The Van der Waal's equation becomes

$$(p_r + 3/(2v_r))(3v_r - 1) = 8 T_r \quad (9)$$

The Van der Waals' Equation above is considered to be universal providing the critical values of  $p, V$ , and  $T$  are measured. All gases then are said to behave identically when in their corresponding states determined by the critical values,  $p_c$ , etc. While corresponding states may not seem to be precise, this principal has had wide use in the fields of equilibrium and transformation properties of pure substances (20). The Principle of Corresponding States has been used to describe incompressible flow behavior where for dynamic similarity, the Reynolds number is frequently used. More recently, Prieto (19) has applied corresponding states to shock thermodynamics.

The development of a universal equation of state to describe shock has been the subject of extensive research in the last 40 years. Prieto has developed an equation which relates the shock thermodynamic variables ( $P, V$ , and  $E$ ) to experimental parameters, i.e., particle velocity, shock, compressibility, and density. In so doing he assumed a linear relation between shock

velocity and particle velocity. Prieto's development of the equation of state in Reference 8 is summarized below. He defines a fractional compression , Z, given by

$$Z = 1 - \rho/\rho_0 = \Delta V/ V_0 \quad (10)$$

where  $\rho$  is density and V is volume.

From Equation 2 it also follows that  $Z = U_p/U_s$ . Combining Equations 2, 3, and 4 with 10 gives

$$P = \rho_0 C^2 Z(1 - sZ)^{-2} \quad (11)$$

Using the principle of corresponding states from Reference 7, Prieto in Reference 19 defines critical ratios

$$Q_2 = K_Q Q_1 \quad (12)$$

where

$$Q = P, Z, \rho, C, s$$

Using the numerals 1 and 2 to refer to different materials and substituting them into Equation 12 leads to

$$s_1 Z_1 = s_2 Z_2 = v_r \quad (13)$$

and

$$P_1/[(\rho_1 C_1^2)/s_1] = P_2/[(\rho_2 C_2^2)/s_2] = p_r \quad (14)$$

and rewriting Equation 12 becomes

$$p_r = v_r (1 - v_r)^{-2} \quad (15)$$

where  $p_r = (\rho_0 C^2)/s$  and  $v_r = sZ$ .

If Equations 13 and 14 are combined with Equation 6 we obtain

$$u_s = 1 + u_p \quad (16)$$

where the reduced shock velocity is  $u_s = U_s/C$  and the reduced particle velocity is  $u_p = U_p/(C/s)$ . This equation predicts that the reduced shock velocity is a linear function of the reduced particle velocity with a slope of one. Thus, Prieto succeeded in expressing the shock velocity equation in terms of reduced variables. Their proof of the validity of Equation 16 lies in its ability to predict experimental values. Prieto made a few comparisons for a few metals which have nearly the same values of  $s$  and he obtained a very close fit to that data as presented in Figure 5 in Reference 6.

## 2.2 Summary Work on Data Correlations at Phillips Laboratory

There is a significant amount of shock data available for evaluating theories about the equation of state (3,4). Recently, it has become possible to produce particle velocities exceeding 10 km/s. Some very extensive experiments using an electric gun have achieved particle velocities exceeding 15 km/s. However, most of the available data lie at velocities below 5 km/s. In addition, experimental techniques have improved with the use of laser interferometers and streak cameras to measure velocities. Instrumentation of pressure transducers has also improved.

Shock data are available for a wide variety of materials and in the range of 0.01 to 5 km/s (3,4). The data for the most part have been generated by flyer-plate tests in which the plate velocity is measured and the shock velocity is determined through momentum transfer to the target. In a few cases, the pressure is measured during shock by means of transducers. Other properties are usually derived from the physics of shock (Equations. 2 to 4). Selected data from the above reference data banks were electronically scanned into a computer and entered into a computer-based spread sheet program. The results of this work was published this summer in a Phillips Laboratory Report (21 ).

The data for shock were manipulated in a special way; viz. the pressure was normalized by dividing by the adiabatic bulk modulus of sound,  $B_S = \rho_0 C^2$ , and the particle velocity was normalized by dividing by the bulk sound velocity,  $C$ . The results are presented in Figure 1 for different materials. The results show that the selections for this normalization of pressure and velocity, while not obvious selections, correct the data to form a master curve. If either normalization step is omitted, the data do not follow a master curve. In retrospect, it is easy to see the validity of the normalization when one considers Prieto's use of The Principle of

Corresponding States as a means of describing the shock process. From Equation 8 one can show that at low ratios of  $U_p/C$ ,  $<0.1$  with  $s$  in the range of 1, the second factor on the right hand side of the equation is of the order of one.

This means that the normalized pressure approximately equals the normalized particle velocity. Therefore the relationship  $P/(\rho_0 C^2)$  to  $(U_p/C)$  should be linear with a slope of 1. This appears to be the case as can be seen in Figure 1 for  $U_p/C < 0.1$ . However, as  $U_p/C$  approaches 0.1, the curve begins to bend upward as the second factor in Equation 8 gradually increases. In essence, Equation 8 is a quadratic in  $U_p/C$  in which the squared term dominates at values of  $U_p/C > 0.1$ . Thus at ratios of  $U_p/C > 0.1$ , the normalized pressure increases non-linearly with normalized particle velocity as can be seen in Figure 1.

What makes Figure 1 remarkable is that eight different materials fit on one curve including one liquid, water. Examination of Equation 8 shows that  $s$  is a parameter of the material; i.e., the slopes vary from one material to another. However the agreement shown in Figure 1 suggests that materials have the same slope,  $s$ , as obtained from the  $U_s$  versus  $U_p$  plots. In fact, a careful review of the literature on shock and of the shock data indicate that materials are reported to have slope values which range from 1 to 5.

The correlation shown in Figure 1 was tested further. Additional materials were checked against the master curve, Figure 1. Ceramic materials such as quartz, corundum, and LiF were compared and each of these ceramics fits the curve. Three other metals were evaluated by normalizing the pressure and particle velocity and we found to superimpose on Figure 1. Polymers, such as epoxy, polysulfone, Mylar, Lucite, and Plexiglas were compared to the master curve and fell on top of the curve. Shock data obtained on iron powders ranging in densities from  $4.7 \text{ g/cm}^3$  to the theoretical density  $7.8 \text{ g/cm}^3$  were compared to the master curve in Figure 1. These comparisons included corrections for both the density and sound velocity changes in iron as a result of the initial powder porosity. When these corrections are performed, the iron powders data superimposed on the master plot. In short, all homogeneous materials evaluated last year exhibit the same normalized (reduced) pressure,  $P/(\rho_0 C^2)$ , response to a collision by a particle traveling at a normalized (reduced) particle velocity,  $U_p/C$ .

Comparisons of a selection of different materials were made using the shock velocity and the particle velocity. The results are shown in Figure 2. As can be seen, the slopes of the different materials within the scatter in the data appear to follow a single slope. Again within experimental error the intercept is equal to the ratio of the shock velocity to the bulk sound velocity for each material. Note that for water  $C = C_L$ ,  $C_S = 0$ .

One issue related to the slope is the problem of phase changes during the shock wave propagation. Shock induced phase transformation complicate the use of Equation (8) that assumes a single bulk sound velocity and a single initial density. Phase changes will definitely

affect both the density and the sound velocity of a material. Therefore the correlation is not completely valid for shock induced phase transformations. Quartz is an example where the shock induced transformations are predicted to occur in the solid state. These phenomena could be reflected in the quartz data that has a slight anomaly in the slope and intercept at high values of the particle velocity above the transition point of the phase change.

### 3.0 Work Performed Under This Grant

#### 3.1 Potential Functions and the Slope of the $U_s$ Vs $U_p$ Curve

King (25) and Pastine (8) have independently established that the slope of the  $U_s$  Vs  $U_p$  curve is to a third order independent of the material. If the interactive potential in the compressive regime can be expressed as a function

$$V(r) = A\Phi(r/r_0) \quad (17)$$

where  $V(r)$  = Interactive potential energy in the compressive region  $r/r_0 < 1$ ,  
 $A$  = Materials Constant  
 $r$  = Separation of Components  
 $r_0$  = Equilibrium Separation  
 $\Phi(r/r_0)$  = Infinite Powers Series in  $(r/r_0)$

then it follows that

$$s = -d^3\Phi/4d\Phi^2 \quad (18)$$

where  $s$  = slope of the  $U_s$  Vs  $U_p$  curve  
 $\Phi = \Phi(r/r_0)$

A typical potential energy function is the Lennard-Jones Potential equation (22,23) for interactions between two components (molecules, ions, or atoms). This equation is

$$V(r) = A/r^m + B/r^n \quad (19)$$

This Lennard-Jones Potential has been extended by Kittel (24) to a crystal with coordination number of 12 where A and B have specific values. If we redefine Equation 19 by dividing  $r$  by  $r_0$  we get

$$V(r/r_0) = C[12.13(r/r_0)^{-m} - 14.45(r/r_0)^{-n}] \quad (20)$$

which is of the form  $V(r) = A\Phi(r)$ . The usual values taken for  $m, n$  are 12 and 6 respectively.



An alternative potential energy equation is the so-called modified Buckingham 6-EXP Equation given by

$$V(r/r_0) = \{\varepsilon/1 - (6/\alpha)\} \{(6/\alpha) \exp (\alpha[1-(r/r_0)]) - (r_0/r)^6\} \quad (21)$$

in which  $\varepsilon$ ,  $\alpha$ , and  $r_0$  are empirical constants depending on the shape of the potential well. The value of  $\varepsilon$  depends on the depth of the well,  $\alpha$  on the shape of the repulsion potential, and  $r_0$  upon the equilibrium spacing, respectively (20 ).

The Buckingham 6-EXP equation is somewhat more realistic than the Lennard-Jones potential for prediction phenomena in the compressive region of the interactive potential. Lennard-Jones did not have a physical model of the repulsive potential. The Buckingham 6-EXP Potential is considered be more realistic because the potential includes dipole and quadrupole interactions and approximates the repulsive potential with an exponential function (20). Ross has also noted that the Lennard-Jones Potential is inadequate because quantum mechanical calculations have shown that the repulsion is softer at short intermolecular distances than the Lennard-Jones Potential predicts (28).

### 3.2 Theoretical Slope Predictions

The value of the slope,  $s$ , can be determined by taking the appropriate derivatives of Equations 19 or 21 and substituting them into Equation 18. According to both King (25) and Pastine (8) the slope of the  $U_s$  Vs  $U_p$  line is related to the ratios of the third derivative of the potential to the second derivative of the potential as given by Equation 18. Since the functional form of  $r$  of Equation 19 is the same as that for Equation 20, the ratios of the derivatives can be calculated and the values of the constants  $A$  and  $B$  in Equation 19 cancel. As a result, the slope is predicted to be independent of the material or its crystal structure, except that  $r_0$  varies from one material to another. Even if Equation 20 were modified for other coordination numbers, the constants would still cancel. Thus, the slope is predicted to be totally independent of the atomic arrangement of the material but depends only on the normalized,  $(r/r_0)$ , and the functional shape of the potential energy curve. The constants in Equation 19 or Equation 21 determine the magnitude of the slope of the  $U_s$  Vs  $U_p$  line. Moreover, the slope would be more or less universal for all materials if the nature of the electrical interaction was more or less the same. In the analysis by King, the application of Equation 18 to predict the slope of the  $U_s$  Vs  $U_p$  line, higher order terms were neglected, i.e., the expression for the potential is assumed to be a power series.

The Lennard-Jones Potential has been used extensively to predict the behavior of gases and condensed vapors. It is used to predict hydrodynamic applications, transport phenomena, and critical phenomena for gases and liquids (20). It has been used successfully in predicting shock behavior and detonations in gases (20). Moreover, the Lennard-Jones equation using

reduced variables (Principle of Corresponding States) has led to good agreement with the observation of liquids and their vapors at or near the critical point. Thus, the Lennard-Jones Potential equation while partly arbitrary is, nevertheless, useful for predicting equilibrium and non-equilibrium phenomena. The predicted universality and constancy of the slope used in Equation 8 implies that liquids and solids would behave the same under shock waves. The above predictions using the Lennard-Jones equation for the potential energy are consistent with the evaluation of shock data for which the slope is apparently universal and constant for homogeneous materials. Moreover, because the Lennard-Jones equation has worked very well in making predictions for liquids and their vapors and for ionic solids, it appears that it may provide an accurate description of the potential energy in the compressive region for all dense solids.

The Modified Buckingham Potential or the 6-EXP Potential equation has had less universal appeal because it is considerably more difficult to make thermodynamic calculations using this equation. The equation is considerably more complicated than the Lennard-Jones equation. However, it is thought to describe the repulsive electric field interactions better than the Lennard-Jones Equation (20). The exponent for the repulsive potential in the Lennard-Jones Potential is arbitrary. The Buckingham 6-EXP Potential takes into account the steepness of the repulsive potential much better than the Lennard-Jones Potential. It includes induced dipole-dipole and quadrupole-quadrupole interactions. In addition, the repulsive potential is an exponential function of the compression rather than a single term in a power series,  $r^m$ . The parameter which governs the steepness of the potential is  $\alpha$ . The dependence upon  $\alpha$  is presented in Figure 3. For these comparisons the steepness varied from  $\alpha = 10$  to 13.5 using Equation 21.

A comparisons of the predicted values of the shock velocity slope using Equations 18 and the expressions for the potential energy given by Equations 19 and 21 are shown in Figure 4. Two values of  $\alpha$ , 10 and 13.5 in the Buckingham 6-EXP Equation and  $m=12$  and  $n=6$  for the Lennard-Jones Equation were used. As can be seen in the figure, the predicted slopes are nearly constant in the range of shock compression,  $V/V_0 = (r/r_0)^3 < 0.5$ . for either potential function as is predicted by the King, Equation 18. Also, the universal value of the slope, ( $s=1.333$ ), closely agree with the calculated slopes of 1.5 to 2. These values are remarkably close considering the uncertainty in the applicability of the Lennard-Jones Potential to the compressive region of the potential curve and the uncertainty in the value of  $\alpha$  for metals. The values of  $\alpha$  used correspond to those extracted by experiment inert gases (20). The prediction of the magnitude of the slope does not depend upon any of the other parameters except  $\alpha$ . The other parameters in Equation 21 drop out of the calculation of the ratio of the derivatives described above. It is interesting to note that over the range of values of compression,  $V/V_0$ , the

slope predicted by the Modified Buckingham Potential is very constant compared to the Lennard-Jones Potential. Moreover, the value of the slope for  $\alpha = 10$  is 1.5 which is very close to the best fit value,  $s = 1.333$ . The predicted slope behavior as a function of the compression,  $V/V_0$ , verify the validity of the constant slope predicted by King (25). In his analysis he assumed that the potential is an infinite series which is another way of describing the exponential function in the Buckingham 6-EXP Potential.

### 3.3 Micro-mechanical Computer Evaluations

Taylor and Dodson (27) have developed a micro-mechanical model for shock impact which is based upon a square array of atoms experiencing a hypervelocity collision. Shock propagation in copper was modeled with the use of the embedded-atom method. Both the Rose potential and the Morse potential were used. Predictions for copper agreed quite well with the shock velocity-particle velocity correlation,  $s = 1.3$ . Particularly noteworthy are the predictions which parallel the data (27).

The computer program developed at Sandia Laboratory by Taylor and Dodson was imported to CSUN for continuing their work by using other potentials such as the Rose potential (15) in micro-mechanical setting. While this work is not complete, the program has successfully been compiled on a CSUN computer and awaits modifications for computer interface of the CSUN mainframe plotter and other minor programming modifications. This work will be continued.

### 3.4 New Data Correlations

Part of the effort this year has focused on the linearity and universality of the slope of the  $U_s$  Vs  $U_p$  curve. Several additional attempts were made to find exceptions to the master curve shown in Figure 1. This included looking at crystal structure, crystal orientation, density effects, and other liquids.

The role of crystal orientation on the slope of the  $U_s$  Vs  $U_p$  curve was evaluated in some detail. Data were evaluated for NaCl with three different crystal orientations, [100],[110], and [111]. The salt specimens were subjected to hypervelocity collisions in each direction. Surprisingly shock waves travel in salt identically with no evidence of a different the slope of the  $U_s$  Vs  $U_p$  curve associated with crystal direction. Moreover the behavior is consistent with the master curve, Figure 1, and the, master equation, Equation 8. The results of the comparison of crystal orientation effects in NaCl on the slope of the  $U_s$  Vs  $U_p$  line are shown in Figure 5. As can be seen the data for shock waves in three direction superimpose on each other. This strongly suggests that the slope of the  $U_s$  Vs  $U_p$  curve is independent of direction of the shock wave travels through the crystal. This result is consistent with the predictions using the Lennard-Jones or the Buckingham 6-EXP. Equation to predict the slope. The repulsive pair-potentials

between nearest neighbor atoms obviously dominates when the atoms are being squeezed together and the interactions from next-nearest neighbors can be neglected.

The majority of the data available for shock in metals has been evaluated by Jeanloz (9). He concluded that the slopes of the  $U_s$  Vs  $U_p$  curves for metals range from 1.1 to 1.6. One observation that may have been missed by Jeanloz et.al., is that FCC metals appear to have a slope is somewhat larger than BCC metals. The FCC metals have reported slopes of 1.3 to 1.6 and BCC metals from 1.1 to 1.4. Without a detailed evaluation of the experimental errors in measuring the shock and particle velocities, it is difficult to determine whether the differences in the reported values of the slopes are real. As can be seen in Figure 6 the slope of tungsten falls slightly below that of gold,  $s = 1.5$  for gold Vs  $s = 1.27$  for tungsten. While atom coordination number (12 nearest neighbors for gold versus 8 nearest neighbors for tungsten), would be expected to play a role during the compression of a crystal, the effect of atom coordination must be very small indeed. A larger group of metals were considered as shown in Figure 7. As can be seen the master curve for metal structures, (body-centered cubic, face-centered-cubic and hexagonal close-packed) do not deviate significantly from a single curved line. As observed above for different crystal orientations shock waves appear to propagate independent of the crystal structure as well as its orientation.

One of the major points found earlier is that the slope of the  $U_s$  Vs  $U_p$  curve for water is very similar to all metals (21). This was discussed earlier for Figure 1. The comparison of water to other liquids was extended for benzene and toluene. As one can see in Figure 8, water, benzene, and toluene behave identically with respect to shock wave propagation. More importantly, the shock velocity intercepts for all liquids is equal to the longitudinal sound speed (shear sound speed is zero) whereas the intercept for solids is equal to the bulk sound velocity. These results conform to the prediction the slope of the shock velocity line is a constant and independent of the atomic arrangement. Liquids do not possess long-range order, but apparently in shock compression behave as solids, or vice versa.

Shock in low density materials such as foams and wood were examined in light of the master equation. It was found that the behavior of woods is an exception to the current correlations as can be seen in Figure 9. While the data do not superimpose, they do converge at high values of the pressure. As was found for iron powders (21), it is necessary to use the theoretical density rather than the apparent density for shock of porous materials. The results must be corrected and a new value of the bulk sound velocity must be determined for a 100% dense woods. Unfortunately, this correction could not be made because the value of the density of 100% dense wood is not known. The sound velocity correction was possible for iron powders because the bulk sound velocity for 100% dense iron is known. Nevertheless, the deviation from a master curve for theoretical dense materials is understandable. If the density and the bulk

sound velocity of a theoretically dense wood were known, then the adjustments to the shock data could be made.

### **3.4 Other Tasks Completed Under This Grant**

Considerable effort was devoted to the review of the open literature on the equation of state for shock. A shock bibliography containing 11 books and 153 references from the open literature was created which pertain the universality of the shock velocity equation.

In addition to the literature review process, two reports were issued this year by Phillips Laboratory (21, 26), which summarize the work performed during the last two summers on the AFOSR Faculty Researchers Program and for the AFOSR Summer Research Initiation Grant for 1992. Finally, presentations of the equation of state analysis were made to the Phillips Laboratory and to Los Alamos National Laboratory. In addition, the author attended the American Institute for Physics Conference on High Pressure Science and Technology on June 28, 1993 in Colorado Springs where the above work was informally discussed with other workers in the shock physics field. A paper is in preparation to the Journal of Applied Physics on the universal shock velocity slope. The author in conjunction with co-authors from the Phillips Laboratory has been invited to present the above work at an upcoming conference sponsored by the Hypervelocity Impact Society.

## **4.0 CONCLUSIONS**

The work performed under this contract as part of the AFOSR Research Initiation Program (Now called SREP) has led to significant understanding of the shock behavior caused by hypervelocity collisions with homogeneous solids. This work has produced a confirmation of a universal slope for the shock velocity line, Equation (6) or its counterpoint, Equation (8). Moreover, this universality was further confirmed for shock data obtained on many other solids, single crystal orientations, and other liquids. The work produced theoretical predictions of a universal slope which agree closely with that determined from shock data. In fact, the magnitude of the universal slope from data agrees with the theoretical value within a factor of two. Thus it now appears that all homogeneous, dense, condensed materials obey a single shock equation with a universal slope,  $s$ .

The work will continue at CSUN to extend the prediction using the Taylor micro mechanical model. This work is important because it can examine the details of the shock behavior and appears to be totally consistent with the macroscopic observations. It can also give insight into shear induced phase transformation due to shock waves.

Future work is definitely needed in several specific areas to render the results of this work useful. Obviously there is a need for verification of the universality of the shock velocity line for higher particle velocities up to a 10 km/s or above. This would require shock waves induced in materials by particle traveling at velocities in the neighborhood of 10 to 15 km/s. A small set of

high velocity impact experiments would verify whether the current shock data base can be reliably extrapolated to higher particle velocities and verify that  $s$  remains constant throughout the velocity regime up to 15 km/s. Secondly, shock experiments are needed on inhomogeneous materials such as composites. The presence of solid-solid interfaces inside a material would be expected to reflect the compressive shock wave much the same as the shock waves are reflected from the free surfaces of a homogeneous target. A composite may behave entirely differently due to the presence of internal interfaces between the macro-constituents of the composite. Thirdly, a thorough statistical evaluation of the uncertainties in the experimental shock data would permit the slope differences reported in the data bases to be evaluated for importance. This analysis suggests a single slope which corresponds to an average value of the reported slopes of the data. The reported slope variation needs to be cleared up. Fourthly, the shock damage model needs to be redefined. If shock waves propagate universally, the damage should be universal. Since it is not the same in all materials, a different model for space debris damage is needed. Heretofore, most shock damage models have associated the damage with the propagation of the shock wave in the material. However, from this study it seems unlikely that the propagation of the shock wave explains damage. More likely, the damage is caused by the reflected waves which transform from compression to tension and shear after reflection at an interface of lower density. Post shock data cannot distinguish between the mechanisms of damage. This will require separating shock compression from shock tension damage by regulating the reflected waves. Finally, additional theoretical calculations of the interatomic interaction during compression of metals is needed. This would involve using quantum mechanics to predict the steepness of the repulsive potential in an attempt to define the steepness parameter in the Buckingham 6-EXP Potential.

#### **5.0 ACKNOWLEDGMENTS**

The author would like to the Air Force Office of Scientific Research for its support through Research Development Laboratories. Also, the author thanks Dr. Charles Stein and TSgt. Robert Robertson for their helpful consultation and advice during this grant. The CSUN Foundation through the Office of Research and Grants and the Center for Research in the School of Engineering and Computer Science is acknowledged for their help in administering this grant. The assistance in migrating the computer program to CSUN by Paul Taylor of Sandia Laboratories is appreciated. Finally, the author would to thank Editha Francisco and Kenneth Nwabueze, student at CSUN, for their help in evaluating the data and performing the potential analyses of the potential functions.

## 6.0 REFERENCES

1. Walsh, John M. and Christian, Russell H., "Equation of State of Metals from Shock Wave Measurements," *The Physical Review*, 97, No. 6, pp. 1544-1556, March 15, 1955.
2. McQueen, R.C. and Marsh, S.P., "Equation of State for Nineteen Metallic Elements from Shock-Wave Measurements to Two Megabars," *Journal of Applied Physics*, 31, No. 7, pp. 1253-1269, July 1960.
3. Marsh, S.P., *Los Alamos Shock Hugoniot Data*, University of California Press, Berkeley, 1980.
4. Kohn, Brian J., *Compilation of Hugoniot Equations of State*, AFWL-TR-69-38, Air Force Weapons Laboratory, Kirtland AFB, NM, April 1969.
5. Hermann, Walter, *Sandia Laboratories Shock Data Base*. Sandia Laboratories, Albuquerque NM, 1992.
6. Prieto, Fernando and Renero, Claude, *The Equation of State of Solids*, *J. Phys.Chem. Solids*, 1976, 37, pp. 151-160.
7. Birch, F., *Journal of Geophysical Research*, 83, 1978 p 1257.
8. Pastine D. Interpolation Formula for the Relationship Between Shock Velocity,  $U_s$ , and Particle Velocity,  $U_p$ , in Solids, *Communications*, p 440, 1968.
9. Jeanloz, Raymond, "Shock Wave Equation of State and Finite Strain Theory," *Journal of Geophysical Research*, 94, No. B5, pp. 5873-5886, May 10, 1989.
10. Rodean, H. Relationship for Condensed Materials Among Heat of Sublimation, shock-wave Velocity and Particle Velocity, *J Chem. Phys.*, 49, No. 9, p 4117, 1968.
11. Rouff, A., Linear Shock-Velocity-Particle-Velocity Relationship, *J Appl. Phys.* 38, No. 13, p 4976, 1967
12. Zel'dovich, Ya and Raizer, Yu, *Physics of Shock Waves and High-Temperature Hydrodynamic Phenomena*, Volume 2, Chapter XI, Academic Press, 1966
13. Slater, J.C., *Introduction to Chemical Physics*, Chapter 14, Mc Graw-Hill, New York, NY, 1939.
14. Dugdale, J.S. and MacDonald, D.K.C., "The Thermal Expansion of Solids," *The Physical Review*, 89, p 832, February 1953
15. Rose, J.; Smith J.; and Ferrante, J., Universal Features of Bonding in Metals, *Phys. Rev. B*, 28, No. 4, p 1835, 1983.
16. Vinet, P.; Ferrante, J.; Smith J.; and Rose J., A Universal Equation of State, *J Phys. C: Solid State Phys.*, 19, L467-L473, 1986.
17. Grover, R., Getting, I.C., and Kennedy, G.C., "Simple Compressibility Relation for Solids," *Physical Review B: Solid State*, 7, No. 2, pp. 567-571, January 1973.
18. Prieto, F. and Renero, C., Equation for the Shock Adiabats, *J. Appl. Phys.*, 41, No. 9, p 3876, 1970.

19. Prieto, Fernando, A Law of Corresponding States for Materials at Shock Pressures, J. Phys. Chem. Solids, 35 pp. 279-286, 1974.
20. Hirschfelder, Joseph; Curtis, Charles; and Bird, R. Byron, Molecular Theory of Gases and Solids, Chapter 4, pp. 234-328, Wiley, 1954.
21. Shively, J.H., Stein, C., and Robertson, R., An Equation of State for Shock in Homogeneous Materials and Comparison to Shock Data, PL-TR-92-1060, Phillips Laboratory, space and Missiles Directorate, Air Force Materiel Command, Kirtland AFB, NM 87117.
22. Lennard-Jones, J and Devonshire, A. Critical Phenomena in Gases I, Proc. Roy. Soc., A163, p 53, 1937.
23. Lennard-Jones, J . The Equation of State of a Gas, Proc. Camb. Phil. Soc., 22, P 105, 1931.
24. Kittel, Charles, Introduction to Solid State Physics, 5th Ed, Chapter 3, pp. 76 - 102, John Wiley, New York, NY, 1973.
25. King, Thomas, Boeing Aircraft, Renton Washington, Private Communication
26. Shively, Jon H. and Roybal, Robert, Chemical and Structural Effects Caused by Hypervelocity Impacts to Polysulfone Graphite Reinforced Composite and Its Resin. PL-92-1076, Phillips Laboratory, Space and Missile Directorate, Air Force Materiel Command, Kirtland AFB, NM 87117, June 1993
27. Taylor. P. and Dodson, B., Propagating Lattice Instabilities in Shock-Loaded Metals, Physical Review B, Vol 42, No. 2, July 1990, p1200ff.
28. Ross, M . and Ree, F., Repulsive Forces of Simple Molecules and Mixtures at High Density, Journal of Chemistry and Physics, 73, No. 12, Dec. 1980, p6146-6152



## **7.0 FIGURES**

**See following pages.**

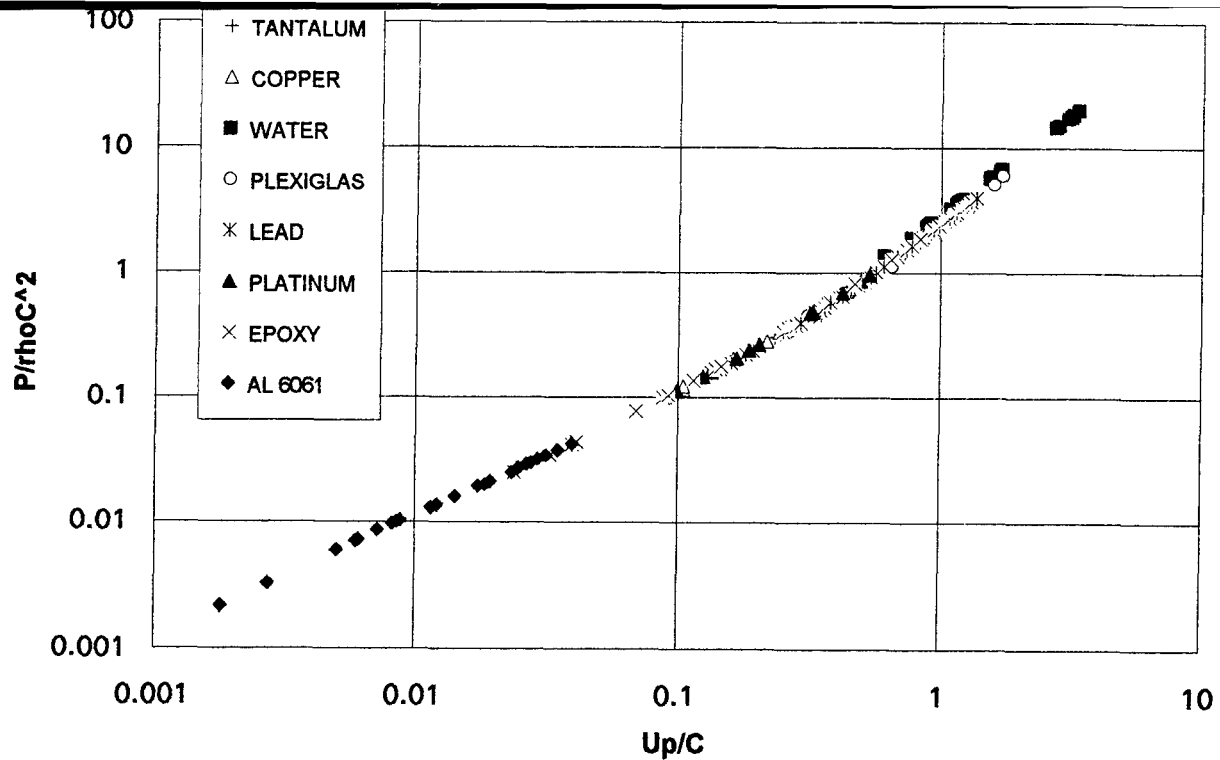


Figure 1. Master curve of normalized pressure for hypervelocity collisions as a function of normalized particle velocity for eight materials.

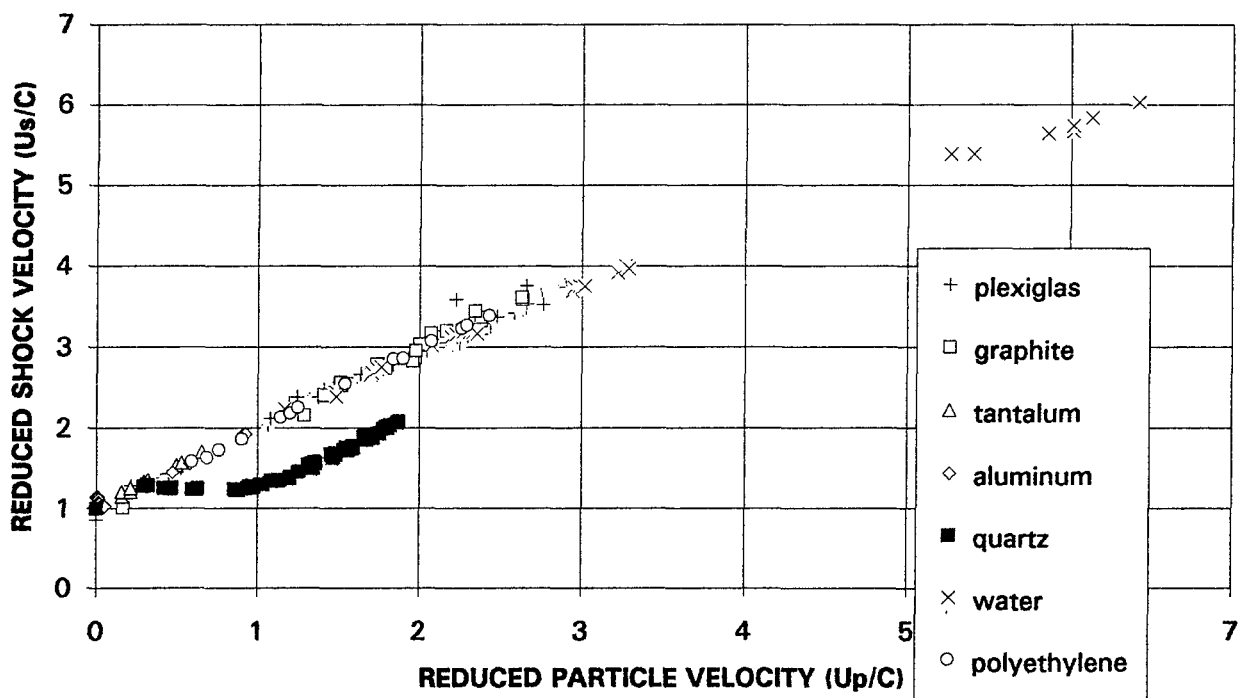


Figure 2. Reduced shock velocity versus reduced particle velocity for eight materials.

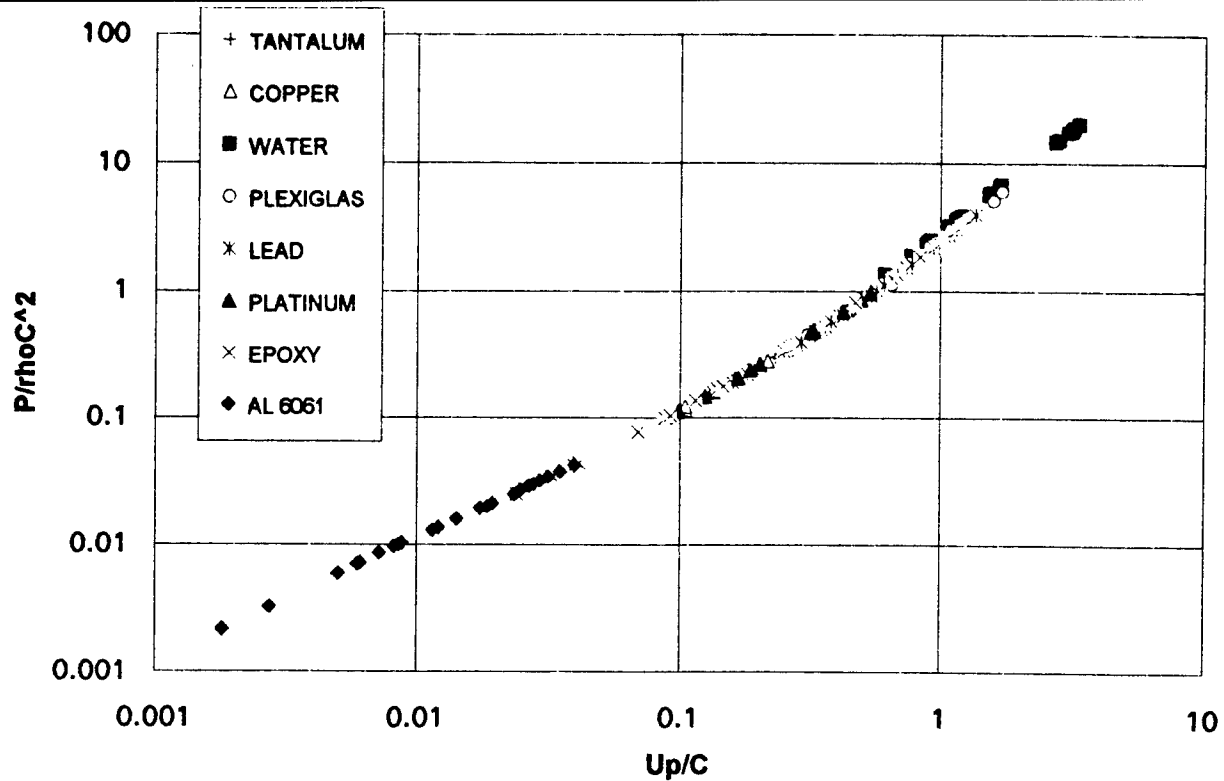


Figure 1. Master curve of normalized pressure for hypervelocity collisions as a function of normalized particle velocity for eight materials.

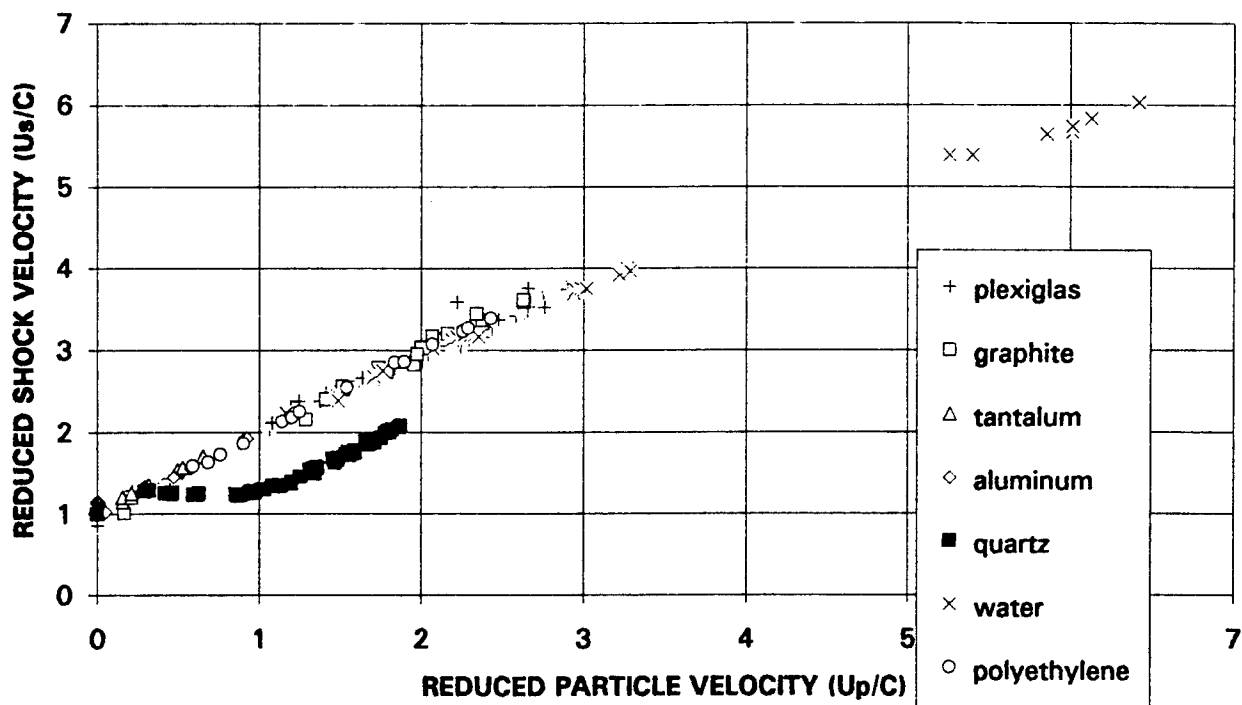


Figure 2. Reduced shock velocity versus reduced particle velocity for eight materials.

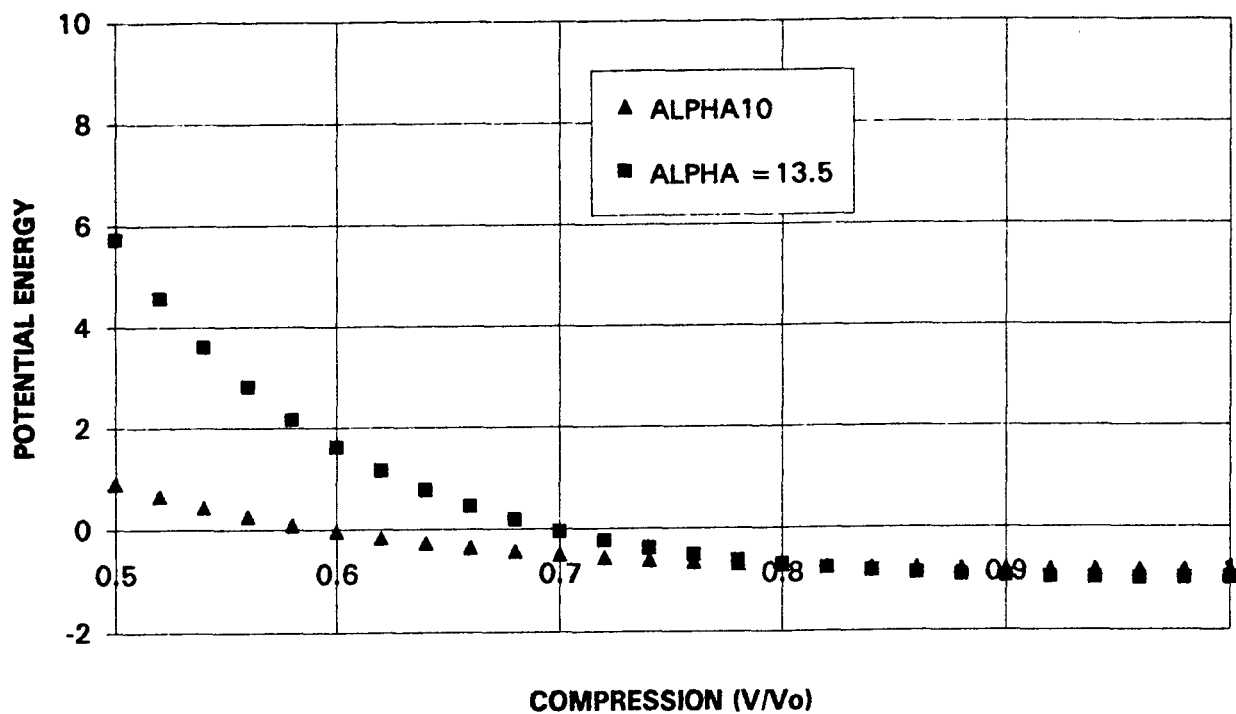


Figure 3. Effect of the steepness parameter,  $\alpha$ , on the shape of the Buckingham 6-EXP Potential

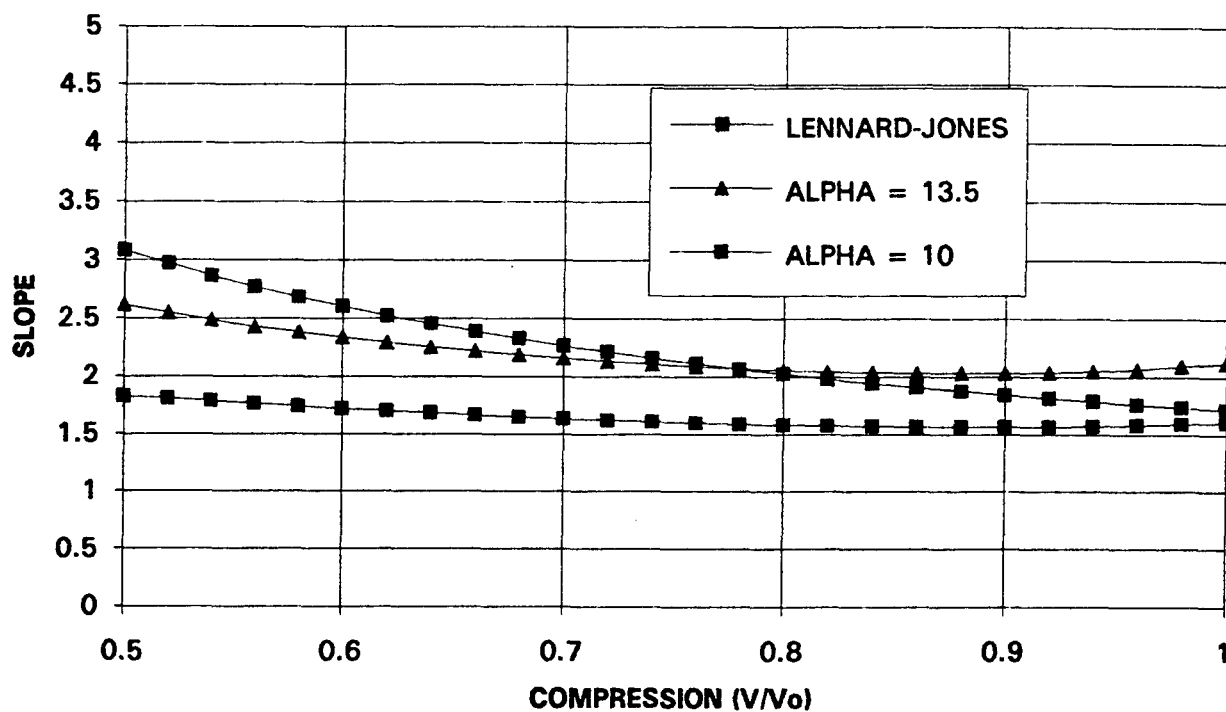


Figure 4. Predicted slope as a function of the compression for Lennard-Jones and the Buckingham 6-EXP Potentials

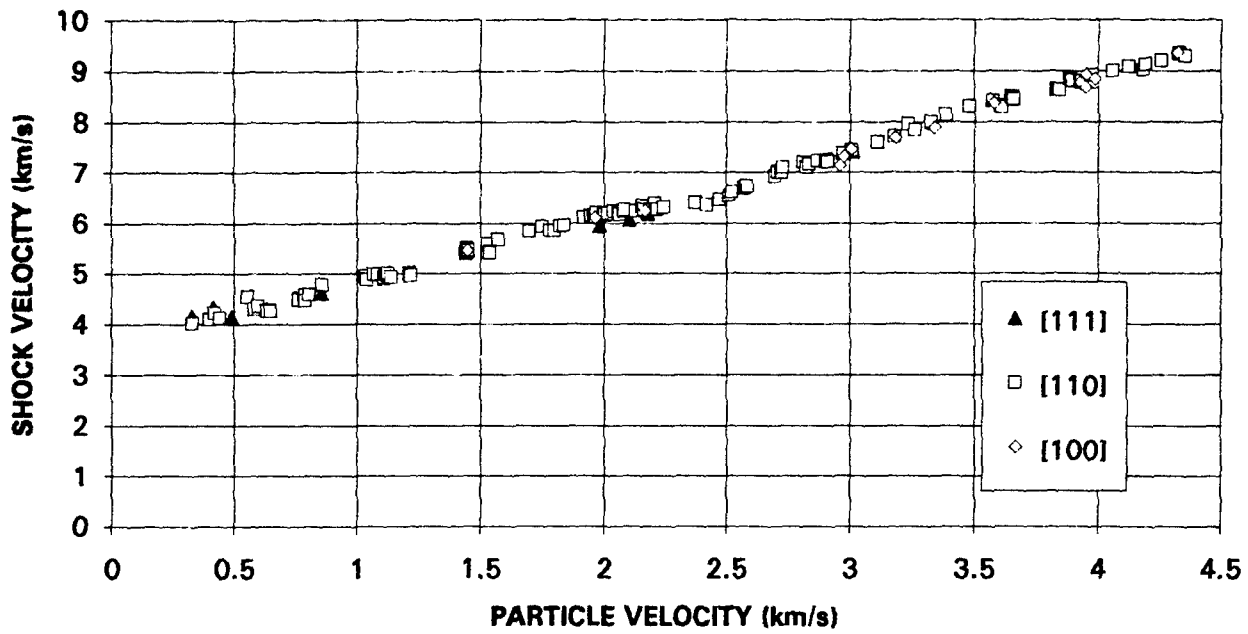


Figure 5. Shock velocity versus particle velocity for three crystal orientations in sodium chloride.

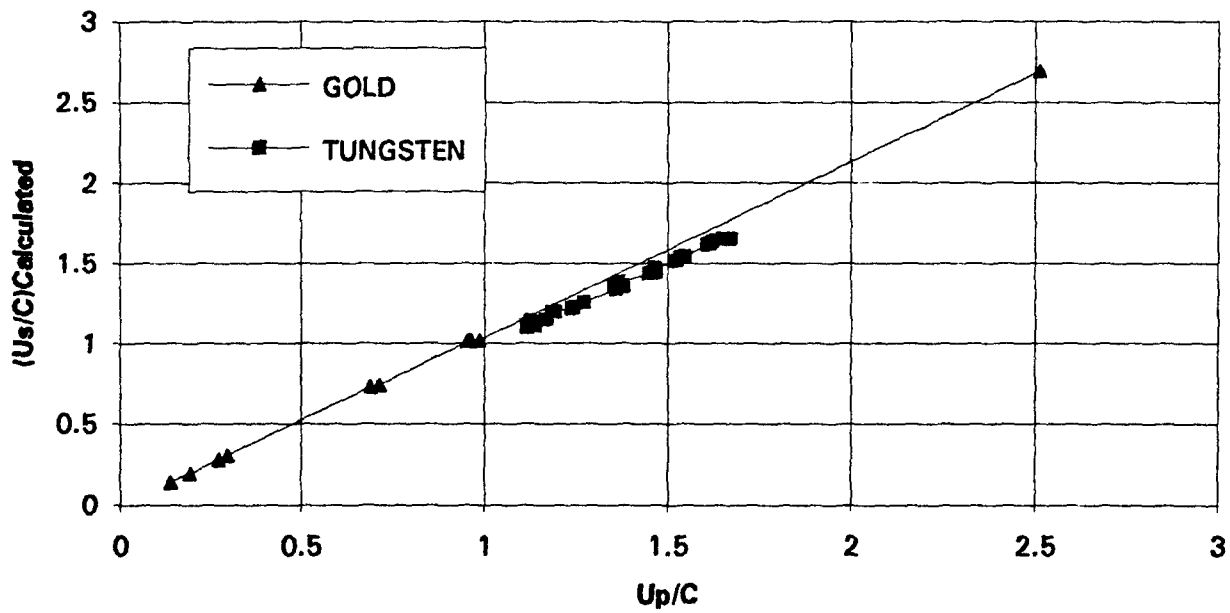


Figure 6. Calculated normalized shock velocity versus normalized particle velocity for two different metallic crystal structures.

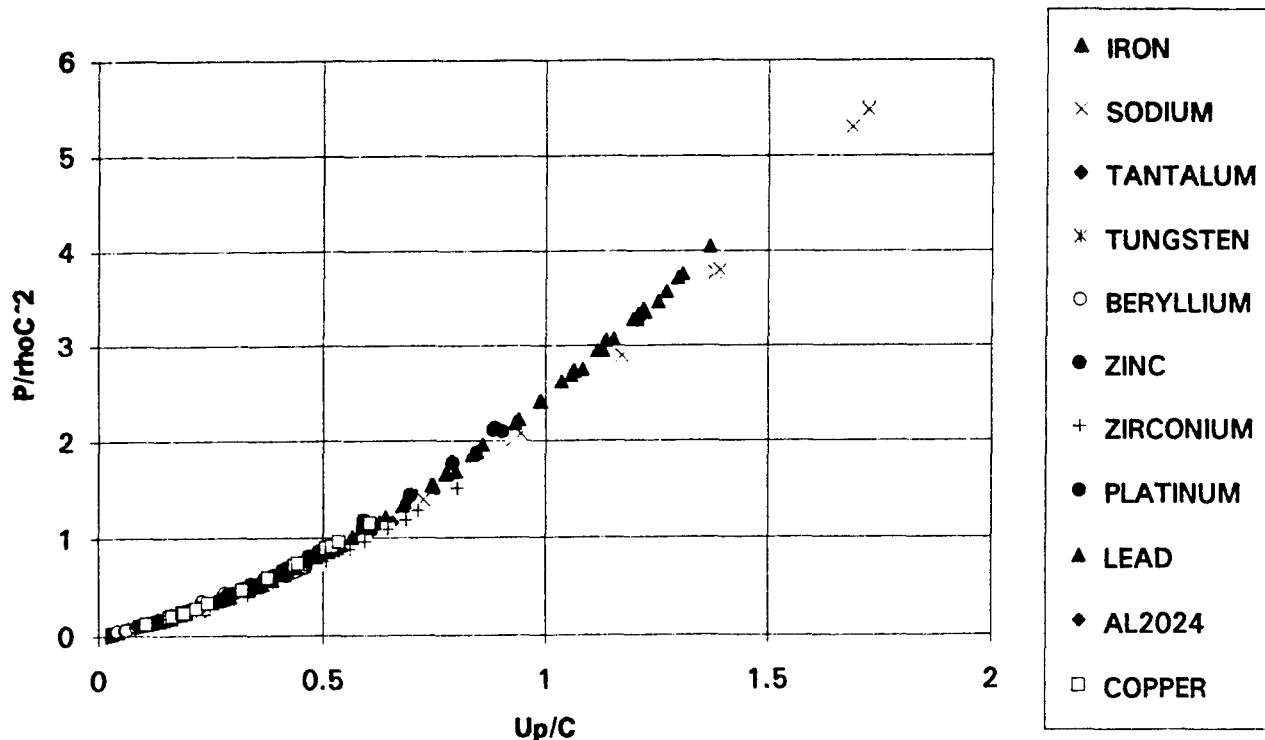


Figure 7. Master curve of reduced pressure versus reduced particle velocity for three sets of metal crystal structures

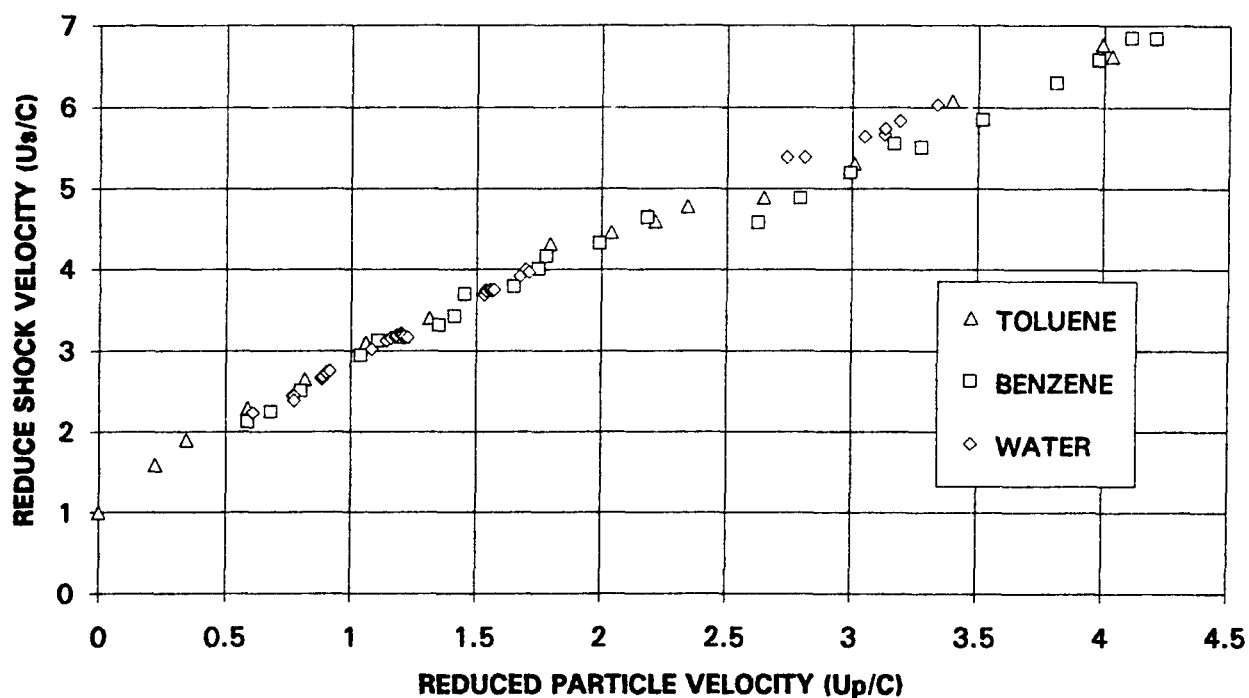


Figure 8. Reduced shock velocity versus reduced particle velocity for three liquids.

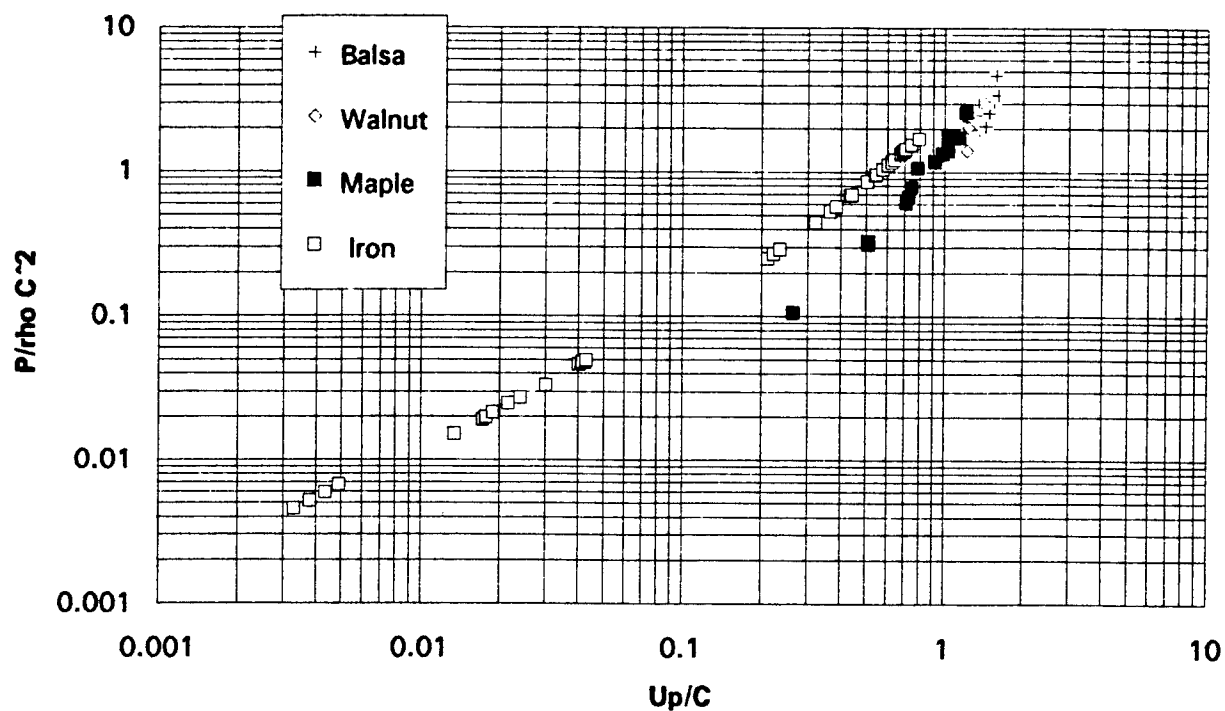


Figure 9. Normalized pressure for hypervelocity collisions as a function of normalized particle velocity for three wood materials and iron.

ANALYSIS OF SOLWIND P78-1 SATELLITE FRAGMENTATION  
USING THEORY AND COMPUTATIONS

Arjun Tan  
Professor  
Department of Physics

Alabama A & M University  
Meridian Street  
Normal, AL 35762

Final Report for:  
Research Initiation Program  
Phillips Laboratory

Sponsored by:  
Air Force Office of Scientific Research  
Bolling Air Force Base, Washington, D.C.

December 1993



ANALYSIS OF SOLWIND P78-1 SATELLITE FRAGMENTATION  
USING THEORY AND COMPUTATIONS

Arjun Tan  
Professor  
Department of Physics  
Alabama A & M University

Abstract

This study analyzes the planned fragmentation event of the Solwind P78-1 satellite from theoretical calculations and numerical computations. The orbital elements of Solwind were taken from the Satellite Fragmentation Catalog. The orbital elements and radar cross-sections of the fragments were obtained from the USAF Cavalier phased-array data and from the USSPACECOM (formerly NORAD) Perimeter Acquisition radar data. The three orthogonal components (radial, down-range and cross-range) of the velocity perturbations received by the fragments were calculated from the orbital elements of the target and those of the fragments, from which the angular distributions of the fragments were determined. Scatter plots of the velocity perturbation components reveal groups of 3 or 4 fragments having similar velocity perturbations, which probably originated from the same parts of Solwind. The possibility that 3 fragments ejected with the greatest velocity changes into the highest energy orbits were parts of the ASAT which ricocheted off Solwind is discussed. The angle of encounter between Solwind and the ASAT as estimated from different methods as well as the velocities of these fragments lend strong support to this possibility based on comparisons with ground-based oblique hypervelocity impact data. The angular distribution of the fragments show a primary and a secondary area of concentration of the fragments, the latter possibly indicating the entry point of the ASAT into its target. A study on the change of the average cross-sectional areas of solids on fragmentation indicates that both Solwind and the ASAT underwent thorough fragmentation during the encounter. The Aerospace Corporation's IMPACT model predicted the general characteristics of the fragmentation. Attempts to model the Solwind fragmentation using analytical codes are still underway.

ANALYSIS OF SAOLWIND P78-1 SATELLITE FRAGMENTATION  
USING THEORY AND COMPUTATIONS

Arjun Tan

INTRODUCTION

The US Air Force solar observation satellite Solwind P78-1 (also referred to as P-78) was launched on February 24, 1979 into a sun-synchronous orbit and was given the international designator 1979-17A (cf. Nauer, 1992). It was built by Ball Brothers Aerospace Corporation and its primary mission was to carry out solar observation experiments. On board was a gamma ray spectrometer experiment for the Defence Advanced Projects Research Agency (*Aviation Week and Space Technology*, 1985). Six secondary experiments (including three from the US Navy, two from the Air Force and one from the Army) were also conducted inside: Solex, Solwind, UV spectrometer, particle detector, X-ray monitor and aerosol monitor (*Aviation Week and Space Technology*, 1985; *Orbital Debris Mon.*, 1989). The six-year mission of Solwind was highlighted by the discovery of six previously undetected sun-grazing comets (cf. Powell, 1987). Having easily outlived its original mission duration of 12 months, the satellite was chosen as a live target for the U.S. Anti-Satellite (ASAT) test program.

On September 13, 1985, an F-15 Eagle jet fighter took off from Edwards Air Force Base, California, attained a height of 35,000 ft. and launched an 18-ft. two-stage rocket. The first stage was a Boeing short-range attack missile (SRAM) whereas the second stage was an LTV Altair III Scout rocket booster (*Aviation Week and Space Technology*, 1985). After the second-stage burnout, an LTV-made miniature homing vehicle (MHV) separated from the rocket. Guided by 8 infrared sensors and telescopes and powered by 64 small steering jets, the cylindrical-shaped MHV successfully converged on Solwind over the Pacific Ocean. At 20:43 GMT, the two objects collided at a relative speed of about 7 km/s and fragmented into over 300 trackable pieces in the perhaps first and only U.S. ASAT experiment against a live target in space (*Aviation Week and Space Technology*, 1985;

Aerospace America, 1985). Telemetry signals from both Solwind (which was still transmitting data) and the ASAT stopped at the same time, confirming the hit.

This study analyzes the Solwind fragmentation event from theoretical calculations and also from numerical computations.

#### DATA

The data for this study come from published references in the open literature.

Physical Characteristics of Solwind. Fig. 1 (after Kling, 1986) is a sketch of the Solwind P-78 satellite before fragmentation. The main body was roughly cylindrical and actually comprised of two cylinders: an octagonal cylinder fused to a circular one. The overall length of the two cylinders was 1.3 m and the diameter 2.1 m (cf. Nauer, 1992). Attached to the main body was one nearly square solar panel of area 47 ft<sup>2</sup> (Remillard, 1990), which translates to a side of 2.1 m. The mass of the satellite proper was 850 kg (Nauer, 1992), while the total mass of the satellite (including the solar panel and peripherals) was 878 kg (Remillard, 1992). According to Air University's *Space Handbook*, the surface density of the solar panel was 1 lb/ft<sup>2</sup> (Remillard, 1990).

Physical Characteristics of the MHV. The MHV projectile, which destroyed P-78, was circular cylindrical in shape having a length of 33 cm (13 in) and diameter 30.5 cm (12 in) and weighed 15.9 kg (35 lb) (Remillard, 1990). It contained a laser gyroscope for guidance and 8 cryogenically cooled infrared detectors for homing. Midcourse corrections were made by 64 single-shot solid-motor rockets (Remillard, 1990).

Orbital Elements of Solwind and Coordinates of the Breakup Point. The orbital elements of a satellite are any set of 6 independent quantities which specify completely the shape (oblateness) and size (energy) of the orbit, its orientation with respect to the earth and the instantaneous location of the satellite on that orbit. Normally, the semi-major-axis ( $a$ ) and eccentricity ( $e$ ) respectively furnish the size and shape of the orbital ellipse. The orientation of the orbit is determined by three angles: the longitude (also the right

ascension) of the ascending node ( $\Omega$ ), inclination ( $i$ ) and the argument of perigee ( $\omega$ ). Finally, the true anomaly ( $v$ ) pinpoints the exact location of the satellite on the defined orbit (cf. Bate, et al., 1971). These six quantities are by no means unique and may be substituted by other combinations of independent quantities. For example,  $a$  and  $e$  may be replaced by the height of apogee ( $h_a$ ) and the height of perigee ( $h_p$ ). In that case, we have

$$a = \frac{2 r_0 + h_a + h_p}{2} , \quad (1)$$

and

$$e = \frac{h_a - h_p}{2 r_0 + h_a + h_p} , \quad (2)$$

where  $r_0$  is the reference radius of the earth (6,378.145 km).

Oftentimes, the mean anomaly ( $M$ ) is given, instead of the true anomaly. In that case, the true anomaly is determined from the mean anomaly via the eccentric anomaly ( $E$ ) by means of the following equations (cf. Van de Kamp, 1964):

$$E = M + e \sin M + \frac{1}{2} e^2 \sin 2M + \frac{1}{8} e^3 (3 \sin 3M - \sin M) , \quad (3)$$

and

$$v = 2 \tan^{-1} \left[ \left( \frac{1+e}{1-e} \right)^{\frac{1}{2}} \tan \frac{E}{2} \right] . \quad (4)$$

The orbital elements of Solwind prior to fragmentation and the coordinates of the point of fragmentation have been gathered from Johnson and Nauer (1987) and Nauer (1992) and from calculations using Eqs. (1) through (4). These are reproduced in Table I.

Table I			
Symbol	Physical Quantity	Value	Reference
$h_a$	Height of Apogee	548.6 km	Johnson & Nauer (1987)

$h_p$	Height of Perigee	518.1 km	Johnson & Nauer (1987)
$a$	Semi-Major-Axis	6911.495 km	Calculated
$e$	Eccentricity	0.0022038	Nauer (1992)
$\Omega$	Longitude of Ascending Node	182°.5017	Nauer (1992)
$i$	Inclination	97°.6346	Nauer (1992)
$\omega$	Argument of Perigee	99°.4081	Nauer (1992)
$M$	Mean Anomaly	260°.9644	Nauer (1992)
$E$	Eccentric Anomaly	260°.9622	Calculated
$v$	True Anomaly	260°.8375	Calculated
$T$	Time Period	95.3 min	Johnson & Nauer (1987)
$h$	Altitude of Fragmentation	525 km	Johnson & Nauer (1987)
$\lambda$	Latitude of Fragmentation	35°N	Nauer (1992)
$\Phi$	Longitude of Fragmentation	234°E	Nauer (1992)

Fig. 2 (after Remillard, 1990) is an overhead view of the Solwind encounter. Solwind was on a northbound pass when the ASAT projectile intercepted it. It must be stated that the state vectors of the ASAT projectile prior to impact are classified information and will remain so indefinitely. Hence not much is certain about the precise direction from which the projectile encountered P-78. This information has, however, been inferred from the momentum transfer calculated from the fragment data (Badhwar, et al., 1990).

Orbital Elements and Radar Cross-Sections of the Fragments. The orbital elements of the fragments as well as their radar cross-sections (RCS) have been taken from USAF Cavalier phased-array radar data and from the NORAD (now USSPACECOM) Perimeter Acquisition radar data (PARCS). A major problem with the

data is that oftentimes, they are days, weeks or even months old and atmospheric drag tends to decay and "circularize" them. To circumvent this problem, they data are propagated backwards to the time of fragmentation by a technique developed by Badhwar and Anz-Meador (1989).

#### METHOD OF ANALYSIS

As stated earlier, both theoretical and numerical techniques have been employed to study the P-78 fragmentation event.

Theory. Most, if not all of the facts pertaining to a breakup are derived retrospectively from the orbital elements and the RCSs of the parent satellite and those of the individual fragments.

Velocity Perturbations of the Fragments. The magnitude, variance and directionality of the velocity perturbations of the fragments can furnish valuable information regarding the nature and intensity of a fragmentation. Exact solutions for the orthogonal components of the velocity perturbations have been obtained by Badhwar, et al. (1990).

To calculate the velocity perturbations imparted to the fragments, it is convenient to use the parent satellite's local frame of reference at the point of breakup. The three orthogonal directions are defined by the radial and down-range directions in the plane of the orbit and the cross-range direction perpendicular to the plane of the orbit and along the angular momentum vector. In this coordinate system, the velocity vector  $\vec{v}$  of the parent satellite has the components ( $v_r$ ,  $v_d$  and 0). From Keplerian Mechanics,

$$v = \left[ \mu \left( \frac{2}{r} - \frac{1}{a} \right) \right]^{\frac{1}{2}}, \quad (5)$$

$$v_d = \left[ \mu a \frac{(1 - e^2)}{r^2} \right]^{\frac{1}{2}}, \quad (6)$$

and

$$v_r = \pm (v^2 - v_d^2)^{\frac{1}{2}}, \quad (7)$$

where  $r$  is the radial distance from the center of the earth to the breakup point and  $\mu = GM$  is the gravitational parameter,  $G$  and  $M$  being the universal gravitational constant and the mass of the earth respectively. In Eq. (7), the plus sign corresponds to the ascending mode of the satellite ( $v < 180^\circ$ ), while the minus sign corresponds to the descending mode ( $v > 180^\circ$ ).

Upon fragmentation, the velocity of a fragment  $\vec{v}'$  will have the components  $v_r + dv_r$ ,  $v_d + dv_d$  and  $dv_x$ , where  $dv_r$ ,  $dv_d$  and  $dv_x$  are the velocity perturbation components received by the fragment during the breakup. The latter can be solved from the energy, angular momentum and plane-change angle equations (Badhwar, et al., 1990). If  $a'$  and  $e'$  are the semi-major axis and eccentricity, respectively, of the fragment's orbit and  $\alpha$  the plane-change angle, then:

$$dv_r = \pm \left[ \mu \left( \frac{2}{r} - \frac{1}{a'} \right) - \frac{\mu}{r^2} a' (1 - e'^2) \right]^{\frac{1}{2}} - v_r, \quad (8)$$

$$dv_d = \frac{\cos \alpha}{r} \left[ \mu a' (1 - e'^2) \right]^{\frac{1}{2}} - v_d, \quad (9)$$

and

$$dv_x = \frac{\sin \alpha}{r} \left[ \mu a' (1 - e'^2) \right]^{\frac{1}{2}}. \quad (10)$$

In Eq. (8), the plus sign corresponds to the ascending mode of the fragment (true anomaly  $v' < 180^\circ$ ), whereas the minus sign corresponds to the descending mode ( $v' > 180^\circ$ ).

The plane-change angle  $\alpha$  can be calculated from the inclinations  $i$  and  $i'$  of the parent's and the fragment's orbits, respectively and  $\lambda$ , the latitude of the breakup point.:

$$\alpha = \pm \cos^{-1} \frac{\cos i \cos i' + [(\cos^2 \lambda - \cos^2 i)(\cos^2 \lambda - \cos^2 i')]^{\frac{1}{2}}}{\cos^2 \lambda} \quad (11)$$

Here the plus sign corresponds to  $i' > i$  and the minus sign corresponds to  $i' < i$  for northbound orbits. The signs are reversed for southbound orbits.

Angular Distribution of the Fragments. The angular distribution of the fragments as they emerge from a breakup may be a potential indicator of the nature of the breakup (Benz, et al., 1987). This distribution may be studied by defining two angles akin to the zenith and azimuth angles of spherical coordinates (Badhwar, et al., 1990):  $\theta = \cos^{-1}(dv_r/dv)$  and  $\phi = \tan^{-1}(dv_x/dv_d)$ , where  $dv$  is the magnitude of the velocity perturbation of the fragment:  $dv = (dv_r^2 + dv_d^2 + dv_x^2)^{1/2}$ .

Mass and Momentum Distributions of the Fragments. A novel technique for determining the masses of orbiting satellites was devised by Badhwar and Anz-Meador (1989). Since the drag coefficient as calculated from orbital decay gives the cross-sectional area to mass ratio and the RCS supplies the cross-sectional area, the two together can furnish the mass of the satellite. Badhwar and Anz-Meador (1989) estimated the masses of hundreds of orbiting satellites, rockets and fragments in this way.

Once the velocity perturbations and the masses of the fragments are obtained, the momentum perturbations and the kinetic energies imparted to the fragments can be calculated.

Change in Cross-Sectional Area in Fragmentation of Solids. A recent study by Tan (1993) revealed the existence of two simple yet fundamental principles of nature as regards the cross-sectional area (CSA) of solids: (1) the average CSA of a flat plate remains constant in a fragmentation; and (2) the average CSA of any solid other than a flat plate must increase upon fragmentation. It is shown that these two principles may be used to extract additional information regarding the fragmentation of satellites in space (Tan, 1993).



## RESULTS AND DISCUSSIONS

Several hours after the fragmentation, at least 321 fragments of Solwind were detected by the NORAD Perimeter radar (Kling, 1986), of which 285 were cataloged (Nauer, 1992). The number of fragments detected by the Cavalier radar immediately following the breakup was almost twice as many (Badhwar, et al., 1990), which means that nearly half of the fragments had deorbited in the first few hours. As of July, 1992, 11 cataloged objects still remained in orbit (Nauer, 1992). It can be shown that a negative downrange velocity perturbation equal to 2% of the orbital speed would be sufficient to deorbit a fragment immediately from the Solwind breakup altitude.

Gabbard Diagram. Fig. 3 (after Kling, 1986; Nauer, 1992) is the Gabbard diagram of 267 objects as detected by NORAD some 11 hours after the breakup. The Gabbard diagram is one of the earliest tools used in breakup analysis and is a plot of the apogee and perigee heights against the orbital period. The "collapsing arms" for the lower period orbits in Fig. 3 indicates orbital decay and "rounding of orbits" due to atmospheric drag. This is to be expected for the breakup altitude of Solwind (525 km).

A close scrutiny of Fig. 3 reveals the existence of groups of 3 objects clustered together in relatively more elliptic orbits compared with the rest. Since the parent orbit was nearly circular ( $e = 0.0022038$ ), these fragments must have received relatively larger velocity perturbations and most likely came from the same parts of Solwind. Most notable are three pieces in highly elliptic and energetic orbits with large orbital periods. They were certainly ejected with the greatest velocity boosts in the forward direction ( $dv_d$ ). One year later, one was still being tracked, but the other two, having smaller RCSs were eventually lost (Kling, 1986). Speculation about these objects ranged from being insulation material (Kling, 1986) to a clamp (private discussion among orbital debris investigators). In this study, we shall examine the possibility that they are parts of the ASAT projectile which ricocheted from the Solwind encounter.

RCS and Inclination of the Fragments. Fig. 4 (after Kling, 1986) is a plot of RCS vs. inclination of the Solwind fragments from the PARCS data. The dotted

line in the figure marks the inclination of the parent satellite ( $i = 97^\circ.6346$ ). Two interesting observations can be made from the figure. First, the fragments having the largest RCSs suffered smaller inclination changes than those having smaller RCSs, thus indicating a negative correlation between the inclination change and size (RCS). Second, a vast majority of the fragments (including the largest ones) suffered positive inclination changes. Consequently, the net inclination change is positive. This is possible only if the fragmentation is due to collision with a sizeable object and not due to internal explosion (in which case there should be no significant net inclination change). It should be stated that the PARCS RCS values are generally smaller than those generated by the Cavalier radar for the same objects (Kling, 1986) but that does not affect the conclusion just arrived at.

Velocity Perturbations. The velocity perturbations received by the fragments have been calculated from both the USAF Cavalier radar data and the NORAD Perimeter radar data using Eqs. (8), (9) and (10). Since the Cavalier data were taken almost immediately following the breakup whereas the Perimeter data were taken several hours later, only the results derived from the former are discussed here. Fig. 5 (after Badhwar, et al., 1990) is a scatter plot of the three orthogonal components of the velocity changes as calculated from the Cavalier data. The figure reveals groups of 3 or 4 fragments (marked 0, 1, 2 and 3) which had suffered similar velocity changes. As discussed earlier, these objects most probably originated from the same parts of Solwind. Most interesting among them is the group marked by 0. This is the group thrown out with the greatest velocity changes into the highest energy orbits found on the extreme right side of the Gabbard diagram that has been the subject of much speculation.

Fig. 6 is a three-dimensional plot of the velocity perturbations components. The groups of fragments marked 0 and 2 are identified in the figure. Clearly, the group 0 separates itself far apart from the rest of the fragments.

Fig. 7 gives the frequency distributions of  $dv_z$ ,  $dv_d$ ,  $dv_x$  and  $dv$ . The distributions of the velocity components are mainly Gaussian (as would be expected) while that of  $dv$  could be fitted by a Beta function (Badhwar, et al.,

1990). The Gaussian curves are not centered around zeros but displaced, showing clearly the signature of a collision with a sizeable object.

The mean values of  $dv_r$ ,  $dv_d$  and  $dv_x$  are -17.6, -4.9 and 22.5 m/s respectively. Assuming that the net momentum is in the same direction of the average velocity, Badhwar, et al. (1990) determined the probable direction in which the ASAT traversed to hit its target. Using the mean velocity components, we have  $\theta = 103^\circ.1$  and  $\phi = 102^\circ.3$ , which implies that from Solwind's frame of reference, the projectile arrived from slightly above the horizontal plane and from a slightly forward direction from the right. If the masses of all fragments were equal, the parallelism assumption between the velocity and momentum vectors would hold and this would be a conclusive inference from the data.

However, when one takes into consideration the 3 fragments (earlier marked 0) ejected into higher energy orbits, this solution poses a problem. For these objects were ejected in a direction of  $\phi$  between  $-70^\circ$  and  $-80^\circ$ . Overlooking the radial component and viewing from above, these fragments had to be thrown out in the same quadrant as from which the projectile arrived. In other words, they had to be nearly backscattered. It is highly improbable that fragments would be ejected in a backward direction with such great velocities and consequently kinetic energies.

Another way of looking at this problem is from the Earth's frame of reference. If one assumes that the projectile had taken a great circle from Edwards AFB ( $34^\circ.7N$ ,  $117^\circ.8W$ ) to the point of encounter ( $35^\circ N$ ,  $126^\circ W$ ), it would have travelled in a generally westwardly direction and would have hit Solwind from slightly behind. In that case, the projectile arrived from quadrant 3 and the 3 fragments were ejected in quadrant 4. The most probable solution is that these fragments were parts of the ASAT which ricocheted off Solwind, rather than parts of Solwind. If it is found to be true, then this could well be the first observed case of ricochet phenomenon in space. The directions of the fragments are not inconsistent with those observed in ground-based oblique hypervelocity impact data (Schonberg and Taylor, 1989; Schonber, 1990). Furthermore, computational results of the oblique hypervelocity impact phenomenon from both

Eulerian and Lagrangian codes indicate that the ricochet fragments typically attain velocities greater than that of the incoming projectile, which can help explain the large velocity perturbations received by the 3 Solwind fragments. It may be noted that the coordinates of the breakup point were revised from (40°N, 232°E) (Johnson and Nauer, 1986) to (35°N, 234°E) (Nauer, 1992). This analysis would be even more plausible, if the earlier figures were more accurate.

One way of finding the angle of encounter is from velocity considerations. If  $\vec{v}_1$  and  $\vec{v}_2$  are the velocities of Solwind and its interceptor respectively,  $\vec{v}$  the relative velocity of the two and  $\beta$  the angle of encounter, then from the law of cosine, we have (cf. Kessler, 1981):

$$\beta = \cos^{-1} \left[ \frac{v_1^2 + v_2^2 - v^2}{2 v_1 v_2} \right] . \quad (12)$$

If we know  $v_1$ ,  $v_2$  and  $v$ , then  $\beta$  can be calculated from Eq. (12). First,  $v_1$  can be calculated from Eq. (5) giving  $v_1 = 7.6034$  km/s. Also it has been widely reported that  $v = 7$  km/s (*Orbital Debris Mon.*, 1989; Chobotov and Spencer, 1991).

Next,  $v_2$  can be calculated if we assume that the interceptor traversed on a sub-orbital trajectory (cf. Chobotov and Spencer, 1991) and attained its apogee at the point of interception. From Keplerian geometry of the sub-orbital ellipse, we have (Tan, unpublished):

$$v_2 = \left[ \frac{\mu}{a} \frac{1-e}{1+e} \right]^{1/2} . \quad (13)$$

In terms of the height of fragmentation  $h$ , the semi-major axis and eccentricity of the sub-orbital ellipse are given by

$$a = \frac{r_0 + h}{1+e} , \quad (14)$$

and

$$e = \frac{h}{h + r_0 (1 + \cos v)} , \quad (15)$$

where  $v$  is the true anomaly at the take-off point. If  $\delta$  is the angular distance

between the take-off point (Edwards AFB) and the breakup point at the center of the Earth, then  $v = 180^\circ - \delta$ . Further, if  $(\lambda_1, \phi_1)$  and  $(\lambda_2, \phi_2)$  are the coordinates of the two location points, then  $\delta$  can be calculated from (cf. *VNR Encyclopedia of Mathematics*, 1977)

$$\delta = \cos^{-1} [ \sin \lambda_1 \sin \lambda_2 + \cos \lambda_1 \cos \lambda_2 \cos(\phi_2 - \phi_1) ] \quad (16)$$

On putting the values, we obtain  $\delta = 6^\circ.734$  whence  $v_2 = 2.566$  km/s and finally,  $\beta = 65^\circ.63$ , an acute angle. This is consistent with our previous solution that the projectile arrived from quadrant 3.

An alternative method to determine the angle of encounter is from the inclinations of the target and the interceptor orbits. If  $i_1$  and  $i_2$  are the inclinations of the orbits of Solwind and the ASAT respectively and  $\lambda$  is the latitude of the fragmentation point, then from Eq. (11):

$$\beta = \cos^{-1} \frac{\cos i_1 \cos i_2 + [(\cos^2 \lambda - \cos^2 i_1)(\cos^2 \lambda - \cos^2 i_2)]^{1/2}}{\cos^2 \lambda} \quad (17)$$

$i_2$  can be calculated from the "launch azimuth"  $\gamma$ . From Bate, et al. (1971):

$$i_2 = \cos^{-1} ( \sin \gamma \cos \lambda ) \quad (18)$$

Since the take-off point and the breakup point are relatively close, we have approximately:

$$\gamma = \tan^{-1} \left[ \frac{\phi_2 - \phi_1}{\lambda_2 - \lambda_1} \right] \quad (19)$$

On substituting the values, one gets  $\gamma = -87^\circ.9$ ,  $i = 144^\circ.9$  and  $\beta = 77^\circ.87$ , once again an acute angle.

$i_2$  can also be calculated from the ground trace of the interceptor, which is a great circle given by (cf. Fox, 1987)

$$\tan \lambda = A \cos(\phi + \alpha) \quad (20)$$

where  $\lambda$  is the latitude,  $\phi$  the azimuth angle and  $A$  and  $\alpha$  are constants. The constants can be determined by substituting from the coordinates of the take-off

and breakup points, giving

$$\alpha = \tan^{-1} \left[ \cot \frac{\phi_2 - \phi_1}{2} \frac{\tan \lambda_1 - \tan \lambda_2}{\tan \lambda_1 + \tan \lambda_2} \right] - \frac{\phi_1 + \phi_2}{2} , \quad (21)$$

and

$$A = \tan \lambda_1 \sec(\phi_1 + \alpha) = \tan \lambda_2 \sec(\phi_2 + \alpha) , \quad (22)$$

whence  $i_2 = \lambda_{\max} = \tan^{-1}A$  or  $180^\circ - \tan^{-1}A$  (for retrograde orbits). On substituting the values, we get  $i_2 = 145^\circ.0$  and  $\beta = 80^\circ.71$ , once again, an acute angle. Thus all three analyses indicate that the interceptor arrived from quadrant 3.

Angular Distribution. The angular distribution of the fragments are obtained by calculating the angles  $\theta$  and  $\phi$  for each fragment and plotting them. Fig. 8 is analogous to a Mercator's projection plot of the fragments. Clearly the distribution is not isotropic. A major concentration area is found around  $(\theta_1 = 155^\circ, \phi_1 = 100^\circ)$  and a secondary concentration area is found near  $(\theta_2 = 100^\circ, \phi_2 = 80^\circ)$ . The secondary concentration area is where the ASAT might have impacted Solwind according to the alternative solution discussed earlier. However, there is no concentration of fragments near its anti-podal point to mark the exit area. Secondly, there is no proper explanation of the major concentration area. If it represents the exit area of the ASAT fragments, then the angle between the entry and exit directions is given by (cf. Arfken, 1985):

$$v = \cos^{-1} [ \cos \theta_1 \cos \theta_2 + \sin \theta_1 \sin \theta_2 \cos (\phi_2 - \phi_1) ] . \quad (23)$$

On putting the values, we have  $v = 56^\circ.7$ , an acute angle. It is virtually improbable for the ASAT fragment to get backscattered in this direction.

Change in Average CSA. From geometrical considerations, Tan (1993) calculated the average CSAs of flat plates, various types of hollow rectangular solids, cylinders, cones, etc. and the total average CSAs when these solids undergo thorough fragmentations. From the known dimensions, the average CSAs of the Solwind main body, solar panel and interceptor are calculated to be:  $\langle S \rangle_{\text{body}} = 3.14 \text{ m}^2$ ,  $\langle S \rangle_{\text{panel}} = 1.77 \text{ m}^2$  and  $\langle S \rangle_{\text{interceptor}} = 0.09 \text{ m}^2$ .

It was observed that the total RCS of the largest 250 fragments of Solwind alone was several times greater than the RCS of the parent satellite (Remillard, 1990). Now the RCS of an object is not exactly the same as its CSA. The RCS, like the CSA, of course varies with the orientation of the object. Sometimes, there is almost an order of magnitude variation in the measured RCS of the same object. The RCS of orbiting satellites are therefore averaged and entered in the catalog (cf. USSPACECOM RCS Catalog). The functional relationship between RCS and CSA have been obtained by Badhwar and Anz-Meador (1989) after analyzing data from hundreds of orbiting satellites, rocket bodies and debris. If  $\langle R \rangle$  is the average value of the RCS, then the CSA averaged over all orientations is

$$\langle S \rangle = 0.5712 \langle R \rangle^{0.7666} . \quad (24)$$

There are three possibilities as to the actual fate accorded to Solwind: (1) the solar panel only was hit and the main body survived; (2) the main body was hit and fragmented but the solar panel survived intact; and (3) both the main body and solar panel were fragmented. In order to determine what actually happened, let us recall that the fragmentation of the solar panel (flat plate) would not increase the average CSA but the fragmentation of the main body would (Tan, 1993). Since there was a several-fold increase in the RCS of the fragments, the first possibility is ruled out. Hence the main body of the satellite was hit. As for the second possibility, we find that the RCS of the largest fragment was only  $1.44 \text{ m}^2$ , which according to Eq. (13) translates to an average CSA of only  $0.76 \text{ m}^2$ . Since the largest fragment (whether it came from the main body or the panel) had a smaller average CSA than that of the solar panel ( $\langle S \rangle_{\text{panel}} = 1.77 \text{ m}^2$ ), the solar panel must also have fragmented. That leaves us with the third and only possibility that both the main body and the solar panel of P-78 were destroyed in the event.

To quantify this breakup a little further, the RCSs of the 267 largest fragments were converted to their average CSAs by means of Eq. (13) and the aggregate CSA of the fragments summed out to be  $16.56 \text{ m}^2$ . Subtracting  $\langle S \rangle_{\text{panel}}$  (which does not change in the fragmentation), we obtain the average CSA of the

body fragments  $\langle S \rangle_{\text{body fragments}} = 14.79 \text{ m}^2$ . Since  $\langle S \rangle_{\text{body}} = 3.14 \text{ m}^2$ , there was at least a 4.71-fold increase in the average CSA in the breakup of the main body. Since the fragmentation of a hollow cylinder merely doubles the average CSA (Tan, 1993), the balance must have been contributed by the internal contents of the main body. This dramatic increase in the average CSA illustrates the fact that the satellite was densely packed with instruments and suffered a thorough fragmentation as a result of the impact.

Computations. Numerical models belonging to two different categories (viz., empirical and analytical) were employed to study the P-78 fragmentation event. The numerical model IMPACT was developed by Aerospace Corporation to simulate satellite fragmentation events due to explosions and collisions (Chobotov and Spencer, 1991). It was originally written to predict the fragment products of the Solwind P-78 and Delta 180 experiments and later modified after the actual test data and also to accommodate data from explosive fragmentation events. The MAGI program is one of several analytical codes currently operational at Phillips Laboratory's Space Kinetic Impact and Debris Branch in Kirtland AFB. It is an SPH (Smoothed Particle Hydrodynamics) code based on the Lagrangian (i.e., finite element) scheme. Its major advantage over an Eulerian code like the CTH is its speed and efficiency.

Empirical Model. An updated version 2.02 of IMPACT was used in this study. The orbital elements and fragmentation data of Table I were used as input. The relative velocity between the target and the projectile was taken to be 7 km/s. IMPACT makes a distinction between a "head-on collision" and a "glancing-blow collision" (Chobotov and Spencer, 1991). The head-on collision is designated for impact between a large object and a small one and was chosen as the proper one for the P-78 scenario. According to IMPACT, the target suffered a thorough fragmentation, producing over 20,000 particles (Fig. 9), including 358 trackable ones (fragments larger than 10 cm in diameter). The latter compares with 285 objects cataloged by NORAD several hours after the event. Since many fragments had reentered the atmosphere by then, this comparison is considered as a favorable one.



According to IMPACT, there were four fragments greater than 1 m in diameter, the largest one having a diameter of 1.445 m (which corroborates with the Cavalier radar data). The distribution of fragments had a sharp peak between 1 and 2 cm (Fig. 9). The shape of the distribution was generally triangular (as normally assumed by debris modellers) but tapered off like a Gaussian curve on either end.

Fig. 10 is the Gabbard diagram of P-78 as generated by IMPACT 2.02. As expected, it exhibits the classic "X" form devoid of signs of decay. It is more orderly compared with the actual Gabbard diagram (Fig. 3) without the "clusters" of fragments around the parent orbit. The ranges of the time periods are similar with the exception of the 3 objects discussed earlier.

Fig. 11 is a plot of the eccentricity against the semi-major axis of the Solwind fragments as generated by IMPACT. The classic "V" shape, unperturbed by atmospheric drag is evident in the figure. The fragments along the arms of the V were driven by the downrange velocity perturbations while those inside the V were driven by the radial velocity perturbations (cf. Johnson, 1987)

Analytical Model. The Solwind satellite was approximated by a hollow cylindrical drum made up of aluminum alloy having a diameter  $d = 2.1$  m, length  $l = 1.3$  m, thickness  $t = 2.1$  cm and density  $\rho = 2.7$  g/cc. With these values, the mass of the satellite as given by

$$m = \frac{1}{2} \pi \rho t [ 4 t^2 - 2 t (l + 2 d) + d (2 l + d) ] \quad (25)$$

turns out to be 858.3 kg. This compares with the actual mass of 850 kg (cf. Nauer, 1992) for the satellite proper. The total mass of Solwind, including the solar panel was reported to be 878 kg (Remillard, 1990).

The interceptor was approximated by a solid cylinder of aluminum alloy having length and diameter both equal to 19.6 cm and mass 15.97 kg. This compares with the actual length of 33 cm, diameter 30.5 cm and mass 15.88 kg (Remillard, 1990).

A vertical impact scenario of the interceptor with Solwind perpendicular to its axis was first considered and later, oblique impact models were planned.

Both 2- and 3-dimensional MAGI codes were tried. But as of this writing, successful completion of the runs have not been achieved. It may be stated that a projectile size of this magnitude have not been considered before. Efforts to resolve this problem are still being undertaken at this time.

#### ACKNOWLEDGEMENTS

The author is thankful to the Air Force of Scientific Research and Research and Development Laboratories for funding this project. Dr. Firooz A. Allahdadi, Chief of Space Kinetic Impact and Debris Branch of Phillips Laboratory selected this proposal and provided useful direction while Lt. Scott Maethner performed the computations for this study. Their efforts are hereby thankfully recorded.

#### REFERENCES

- Aerospace America, Nov. 1985, p.10.
- G. Arfken, *Mathematical Methods for Physicists*, Academic Press, New York, 1985.
- Aviation Week and Space Technology, 23 Sept. 1985.
- G. D. Badhwar and P. D. Anz-Meador, *Earth, Moon and Planets*, 45, 29, 1989.
- G. D. Badhwar, A. Tan and R. C. Reynolds, *J. Spacecr. and Rockets*, 27, 299, 1990.
- R. R. Bate, D. D. Mueller and J. E. White, *Fundamentals of Astrodynamics*, Dover, New York, 1971.
- F. J. Benz, C. V. Bishop and M. B. Eck, *Proc. Upper Stage Breakup Conf.*, Houston, May 1987.
- V. A. Chobotov and D. B. Spencer, *J. Spacecr. Rockets*, 28, 670, 1991.
- C. Fox, *An Introduction to the Calculus of Variations*, Dover, New York, 1987.
- N. L. Johnson, *Teledyne Brown Engg. Rept. CS87-LKD-003*, 1987.
- N. L. Johnson and D. J. Nauer, *History of On-Orbit Satellite Fragmentation*, 3rd Ed., Teledyne Brown Engg. Rept. CS88-LKD-001.
- D. J. Kessler, *Icarus*, 48, 39, 1981.
- R. Kling, *Postmortem of a Hypervelocity Impact*, Teledyne Brown Engg. Rept. CS86-LKD-001, 1986.
- D. J. Nauer, *History of On-Orbit Satellite Fragmentations*, 6th Ed., Teledyne

Brown Engg. Rept. CS92-TR-JSC-007, 1992.

*Orbital Debris Mon.*, 2(2), 5, 1989.

J. W. Powell, *J. Brit. Interplanet. Soc.*, 40, 513, 1987.

S. K. Remillard, *Master's Thesis*, Air Force Institute of Technology, 1990.

W. P. Schonberg and R. A. Taylor, *AIAA J.*, 27(5), 639, 1989.

W. P. Schonberg, *J. Aerospace Engg.*, 3(3), 173, 1990.

A. Tan, *USAF Phillips Lab. Int. Rept. WSSD-93-01*, June 1993.

P. Van de Kamp, *Elements of Astromechanics*, Freeman, San Francisco, 1964.

*VNR Encyclopedia of Mathematics*, Van Nostrand Reinhold, New York, 1977.

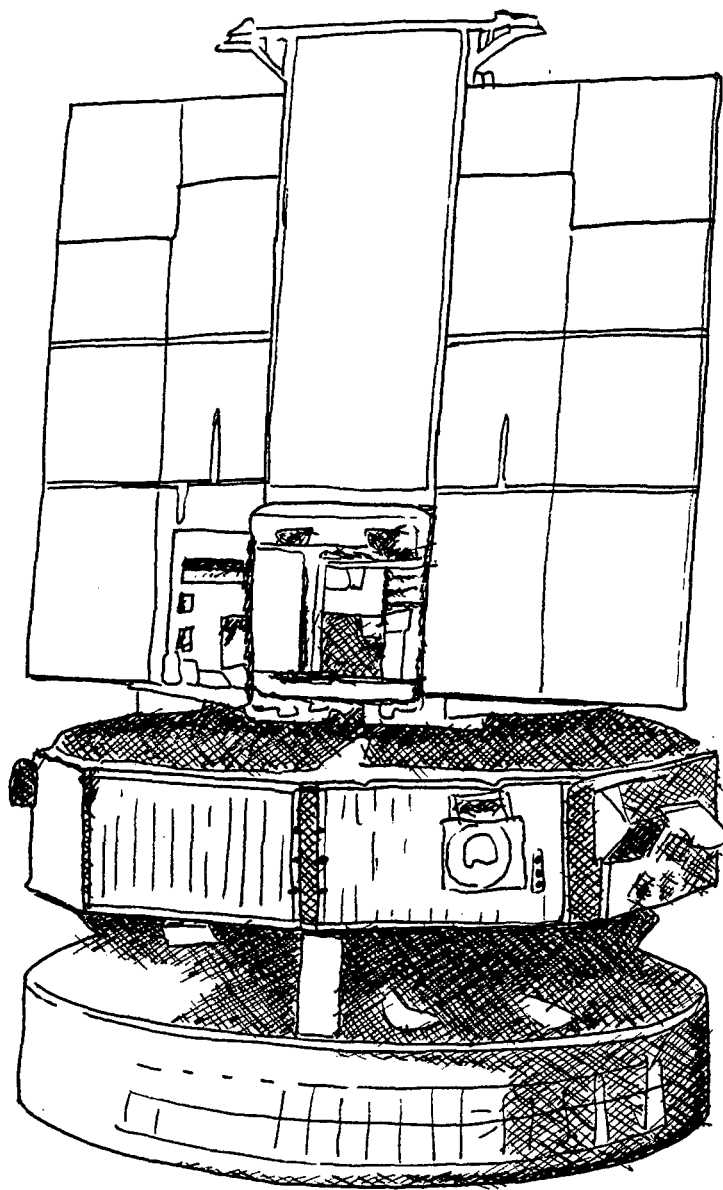


Fig. 1. Sketch of Solwind P78-1 satellite before fragmentation.

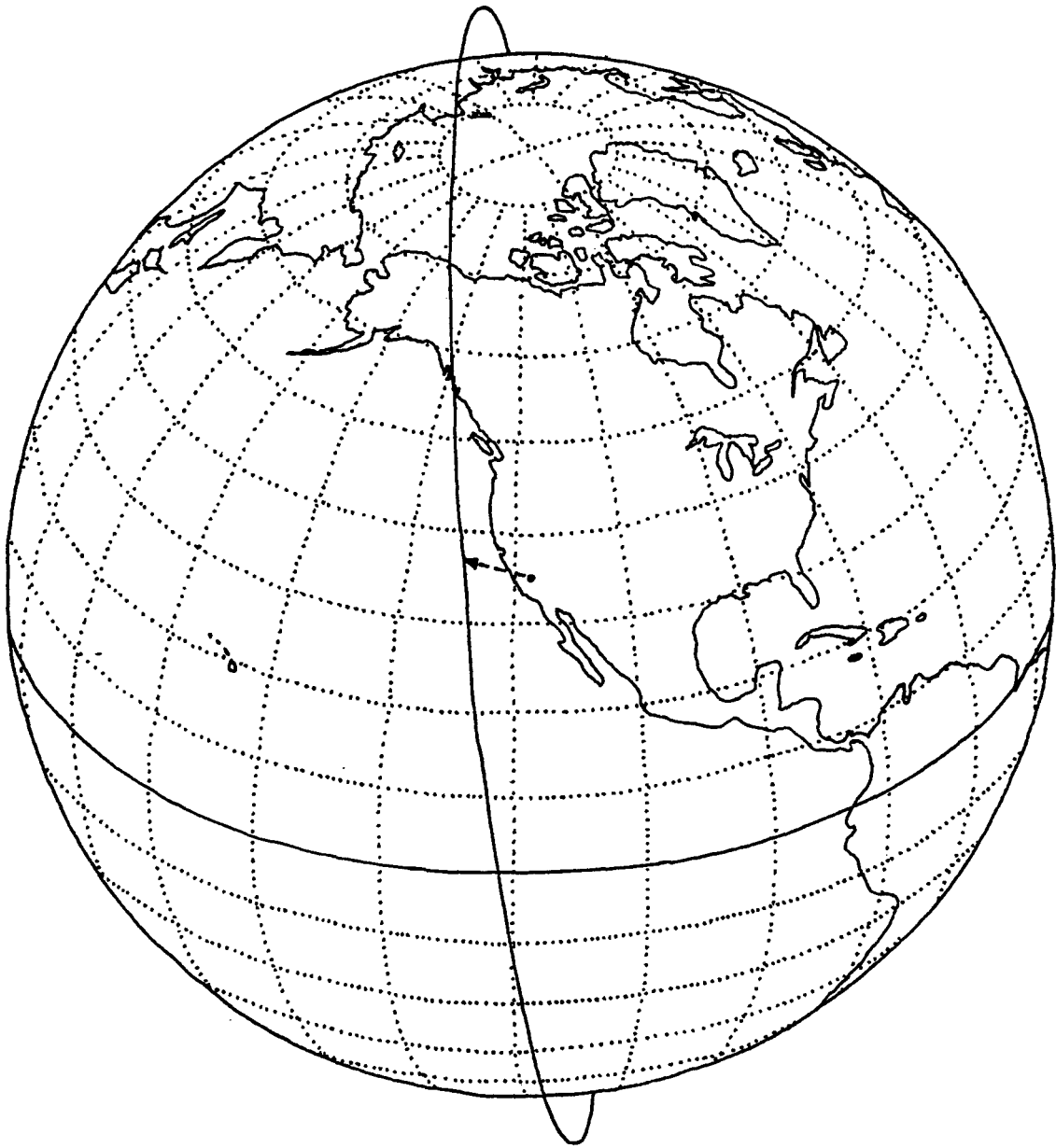


Fig. 2. Overhead view of the Solwind encounter.

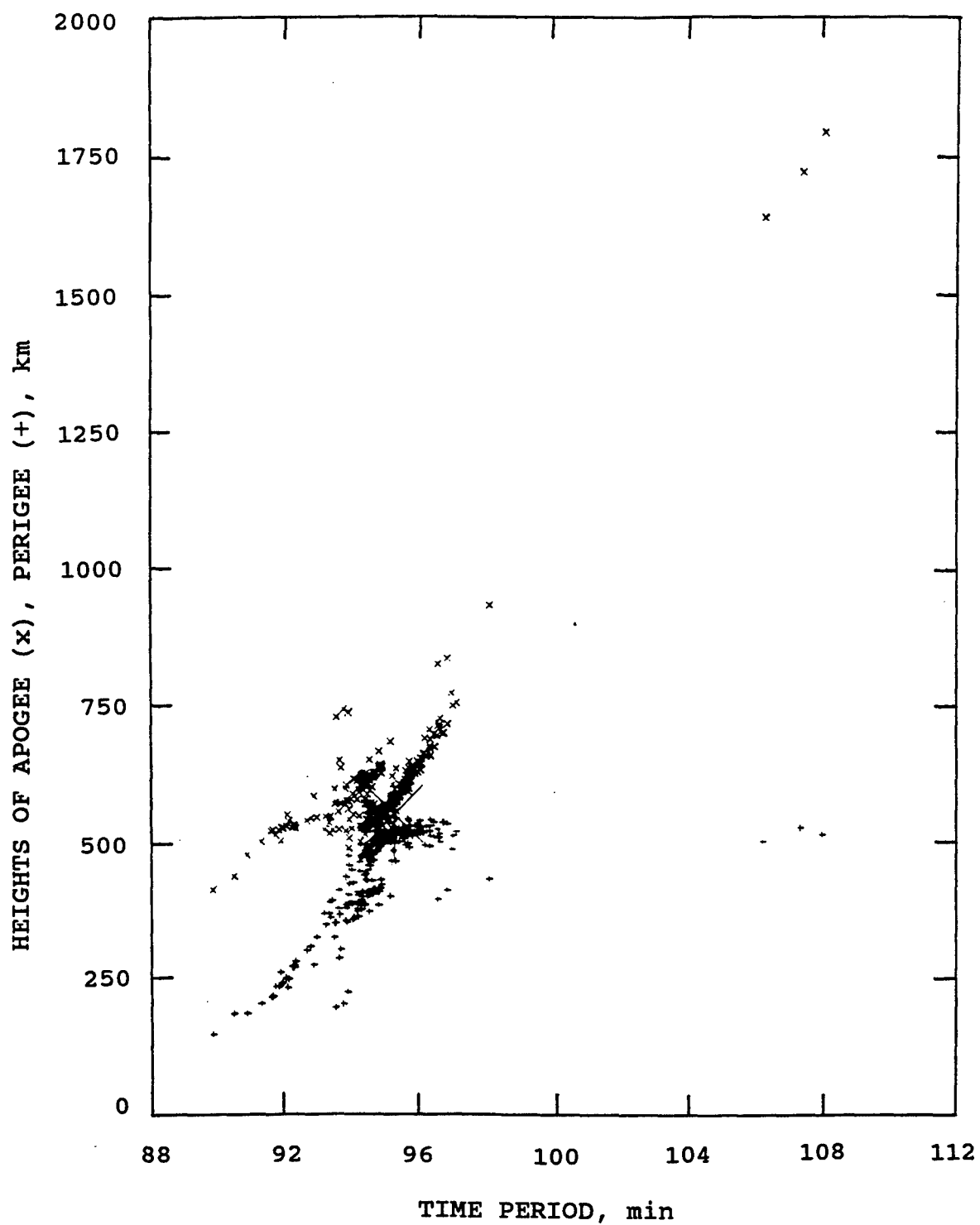


Fig. 3. Gabbard Diagram of Solwind Fragments.

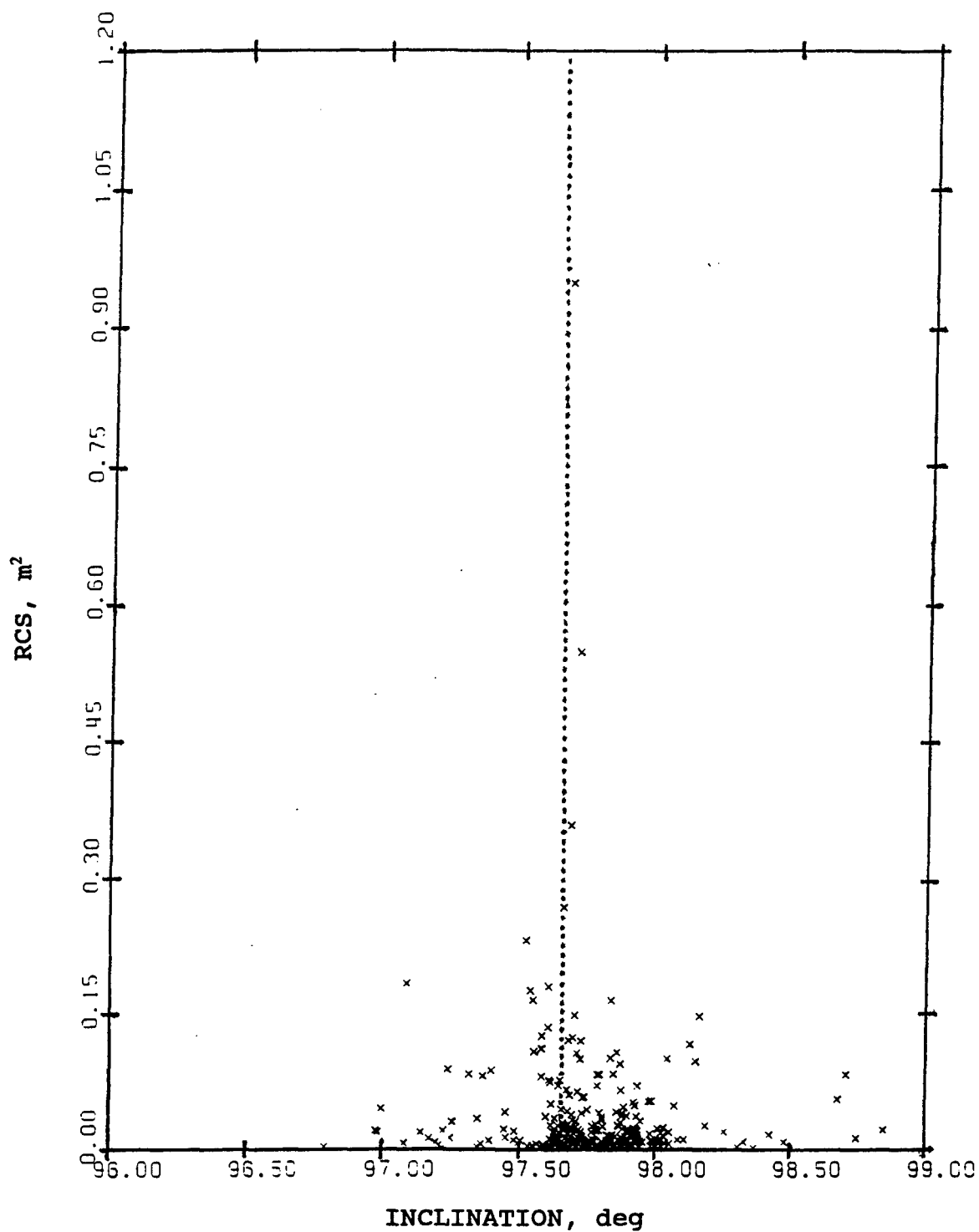


Fig. 4. RCS vs. Inclination of the Solwind Fragments.

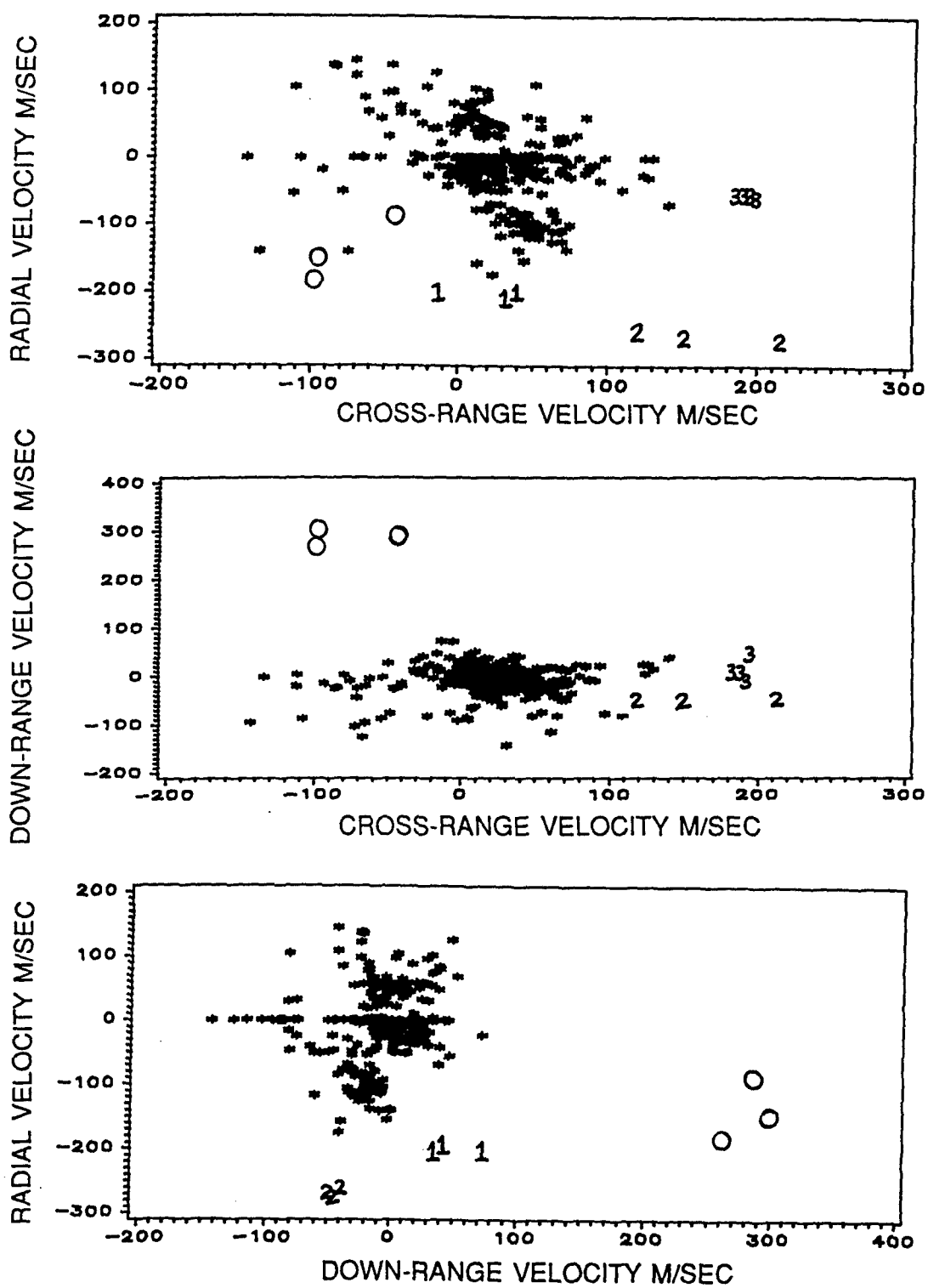


Fig. 5. Scatter Plots of the Velocity Perturbations Components.



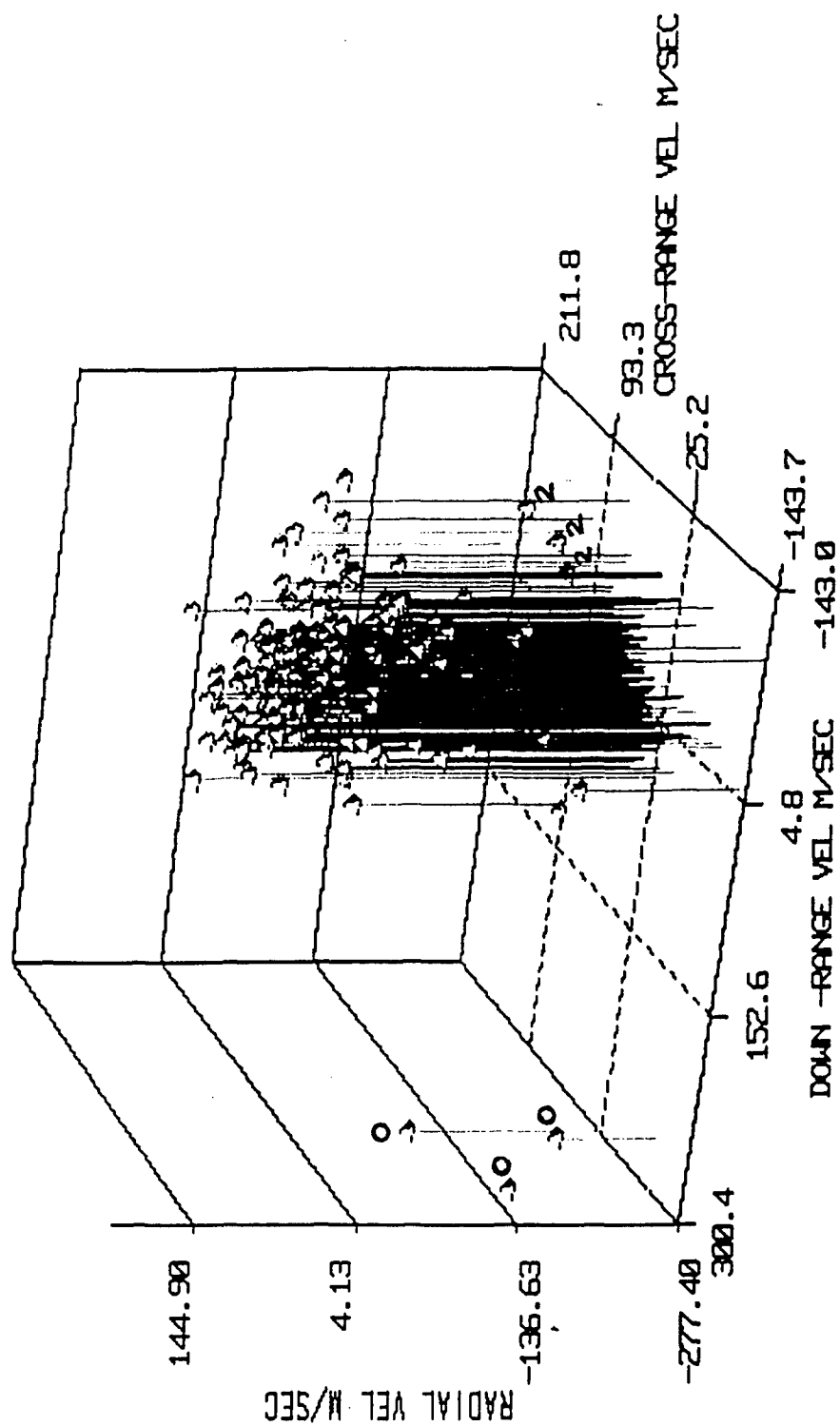


Fig. 6. Three-dimensional plot of the Velocity Perturbations Components.

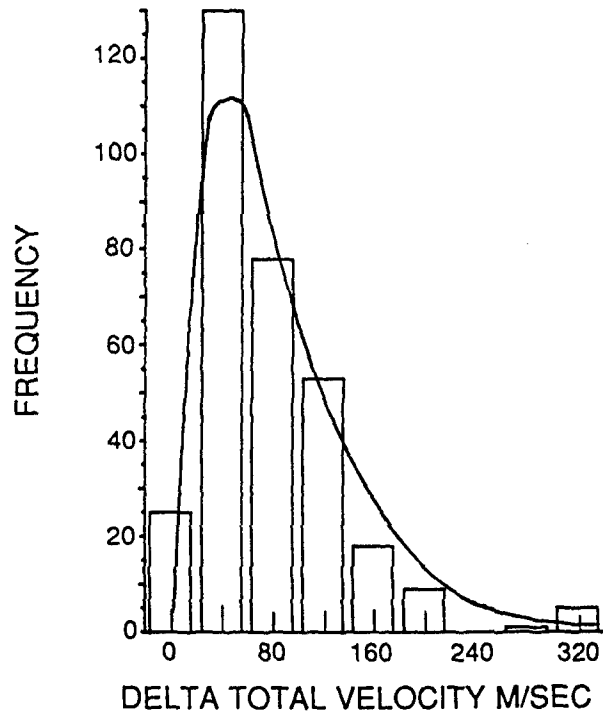
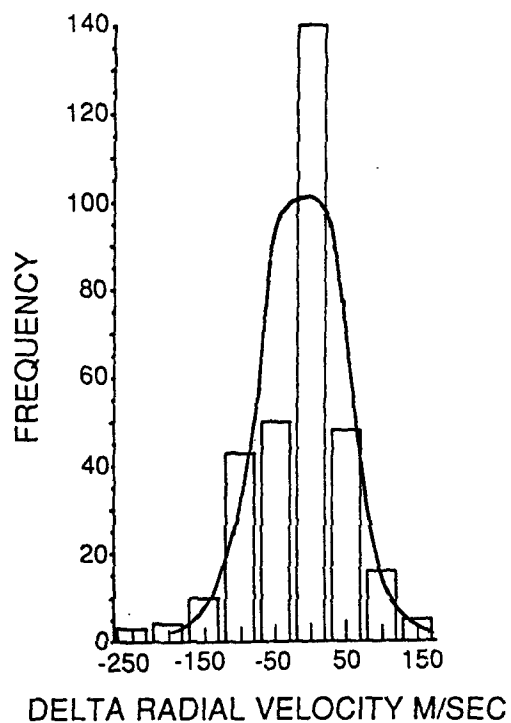
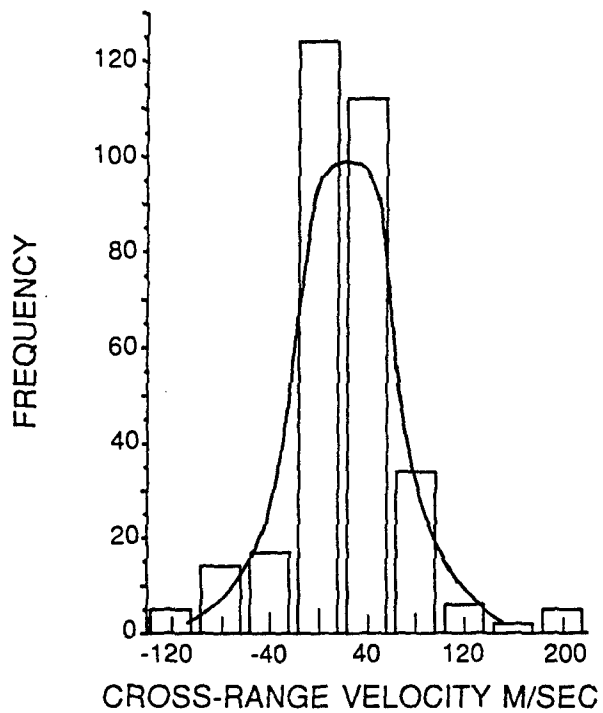
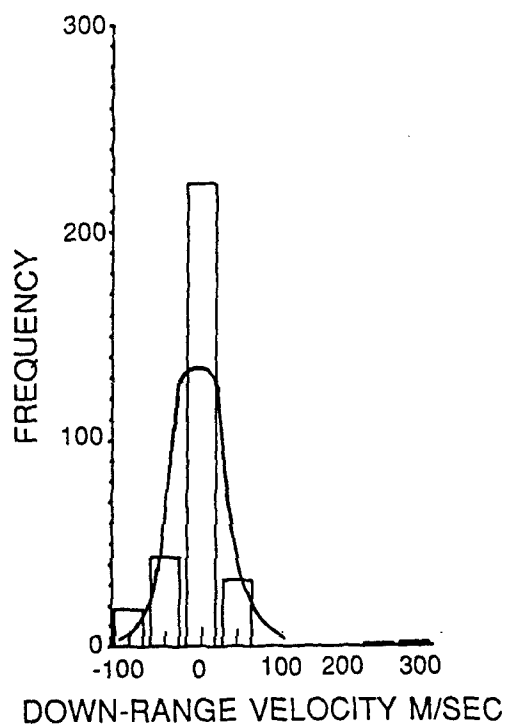


Fig. 7. Histograms of  $dv_r$ ,  $dv_d$ ,  $dv_x$  and  $dv$ .

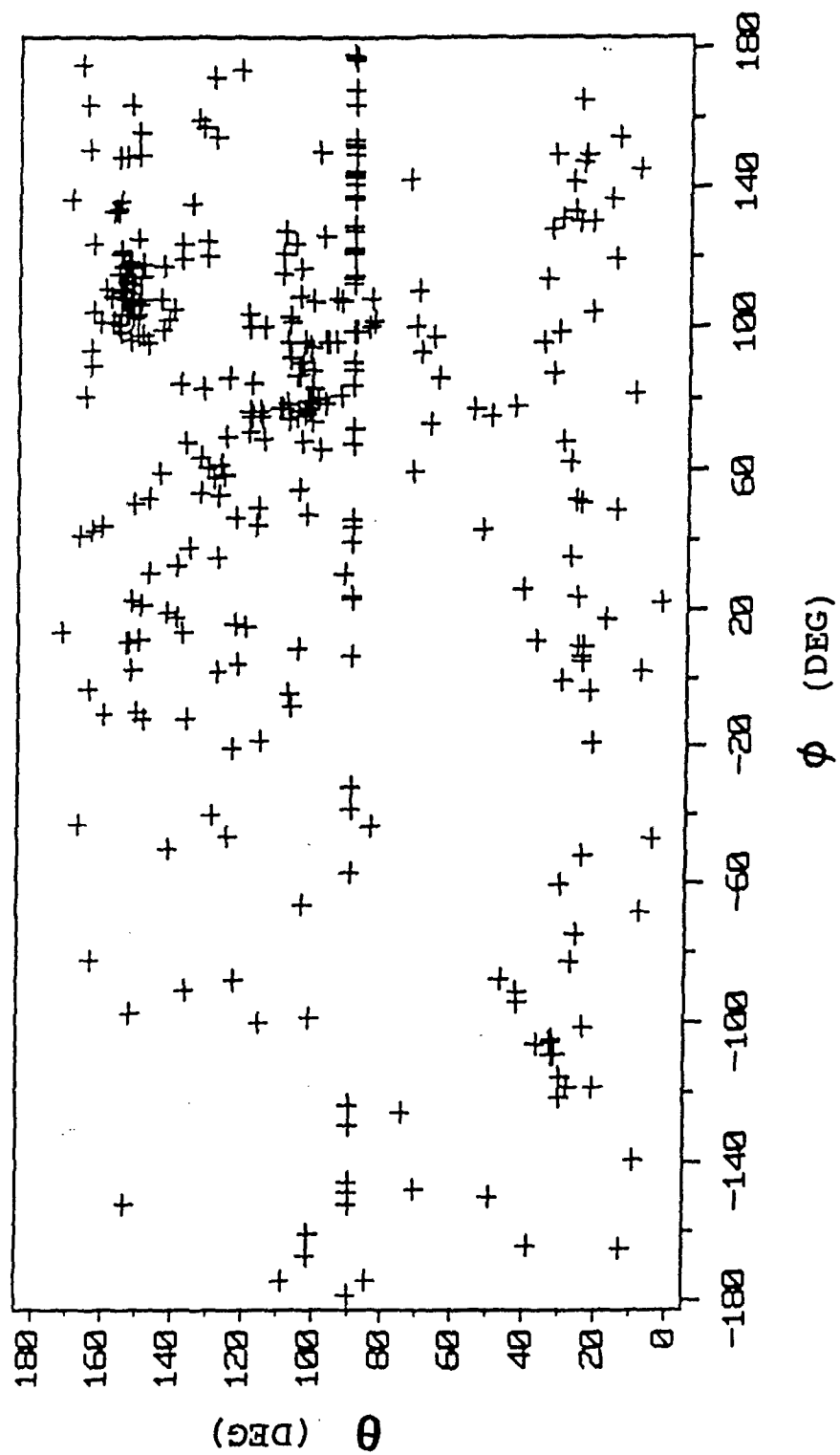


Fig. 8. Angular Distribution of the Fragments.

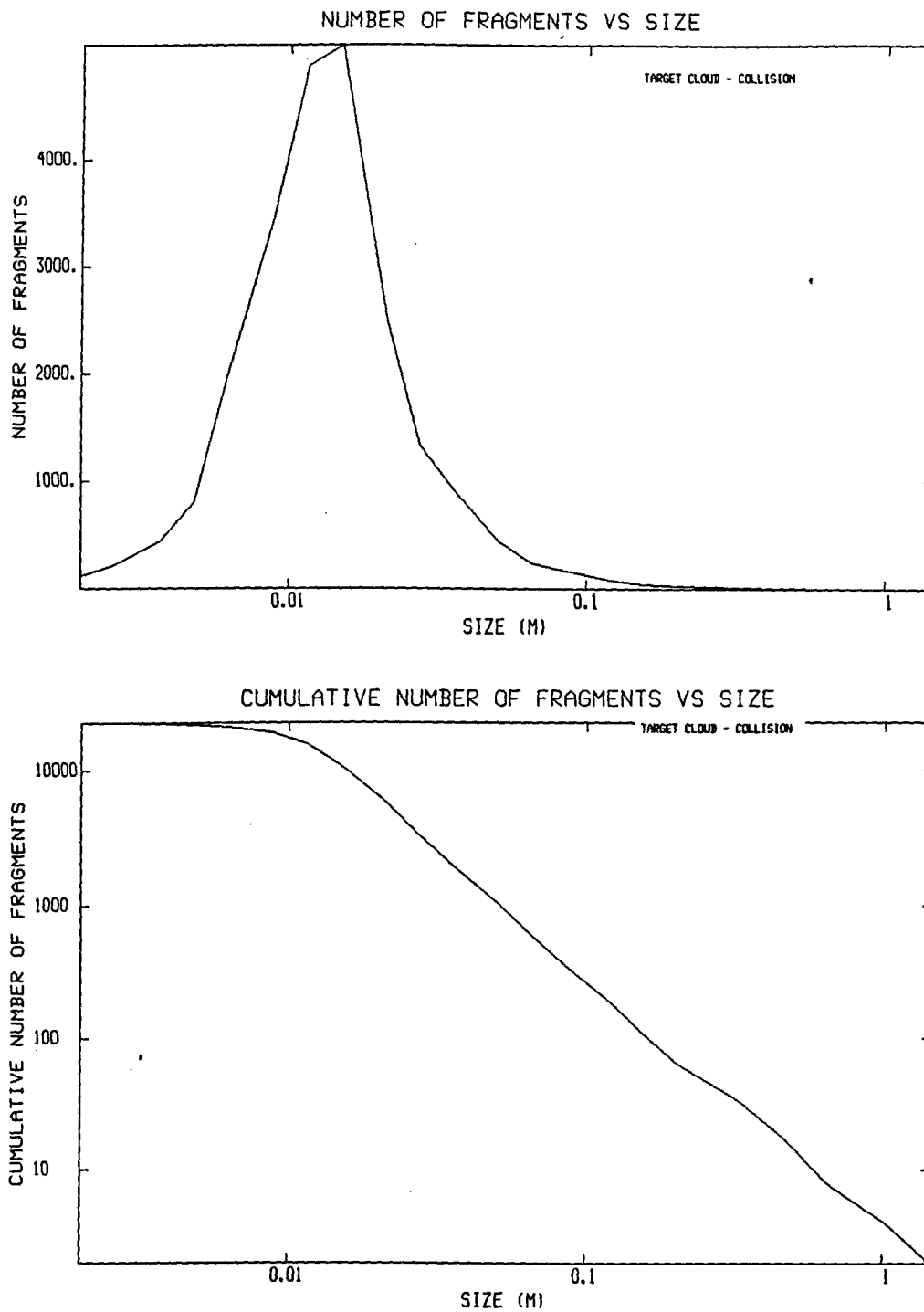


Fig. 9. Size and Cumulative Size Distributions of the Fragments.

# GABBARD DIAGRAM (358) FRAGMENTS

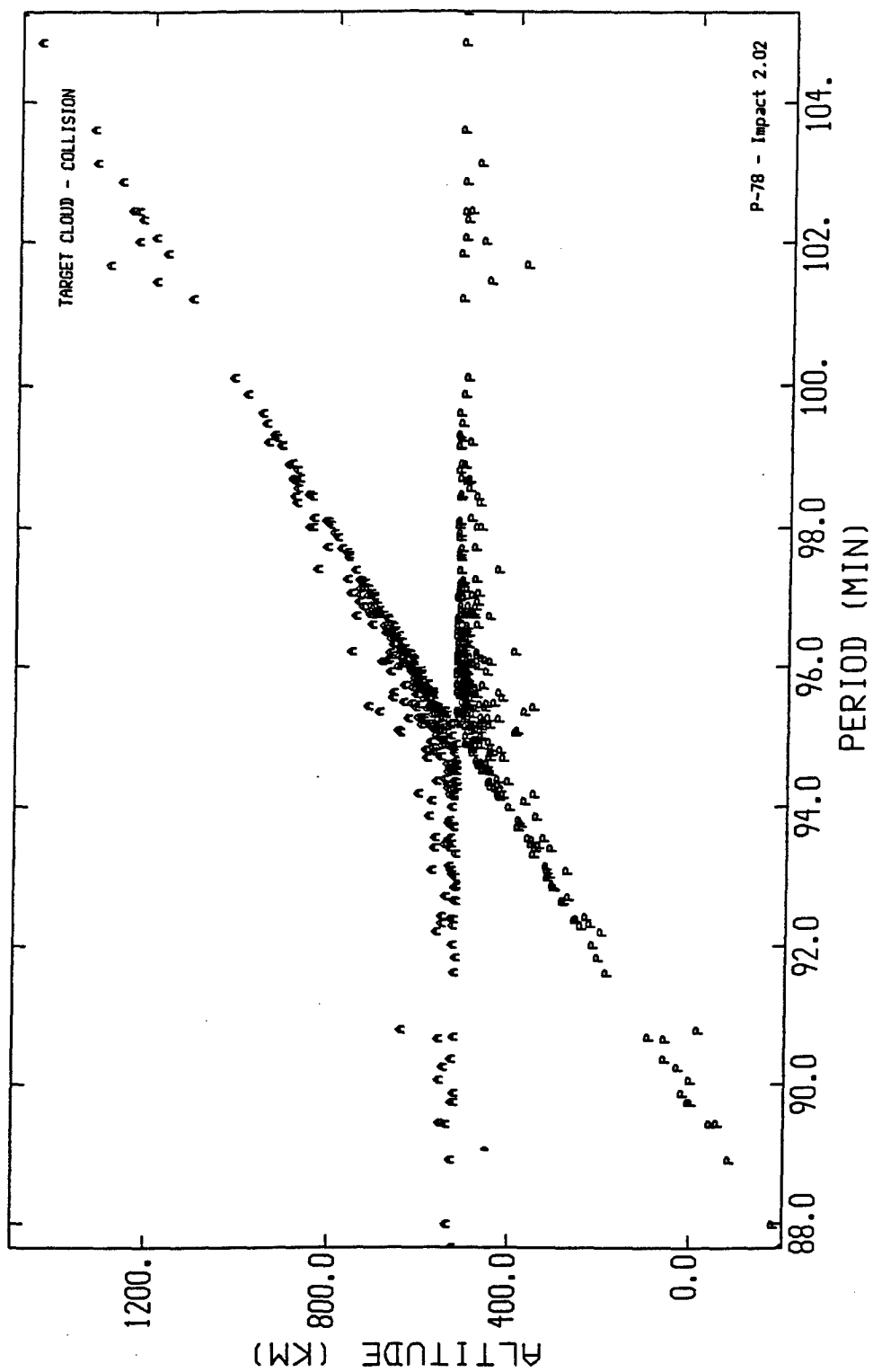


Fig. 10. Gabbard Diagram of Solwind fragments as generated by IMPACT.

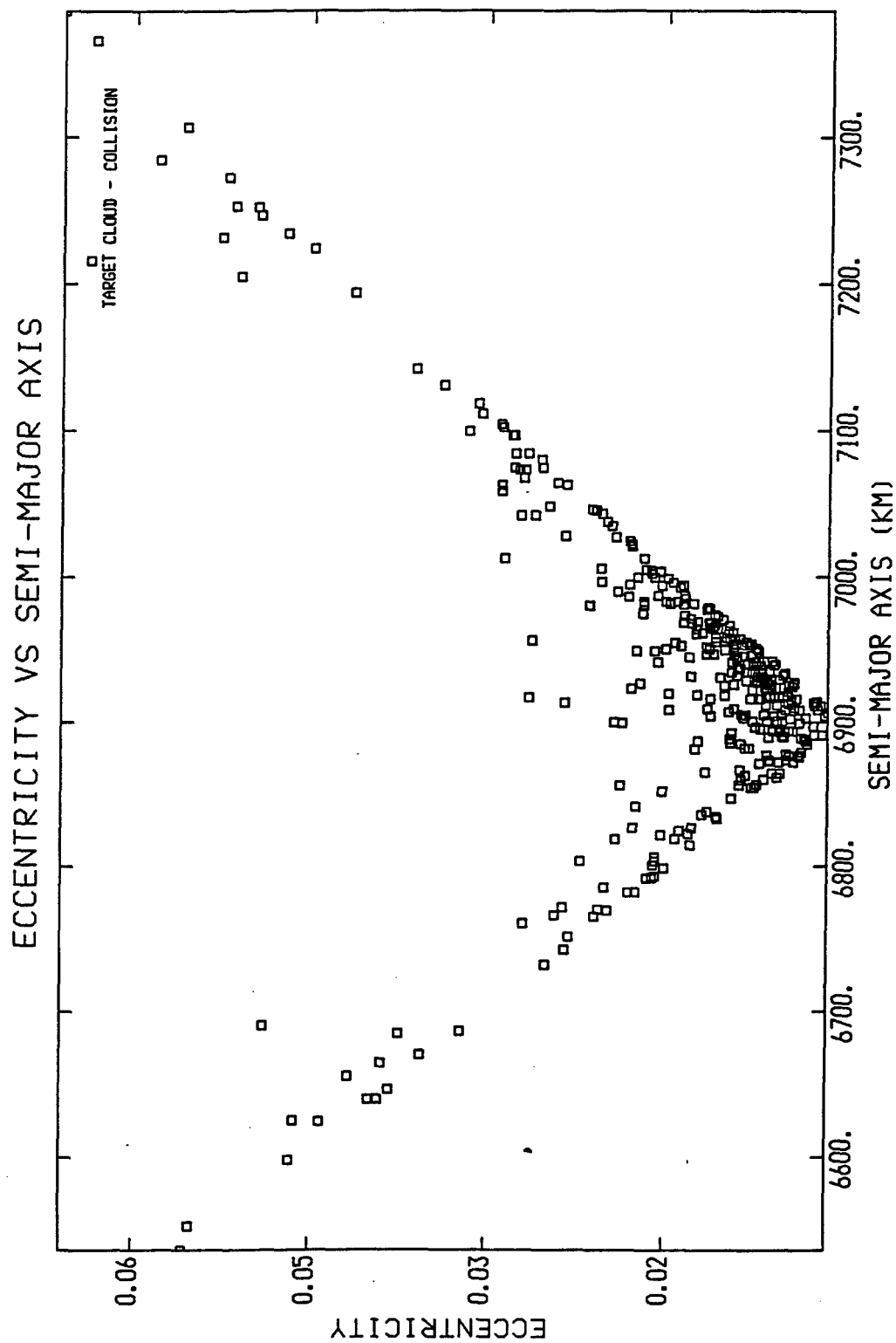


Fig. 11. Eccentricity vs. Semi-major axis of solwind fragments as predicted by IMPACT.

**THE IMPACT OF CONDENSING WATER VAPOR IN  
CHEMICAL OXYGEN IODINE LASERS**

**Philip D. Whitefield  
Research Associate Professor  
Departments of Physics and Chemistry**

**Donald E. Hagen  
Associate Professor  
Department of Physics**

**and**

**W. Mark Barnett  
Graduate Student  
Department of Chemistry**

**Cloud and Aerosol Sciences Laboratory  
University of Missouri-Rolla  
Norwood Hall G-7  
Rolla, MO 654041**

**Final Report for:  
Summer Research Extension Program  
Phillips Laboratory (PL/LIDB)**

**Sponsored by:  
Air Force Office of Scientific Research  
Bolling Air Force Base, Washington, D.C.**

**and**

**University of Missouri-Rolla**

**April 1994**

THE IMPACT OF CONDENSING WATER VAPOR IN  
CHEMICAL OXYGEN IODINE LASERS.

Philip D. Whitefield  
Research Associate Professor  
Departments of Physics and Chemistry  
and  
W. Mark Barnett  
(Graduate Student - Chemistry)  
Cloud and Aerosol Sciences Laboratory  
University of Missouri - Rolla

Abstract

This final report describes the results and interpretation of a joint research project sponsored by (i) AFOSR through its SRE, SFR and GSR programs and (ii) the University of Missouri - Rolla, to investigate the impact of condensing water vapor in the reacting flow regimes of chemical oxygen iodine lasers (COIL's). The "condensation shock phenomenon" first reported in 1991 has been successfully simulated and recreated under non-reacting flow conditions in two independent COIL devices. The two-phase singlet oxygen generator has been identified as the major source of particulates (condensation nuclei), especially those upon which heterogeneous nucleation can take place. These particulates have been characterized in terms of size distribution, total concentration, hydration and dependence on typical generator operating parameters such as chlorine flow rate, disc rotation rate, basic hydrogen peroxide concentration and temperature. Based on the heterogeneous nucleation characterization and known heat released into the laser supersonic flow during the "condensation shock" it is reasonable to conclude that both homogeneous and heterogeneous nucleation are responsible for water vapor condensation in the COIL devices, however, homogeneous nucleation is the dominant step in "condensation shock". Furthermore, the onset of the shock is readily observed at very low BHP temperatures.



# THE IMPACT OF CONDENSING WATER VAPOR IN CHEMICAL OXYGEN IODINE LASERS.

Philip D. Whitefield and Wm. Mark Barnett

## INTRODUCTION

Water vapor, when supersaturated, will spontaneously condense both heterogeneously and homogeneously, growing water droplets or aerosols provided the appropriate supersaturation is sustained. Heterogeneous nucleation requires the presence of condensation nuclei (CN) in the flow. The soluble mass fraction of the CN will determine its critical supersaturation spectrum which in turn determines the specific water vapor supersaturation for a given CN to grow without bound. Heterogeneous nucleation occurs at low supersaturations of water vapor typically  $< 5\%$ . At very high water vapor supersaturations homogeneous nucleation will occur. In this case it is thermodynamically favorable for molecules of water vapor to spontaneously cluster to form aerosols. In both cases the concomitant heat of condensation will be released into the gas flow. The criteria for both types of nucleation exist in supersonic COIL's and a massive heat release has been reported immediately following the supersonic expansion in several devices, especially where the water vapor pressure in the gas flow was thought to be high (typically 5 mole%).[1] Any increase in temperature in the cavity will manifest itself as a ramp in the laser cavity pressure profile, and will diminish the gain of the laser and reduce the optimum laser performance.[2] The relative importance of either type of nucleation channel must be determined for COILs if the impact of condensing water on the devices is to be characterized.

This report describes how the UMR Mobile Aerosol Sampling System (MASS) is being used in conjunction with a small scale supersonic COIL device (SSSC) to continue a study, initiated in 1992,[3,4] investigating the impact of condensing water vapor on the performance of COIL devices. The conclusions and recommendations from the 1992 study were as follows[3,4]:

- o Heterogeneously nucleated aerosols are present in COILs.
- o They are mechanically produced in the generator and their production rate and

size are governed by generator operating parameters.

- o The relationship between these parameters and aerosol production should be explored in detail.
- o The limits of detectability of aerosols using the UMR-MASS in its current state of the art configuration may have led to an underestimate of the total concentration of aerosols produced in the generator. As a result of the studies to date, design upgrades should be made to the sampling probe system and counting system to customize the UMR-MASS to this COIL investigation
- o The inability to simulate the pressure ramp in the supersonic nozzle flow system indicates that the pressure ramp is not a simple gas dynamic effect arising from the enthalpy of condensation associated with a homogeneous nucleation event.
- o The calculations upon which the homogeneous nucleation rational are based should be re-examined.
- o The principles of operation and performance of the spray generator concepts, as singlet oxygen generators for COIL's, should be examined to determine whether submicron aerosol formation will occur in these devices and whether it will affect their predicted performance.

The investigative approach in the preliminary study relied upon the UMR MASS to characterize any heterogeneous nucleation. In this very limited study although heterogeneous nucleation was observed it was not possible to correlate nucleus formation to generator operating parameters, or to quantify total nucleus production concentrations. As a result, it was impossible to determine what proportion of the heat release driving the pressure ramp in the cavity was due to heat of heterogeneous condensation. Using the experience gained from the preliminary studies a methodology was rationalized, to complete the characterization of the heterogeneous processes. The methodology and results of these experiments are described below.

Attempts were also made, in the preliminary study, to simulate or recreate the cavity pressure profile ramp downstream of a particle free supersonic expansion of a water laden gas flow, the rationale being that the cavity pressure profile ramp was a physical indication of a

purely gas dynamic "condensation shock"[5]. These experiments were not successful. Once again, based on the experience gained in the preliminary study a methodology was rationalized and a series of experiments were carried out to test the negative results of the preliminary study. This approach has led, in 1993, to several successful demonstrations of the condensation shock phenomena. The methodology and results of these experiments are, also described below.

## METHODOLOGY

The basic methodology behind the condensation shock phenomenon experiments has been described previously [3,4] and will not be repeated here. A novel approach in the 1993 studies involved the use of a pitot tube pressure sensor to define the boundary layers in the various COIL's examined in this study. The pitot tube methodology is described below. The heterogeneous nucleation experiment methodologies are those of the UMR MASS and have been described in detail elsewhere [6-8] and therefore only a brief summary will be given here. The setup and operation of the laser device and supersonic nozzle facility is not described in this report. Detailed descriptions of this activity can be found elsewhere [9,10].

*The Pitot Tube - design and principles of operation:* In order to better understand the nature of the boundary layers in the nozzle and cavity flow regimes of the various COIL devices at our disposal during this study, a pitot tube was designed and constructed to measure the total pressure profile as a function of the vertical displacement of the pitot tube at various positions along the flow axis of the cavity, but in particular close to the expansion nozzles. Flow velocity can be interpreted in terms of "static" and "dynamic" pressure at any point in a flow regime. "static" pressure is measured at the cavity walls perpendicular to the supersonic flow direction. It is assumed to be fairly constant throughout a given cross-section. The "dynamic" pressure is extracted from pressure measurements made with the pitot tube. The pitot tube measures the total pressure of the supersonic flow by sampling parallel with and into the

supersonic flow direction. The thrust or "dynamic" pressure attributed to the supersonic flow is the difference between the total and "static" pressures, measured at any point in the flow. A schematic diagram of the "static" and total pressure measurement approach is given in figure (1). The orifice of the pitot tube has a diameter is  $8.1 \times 10^{-5} \text{m}$  and all pressure measurements were made using MKS Baratron pressure transducers calibrated against an NIST standard.

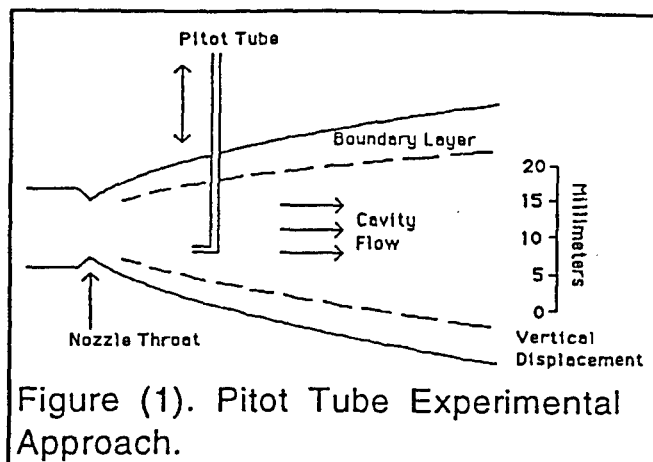


Figure (1). Pitot Tube Experimental Approach.

For the purposes of this experiment the boundary layer is defined in terms of the pitot tube measurements as that region of the vertical crosssection "dynamic" pressure profile where the difference between the "dynamic" pressure and the "static" pressures approaches zero.

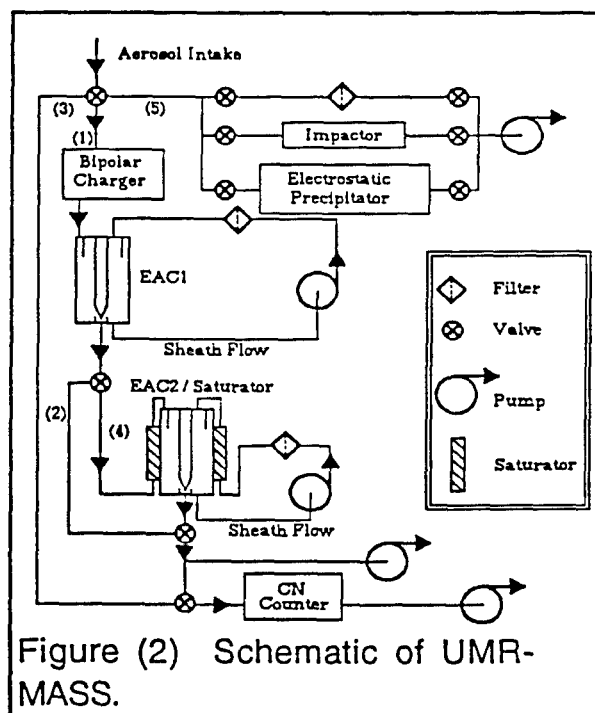


Figure (2) Schematic of UMR-MASS.

*Heterogeneous Nucleation Characterization Using the UMR/MASS:* The Mobile Aerosol Sampling System (UMR-MASS), figure (2) was employed to characterize aerosols in the gas flow of a COIL in terms of their total number density, size distribution and/or hydration properties. The MASS was operated in its rapid sample acquisition/storage mode, with off line sample analysis. This mode is employed under test conditions where it is not possible to characterize aerosol in real-time because the aerosol generation system (in this case the COIL) cannot be run continuously with fixed operating parameters for the time periods required to perform the characterization tests in

real time. Typical minimum continuous operation times of 3 minutes are required. The experimental sequence of events is as follows:

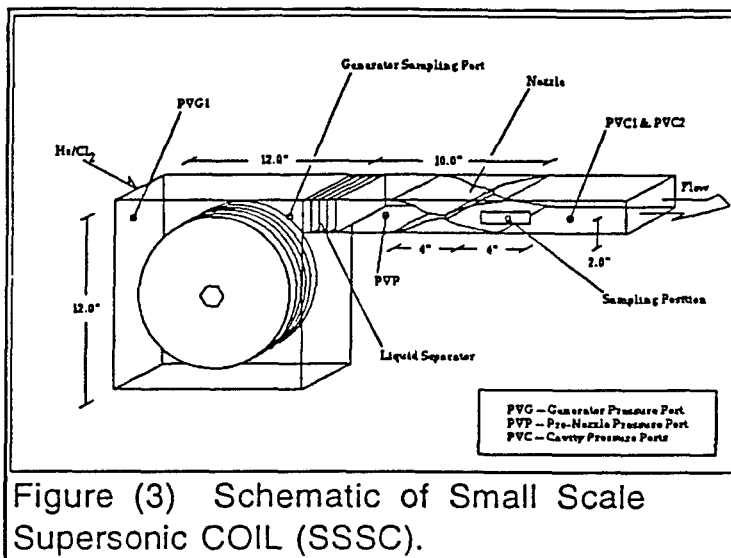
(a) Particulate Concentration Size Distributions - The particulate stream emanating from the sampling probe and dilution facility is sent through, initially, an alcohol counter to examine the total size range of aerosols sampled and determine the total concentration. For a size distribution the aerosol is charged with a bipolar charger and is then sized via its electric mobility using an electric aerosol classifier (EAC). The EAC passes only particles contained in a narrow size range (typically 10% of mean size). A specific particle size is set by the EAC voltage. This voltage and hence the selected particle size is variable. The resulting monodisperse particle stream is then passed through the alcohol counter where it is exposed to a fixed supersaturation of alcohol of sufficient magnitude to condense alcohol on the particle, thus forming aerosols large enough to be detected by the optical particle counter, OPC, sub system of the counter. The enlarged aerosols are passed through the OPC where individual aerosols are counted and the aerosol concentration is determined.

(b) Hydration Properties - For particulate hydration property measurements, specifically the critical supersaturation spectrum (i.e. the minimum supersaturation of water that will cause condensation of water onto a particle to produce a continuously growing droplet presented as a function of particle diameter) is measured. The particulate stream is first passed through an EAC to select a specific size element of the sample distribution. The resulting monodisperse element is then passed through a saturation chamber holding water vapor at 100% relative humidity. As the aerosols pass through the chamber they deliquesce and increase in diameter. This growth is monitored by passing the droplets, after they exit the saturator, through a second EAC, the output of which can be monitored by the alcohol counter. Should a particulate prove difficult to hydrate ( i.e. require significant supersaturation (>1%) of water a continuous flow diffusion chamber (CFD) is employed. (For a more detailed description of the overall UMR approach to particulate measurements, see references 11-14).[11-14]

## RESULTS

### Simulation of "Condensation Shock" in COILs operated under cold flow conditions.

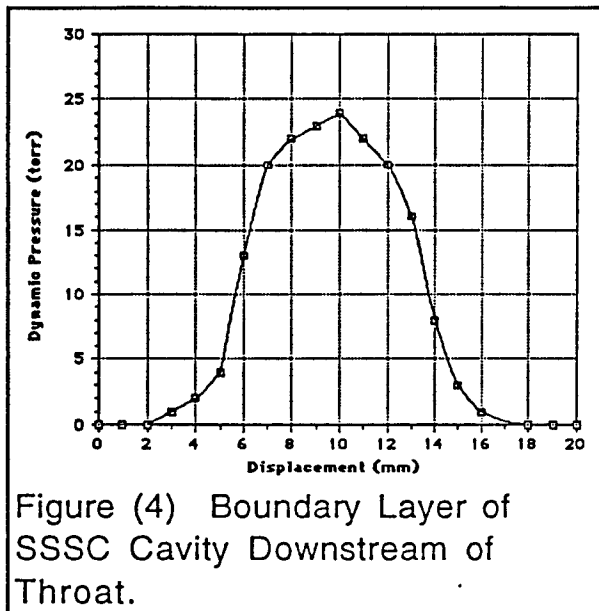
*The Small Scale Supersonic Device (Preliminary Results):* In the preliminary study, [3,4] of the condensation shock phenomenon an SSSC was used to attempt the simulation. A schematic diagram of this device indicating the various components, flow regimes and sampling ports is given in figure (3). During the 1992 experimental campaign this device was considered to be identical to the COIL device in which the pressure ramp had originally been detected[1] and similar results were expected from the SSSC. As reported initially [3,4] no pressure ramp could be detected. This was later explained by an over-simplification of the gas mixtures employed in those initial simulation studies where just nitrogen and water vapor were employed. The actual laser mixture



constituents are helium, oxygen and water vapor, with helium as the bath gas constituting the major part of the flow (75%)[10]. In retrospect, it was reasonable to substitute oxygen with nitrogen but not helium with nitrogen. The significant difference in their heat capacities forfeits such a substitution ( $C_{(\text{Nitrogen})} = 29.124 \text{ J/}[\text{mole}\cdot\text{K}]$  ,  $C_{(\text{Helium})} = 20.786 \text{ J/}[\text{mole}\cdot\text{K}]$ ).[15]

Further simulation experiments were performed after the submission date of the 1992 report [3] using helium, nitrogen, water vapor mixtures. They were successful in detecting pressure ramps in the cavity, however, the increases in pressure were small compared to the original experimental results. These data have subsequently been published elsewhere[16]. A typical maximum pressure increase was found to be on the order of 10-20% significantly smaller than the originally reported 40% [1]. The assumption that the devices could be considered identical was re-examined. There was some indication that the supersonic expansion nozzle configurations were different. If this were so it would be reasonable to assume that the boundary layers, created in the nozzle region during the supersonic expansion, in each of these devices could be different. Dissimilar boundary layers would explain the difference in the

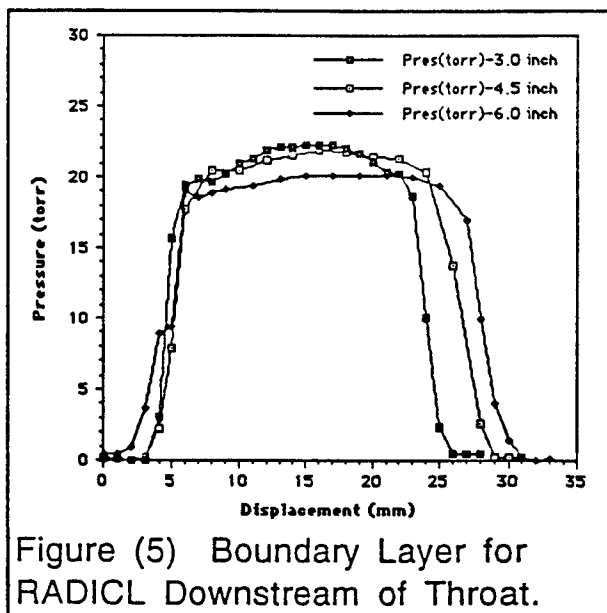
pressure ramps since these boundary layers define the supersonic flow cross-section and the effective gas volume into which any heat of condensation could be released. For example a thick boundary layer will reduce the effective supersonic flow volume which in turn will result in a diminished pressure ramp.



device. These data are presented in figure (4), where the flow parameters were, for the primary flow: He -  $110 \times 10^{-3}$  mole.s $^{-1}$ , N $_2$  -  $35 \times 10^{-3}$  mole.s $^{-1}$  and the secondary flow: He -  $60 \times 10^{-3}$  mole.s $^{-1}$  with the pitot tube port located 2.5 inches (0.06 meters) downstream of the nozzle throat. These data clearly reveal a massive boundary layer occupying as much as 50% of the cavity flow volume in the region of the vertical displacement of the pitot tube. The rounded appearance of the pressure profile indicates that the boundary layers converge. The profile was only measured at one position in the cavity however successive measurements demonstrated excellent reproducibility.

It was not possible to define the actual boundary layer conditions of the device in which the original shock observations were made.[1] However, another COIL device (RADICL) [9, 10], was available, although, much larger than the SSSC device that had been used to date. The boundary layer for this device was characterized using the pitot tube method

*Boundary Layer Definition:* Before proceeding further with the simulation experiments it was decided that the boundary layer issue should be resolved. The pitot tube pressure sensor, described above, was used to measure the "dynamic" pressure, as a function of the vertical displacement in the cavity close to the supersonic nozzle exit plane in the small scale



described above. The data from these experiments is given in figure (5). In the case of the RADICL measurements, profiles were obtained at four discrete locations along the flow axis in the cavity. Even though the geometry of the RADICL cavity differs slightly from that of the SSSC device, it is clear that the boundary layer in RADICL is much smaller. Also, in the region of high total pressure (typically 85% of the flow volume) the profiles are flat indicating the supersonic core is broad and uncompromised.

*Condensation Shock Simulation with RADICL:* The boundary layer results for RADICL indicated that a measurable shock would be more likely to be observed in RADICL than in the SSSC device, therefore, shock simulation studies were transferred to RADICL. Unlike the small scale device RADICL cannot be run by one or two individuals with a few minutes notice. Instead all experiments have to be scheduled in advance or have to be "piggybacked" on previously scheduled tests. Nevertheless, data were obtained. The shock indicator, as described previously, is a change in magnitude of the ratio of the "static" pressure in the supersonic cavity to that in the subsonic generator region ( $P_{cav} : P_{gen}$ ). In the absence of a condensation shock, a condition that can be achieved by

eliminating all water vapor from the flow, this ratio remains constant for a fixed set of run conditions. A typical plot of the constant pressure ratio profile as a function of time is given by the solid line in figure (6a). When water vapor is added to the flow, if the condensation shock model is correct, at an appropriate water vapor concentration, to be determined, the threshold supersaturation of water vapor in the cavity will exceed that required for homogeneous nucleation. Nucleation occurs instantaneously under these conditions and is accompanied by a rapid release of heat (heat of condensation), this is the so called shock. This heat is released into the supersonic gas flow and manifests itself as a localized pressure increase in the cavity.

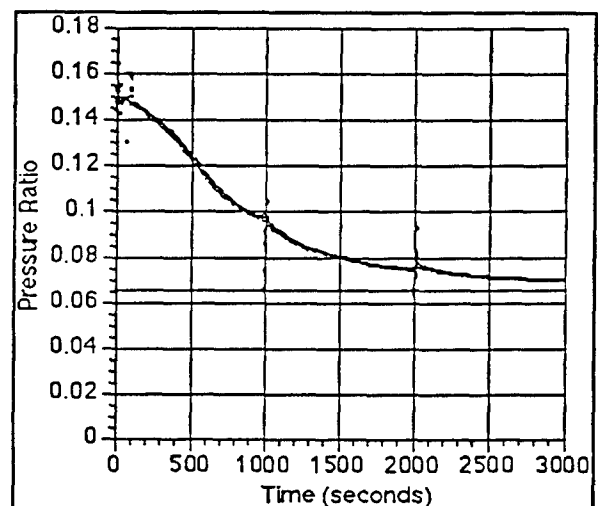


Figure (6a) RADICL Pressure Ratio Profile with Respect to Time.

A thermally controlled 30% aqueous solution of potassium hydroxide, initially cooled to 243K, was used as a variable water vapor concentration source. The cold solution was placed in



the RADICL generator, a helium nitrogen (3:1) mixture was passed at subsonic speeds through the generator and duct, where it entrained water vapor, the concentration of which was controlled by the bulk solution temperature. In the absence of any active cooling of the KOH solution, the solution temperature steadily increased with time as it sought to come to thermal equilibrium with its surroundings. During this period the KOH solution temperature, and the pressure ratio of the cavity to the duct were monitored. The pressure ratio profile is plotted in figure (6a) and the temperature profile is plotted in figure (6b).

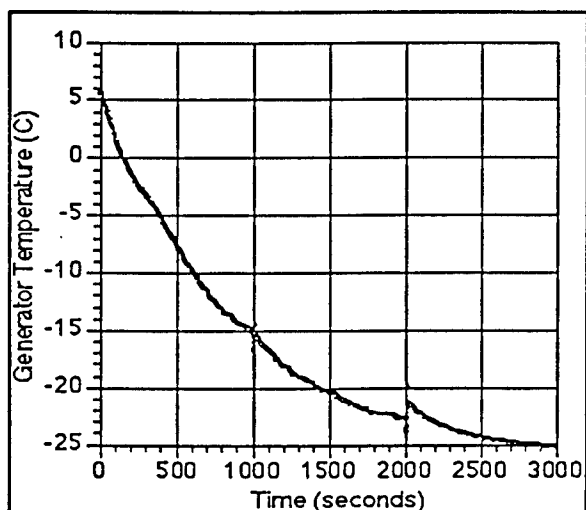


Figure (6b) RADICL Generator Temperature Profile with Respect to Time.

#### Characterization of Heterogeneous Nucleation:

Based on the findings of the preliminary study of heterogeneous nucleation [3, 4] the measurements in the current study were confined to samples taken in the subsonic, post-generator, pre-cavity regions of the SSSC device (see figure (3)). Since it was clear from the preliminary study, that the particulate production rate was not coupled to either, the bulk temperature in the generator, or the presence of iodine in the flow these parameters were not re-investigated in the current study. As previously reported the largest particulate production rates occurred in

the immediate vicinity of the rotating disc generator during the passage of chlorine gas over the BHP wetted disc walls. In the current study, therefore, the parameters: disc rotation rate, BHP concentration as a function of the age of BHP mixture, neutralization salt concentration, also as a function of the age of the BHP mixture and chlorine flow rate were examined for any correlation to particulate production rate.

**Disc Rotation Rate:** Disk rotation rates were varied within the range 0-45 rpm (where 45rpm is considered the optimum disc rotation rate for singlet oxygen production). The discs were rotated in a BHP solution but in the absence of a chlorine flow. The particle number densities increased with increasing rotation rate, however, at 45rpm the maximum particle number densities recorded did not exceed  $5 \text{ cm}^{-3}$

**BHP Concentration:** During the course of a days testing on a single batch of BHP, periodic samples of BHP were drawn from the generator and titrated for the hydroperoxide anion [17]. These titrations repeatedly showed the concentration of the hydroperoxide ion to be relatively constant during the lifetime of the mixture during which time the BHP was being exhausted. For example a typical batch had a 9.5M hydroperoxide ion concentration, initially, and a 9.1M concentration at the end of the test, with a 9.3M mid-test value.

**Neutralization Salt Concentration:** As a batch of BHP solution is exhausted, during the course of a days testing, large concentrations of potassium chloride (KCl) build up in solution and eventually start to precipitate as the BHP solution approaches saturation with respect to KCl (~2% mass solubility in BHP). Observations of the particulate number densities present in the generator measured, between chlorine flow periods, but with a disc rotation rate of 45rpm in an aging BHP mixture demonstrated a reproducible increase in particulate number density with KCl build-up. For example a fresh BHP solution would yield typically  $5 \text{ cm}^{-3}$  at 45rpm and after 5 chlorine runs this number would increase to  $60 \text{ cm}^{-3}$ .

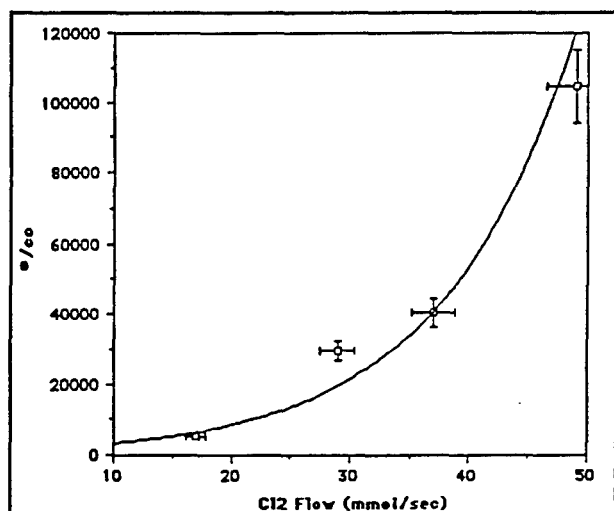


Figure (7) Particulate Concentration as a Function of Chlorine Flow Rate.

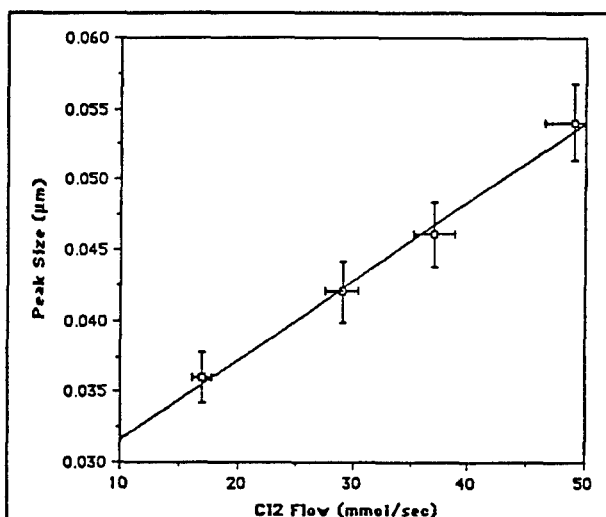


Figure (8) Peak Particle Diameter as a Function of Chlorine Flow Rate.

**Chlorine Flow rate:** At a typical chlorine flowrate of  $37 \times 10^{-3} \text{ moles.s}^{-1}$  and a total generator pressure of 56 torr the mean particulate concentration is  $1.45 \times 10^4 \text{ cm}^{-3}$ . This is three orders of magnitude greater than the concentrations generated by any other process. The total concentration of particles is determined either by integrating the size distribution function

over a specific size range or by monitoring the total concentration of particulates with a CNC counter. Both methods were employed in this study and good agreement was obtained between them. Figure (7) is a plot of the total concentration as a function of chlorine flow rate. The particulate yield correlates exponentially with the chlorine flowrate over the flow range studied (i.e. 0 - 50 x 10<sup>-3</sup> moles.s<sup>-1</sup>, yielding a maximum particulate concentration in excess of 1 x 10<sup>6</sup> cm<sup>-3</sup>. These data are a clear indication that chlorine flow rate is the primary generator operating parameter controlling particulate production. The peak size of the particulates demonstrates a linear correlation with the chlorine flow rate, indicating a shift in the size distributions to larger mean particulates at higher chlorine flows. Typical data are presented in figure (8).

## DISCUSSION

### Condensation Shock Simulation

These data represent the first detailed investigation of the potential for, and characteristics of "condensation shock" in COIL devices. The simulation experiments described here, when combined with the findings of the heterogeneous nucleation studies, also described here, lead to the following inferences.

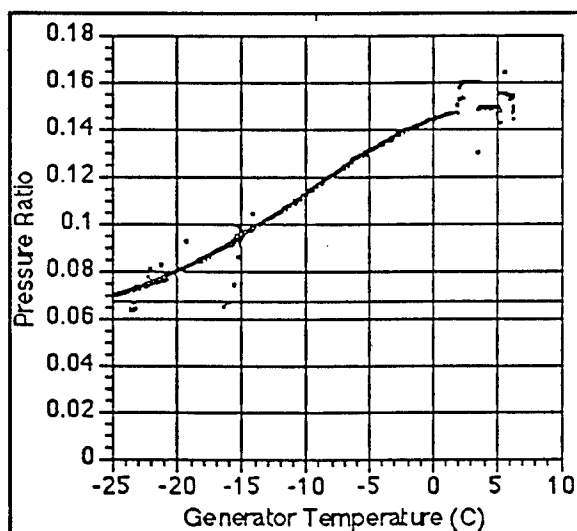


Figure (9) RADICL Pressure Ratio as a Function of Generator Temperature.

A gas dynamic condensation shock can be induced in COIL devices in the absence of any condensation nuclei. Figure (9) is a plot of pressure ratio versus temperature for RADICL derived from the data in figures (6a) and (6b). The dry system pressure ratio line is included for comparison. The P(ratio) versus T plot can be seen to diverge from the "dry line" as T increases. The rate of divergence increases from 253K to 268K. It, then, slows and approaches zero at T = 278K. This divergence is direct evidence of the onset of condensation shock and can be entirely attributed to the heat released during the "shock". Calculations using the 3-D MINT code by Plummer

and coworkers at RDA-Logicon [18] successfully model these results and explain the asymptotic behavior as the onset of choked flow in the cavity due to the heat of condensation released into the flow during the shock.

The concentrations of aerosols emanating from the generator, ( $\sim 10^6 \text{ cm}^{-3}$ ), are not large enough to contribute significantly to the total heat released into the flow through condensation. It is reasonable to assume, however, that heterogeneous and homogeneous condensations are taking place simultaneously in COILS. Furthermore, in the case of RADICL, evidence of the shock (in the P ratio vs T plot) at very low temperatures (i.e. low partial pressures of water) is clearly observed. It is not possible to determine the total water concentration with the current experimental configuration. An upper limit for this concentration could be taken as the equilibrium vapor pressure of water above the KOH solution. A sensitive absolute water vapor concentration diagnostic is being constructed currently. It will be used to profile the massive change in the water vapor concentration in the laser cavity at the onset of the shock. The latter will be monitored by the pressure versus temperature profile as in figure (9). Such data will unequivocally validate the theory of condensation shock as it affects COIL devices. These experiments are planned for this fall when the state of the art water vapor diagnostic is to be delivered. It is hoped that these results will then be incorporated into the AIAA paper planned for publication of this work and the SREP contract report due in December 1993.

#### Heterogeneous Nucleation

The results of this study and the preceding preliminary study clearly demonstrate that heterogenous nucleation is not necessary to create a condensation shock in COIL devices. They further demonstrate, that the maximum concentration of particulates generated under typical COIL operating conditions, although large, is orders of magnitude too small to account for the heat release detected via the pressure ratio divergence data as seen in figure (9). These nucleation data, however, are important. A production mechanism was suggested in the preliminary study: " These results indicate that heterogeneously nucleated aerosols are mechanically generated during the explosion of gas bubbles on the basic hydrogen peroxide (BHP)/chlorine interface and that certain generator operating parameters such as disc velocity and degree of neutralization of the BHP can strongly influence the aerosol production rate." [3,4]. The data from the current study support this mechanism but take our understanding of the process further. The particulate production rate and size distributions depend primarily on the chlorine flow rate. The data acquired to date indicates the dependence to be exponential for total concentration and linear with respect to the shift in the peak size of the size distribution. The sampling techniques and dilutions employed in this study eliminate the potential for agglomeration of particulates, that might skew the data in such a manner [19].

## CONCLUSIONS

The following conclusions can be drawn from this study:

- Condensation shock occurs in COIL devices even at extremely low water vapor concentrations.
- The onset of the shock will directly impact the gain of the device in which it occurs.
- Heterogeneous nucleation is controlled primarily by the chlorine flow rate into the generator.
- Nuclei production rates grow exponentially with increasing chlorine flow rate.
- Nuclei diameters increase with increasing chlorine flow rate (0.033-0.055  $\mu\text{m}$  for the chlorine flow range investigated in this work).
- The onset of foaming in the generator is indicative of massive sub-micron nuclei production rates.
- The next generation of COILs may employ spray generators. These generators should be examined to define their characteristics with respect to condensation shock and heterogeneous nucleation if their performance is to be accurately compared to current wetted-wall type generators as are found in the SSSC and RADICL.

## REFERENCES

- ( 1 ) Private Communication, D. Plummer RDA, 19 July 1991.
- ( 2 ) RDA Memo 87-A/K-3-02-752 Particulates/Aerosols in Oxygen/Iodine Lasers, P.G. Crowell, January 1989.
- ( 3 ) Whitefield, P.D., AFOSR-SFRP Final Report September 1992.
- ( 4 ) Whitefield, P.D., AFOSR-SREP Final Report December 1992.
- ( 5 ) Fundamentals of Gas Dynamics, Editor H.W. Emmons, Princeton University Press, 1958.
- ( 6 ) Hagen, D.E., M.B. Trueblood, and J. Podzimek, "Combustion Aerosol Scavenging", Atmos. Env. 25A, 2581 (1991).
- ( 7 ) Hagen, D.E., Whitefield P.D., and M.B. Trueblood, "A field Sampling of Jet Exhaust Aerosols." Particulate Science and Technology, 10, 53, 1992.
- ( 8 ) Whitefield, P.D., M.B. Trueblood and D.E. Hagen, "Size and Hydration Characteristics of Laboratory Simulated Jet Engine Combustion Aerosols," Particulate Science and Technology, 11, 25, 1993.
- ( 9 ) Review of Modern Physics vol. 59, No.3 paper II, July 1987 pp 541-546
- ( 10 ) Oxygen Iodine Supersonic Technology Program, Part III - Management and Technical

Proposal, MDRL/MDAC Report No. D9299-953003, June 1982.

- (11) Alofs, D.J., "Performance of a dual-range cloud nucleus counter", J. Appl. Meteor. 17, 1286-1297 (1978).
- (12) Alofs, D.J., M.B. Trueblood, D.R. White, and V.L. Behr, "Nucleation experiments with monodisperse NaCl aerosols", J. Appl. Meteor. 18, 1106-1117 (1979).
- (13) Hagen, D.E., and D.J. Alofs, "A Linear Inversion Method to Obtain Aerosol Size Distributions from Measurements with a Differential Mobility Analyzer", Aerosol Sci. and Tech. 2, 465-475 (1983).
- (14) Alofs, D.J. and M.B. Trueblood, "UMR Dual Mode CCN Counter (Modes:CFD plus Haze)," J. Rech. Atmos. 15, n° 3-4, 219-223 (1981)
- (15) CRC Handbook of Physics and Chemistry 73rd Edition, 1992.
- (16) Whitefield, P.D., D.E. Hagen, M.B. Trueblood, W.M. Barnett and C. Helms, SPIE vol 1871 Intense Laser Beams and Applications (1993) pp 277-288.
- (17) Richardson, R.J., Wiswall, C.E., Carr, P.A.G., Hovis, F.E., and Lilenfeld, H.V., "An Efficient Singlet Oxygen Generator For Chemically Pumped Iodine Lasers", J. Appl. Phys. 52, 4962-4969, (1981).
- (18) RADICL Data presented at a briefing on the condensation shock phenomena by D. Plummer RDA, August 1992.
- (19) Whitefield, P.D., D. E. Hagen and H.V. Lilenfeld Geophysica Acta (submitted September 1993)